LABORATORY STUDIES OF PYRRHOTITE OXIDATION

MEND Project 1.21.2

This work was done on behalf of MEND and sponsored by
INCO Limited,
Noranda Inc.,
the Ontario Ministry of Northern Development and Mines and
the Canada Centre for Mineral and Energy Technology (CANMET)
through the CANADA/Northern Ontario Development Agreement (NODA)

March 1998

LABORATORY STUDIES
OF PYRRHOTITE OXIDATION

Final Report
To

CANMET - Contract No. 23440-4-1198/01
Inco Limited
Centre Technologie Noranda

Principal Investigators

R.V. Nicholson, Department of Earth Sciences

J.M. Scharer, Department of Chemical Engineering

Research Assistants

E.C.M. Kwong, Department of Chemical Engineering

M.P. Janzen, Department of Earth Sciences

University of Waterloo

Waterloo, ON N2L 3G1

March, 1998

EXECUTIVE SUMMARY

Pyrite and pyrrhotite are the most abundant sulphides in mine wastes worldwide. While there is a large body of information related to the weathering of pyrite and the effects of this process on water quality, there is a significant deficiency of information on the weathering reactions and the controls on pyrrhotite reaction rates. Unlike pyrite, pyrrhotite represents a range of chemical composition as indicated by the formula $Fe_{1-x}S$ in which x can vary from 0 to 0.125. This also implies that there is an inherent deficiency of iron in the crystal structure, possibly representing less structural stability than that of pyrite. Several crystallographic forms of pyrrhotite are known.

The objectives of this investigation were:

1) to assess the kinetic controls on pyrrhotite oxidation;
2) investigate the effects of crystal structure, metal impurities, surface area, and bacterial catalysis on oxidation reaction rates;
3) assess the dynamics and effects on water quality of pyrrhotite oxidation in tailings column studies; and
4) develop a modelling approach consistent with the mechanisms and controls on pyrrhotite oxidation reactions.

This study was conducted in three distinct phases. The first phase involved twelve distinct pyrrhotite samples for a detailed study of fundamental chemical kinetics of oxidation by oxygen and ferric iron. The second phase comprised characterization and kinetic studies on actual pyrrhotite concentrate obtained from the Inco Clarabell Mill (Sudbury). The pyrrhotite concentrate material was studied to assess the oxidation kinetics for different conditions of temperature, pH and bacterial catalysis. The third phase of the investigation involved testing of pyrrhotite tailings material in columns designed to assess the effects of sulphur content (2 % to 6 % S^{2-}), bacterial inoculation (*Thiobacillus ferrooxidans*), the presence of calcite (1 % $CaCO_3$) and enstalite (5 % $MgSiO_3$) as neutralizing solids, and the presence of fine-grained pyrrhotite material (< 45 μm) in the tailings.

The specific surface areas (area/mass) of selected particle size-fractions varied significantly among

pyrrhotite specimens and exhibited values that were a factor of 2 to 10 times greater than those of similar size pyrite particles and 6 to 40 times greater than calculated theoretical surface areas assuming spherical smooth geometry. The rates of abiotic oxidation by oxygen as exhibited by iron production were, on average, ten times greater than rates for pyrite oxidation under similar conditions. Oxidation rates by ferric iron, however, were about one-fourth of those for pyrite oxidation under similar conditions. The effect of temperature was similar to that observed for pyrite oxidation with activation energy values in the range of 50 to 60 kJ mol^{-1}. Crystallographic structure and trace metal content showed no consistently significant effects.

The effect of bacterial inoculation differed with pH and temperature. The maximum biologic rate of sulphate production was observed at pH = 4 with rates that were approximately 10 times those in non-biologic tests. Non-biologic rates and biologic rates approached similar values at pH values of 2 and 6. The column studies confirmed the effects of bacterial activity on oxidation rates with similar behaviour in a column that had been inoculated and one that had not been inoculated. Oxidation rates and loading rates for sulphate, iron and nickel were similar in both columns containing 6 % S^{2-}. Only slightly lower loading rates for sulphate and iron were observed in the column containing 2 % S^{2-} but nickel release rates were higher than those in the 6 % S^{2-} column. The oxygen consumption rates reflected the loading rates of pyrrhotite oxidation products. In general, the oxygen consumption rates were a factor of 3 to 10 higher than the stoichiometrically equivalent sulphate production rates initially but oxygen consumption and sulphate release rates converged with time. The average molar ratio of Fe : SO_4 was about 0.9 to 0.96 suggesting that, on average, pyrrhotite oxidation produced Fe^{2+} and SO_4^{2-} stoichiometrically.

The presence of calcite in the 6 % S^{2-} tailings resulted in similar oxygen consumption and sulphate release rates to those observed for the non-carbonate tailings. However, the calcite maintained a near neutral pH condition in the pore water with the result that Fe and Ni release rates were significantly lower. The presence of enstatite, representing a silicate buffer, resulted in porewater with pH = 4 to 5 and some additional ferric hydroxide precipitation with subsequent decreases in nickel release rates compared to the control. The difference between the carbonate and silicate buffered tailings was the pH of the porewater with the carbonate column maintaining near neutral pH and causing almost complete precipitation of the iron.

The results indicate that characteristics of pyrrhotite such as metal impurities and crystallographic form do not affect oxidation rates significantly. The surface area of the pyrrhotite particles is by far, the most significant parameter required to assess oxidation rates for pyrrhotite in tailings. The results of the column tests indicate that oxygen transport is the most important phenomenon and small uncertainties in reaction kinetics will not significantly affect long-term predictions for tailings oxidation when both kinetics and oxygen mass transport are considered in geochemical modeling.

SOMMAIRE

La pyrite et la pyrrhotine sont les sulfures les plus abondants dans les déchets miniers du monde entier. Bien qu'il existe un important corpus d'information relative à l`altération de la pyrite et aux effets de ce phénomène sur la qualité de l'eau, on connaît mal les réactions intervenant dans l`altération et les facteurs qui contrôlent le taux de réaction de la pyrrhotine. Contrairement à la composition chimique de la pyrite, celle de la pyrrhotine varie beaucoup comme l'indique la formule $Fe_{1-x}S$ où x peut varier de 0 à 0,125. Ceci indique aussi une carence inhérente en fer dans la structure cristalline, correspondant peut-être à une moins grande stabilité structurale que dans le cas de la pyrite. La pyrrhotine se présente sous plusieurs formes cristallographiques connues.

Les objectifs de ces travaux étaient les suivants:

1) évaluer les facteurs cinétiques qui influencent l'oxydation de la pyrrhotine;
2) étudier les effets de la structure cristalline, des impuretés de métal, de la surface et de la catalyse bactérienne sur le taux d'oxydation;
3) évaluer la dynamique et les effets sur la qualité de l'eau de l'oxydation de la pyrrhotine dans des études portant sur des colonnes de résidus;
4) élaborer une approche de modélisation qui concorde avec les mécanismes et les facteurs de contrôle s'exerçant sur les réactions d'oxydation de la pyrrhotine.

Cette étude a été réalisée en trois phases distinctes. La première phase consistait à étudier de manière détaillée douze échantillons de pyrrhotine la cinétique chimique fondamentale de l'oxydation par l'oxygène et l'ion ferrique. La deuxième phase consistait à caractériser le concentré de pyrrhotine obtenu de Clarabell Mill (Inco-Sudbury) et à en étudier la cinétique. On a étudié le concentré de pyrrhotine pour évaluer la cinétique de l'oxydation dans différentes conditions de température, de pH et de catalyse bactérienne. La troisième phase de l'étude consistait à tester des résidus de pyrrhotine dans des colonnes conçues pour évaluer les effets de la teneur en soufre (2 % à 6 % S^{2-}), de l'inoculation bactérienne (*Thiobacillus ferrooxidans*), de la présence de calcite (1 % $CaCO_3$) et d'enstalite (5 % $MgSiO_3$) comme solides neutralisants,

ainsi que de la présence de pyrrhotine à fine granulométrie (< 45 μm) dans les résidus.

La surface spécifique (aire/masse) de certaines fractions granulométriques variait beaucoup d'un échantillon de pyrrhotine à l'autre et elle pouvait être 2 à 10 fois plus élevée que celles des particules de pyrite de taille analogue et 6 à 40 fois supérieures aux surfaces théoriques calculées en supposant une géométrie sphérique lisse. Le taux d'oxydation abiotique par l'oxygène indiqué par la production de fer était en moyenne dix fois plus élevé que le taux d'oxydation de la pyrite dans des conditions analogues. Le taux d'oxydation par l'ion ferrique était toutefois le quart environ du taux d'oxydation de la pyrite dans des conditions analogues. L'effet de la température était analogue à celui qu'on observait pour l'oxydation de la pyrite avec des énergies d'oxydation variant de 50 à 60 kJ mol^{-1}. La structure cristallographique et la teneur en métaux à l'état de traces n'avait pas d'effet important de manière soutenue.

L'effet de l'inoculation bactérienne variait en fonction du pH et de la température. Le taux maximal de production biologique de sulfate a été observé à pH = 4; les taux mesurés étaient à peu près 10 fois plus élevés que ceux qui avaient été observés dans le cadre d'essais non biologiques. À pH 2 et 6, les taux non biologiques et les taux biologiques étaient à peu près analogues. Les essais en colonne ont confirmé les effets de l'activité bactérienne sur le taux d'oxydation : on a constaté un comportement analogue dans une colonne inoculée et dans une colonne non inoculée. Le taux d'oxydation et d'apport dans le cas du sulfate, du fer et du nickel étaient analogues dans les deux colonnes renfermant 6 % S^{2-}. Les taux d'apport dans le cas du sulfate et du fer n'étaient que légèrement inférieurs dans la colonne renfermant 2 % S^{2-}, mais le taux de libération du nickel était supérieur par rapport à la colonne renfermant 6 % S^{2-}. Le taux de consommation de l'oxygène suivait le taux d'apport des produits d'oxydation de la pyrrhotine. En général, le taux de consommation de l'oxygène était initialement 3 à 10 fois plus élevé que le taux de production de sulfate, équivalent au point de vue stoechiométrique, mais avec le temps, le taux de consommation d'oxygène et le taux de libération de sulfate convergeaient. Le rapport molaire moyen de Fe : SO_4 était d'environ 0,9 à 0,96, ce indique qu'en moyenne, l'oxydation de la pyrrhotine produisait du Fe^{2+} et du SO_4^{2-} de manière stoechiométrique.

La présence de calcite dans les résidus renfermant 6 % S^{2-} donnait lieu à des taux de

consommation d'oxygène et de libération de sulfate analogues à ceux qui étaient mesurés dans le cas des résidus ne contenant pas de carbonates. Toutefois, la calcite assurait le maintien d'un pH presque neutre dans l'eau interstitielle, ce qui donnait des taux de libération du Fe et du Ni beaucoup plus faibles. La présence d'enstatite, un tampon de silicate, donnait à l'eau interstitielle un pH de 4 à 5 et faisait précipiter un peu plus d'hydroxyde ferrique, ce qui faisait diminuer le taux de libération du nickel par rapport au témoin. La différence entre les résidus tamponnés avec du carbonate et du silicate était liée au pH de l'eau interstitielle, la colonne de carbonate maintenant un pH à peu près neutre et provoquant la précipitation presque complète du fer.

Les résultats indiquent que des caractéristiques de la pyrrhotine comme la présence d'impuretés métalliques et la forme cristallographique n'influent pas beaucoup sur le taux d'oxydation. La surface des particules de pyrrhotine est de loin le paramètre le plus important permettant d'évaluer le taux d'oxydation de la pyrrhotine dans les résidus. Les résultats des essais effectués en colonne indiquent que le transport de l'oxygène est le phénomène le plus important et que de petites incertitudes relatives à la cinétique de la réaction n'influent pas beaucoup sur la prévision à long terme de l'oxydation des résidus lorsqu'on tient compte à la fois de la cinétique et du transport de masse de l'oxygène dans la modélisation géochimique.

TABLE OF CONTENTS

Pages

EXECUTIVE SUMMARY II

SOMMAIRE V

TABLE OF CONTENTS VIII

LIST OF TABLES X

LIST OF FIGURES XI

INTRODUCTION 1

1 LITERATURE REVIEW 5

1.1 Physio-chemical Properties of Pyrrhotite 5
1.1.1. Chemical Compositions 5
1.1.2. Mineralogical Compositions 7

1.2 Dissolution Pathway of Sulphide Minerals 9
1.2.1 Oxidant-free (Non-Oxidative) Dissolution 11
1.2.2 Chemical (Abiotic) Oxidation 12
1.2.3 Anoxic Oxidation by Ferric Iron 15
1.2.4 Biological Oxidation 16

1.3 Transport Processes and Geochemistry in Mine Tailings 22
1.3.1 Gaseous Transport - Fick's Law Diffusion 23
1.3.2 Neutralizing Reactions and Formation / Dissolution of Secondary Minerals 24
1.3.3 Weathering of Rock-Forming Minerals 25

2 MATERIALS AND METHODS 27

2.1 Material Characterization 27
2.1.1 Particle Size Distribution 28
2.1.2 Chemical Composition 28
2.1.3 Mineralogical Composition 28
2.1.4 Microprobe Analysis 29
2.1.5 Specific Surface Area 30

2.2 Determination of Intrinsic Kinetics 30
2.2.1 Reactor Configurations 31

2.3 Bacterial Inoculum 36

2.4 Coupling of Mass Transfer with Oxidation Kinetics 38
2.4.1 Column Configurations 38

2.5 Analytical Techniques 44
2.5.1 Ferrous Iron (Fe^{2+}) Analysis - Bathophenanthroline Method 44
2.5.2 Total Iron Analysis 44
2.5.3 Nickel (Ni^{2+}) Analysis - Atomic Absorption 45
2.5.4 Sulphate (SO_4^{2-}) Analysis - Ion Chromatography 45
2.5.5 Surface Texture - Scanning Electron Microscopy (SEM) 46

3 RESULTS AND DISCUSSION 47

3.1 Physical and Chemical Characteristics of Pyrrhotite Samples 47
3.1.1 Specimen-Grade Pyrrhotite Samples 47
3.1.2 Inco Copper Cliff Pyrrhotite Tailings Concentrate 60

3.2 Fundamental Kinetics 62
3.2.1 Comparison of Kinetic Rates among Specimen Grade Samples 62
3.2.2 Kinetics of Pyrrhotite Oxidation in Tailings Concentrate 76

3.3 Column Studies on Pyrrhotite Tailings 88
3.3.1 Effect of Sulphur Content 94
3.3.2 Effect of Bacterial Inoculation 98
3.3.3 Effect of Neutralizing Minerals 101
3.3.4 Effect of Fine Particles 104

4 CONCLUSIONS 108

5 REFERENCES 111

Appendix A – Material Characterization of Pyrrhotite Samples

Appendix B – Non-Oxidative Dissolution of Specimen Grade Pyrrhotite Samples

Appendix C – Ferric Iron Oxidation of Specimen Grade Pyrrhotite Samples

Appendix D – Kinetic Oxidation of Inco's Copper Cliff Pyrrhotite Concentrate

Appendix E – Column Studies of Inco's Copper Cliff Pyrrhotite Concentrate

LIST OF TABLES

Pages

Table 2.1: Common ionic molecular forms of aqueous sulphur species. 6

Table 2.2: Thermodynamic data for iron-sulphur minerals (Woods and Garrels, 1987). 11

Table 2.3: Acidophilic bacteria in metal ore leaching environments (adopted from Olson and Kelly, 1986). 17

Table 2.4: Solubility products of secondary minerals in mine tailings (Stumm, 1992; Brownlow, 1996) 25

Table 2.5: Silicate and phosphate minerals that provide buffering capacities at 25°C (Lowson and Brown, 1996). 26

Table 3.1: Descriptions, suppliers, and localities of the twelve pyrrhotite samples. 27

Table 3.2: Theoretical chemical compositions of sulphide mineral in Sudbury, ON. 29

Table 3.3: Chemical composition of aqueous growth media for *Thiobacillus ferrooxidans* 36

Table 3.4: Conditions used in packed columns. 39

Table 4.1: Specific surface area of two pyrrhotite samples after 15 months of oxidation. 50

Table 4.2: Trace metal contents of pyrrhotite samples. 55

Table 4.3: Accessory minerals present in the pyrrhotite samples. 57

Table 4.4: Hexagonal, monoclinic and orthorhombic crystal forms in the pyrrhotite samples. 59

Table 4-5: Chemical composition of Inco Copper Cliff pyrrhotite concentrate. 61

Table 4.6: Non-oxidative dissolution rates of the pyrrhotite samples. 63

Table 4.7: Rates of oxidation of the pyrrhotite samples by oxygen. 65

Table 4.8: Oxidation of the pyrrhotite samples by ferric iron. 67

Table 4.9: The rate order dependence of pyrrhotite oxidation on Fe^{3+} at pH=2.0. 70

Table 4.10: Activation energies for pyrrhotite oxidation by oxygen. 74

Table 4.11: Activation energies for pyrrhotite oxidation by ferric iron. 74

Table 4.12: Activation energies for abiotic pyrrhotite oxidation (based on sulphate release). 84

Table 4.13: Conditions used in packed columns. 88

LIST OF FIGURES

Figure 1.1: General concepts adopted for modelling of mine wastes. 3

Figure 2.1: Suggested scheme for sulphur oxidation in oxidative environments (adopted from Kuenen, 1993). 6

Figure 2.2: The NaCl-type and NiAs-type crystal structures: (a) NaCl structure showing the coordination of ions and the linking of octahedral units; (b) linkage of ions in a unit cell of NiAs structure and stacking of octahedral units (adopted from Vaughan and Craig, 1978). 8

Figure 2.3: Projection of Fe and S atoms on the basal plane (c-axis) in the troilite super-structure (adopted from Vaughan and Craig, 1978). 8

Figure 2.4: Direct biological leaching without diffusion limitation (adopted from Boon and Heijnen, 1993). 17

Figure 2.5: Indirect biological leaching by ferric iron without diffusion limitation (adopted from Boon and Heijnen, 1993). 18

Figure 2.6: Indirect biological leaching by ferric iron and biological oxidation of sulphide without diffusion limitation (adopted from Boon and Heijnen, 1993). 18

Figure 2.7: Indirect biological leaching with diffusion limitation (adopted from Boon and Heijnen, 1993). 19

Figure 3.1: Internal spilt-flow airlift reactor 32

Figure 3.2: Stirred tank reactor 34

Figure 3.3: Flow chart for the program IRON SOLVER 35

Figure 3.4: Column layout 37

Figure 3.5: Headspace oxygen consumption cap with galvanic oxygen sensor 41

Figure 3.6 Lysimeter for porewater extraction 42

Figure 3.7 Oxygen profile sampling port with galvanic oxygen sensor 43

Figure 4.1: Adsorption isotherm for N_2 gas, at 77.4°K, on pyrrhotite 48

Figure 4.2: Specific surface area comparisons among the twelve pyrrhotite samples, a pyrite sample from Colorado, and the theoretical geometrical specific surface area based on particle size plotted on a log - log axis. 48

Figure 4.3: The effects of grinding techniques on pyrrhotite specific surface area. 49

Figure 4.9: XRD standardization - Correlation between peak area and hexagonal composition. 53

Figure 4.10: Impurity concentrations of the pyrrhotite samples. 54

Figure 4.11: A comparison between measured microprobe atomic Fe %

and predicted atomic Fe %. 56
Figure 4.12: XRD intensity spectra for: (a) pure hexagonal pyrrhotite, (b) pure monoclinic pyrrhotite, (c) mixed hexagonal and monoclinic pyrrhotite, and (d) mixed hexagonal, monoclinic and troilite containing pyrrhotite 58
Figure 4.13: Particle size distributions of pyrrhotite concentrate and quartz sand. 61
Figure 4.14: Non-oxidative dissolution at pH=2.75, 25°C for Po-M-7-94 measured in closed stirred tank reactors. 63
Figure 4.15: Oxidation of pyrrhotite by oxygen at pH=2.75, 25°C for Po-M-15-93 measured in internal split-flow airlift reactors. 65
Figure 4.16: Oxidation by Fe^{+3} of Po-C-5-94 at pH=2.50, 25°C, $Fe^{+3}_{int}=1\times10^{-3}$ [M] measured in closed stirred tank reactors. 68
Figure 4.17: Oxidation by Fe^{+3} of Po-C-5-94 at pH=2.00, 25°C, $Fe^{+3}_{int}=1\times10^{-2}$ [M] measured in closed stirred tank reactors. 68
Figure 4.18: The dependence of pyrrhotite oxidation on Fe^{+3} ($Fe^{+3}_{int}=2\times10^{-4}$ [M], 25°C, pH=2.75, Po-C-5-94). 69
Figure 4.19: The dependence of pyrrhotite oxidation on Fe^{3+} ($Fe^{3+}_{int}=1\times10^{-2}$ [M], 25°C, pH=1.99, Po-C-5-94). 70
Figure 4.20: The linearized adsorption model (Po-M-2-94). 71
Figure 4.21: The use of ferrous iron production to predict pyrrhotite oxidation completeness. 73
Figure 4.22: The influence of crystal structure on pyrrhotite oxidation rate by oxygen (pH=2.75, 25°C). 76
Figure 4.23: The influence of total trace metal content on pyrrhotite oxidation by oxygen (pH=2.75, 25°C). 76
Figure 4.24: Sulphate release under abiotic pyrrhotite oxidation at 30 °C and various pH values. 77
Figure 4.25: Iron release under abiotic pyrrhotite oxidation at 30 °C and various pH values. 78
Figure 4.26: The sulphate production rate for abiotic pyrrhotite oxidation by oxygen. 79
Figure 4.27: The iron production rate for abiotic pyrrhotite oxidation by oxygen. 80
Figure 4.28: The nickel production rate for abiotic pyrrhotite oxidation by oxygen. 81
Figure 4.29: Effect of pH on abiotic pyrrhotite oxidation rates (based on sulphate release) at various temperatures. 83

Figure 4.30: Effect of pH on abiotic pyrrhotite oxidation rates (based on iron release) at various temperatures. 83
Figure 4.31: Arrhenius plots of abiotic pyrrhotite oxidation rates (based on sulphate) with temperature at various pH values. 84
Figure 4.32: Effect of chelating agent (EDTA) on abiotic pyrrhotite oxidation rate (based on iron release). 86
Figure 4.33: Effect of chelating agent (EDTA) on abiotic pyrrhotite oxidation rate (based on nickel release). 86
Figure 4.34: Effect of bacterial inoculation on pyrrhotite oxidation rate (based on sulphate release). 87
Figure 4.35: Effect of bacterial inoculation on pyrrhotite oxidation rate (based on iron release). 87
Figure 4.36: The sulphate, iron and nickel production loading in base case column. 89
Figure 4.37: Iron to sulphate production ratio in the column. 90
Figure 4.38: Nickel to sulphate production ratio in the column. 90
Figure 4.39: The oxygen consumption rate in column. 92
Figure 4.40: Concentration profile in the base case column after 126 days: (a) pH profile, (b) iron concentration profile, (c) nickel concentration profile, (d) sulphate concentration profile, and (d) normalized oxygen gas concentration profile. 93
Figure 4.41: Comparison of sulphate loading between the base case and the 2 % S^{2-} columns. 94
Figure 4.42: Comparison of iron loading between the base case and the 2 % S^{2-} columns. 95
Figure 4.43: Oxygen concentration profile in the 2 % S^{2-} column after 138 days. 96
Figure 4.44: Comparison of oxygen consumption rate between the base case and 2 % S^{2-} columns. 97
Figure 4.45: Comparison of nickel loading between the base case and the 2 % S^{2-} columns. 98
Figure 4.46: Comparison of sulphate loading between the base case and the inoculated columns. 99
Figure 4.47: Comparison of oxygen consumption rate between the base case and the inoculated columns. 100
Figure 4.48: Comparison of nickel loading between the base case and the inoculated columns. 100
Figure 4.49: Comparison of sulphate loading between the base case and the mineral buffered columns. 102
Figure 4.50: Comparison of oxygen consumption rate between in the base case and the mineral buffered columns. 102
Figure 4.51: Comparison of iron loading between the base case and the

mineral buffered columns.....103
Figure 4.52: Comparison of nickel loading between the base case and the mineral buffered columns.....103
Figure 4.53: Concentration profile in the 1 % calcite column after 101 days: (a) iron concentration profile, and (b) nickel concentration profile. 104
Figure 4.54: Comparison of sulphate loading between the base case and the column with fines. 105
Figure 4.55: Comparison of iron loading between the base case and the column with fines. 106
Figure 4.56: Comparison of nickel loading between the base case and the column with fines. 106
Figure 4.57: Comparison of oxygen consumption rate between the base case and the column with fines.....107

INTRODUCTION

Base metal tailings often contain significant quantities of sulphide minerals, often as mixtures of pyrite (FeS_2) and pyrrhotite ($Fe_{1-x}S$). Exposure of pyrrhotite at the ground surface to atmospheric oxygen and water results in oxidation and the release of oxidation products, namely sulphate (SO_4^{2-}) and dissolved iron species (Fe^{2+} and Fe^{3+}). The acidic drainage generated from waste sulphide oxidation is recognized as the cause of severe environmental degradation in the mining regions. Consequently, the prediction and control of acid mine drainage (AMD) from mine tailings are recognized as major environmental issues (Filion and Ferguson, 1990).

Assessment of the acid generating potential of mine wastes and long-term treatment options are required by the mine operators under environmental regulations. A common method of assessment is an accelerated short-term laboratory leaching tests under highly oxidative conditions, which often do not represent the natural conditions (SENES Consultants Ltd., 1994). In order to develop an effective process or preventive management strategy, there is a need to assess or predict water quality on a regional scale. There is no singular standard method for assessing long-term impacts of acidic drainage from mine wastes on surrounding environments. In addition to each tests, mathematical models, such as RATAP (Reactive Acidic Tailings Assessment Program) and WATAIL (Waterloo Tailings Program) provide alternative methods for long-term prediction.

The computer model RATAP was the result of CANMET's initiative to conduct studies on the factors and processes which controls acid generation in mine tailings. The program simulates one-dimensional transport of oxygen and porewater through tailings. The tailings solids profile is divided into twenty layers comprising the unsaturated zone, the capillary fringe and the water table. The major processes in the model are abiotic and biotic oxidation of sulphide minerals and the diffusive flux of oxygen through the unsaturated zone. RATAP is designed to run in a probabilistic manner and utilizes a Monte Carlo type subroutine for the allocation of distributed parameter values. The program has been employed successfully to simulate field data at several tailings sites.

The WATAIL model was developed to predict water quality associated with different tailings management options (Scharer et al., 1993). The program provides comparisons in contaminant loading rates from tailings discharge. The model focuses on the effects of treatment or management strategies based on reasonable engineering intervention, such as soil covers or various degrees of flooding. The model consists of three fundamental components: oxidation rates controlled by the estimated diffusive resistance to oxygen transport, pertinent chemical

reactions between oxidation products, and water balance and flow between waste sites. The model allows tailings to be divided into zones of different characteristics (physical and chemical). Each zone is divided into several horizontal segments known as control volumes (layers) and the parameters (diffusion coefficient, reaction rate, etc.) are evaluated in each control volume for each time interval (Figure 1.1).

The current kinetic model is based on the concept that sulphide oxidation is a surface phenomenon that is controlled by the rate of oxygen transport from the atmosphere to the reactive surface of the sulphide wastes. The surficial sulphide reaction is subdivided into chemical (dissolved oxygen) and biological oxidation. The two reaction mechanisms are assumed to be additive to provide an overall reaction rate. In the absence of oxygen, sulphide dissolution is assumed to be zero. However, this approach did not account for the oxidation of sulphide mineral by ferric iron and other chemical oxidants in the absence of dissolved oxygen.

In order for a model to provide accurate assessment of drainage qualities, fundamental information on the kinetics and mechanisms that affect the oxidation of sulphide minerals under various conditions are required. For many sulphide minerals, this fundamental information is lacking. Pyrite oxidation is relatively well understood in comparison to the oxidation of pyrrhotite. It should be noted that pyrite is the dominant sulphide waste mineral in North American coal mining and AMD from coal wastes has been a major concern of the US regulatory authorities. A number of investigations and several major reviews on the oxidation of pyrite have appeared in the literature (e.g. Lowson, 1982; de Hann, 1991; Nicholson, 1994). In contrast, pyrrhotite is the primary sulphide waste at many base metal mines across northern Canada and the oxidation of pyrrhotite has been generally ignored. The few previous investigations to date, however, indicate that reaction rates of pyrrhotite may be significantly higher than reaction rates of pyrite.

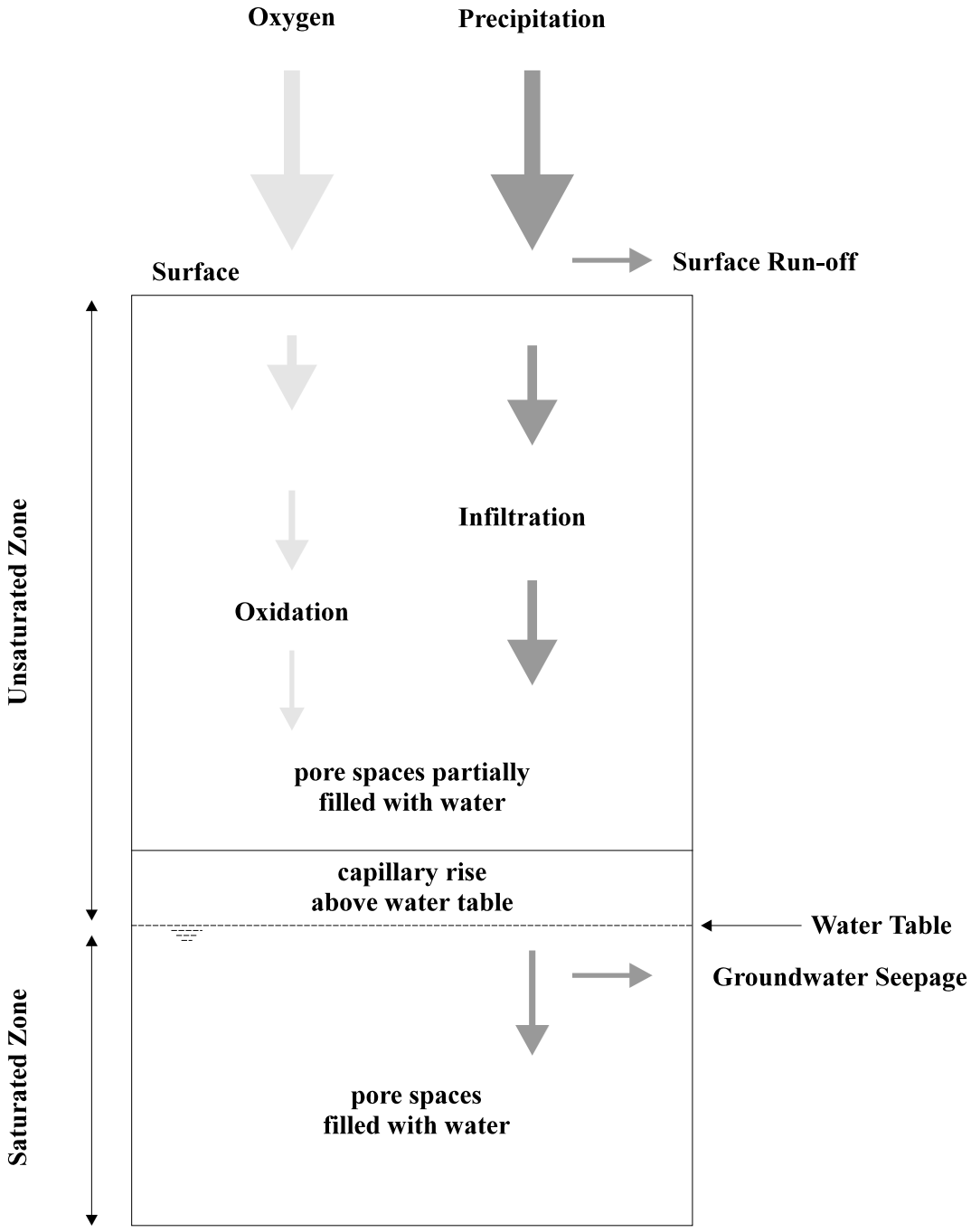

Figure 1.1: General concepts adopted for modeling of mine wastes.

Pyrrhotite chemistry is complicated by the iron deficiency in the crystal structure. The general formula is $Fe_{1-x}S$, where x can vary from 0.0 (FeS) to 0.125 (Fe_7S_8) (Deer et al., 1992). Furthermore, pyrrhotite exists in three crystal forms, hexagonal and monoclinic being the most common (Yund and Hall, 1969). The iron deficient form of pyrrhotite (Fe_7S_8) is monoclinic

while the equimolar variety (FeS) is hexagonal. The non-stoichiometric formula of pyrrhotite is caused by the vacancy of iron in the crystal structure. This vacant metal sites resulting in lower crystal symmetry and giving rise to potentially higher reactivity. Small amounts of Co, Cu, Mn, Pb, Ni and Zn can substitute for Fe in pyrrhotite but most are present as impurities, such as Cu in chalcopyrite ($CuFeS_2$), Pb in galena (PbS), Ni in pentlandite $(Fe,Ni)_9S_8$ and Zn in sphalerite (ZnS).

The objective of this study was to investigate the mechanism and controlling factors affecting the oxidation of pyrrhotite. The laboratory studies were designed to acquire fundamental data, on intrinsic kinetics and transport processes related to pyrrhotite oxidation, for predictive purposes and refinements of model concepts to accommodate pyrrhotite oxidation in tailings under various reaction conditions.

PHYSIO-CHEMICAL PROPERTIES OF PYRRHOTITE

The iron-sulphur mineral system is the most important binary sulphide system because it contains the only sulphides common enough to be considered rock-forming minerals (pyrite and pyrrhotite). Phase equilibria for Fe-S system are well established above 300 °C but remain unresolved at lower temperatures, especially in the pyrrhotite composition region.

Previous studies were generally performed using pyrite (FeS_2) as the reactive mineral. This is particularly evident with regard to reaction mechanisms and kinetic expressions for both abiotic and biotic oxidation. There are some indications, however, that the oxidative mechanism of sulphide moiety of the two minerals as similar. In fact, the initial high release of iron during pyrrhotite oxidation may result in a sulphide-rich layer surrounding the pyrrhotite particle. This layer resembles pyrite. For these reasons, relevant studies pertaining to pyrite oxidation are included in the review when no comparable information on pyrrhotite was available.

Besides the kinetic aspects, the gaseous transport in tailings is reviewed briefly. The most important transport mechanism in tailings is diffusive molecular transport of oxygen and other transport mechanisms such as convective transport caused by thermal gradients, barometric pumping or wind are acknowledged but their importance in tailings environment is generally accepted to be secondary.

1.1.1. Chemical Compositions

A 'sliding scale' X-ray spacing curve was developed by Toulmin and Barton (1964) for determination of pyrrhotite composition. Yund and Hall (1969) have compiled and evaluated the X-ray data of previous workers and calculated the following expression to relates the d_{102} of hexagonal pyrrhotites and their compositions in terms of atomic percent iron.

$$Atomic\,\%\,iron \;=\; 45.212 + 72.86\left(d_{102} - 2.040\right) + 311.5\left(d_{102} - 2.040\right)^2 \qquad (2.1)$$

Pyrrhotite ($Fe_{1-x}S$) had been generally considered having composition range from FeS to Fe_7S_8 (x range from 0 to 0.125), which translates to an atomic percent of iron range from 50 % to 43.75 %.

The multiple valency states of sulphur result in several reaction pathways for the sulphur species. The more common ionic molecular forms of aqueous sulphur species are given in Table 2.1. A simplified reaction pathway proposed by Kuenen (1993) illustrated the aqueous sulphur species and their respective reactions under oxidative environments (Figure 2.1).

Table 2.1: Common ionic molecular forms of aqueous sulphur species.

Valence of sulphur	Molecules	Ions	
+6	H_2SO_4 (sulphuric acid)	HSO_4^- (bisulphate)	SO_4^{2-} (sulphate)
+4	H_2SO_3 (sulphurous acid)	HSO_3^- (bisulphite)	SO_3^{2-} (sulphite)
+2		$HS_2O_3^-$ (bithiosulphate)	$S_2O_3^{2-}$ (thiosulphate)
0			
-2/x	H_2S_x (hydrogen polysulphide)	HS_x^- (bipolysulphide)	S_x^{2-} (polysulphide)
-2	H_2S (hydrogen sulphide)	HS^{2-} (bisulphide)	S^{2-} (sulphide)

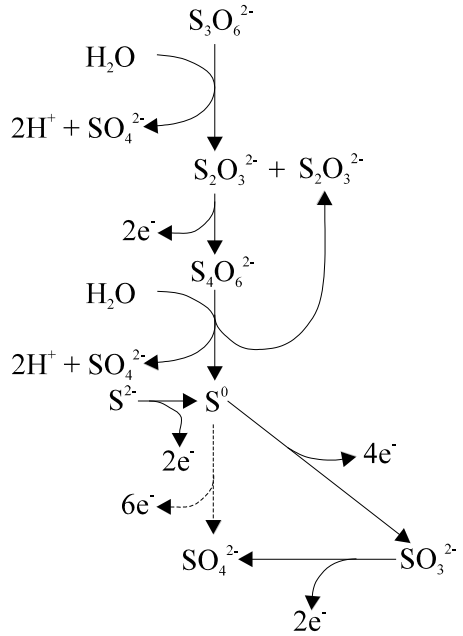

$$S_3O_6^{2-} + H_2O \rightarrow S_2O_3^{2-} + SO_4^{2-} + 2H^+ \quad (2.2)$$

$$S_2O_3^{2-} + S_2O_3^{2-} \rightarrow S_4O_6^{2-} + 2e^- \quad (2.3)$$

$$S_4O_6^{2-} + H_2O \rightarrow S_2O_3^{2-} + S^0 + SO_4^{2-} + H^+ \quad (2.4)$$

$$S^{2-} \rightarrow S^0 + 2e^- \quad (2.5)$$

$$S^0 + 3H_2O \rightarrow SO_3^{2-} + 6H^+ + 4e^- \quad (2.6)$$

$$SO_3^{2-} + H_2O \rightarrow SO_4^{2-} + 2H^+ + 2e^- \quad (2.7)$$

Figure 2.1: Suggested scheme for sulphur oxidation in oxidative environments (adopted from Kuenen, 1993).

Despite the wide variety of possible sulphur species, only HSO_4^-, SO_4^{2-}, H_2S (aq), HS^- and S^{2-} are

of significance in aqueous solutions under reasonable near surface conditions of pH and oxygen activity.

The vacancy of iron in pyrrhotite is often substituted with other trace metal ions, such as Co, Cu, Mn, Pb, Ni and Zn. The trace metals can also be present as minerals, such as pentlandite, chalcopyrite, galena and sphalerite etc., which inter-grow with the pyrrhotite crystal structure. Semi-quantitative analysis of the oxidation of monoclinic pyrrhotite was performed by Kwong (1993). Pyrrhotite with high trace metal content appeared to oxidize slower under abiotic conditions than pyrrhotite samples with a lower trace metal content.

1.1.2. Mineralogical Compositions

Pyrrhotite is classified as having a distorted NiAs structure. The hexagonal NiAs structure is one of the most important in transitional metal chemistry (Vaughan and Craig, 1978). It occupies a unique position in crystal chemistry, being related to the predominantly 'ionic' NaCl structure, while also related to the intermetallic compounds having the CsCl structure (Figure 2.2).

Stoichiometric FeS has the true NiAs structure at a temperature above 140 °C. Below this temperature, a distorted form exists so that the unit cell is related to the simple NiAs structure by 'a' ≈ A√ = B and 'c' ≈ 2C, where A and C represent the a and c parameters of the simple NiAs-type cell and the superstructure is defined as B, 2C according to the nomenclature of Wuensch (1963). The low temperature form exists naturally as the mineral troilite. The directions of the displacements of the iron atoms are indicated on a c-axis projection (Figure 2.3). The iron atoms are displaced only in the *x* and *y* directions while sulphur atoms are displaced along the c-axis. The result is that the iron atoms form triangles, some of which are contracted and some dilated. Sulphur atoms above or below the centres of these triangles are displaced away from contracted triangles and towards the dilated triangles.

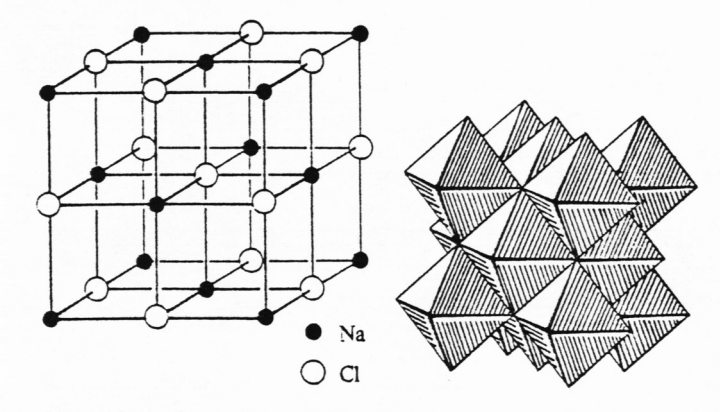

(a)

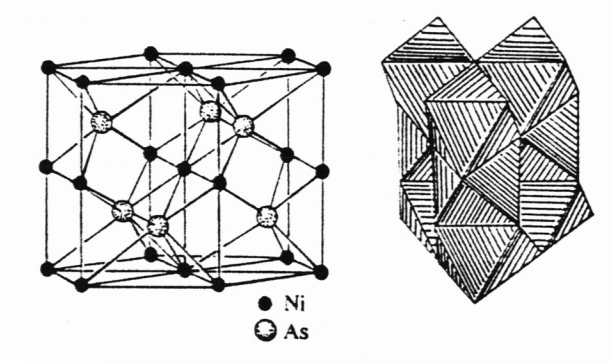

(b)

Figure 2.2: The NaCl-type and NiAs-type crystal structures: (a) NaCl structure showing the coordination of ions and the linking of octahedral units; (b) linkage of ions in a unit cell of NiAs structure and stacking of octahedral units (adopted from Vaughan and Craig, 1978).

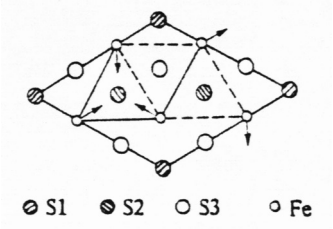

Figure 2.3: Projection of Fe and S atoms on the basal plane (c-axis) in the troilite super-structure (adopted from Vaughan and Craig, 1978).

Non-stiochiometry of the type $Fe_{1-x}S$ has been attributed to vacancies on the Fe sites rather than excess of S atoms (Deer et al., 1992). The pyrrhotite with composition of Fe_7S_8 has a monoclinic structure related to the NiAs-type structure. A large number of structures and superstructures for natural and synthetic pyrrhotites in addition to the troilite and monoclinic pyrrhotites have been

found (Arnold, 1967).

The most abundant natural pyrrhotites are the monoclinic (4C) and troilite (2C) types and the intermediate pyrrhotites, which can be generally categorized as nC (Morimoto et al., 1975). The 5C and 6C types are special cases of the nC type which tend to be more widespread. Commonly, the nC type pyrrhotite is found intergrown with either the 2C or 4C type, and intergrown involving more than one type of nC pyrrhotite are rare.

DISSOLUTION PATHWAY OF SULPHIDE MINERALS

Although the details of the reaction and mechanism of pyrrhotite oxidation are unclear at the present, it is generally believed that the following reactions represent the overall oxidation of pyrrhotite ($Fe_{1-x}S$).

$$Fe_{1-x}S + \left(2 - \frac{x}{2}\right) O_2 + x\,H_2O \;\rightarrow\; (1-x)\,Fe^{2+} + SO_4^{2-} + 2x\,H^+ \qquad (2.8)$$

Equation (2.8) shows the oxidation of pyrrhotite using oxygen as the primary electron acceptor under aerobic conditions. At low pH (below 4.5), pyrrhotite oxidation may be catalyzed by bacteria, particularly *Thiobacillus ferrooxidans* (Ingledew, 1986; Tuovinen, 1986). Bacteria derive metabolic energy for carbon dioxide fixation and growth from oxidation of ferrous iron to ferric iron (Equation 2.9) and sulphide to sulphate (Equation 2.10).

$$Fe^{2+} + \frac{1}{4} O_2 + H^+ \;\rightarrow\; Fe^{3+} + \frac{1}{2} H_2O \qquad (2.9)$$

$$S^{2-} + 2\,O_2 \;\rightarrow\; SO_4^{2-} \qquad (2.10)$$

Although the oxidation of Fe^{2+} to Fe^{3+} can occur in an abiotic environment, the reaction is greatly accelerated by the presence of chemolithotropic bacteria, particularly acidophiles. The resulting ferric iron can act as oxidant to oxidize pyrrhotite (Equation 2.11). Therefore, the enzymatic oxidation of ferrous iron is referred to as the indirect biological oxidation mechanism.

$$Fe_{1-x}S + (8 - 2x)\,Fe^{3+} + 4\,H_2O \;\rightarrow\; (9 - 3x)\,Fe^{2+} + SO_4^{2-} + 8\,H^+ \qquad (2.11)$$

Alternatively, oxidation may not proceed to completion. Field observations indicate that elemental sulphur can exist in quantities up to 2.5 % in well oxidized tailings as a result of partial oxidation of pyrrhotite (Steger and Desjardins, 1978; Jambor, 1994). The partial oxidation of pyrrhotite by dissolved oxygen and ferric iron is illustrated in Equation (2.12) and (2.13):

$$Fe_{1-x}S + \left(\frac{1-x}{2}\right)O_2 + 2(1-x)H^+ \rightarrow (1-x)Fe^{2+} + S^0 + (1-x)H_2O \qquad (2.12)$$

$$Fe_{1-x}S + (2-2x)Fe^{3+} \rightarrow (3-3x)Fe^{2+} + S^0 \qquad (2.13)$$

Elemental sulphur formed from the partial oxidation of pyrrhotite can further undergo oxidation to sulphate. The relative rate of oxidation of elemental sulphur compared to partial oxidation of pyrrhotite has not been established presently. The oxidation of elemental sulphur by dissolved oxygen is relatively slow under abiotic condition, while the reaction is greatly accelerated by the presence of *T. ferrooxidans* and *T. thiooxidans* (Equation 2.14). The chemical oxidation of elemental sulphur to sulphate by ferric iron can also occur (Equation 2.15).

$$S^0 + \frac{3}{2}O_2 + H_2O \rightarrow SO_4^{2-} + 2H^+ \qquad (2.14)$$

$$S^0 + 6Fe^{3+} + 4H_2O \rightarrow SO_4^{2-} + 6Fe^{2+} + 8H^+ \qquad (2.15)$$

Sulphur enrichment on the surface of pyrrhotite can occur through oxidative conversion of pyrrhotite to pyrite or marcasite (FeS_2). There is field evidence that pyrite is an intermediate product of pyrrhotite oxidation in the mineral zoning of oxidized ore deposits (Nickel et al, 1974; Thornber, 1975a,b; Thornber et al, 1981). The conversion reaction is shown in Equation (2.16).

$$2Fe_{1-x}S + \left(\frac{1}{2}-x\right)O_2 + (2-4x)H^+ \rightarrow FeS_2 + (1-2x)Fe^{2+} + (1-2x)H_2O \qquad (2.16)$$

Thermodynamic data also indicate the feasibility of such oxidative conversion. It is evident that pyrite and marcasite are both more stable than pyrrhotite. However, under an oxidative environment, pyrite and marcasite are only metastable and will be eventually oxidized further.

Table 2.2 is a summary of the thermodynamic data for iron-sulphur solid species that are common in mine tailings.

Table 2.2: Thermodynamic data for iron-sulphur minerals (Woods and Garrels, 1987).

Formula	Minerals	ΔH_f (kJ·mol^{-1})	ΔG_f (kJ·mol^{-1})	S° (J·mol^{-1}·K^{-1})
FeS	α Troilite	-98.7	-99.8	62.7
	Pyrrhotite	-100.4	-100.8	60.3
	(Iron-rich)	-100.0	-100.4	60.3
	(Sulfur-rich)	-92.0	-93.6	60.7
	Mackinawite		-93.3	
FeS_2	Pyrite	-174.3	-163.1	52.9
	Marcasite	-160.0	-158.4	53.9
$Fe_2(SO_4)_3$		-2580.1	-2248.4	270.9
$FeSO_4 \cdot H_2O$	Szomolnokite	-1243.9		
$FeSO_4 \cdot 7H_2O$	Melanterite	-3014.5	-2509.9	409.2

The presence of elemental sulphur and disulphide (pyrite and marcasite) as intermediate products of pyrrhotite oxidation may have important implications in the determination of the oxidation rates.

Oxidant-free (Non-Oxidative) Dissolution

Electrochemical conversion of pyrrhotite to pyrite or marcasite in natural environments was observed previously (Thornber, 1975a; Jambor, 1994). The anodic conversion of pyrrhotite to pyrite was accompanied by anodic conversion of pentlandite ($(Ni,Fe)_9S_8$) to violarite ($(Ni,Fe)_3S_4$) in the absence of oxygen. The reaction of pyrrhotite and pentlandite are as follows:

$$Fe_{1-x}S \rightarrow \frac{1}{2}FeS_2 + \left(\frac{1}{2} - x\right)Fe^{2+} + (1-2x)e^- \quad (4.17)$$

$$(Ni,Fe)_9S_8 \rightarrow 2(Ni,Fe)_3S_4 + 3(Ni,Fe)^{2+} + 6e^- \quad (4.18)$$

In the absence of oxygen, sulphide sulphur acts as the electron acceptor, and the evolution of hydrogen sulphide enhances pyrrhotite dissolution according to the following reaction:

$$Fe_{1-x}S + 2H^+ + 2x\,e^- \rightarrow (1-x)\,Fe^{2+} + H_2S_{(g)} \qquad (4.19)$$

The rate controlling step for the reaction is either the stripping of H_2S from this reaction system or the availability of H^+ ions. The presence of trace metal sulphides provides extra electrons for Equation (4.19). Van Weert et al. (1974) observed that H_2S gas evolution occurs when the Eh potential dropped below 0 V.

There were inconsistencies concerning the controlling mechanism of non-oxidative dissolution. Nichol and Scott (1979) suggested that pyrrhotite dissolution was governed by the mass transfer of ferrous iron and sulphide ions from the mineral surface. Tewari and Campbell (1976) and Bugajski and Gamsjäger (1982) performed rotating disk electrode experiments in sulphuric acid environments, using troilite and monoclinic pyrrhotite, respectively. The measured activation energies for oxidant-free dissolution were 60 and 58.6 $kJ \cdot mol^{-1}$ respectively, which indicated a kinetic control mechanism. A transport limited process would have activation energies in the range of 10 - 20 $kJ \cdot mol^{-1}$.

Despite field observation of pentlandite conversion to violarite (Thornber, 1975a,b), laboratory experiments by Janzen (1996) did not show any correlation between pyrrhotite dissolution with trace nickel content. The non-oxidative dissolution rates ranged from 9.32×10^{-11} to 9.21×10^{-10} $mol \cdot m^{-2} \cdot s^{-1}$ at pH 2.75 in a closed reactor which were almost an order of magnitude lower than the rate measured by Kwong (1995) (5×10^{-9} $mol \cdot m^{-2} \cdot s^{-1}$) at pH 2.0 in an open airlift reactor. The discrepancies were explained by Janzen as the result of stripping of hydrogen sulphide gas (from Equation 4-19) from solution by the nitrogen carrier gas. The closed system used by Janzen prevented the escape of hydrogen sulphide.

Chemical (Abiotic) Oxidation

There are relatively few studies and scarce literature on the oxidation of pyrrhotite by dissolved oxygen. In contrast, the reaction kinetics of pyrite oxidation by dissolved oxygen has been studied extensively in the past. Lowson (1982) reviewed the combined effect of aqueous

oxidation of pyrite and ferrous iron by molecular oxygen, and oxidation of pyrite by ferric iron. Lowson proposed the following rate equation for the overall pyrite oxidation:

$$r_c = A \cdot e^{-E_a/RT} \left[O_2\right] \cdot 10^{-x\,pH} \tag{2.20}$$

The oxidation reaction is a heterogeneous surface reaction between aqueous dissolved oxygen and the surface mineral. Despite Lowson's (1982) suggestion of a first order dependence of the kinetic rate on the oxygen concentration, the specific reaction rate of pyrite oxidation was generally found to be half order with respect to dissolved oxygen when mass transport was not limiting (McKibben and Barnes, 1986; Williamson and Rimstidt, 1994). The rate limiting reaction of abiotic pyrite oxidation is not strongly pH dependent. The pH dependence ranges from zero order (McKibben and Barnes, 1986; Moses and Herman, 1991) to fractional order (Williamson and Rimstidt, 1994). The generally accepted reaction rate equations are as follows:

Williamson and Rimstidt: $$r = 10^{-8.19(\pm 0.10)} \frac{\left[O_2\right]^{0.5(\pm 0.04)}}{\left[H^+\right]^{0.11(\pm 0.01)}} \tag{2.21}$$

McKibben and Barnes: $$r = 10^{-9.74} \left[O_2\right]^{0.5} \tag{2.22}$$

At high dissolved oxygen levels, the reaction of pyrite is believed to be controlled by the adsorption of reactant (dissolved oxygen) and products (ferrous iron and sulphate) (Moses and Herman, 1991; Nicholson et al., 1988). Assuming monolayer (Langmuir) adsorption behaviour, the pyrite surface becomes saturated with oxygen as the oxygen partial pressure increases. The reaction rate then becomes zeroth order with respect to dissolved oxygen.

Moses et al. (1987) proposed that sulphate production during pyrite oxidation is controlled by the oxidation of sulfoxy intermediates. The production and accumulation of sulfoxy intermediates depends on the pH and the presence of other intermediates. The most important reaction involves the formation of sulphite from a mixture of sulfoxy intermediates:

$$S_nO_6^{2-} + S_2O_3^{2-} \leftrightarrow S_{n+1}O_6^{2-} + SO_3^{2-} \tag{2.23}$$

Sulphur enrichment on the pyrrhotite surface was found after surface oxidation by either acid leaching and / or molecular oxygen (Hamilton and Woods, 1981; Jones et al., 1992; Pratt et al.,

1994). Linear potential sweep voltammetry performed by Hamilton and Woods (1981) identified elemental sulphur as the major sulphur product for pyrrhotite oxidation at all potentials investigated. The quantity of sulphur formed on pyrite is much less than on pyrrhotite.

Surface characterization studies by Jones et al. (1992) and Pratt et al. (1994) suggested that a layer of Fe(III)-oxyhydroxide layer overlies an iron-deficient sulphide structure. The oxide / hydroxide overlayer is approximately 1 to 3 nm in thickness. A sulphur-enriched layer existed below the oxide / hydroxide overlay. Pratt et al. (1994) suggests that the sulphur enrichment resulted from iron diffusion to the surface oxide layer. The enriched layer is comprised of various iron-deficient sulphides ranging from FeS_2 to Fe_2S_3. The combination of oxide / hydroxide and sulphur rich layers can create a mass transport barrier.

The oxidation of pyrrhotite by molecular oxygen was studied by Kwong (1995) in airlift reactors using air as carrier gas. The measured oxidation kinetic rates were 2.28×10^{-9} mol·m^{-2}·s^{-1} based on iron release and 8.51×10^{-10} mol·m^{-2}·s^{-1} based on sulphate production. The production of sulphate was found to lag behind iron release (SO_4^{2-} / Fe^{2+} = 0.37), which was consistent with a build-up of sulphur rich component on the surface of pyrrhotite (Jones et al., 1992).

The oxidation rate was found to be dependent on the temperature by the Arrhenius relationship. The activation energies for pyrrhotite oxidation by molecular oxygen ranged from 58.1 to 100.4 kJ·mol^{-1} depending on pH conditions (Kwong, 1995). The activation energies suggested a kinetic controlled mechanism.

The kinetics of the oxidation of ferrous iron by dissolved oxygen is a function of the medium, pH, temperature, ferrous concentration, dissolved oxygen concentration and the presence of catalytic materials (Lowson, 1982). In an acidic environment under ambient conditions, the rate equation is given by:

$$-\frac{dFe^{2+}}{dt} = k\left[Fe^{2+}\right]^x\left[OH^-\right]^y P_{O_2} \qquad (2.24)$$

At pH below 2, the rate of reaction is very slow, independent of pH (y = 0), first order with respect to the partial pressure of oxygen and second order with respect to ferrous ion concentration (x = 2). The corresponding reaction rate constant (k) is reported to be approximately 2.5×10^{-6} mol·L^{-1}·atm^{-1}·s^{-1} (Lowson, 1982). At pH values between 2 and 5, the oxidation of ferrous iron is first order with respect to ferrous iron (x = 1) and hydroxyl ion (y =

1). The corresponding rate constant is 1.7×10^{-9} $atm^{-1}\cdot s^{-1}$.

The electrochemical reaction of ferrous iron oxidation by air or molecular oxygen in acidic solution can be accelerated by the presence of other trace metal ions (Cu^{2+}, Ni^{2+}, etc.). At low copper concentration (10^{-5} - 10^{-3} $mol\cdot L^{-1}$), the oxidation of ferrous iron is enhanced by the an additional term:

$$-\frac{dFe^{2+}}{dt} = k\left[Fe^{2+}\right]P_{O_2} + k_1\left[Fe^{2+}\right]\left[Cu^{2+}\right] \qquad (2.25)$$

The enhancement is first order with respect to ferrous and cupric ions. The reaction rate constant (k_1) for the enhancement term is found to be 7.6×10^{-3} $mol\cdot L^{-1}\cdot s^{-1}$.

Anoxic Oxidation by Ferric Iron

The oxidation of pyrite by ferric ion is found to be more complicated than oxidation by molecular oxygen. In an abiotic environment, ferric iron is consumed in the oxidation of pyrite while it is being formed during the oxidation of ferrous iron (Equation 2.11 and Equation 2.9 for pyrrhotite oxidation system).

When oxygen was present, the oxidation of pyrite by ferric iron was found to be independent of the pH (Williamson and Rimstidt, 1994). The reaction (Equation 2.26) was found to be approximately first order with respect to ferric ion concentration and inverse half order with respect to the ferrous iron.

$$r = 10^{-6.07(\pm0.57)}\frac{\left[Fe^{3+}\right]^{0.93(\pm0.07)}}{\left[Fe^{2+}\right]^{0.40(\pm0.06)}} \qquad (2.26)$$

However, under anoxic conditions, pyrite oxidation by ferric iron was found to be pH sensitive. There is an inconsistency in the literature concerning the dependence of the reaction on the ferrous ion concentration. McKibben and Barnes (1986) found that the oxidation of pyrite by ferric iron under anoxic condition was independent of ferrous iron, while Williamson and Rimstidt (1994) reported a half order dependence.

McKibben and Barnes $$r = 10^{-9.74} \frac{\left[Fe^{3+}\right]^{0.5}}{\left[H^{+}\right]^{0.5}} \quad (2.27)$$

Williamson and Rimstidt $$r = 10^{-6.07(\pm 0.57)} \frac{\left[Fe^{3+}\right]^{0.30(\pm 0.02)}}{\left[Fe^{2+}\right]^{0.47(\pm 0.03)} \left[H^{+}\right]^{0.32(\pm 0.04)}} \quad (2.28)$$

In both cases, the reaction dependence on ferric iron was reduced to half order or less. Williamson and Rimstidt (1994) also showed the pyrite oxidation by ferric iron is enhanced at high ferric to ferrous ratio under oxic condition, whereas the reverse holds under anoxic condition. This illustrates a change in reaction mechanisms between oxic and anoxic conditions for pyrite oxidation.

Investigations by Kwong (1995) using an airlift reactor at initial ferric iron concentration of 1×10^{-3} M yielded a similar reaction rate (1.14×10^{-8} mol·m^{-2}·s^{-1}). There was no significant amount of hydrogen sulphide gas evolution detected in the open airlift system. In both studies, the sulphate production significantly lagged behind the iron release. Sulphate release was estimated to be 14 % of the iron release during anoxic ferric iron oxidation of pyrrhotite (Kwong, 1995). The sulphate to iron ratio with ferric iron oxidation was found to be less than the oxidation by molecular oxygen. The oxidation rates of pyrrhotite by ferric iron were consistently higher than the oxidation by molecular oxygen.

Biological Oxidation

The biological oxidation of sulphide minerals has received substantial research attention in the past 20 years. However, much of the focus on the sulphide oxidation involved the microbial recovery of metal values (Campbell et al., 1985; Olson and Kelly, 1986; Debus, 1990). The bacterial oxidation of sulphide minerals, predominantly pyrite and pyrrhotite, regarding environmental concerns emerged as an important key area of research in recent years (Singh and Bhatngar, 1985; Evangelou and Zhang, 1995).

Among many acidophiles and neutrophiles identified from acid mine drainage or mine waste site, the chemolithotrophic bacteria of the genus *Thiobacillus* were the more important microorganism in the oxidation of sulphide minerals (Leduc and Ferroni, 1994; Johnson, 1991). Recently, there was evidence that *Leptospirillum ferrooxidans* played an important role in

ferrous iron oxidation in acidic environments (Sand et al., 1992; McGinness and Johnson, 1993). Some of the common bacteria in AMD and the respective growth conditions are given Table 2.3.

Table 2.3: Acidophilic bacteria in metal ore leaching environments (adopted from Olson and Kelly, 1986).

Organism	**Energy Sources**	**Growth Temperature**	**Primary Carbon Sources**
Thiobacillus ferrooxidans	Fe^{2+}, S^0	mesophile	CO_2
Leptospirillum ferrooxidans	Fe^{2+}	mesophile	CO_2
Thiobacillus thiooxidans	S^0	mesophile	CO_2
Sulfolbus species	S^0, organic C, Fe^{2+}	thermophile	CO_2, organic C
Acidophilium cryptum	organic C	mesophile	organic C

The bacterium *Thiobacillus ferrooxidans* is the most dominant iron-oxidizing bacterium. This organism is able to use both reduced sulphur species and ferrous iron as the energy source for growth, and obtains its cellular carbon needs from fixation of CO_2. The optimal growth conditions were determined at pH 2-3 and temperature range from 20 to 35°C.

The biological oxidation of sulphide mineral can occur according to two different pathways: direct biological oxidation and indirect biological oxidation (Boon and Heijnen, 1993). Direct biological oxidation occurs when bacteria directly utilize both the metal component (predominantly iron) and sulphide sulphur from the surface of the mineral. Formation of diffusive layers on the surface of the mineral will terminate this process. The direct biological process can be illustrated in Figure 2.4.

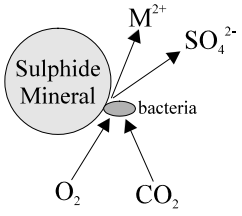

$$r_{MS,bio-ox} = \frac{r_{x,MS}}{Y_{MS,x}} + m_{MS} \cdot C_x \qquad (2.29)$$

$$r_{x,MS} = \mu_{MS} \cdot C_x \qquad (2.30)$$

Figure 2.4: Direct biological leaching without diffusion limitation (adopted from Boon and Heijnen, 1993).

Indirect biological oxidation refers to biological oxidation of aqueous ferrous iron to ferric iron,

which results in the chemical oxidation of the sulphide mineral with ferric iron. Complete chemical (ferric iron as oxidant) oxidation of sulphide mineral will result in metal and sulphate ions. The coupled process between biological ferrous oxidation and complete chemical oxidation is illustrated in Figure 2.5.

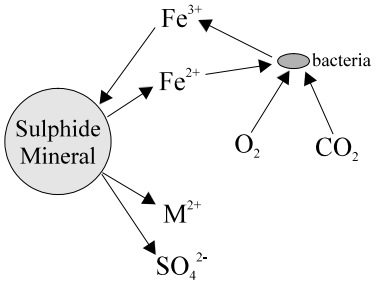

$$r_{MS,chem-ox} = k_{A,chem} \cdot A_{MS,surf} \quad (2.31)$$

$$r_{x,Fe^{2+}} = \mu_{Fe^{2+}} \cdot C_x \quad (2.32)$$

$$r_{Fe^{2+},bio-ox} = \frac{r_{x,Fe^{2+}}}{Y_{Fe^{2+},x}} + m_{Fe^{2+}} \cdot C_x \quad (2.33)$$

Figure 2.5: Indirect biological leaching by ferric iron without diffusion limitation (adopted from Boon and Heijnen, 1993).

Incomplete chemical oxidation of the sulphide mineral will result in the formation of elemental sulphur, which is followed by biological oxidation to sulphate. This is shown in Figure 2.6.

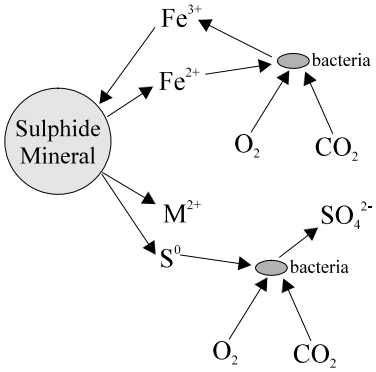

$$r_{x,S^0} = \mu_{S^0} \cdot C_x \quad (2.34)$$

$$r_{S^0,bio-ox} = \frac{r_{x,S^0}}{Y_{S^0,x}} + m_{S^0} \cdot C_x \quad (2.35)$$

Figure 2.6: Indirect biological leaching by ferric iron and biological oxidation of sulphide without diffusion limitation (adopted from Boon and Heijnen, 1993).

A diffusive barrier could emerge if the formation rate of elemental sulphur exceeds the biological oxidation rate of sulphur, or if the precipitation of ferric iron ($Fe(OH)_3$) or jarosite ($KFe_2(SO_4)_2(OH)_6$) takes place due to changes in environmental conditions, such as pH. Chemical oxidation at the mineral surface is in series with diffusion of reactants and products through the diffusive barrier. The overall coupling of diffusive transport and biological oxidation process is illustrated in Figure 2.7.

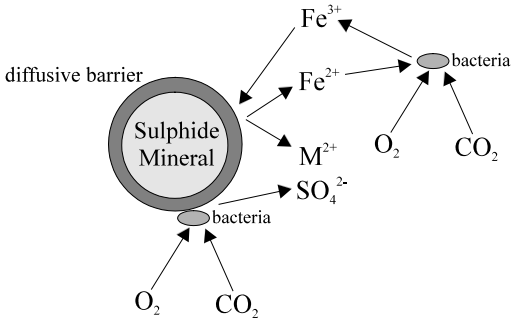

Figure 2.7: Indirect biological leaching with diffusion limitation (adopted from Boon and Heijnen, 1993).

The overall sulphide dissolution rate is determined by the coupling of diffusion transport and biological oxidation. The nature of the diffusive barrier will be discussed in a later section.

The biological oxidation of sulphide mineral can be considered as two distinct oxidation processes, ferrous (Fe^{2+}) oxidation and sulphide (S^{2-}) oxidation. The biological oxidation of ferrous iron has been studied extensively due to the important characteristics of ferric iron as chemical oxidant in the oxidation of sulphide minerals (Pronk and Johnson, 1992; Ingledew, 1986; Pesic, 1993; Ahonen and Tuovinen, 1989; Nakamura et al, 1986; Jensen and Webb, 1995; Toro et al, 1988). The significant increase in the biological oxidation of the reduced sulphur species compared to the chemical oxidation, the bioenergetics of acidophilic *Thiobacilli* had been studied extensively (Kuenen et al, 1993; Lorbach et al, 1993; Suzuki et al, 1990; Kulpa et al, 1990; Sugio et al, 1992).

It was stated by Boogerd et al (1991) that ferric iron oxidation of pyrite did not result in the accumulation of elemental sulphur at ferric iron concentrations less than 0.1 mM. In a biological system, ferric iron concentrations often exceeded 0.1 mM. Under high ferric iron concentration, formation of elemental sulphur or polysulphide, during mineral dissolution, was observed in surface species analysis (Mustin et al, 1993a). The oxidation of sulphur by ferric iron was slow compared to the release of metal ions. Electrochemical studies have shown that the bacterial oxidation of elemental sulphur, formed from ferric iron oxidation of sulphide minerals, greatly increases sulphide dissolution (Tributsch and Bennett, 1981a,b; Mehta and Murr, 1983; Choi et al, 1993).

The oxidation of elemental sulphur and pyrite by *Thiobacillus thiooxidans* was investigated based on oxygen consumption (Lizama and Suzuki, 1990). The oxidation of sulphide and

elemental sulphur was found to be competitively inhibited by increasing concentrations of cells. The biological oxidation of pyrite with *Thiobacillus ferrooxidans* was investigated by Scharer et al. (1991), and proposed the following rate equation.

$$r_b = b\frac{\mu_{\max}\cdot\sigma}{Y_{x/s}}e^{-E_a/RT}\frac{[O_2]}{K_0+[O_2]}\frac{1}{1+10^{2.5-pH}+10^{pH-4}} \quad (2.36)$$

Bacterial oxidation of pyrrhotite was examined in airlift reactor by Scharer et al. (1993) and Kwong (1995), the reaction rate was determined to be approximately 7×10^{-9} mol·m^{-2}·s^{-1} with respect to both iron and sulphate release. The equimolar production of iron and sulphate suggested the importance of bacterial catalysis of sulphide oxidation, while abiotic oxidation produced significant accumulation of sulphur species on the pyrrhotite surfaces.

The effects of pH, temperature and initial density of bacteria on the *T. ferrooxidans* oxidation of ferrous iron was studied by Pesic et al. (1989). Using the continuous measurements of redox potential, the rate equation for the biological oxidation of ferrous iron can be written as follows.

$$-\frac{d[Fe^{2+}]}{dt} = 1.62\times10^{11}\cdot C_{bacteria}\cdot[H^+][Fe^{2+}]\cdot P_{O_2}\cdot e^{-58.77/RT} \quad (2.37)$$

where:

$C_{bacteria}$ concentration of bacteria
P_{O2} partial pressure of oxygen

The biological growth rate of heterotrophic acidophiles generally followed Monod type growth kinetics (Equation 2.38). The growth kinetics were found to depend on substrate, such as ferrous iron (Fe^{2+}), elemental sulphur (S^0) or sulphide minerals (Suzuki et al., 1990). *T. ferrooxidans* grown on sulphide ore and elemental sulphur showed good ferrous and elemental oxidation activities, while cells grown on ferrous iron had mixed results on S^0 and Fe^{2+} activities when transferred to sulphur substrate system.

$$b\frac{\mu_{\max}\cdot\sigma}{Y_{x/s}}f(substrates, products) \quad (2.38)$$

where:

b biological scaling factor
μ_{max} specific growth rate (s^{-1})
σ specific surface coverage (g·m^{-2})

$Y_{x/s}$ growth yield ($g \cdot mol^{-1}$)

There is evidence for the direct oxidation of sulphur moiety of pyrite by *T. ferrooxidans* (Arkesteyn, 1979). Bacterial oxidation of Fe^{2+} to Fe^{3+} was negligible at pH 5 or above, while pyrite and elemental sulphur utilization continued above this pH. Carbon dioxide fixation (per mole of oxygen consumed) was highest at pH 4 for sulphur metabolism while lowest for ferrous metabolism. This is consistent with direct oxidation of sulphide sulphur by *T. ferrooxidans*.

Oxygen is essential for bacterial catalysis and growth (Nagpal et al., 1993). Bacterial growth was inhibited at dissolved oxygen concentrations less than 0.20 $mg \cdot L^{-1}$ (Liu, 1988; Hansford and Bailey, 1993). Reduction in the dissolved oxygen concentration below optimal levels leads to reduced oxidation rate and bacterial growth.

The bacterial growth rate and sulphide dissolution rate were found to increase linearly with increasing aqueous carbon dioxide concentration (Liu et al, 1988), which was consistent with data obtained by Torma et al (1972). However, a study performed by Nagpal (1993) in a continuous stirred tank reactor showed that the bacterial activities increased from zero carbon dioxide to an optimal aqueous phase carbon dioxide concentration of 3 to 7 $mg \cdot L^{-1}$, and concentrations above 10 $mg \cdot L^{-1}$ were found to be inhibitory. Based on Monod kinetics, Nagpal proposed the following equation for the uptake of carbon dioxide.

$$Q_{CO_2} = \frac{\mu_{\max} \cdot X}{1 + \frac{K_1}{C_{CO_2}} + \frac{C_{CO_2}}{K_2}} \qquad (2.39)$$

The parameters were determined to be $K_1 = 4.29\ mg \cdot L^{-1}$ and $K_2 = 5.81\ mg \cdot L^{-1}$ and $\mu_{max} \cdot X$ was a function of the growth conditions.

Although glucose was reported to be inhibitory to *Thiobacillus ferrooxidans* growth, controlled amount of glucose in the growth medium gave a 7-fold population increase (Kai et al., 1996).

The toxicity of metal ions in acid mine drainage on *Thiobacillus ferrooxidans* had been studied by Kamarov et al, 1993. The study showed that the bacterium could withstand metal concentration of up to 10 $g \cdot L^{-1}$ copper, 20 $g \cdot L^{-1}$ iron, 25 $g \cdot L^{-1}$ nickel and 10 $g \cdot L^{-1}$ sulphuric acid (H_2SO_4).

T. ferrooxidans are able to grow at pH values between 1 and 6 (Jensen and Webb, 1995), the

optimal pH is generally accepted to be between 2.0 and 2.3 for ferrous iron and somewhat higher for sulphide mineral substrates (Arkesteyn, 1979). However, there were discrepancies concerning the pH effects in attached growth environment, such as the biofilm system. Nakamura et al. (1986) found that the ferrous iron oxidation rate remained constant for pH values ranging from 1.5 to 2.5, but there were significant effects outside this pH range. The biological growth and oxidation activities were found to follow Arrhenius relationship (Ahonen and Tuovinen, 1989 & 1991). The activation energies for the oxidation of pyrrhotite and pyrite were determined to be 40 and 95.5 $kJ \cdot mol^{-1}$ respectively. The activation energy for the ferrous iron oxidation was found to be 83 $kJ \cdot mol^{-1}$.

When two sulphide minerals are in electrical contact in an acid-aqueous solution, the mineral with lower electrode potential dissolves preferentially while the higher member is galvanically protected (Mehta and Murr, 1983; Lizama and Suzuki, 1987). Under rapid galvanic dissolution, sulphide sulphur is often partially converted to elemental sulphur on the mineral surface. Bacteria can enhance the removal of elemental sulphur and other sulphur constituents by oxidation to sulphate (Mehta and Murr, 1982). The combination of bacterial catalysis and galvanic interaction of sulphide minerals enhances the dissolution of sulphide mineral with lower electrode potential.

In the absence of bacterial activity, surface buildup of sulphur constituents will result in mass transport limitation and reduction in galvanically induced reactions (Mehta and Murr, 1983). Therefore, without bacterial catalysis of elemental sulphur to sulphate, galvanic interaction is less significant.

The difficulties in studying the bacterial catalysis of sulphide oxidation is the attachment of bacteria on solid surfaces (Suzuki et al., 1990). Amaro et al. (1993) showed that phosphate starvation of *T. ferrooxidans* increased the extent of attachment to sulphide and elemental sulphur surfaces. Cell attachment potentially reduced the accuracy of cell enumeration, and free cells might have shown different oxidation activities compared to attached cells.

TRANSPORT PROCESSES AND GEOCHEMISTRY IN MINE TAILINGS

There are many other processes occurring in mine tailings in conjunction with sulphide oxidation. Transport processes and equilibrium reactions are coupled with kinetic. A brief review of these is presented below. The simplified schematic in Figure 1.1 has shown the

vertical transport of liquid and gaseous constituents in the unsaturated zone of a tailings column. In addition to liquid and gas transport, there are also buffering reactions, silicate weathering, formation and dissolution of secondary minerals (precipitates) and adsorption processes occurring in mine tailings.

Gaseous Transport - Fick's Law Diffusion

The most important gaseous transport in mine tailings is the penetration of oxygen into the inter-particle pore space of the tailings. Both diffusion and advection transport of oxygen can occur in tailings. There are three basic transport processes for oxygen movement in tailings: (1) barometric pumping, (2) dissolved oxygen transport in infiltrating water and (3) diffusion in the gas phase.

The change in barometric pressure can create advective transport of gas into the unsaturated materials. The atmospheric pumping was related to the thickness of materials and change in barometric pressure by Massmann and Farrier (1992).

$$\frac{\Delta Z}{Z_0} = \frac{\Delta P}{P_o + \Delta P} \tag{2.40}$$

where:

Z_0 depth to saturated zone
ΔZ depth of penetration
P_0 initial barometric pressure
ΔP changes in barometric pressure

The magnitude of barometric pumping was found to be insignificant for mine tailings when changes in pressure were less than 3 % and shallow unsaturated depth.

The transport of oxygen via dissolved oxygen in infiltrating water follows the Henry's law equilibrium for oxygen partition between gas and liquid phases.

$$F_{O_2} = Q \cdot \left(P_{O_2} K_H \right) \tag{2.41}$$

where:

F_{O2} flux of oxygen transport
Q rate of water infiltration
P_{O2} partial pressure of oxygen in gas phase
K_H Henry's law constant for oxygen

The low solubility of oxygen in water reduces the effectiveness of oxygen transport by this transport mechanism.

The predominant mechanism for oxygen transport is based on diffusion (Jaynes et al, 1984; Nicholson et al, 1989). The one-dimensional diffusion transport estimated by Fick's law can be written as follows.

$$F_{O_2} = -D_{eff} \frac{dC_{O_2}}{dz} \quad (2.42)$$

where:

D_{eff} effective diffusion coefficient

dC_{o2} / dz oxygen concentration gradient

The effective diffusion coefficient is the combination of diffusion of oxygen in both gas and liquid phases. Diffusion in gas phase depends on the diffusion coefficient for oxygen in air, available gas-filled pore-space and tortuosity (Collin and Rasmuson, 1988). Using data from Reardon and Moddle (1986), a correlation calculating the effective diffusion coefficient was reported by David (1993).

$$D_{eff} = \tau D_a^0 (1-S)^{\alpha} + \frac{\tau S D_w^0}{K'_H} \quad (2.43)$$

where:

D_a^0 coefficient of free diffusion for oxygen in air

D_w^0 diffusion coefficient of oxygen in water

S degree of saturation

τ, α parameters derived from non-linear regression (0.273 and 3.28 respectively)

K'_H unitless Henry's law constant (23.6 at 10 °C)

Neutralizing Reactions and Formation / Dissolution of Secondary Minerals

The presence of buffering minerals will maintain higher pH in the mine tailings even if significant sulphide oxidation occurs. The most common buffering minerals present in mine tailings are calcite ($CaCO_3$), dolomite ($CaMg(CO_3)_2$), siderite ($FeCO_3$), amorphous aluminum hydroxide ($Al(OH)_3$) and gibbsite and amorphous ferric hydroxide ($Fe(OH)_3$) and goethite.

The buffering capacity results from the consumption of protons (H^+) during dissolution. Dissolution of the buffering minerals are shown below:

$$CaCO_3 + 2H^+ \rightarrow Ca^{2+} + H_2CO_3 \quad (2.44)$$

$$CaMg(CO_3)_2 + 4H^+ \rightarrow Ca^{2+} + Mg^{2+} + 2H_2CO_3 \quad (2.45)$$

$$FeCO_3 + 2H^+ \rightarrow Fe^{2+} + H_2CO_3 \quad (2.46)$$

$$Al(OH)_3 + 3H^+ \rightarrow Al^{3+} + 3H_2O \quad (2.47)$$

$$Fe(OH)_3 + 3H^+ \rightarrow Fe^{3+} + 3H_2O \quad (2.48)$$

The formation and dissolution of secondary minerals are based on solid-liquid equilibrium in the aqueous phase. The general formula for the solid-liquid equilibrium is based on the solubility products of the secondary minerals. Table 2.4 provided solubility products data for carbonate buffering minerals.

$$K_{sp} = [metal]_{aq} \cdot [ligand]_{aq} \quad (2.49)$$

where:
K_{sp} solubility product constant

Table 2.4: Solubility products of secondary minerals in mine tailings (Stumm, 1992; Brownlow, 1996)

Minerals	**-log K_{sp}**
Calcite $CaCO_3$	8.42
Magnesite $MgCO_3$	7.46
Dolomite $CaMg(CO_3)_2$	17.09
Siderite $FeCO_3$	10.68
Gypsum $CaSO_4 \cdot 2H_2O$	4.6
Ferric hydroxide $Fe(OH)_3$	38.7

Weathering of Rock-Forming Minerals

The are numerous silicate and phosphate minerals that can be found with mine tailings materials, but only a few minerals appear to have any significant effects on the major ion chemistry and pH of mine drainage. Table 2.5 illustrates silicate and phosphate minerals that provide neutralizing capacities when dissolved in acidic environment.

The weathering reaction rates of silicate and phosphate minerals are generally 10^{-3} to 10^{-10}

slower than the oxidation rate of sulphide minerals. Therefore, the dissolution of such minerals will not buffer the pH at higher value, but will have some effect on the overall chemistry of the mine drainage.

Table 2.5: Silicate and phosphate minerals that provide buffering capacities at 25°C (Lowson and Brown, 1996).

Mineral	**Weathering Reaction**	**Rate Constant ($mol \cdot dm^{-2} \cdot s^{-1}$)**
Muscovite / Mica	$2KAl_2(AlSi_3O_{10})(OH)_2 + 2H^+ + 3H_2O \rightarrow 2K^+ + 3Al_2Si_2O_5(OH)_4$	2.5×10^{-15} ($mol^{0.63} \cdot dm^{-0.89} \cdot s^{-1}$)
Kaolinite	$3Al_2Si_2O_5(OH)_4 + 6H^+ \rightarrow 2Al^{3+} + 2H_4SiO_4 + H_2O$	1.8×10^{-15}
Chlorite	$(Mg,Fe^{2+},Fe^{3+})_6AlSi_3O_{10}(OH)_8 + 16H^+ \rightarrow 6(Mg,Fe^{2+},Fe^{3+}) + Al^{3+} + 3H_4SiO_4 + 6H_2O$	1.8×10^{-16}
Feldspar	$2KAlSi_3O_8 + 2H^+ + 9H_2O \rightarrow 2K^+ + 4H_4SiO_4 + Al_2Si_2O_5(OH)_4$	1.6×10^{-15}
Apatite	$Ca_5(PO_4)_3F + 9H^+ \rightarrow 5Ca^{2+} + 2H_3PO_4 + F^-$	4.9×10^{-8}
Pyroxene	$CaMg(SiO_3)_2 + 4H^+ + 2H_2O \rightarrow Ca^{2+} + Mg^{2+} + 2H_4SiO_4$	3.0×10^{-13} ($mol^{0.5} \cdot dm^{-0.5} \cdot s^{-1}$)

MATERIALS AND METHODS

The laboratory experiments included physical methods (particle size and specific surface area), physico-chemical methods (mineral composition), wet chemical methods (water chemistry), and microbiological methods (bacterial inoculum, enumeration). The methods are presented below.

MATERIAL CHARACTERIZATION

Museum (or specimen) grade pyrrhotite samples were obtained from several mineral supply companies across North America. Sample locations included Abitibi Quebec, Northern Ontario, Virginia, Montana, New York, and Eastern Quebec. Table 3.1 lists the descriptions of the various pyrrhotite samples, the localities where the pyrrhotite samples were obtained, and the mineral supply companies where the pyrrhotite samples were purchased.

Table 3.1: Descriptions, suppliers, and localities of the twelve pyrrhotite samples.

Sample ID	Pyrrhotite Description	Supplier	Locality
Po-M-1-93	Massive	Hawthorneden	D'Alambert, Abitibi
Po-M-2-94	Massive	Mineralogical Research Co.	Near Crown Pt. Adirondack Mts. Essec Co. NY
Po-M-3-94	Massive	Continental Minerals	Cable Mine Deer Lodge Co. Montana
Po-M-4-94	Massive	Continental Minerals	Movat Mine Nye, Stillwater Co. Montana
Po-C-5-94	Crystalline	Hawthorneden	Mina Potasi, Santa Eulalia, Chihuahua, Mexico
Po-M-6-94	Massive	Hawthorneden	Cornog, PA
Po-M-7-94	Massive	Hawthorneden	Gaspe
Po-M-8-93	Massive	unknown	Unknown
Po-M-9-91	Massive	unknown	Unkown
Po-M-15-93	Massive	Wards Sci.	Virgina
Po-M-17-93	Massive	Hawthorneden	Northern Ontario
Po-M-19-94	Massive	Hawthorneden	Eastern Township, Quebec

Pyrrhotite samples were visually inspected for any apparent impurities. On two samples, visual impurities were chipped away before crushing. Samples were crushed in a jaw crusher and

further ground in a ceramic ball mill. A single sample was ground first in a jaw crusher, equally subdivided and size reduced by a sledge hammer, shatterbox, and ball mill to assess the effects of grinding method on specific surface area. The ball mill samples were reduced by a wet and dry grind, and a grind with increased rotational speed.

Pyrrhotite concentrates were collected from Inco Limited Copper Cliff Mill in December 7, 1995. The pyrrhotite concentrates were collected prior to discharge and therefore can be assumed to represent the waste materials in the pyrrhotite tailings.

Particle Size Distribution

A typical 200 gram sample was wet sieved through a 45 μm (325 mesh) Tyler screen pan to remove very fine particles (clay-sized material). The minus 45 μm sample was collected for weight measurement. The larger size fraction was sieved through five screen pans with openings of 45 μm, 63 μm (250 mesh), 90 μm (170 mesh), 125 μm (120 mesh) and 180 μm (80 mesh), using a Rototap shaker. The weight of each size fractions was measured to determine the particle size distribution.

Chemical Composition

The chemical composition of the pyrrhotite concentrate was determined using neutron activation analysis (INAA) and inductively coupled plasma emission spectrometry (ICP).

The pyrrhotite samples were submitted for quantitative analysis of cations and total sulphur. The analysis of cations utilizes both INAA and 4 acids digestion followed by ICP. This analytical protocol gave reliable cation compositions at a reasonable cost. The total sulphur content was measured using a Leco Carbon-Sulphur analyzer, which uses an infrared spectrometry technique.

Mineralogical Composition

A Siemens™ Diffractometer D-500 was used for all X-ray diffraction (XRD) measurements. Standard X-ray powder techniques were employed using CuK_α radiation (λ=1.5418 Å) generated at 40 kV and 30 mA. Scans of the pyrrhotite samples were taken between 43° and 45°, 2θ (d-spacing=2.103 to 2.015 Å) to determine hexagonal and monoclinic composition employing techniques similar to those reported by Graham (1969) and Arnold (1966). The resulting spectra between 43° and 45°, 2θ were separated using a peak fitting computer program employing

Gaussian techniques. The hexagonal variety produces a sharp single peak at about 43.8°, 2θ (d-spacing=2.066 Å) while monoclinic pyrrhotite gives doublets of approximately equal intensity at about 43.9°, 2θ (d-spacing=2.064 Å) and 44.1°, 2θ (d-spacing=2.054 Å). Troilite produces a single peak at 43.2°, 2θ (d-spacing =2.093 Å). A second random powder scan between 3° and 90°, 2θ (d-spacing=29.450 to 1.090 Å) on the pyrrhotite samples was used to determine the presence of mineral impurities.

The X-ray diffraction measurements can identify qualitatively the presence of minerals in the pyrrhotite sample, but cannot provide an accurate quantitative value. Given the knowledge of the mineral present, an estimate of the mineralogical composition can be made using the cations and sulphur concentration based on the theoretical mass balance (such as: chalcopyrite as CuFeS, pentlandite as $Ni_5Fe_4S_8$ (with 1.2% trace cobalt), galena as PbS, pyrrhotite as Fe_7S_8 (with 0.8% trace nickel), pyrite as FeS_2 and sphalerite as ZnS(with 1.2% trace iron)) listed in Table 3.2.

Table 3.2: Theoretical chemical compositions of sulphide mineral in Sudbury, ON.

Mineral	Composition (%)						
	Cu	Co	Ni	Pb	Zn	Fe	S
Chalcopyrite	34.62					30.43	34.95
Pentlandite		1.20	35.80			29.80	33.20
Galena				86.58			13.42
Sphalerite					65.90	1.20	32.90
Pyrrhotite			cNiPo (0.80)			59.60	39.60
Pyrite						46.55	53.45

Microprobe Analysis

Trace metals in the pyrrhotite matrix were determined for the twelve pyrrhotite samples using a JOEL JXA-8600 SUPERPROBE. The samples were measured on a faraday cup with an accelerating voltage of 25 kV and probe current of 50 nanoamps. The probe counted 20 seconds on both the peak and background for iron and sulphur, and 30 seconds on the peak and background for the trace elements. The elements analyzed, with their detection limits expressed

as weight percent, were: Mn, 0.013 %; Co, 0.014 %; Ni, 0.015 %; and Cu, 0.018%. The standards for calibration were stoichometric FeS for Fe and S, millerite (NiS) for nickel, chalcopyrite ($CuFeS_2$) for copper, pure Co metal for Co and pure Mn metal for Mn.

Specific Surface Area

Specific surface area values were determined for most size fractions for the twelve pyrrhotite samples using a GEMINI II 2375 BET surface area analyzer. The samples were evacuated on the GEMINI sample preperation unit for 24 hours or until the gas pressure inside the chamber tube fell below 25 millitorr. The instrument's detection limit quoted by the manufacturer is 0.01 $m^2 \cdot g^{-1}$ with nitrogen used as the adsorptive gas. Approximately 12 grams of sample were used in each analysis. A five point BET measurement was used to calculate the specific surface area.

DETERMINATION OF INTRINSIC KINETICS

Kinetic experiments were performed under four different conditions: i) oxidant-free (anoxic and without chemical oxidant), ii) chemical oxidation (anoxic and ferric iron as oxidant), iii) abiotic oxidation (aerobic and molecular oxygen as primary oxidant) and iv) biotic oxidation (aerobic and bacterial catalysis). Experiments were performed under various physio-chemical conditions of pH and temperature to examine the effects of these variables on oxidation kinetics. Chelating agents such as EDTA were used in the abiotic experiments to clarify the effects of oxidation of ferrous to ferric iron by molecular oxygen without hydroxide precipitation.

The pyrrhotite samples were wet sieved through 45 μm screen pan to remove very fine particles (clay-sized material). Materials larger than 45 μm will then be sieved through five sieves using a rototap shaker for 30 minutes. The mass fractions sized between 63 and 90 μm (75 μm nominal particle diameter), and 90 and 125 μm (106 μm nominal particle diameter) was used for the kinetic studies.

Individual size fractions were cleaned to remove residual fine particles and oxidation products in the following way. The sieved sample was suspended in methanol by stirring repeatedly until a clear supernatant was obtained. The sample was then cleaned for 30 to 45 seconds in an ultrasonic cleaner. The sample was rinsed in methanol repeatedly until the supernatant appeared clear and colourless. The sample was further washed with 6N HCl followed by distilled water, and rinsed several times with fresh methanol and air dried.

The washed pyrrhotite samples were be re-sieved to obtain the size fraction between 63 and 90 μm and size fraction between 90 and 125 μm.

Reactor Configurations

Kinetic studies were conducted using two type of reactor systems. Majority of the kinetic experiments were conducted using 0.65 L internal split-flow airlift reactors. The second reactor system was a continuous stirred tank reactor.

Internal Split-Flow Airlift Reactor

The internal split-flow airlift reactor system was used to determine the effect of each controlling factor (pH, temperature, bacterial catalysis) on the rate of pyrrhotite oxidation. The reactors had a total volume of 0.65 L, and consisted of an internal diameter of 5.6 cm and a height to diameter aspect ratio of 7 (Figure 3.1). Each reactor was water jacketed to maintain a constant temperature set between 4°C to 40°C ±0.1°C. Oxygen transfer and fluid mixing were provided by sparging air or nitrogen through a 110 μm sintered glass sparger at the bottom of the reactor. The solids loading varied from 1.67 g/L (1 g in 0.6 L) to 8.33 g/L (5 g in 0.6 L). The airlift reactor was operated under continuous flow-through mode, fresh medium was continuously delivered into the airlift reactor at a rate of 30 $mL \cdot hr^{-1}$ while the effluent was withdrawn from the top of the reactor at the same flow rate. Solids were retained in the reactor by cotton filters installed at the inlet and outlet ports. Under continuous operation, the pseudo steady-state extent of the pyrrhotite oxidation could be obtained from the difference in dissolved sulphate and iron concentrations between the inlet and outlet streams.

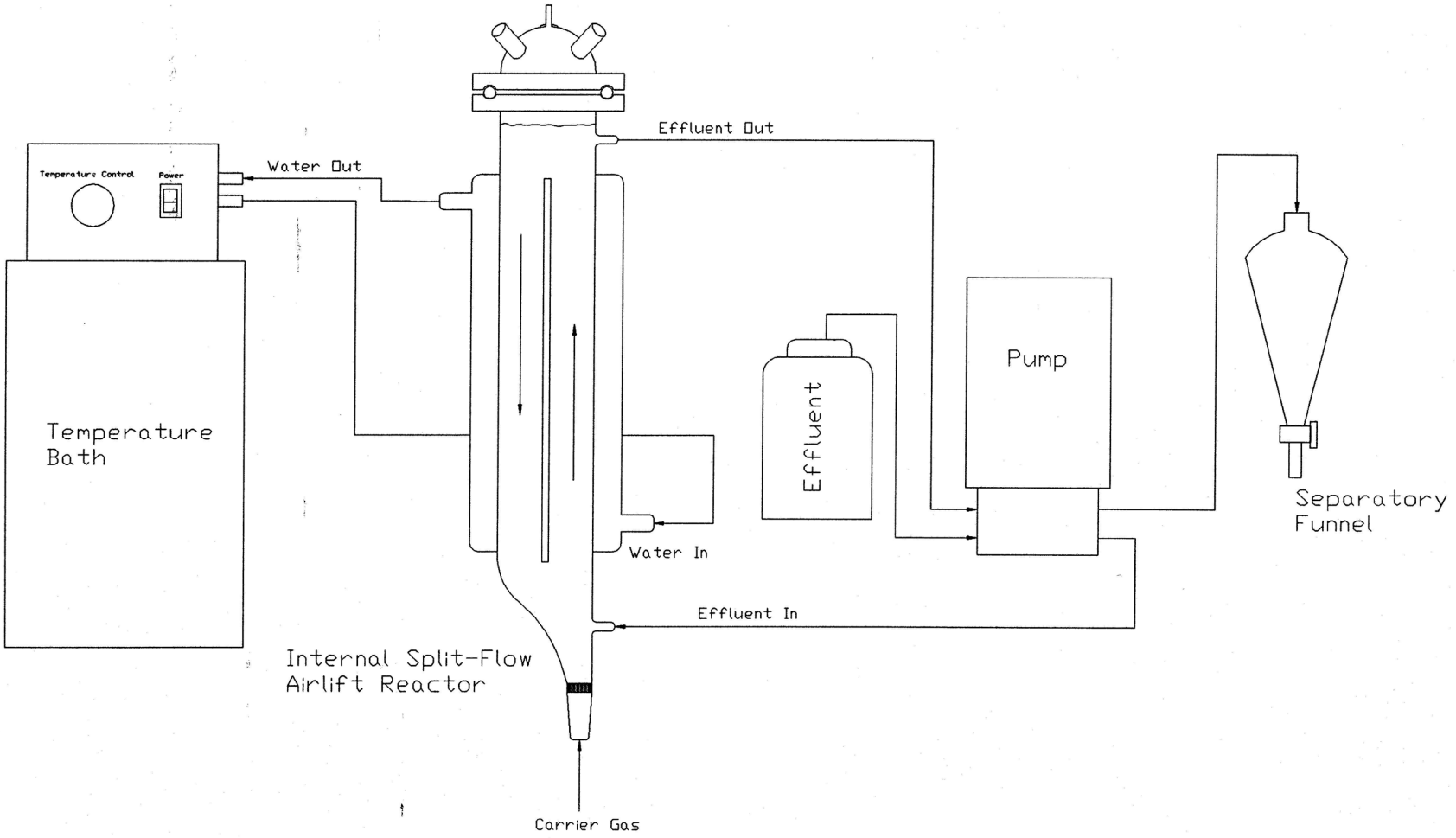

Figure 3.1: Internal spilt-flow airlift reactor

Stirred Tank Reactor

Stirred tank reactors were used for investigation of anoxic dissolution of pyrrhotite, such as non-oxidative pyrrhotite dissolution and anoxic ferric iron oxidation on pyrrhotite. Experiments performed in airlift reactors had no control on the formation of hydrogen sulphide, therefore it was difficult to close the sulphur balance. The stirred tank reactor (Figure 3.2) was operated as a closed reactor to maintain anoxic conditions within the reacting system and minimize evolution of H_2S.

Oxidation studies with Fe^{3+} were performed in 0.43 L, cylindrical, closed, stirred, glass reactors immersed in a water bath and held at constant temperatures ranging from 7.5 °C to 35 °C ±0.1°C as described by Janzen (1996). Oxygen removal was accomplished by passing N_2 through a sparger near the bottom of the vessel. The solution pH was adjusted in both reactors with HCl to pH values between 2 and 3. The solids loading rate used in the kinetic studies was 3.9 $g \cdot L^{-1}$. Liquid samples were extracted from the reactors periodically. During sampling, 20 mL of DI water (adjusted to the starting pH value of the reactor) was delivered into the reactor while 20 mL was simultaneously removed. Known quantities of $FeCl_3 \cdot 6H_2O$ were added to the continuous stirred reactors to establish initial Fe^{+3} concentrations between 1 x 10^{-2} and 1x10^{-4} $mol \cdot L^{-1}$. Solution samples were taken at the beginning and at the end of each run. The remaining measurements were made via a platinum electrode using a method similar to Rimstidt et al., (1994). The electrode readings were collected by a computer and a data logger. The response of the platinum electrode was measured periodically between experiments in Zobell solution (Langmuir, 1970) and never deviated more than 2 mV from the theoretical reading. Electrode measurements were collected every 30 seconds. A FORTRAN computer code (IRON SOLVER) was also developed specifically to convert the platinum electrode readings (mV) collected during the Fe^{3+} oxidation experiments to Fe^{3+} and Fe^{2+} concentrations. The Eh measurements were converted to Fe^{2+} and Fe^{3+} concentrations using the measured initial and final total iron concentrations and accounting for total iron increase at each time step. A flow chart for the computer code IRON SOLVER appears in Figure 3.3.

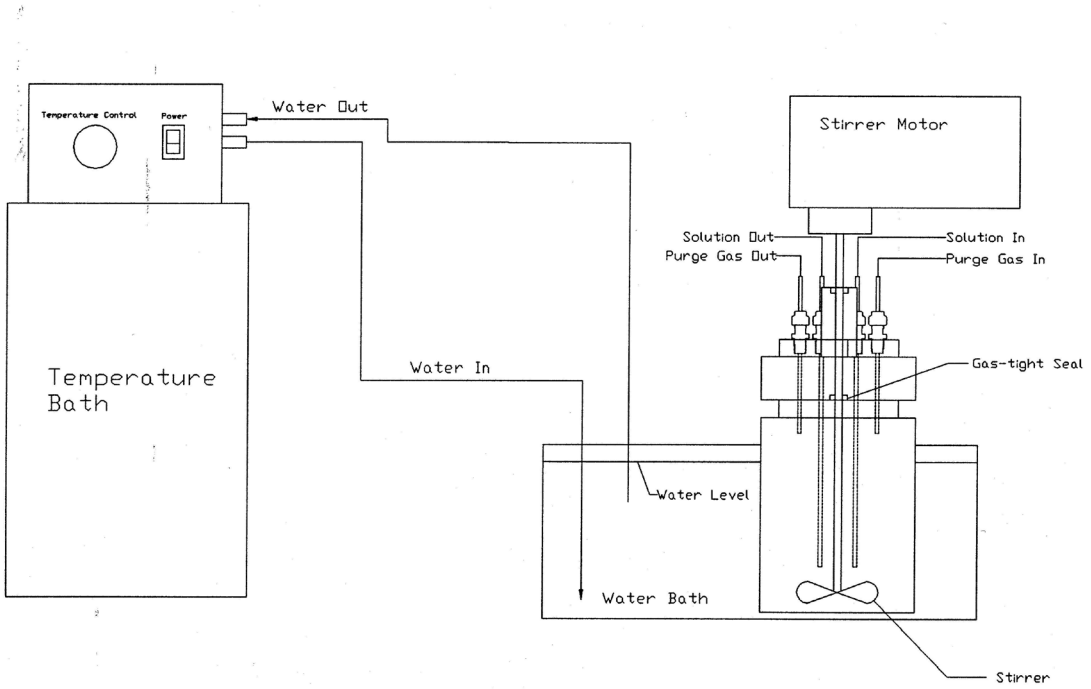

Figure 3.2: Stirred tank reactor

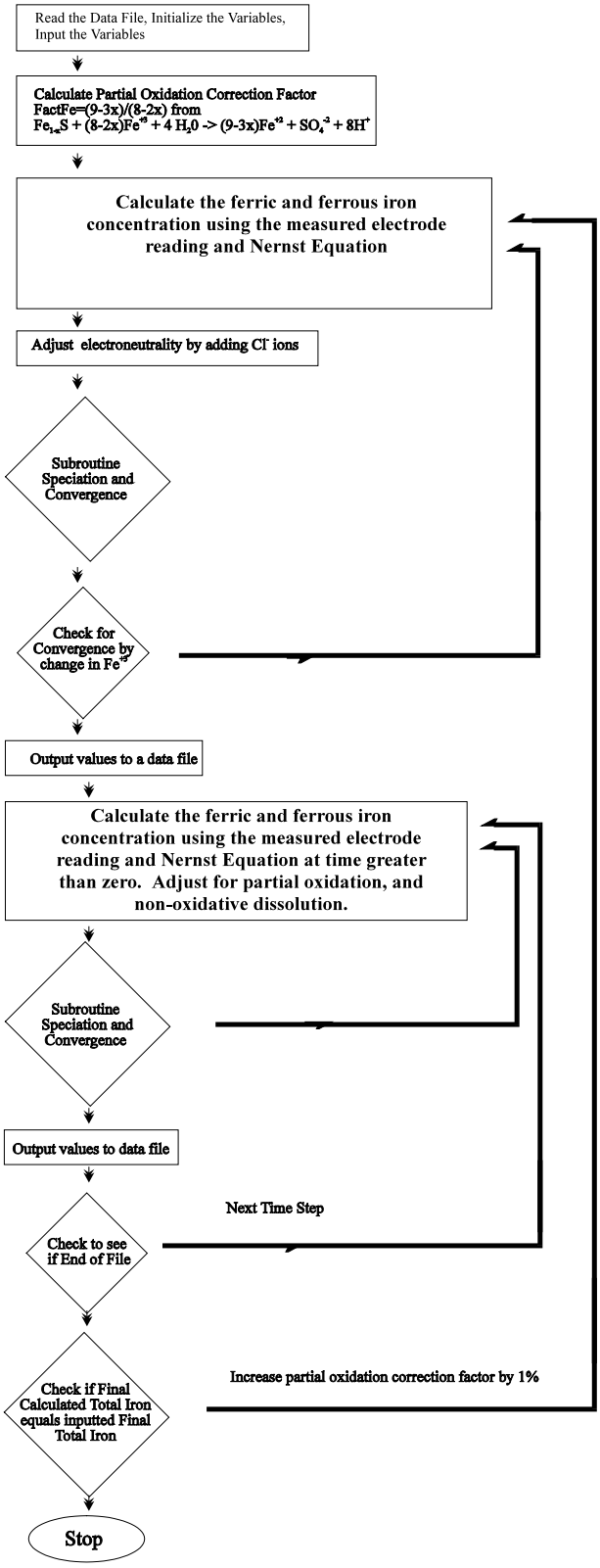

Figure 3.3: Flow chart for the program IRON SOLVER

BACTERIAL INOCULUM

The biological inoculum for the biological studies was obtained from acid mine drainage at Elliot Lake, Ontario, Canada. After one year of acclimatization with pure pyrrhotite, an essentially monotypic culture of *Thiobacillus ferrooxidans* was attained. The pyrrhotite samples used for bacterial enumeration experiments were wet sieved through 45 μm screen pan and washed with methanol to minimize biological growth on the sample during storage.

The aqueous medium used for the growth of *Thiobacillus ferrooxidans* was essentially identical to the standard medium used by other researchers, except the 9K medium used for the studies was comparatively more diluted. The modified 9K medium used for the biological studies was designed to be as simple as possible. The chemical composition of the aqueous medium is shown in Table 3.3.

Table 3.3: Chemical composition of aqueous growth media for *Thiobacillus ferrooxidans*

Components	**Modified 9K medium (per litre)**	**Starkey medium (per litre)**
$(NH_4)_2SO_4$	0.25 g	0.30 g
$MgSO_4 \cdot 7H_2O$	0.04 g	0.5 g
K_2HPO_4	0.125 g	
KH_2PO_4		3.5 g
$CaCl_2 \cdot 2H_2O$		0.25 g
H_2SO_4 (pH adjustment)	to pH = 2 or 3	to pH = 4.5
Energy Source	50 g of $FeSO_4$, or 50 g of pyrrhotite	10 g of precipitated sulphur

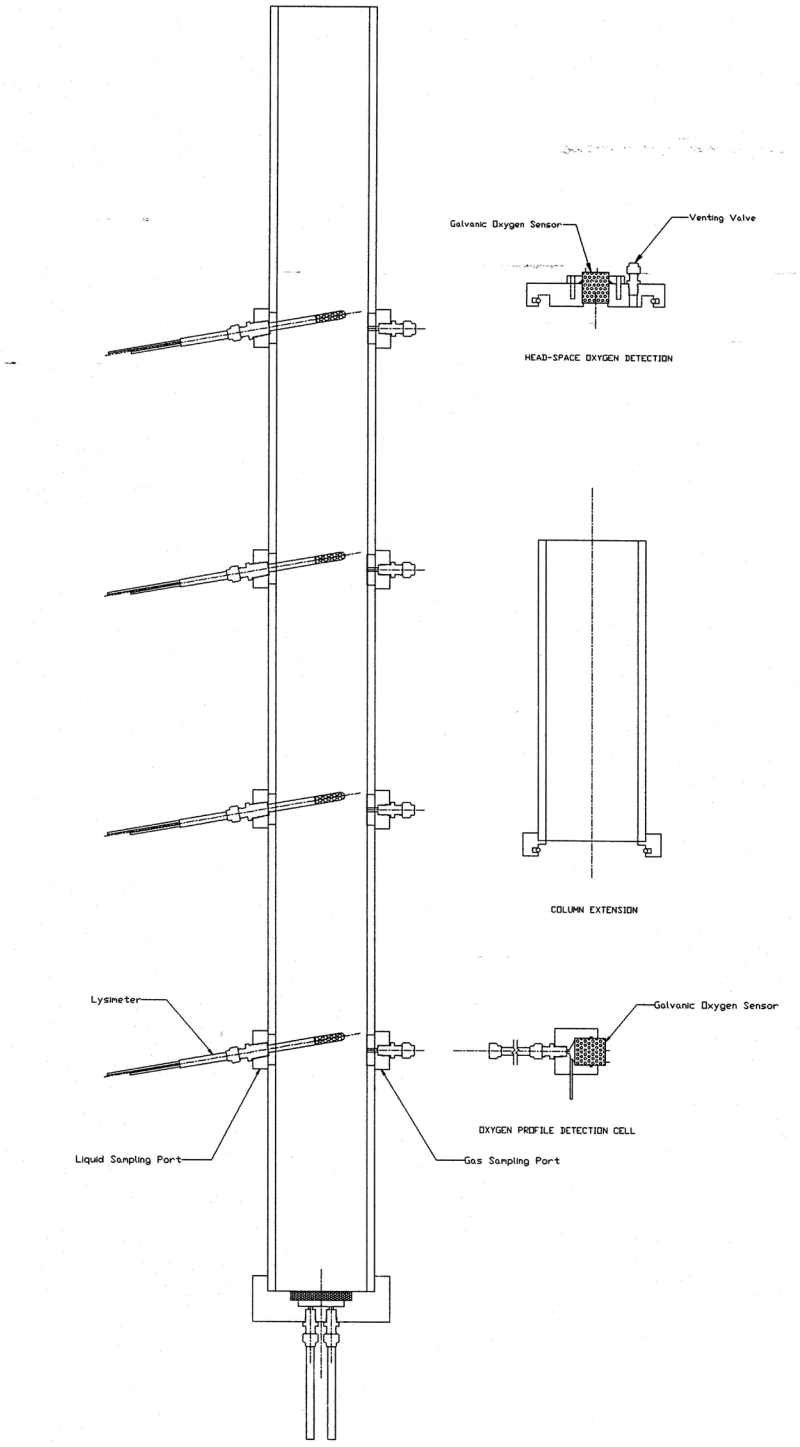

Figure 3.4: Column layout

The ingredients potassium chloride (KCl) and calcium nitrate ($Ca(NO_3)$) were omitted from the modified 9K medium used in the biological oxidation of ferrous and mineral sulphide. Potassium and chloride ions were supplied as K_2HPO_4 and $CaCl_2$, respectively. The nitrogen requirement is met by (NH4)2SO4, therefore, no addition of $Ca(NO_3)_2$ is necessary.

Double de-ionized water was used for the preparation of the biological media. The media were heat sterilized before the addition of an 'energy source', at 120 °C and 1.2 atm for approximately 15 minutes. The inoculum size ranged from 10 % (by volume) for cell culture and 5 % (by volume) for kinetic testing.

Shake flask cultures (500 mL) with 10 % inoculum (v/v) were grown in 1 L Erlenmeyer flasks at ambient temperature on a rotary shaker at 175 rpm for 21 days.

COUPLING OF MASS TRANSFER WITH OXIDATION KINETICS

Column Configurations

Altogether 6 columns packed with tailings analogues were employed. Each packed column had an internal diameter of 7.62 cm and a height of 1.05 metres (Figure 3-4). Each column was equipped with four liquid sampling ports and four gas sampling ports for measurement of porewater concentrations and oxygen concentrations at different heights in the column. The moisture content in the column was adjusted using a porous ceramic disk installed at the bottom of the column.

The column was packed to a height of 1 metre and contained approximately 4.56 litres of solids in bulk volume. Inco pyrrhotite concentrate was used as the sulphide component of the solids in the column. The pyrrhotite concentrate was pre-sieved through a 45 μm sieve to remove fine particles. Quartz sand was mixed with the pyrrhotite concentrate to lower the sulphide content (2 % and 6 %) in order to accelerate the profile development in the packed column. Each of the six columns was set to a different condition to investigate different scenarios that may be encountered in the field. The combinations used in each of the six columns are listed in Table 3.4.

Table 3.4: Conditions used in packed columns.

Condition	Designation	Approximate Sulphur Content (%)	Special Conditions
#1	Base Case	6	None
#2	2 % S^{2-}	2	None
#3	Bacterial inoculated	6	with *Thiobacillus ferrooxidans* inoculations
#4	1% Calcite	6	with 1 % calcite buffer
#5	5 % Enstatite	6	with 5 % buffering silicate (Enstatite)
#6	With Fines	6	with minus 45 μm particles

The packed column was designed to investigate the coupling of oxidation kinetics with geochemical and transport processes, such as diffusion of oxygen, buffering reactions, precipitation and adsorption. These processes were measured using overall contaminant loading data, headspace oxygen consumption measurements, porewater chemistry and pore-space oxygen concentration profiles. Sampling was performed biweekly to allow sufficient time for sulphide oxidation to occur between samples.

Contaminant Loading

Overall contaminant loading was obtained by flooding the column from the bottom until a 16 cm water head was obtained above the top of the soil surface (a special column extension is used for the flooding of the column). Flooding from the bottom of the column prevented entrapment of air pockets in the column. The column was allowed to drain with the water table set at vertical distance of 1.5 m below the bottom of the column. The column was allowed to drain for 1 to 2 days before the water table was reset to the operating level (bottom of the column).

The drained liquid was analysed for pH, total iron, nickel, and sulphate concentrations. Since the environment was not anoxic, the use of Eh conjunction with the computer program IRONSOLVER was not applicable.

Headspace Oxygen Consumption

Headspace oxygen consumption measurements can provide data for maximum sulphide oxidation rates with no prior knowledge of the diffusion coefficient for oxygen in the column. A

special cap equipped with a galvanic oxygen sensor to provide oxygen concentration decline in the fixed headspace gas volume was designed. An o-ring was installed in the sensor cap to ensure that no gas transfer occurs during measurement. The sensor cap is shown on Figure 3.5. The sensor cap, with the venting valve open, was placed on the column after a pseudo steady-state condition was achieved between flooding. All flooding and drainage tubes were closed to prevent any atmospheric pressure effect during sampling. Measurement was initiated by closing the venting valve. The oxygen concentration data were obtained using a multi-channel voltmeter connected to a computer.

Porewater Concentration Profiles

Four suction lysimeters were installed in the column at a distance of 20 cm apart. The lysimeter employed a porous ceramic cap that allows liquid passage only, without gas entry up to a suction pressure of 0.5 bar (approximately 50 kPa). The lysimeter is shown in Figure 3.6. The lysimeters were connected to a vacuum pump at 36 kPa suction pressure. Approximately 5 to 10 mL of porewater was drawn through the lysimeter into a sample bottle from each of the sampling ports. The porewater samples were analyzed for pH, total iron, ferrous iron, nickel and sulphate concentrations. The presence of dissolved oxygen in some of the samples precluded the application of the IRONSOLVER program. These data provide a concentration-height profile for each contaminant, which was used for estimation of precipitation and adsorption reactions in the column.

Pore-space Oxygen Concentration Profiles

To identify the location of the oxidation zone and buffering region in the column, the pore-space oxygen concentration data could be used to indicate the region where highest oxygen consumption occurred. A galvanic oxygen sensor cell was installed with a connecting unit, and was attached to the gas sampling port (20 cm apart) along the column. The detection cell is shown in Figure 3.7. After the sensor was attached to the column, 5 mL of gas was drawn off the remove oxygen in the stagnant space adjacent to the sensor. This significantly shortens the time necessary for the measurement. The duration of each measurement was approximately 3 hours. The oxygen data were logged using a multi-channel voltmeter connected to a computer.

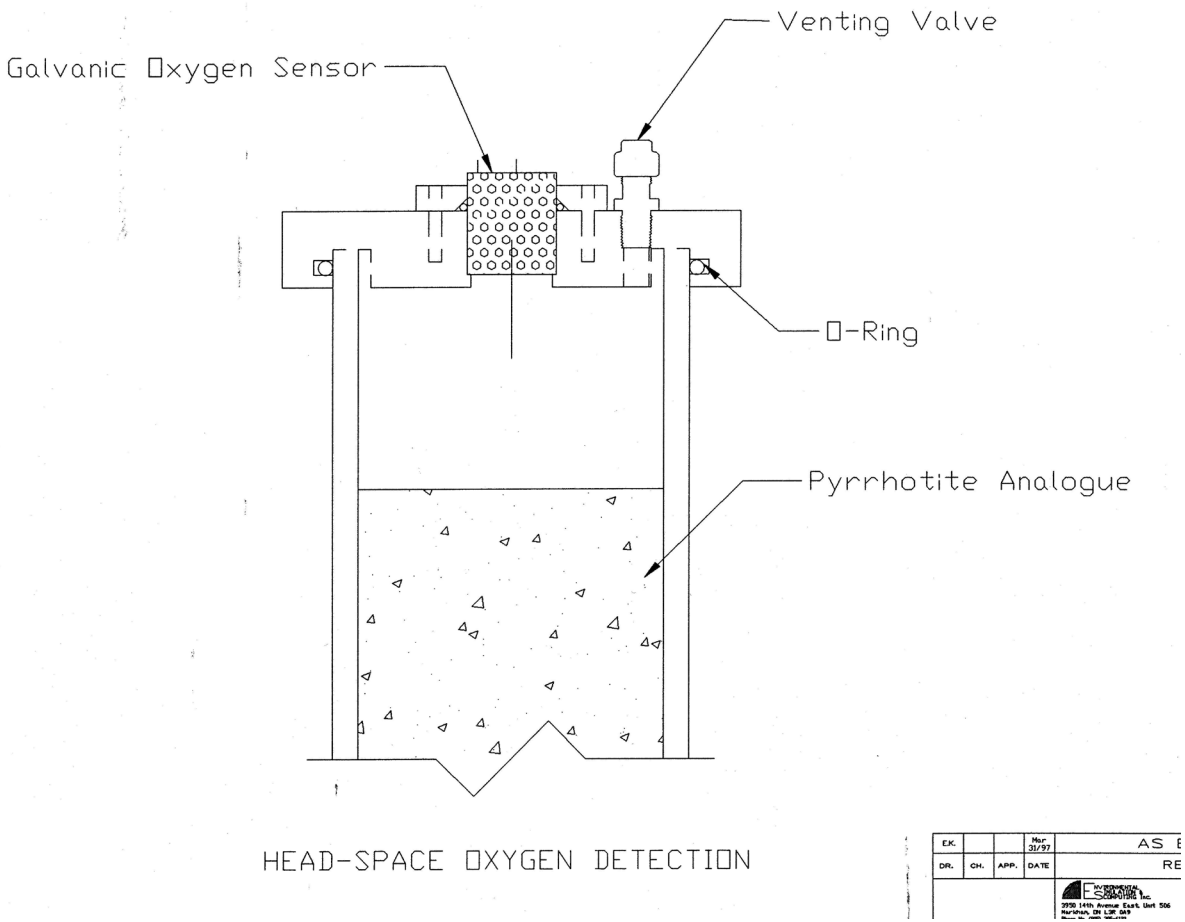

Figure 3.5: Headspace oxygen consumption cap with galvanic oxygen sensor

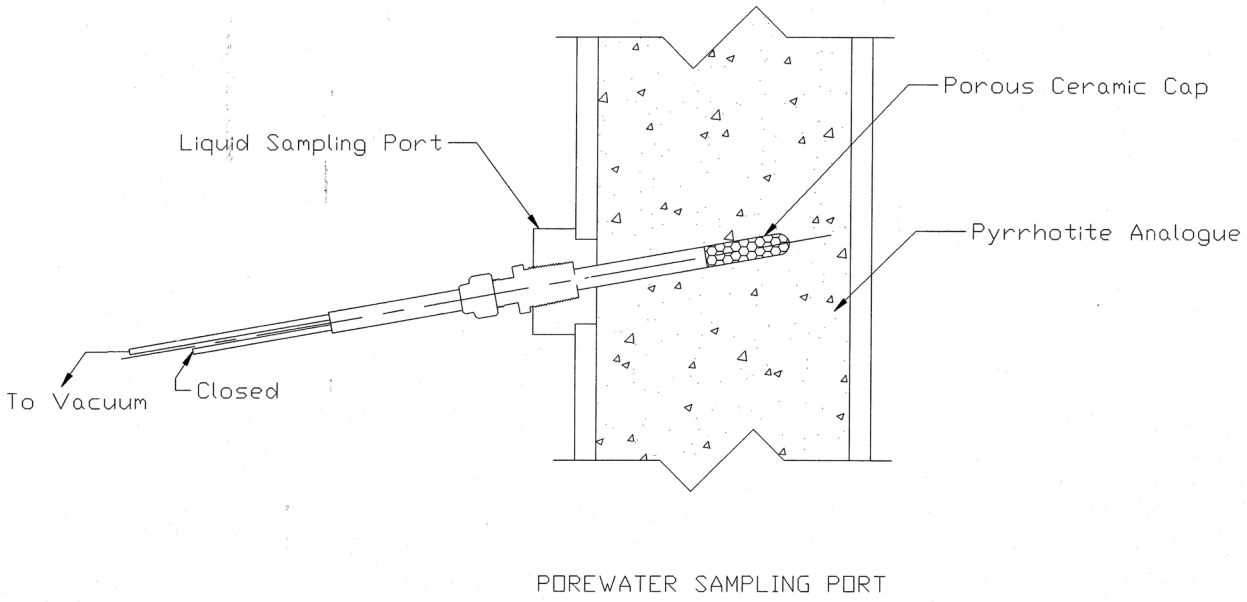

Figure 3.6 Lysimeter for porewater extraction

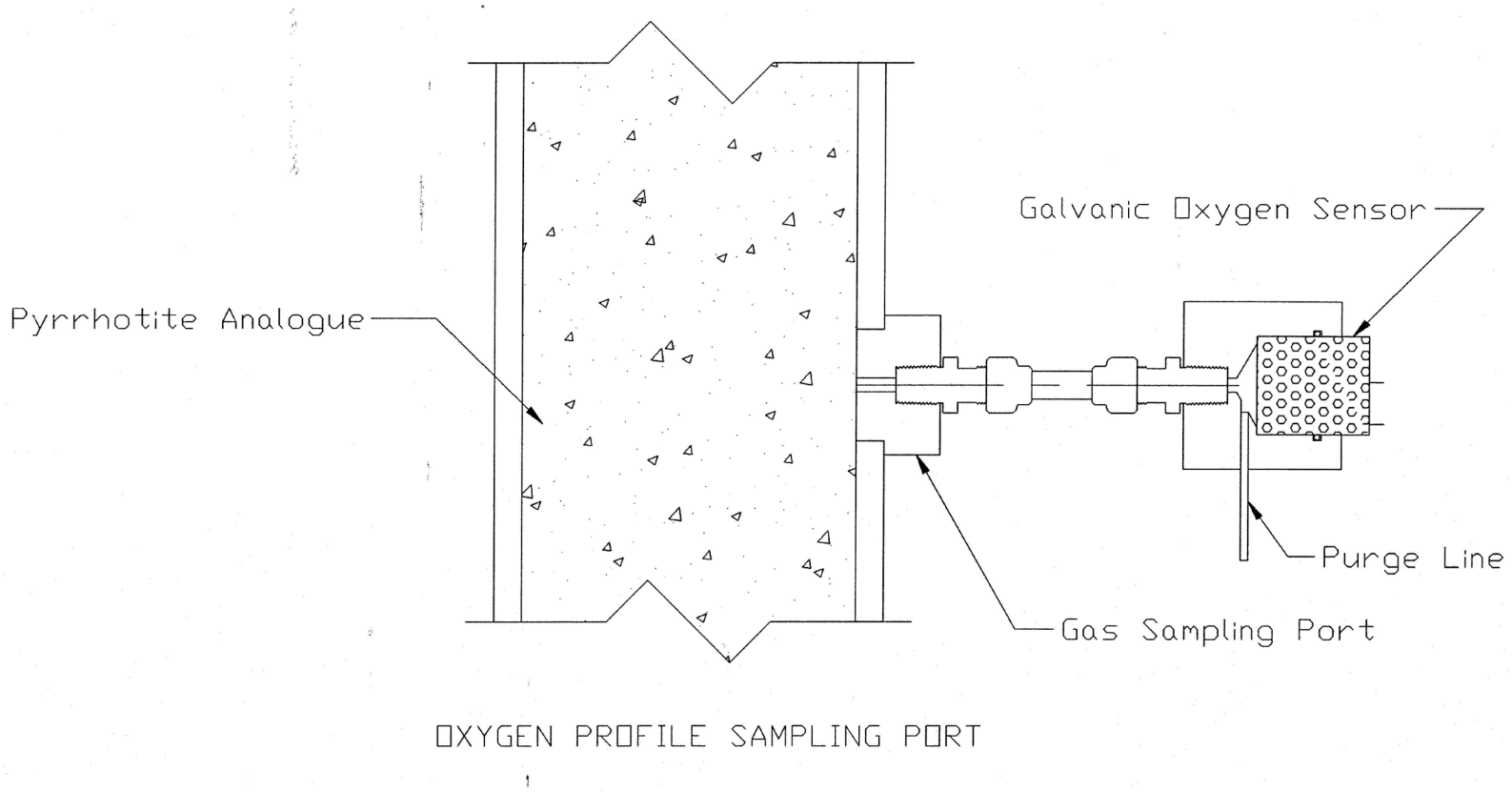

Figure 3.7 Oxygen profile sampling port with galvanic oxygen sensor

ANALYTICAL TECHNIQUES

Liquid samples taken during the kinetics and column experiments were analyzed for dissolved ferrous (Fe^{2+}), total dissolved iron, dissolved nickel (Ni^{2+}) and sulphate (SO_4^{2-}). Selected solid samples after experimentations were sent for chemical compositions and surface textures by scanning electron microscopy.

Ferrous Iron (Fe^{2+}) Analysis - Bathophenanthroline Method

The ferrous iron concentration in the liquid samples were determined colorimetrically using bathophenanthroline (4,7-phenyl-1,10-phenanthroline) reagent as described by Lee and Stumm (1960). This non-oxidative method is reported to be specific for ferrous iron. The presence of other transient metal ions in their lower oxidation state such as manganese, reduced dissolved sulphur compounds (sulphide, thionates, thiosulphates) and dissolved organics (EDTA, products of bacterial activity) preclude the use of methods based on titration by an oxidizing agent. Liquid samples ranging from 0.5 to 1.0 mL are pipetted into a 125 mL separatory funnel and 4 mL of 10 % (wt / vol) sodium acetate ($NaC_2H_3O_2$) solution was then added to buffer the pH at approximately 4. Approximately 15 mL of 0.001M bathophenanthroline was added to complex with the ferrous iron to give a red colour. The iron-bathophenanthroline complex was then extracted from the aqueous phase into an organic phase by adding 10 mL of n-hexanol ($C_6H_{13}OH$). The separatory funnel was then thoroughly shaken and allowed to separate for at least 5 minutes after mixing. The aqueous phase was then drawn off and discarded, while the organic phase was drawn into a 25 mL volumetric flask. The separatory funnel was rinsed with 2 to 3 mL of ethanol to ensure all iron-bathophenanthroline complexes were washed into the volumetric flask. The organic solution was diluted with ethanol to a 25 mL volume.

The colorimetric measurement is based on the absorbance of the organic solution at a wavelength of 533 nm. The relationship between absorbance and ferrous concentration conforms to Beer's law (i.e. absorbance is directly proportional to iron concentration). Ethanol was be used as a blank for the analysis and calibration line was obtained using known concentrations of ferrous ammonium sulphate ($Fe(NH_4)_2(SO_4)_2$) solution.

Total Iron Analysis

There were two analytical methods used for the determination of total dissolved iron. For liquid

samples that had volume greater than 5 mL, atomic absorption analysis was used. Bathophenanthroline analysis was used for liquid samples that had volume less than 5 mL, such as porewater samples extracted from the column experiments.

Atomic Absorption

The atomic absorption spectrometric measurements were performed on an atomic absorption spectrometer (Perkin Elmer Atomic Absorption Spectrometer 3100) employing air as oxidant and acetylene as fuel. The absorption wavelength was set at 279.3 nm with detection slit setting was set at 0.2 and high. Each analysis was performed in triplicate. The absorbance was automatically recorded and integrated by a software package installed on an on-line personal computer. The absorption to concentration relationship follows Beer's law and the calibration curve was obtained using known dilution of iron atomic adsorption standard.

Bathophenanthroline Method

The procedures used to determine the total dissolved iron by bathophenanthroline was the same as those used for ferrous analysis, except ferric iron was reduced to ferrous prior to addition of sodium acetate. The reduction of ferric iron to ferrous was done by the addition of 2 mL of hydroxylamine hydrochloride.

Nickel (Ni^{2+}) Analysis - Atomic Absorption

The nickel analysis procedure was similar to that used for total iron analysis by atomic absorption. The absorption wavelength for nickel is 232.0 nm with detection slit setting at 0.2 and high. The absorption to concentration relationship follows Beer's law and the calibration curve was obtained using known dilution of nickel atomic adsorption standard.

Sulphate (SO_4^{2-}) Analysis - Ion Chromatography

Ion Chromatography with a conductivity detector was used to determine sulphate concentration in liquid samples. The anions separation was achieved by using a Dionex IonPac® AS4A anion separation column with carbonate / bicarbonate buffer eluent (0.18mM sodium carbonate (Na_2CO_3) and 0.17mM sodium bicarbonate ($NaHCO_3$)). A post column suppressor (Dionex Anion Micro-Membrane Suppressor) was used to reduce solution background conductivity due to carbonate / bicarbonate eluent. Conductivity measurements were performed on at least 10 concentrations in the range between 0 to 50 $mg \cdot L^{-1}$ to verify linearity. The conductivity-concentration relationship was calibrated using double de-ionized water as blank and a 50 $mg \cdot L^{-1}$

of sulphate standard (prepared from ferrous ammonium sulphate). The standard conductivity measurements were stored internally by a computer program and used to estimate the concentrations of subsequent samples by employing software supplied by the manufacturer.

Surface Texture - Scanning Electron Microscopy (SEM)

Surface characteristics of the pyrrhotite particles before and after dissolution were investigated using scanning electron microscopy. Dry particles were secured onto a conductive sample stud using a conductive double-sided adhesive tape. Sample studs were coated with gold at a thickness of 120 Å. The gold coating provided additional secondary electrons for better imaging.

PHYSICAL AND CHEMICAL CHARACTERISTICS OF PYRRHOTITE SAMPLES

Detailed characterization of pyrrhotite materials was performed on several specimen-grade pyrrhotite samples in order to access potential effects on reaction rates. Based on those results, a more focused characterization of the pyrrhotite tailings (concentrate) was conducted for materials used in the column experiments.

Specimen-Grade Pyrrhotite Samples

Specific Surface Area

Plots of P/P_o versus N_2 adsorbed were used to determine the linear range of the isothermal adsorption of N_2 on pyrrhotite. A sample plot appears in Figure 4.1. The linear range was determined to be valid from 0.1 to 0.3 relative pressure. Isothermal adsorption of N_2 varies from one material to the next. For example, the linear range of the isothermal adsorption of N_2 on synthetic goethite appears to be valid from 0.1 to 0.25 (Davis and Kent, 1990). N_2 adsorption on goethite appears to be quite different from pyrrhotite illustrating that the linear range of the isothermal adsorption of N_2 needs to be determined for different materials since points in the linear range are used in calculating BET specific surface area (area per unit mass).

Specific surface area measurements are compared graphically to the theoretical geometric specific surface area (based on spheres) and to the specific surface area of cleaned pyrite particles on a log-log plot in Figure 4.2. As the grain fraction decreases in size, the specific surface area of the pyrrhotite increases. Both the pyrite and pyrrhotite specific surface areas were higher than the predicted geometric specific surface areas. This plot clearly shows an envelope for the specific surface areas of pyrrhotite particles that follows a slope similar to the calculated geometric specific surface area. The measured pyrrhotite specific surface areas are a factor of 6-40 times greater than the theoretical geometric specific surface area and a factor of 2-10 times greater than the measured specific surface area of pyrite.

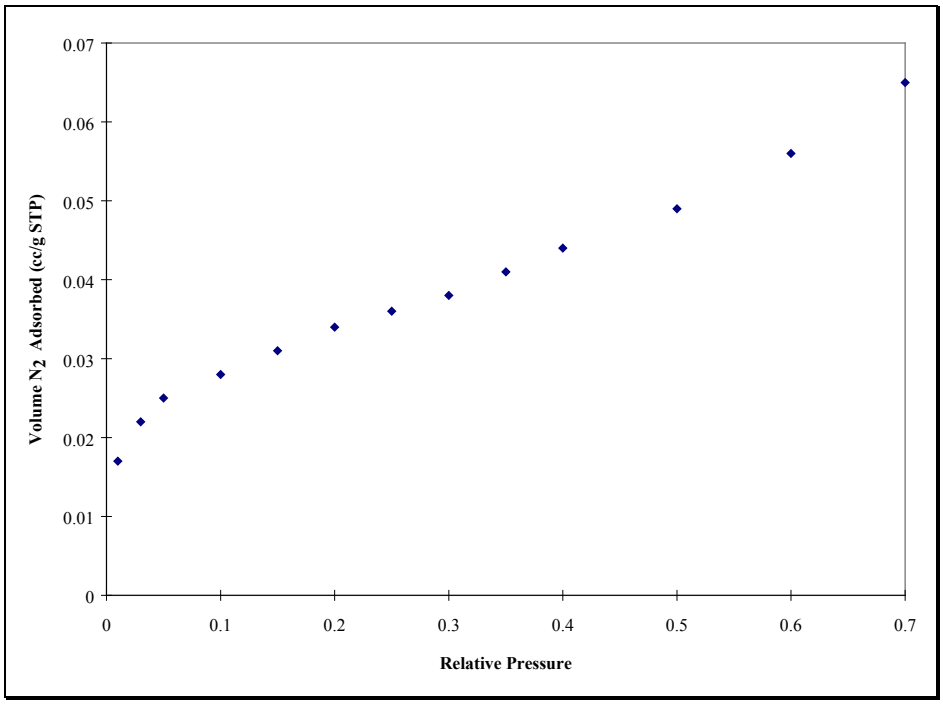

Figure 4.1: Adsorption isotherm for N_2 gas, at 77.4°K, on pyrrhotite.

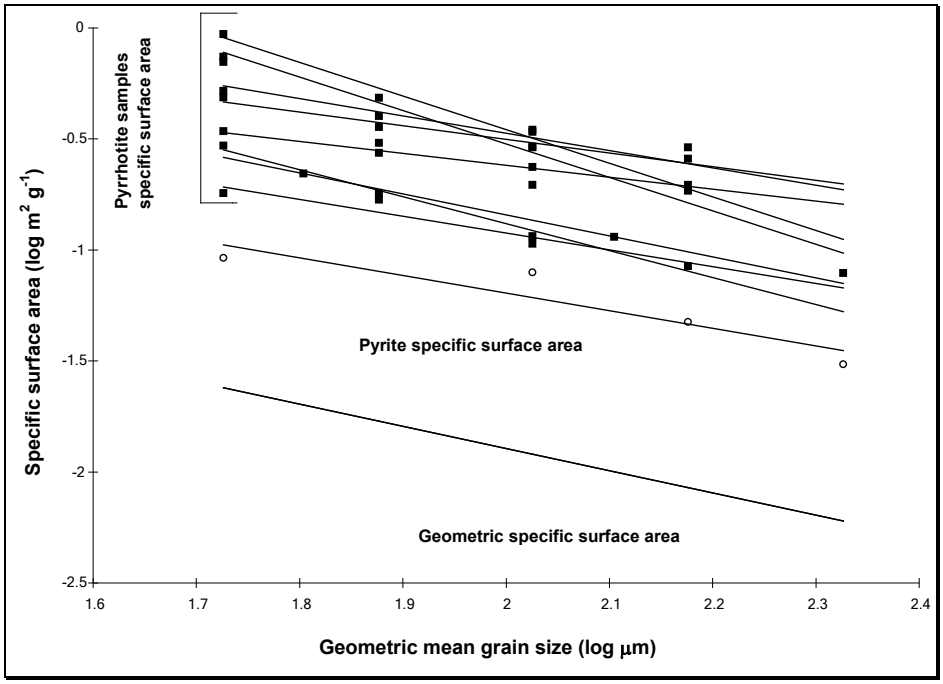

Figure 4.2: Specific surface area comparisons among the twelve pyrrhotite samples, a pyrite sample from Colorado, and the theoretical geometrical specific surface area based on particle size plotted on a log - log axis.

The effects of different grinding techniques on specific surface of pyrrhotite were evaluated since some of the original samples were crushed by unknown techniques by previous investigations. The results are shown in Figure 4.3. The specific surface areas of pyrrhotite treated by various grinding methods converge at grain size 212 μm - the initial starting grain size used before applying separate crushing techniques. However as the particles were further reduced in size and become more characteristic of the different size reduction methods, the specific surface area values of the pyrrhotite samples diverge. A maximum factor of three separating the largest and smallest surface area values for the various crushing techniques. SEM pictures confirmed that the particles were thoroughly cleaned of fine particles prior to surface area analysis. Therefore, it appears that as different forces and strains are imposed on the pyrrhotite sample by different size reduction methods, the specific surface area of pyrrhotite for a given grain size may change.

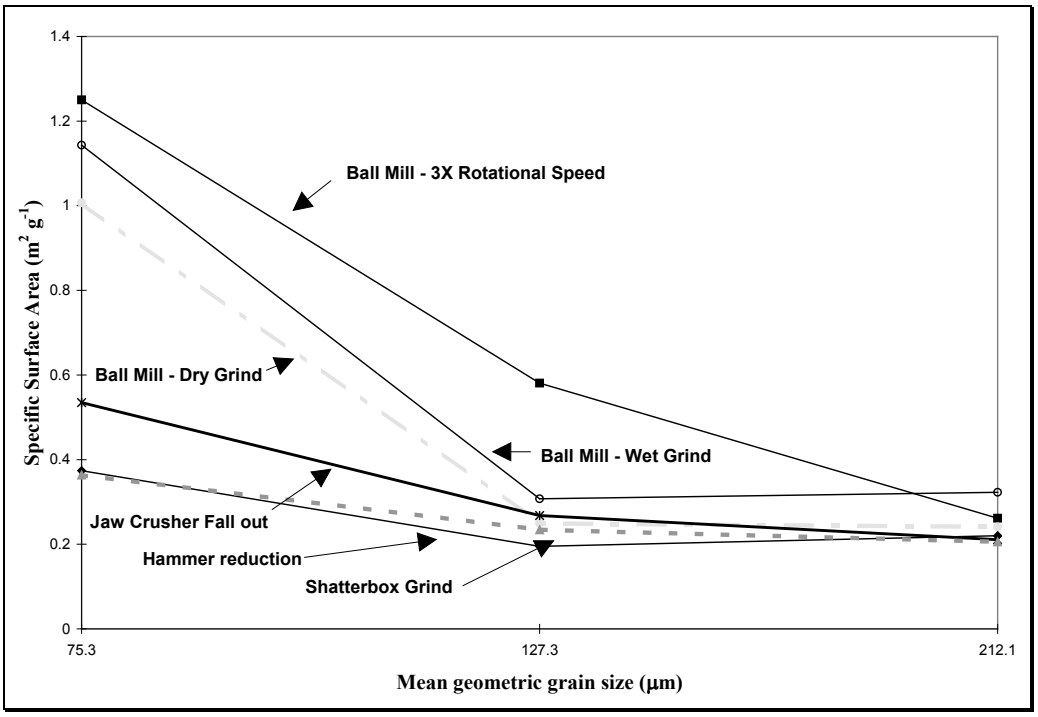

Figure 4.3: The effects of grinding techniques on pyrrhotite specific surface area.

The change in surface area from long term pyrrhotite oxidation by oxygen in air during storage is illustrated in Table 4.1. After 15 months of storage in a dessicator, the specific surface areas of two pyrrhotite samples were re-examined. The specific surface area of both pyrrhotite samples decreased noticeably. Cleaning the pyrrhotite samples in an acid solution revealed that iron oxides/hydroxides formation had occurred on the pyrrhotite surface. The colorless washing

solution turned a rusty brown colour that was characteristic of iron oxides. After cleaning, the surface area for both samples increased.

Table 4.1: Specific surface area of two pyrrhotite samples after 15 months of oxidation.

Sample ID	Condition	Specific Surface Area (m^2 g^{-1})	% of Original Area
Po-M-4-94	Initial specific surface measurement	1.78	-
Po-M-4-94	Air dried sample undergoes O_2 oxidation in storage for 15 months	0.20	11
Po-M-4-94	Sample re-cleaned in HCl acid solution	0.45	25
Po-M-15-93	Initial specific surface measurement	2.10	-
Po-M-15-93	Air dried sample undergoes O_2 oxidation in storage for 15 months	0.32	15
Po-M-15-93	Sample re-cleaned in HCl acid solution	1.81	86

Significant variations in measured specific surface area existed among the pyrrhotite samples, ranging from 0.17 to 2.1 $m^2 \cdot g^{-1}$, for particles in the grain fraction 125-180 μm. Initially, it was thought that the pyrrhotite particles were improperly cleaned (i.e. fine particles remained adhering to the larger particles after cleaning). Secondary particles or "dust" may partially cover larger particles increasing the apparent specific surface area (Nicholson et al., 1988). The fine particles, if not removed, will oxidize more rapidly leading to apparent non-linear rates and misinterpretation of kinetic results. After rigorous cleaning, however, SEM photographs revealed clean surfaces. Surface roughness and fractures are the cause of the higher than expected specific surface areas for pyrrhotite samples (Figure 4.4 to Figure 4.7). The fractures seem to vary in thickness and occur along cleavage planes of the pyrrhotite particles. The fractures are not merely near surface effects; rather, the fractures were found to extend into the pyrrhotite grains (Janzen, 1996). Pyrite surfaces are smooth and absent of fractures (see Figure 4.8) in comparison to the surface morphology of pyrrhotite. These features resulted in a measured specific surface areas for particles of pyrite that were 2-10 times smaller than pyrrhotite particles of a similar size range. Specific surface area was compared graphically to crystal structure and trace metal content (Janzen, 1996). It appears that specific surface area is not related to crystal structure or trace metal content (Janzen, 1996). However, this study has shown that grinding method

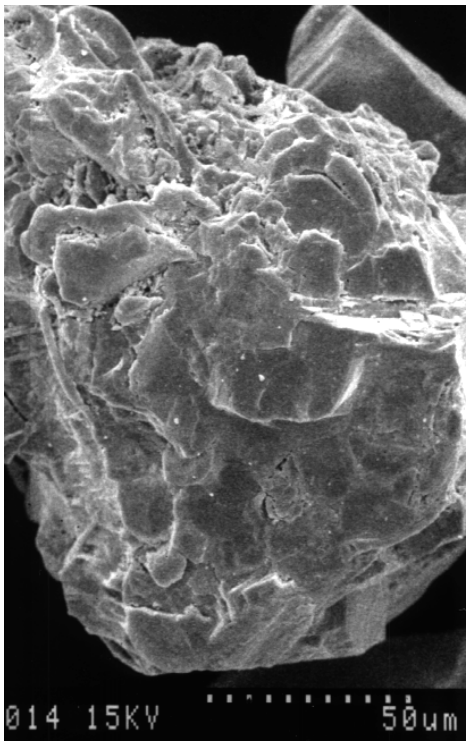

Figure 4.4: SEM photograph of a pyrrhotite grain

Figure 4.5: SEM photograph of a pyrrhotite grain illustrating fractures

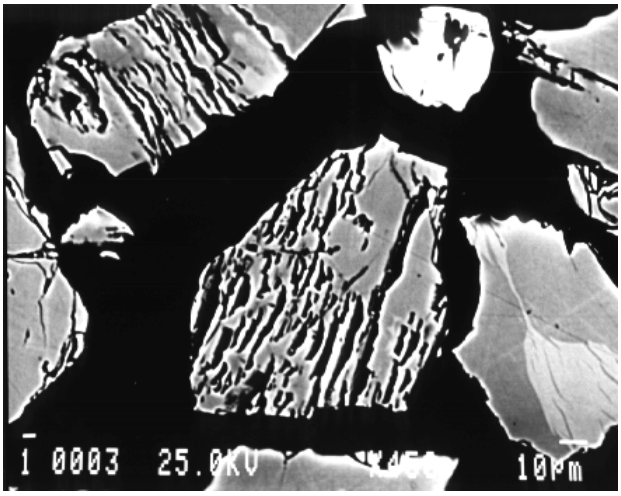

Figure 4.6: Polished section of a pyrrhotite grain illustrating extended fracture network

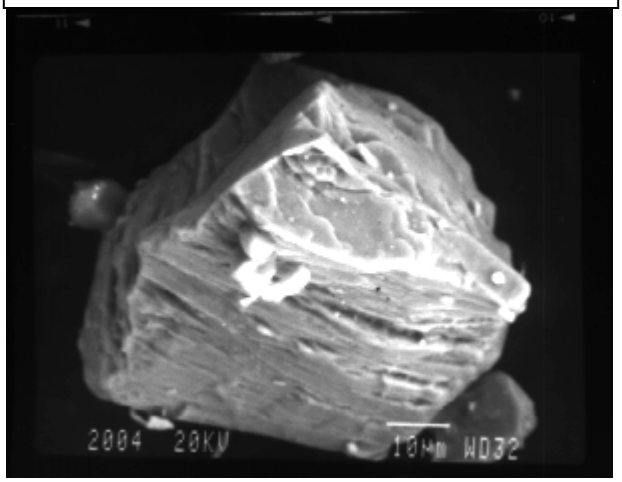

Figure 4.7: SEM photograph of a pyrrhotite grain illustrating fracture surface

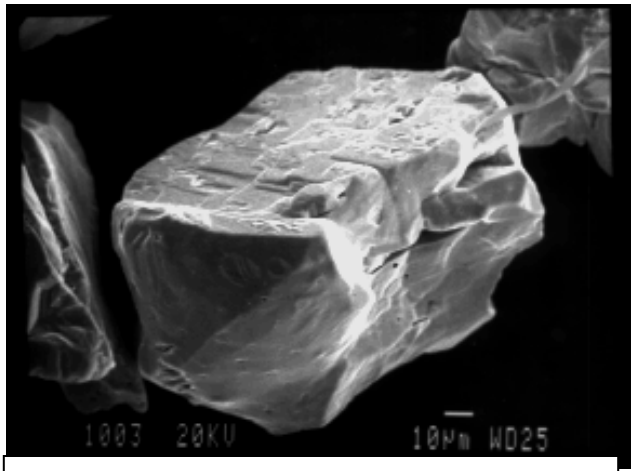

Figure 4.8: SEM photograph of a pyrite grain

can influence specific surface area and may be part of the reason for differences in surface area and apparent differences in observed rates for crushed pyrrhotite samples.

Insight into pyrrhotite oxidation mechanisms was obtained by examining two pyrrhotite samples with high specific surface area. After 15 months of storage, the specific surface areas of two pyrrhotite samples were re-examined. The specific surface area of both pyrrhotite samples decreased noticeably. Cleaning the pyrrhotite samples in an acid solution revealed that iron oxides/hydroxides formation had occurred on the pyrrhotite surface. Based on the previous two observations that oxidation occurred and that the specific surface area decreased leads to the conclusion that pyrrhotite oxidation occurred preferentially in fractures. Preferential oxidation observations at areas of high strain agree with observations from other researchers in the studies of pyrite oxidation (Rimstidt et al, 1994, McKibben and Barnes, 1986) and feldspar weathering (Holdren and Speyer, 1985). After the iron hydroxides/oxides partially were dissolved and removed from the fractures, the specific surface area of both pyrrhotite samples increased.

X-ray Diffraction (XRD) Calibration

A standard curve relating peak areas to hexagonal composition was prepared by adding known amounts of pure hexagonal pyrrhotite with known amounts of pure monoclinic pyrrhotite to produce different compositions of hexagonal and monoclinic pyrrhotite to affirm that peak area distinguishes between hexagonal and monoclinic pyrrhotite. X-ray diffraction scans were performed and interpreted using the techniques described in the method section. The correlation between peak area and percent hexagonal pyrrhotite gave a R^2=0.98 as demonstrated by Figure 4.9. However, the standard curve demonstrates the difficulty in determining low quantities of hexagonal pyrrhotite in the samples as also concluded by Arnold (1966). The detection limit for hexagonal pyrrhotite is approximately 7.5%.

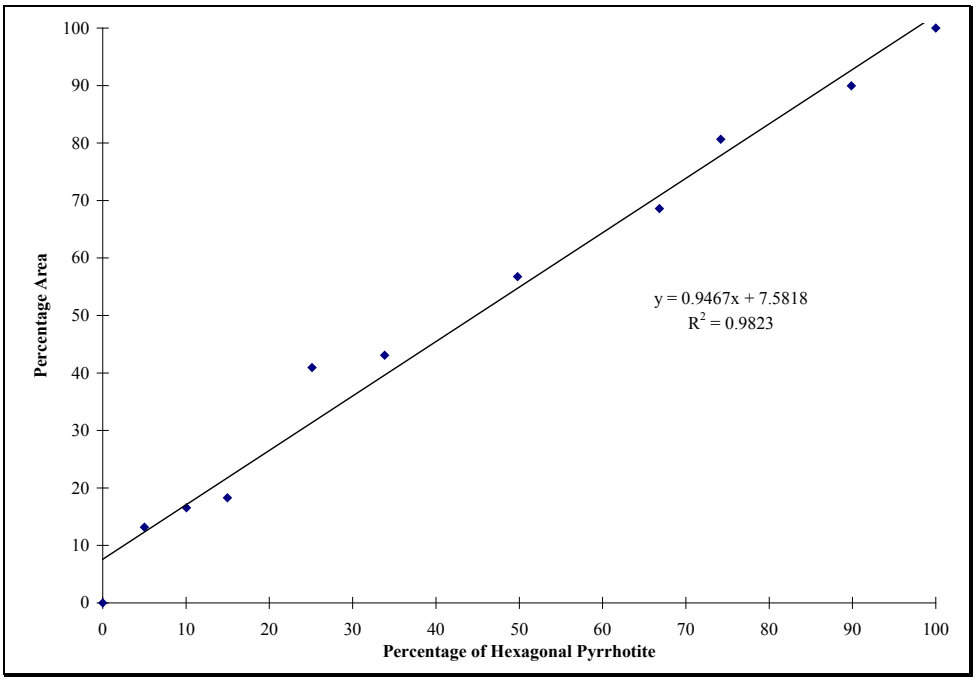

Figure 4.9: XRD standardization - Correlation between peak area and hexagonal composition.

Only cobalt, nickel, and small amounts of copper and manganese were found to substitute for iron in the pyrrhotite samples examined in this study, in agreement with the findings of Arnold (1967), and Deer et al. (1992). Manganese and copper substitution were apparently not significant in the pyrrhotite samples as Mn and Cu were not detected at levels much greater than the detection limit during electron microprobe analysis. No other elements were likely present in significant quantities in the pyrrhotite structure because the mass of iron, sulphur and the four trace elements (not shown) accounted for practically 100% of the mineral composition taking into account instrument error (electron microprobe). The increase in nickel substitution appears to correspond with an increase in bulk nickel concentration (by chemical analysis) in the pyrrhotite sample representing nickel present in accessory minerals plus nickel substituting for iron in pyrrhotite. Cobalt substitution follows a similar trend whereas copper and manganese substitution for iron do not follow this trend.

Bulk Chemical Impurities

The results of the bulk chemical analysis determined by multi-acid extraction followed ICP-AES measurement of the elements for the twelve pyrrhotite samples are plotted in Figure 4.10. Only the major bulk impurities are plotted. The remaining elements are listed in Janzen, 1996. The bulk chemical analysis of the twelve pyrrhotite samples, determined by multi-acid extraction and

ICP, demonstrated that pyrrhotite samples contain a range of impurities. The major impurities were cobalt, copper, manganese, nickel, lead, and zinc (Figure 4.10).

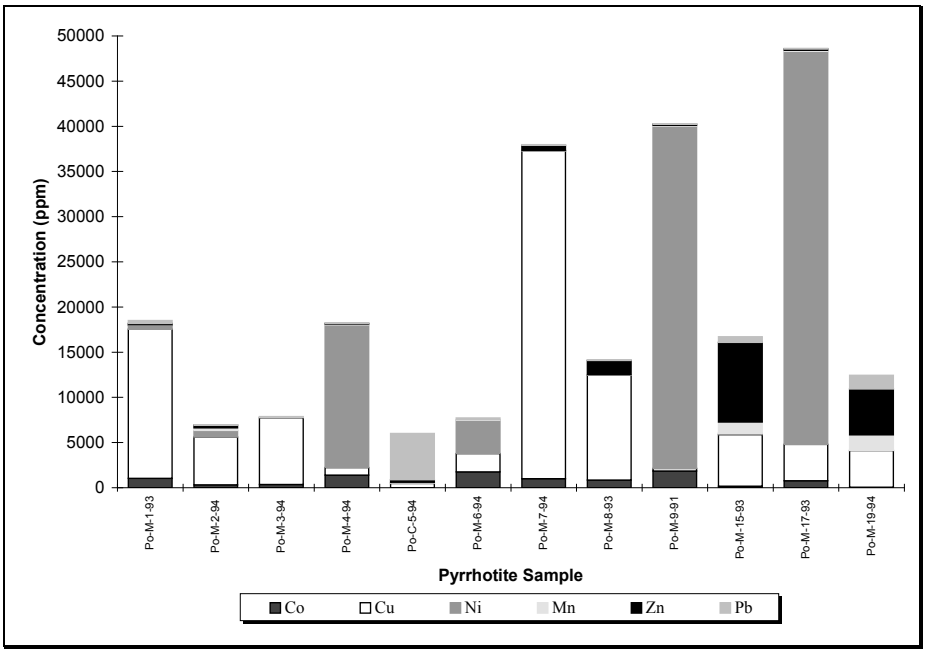

Figure 4.10: Impurity concentrations of the pyrrhotite samples.

Trace Metal Content from Electron Microprobe Analysis

The average trace metal content of the twelve pyrrhotite samples analyzed by electron microprobe appear in Table 4.2. Samples that had distinguishable differences in metal content amongst the measured grains were separated into two groups (Po-M-2-94, Po-M-4-94, Po-C-5-94 - the light, bright, and dark descriptions refer to the colour of the grains relative to one another). It is clear from Table 4.2 that significant differences in trace metal content among the twelve pyrrhotite samples exist. All pyrrhotite samples contain Co of varying proportions; however, the range of Co composition was small, 513 to 2407 ppm, compared to the range Ni values observed. The proportions of trace nickel in the pyrrhotite samples varied from 0 to 9450 ppm. Overall, the mean total trace metal content in the twelve pyrrhotite samples is 3055 ppm ± 3171 with a median of 1593 ppm.

Table 4.2: Trace metal contents of pyrrhotite samples.

Sample	Co (mg/kg)	Cu (mg/kg)	Mn (mg/kg)	Ni (mg/kg)	Total Trace Metals (mg/kg)
Po-M-1-93	1414	462	24	54	1954
Po-M-2-94 bright	694	45	0	5	744
Po-M-2-94 dark	1150	5	20	2898	4073
Po-M-2-94 smoke	651	0	0	90	741
Po-M-3-94	935	5	5	63	1008
Po-M-4-94 dark	600	17	0	3477	4093
Po-M-4-94 bright	640	0	100	130	870
Po-C-5-94 dark	525	10	40	0	575
Po-C-5-94 light	520	0	100	0	620
Po-M-6-94	2407	0*	0*	3810	6217
Po-M-7-94	1577	0*	0*	27	1603
Po-M-8-94	1583	0*	0*	0	1583
Po-M-9-91	685	0*	0*	6794	7479
Po-M-15-93	765	0*	0*	15	780
Po-M-17-93	640	0*	0*	9450	10090
Po-M-19-94	513	10	10	27	560

where *= not measured

Accurately measured iron contents of the twelve pyrrhotite samples by the electron microprobe permits a verification of the equation presented by Yund and Hall (1969) relating atomic percent iron of hexagonal pyrrhotites and X-ray powder diffraction measurements.

$$X = 45.212 + 72.86(d_{102}\text{-}2.0400) + 311.5(d_{102}\text{-}2.0400)^2 \qquad (4.1)$$

where X is the composition of hexagonal pyrrhotite in atomic percent iron, and d_{102} is the strong refraction of hexagonal pyrrhotite (d-spacing=2.066 Å). In Figure 4.11, a comparison of measured and predicted iron contents for each method is shown (error bars allow for one standard deviation for each estimation technique). Only pyrrhotite samples with greater than 74% hexagonal pyrrhotite were used for the comparison since the equation predicts hexagonal atomic percent iron for a pure hexagonal sample. Skinner and Luce (1971) stated that appreciable quantities of nickel, cobalt, or manganese substituting for iron may invalidate

Equation 4.1. The authors showed that the presence of manganese in the crystal structure expands the (d_{102}) spacing appreciably, but Arnold and Reichen (1962) demonstrated that if nickel + cobalt + copper is less than 0.6% (by weight), there is no measurable effect on the (d_{102}) spacing. The total trace metal content for all the pyrrhotite samples used in this comparison fit the stated criteria. There were significant differences observed between predicted and measured hexagonal iron contents even for samples with low trace metal contents. Therefore, care should be used when applying the Yund and Hall (1969) equation.

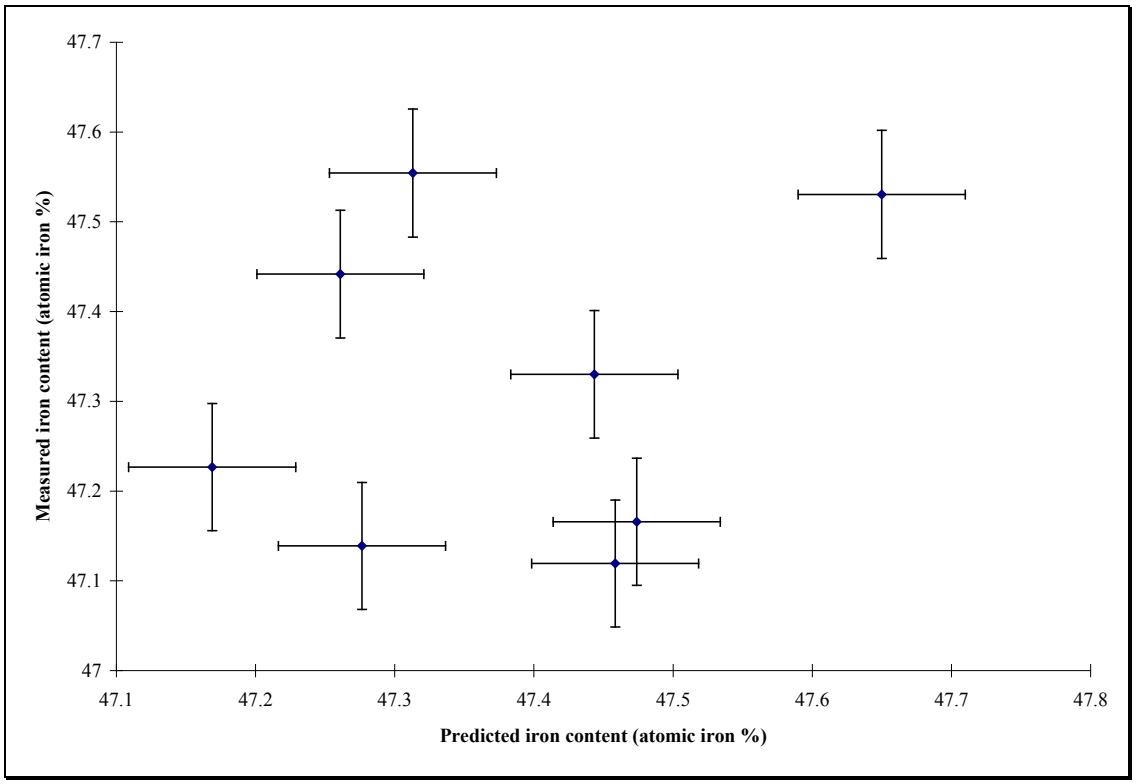

Figure 4.11: A comparison between measured microprobe atomic Fe % and predicted atomic Fe %.

Accessory Minerals and Pyrrhotite Composition

Accessory minerals were determined in the pyrrhotite samples by XRD scans and by electron microprobe analysis. The results of the interpretation of the X-ray diffraction scans between 3° and 90°, 2θ to determine the presence of accessory minerals is summarized in Table 4.3. The results indicate that a wide ranges of accessory minerals are probably present in the different pyrrhotite samples. Electron microprobe analysis was also used to determine accessory minerals present with the pyrrhotite (Janzen, 1996). Both methods identified the same accessory minerals

in each sample with a few exceptions (Janzen, 1996).

Table 4.3: Accessory minerals present in the pyrrhotite samples.

Sample ID	Accessory Minerals
Po-M-1-93	Chalcopyrite ($CuFeS_2$), Akaganeite ($FeO(OH)_\beta$)
Po-M-2-94	Bravoite ($(Fe,Ni)S_2$), Magnetite (Fe_3O_4),Chalcopyrite ($CuFeS_2$)
Po-M-3-94	Chalcopyrite($CuFeS_2$), Pyrite (FeS_2), Goethite ($FeO(OH)_\alpha$)
Po-M-4-94	Pentlandite ($(Fe,Ni)_9S_8$)
Po-C-5-94	Pyrite (FeS_2), Quartz (SiO_2), Galena (PbS)
Po-M-6-94	Chalcopyrite ($CuFeS_2$), Quartz (SiO_2)
Po-M-7-94	Chalcopyrite ($CuFeS_2$)
Po-M-8-93	Chalcopyrite ($CuFeS_2$), Quartz (SiO_2)
Po-M-9-91	Pentlandite ($(Fe,Ni)_9S_8$), Silicates, Carbonates
Po-M-15-93	Chalcopyrite ($CuFeS_2$), Pyrite (FeS_2), Wurtzite (ZnS), Goethite ($FeO(OH)_\alpha$), Dolomite ($CaMg(CO_3)_2$), Sphalerite (β-ZnS), Silicates, Dolomite-ferroan ($Ca(Fe,Mg)(CO_3)_2$)
Po-M-17-93	Pentlandite ($(Fe,Ni)_9S_8$), Chalcopyrite ($CuFeS_2$), Nickel Sulfide ($Ni_{1-x}S_2$)
Po-M-19-94	Chalcopyrite ($CuFeS_2$), Dolomite ($CaMg(CO_3)_2$), Sphalerite (β-ZnS), Pyrite (FeS_2), Teallite ($PbSnS_2$)

The findings from the 43° to 45°, 2θ XRD scans are presented in Table 4.4. There is wide compositional range between monoclinic and hexagonal pyrrhotite with two pyrrhotite samples containing troilite (FeS). The compositions range from pure hexagonal (e.g. Po-M-1-93) to nearly pure monoclinic (e.g. Po-C-5-94). Triolite presence was verified in sample Po-M-2-94 and Po-M-4-94 by electron microprobe. Sample plots for the 43° to 45°, 2θ scans are shown in Figure 4.12. The figure show a nearly pure monoclinic pyrrhotite, a pure hexagonal pyrrhotite, a mixture of hexagonal and monoclinic pyrrhotite, and a mixture of hexagonal, monoclinic and troilite.

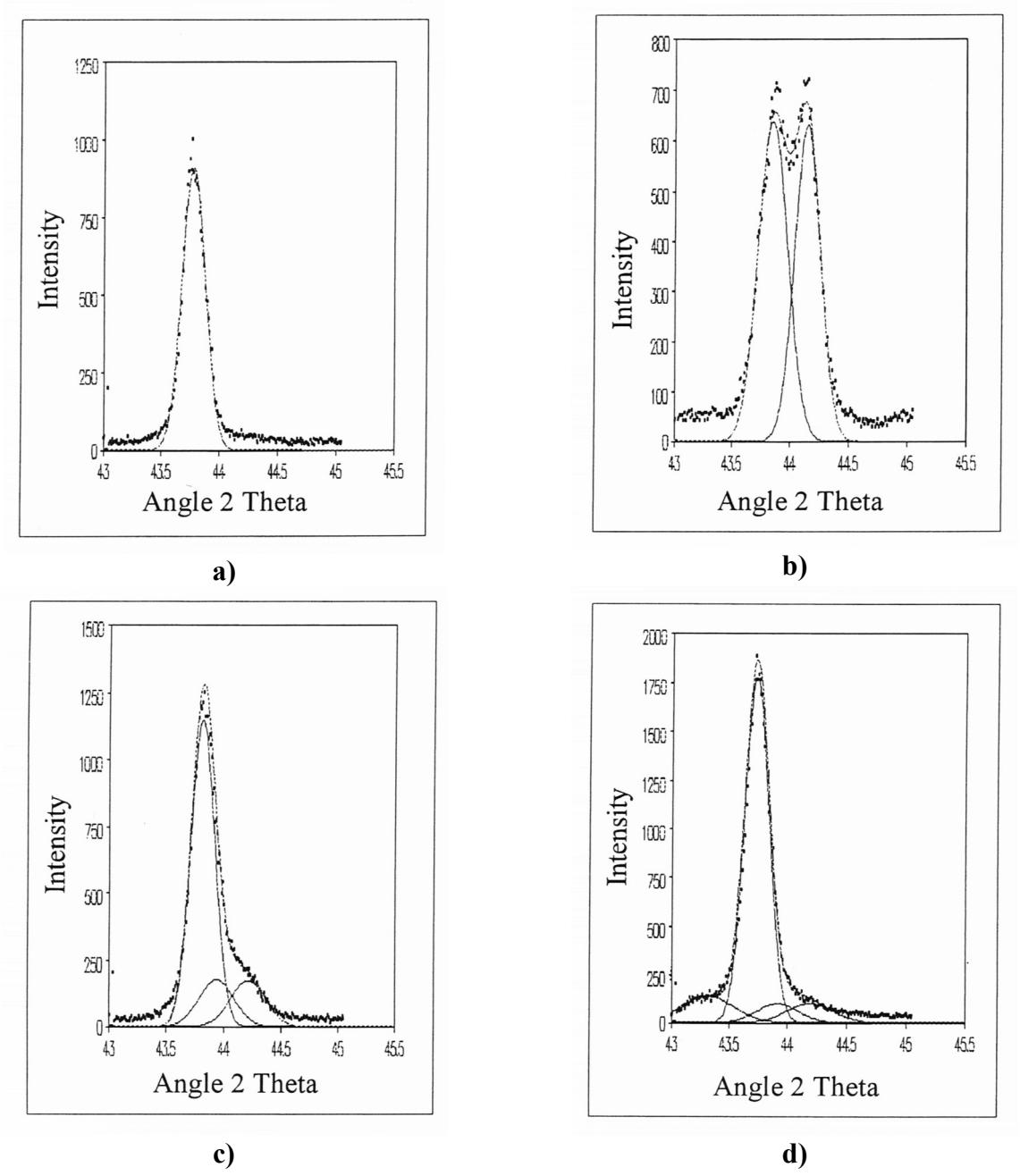

Figure 4.12: XRD intensity spectra for: (a) pure hexagonal pyrrhotite, (b) pure monoclinic pyrrhotite, (c) mixed hexagonal and monoclinic pyrrhotite, and (d) mixed hexagonal, monoclinic and troilite containing pyrrhotite

Table 4.4: Hexagonal, monoclinic and orthorhombic crystal forms in the pyrrhotite samples.

Sample ID	Monoclinic Composition (%)	Hexagonal Composition (%)	Troilite Composition (%)
Po-M-1-93	0	100	0
Po-M-2-94	10	74	16
Po-M-3-94	55	45	0
Po-M-4-94	8	81	11
Po-C-5-94	100	trace	0
Po-M-6-94	19	81	0
Po-M-7-94	0	100	0
Po-M-8-93	0	100	0
Po-M-9-91	86	14	0
Po-M-15-93	22	78	0
Po-M-17-93	95	5	0
Po-M-19-94	14	86	0

The presence of different accessory mineral accounts for the wide compositional range for the concentrations of the bulk impurities observed in the pyrrhotite samples. Although, electron microprobe analysis indicated that substitution of nickel and cobalt for iron in the pyrrhotite may be a significant source of cobalt and nickel in these pyrrhotite samples. SEM photographs show that the accessory minerals were present both as separate grains and as embedded impurities in the pyrrhotite grains (Janzen, 1996).

Both electron microprobe and XRD methods are valid methods for determining the presence of accessory minerals. With a few exceptions, both methods identified the same accessory minerals present in the pyrrhotite samples. Chalcopyrite was found to be a dominant mineral associated with pyrrhotite. Nine out of the twelve pyrrhotite samples contained chalcopyrite in detectable amounts. Other sulphide minerals such as pyrite, pentlandite, sphalerite, and galena were also found in some samples. A few samples contained some silicates and carbonates. The accessory minerals were present both as separate grains and as embedded impurities in the pyrrhotite grains. The accessory minerals found during this study match closely to those observed by Arnold (1967). The pyrrhotite samples ranged in composition from pure hexagonal to nearly pure monoclinic. Most were mixed, while two contains troilite. Troilite formed lamellae in a hexagonal matrix in both samples (Janzen, 1996) where troilite was detected by XRD (Po-M-2-94 and Po-M-4-94). The mixing of pyrrhotite crystalline forms have been observed by Arnold (1967).

The pyrrhotite compositions were determined by XRD methods similar to those described by Graham (1969) and Arnold (1966). These authors however only described techniques for

separating monoclinic and hexagonal pyrrhotite, and did not discuss troilite composition. Troilitic composition can be determined by examining the XRD peak of hexagonal pyrrhotite at 43.2°, 2θ(d-spacing=2.093 Å). Care must be taken though as other minerals have a peak at this position (e.g. calcite, chromite). However, troilite confirmation can be obtained by examining other peaks in a wider XRD scan (e.g. 3° to 90°, 2θ). The mineral composition of the samples determined by powder diffraction was verified by electron microprobe analysis. Grains were found in Po-M-2-94 and Po-M-4-94 that had a Fe to S atomic percent ratio very close to 1 confirming XRD data.

Inco Copper Cliff Pyrrhotite Tailings Concentrate

The particle size distribution of the Inco pyrrhotite tailings was determined for the estimation of reactive surface area. The particle size distribution is shown in Figure 4.13. The particle size distribution of the quartz sand (Barco 71) was provided by the manufacturer. The larger particle size of quartz sand would significantly improve the drainage characteristics of the packed column.

The quartz sand is coarser grained than the pyrrhotite tailings and was selected to provide a higher hydraulic conductivity to enhance drainage. Because the columns were designed to be 1 m in length and gravity drained, it was desirable to allow drainage so that capillary forces did not maintain near-saturated conditions which resulting low gas diffusion coefficients in the columns.

The chemical composition of the Inco's pyrrhotite concentrate was analyzed by the combination of INAA and ICP [Activation Laboratories Ltd.]. The contents of major chemical elements in the pyrrhotite concentrate are listed in Table 4-5.

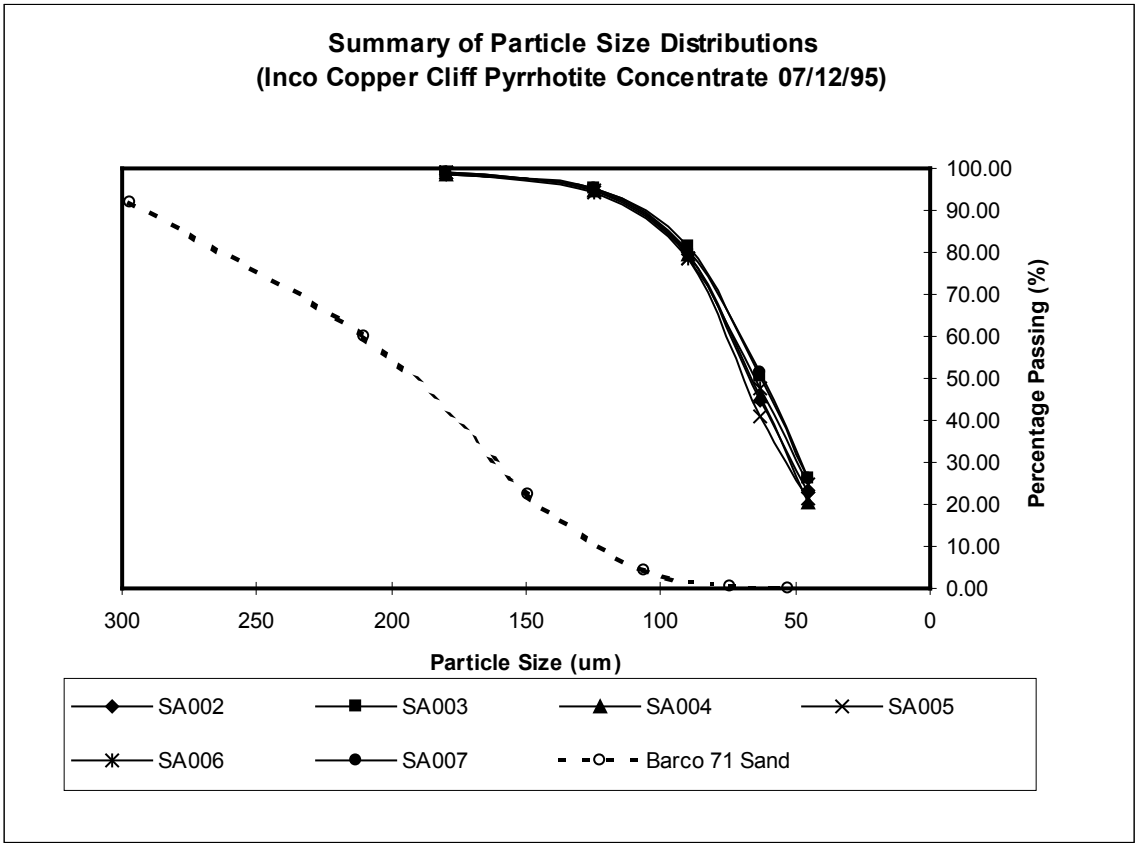

Figure 4.13: Particle size distributions of pyrrhotite concentrate and quartz sand.

Table 4-5: Chemical composition of Inco Copper Cliff pyrrhotite concentrate.

unit	Fe %	S %	Co ppm	Cr ppm	Cu ppm	Mn ppm	Ni ppm	Pb ppm	Zn ppm	Ca %	Mg %	Al %	Na %	K %
Po	52.9	22.8	200	260	680	432	9846	51	61	0.46	0.46	0.67	0.13	0.09

Mineralogical composition based on chemical composition of mineral outlined in Table 3.2, the Inco pyrrhotite concentrate contained approximately 56 % pyrrhotite, 1.5 % pentlandite, 25 % iron oxide and silicate minerals made up the rest. This yielded an average sulphur content of 23 %. The quartz sand used in the columns was reported to be essentially pure silicon oxide (99.8 % SiO_2) by the manufacturer.

FUNDAMENTAL KINETICS

Kinetic studies were conducted on specimen-grade pyrrhotite samples to assess the effects of chemical and crystallographic differences on reaction rates. More detailed chemical and biologic kinetic studies were then conducted on the pyrrhotite concentrate (Inco tailings) to provide fundamental data on this material and to provide a basis for interpretation of the column studies results.

Comparison of Kinetic Rates among Specimen Grade Samples

Non-Oxidative Dissolution of Pyrrhotite

Experiments were performed to determine the contribution of non-oxidative dissolution to ferrous iron release from pyrrhotite (Po) in acidic solutions. The experimental results for the twelve pyrrhotite samples are summarized in Table 4.6. This table shows that all the pyrrhotite samples seem to dissolve at roughly the same rate. The mean dissolution rate for the 12 pyrrhotite samples, as measured by Fe^{2+} release, was 5×10^{-10} ($\pm$ 3×10^{-10}) $mol\cdot m^{-2}\cdot s^{-1}$. The non-oxidative dissolution rates ranged from 9.21×10^{-11} to 9.20×10^{-10} $mol\cdot m^{-2}\cdot s^{-1}$ for the twelve pyrrhotite samples (Janzen, 1996). The result of a typical non-oxidative dissolution experiment is illustrated in Figure 4.14. As shown in Figure 4.14, the iron production rates were constant during the experimental run conducted for over one week. Dissolved sulphate concentrations were determined for a single non-oxidative run. It was found that while the ferrous iron concentration increases linearly with time, sulphate values remain unchanged at levels fluctuating around the detection limit (0.05 ppm). Sulphur from pyrrhotite therefore appears to remain in a reduced state during dissolution as indicated by the lack of sulphate production.

Table 4.6: Non-oxidative dissolution rates of the pyrrhotite samples.

Pyrrhotite Sample	Pyrrhotite Dissolution ($mol \cdot m^{-2} \cdot s^{-1}$)
Po-M-1-93	8.24×10^{-10}
Po-M-2-94	3.53×10^{-10}
Po-M-3-94	4.72×10^{-10}
Po-M-4-94	9.21×10^{-11}
Po-C-5-94	1.67×10^{-10}
Po-M-6-94	6.11×10^{-10}
Po-M-7-94	3.24×10^{-10}
Po-M-8-94	9.32×10^{-10}
Po-M-9-91	3.70×10^{-10}
Po-M-15-93	9.20×10^{-10}
Po-M-17-93	4.76×10^{-10}
Po-M-19-94	4.75×10^{-10}
Mean	5×10^{-10}
Standard Deviation of the Mean	8.7×10^{-11}

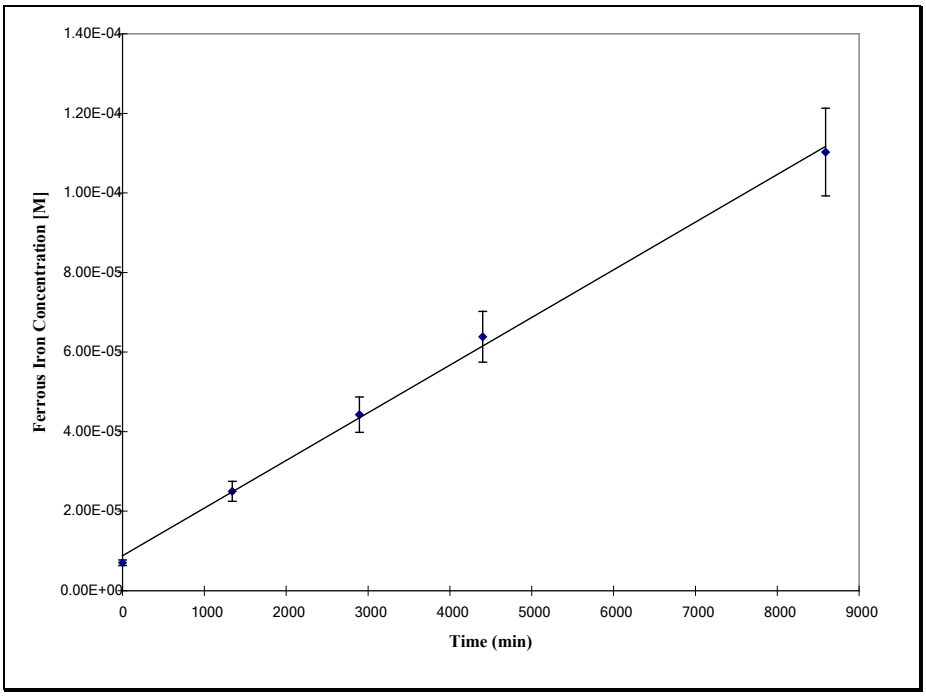

Figure 4.14: Non-oxidative dissolution at pH=2.75, 25°C for Po-M-7-94 measured in closed stirred tank reactors.

Non-oxidative dissolution rates are variable and but are generally about 1-10% of the oxidative rates. The non-oxidative dissolution rates observed in this study were comparable to the rates

observed by Tewari and Campbell (1976) for troilite dissolution in sulphuric acid (10^{-9} to 10^{-10} $mol \cdot m^{-2} \cdot s^{-1}$ at pH = 2 to 5), however, they were considerably lower than the rates observed by Nichol and Scott (1979) for pyrrhotite dissolution in perchloric acid (10^{-6} to 10^{-7} $mol \cdot m^{-2} \cdot s^{-1}$ at pH = 3). The reason for the differences in non-oxidative dissolution rates among the twelve pyrrhotite samples at this time remains unknown. Attempts to correlate the reaction rates with other variables were unsuccessful. No correlation between dissolution rate and crystal structure or trace metal content was observed (Janzen, 1996). The differences in rates may be due to surface features such as roughness and cleavages that are difficult to express quantitatively.

Pyrrhotite Oxidation by Oxygen

In this study, oxygen was confirmed to be a significant oxidant in pyrrhotite oxidation. Table 4.2 lists the oxidation rates for the twelve pyrrhotite samples by oxygen for both Fe^{2+} and sulphate release. Correlation coefficients for the linear regressions are also listed. The mean oxidation rate based on ferrous iron release for the twelve pyrrhotite samples was 4×10^{-9} ($\pm$ 6×10^{-10}) $mol \cdot m^{-2} \cdot s^{-1}$. The mean oxidation rate based on sulphate release for the twelve pyrrhotite samples was 4×10^{-10} ($\pm$ 6×10^{-11}) $mol \cdot m^{-2} \cdot s^{-1}$ (Janzen, 1996). A sample run is illustrated in Figure 4.15. It is evident from the study that rates of oxidation based on iron release are more than one order magnitude higher than the oxidation rates based on sulphate production. Table 4.7 illustrates not only differences in reaction rates but also the differences in correlation coefficients between oxidation based on iron release and sulphate production. All correlation coefficients between species concentrations and time for oxidation by oxygen based on ferrous iron release were near 1, while the linear correlation coefficients for sulphate production ranged, with one notable exception, from 0.810 to 0.999.

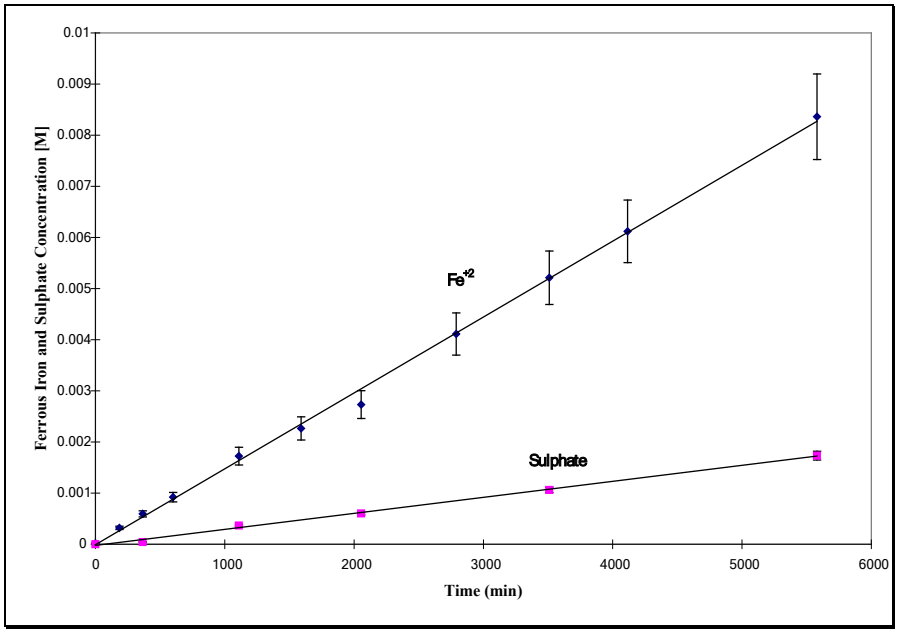

Figure 4.15: Oxidation of pyrrhotite by oxygen at pH=2.75, 25°C for Po-M-15-93 measured in internal split-flow airlift reactors.

Table 4.7: Rates of oxidation of the pyrrhotite samples by oxygen.

Po Sample	Oxidation rate based on iron release ($mol \cdot m^{-2} \cdot s^{-1}$)	R^2 for iron release	Oxidation rate based on sulphate production ($mol \cdot m^{-2} \cdot s^{-1}$)	R^2 for sulphate Production
Po-M-1-93	4.03×10^{-9}	0.997	2.70×10^{-11}	0.999
Po-M-2-94	4.73×10^{-9}	0.998	4.18×10^{-10}	0.810
Po-M-3-94	9.76×10^{-9}	0.986	4.02×10^{-10}	0.956
Po-M-4-94	3.53×10^{-9}	0.996	1.09×10^{-10}	0.850
Po-C-5-94	1.58×10^{-9}	0.998	8.15×10^{-12}	0.840
Po-M-6-94	2.94×10^{-9}	0.996	4.15×10^{-11}	0.848
Po-M-7-94	4.22×10^{-9}	0.990	5.64×10^{-11}	0.861
Po-M-8-94	1.33×10^{-9}	0.999	1.38×10^{-11}	0.975
Po-M-9-91	1.60×10^{-9}	0.996	1.59×10^{-11}	0.183
Po-M-15-93	3.07×10^{-9}	0.998	5.86×10^{-10}	0.998
Po-M-17-93	1.65×10^{-9}	0.997	6.59×10^{-11}	0.937
Po-M-19-94	5.54×10^{-9}	0.996	4.31×10^{-10}	0.876
Mean	4×10^{-9}		2×10^{-10}	
Standard Error of the Mean	6×10^{-10}		6×10^{-11}	

In the case of pyrrhotite oxidation by oxygen, this study demonstrated that the rate of release of

ferrous iron does not equal the rate of production of sulphate as implied by the stoichometry of the pyrrhotite oxidation reaction. Discrepancies between values for oxidation rates based on iron release and sulphate production were also observed by Kwong (1995) who found that molecular oxygen did not completely oxidize all the sulphide sulphur component in pyrrhotite to sulphate. Based on ferrous iron release, only 37 % of the expected sulphur component were transformed to sulphate. Partial oxidation of sulphide sulphur to sulphate and differences in ferrous and sulphate ion release were anticipated. Numerous researchers have identified sulphur oxidation products other than sulphate during pyrrhotite oxidation experiments (Steger 1982, Jambor 1986, Plyusnin et al. 1990, Pratt et al. 1994 and others). Both elemental sulphur formation and sulphur enrichment on the pyrrhotite surface (FeS_2 formation) had been observed by other investigators. No attempt was made to assess the surface products or sulphur species on the solid phase in this study.

Pyrrhotite Oxidation by Ferric Iron

Published reaction rate data for other sulphide minerals such as pyrite have shown that ferric iron is a more reactive oxidizing agent than oxygen. Continuous-stirred closed reactors were used to assess the oxidation rates by ferric iron. The standard oxidation rate tests at various pH values and initial ferric iron concentrations are listed in Table 4.8. The mean oxidation rate for the different conditions were: 3.5×10^{-8} mol $Fe^{3+}\cdot m^{-2}\cdot s^{-1}$ (at pH = 2.75, with $Fe^{3+}_{int} = 2\times10^{-4}$ M); 3.1×10^{-8} mol $Fe^{3+}\cdot m^{-2}\cdot s^{-1}$ (at pH = 2.50, with $Fe^{3+}_{int} = 2\times10^{-4}$ M), and 6.8×10^{-8} mol $Fe^{3+}\cdot m^{-2}\cdot s^{-1}$ (at pH = 2.50, with $Fe^{3+}_{int} = 1\times10^{-3}$ M) (Janzen, 1996). For comparison purposes between pyrrhotite oxidation by oxygen and ferric iron, Janzen, (1996) demonstrated that approximately 3 moles of ferric iron are required to oxidize 1 mole of pyrrhotite assuming stoichometric pyrrhotite FeS.

Generally, the oxidation rate increased as the initial concentration of the oxidant, ferric ion increased from 2×10^{-4} M to 1×10^{-3} M. Slight increases in the oxidation rates were also observed with pH increases from pH = 2.5 tp pH = 2.75. Typical ferric iron oxidation data are shown in Figure 4.16 and Figure 4.17. These figures illustrated, that initially, when the ferric ion concentration is high, ferric ion consumption proceeds at a relatively constant rate. This is consistent with a zero order dependence of the reaction rate on ferric ion. As the ferric ion became exhausted, a distinct curvature in the plots becomes evident. Thus, the reaction rate

order changes continuously from order zero to order one. This change in order with reactant (oxidant) concentration is characteristic of heterogeneous reactions involving solid surfaces and is known as Langmuir-Hinshelwood mechanism. At high oxidant concentrations the surface is saturated with the oxidant, hence, the reaction rate depends on the reacting surface only. Partial saturation of the surface is expected to result in fractional order. The rate becomes first order at very low limiting reactant concentrations. At low reactant concentrations, the surface is becomes unsaturated with oxidant.

Table 4.8: Oxidation of the pyrrhotite samples by ferric iron.

Po Sample	Oxidation Rate by Ferric Iron (mol $Fe^{3+}\cdot m^{-2}\cdot s^{-1}$)		
	$Fe^{3+}_{int}=2\times10^{-4}$[M] pH=2.75, 25 °C	$Fe^{3+}_{int}=2\times10^{-4}$[M] pH=2.50, 25 °C	$Fe^{3+}_{int}=1\times10^{-3}$[M] pH=2.50, 25 °C
Po-M-1-93	3.51×10^{-8}	4.12×10^{-8}	5.34×10^{-8}
Po-M-2-94	3.11×10^{-8}	2.71×10^{-8}	4.57×10^{-8}
Po-M-3-94	3.04×10^{-8}	3.24×10^{-8}	8.53×10^{-8}
Po-M-4-94	1.76×10^{-8}	1.69×10^{-8}	6.73×10^{-8}
Po-C-5-94	1.96×10^{-8}	1.39×10^{-8}	2.46×10^{-8}
Po-M-6-94	5.17×10^{-8}	4.03×10^{-8}	6.83×10^{-8}
Po-M-7-94	4.06×10^{-8}	3.42×10^{-8}	3.96×10^{-8}
Po-M-8-94	1.39×10^{-8}	1.32×10^{-8}	2.34×10^{-8}
Po-M-9-93	2.83×10^{-8}	2.85×10^{-8}	4.16×10^{-8}
Po-M-15-93	2.84×10^{-8}	Not Analyzed	7.05×10^{-8}
Po-M-17-93	5.49×10^{-8}	3.80×10^{-8}	1.08×10^{-7}
Po-M-19-94	6.31×10^{-8}	5.26×10^{-8}	1.85×10^{-7}
Mean	3.5×10^{-8}	3.1×10^{-8}	6.8×10^{-8}
Standard Error of the Mean	4.3×10^{-9}	3.5×10^{-9}	1.3×10^{-9}

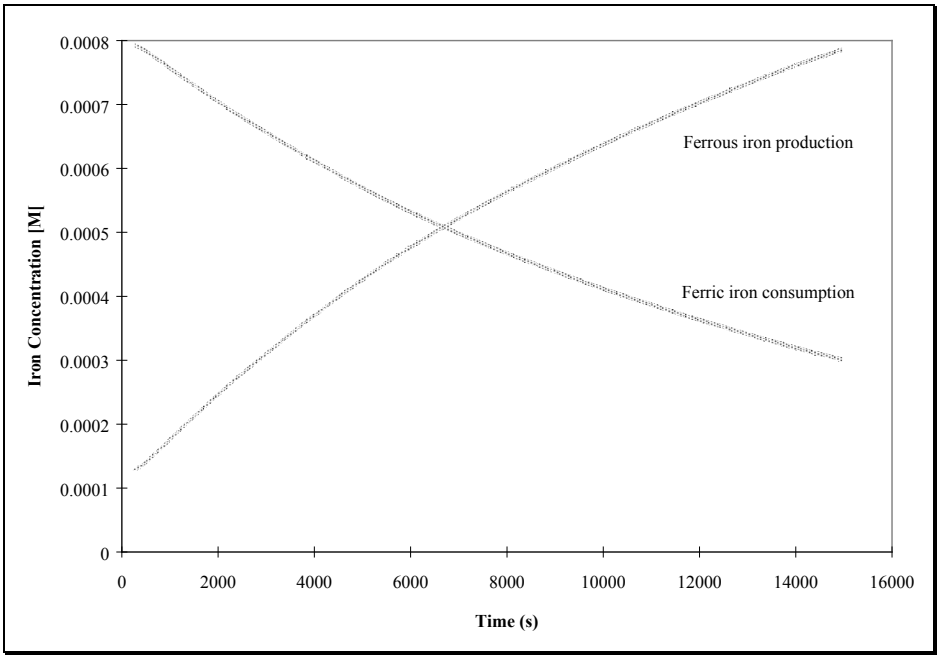

Figure 4.16: Oxidation by Fe^{+3} of Po-C-5-94 at pH=2.50, 25°C, $Fe^{+3}_{int}=1\times10^{-3}$ [M] measured in closed stirred tank reactors.

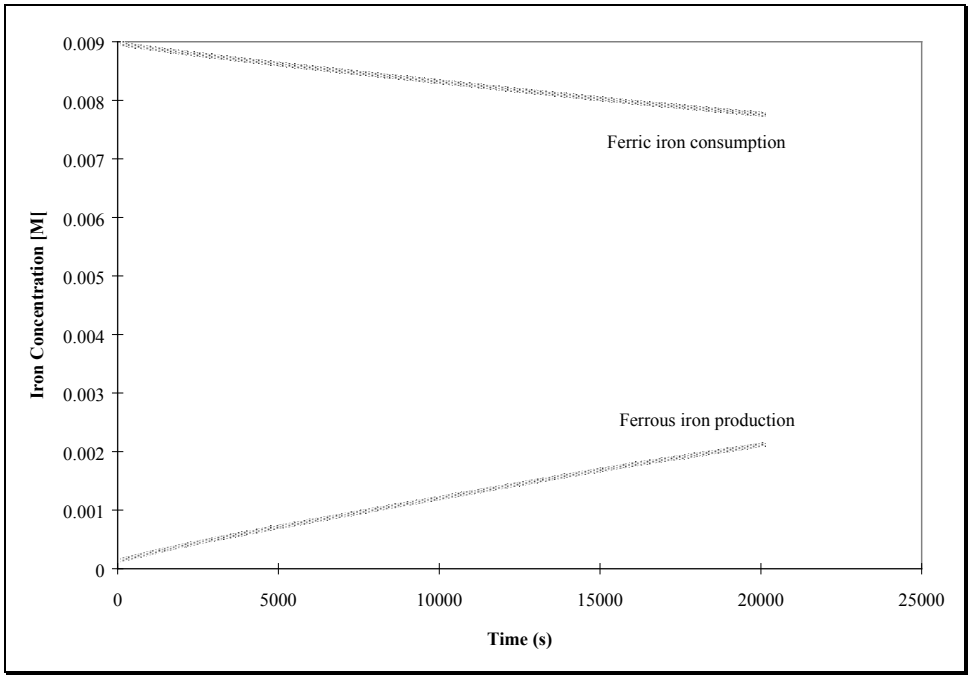

Figure 4.17: Oxidation by Fe^{+3} of Po-C-5-94 at pH=2.00, 25°C, $Fe^{+3}_{int}=1\times10^{-2}$ [M] measured in closed stirred tank reactors.

Oxidation rates with ferric iron as the oxidant ion exceeded all other reaction rates. In

accordance with the Langmuir-Hinshelwood adsorption mechanism for heterogeneous reactions, there is an approximate half-order (i.e. fractional order) dependence on ferric iron concentration at low levels (Figure 4.18). Numerous other plots using the same initial ferric concentration (2×10^{-4} [M]) showed similar fractional order of dependence ranging from 0.45 to 0.66. Half order dependence on ferric iron was also observed by McKibben and Barnes (1986) for pyrite oxidation by ferric iron. However, as the initial ferric ion concentration increases, the half-order dependence on concentration changes to a more complex rate dependence. At high initial ferric iron concentrations (1×10^{-2} [M]), zero-order dependence on ferric iron concentration was observed, as shown by the constant slope of Fe^{3+} with time in Figure 4.19. Table 4.9 shows the change in order with concentration for two pyrrhotite samples. The fractional order of dependence generally implies a mechanism involving control by sorption or desorption processes. This loss of half-order dependence and the change to a zero-order dependence suggested that an adsorption mechanism apply to pyrrhotite oxidation by ferric iron.

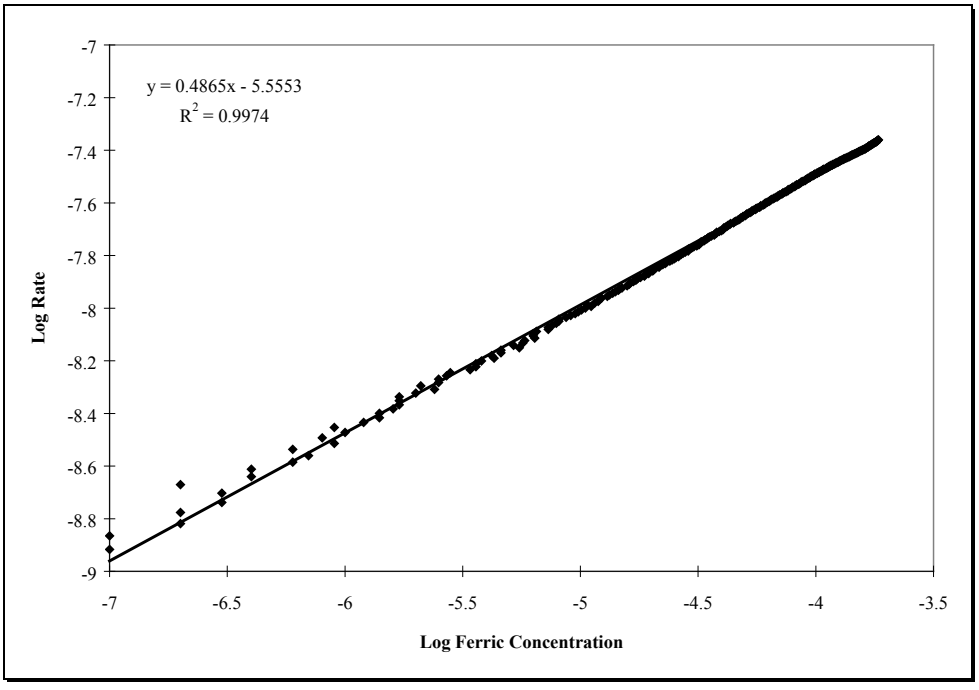

Figure 4.18: The dependence of pyrrhotite oxidation on Fe^{+3} ($Fe^{+3}_{int}=2\times 10^{-4}$ [M], 25°C, pH=2.75, Po-C-5-94).

Table 4.9: The rate order dependence of pyrrhotite oxidation on Fe^{3+} at pH=2.0.

Pyrrhotite Sample	$Fe^{3+}_{int}=2\times10^{-4}$ [M]	$Fe^{3+}_{int}=1\times10^{-3}$[M]	$Fe^{3+}_{int}=1\times10^{-2}$ [M]
Po-M-2-94	.55	0.2	0
Po-C-5-94	0.6	0.4	0

An adsorption mechanism has been used to explain rate control phenomena for pyrite oxidation. Williamson and Rimstidt (1994) suggested that a Freundlich non-site specific adsorption model describe the pyrite oxidation by ferric iron. Alternatively, Smith et al. (1968) proposed that pyrite oxidation by ferric iron follows a Hougen and Watson adsorption model. Similarly, Zheng et al. (1986) proposed that pyrite oxidation by ferric sulphate can be represented by a *dual-site* adsorption model. Initial rates were plotted for pyrrhotite samples that have three different measured ferric iron concentrations and using a linearized Langmuir equation as suggested by Nicholson et al. (1988) for oxidation of pyrite by oxygen.

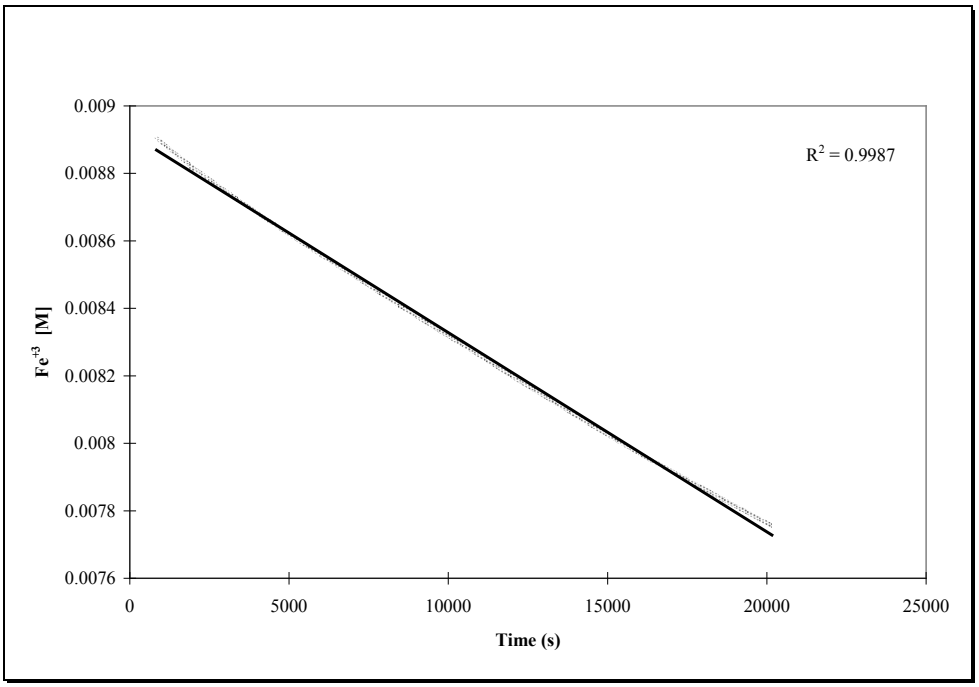

Figure 4.19: The dependence of pyrrhotite oxidation on Fe^{3+} ($Fe^{3+}_{int}=1\times10^{-2}$ [M], 25°C, pH=1.99, Po-C-5-94).

$$C/R=1/(R_mK) + C/R_m \quad (4.2)$$

where R is the rate of oxidation, R_m is the rate based on maximum saturation of available surface sites, K is the adsorption equilibrium constant for ferric iron on pyrrhotite, and C is the concentration of ferric iron. Figure 4.20 suggests that the data is consistent with a Langmuir type model. The calculated values, based on ferric iron consumption, gave R_m and K as 2.5×10^{-8} $mol\cdot m^{-2}\cdot s^{-1}$, and 972 M^{-1} respectively. Further measurements of rates at different ferric concentrations would assist in this interpretation and confirm the adsorption mechanism.

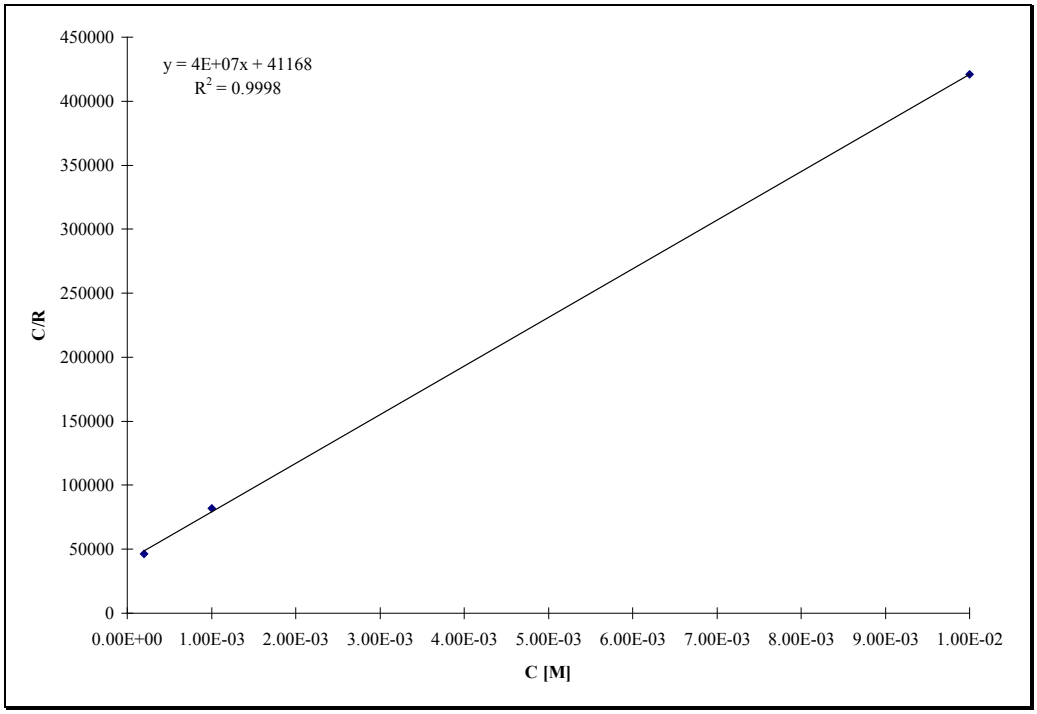

Figure 4.20: The linearized adsorption model (Po-M-2-94).

Pyrrhotite oxidation by ferric iron also exhibits incomplete transformation of the sulphide sulphur to sulphate. A computer model (IRON SOLVER) was developed to quantify electron transfer during the oxidation process. The use of an electron balance to assess reaction completeness is a novel aspect of this study. Figure 4.21 illustrates different scenario's for pyrrhotite reaction completeness (for a simple zero order reaction). The quantity of ferrous iron produced during pyrrhotite oxidation by ferric iron decreases with an increase in sulphate production. Therefore indirectly from ferrous iron production, the extent of pyrrhotite oxidation

reaction completeness can be assessed. Based on the IRON SOLVER, pyrrhotite oxidation by ferric iron was 18% complete with respect to sulphide sulphur oxidation to sulphate. Measured sulphate values also indicated that not all the sulphide sulphur was oxidized to sulphate during oxidation by ferric iron, although these values suggested even less transformation to sulphate than values estimated by the computer model. Similar sulphate production rates were reported by Kwong (1995), demonstrated that sulphate production lagged behind iron release. These partial oxidation trends for pyrrhotite are consistent with the general oxidative mechanism proposed by Loten and Wesker (1987) for mono-sulphide minerals. A single electron transfer agent (e.g. Fe^{3+}) should produce more elemental sulphur and less sulphate than a double electron transfer agent (e.g. O_2) since different hydrolysis reactions take place. Loten and Wesker (1987) also proposed that a single electron transfer agent would react more rapidly than a double electron transfer agent. This hypothesis is supported by the results of this study. Although thiosalt production is possible, and products such thiosulphate and dithionate can form as intermediate products as observed in many mill circuits, oxidation of these species is relatively rapid in acidic solution and sulphate would be the major product in tailings. Alternatively, thionates and thiosulphate are unstable under even mild acid conditions and decompose to elemental sulphur and sulphate.

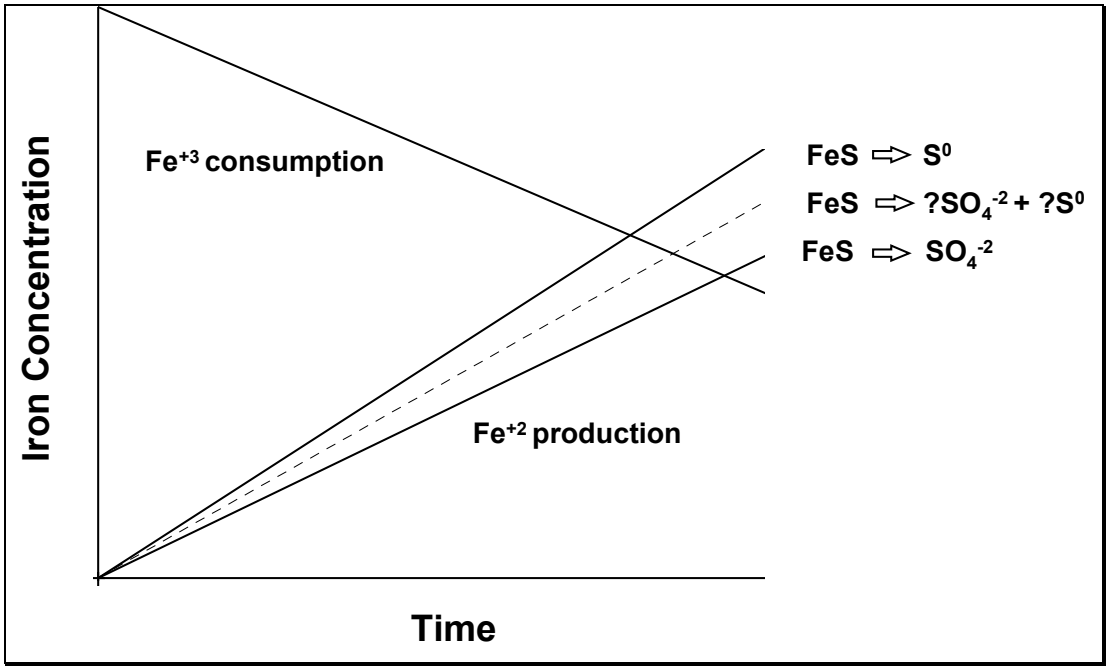

Figure 4.21: The use of ferrous iron production to predict pyrrhotite oxidation completeness.

Dependence of Oxidation Reactions on Controlling Factors

Dependence of Oxidation Reactions on pH

The dependence of the oxidation reactions on pH was assessed for oxidation reactions by ferric iron. Generally, the rate appears to increase with increasing pH values for most samples, but the results are not consistent for all pyrrhotite samples over the range of pH. Further research is needed to explain these inconsistencies. Similar relationships between pH values and oxidation rate have been shown during pyrite oxidation. Results of Williamson and Rimstidt (1994) and McKibben and Barnes (1986) demonstrated that an increase in pH increases the rate of oxidation of pyrite by ferric iron (in N_2-purged system). The dependence of pyrrhotite reaction rate on pH values suggests that H^+ may be competing with Fe^{3+} (and possibly Fe^{2+}) for adsorption sites on the pyrrhotite surface.

Dependence of Oxidation Reactions on Temperature

Pyrrhotite oxidation rates by oxygen were measured at 25°, 35°, and 45°C. Activation energies for oxidation by oxygen were calculated for 3 samples (Table 4.10) using Arrhenius type plots. There are distinctive differences between the activation energies calculated from iron release compared to the activation energy based on sulphate production. All activation energies have

correlation coefficients close to unity except for a single sample using sulphate based rates. The one sample exhibited no significant correlation coefficient (R^2 = 0.27) and a low calculated activation energy value that should not be considered as valid.

Table 4.10: Activation energies for pyrrhotite oxidation by oxygen.

Po Sample	Activation energy based on iron release (kJ×mole^{-1})	R^2 for iron release	Activation energy based on sulphate production (kJ×mole^{-1})	R^2 for sulphate Release
Po-M-1-93	47.7	0.97	79.1	0.978
Po-M-2-94	62.5	0.995	12.4	0.272
Po-C-5-94	50.0	1	106.0	0.997

The activation energies of the oxidation with ferric ion were also determined. Pyrrhotite oxidation by ferric iron was measured at 7.5°, 25°, and 35°C. The results are shown in Table 4.11. Notwithstanding a single exception, the activation energies are comparable with pyrrhotite oxidation using oxygen.

Table 4.11: Activation energies for pyrrhotite oxidation by ferric iron.

Pyrrhotite Sample	Activation Energy (kJ×mole^{-1})
Po-M-1-93	63.0
Po-M-2-94	59.1
Po-M-3-94	22.8
Po-M-4-94	47.5
Po-C-5-94	50.8

Oxidation rates by oxygen increase by 3 to 5 times for an increase in temperature of 20 °C while oxidation rates by ferric iron increased 2 to 11 times for a temperature increase of 30 °C. Activation energies for pyrrhotite oxidation by oxygen ranged from 48 kJ·mol^{-1} to 63 kJ·mol^{-1} based on iron release and 79.1 kJ·mol^{-1} to 106 kJ·mol^{-1} based on proven sulphate release. Similar activation energies based on iron release were found for pyrrhotite oxidation by ferric iron except for a single sample (47 kJ·mol^{-1} to 63 kJ·mol^{-1}). The exceptional pyrrhotite sample, with a value of 22.8 kJ·mol^{-1} was the most reactive of the twelve pyrrhotite samples.

Both molecular oxygen and ferric iron oxidation reactions obeyed an Arrhenius type equation (Janzen, 1996). Although pyrrhotite oxidation cannot be represented by a simple elementary-type reaction that the Arrhenius equation was intended to model, the equation applies well to pyrite (Nicholson, 1994). From the results of this study, it is evident that the Arrhenius equation

applies to pyrrhotite oxidation as well. The high activation energy values suggest that the rate-controlling step is a chemical reaction rather than control by transport processes (Nicholson, 1994). Reasons for the differences in activation energies between pyrrhotite oxidation rates by oxygen based on iron and sulphate release are unknown at this time. However, it does suggest that iron release and sulphate production are controlled by different mechanisms.

The activation energies for oxygen and ferric iron found in this study compare well with published values. Nicholson and Scharer (1994) reported activation energies of 58.1 $kJ \cdot mol^{-1}$ and 52.4 $kJ \cdot mol^{-1}$ at pH=2 and pH=4 for oxygen oxidation of a pyrrhotite of unknown composition and origin. Orlova et al. (1988) reported activation energies of 50.2 $kJ \cdot mol^{-1}$ and 46.2 $kJ \cdot mol^{-1}$ for oxidation of monoclinic and hexagonal pyrrhotite samples, respectively, by oxygen.

Crystal Structure and Trace Metal Content

The findings from the 43° to 45°, 2θ XRD scans indicated that there is wide compositional range between monoclinic and hexagonal pyrrhotite with two samples containing troilite among the twelve pyrrhotite samples. The compositions range from pure hexagonal to nearly pure monoclinic (Janzen, 1996). Numerous researchers have suggested that crystal structure of pyrrhotite will affect oxidation rates (Orlova et al. 1988, Yakhontova et al. 1983). The results of this study do not support this hypothesis. Figure 4.22 illustrates the effect of crystal structure on pyrrhotite oxidation by oxygen. No apparent correlation is observed between pyrrhotite oxidation by oxygen and crystal structure or between pyrrhotite oxidation by ferric iron and crystal structure (Janzen, 1996). Using the Student "t" test, the regression of the oxidation rate with respect to crystal structure was not statistically significant (see Figure 4.22).

Kwong (1993) observed visible corrosion of pyrrhotite samples of mostly monoclinic structure, and concluded that samples with a relatively high trace metal content oxidized slower than pyrrhotite with a lower trace metal content. Comparisons between oxidation rates and trace metal contents were completed in this study to quantify this effect. Significant differences in trace metal content amongst the 12 pyrrhotite samples exist (Janzen, 1996). As in the case of crystal structure, trace metal content (individual metals and sum of trace metals) had no statistically significant trend on the oxidation rate (Figure 4.23).

Orlova et al. (1988) argued that hexagonal pyrrhotite exhibited a significantly lower activation energy than monoclinic pyrrhotite for oxidation by oxygen (46.2 $kJ \cdot mol^{-1}$ compared to 50.2 $kJ \cdot mol^{-1}$ respectively). However, the results of this study did not show any consistent trends of

activation energy related to pyrrhotite crystal form.

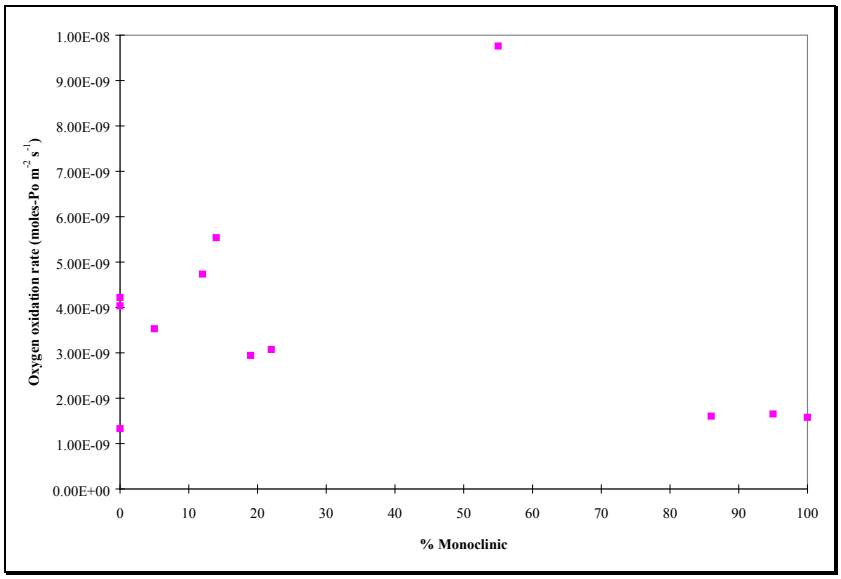

Figure 4.22: The influence of crystal structure on pyrrhotite oxidation rate by oxygen (pH=2.75, 25°C).

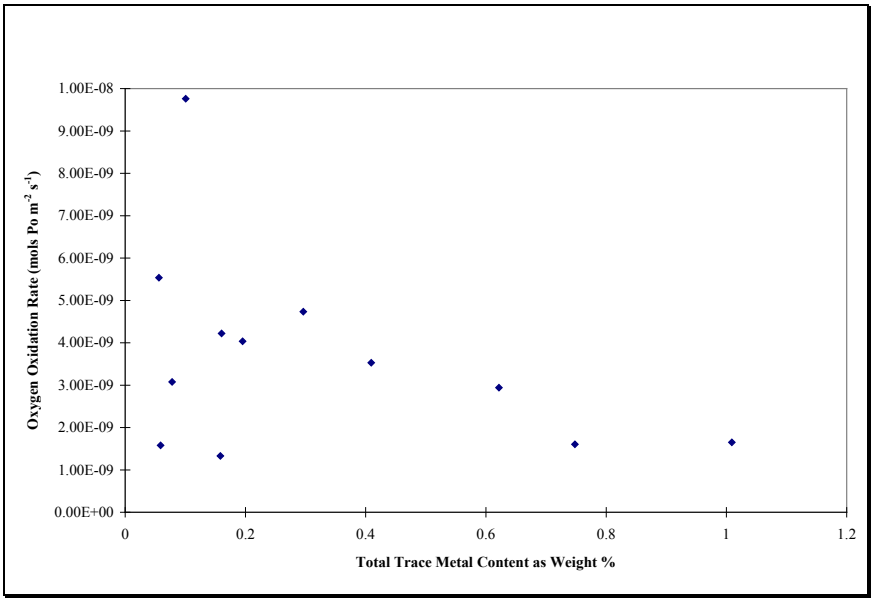

Figure 4.23: The influence of total trace metal content on pyrrhotite oxidation by oxygen (pH=2.75, 25°C).

Kinetics of Pyrrhotite Oxidation in Tailings Concentrate

The oxidation rates for pyrrhotite were found to be consistently higher than those observed for

oxidation of pyrite. Kinetic experiments investigating the effects of controlling factors, such as temperature, pH, addition of chelating agent and bacterial inoculation, for pyrrhotite oxidation by oxygen has been performed. The effect of each controlling factor on the oxidation rate of pyrrhotite is compared on the basis of sulphate, iron and nickel release rates. An example of the sulphate release and iron release plots at 30 °C and various pH values are given in Figure 4.24 and Figure 4.25, respectively. The oxidation rates were calculated from the latter section of the release data (after 1500 minutes), at which the sulphate loading rates tend to become constant. The highest loading rate was observed at pH 4.

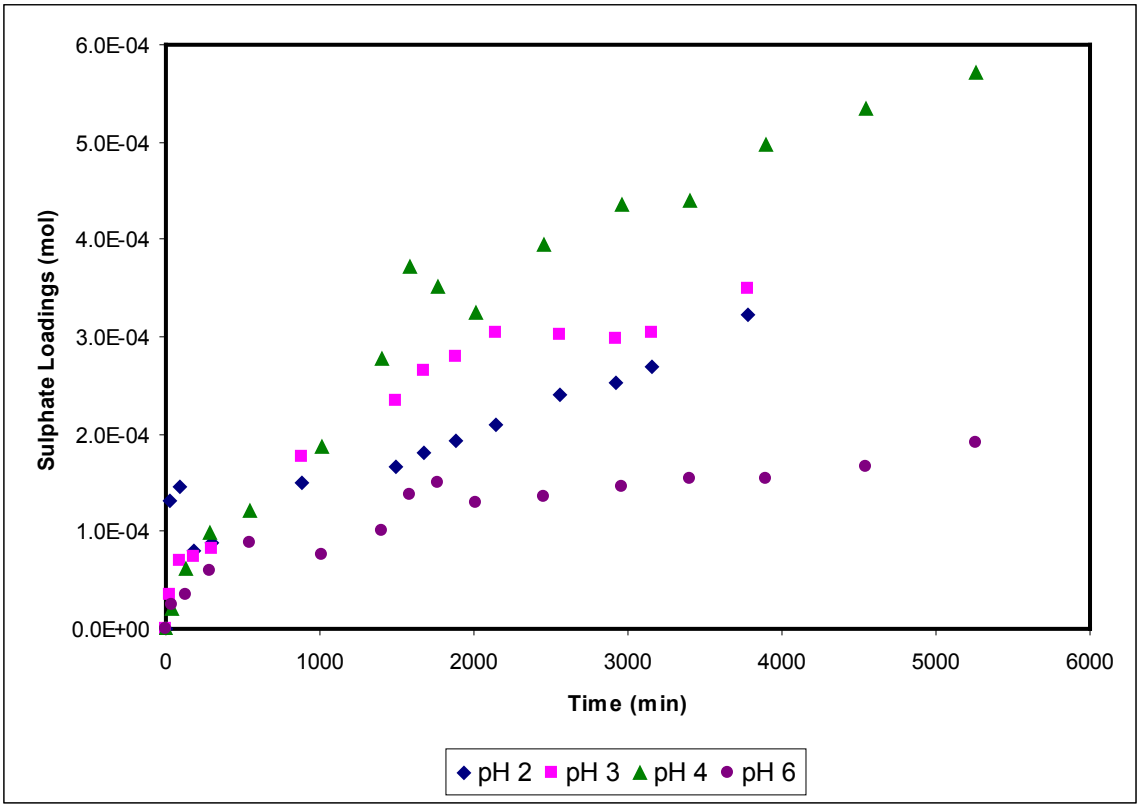

Figure 4.24: Sulphate release under abiotic pyrrhotite oxidation at 30 °C and various pH values.

There was a significant difference in the effect of pH on the sulphate release compared to iron release during oxidation of pyrrhotite. As shown in Figure 4.25, the maximum iron release rate occurs at pH = 2.0. Ferric ion tends to precipitate as ferric hydroxide at pH values above 4.0, hence, the apparent iron loading in the liquid phase decreases as the pH increases. In contrast, sulphate is not expected to precipitate in the pH range of pH = 2.0 to pH = 6.0. Consequently, the sulphate release data may be a better indicator of pyrrhotite oxidation than the iron release at pH values above pH 3.0.

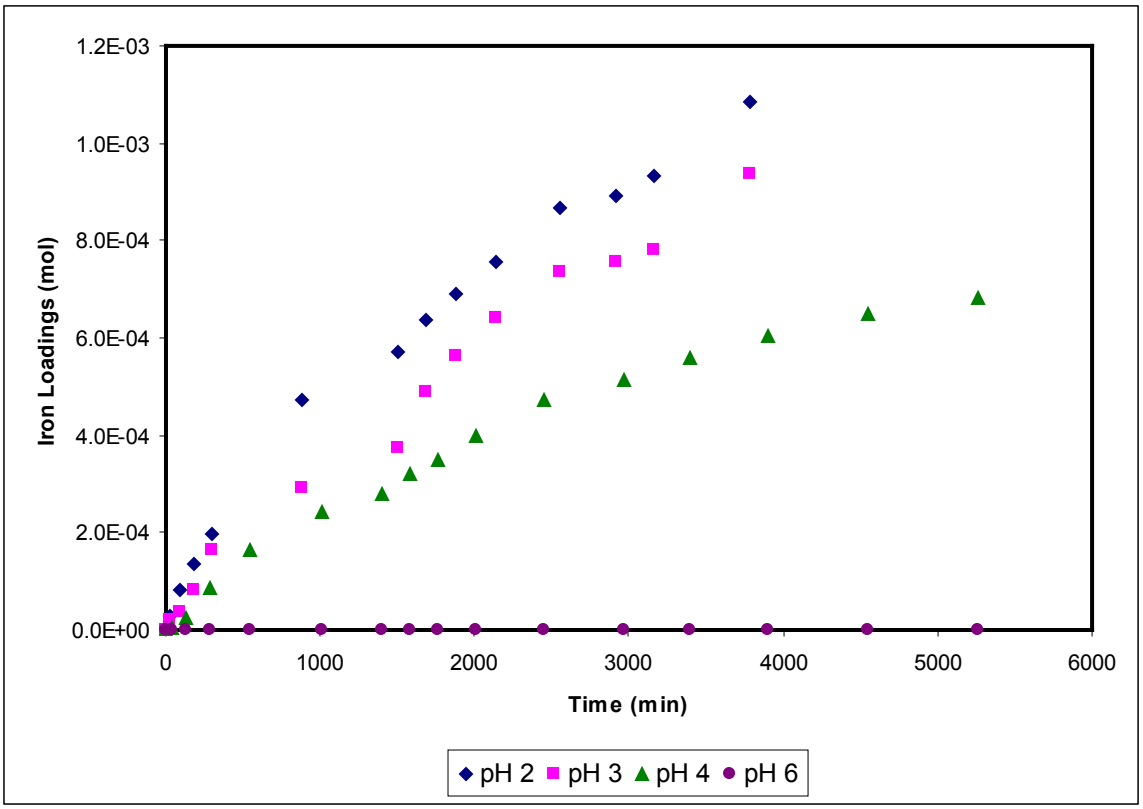

Figure 4.25: Iron release under abiotic pyrrhotite oxidation at 30 °C and various pH values.

The calculated pyrrhotite oxidation rates based on sulphate and iron under various temperatures and pH conditions are shown in Figure 4.26 and Figure 4.27. A comparison of the oxidation rate calculated from sulphate and oxidation rate calculated from iron release illustrates a significant mass transport difference between the sulphate release process and iron release process. At 40 °C, the maximum sulphate release rate was observed at pH = 2.0 while at 30 °C the maximum rate occurred at pH = 4.0. Maximum iron release rate occurred at 30 °C and pH = 3.0. The oxidation rates based on sulphate release ranged from 2.07×10^{-10} to 9.06×10^{-9} $mol\cdot m^{-2}\cdot s^{-1}$ and the oxidation rates based on iron ranged from 1.00×10^{-12} to 8.17×10^{-9} $mol\cdot m^{-2}\cdot s^{-1}$. A detailed discussion of temperature and pH effects on pyrrhotite oxidation is given in following sections.

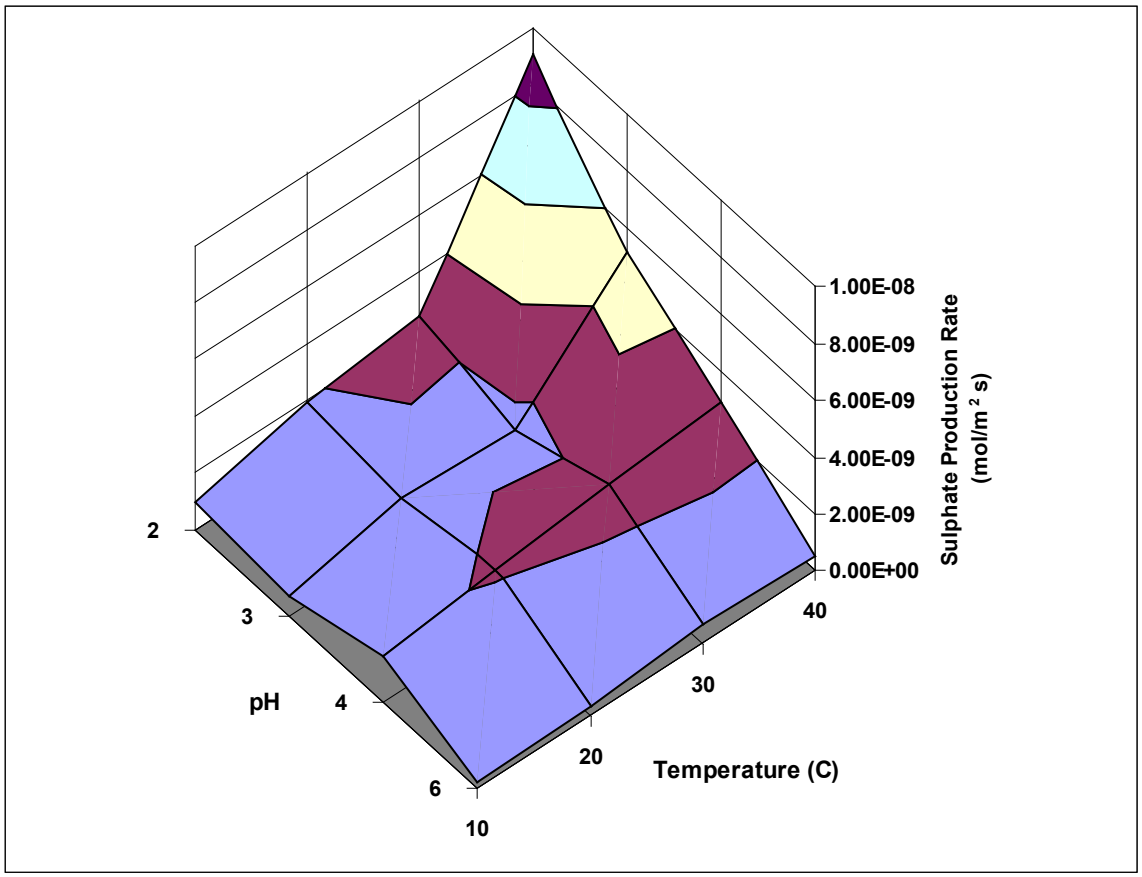

Figure 4.26: The sulphate production rate for abiotic pyrrhotite oxidation by oxygen.

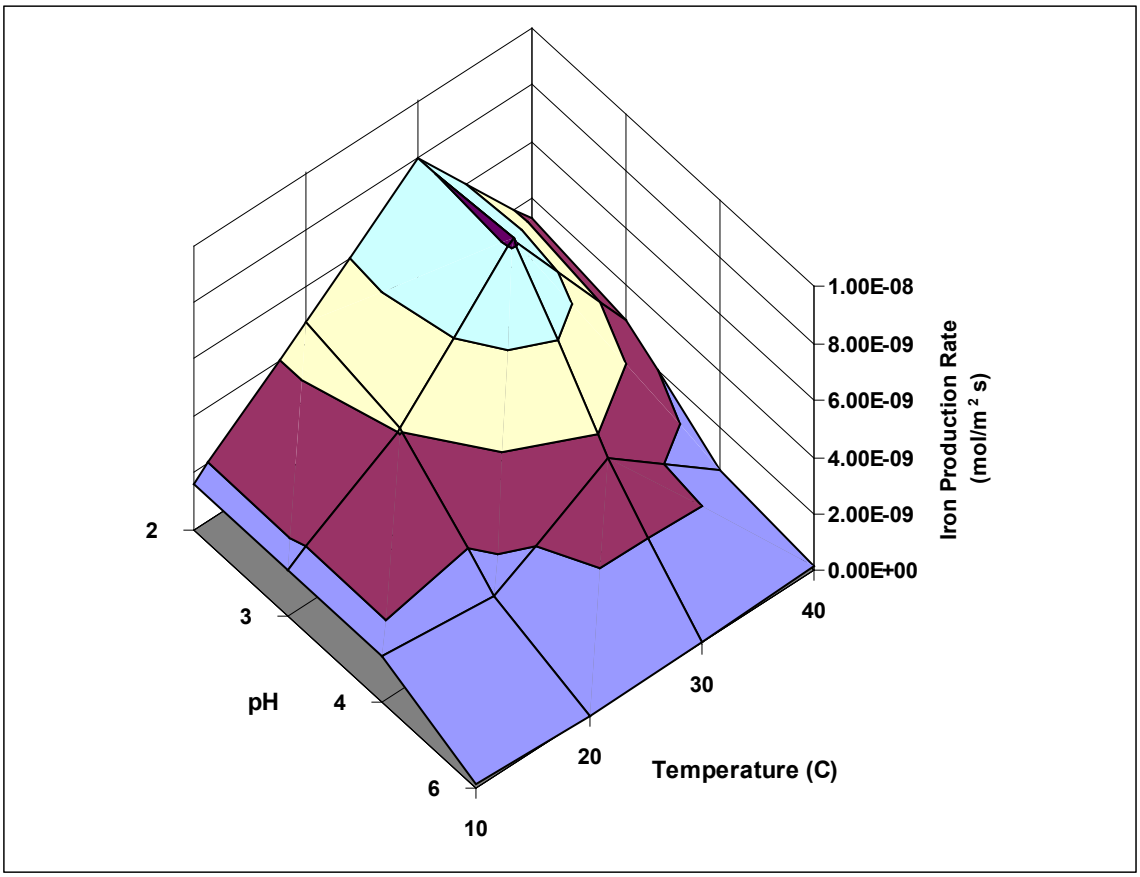

Figure 4.27: The iron production rate for abiotic pyrrhotite oxidation by oxygen.

The nickel content of the Inco pyrrhotite concentrates was estimated to be 0.8 %, therefore the nickel release rate can also possibly be used to investigate the oxidation rate. The nickel release rates are shown in Figure 4.28. The nickel release rate showed no consistent trend with either sulphate or iron release rates. The nickel release rates ranged from 1.01×10^{-11} to 1.60×10^{-10} $mol\cdot m^{-2}\cdot s^{-1}$ and were found to reach a peak at pH = 4 and 30 °C.

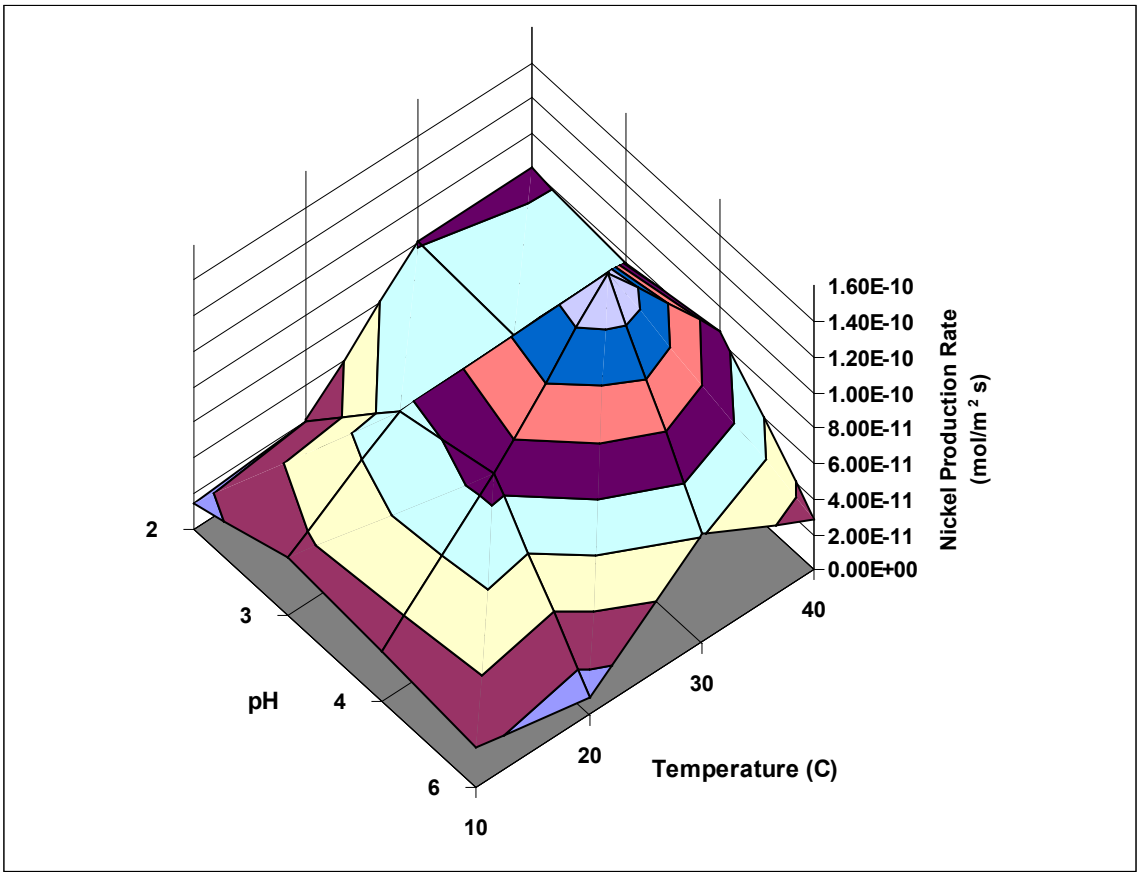

Figure 4.28: The nickel production rate for abiotic pyrrhotite oxidation by oxygen.

Effect of Temperature

The effect of temperature on the pyrrhotite oxidation rate observed in Figure 4.26 was found to be consistent with those observed for pyrite oxidation. The dependence of sulphate and iron release rate on temperature under various pH conditions are shown in Figure 4.29 and Figure 4.30. The oxidation rates (based on sulphate release) were proportionally dependent on temperature, i.e. higher oxidation rates at higher temperatures. However, the iron release rate was found to be highest at 30 °C.

The Arrhenius plots for the abiotic oxidation of pyrrhotite (based on sulphate release) are shown in Figure 4.31 and the activation energies at each pH are given in Table 4.12. The activation energies obtained for pH = 2 and pH = 3 were 42.6 and 51.8 $kJ \cdot mol^{-1}$, respectively. Typically, diffusion controlled reactions exhibit activation energies of 12 – 25 $kJ \cdot mol^{-1}$. Reactions controlled by molecular collisions or chemical bond rearrangements usually have activation energies in excess of 30 $kJ \cdot mol^{-1}$. The above activation energies indicate reaction processes as the controlling mechanism and that the reactions are not diffusion controlled. The corresponding activation energies for pH = 4 and pH = 6 were 14.5 and 23.7 $kJ \cdot mol^{-1}$, respectively, and are consistent with mass transport or diffusion control. This change in controlling mechanism with pH was not observed previously for pyrite oxidation.

Effect of pH

The pH seemed to affect the activation energies. Figure 4.29 and Figure 4.30 illustrated the effect of pH on the sulphate and iron release rates under various temperatures. The overall trend of oxidation rates (both sulphate and iron release) are inversely dependent on pH, i.e. higher oxidation rates at lower pH values. The effect of pH on pyrrhotite oxidation rates was found to converge to a more or less constant oxidation rate at pH = 6 at all temperature tested. At pH = 6, the pyrrhotite oxidation rates appeared to be independent of temperature. It has been noted above that there may be a change in reaction mechanism, hence temperature effects between pH = 3 and pH = 4. At pH = 3 and below, the apparent reaction mechanism is controlled by chemical processes, while at pH = 4 and above the rate controlling step appears to be diffusive transport.

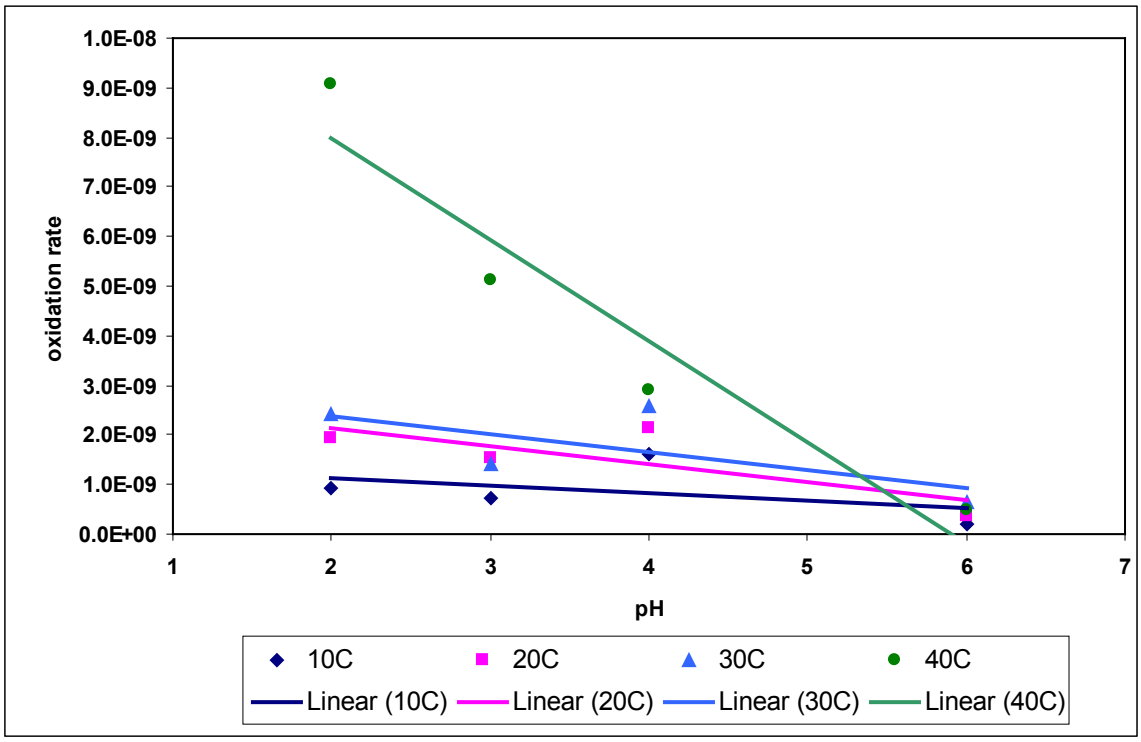

Figure 4.29: Effect of pH on abiotic pyrrhotite oxidation rates (based on sulphate release) at various temperatures.

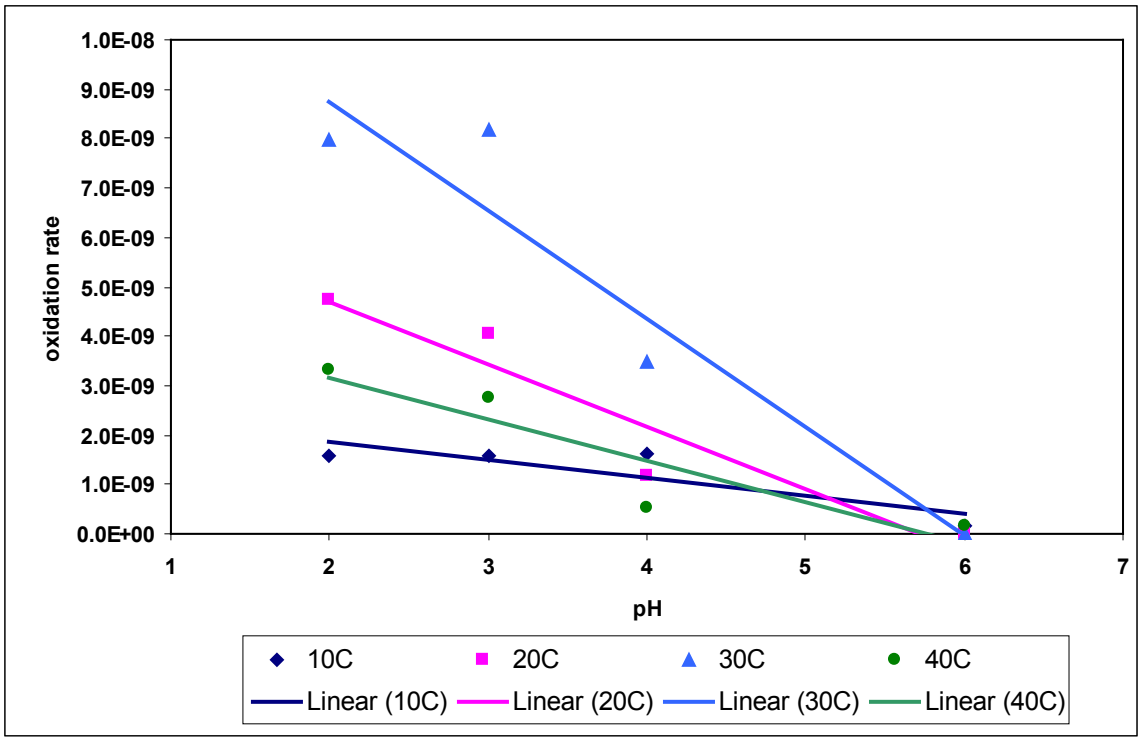

Figure 4.30: Effect of pH on abiotic pyrrhotite oxidation rates (based on iron release) at various temperatures.

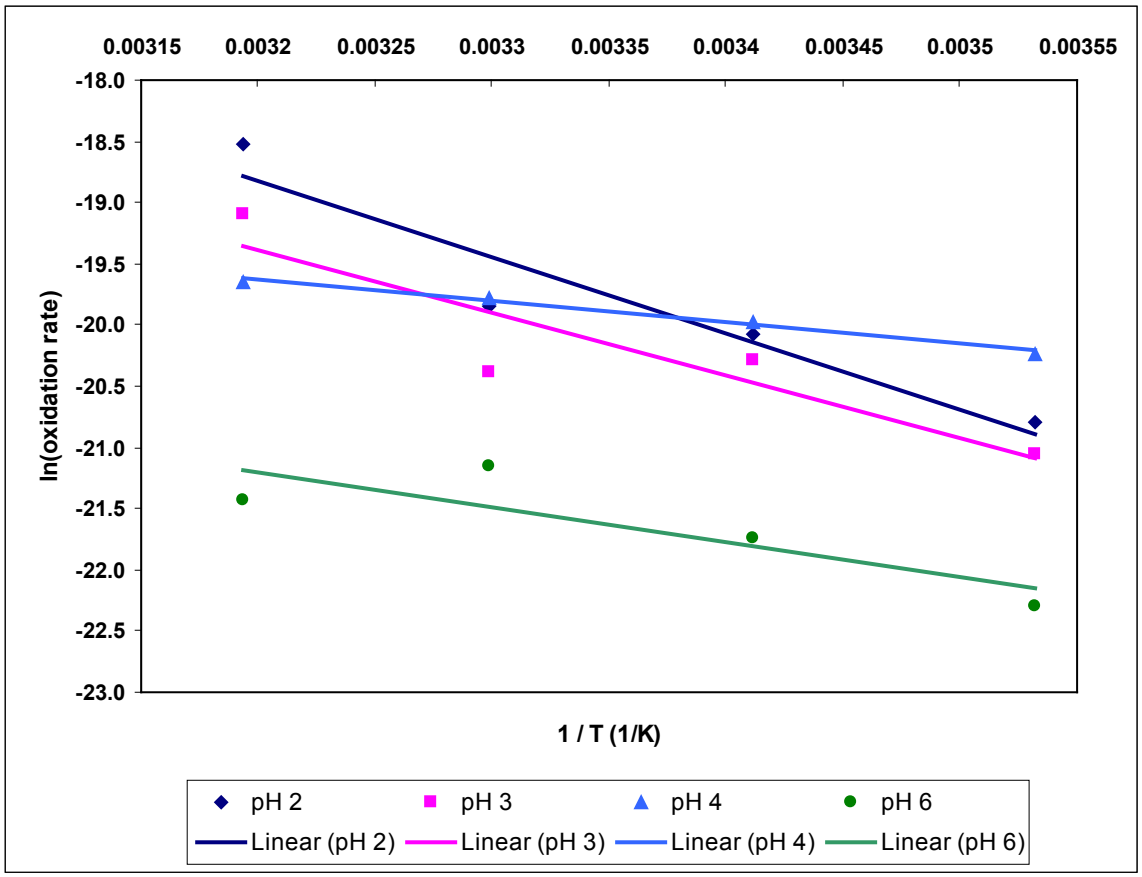

Figure 4.31: Arrhenius plots of abiotic pyrrhotite oxidation rates (based on sulphate) with temperature at various pH values.

Table 4.12: Activation energies for abiotic pyrrhotite oxidation (based on sulphate release).

Activation Energy (J/mol·K)	**pH**			
	2	**3**	**4**	**6**
	51851	42606	14509	23761

Effect of Chelating Agent

The addition of chelating agent, such as EDTA, was used to prevent the precipitation of ferric hydroxide, which, in turn, was used to investigate the significance of transport limitation in the kinetic experiments. The addition of EDTA did not have any significant effect on the iron release for pH ≤ 4 (Figure 4.32). Despite the addition of EDTA, which could potentially act as a leaching agent, there was no significant increase of iron release with EDTA compared to the experiments without EDTA. Therefore, the lower rates and lower activation energy values at pH

values of 4 and 6 that implied mass transport control of the pyrrhotite oxidation (discussed in previous sections) did not result from the precipitation of ferric hydroxide on the particle surface. The combined results strongly indicate that the controlling mechanism at pH 2 and 3 is kinetic oxidation, while at pH 4 and 6, the controlling mechanism is possibly due to dissolution reaction at pyrrhotite particles.

The nickel release rates in Figure 4.33 also showed no significant differences between tests with or without EDTA.

Effect of Bacterial Inoculation

The presence of bacteria, such as *Thiobacillus ferrooxidans*, is known to accelerate the oxidation of sulphide minerals. The effects of bacteria on pyrrhotite oxidation rates are shown in Figure 4.34 and Figure 4.35 based sulphate release and iron release. The sulphate release rates with bacteria were significantly higher than those that were not inoculated. The maximum biological rate at 40 °C was observed at pH 4 (3.53×10^{-8} mol·m^{-2}·s^{-1}), and was approximately 10 times higher than the abiotic oxidation rate (2.92×10^{-9} mol·m^{-2}·s^{-1}).

Despite significant increase of sulphate release rates, however, the inoculation with bacteria had no effect on the iron release rates during pyrrhotite oxidation (Figure 4.34). Therefore, the importance of bacteria during pyrrhotite oxidation appears to be related to the sulphide metabolism. Even ignoring the results at pH = 6, for which bacteria are not expected to be important and ferric iron should precipitate, it is evident that bacterial catalysis is different for the sulphate and iron components of the oxidation reaction. These results suggest that sulphate release rates may increase by a factor of 10 as a result of bacterial involvement.

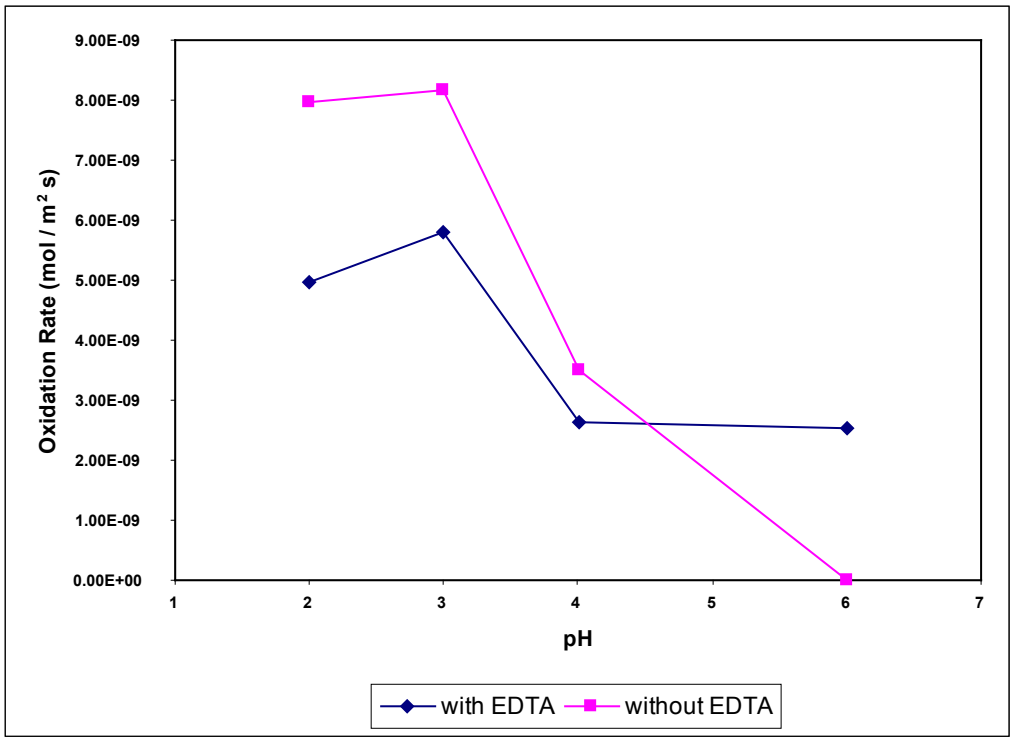

Figure 4.32: Effect of chelating agent (EDTA) on abiotic pyrrhotite oxidation rate (based on iron release).

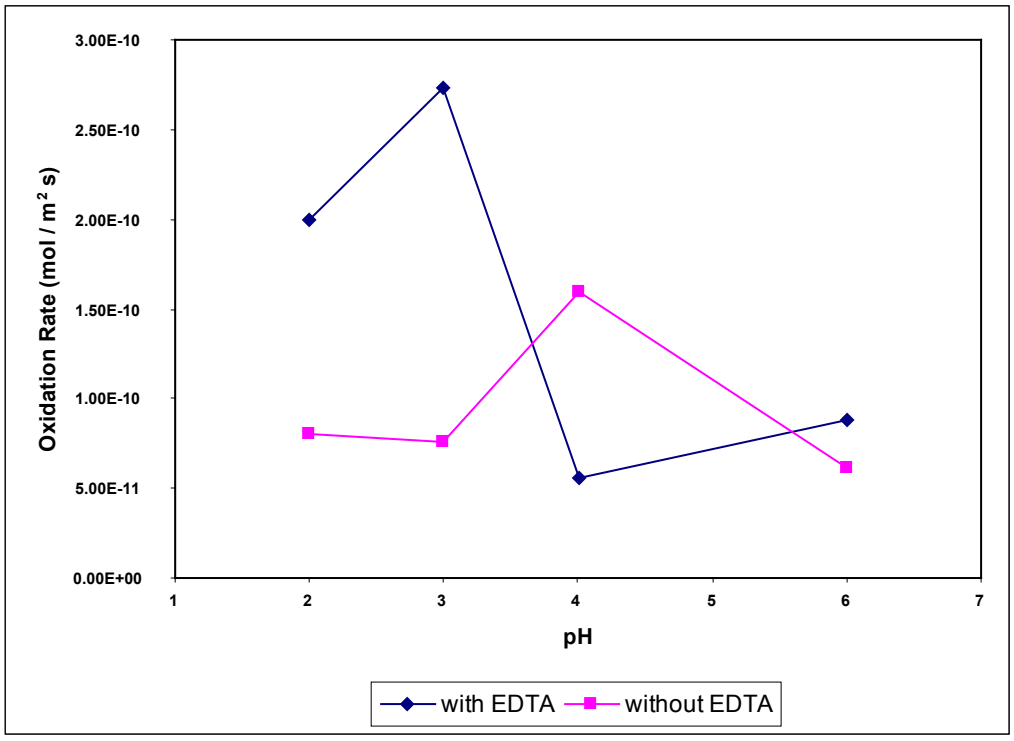

Figure 4.33: Effect of chelating agent (EDTA) on abiotic pyrrhotite oxidation rate (based on nickel release).

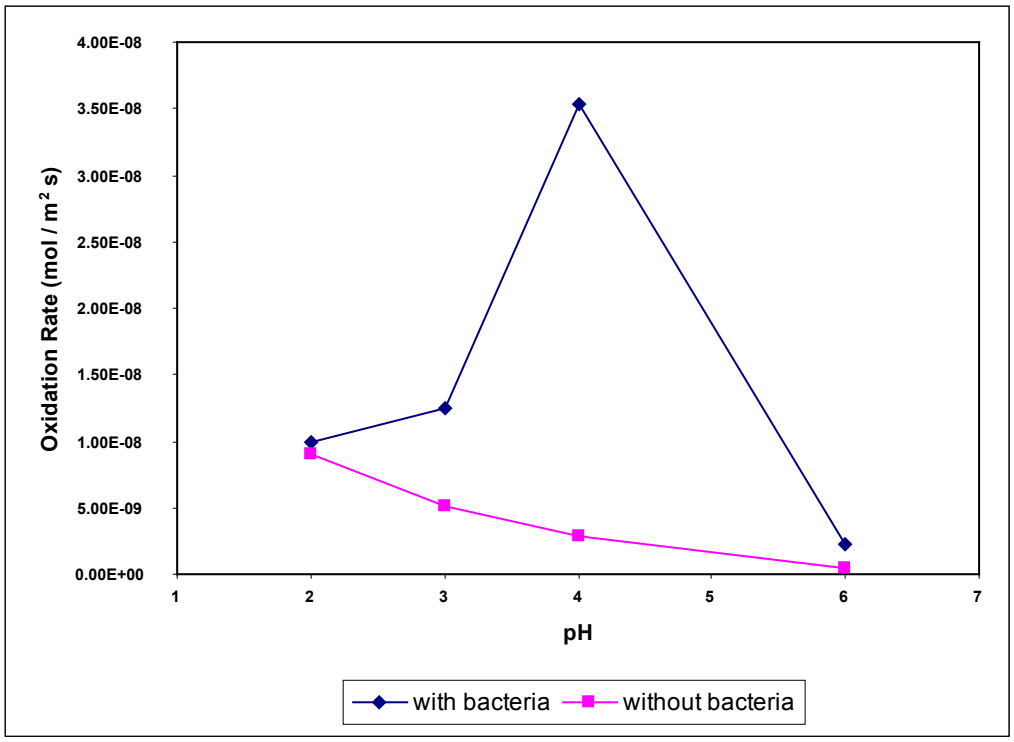

Figure 4.34: Effect of bacterial inoculation on pyrrhotite oxidation rate (based on sulphate release).

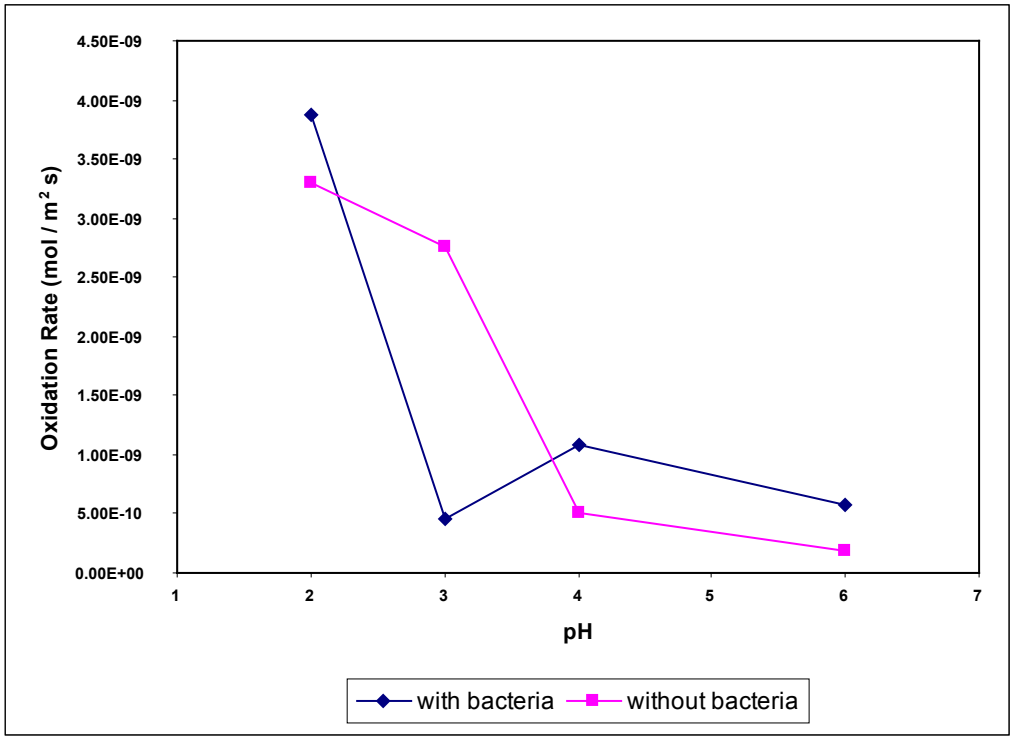

Figure 4.35: Effect of bacterial inoculation on pyrrhotite oxidation rate (based on iron release).

COLUMN STUDIES ON PYRRHOTITE TAILINGS

The acid generation rate of mine tailings depended on oxidation kinetics of sulphide minerals and transport processes. The packed columns are designed to investigate the coupling of the oxidation kinetics with geochemical and transport processes, such as diffusion of oxygen, buffering reactions, precipitation and adsorption. These processes were measured using overall contaminant loading data, headspace oxygen consumption measurements, porewater chemistry and pore-space oxygen concentration profiles.

Altogether, 6 columns were constructed to investigate the coupling of pyrrhotite oxidation kinetics and transport processes. The Inco pyrrhotite concentrate was mixed with quartz sand to lower the sulphur content to 2 % and 6 % S^{2-}. A single column was packed with 2 % S^{2-} mixture, while 5 other columns were packed with 6 % S^{2-} mixture. The column conditions are given in Table 4.13.

Table 4.13: Conditions used in packed columns.

Condition	Designation	Approximate Sulphur Content (%)	Special Conditions
#1	Base Case	6	none
#2	2 % S^{2-}	2	none
#3	Bacterial inoculated	6	with *Thiobacillus ferrooxidans* inoculations
#4	1% Calcite	6	with 1 % calcite buffer
#5	5 % Enstatite	6	with 5 % buffering silicate (Enstatite)
#6	With Fines	6	with minus 45 μm particles

The 6 % S^{2-} column will be used as the base case scenario to compare the effects of geochemical parameters, such as sulphur content, bacterial catalysis, buffering minerals and fine particles.

The cumulative loading of sulphate, iron and nickel from the base case (6 % S^{2-}) column are presented in Figure 4.36.

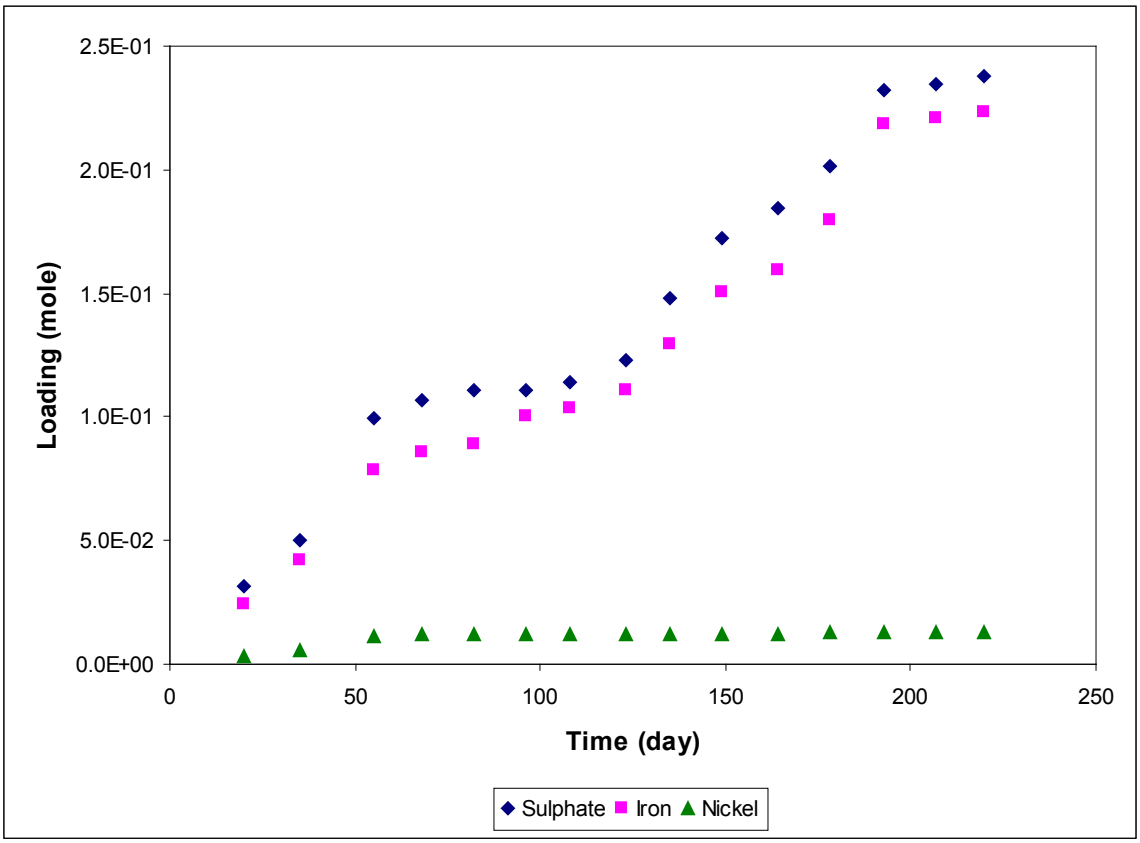

Figure 4.36: The sulphate, iron and nickel production loading in base case column.

The sulphate loading data above show the cumulative sulphate generation for a period of approximately 220 days. The corresponding sulphate generation rate ranged from 1.90×10^{-4} to 2.48×10^{-3} mol·day^{-1}. The iron production rate ranged from 1.63×10^{-4} to 2.61×10^{-3} mol·day^{-1}. The nickel loading rates were significantly lower than those of sulphate and iron, and ranged from 1.59×10^{-6} to 2.82×10^{-4} mol·day^{-1}.

The ratios of iron to sulphate production rate are shown in Figure 4.37. The average iron to sulphate ratio of 0.899 is slightly lower than the stoichiometric ratio of iron to sulphide in pyrrhotite. A ratio of iron to sulphate production rate below unity indicates accumulation of iron (in form of ferric hydroxide) in the column. The corresponding ratio between nickel production rate and sulphate production rate decreased from 0.11 at start to 0.01. The time profile of the nickel to sulphate production ratio is given in Figure 4.38. The nickel to sulphate ratios combined with loading data of nickel indicate the nickel release was not proportional to the pyrrhotite oxidation rate over the first 50 days.

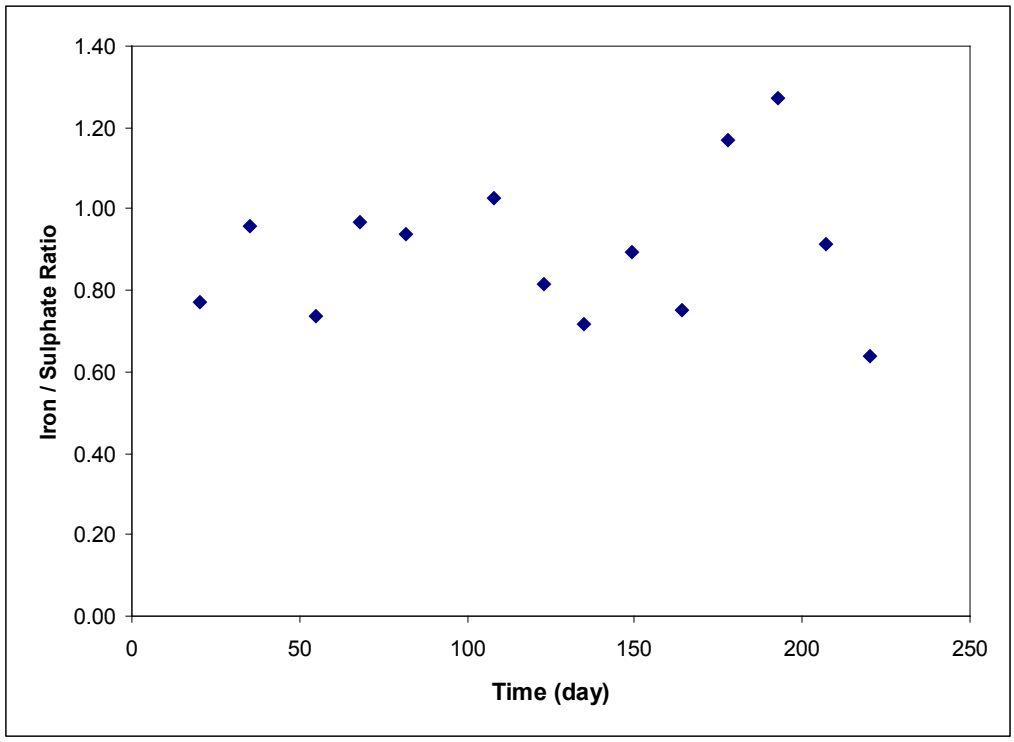

Figure 4.37: Iron to sulphate production ratio in the column.

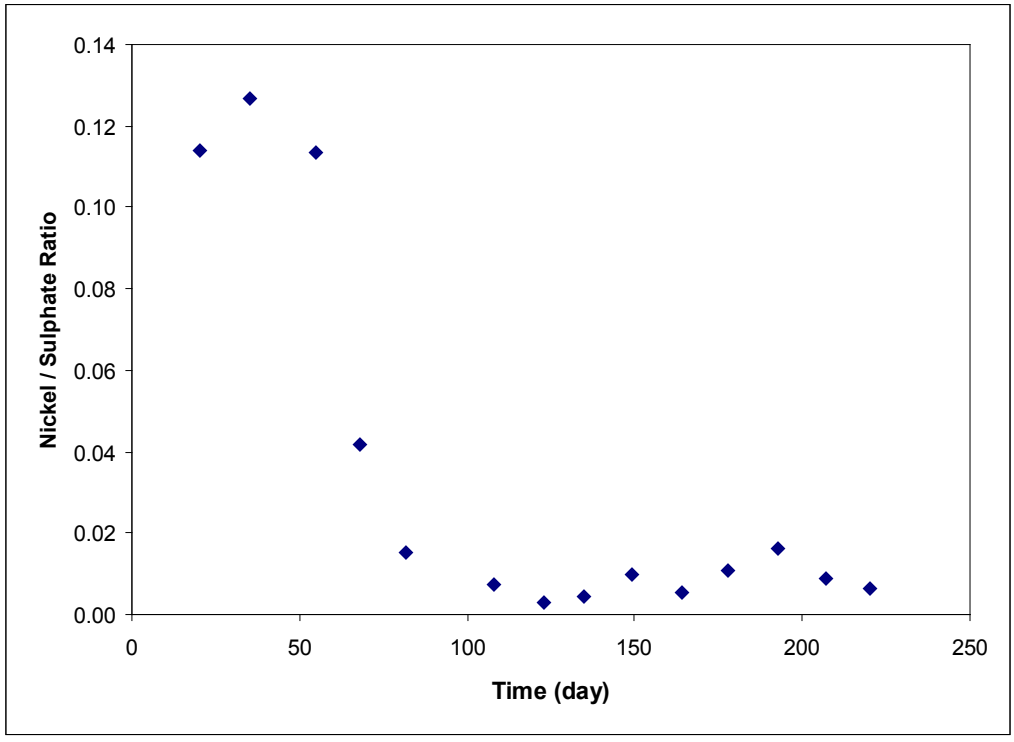

Figure 4.38: Nickel to sulphate production ratio in the column.

Based on the nickel production rate for Inco pyrrhotite (0.8 % nickel content by mass), the

theoretical ratio of the nickel production rate to sulphate production rate is 0.014. The observed ratio of nickel to sulphate production rate at the start was significantly higher than the theoretical ratio. The higher nickel production rate at the early stage was likely as the result of pentlandite oxidation (approximately 0.25 % by mass in the base case column). As pentlandite was depleted from the reactive surface, the nickel production rate decreased. After 50 days, the nickel to sulphate production ratios varied close to the theoretical ratio related to the nickel content of the pyrrhotite. Co-precipitation and adsorption of nickel to ferric hydroxide may have contributed to the lower nickel release rates.

The oxygen consumption rate data yielded results comparable to those observed from the loading rates. A plot of the oxygen consumption rates with time for the base case is shown in Figure 4.39. The oxygen consumption rates in the column decreased with time, from an initial high of 1.52×10^{-2} to low of 4.42×10^{-3} mol·day^{-1}, which indicated a possible switch from kinetic to mass transport control. As pyrrhotite content depleted at the surface layer of the column, the reactive layer migrated deeper into the column. Therefore, oxygen diffusion became more significant in comparison to oxidation kinetics of pyrrhotite. The diffusion effect may also be enhanced with precipitation of ferric hydroxide in the column, which can reduce the effective diffusion coefficient of oxygen through the tailings or at the surface of the pyrrhotite particles.

The corresponding oxygen consumption flux obtained from the packed column ranged from 1218 initially to 354 mol $O_2 \cdot m^{-2} \cdot yr^{-1}$. These data are in the same range as those observed by Tibble and Nicholson (1997) in field measurements on pyrrhotite tailings using similar methodology. The field-measured oxygen consumption flux ranged 200 to 700 mol $O_2 \cdot m^{-2} \cdot yr^{-1}$ in tailings containing 15 % S as pyrrhotite. This demonstrated that the column experiment can provide representative data for site characterization and the oxygen consumption technique is suitable for both packed column and field measurements.

The theoretical ratios between the oxygen consumption rate and sulphate production rate are 2 for pyrrhotite oxidation to Fe^{2+} and SO_4^{2-} and 2.25 for conversion to Fe^{3+} and SO_4^{2-}. The experimental ratio of oxygen consumption rate and sulphate production rate ranged from 33 to 2.64. The high ratios between oxygen consumption and sulphate production may be the result of partial oxidation of sulphide S^{2-} to elemental sulphur S^0 or conversion of pyrrhotite to amorphous FeS_2 as suggested by other studies.

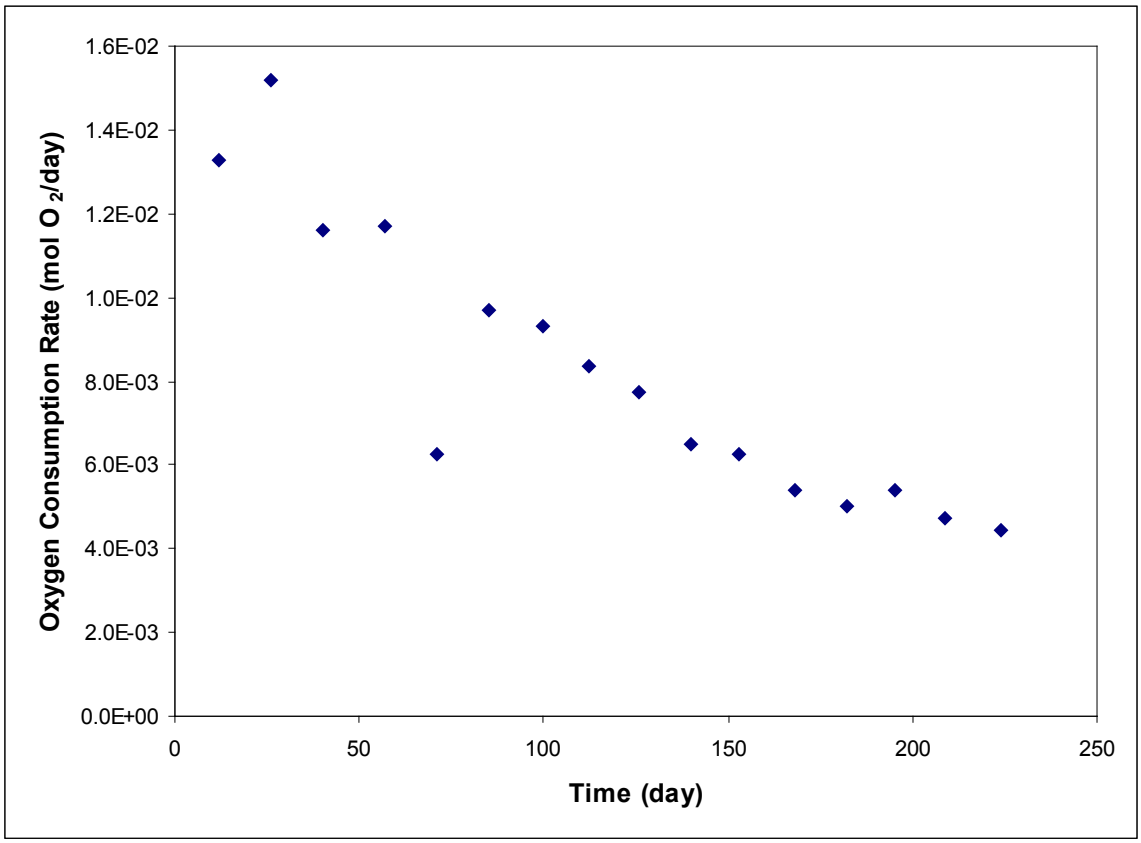

Figure 4.39: The oxygen consumption rate in column.

The concentration profiles for the base case column did not change significantly during 220 days. Examples of the concentration profiles are given in Figure 4.40. Visual observation of the column suggested hardpan formation in the upper layer if the column, which could the also seen from the iron concentration profile. The significant reduction of nickel concentration between the oxidation zone and the lower layer of the column indicated precipitation or adsorption of nickel from the porewater. The measured porewater concentration of sulphate reached levels above 10000 $mg \cdot L^{-1}$. The sulphate concentration profile demonstrated no significant secondary reaction, such as gypsum precipitation, occurring in the column with respect to sulphate. The oxygen was consumed within the top 40 cm. Therefore, the zone of oxidation was restricted to the top 40 cm in the column during the 200 days experiment.

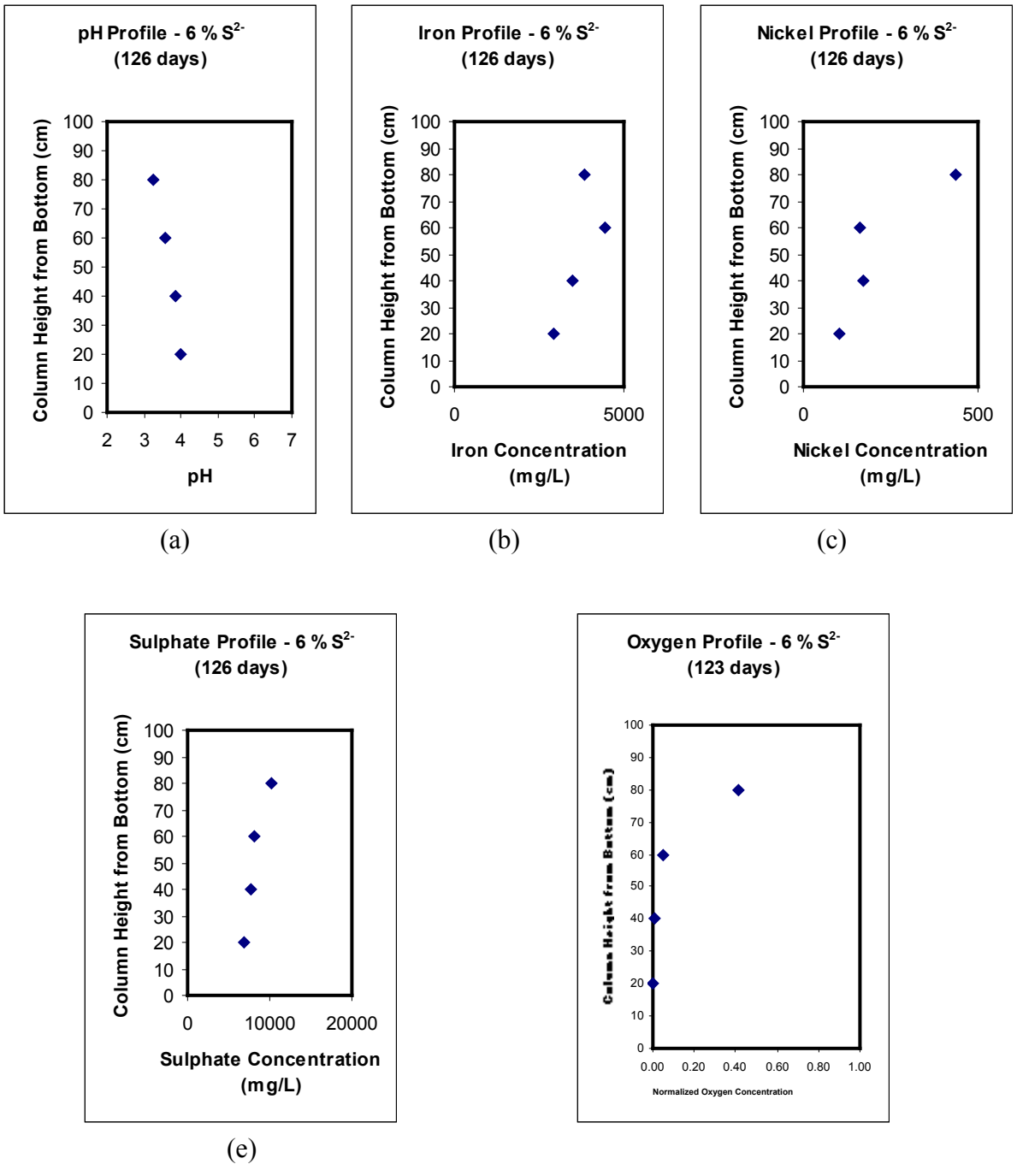

Figure 4.40: Concentration profile in the base case column after 126 days: (a) pH profile, (b) iron concentration profile, (c) nickel concentration profile, (d) sulphate concentration profile, and (d) normalized oxygen gas concentration profile.

Effect of Sulphur Content

The sulphate generation rate in a tailings mass is expected to be proportional to the sulphur content in the absence of other reaction controls, such as gas diffusion. The sulphate production rate obtained from the 2 % S^{2-} column ranged from 1.63×10^{-3} to 6.14×10^{-4} mol·day^{-1}. These production rates were within the range of those obtained for the base case column. Figure 4.41 and 4.42 provide a comparison of sulphate and iron loading between the 2 % S^{2-} and base case columns. Production rate is the first derivative (i.e. the local slope) of the loading data. The average iron to sulphate production ratio in the 2 % S^{2-} column was 0.955. The higher iron to sulphate ratio indicated less iron accumulated as ferric hydroxide in the 2 % S^{2-} column.

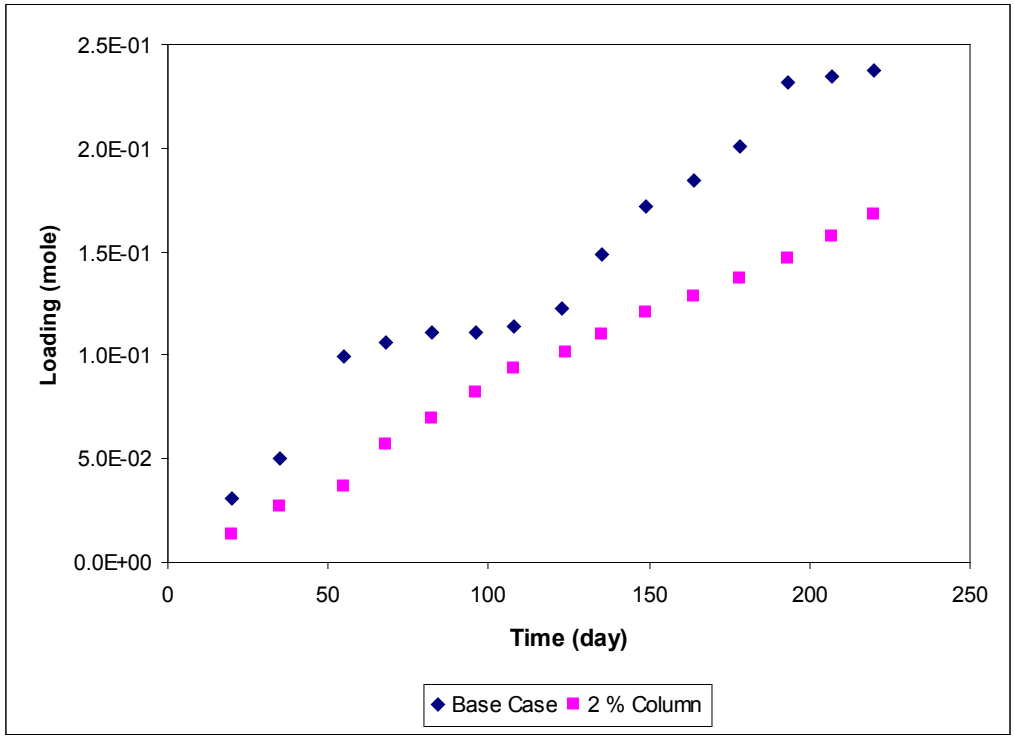

Figure 4.41: Comparison of sulphate loading between the base case and the 2 % S^{2-} columns.

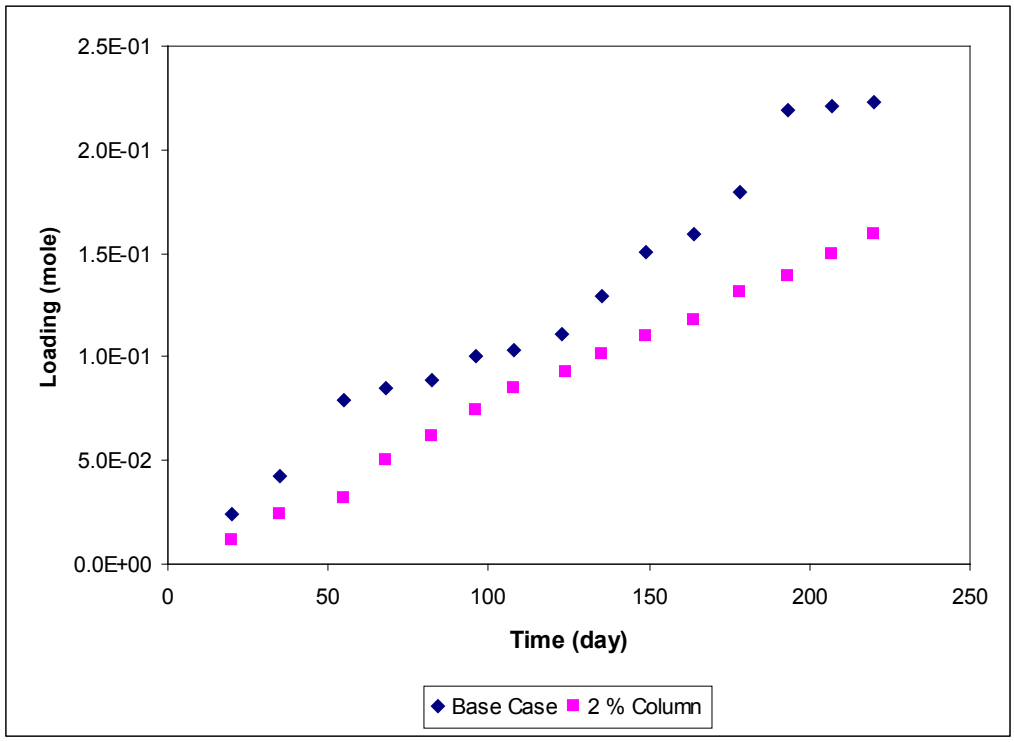

Figure 4.42: Comparison of iron loading between the base case and the 2 % S^{2-} columns.

The sulphate and iron generation rates in the 2 % S^{2-} column (6.1×10^{-4} to 1.6×10^{-3}mol·day^{-1}) were comparable to those of the base case column (1.9×10^{-4} to 2.3×10^{-3}mol·day^{-1}). The lower sulphide content in the 2 % S^{2-} column allowed deeper oxygen penetration and resulted in a deeper oxidation zone. The 2 % S^{2-} column also retained less water under gravity because it contained less fine-grained tailings concentrate and there would be expected to have a higher gas diffusion coefficient. The oxygen concentration profile for 2 % S^{2-} column is given in Figure 4.43. The profile demonstrated that oxygen penetrated the entire column, which indicated the importance of mass transport control in tailings with higher gas diffusion coefficients (better drained) or with a lower sulphide content.

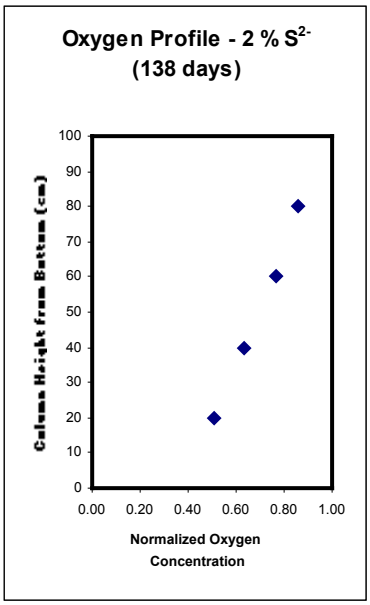

Figure 4.43: Oxygen concentration profile in the 2 % S^{2-} column after 138 days.

Despite the high oxygen penetration in the 2 % S^{2-} column, the lower sulphide content resulted in significantly lower oxygen consumption initially. The oxygen consumption profiles are shown in Figure 4.44. The rates of oxygen consumption declined continually in the base case column. In contrast, the oxygen consumption rates were lower, but remained relatively constant in the 2 % S^{2-} column. This implies, that at the lower sulphide content pyrrhotite oxidation remained under kinetic control, while at higher sulphide concentrations a gradual transition from kinetic control to diffusive control occurred. The stoichiometric molar ratio for oxygen consumption and sulphate production for pyrrhotite is approximately 2.5. The experimentally observed ratio ranged from 1.51 to 6.53. Any ratio greater than 2.5 implies incomplete sulphide-sulphur oxidation, while a ratio less than 2.5 implies the presence and complete oxidation of elemental sulphur as well as the complete oxidation of pyrrhotite. It is noteworthy that the theoretical lower limit of the ratio of oxygen consumption to sulphate production is 1.5 in a pyrrhotite-sulphur environment. The ratio between oxygen consumption rate and sulphate production rate ranged from 6.53 to 1.51. The lower oxygen consumption / sulphate production ratio and comparable sulphate production rate with the base case indicated higher percentage conversion of sulphide (S^{2-}) to sulphate (SO_4^{2-}).

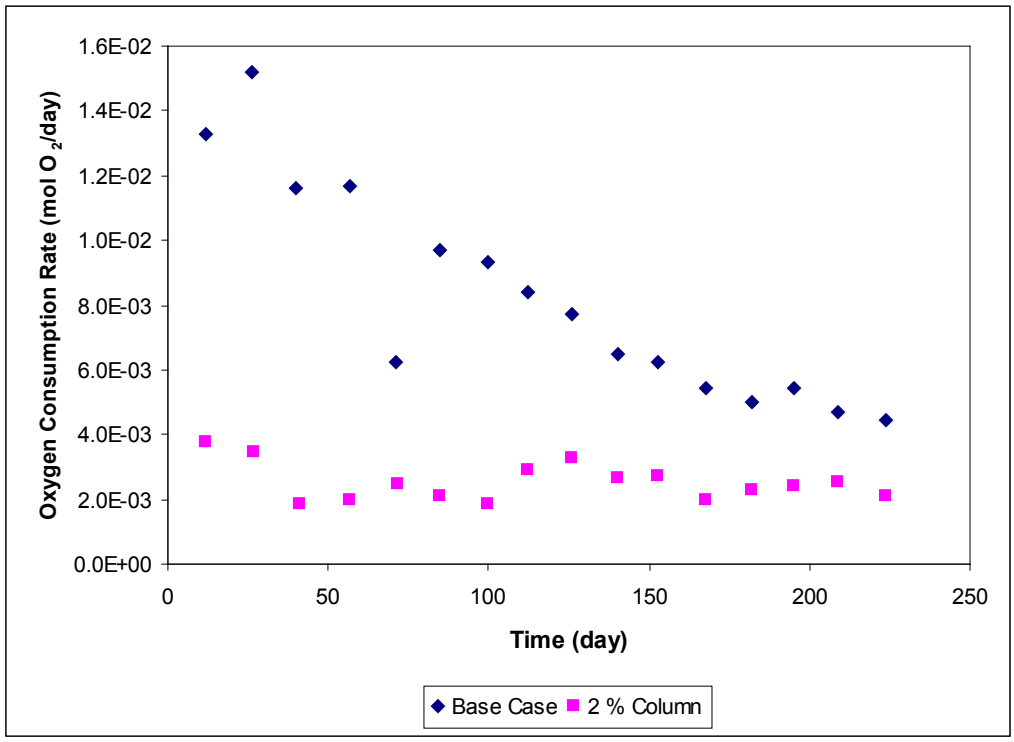

Figure 4.44: Comparison of oxygen consumption rate between the base case and 2 % S^{2-} columns.

The nickel production rate with time was different in the 2 % S^{2-} column compared to the base case column (Figure 4.45). The nickel production rate ranged from 2.40×10^{-4} to 2.56×10^{-5} mol·day^{-1}. The nickel production rate remained high compared to the base case. As observed from the ratio between the iron to sulphate production rates, lower accumulation of iron in the column results in less coprecipitation of nickel or adsorption of nickel on ferric hydroxide.

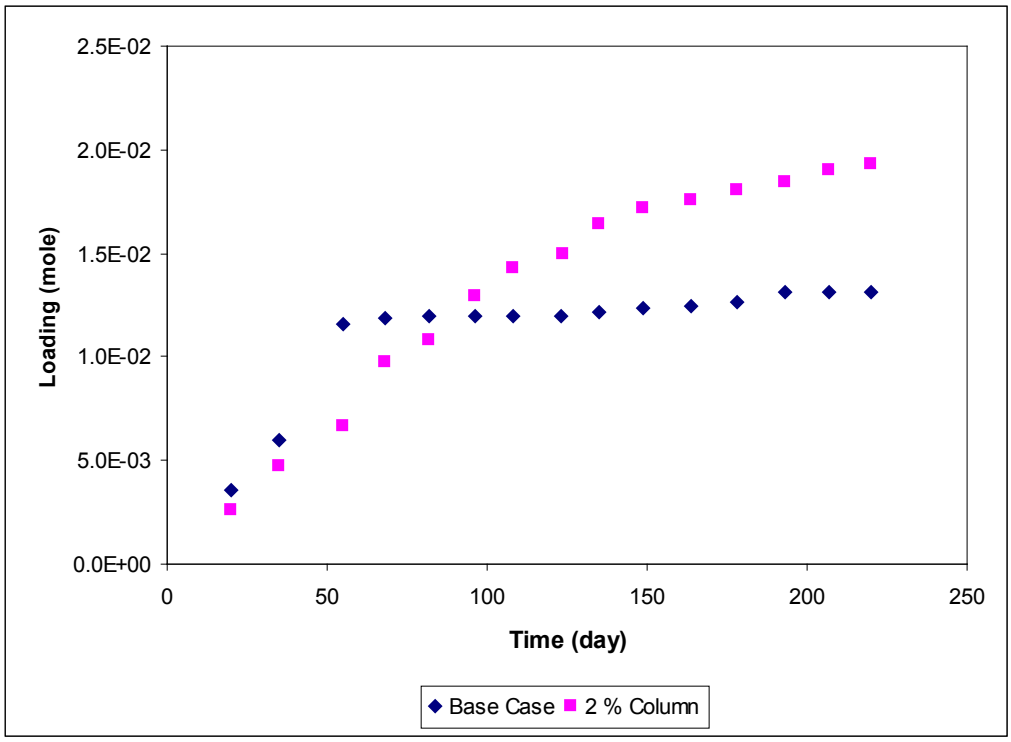

Figure 4.45: Comparison of nickel loading between the base case and the 2 % S^{2-} columns.

Effect of Bacterial Inoculation

Bacteria such as *Thiobacillus ferrooxidans*, can significantly enhance the sulphide S^{2-} conversion to SO_4^{2-}. Sulphate loading in the base case column is compared with the inoculated column in Figure 4.46. There were no significant differences between the sulphate production rate between the bacterial inoculated column and the base case. Similar observation was also true for the iron production rate. The nearly exponential increases of sulphate loading followed by a constant rate suggest the development of steady state bacterial population. The definite inflection point after 120 days and the essentially identical sulphate production rates suggest a possible cross contamination of the base case column with bacteria. The oxygen consumption rate for the bacterial inoculated column was found to be the essentially the same as the base case (Figure 4.47). The continuous decline of the oxygen consumption rate in both the base case and the inoculated column indicates the increasing importance of mass transfer (i.e. diffusion) as time progresses.

The average ratio of the iron to sulphate production rate was 0.789. The lower iron to sulphate ratio indicated bacterial catalysis of Fe^{2+} to Fe^{3+} reaction and higher ferric hydroxide accumulation in the bacterial inoculated column. The ratios between oxygen consumption to sulphate production were in the same range as those observed in the base case column.

Concentration profiles in the inoculated column were similar to those of the base case. The

sulphate concentration in the oxidation layer reached a level of 12000 mg·L^{-1} (see Appendix E). Similarity of concentration profiles between the bacterial inoculated column and the base case column confirmed mass transfer of oxygen as the controlling factor.

The nickel production rates in the inoculated column were significantly lower than those in the base case column (Figure 4.48). The higher accumulation of iron in the form of ferric hydroxide likely retained the nickel in the column through coprecipitation and adsorption processes.

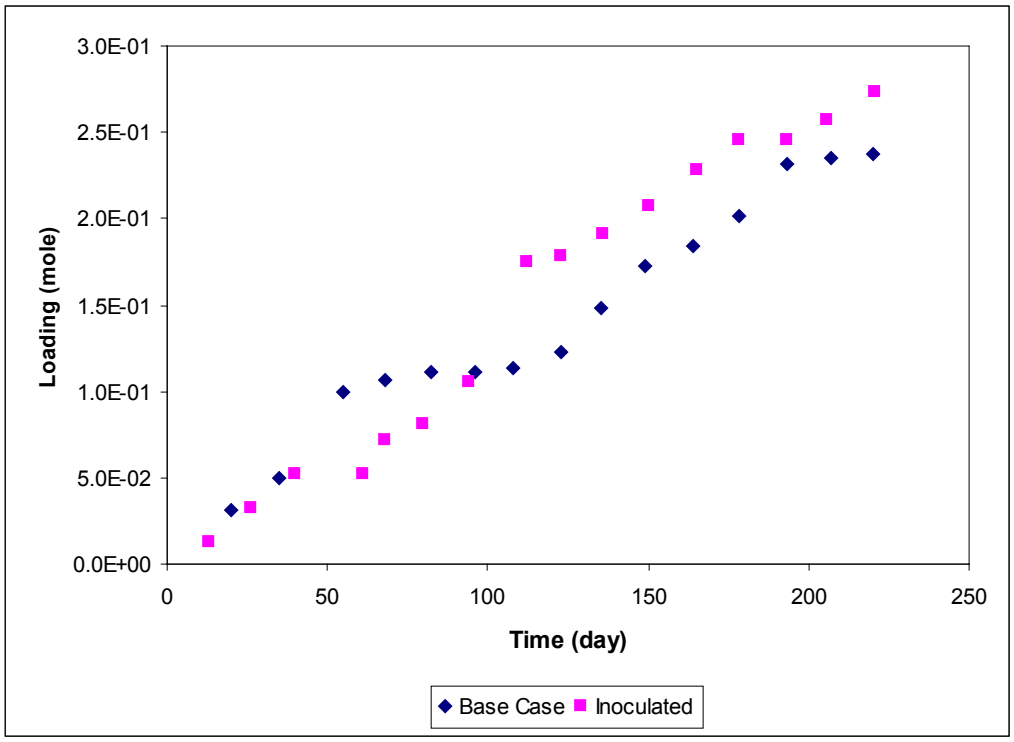

Figure 4.46: Comparison of sulphate loading between the base case and the inoculated columns.

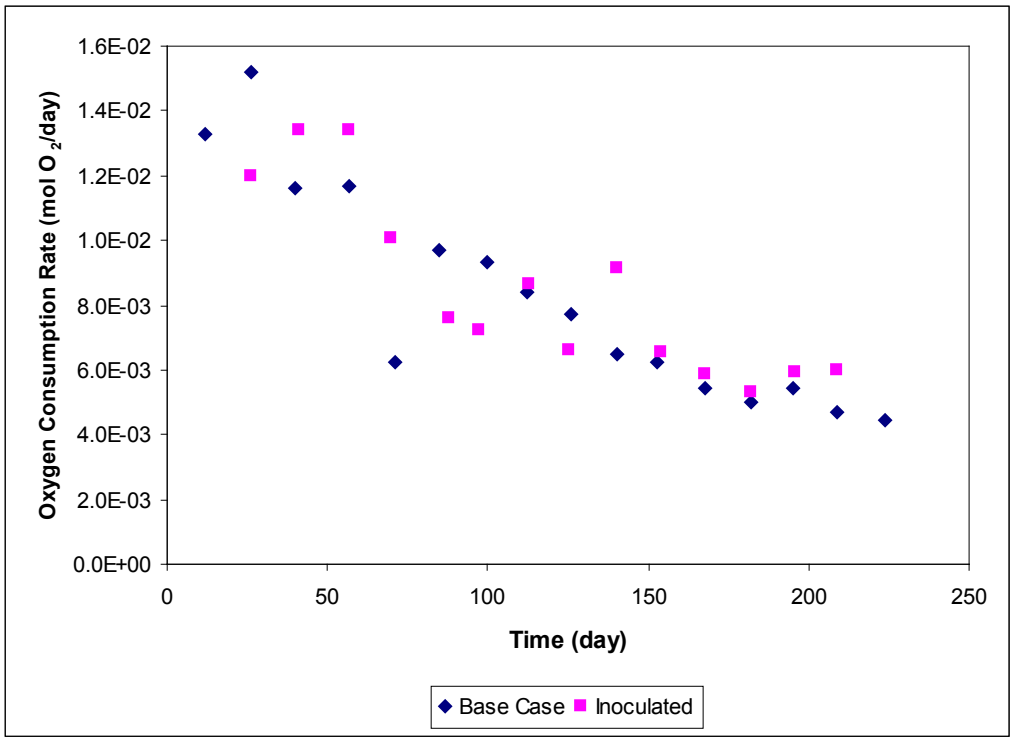

Figure 4.47: Comparison of oxygen consumption rate between the base case and the inoculated columns.

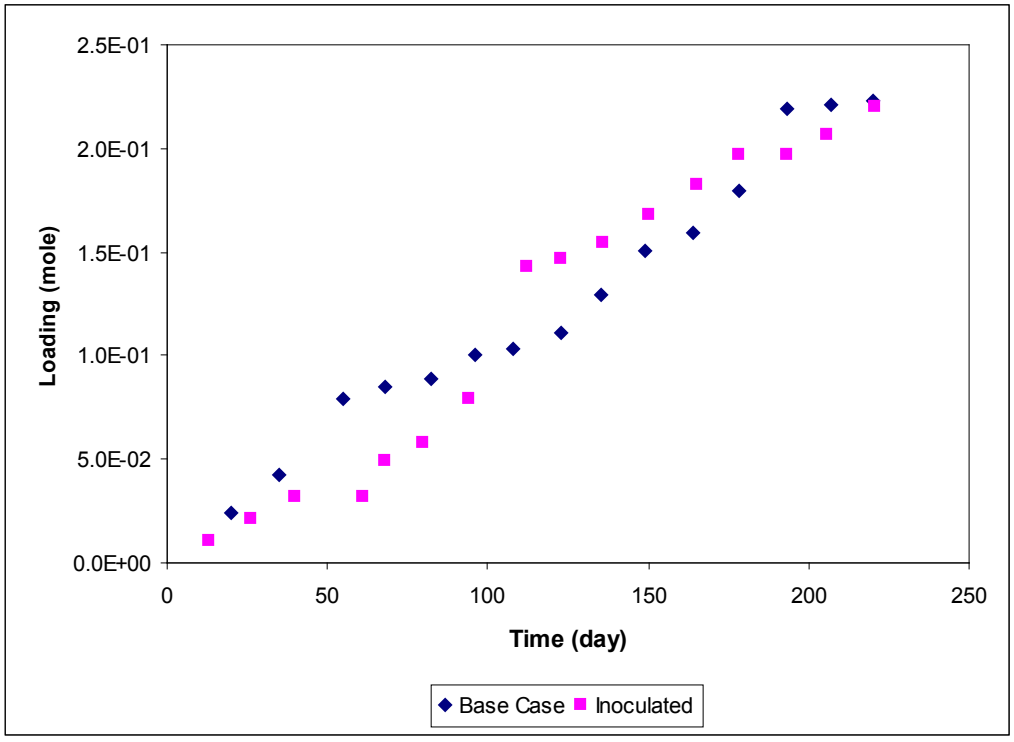

Figure 4.48: Comparison of nickel loading between the base case and the inoculated columns.

Effect of Neutralizing Minerals

The addition of neutralizing minerals gives rise to higher pH values in the packed column compared to base case column. Calcite and enstatite were added to two packed columns to investigate the effect of these minerals on the contaminant release. The presence of buffering minerals had little effect on the sulphate production rate and the oxygen consumption rate. The time profiles of sulphate production rate and oxygen consumption rate are shown in Figure 4.49 and Figure 4.50, respectively. The measured ratios between oxygen consumption and sulphate production for both calcite and enstatite columns are in the same range as those observed for the base case column. Oxidation kinetics of pyrrhotite is inversely dependent on pH, therefore higher pH should result in lower oxidation rate. The approximately identical sulphate production rates suggest that kinetic control was not significant in the packed column. The general trends of the sulphate and oxygen concentration profiles in the buffered columns were similar to those of the base case column. The lack of inflection point in the 5 % enstatite and the 1 % calcite column indicates no effects from bacterial cross-contamination or from bacterial effects. However, the highest sulphate concentration reached in the calcite buffering column was only 5000 $mg \cdot L^{-1}$ (see Appendix E), which was approximately one half the highest concentration measured in the base case column. The lower porewater sulphate concentration and identical sulphate production rate indicated the formation of gypsum in the pore-space that likely dissolved during the flooding and flushing process.

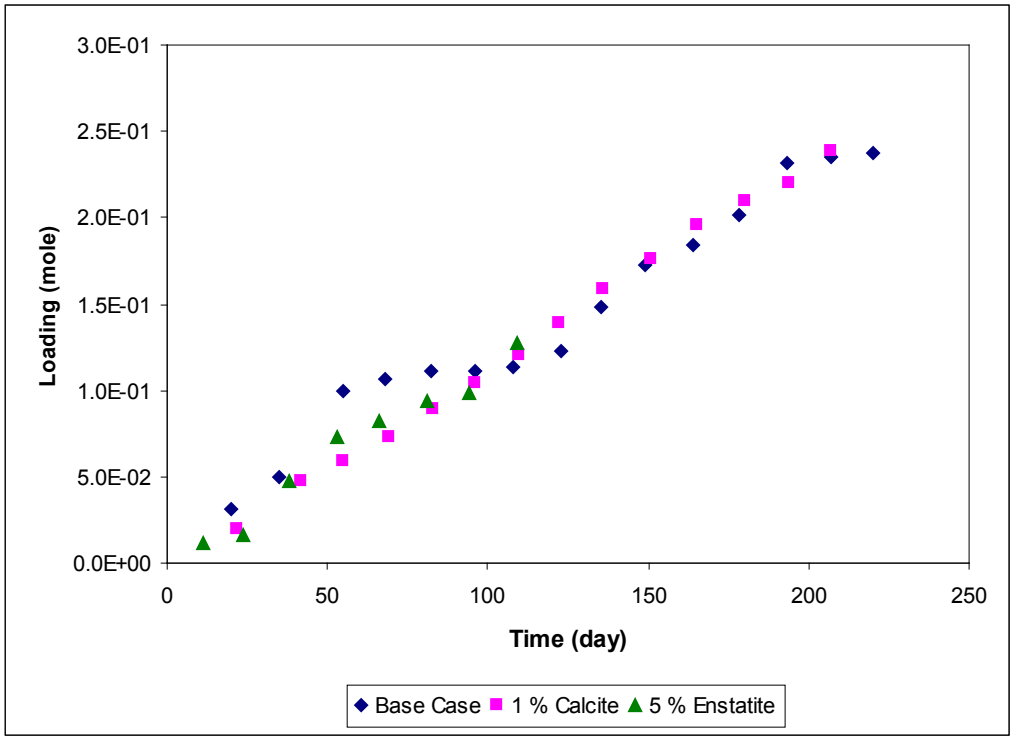

Figure 4.49: Comparison of sulphate loading between the base case and the mineral buffered columns.

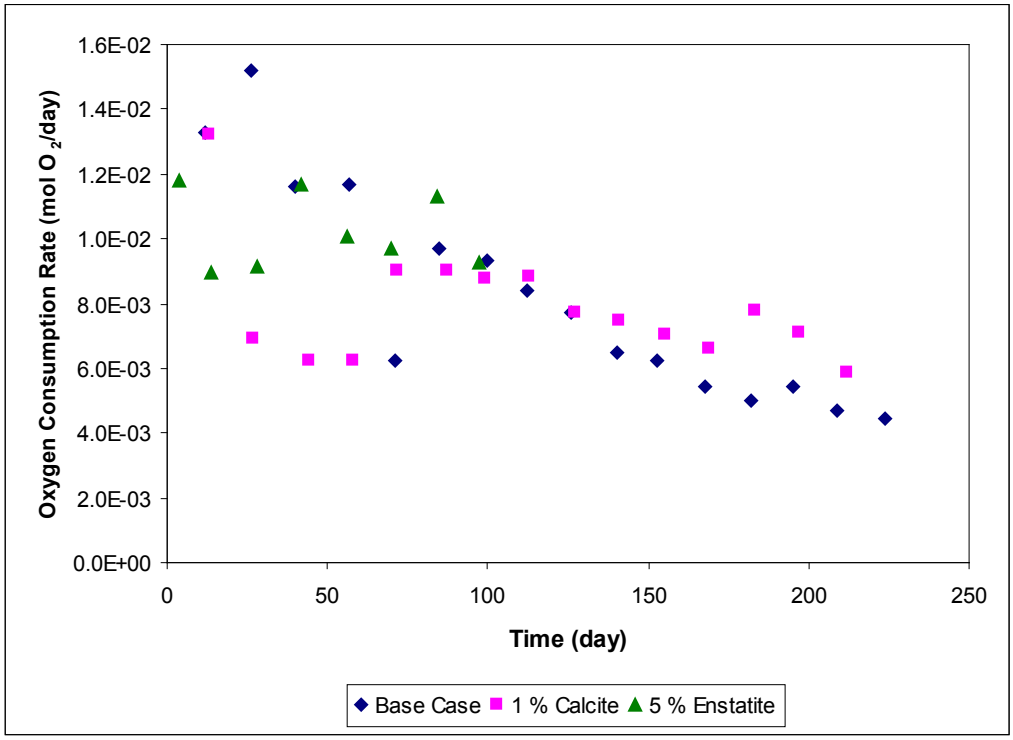

Figure 4.50: Comparison of oxygen consumption rate between in the base case and the mineral buffered columns.

Although the presence of buffering minerals had little effect on the sulphate production rate and the oxygen consumption rate, the iron and nickel production rates were significantly lower in the calcite buffered columns. The iron production rate from the 5 % enstatite column over the first 100 days was also slight lower than that in the base case column. Since the nickel production rate was shown previously to depend on accumulation of iron in the packed column, the major increase in iron accumulation should reduce nickel production rates. Th iron and nickel production rates are given in Figure 4.51 and Figure 4.52.

Majority of the iron in the 1 % calcite column was precipitated as ferric hydroxide due to high porewater pH (approximately 7.0). The high iron accumulation resulted in significant nickel retention in the column through either entrainment of nickel in the ferric hydroxide matrix or adsorption on the surface of the ferric hydroxide precipitate. The porewater concentration profiles for iron and nickel (Figure 4.53) also confirmed the accumulation of nickel in secondary iron precipitates. The enstatite resulted in porewater pH values of 4 to 5 and therefore less iron precipitated than the calcite column. This resulted in nickel loadings that were intermediate between the base case and the 1 % calcite column.

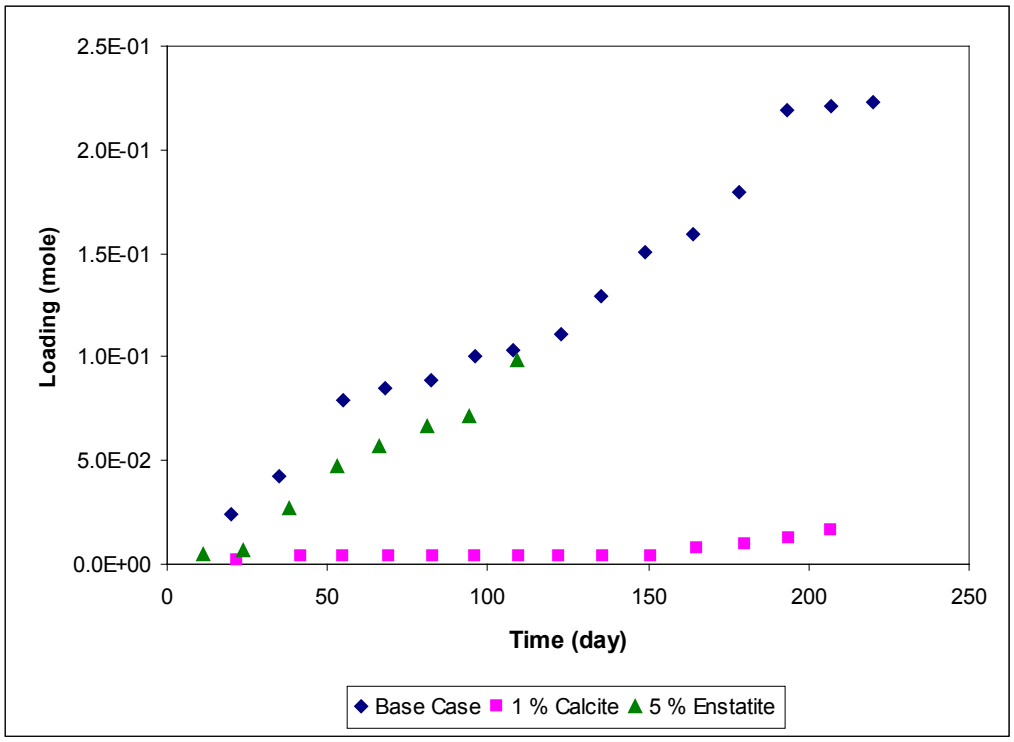

Figure 4.51: Comparison of iron loading between the base case and the mineral buffered columns.

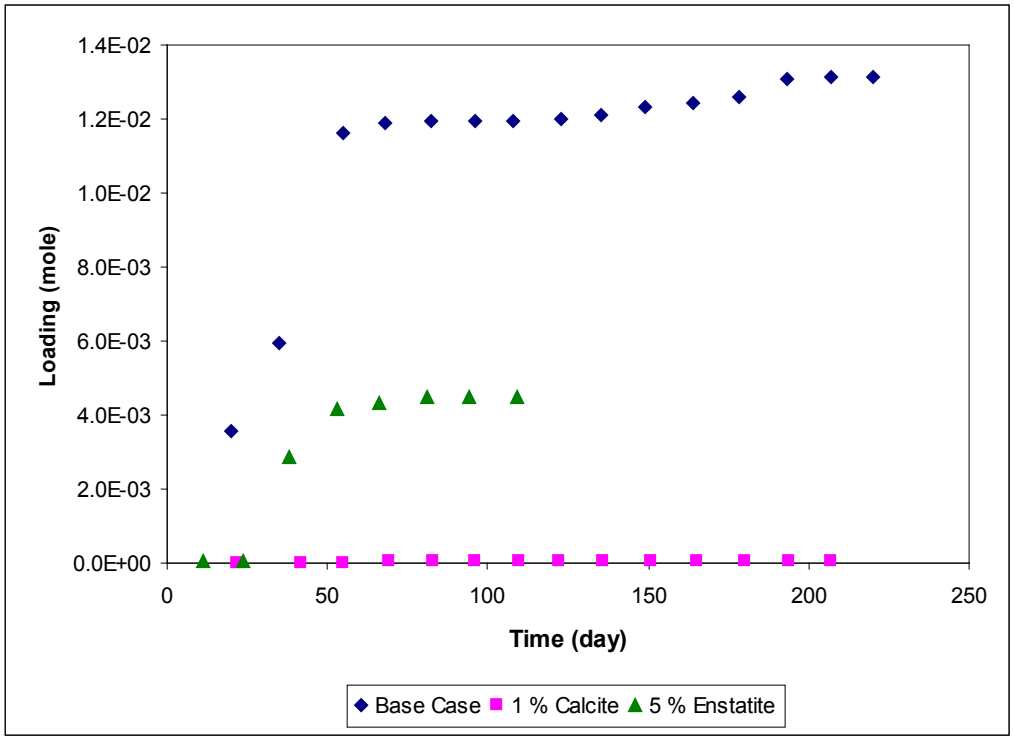

Figure 4.52: Comparison of nickel loading between the base case and the mineral buffered columns.

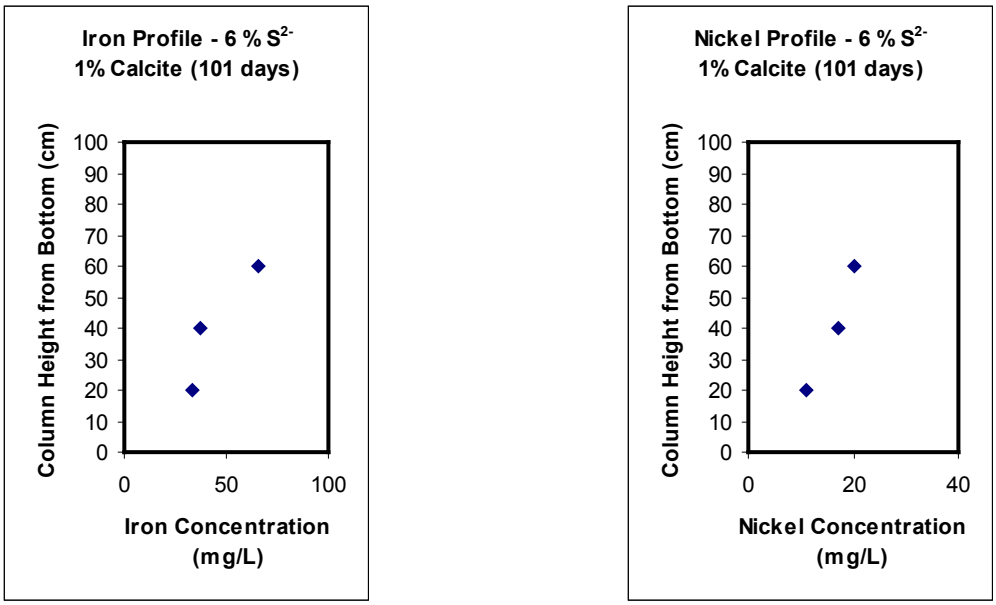

(a) **(b)**

Figure 4.53: Concentration profile in the 1 % calcite column after 101 days: (a) iron concentration profile, and (b) nickel concentration profile.

Effect of Fine Particles

The column including the fine particles exhibited a significantly lower production of sulphate and iron. This may be due to altered mass transfer characteristics. The presence of fine particles increases the water content in the pore-space, which reduces the diffusion of oxygen in the column. The oxygen concentration profiles in the column indicated no oxygen penetration beyond a depth of 20 cm from the surface. The zone of shallow oxygen penetration restricted the amount of material available for oxidation. The shallow oxidation layer would reduce the production rate of contaminants, which can be seen in Figure 4.54 to Figure 4.56 for sulphate, iron and nickel. The lower levels of contaminant porewater concentrations observed in the column with fines were in agreement with lower overall oxidation of pyrrhotite.

Despite the shallow oxygen penetration in the column with fines, the presence of fine particles increased the reactive surface area of the fresh material. Therefore, the initial oxygen consumption rates for the column the fines were significantly higher than those observed in the base case column (Figure 4.57). The initial oxygen consumption rate was approximately 1.80×10^{-2} mol $O_2\cdot day^{-1}$ and decreased rapidly to a steady state value of approximately 4.00×10^{-3} mol $O_2\cdot day^{-1}$. The inflection in the loading profile suggests potential cross contamination of the fine column with bacteria.

The high initial oxygen consumption rate yielded a very high ratio of oxygen consumption to

sulphate production (24 to 63). The combination of low sulphate production rate and high oxygen consumption rate suggested highly significant partial oxidation of pyrrhotite occurred in the column with fines.

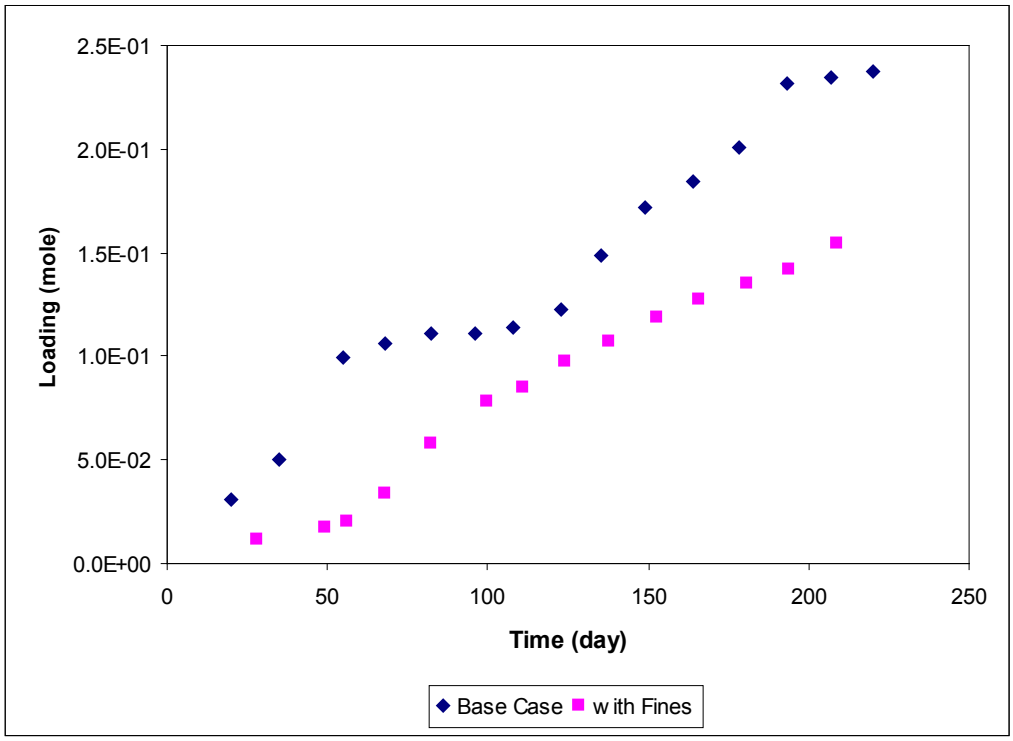

Figure 4.54: Comparison of sulphate loading between the base case and the column with fines.

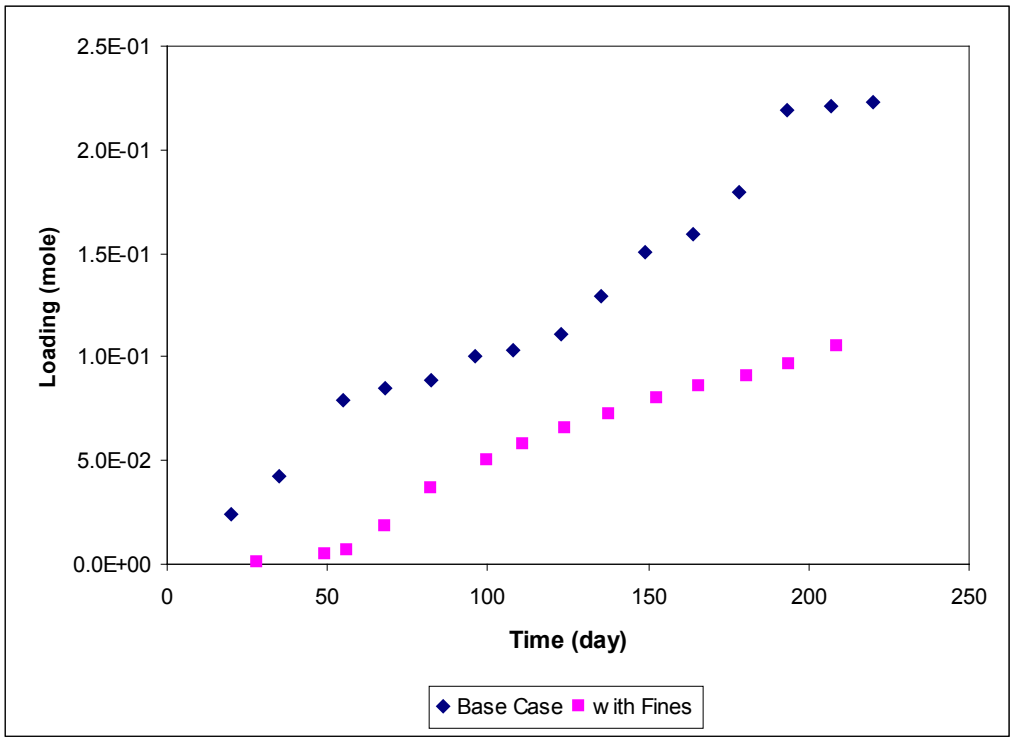

Figure 4.55: Comparison of iron loading between the base case and the column with fines.

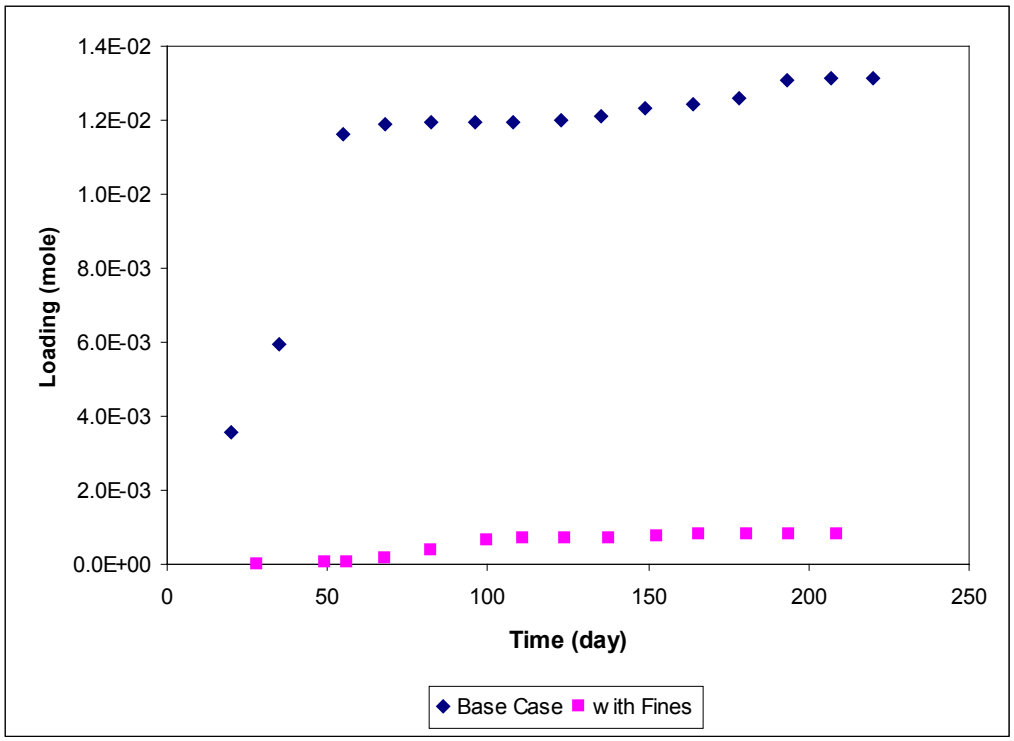

Figure 4.56: Comparison of nickel loading between the base case and the column with fines.

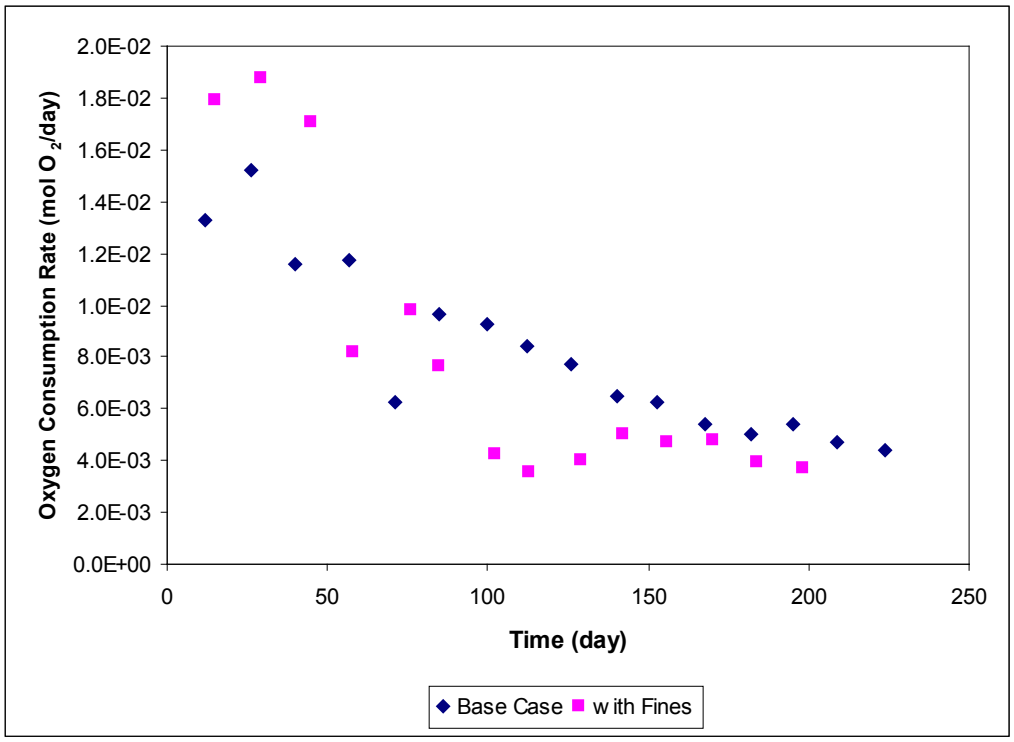

Figure 4.57: Comparison of oxygen consumption rate between the base case and the column with fines.

CONCLUSIONS

1. There is considerable variation among the specific surface area values for different pyrrhotite samples. Differences in specific surface area values among pyrrhotite samples appear random and not correlated to crystal structure or trace metal substitution for iron in the pyrrhotite matrix. Preferential oxidation appears to occur at areas of high strain on the pyrrhotite surface. In granular material such as tailings, surface area may be influenced by method of size reduction. Specific surface area values calculated from a spherical geometry are poor estimators for BET measured specific surface areas. Measured pyrrhotite specific surface areas were 6 to 40 times greater than the theoretical specific surface area. Fractures along cleavage planes and surface roughness cause the specific surface area of pyrrhotite to be higher than the theoretical geometrical specific surface area and pyrite specific surface area. The fractures are not simply near-surface features, but appear to extend into the pyrrhotite structure. Pyrrhotite can have specific surface area values as much as 10 times higher than pyrite. Pyrite does not exhibit crystallographic cleavage like pyrrhotite. Accurate BET measured specific surface areas on site specific pyrrhotite samples are therefore required to properly assess oxidation rates in mine tailings containing pyrrhotite.
2. There are differences in bulk impurity compositions (determined by multi-acid extraction and ICP-AES analysis) among the twelve pyrrhotite samples. The major impurities included were cobalt, copper, manganese, nickel, lead, and zinc. The concentrations of impurities were attributed to accessory minerals present with pyrrhotite. Cobalt substituted for iron in all twelve pyrrhotite samples. Nickel content varied more widely than cobalt in the twelve pyrrhotite samples. Manganese and copper substitution were not significant in the twelve pyrrhotite samples. Both XRD and electron microprobe analysis are effective techniques for identifying accessory minerals associated with the pyrrhotite particles. Chalcopyrite was the dominant accessory mineral associated with pyrrhotite and was present in detectable amounts for 9 of 12 samples. The twelve samples varied in composition from pure hexagonal to pure monoclinic. XRD Peak area is a valid method to determine the composition of hexagonal and monoclinic pyrrhotite. The limit of detection for hexagonal pyrrhotite is close to 8 %. Care should be used when applying the Yund and Hall (1969) equation to estimate atomic percent iron in pyrrhotite samples.
3. Several different aspects of pyrrhotite oxidation were examined in this study. The mean non-oxidative dissolution rate of pyrrhotite for twelve pyrrhotite samples was 5×10^{-10} $mol\cdot m^{-2}\cdot s^{-1}$. The reasons for the variation in dissolution rates remain unclear. Pyrrhotite crystal structure and trace metal content do not appear to have a consistent effect on the control of pyrrhotite

oxidation rates by either oxygen or ferric iron. Non-oxidative dissolution of pyrrhotite appears to be a potentially significant contributor of ferrous iron release in pyrrhotite weathering in acidic solutions. These rates should be considered in prediction models that include pyrrhotite weathering in tailings. The mean oxidation rate of pyrrhotite by oxygen for the twelve pyrrhotite samples was 4×10^{-9} mol·m^{-2}·s^{-1}. Oxidation by ferric iron exhibited more rapid rates than oxidation of pyrrhotite by oxygen. At pH=2.75 with an initial Fe^{3+} concentration of 2×10^{-4} M, the mean oxidation rate by ferric iron for the twelve pyrrhotite samples was 3.5×10^{-8} mol Fe^{3+}·m^{-2}·s^{-1}. Pyrrhotite oxidation by ferric iron appears to follow an adsorption type of mechanism. In spite of the high sample variances, the difference between mean non-oxidative reaction rates was significant at the 5 % significance level.

4. Oxidation reactions of pyrrhotite by either ferric iron or oxygen resulted in incomplete oxidation for some of the sulphide sulphur with only partial transformation to sulphate. Sulphur enrichment on particle surfaces and elemental sulphur formations are likely reasons for the incomplete oxidation of sulphide sulphur to sulphate.
5. Calculated activation energies for pyrrhotite oxidation by oxygen ranged from 47 kJ·mol^{-1} to 63 kJ·mol^{-1} based on iron release. Similar activation energies were found for ferric iron oxidation. Surface area is a controlling factor in reaction kinetics. Accurate BET measured specific surface areas on location-specific pyrrhotite samples are therefore required to properly assess oxidation rates in mine tailings containing pyrrhotite. The high reactivity of pyrrhotite on the mass basis as reported in previous papers is attributable to the high specific surface area of pyrrhotite in comparison to the other minerals.
6. Detailed kinetic studies on the pyrrhotite tailings concentrate indicated that; a) oxidation rates varied consistently with temperature, b) abiotic rates were higher at pH = 2 and lower at pH = 6, c) bacterial catalysis of pyrrhotite oxidation enhanced sulphate but not iron production rates, and d) nickel release rates reflected iron release rates for pH values of 2, 3 and 4.
7. The results of the column studies showed that; a) oxygen consumption rates were higher than expected from the release rates for sulphate. This may be due to the partial oxidation of sulphide in the pyrrhotite, b) iron and sulphate release rates were close to the stoichiometric ratio of 1 : 1 even though precipitation of ferric hydroxide was evident and lower iron : sulphate ratios were expected, c) oxidation rates in the 6 % S columns generally decreased with time, reflecting sulphide depletion and an increasing importance of oxygen diffusion

controls with time, d) sulphate release rates in the 2 % S column were only slightly lower than those in the 6 % S column, e) nickel release rates were higher in the 2 % S column, f) the precipitation of ferric hydroxide solids in the tailings was responsible for attenuating the release of nickel from the tailings porewater, g) although carbonate buffering did not significantly affect the rates of pyrrhotite oxidation as exhibited by sulphate production and oxygen consumption rates, iron and nickel release was significantly lower as a result of enhanced ferric hydroxide precipitation, h) silicate (enstatite) provided a partial buffering that resulted in iron and nickel loadings that were lower than the non-buffered columns, and i) the presence of pyrrhotite "fines" in the tailings, with the potential for higher reactivity than the coarse pyrrhotite actually resulted in lower rates because of the increased moisture retention and decreased gas diffusion coefficient that controls oxygen transport.

It is evident that kinetic data are required to assess pyrrhotite oxidation rates in tailings. However, because most of the variation in rates is due to the variation in specific surface area of pyrrhotite particles, this parameter should be measured on location-specific samples. The results of this study have shown that oxygen diffusion (or mass transfer) has a significant and overriding effect on the observed rates in tailings that becomes increasingly significant with time. This implies that uncertainties in oxidation rate kinetics will result in less uncertainty in rate predictions when both kinetics and mass transport are considered in tailings oxidation calculations. This means that small uncertainties in the estimates of kinetic parameters may not significantly affect long-term predictions of loading rates of pyrrhotite oxidation products. This is a positive outcome in that detailed long-term kinetic testing is not required for model input data to evaluate long-term behaviour of pyrrhotite tailings. By inference, and the less complex nature of pyrite oxidation, similar conclusions likely hold for pyrite oxidation.

REFERENCES

Ahonen L. and O.H. Tuovinen. 1989. Microbiological oxidation of ferrous iron at low temperatures. Applied and Environmental Microbiology *55*:312-316.

Ahonen L. and O.H. Tuovinen. 1991. Temperature effects on bacterial leaching of sulfide minerals in shake flask experiments. Applied and Environmental Microbiology *57*:138-145.

Amaro, A. M., Seeger, M., Arredondo, R., Moreno, M., and Jerez, C. A. The growth conditions affect *Thiobacillus ferrooxidans* attachment to solids. 2, 577-585. 1993. Proceedings of International Biohydrometallurgy Symposium.

Arkesteyn G.J.M.W. 1978. Pyrite oxidation by *Thiobacillus ferrooxidans* with special reference to the sulphur moiety of the mineral. Antonie van Leeuwenhoek *45*:423-435.

Arnold R.G. and L.E. Reichen. 1962. Measurement of the metal content of naturally occurring, metal-deficient, hexagonal pyrrhotite by an x-ray spacing method. The American Mineralogist *47*:105-111.

Arnold R.G. 1966. Mixtures of hexagonal and monoclinic pyrrhotite and the measurement of the metal content of pyrrhotite by x-ray diffraction. The American Mineralogist *51*:1221-1227.

Arnold R.G. 1967. Range in composition and structure of 82 natural terrestrial pyrrhotites. Canadian Mineralogy *9*:31-50.

Boogerd F.C., C. van den Beemd, T. Stoelwinder, P. Bas and J.G. Kuenen. 1991. Relative contributions of biological and chemical reactions to the overall rate of pyrite oxidation at temperatures between 30ºC and 70ºC. Biotechnology and Bioengineering *38*:109-115.

Boon, M. and Heijnen, J. J. Mechanisms and rate limiting steps in bioleaching of sphalerite, chalcopyrite and pyrite with *thiobacillus ferrooxidans*. 1, 217-235. 1993. Proceedings of International Biohydrometallurgy Symposium

Brownlow A.H. 1996. Geochemistry. Prentice-Hall, Inc.,

Bugajski J. and H. Gamsjager. 1982. The kinetics of the dissolution of monoclinic pyrrhotite in aqueous acidic solutions. Monatshefte fur Chemie *113*:1087-1092.

Choi W.K., A.E. Torma, R.W. Ohline and E. Ghali. 1993. Electrochemical aspects of zinc sulphide leaching by *Thiobacillus ferrooxidans*. Hydrometallurgy *33*:137-152.

Collin M. and A. Rasmuson. 1988. A comparison of gas diffuivity models for unsaturated porous media. Soil Sci.Soc.Am.J. *53*:1559-1565.

David, D. J. and Nicholson, R. V. Field measurements for determing rates of sulphide oxidation. 1, 201-210. 1995. Proceeding of Sudbury'95. 1995.

Davis, J. A. and Kent, D. B. Surface complexation modeling in aqueous geochemistry. Hochella, M. F. Jr. and White, A. F. (23), 87-128. 1990. Mineralogical Society of America. Reviews in Mineralogy - Mineral-Water Interface Geochemistry.

de Haan S.B. 1991. A review of the rate of pyrite oxidation in aqueous systems at low temperature. Earth Sciencr Review *31*:1-10.

Deer W.A., R.A. Howie and J. Zussman. 1992. An introduction to the rock-forming minerals. Longman Scientific & Technical,

Evangelou V.P. and Y.L. Zhang. 1995. A review: pyrite oxidation mechanisms and acid mine drainage prevention. Critical Reviews in Environmental Science and Technology *25*:141-199.

Graham R.A. 1969. Quantitative determination of hexagonal and monoclinic pyrrhotites by x-ray diffraction. The Canadian Mineralogist *10*:4-24.

Hamilton I.C. and R. Woods. 1981. An investigation of surface oxidation of pyrite and pyrrhotite by linear potential sweep voltammetry. Journal of Electroanalytical Chemistry *118*:327-343.

Hansford, G. S. and Bailey, A. D. Oxygen transfer limitation of bio-oxidation at high solids concentration. 1, 469-478. 1993. Biotechnological Technologies - Proceedings of international biohydrometallurgy symposium.

Holdren G.R. and P.M. Speyer. 1985. Reaction rate - surface area relationships during the early stages of weathering - I. initial observations. Geochimica et Cosmochimica Acta *49*:675-681.

Ingledew W.J. 1986. Ferrous iron oxidation by *Thiobacillus ferrooxidans*. Biotechnology and Bioengineering Symp. *16*:23-33.

Jambor, J. L. Detailed mineralogical examination of alteration products in core WA-20 from Waite Amulet tailings. CANMET Division Report MSL 86-137(IR). 1986. Dept. Energy Mines Resources Canada.

Jambor J.L. 1994. Mineralogy of sulfide-rich tailings and their oxidation products. In: Jambor J.L. and D.W. Blowes, eds. Geochemistry of Sulfide Mine Wastes. Mineralogical Society of America. 59-102.

Janzen, M. P. Role of ferric iron, trace metal content and crystal structure on pyrrhotite oxidation. 1996. University of Waterloo. 1996.

Jaynes D.B., H.B. Pionke and A.S. Rogowski. 1984. Acid mine drainage from reclaimed coal strip mines, 2. simulation results of model. Water Resour.Res. *20*:243-250.

Jensen A. and C. Webb. 1995. Ferrous sulphate oxidation using *Thiobacillus ferrooxidans*: a review. Process Biochemistry *30*:225-236.

Johnson, D. B. Diversity of microbial life highly acidic, mesophilic environments. 1991. Elsvier Science B.V. Diversity of Environmental Biogeochemistry.

Jones C.F., S. LeCount, R.St.C. Smart and T.J. White. 1992. Compositional and structural alteration of pyrrhotite surfaces in solution : XPS and XRD studies. Applied Surface Science *55*:65-85.

Kuenen, J. G., Pronk, J. T., Hazeu, W., Meulenberg, R., and Bas, P. A review of bioenergetics and enzymology of sulfur compound oxidation by acidophilic *Thiobacillui.* 2, 487-494. 1993. Proceedings of International Biohydrometallurgy Symposium. 1993.

Kulpa C.F.Jr., N. Mjoli and M.T. Roskey. 1986. Comparison of iron and sulfur oxidation in *Thiobacillus ferrooxidans*: inhibition of iron oxidation by growth on sulfur. Biotechnology and Bioengineering Symp. *16*:289-295.

Kwong, E. C. M. Abiotic and biotic pyrrhotite dissolution. 1-101. 1995. 1995.

Kwong, J. Y. T. Prediction and prevention of acid rock drainage from a geological and mineralogical perspective. Mend Project 1.32.1. 1993.

Leduc L.C. and G.D. Ferroni. 1994. The chemolithotrophic bacterium *Thiobacillus ferrooxidans*. FEM Microbiology Reviews *14*:103-120.

Liu M.S., R.M.R. Branion and D.W. Duncan. 1988. The effects of ferrous iron, dissolved oxygen , and inert solids concentrations on the frowth of *Thiobacillus ferrooxidans*. The Canadian Journal of Chemical Engineering *66*:445-451.

Lizama H.M. and I. Suzuki. 1988. Bacterial leaching of a sulfide ore by *Thiobacillus ferrooxidans* and *Thiobacillus thiooxidans*: I. shake flask studies. Biotechnology and Bioengineering *32*:110-116.

Lizama H.M. and I. Suzuki. 1990. Kinetics of sulfur and pyrite oxidation by *Thiobacillus thiooxidans*. Competitive inhibition by increasing concentrations of cells. Canadian Journal of Microbiology *37*:182-187.

Lorbach, S. C., Buonfiglio, V., Bauld, J. M., and Shively, J. M. Oxidation of reduced sulfur compounds by *Thiobacillus ferrooxidans*23270 and *Thiobacillus ferrooxidans* F.C. 2, 443-452. 1993. Biohydrometallurgical Technologies - Proceedings of international biohydrometallurgy symposium. 1993.

Loten J.P. and E. Wesker. 1987. The behaviour of sulphur in the oxidative leaching of sulphidic minerals. Hydrometallurgy *18*:39-54.

Lowson R.T. 1982. Aqueous oxidation of pyrite by molecular oxygen. Chemical Reviews *82*:461-497.

Massmann J. and D.F. Farrier. 1992. Effects of atmospheric pressures on gas transport in the vadose zone. Water Resour.Res. *28*:777-791.

McGinness S. and D.B. Johnson. 1993. Seasonal variations in the microbiology and chemistry of an acid mine drainage stream. The Science of the Total Environment *132*:27-41.

McKibben M.A. and H.L. Barnes. 1986. Oxidation of pyrite in low temperature acidic solutions: rate laws and surface textures. Geochimica et Cosmochimica Acta *50*:1509-1520.

Mehta A.P. 1982. Kinetic study of sulfide leaching by galvanic interaction between chalcopyrite, pyrite, and sphalerite in the presence of *T. ferrooxidans* (30ºC) and a thermophilic microorganism (55ºC). Biotechnology and Bioengineering *24*:919-940.

Mehta A.P. and L.E. Murr. 1983. Fundamental studies of the contributioin of galvanic interaction to acid-bacterial leaching of mixed metal sulfides. Hydrometallurgy *9*:235-256.

Morimoto N., A. Gyobu, H. Mukaiyama and E. Izawa. 1975. Superstructure and nonstoichiometry of intermediate pyrrhotite. Am.Mineral. *60*:240-248.

Moses C.O., D.K. Nordstrom, J.S. Herman and A.A. Mills. 1987. Aqueous pyrite oxidation by dissolved oxgen and ferric iron. Geochimica et Cosmochimica Acta *51*:1561-1571.

Moses C.O. and J.S. Herman. 1991. Pyrite oxidation at circumneutral pH. Geochimica et Cosmochimica Acta *50*:1509-1520.

Mustin, C., de Donato, Ph., and Berthelin, J. Surface oxidized species, a key factor in the study of bioleaching processes. Part II: investigation of superficial oxidized species developed during the bacterial oxidation of pyrite by *Thiobacillus ferrooxidans*. 1, 175-184. 1993. Biohydrometallurgical Technologies - Proceedings of international biohydrometallurgy sumposium. 1993.

Nagpal E., D. Dahlstrom and T. Oolman. 1993. Effect of carbon dioxide concentration on the bioleaching of a pyrite-arsenopyrite ore concentrate. Biotechnology and Bioengineering *41*:459-464.

Nakamura K., T. Noike and J. Matsumoto. 1986. Effect of operation conditions on biological Fe^{2+} oxidation with rotating biological contactors. Water Resources *20*:73-77.

Nichol M.J. and P.D. Scott. 1979. The kinetics and mechanism of the non-oxidative dissolution of some iron sulphides in aqueous acidic solutions. Journal of the South African Institute of Mining and Metallurgy 298-305.

Nicholson R.V., R.W. Gillham and E.J. Reardon. 1988. Pyrite oxidation in carbonate-buffered solution: I. experimental kinetics. Geochimica et Cosmochimica Acta *52*:1077-1084.

Nicholson R.V., R.W. Gillham and E.J. Reardon. 1989. Pyrite oxidation in carbonate-buffered solution: II. rate control by oxide coatings. Geochimica et Cosmochimica Acta *54*:395-402.

Nicholson R.V. 1994. Iron-sulfide oxidation mechanisms: laboratory studies. In: Jambor J.L. and D.W. Blowes, eds. Environmental Geochemistry of Sulfide Mine-Wates. Mineralogical Society of America. 163-183.

Nickel E.H., J.R. Ross and M.R. Thornber. 1974. The supergene alteration of pyrrhotite-pentlandite ore at Kambalda, Westen Australia. Economic Gelogy *69*:93-107.

Olson G.J. and R.M. Kelly. 1986. Microbiological metal transformations. Biotechnology Progress *2*:1-15.

Orlova T.A., V.M. Stupnikov and A.L. Krestan. 1988. Mechanism of oxidative dissolution of sulphides. Zhurnal Prikladnoi Khimii *61*:2172-2177.

Pesic, B. Redox potential technique to study the factors of importance during reactions of *T. ferrooxidans* with Fe^{3+}. 1, 545-560. 1993. Biohydrometallurgical Technologies - Proceedings of international biohydrometallurgy symposium. 1993.

Plysunin A.M., A.G. Mironov, N.V. Belomestrova and S.Ye. Chernigova. 1990. Laboratory studies on gold-bearing sulfide oxidation. Geokhimya *1*:51-60.

Pratt A.R., H.W. Nesbitt and I.J. Muir. 1994. Generation of acids from mine waste: oxidative leaching of pyrrhotite in dilute H_2SO_4 solutions at pH 3.0. Geochimica et Cosmochimica Acta *58*:5147-5159.

Pratt A.R., I.J. Muir and H.W. Nesbitt. 1994. X-ray photoelectron and Auger electron spectroscopic studies of pyrrhotite and mechanism of air oxidation. Geochimica et Cosmochimica Acta *58*:827-841.

Pronk J.T. and D.B. Johnson. 1992. Oxidation and reduction of iron by acidophilic bacteria. Geomicrobiology Journal *10*:153-171.

Reardon E.J. and P.M. Moddle. 1985. Gas diffusion coefficient measurements on uranium mill tailings: implications to cover layer design. Uranium *2*:111-131.

Rimstidt, J. D., Chermak, J. A., and Gagen, P. M. Rates of reaction of galena, shpalerite, chalcopyrite, and arsenopyrite with Fe(III) in acidic solutions. 2-13. 1994. Environmental Geochemistry of Sulfide Oxidation.

Sand W., K. Rohde, B. Sobotke and C. Zenneck. 1992. Evaluation of *Leptospirillum ferrooxidans* for leaching. Applied and Environmental Microbiology *58*:85-92.

Scharer, J. M., Garga, V., Smith, R., and Halbert, B. E. Use of steady state models for assessing acid generation in pyritic mine tailings. 2, 211-230. 1991. Proceeding of 2nd ICARD. 1991.

Scharer, J. M., Byerley, J. J, Kwong, E. C. M., and Nicholson, R. V. Role of biologically assisted pyrrhotite oxidation in acid mine drainage. 2, 255-265. 1993. Proceedings of International Biohydrometallurgy Symposium. 1993.

Scharer, J. M., Annable, W. K., and Nicholson, R. V. WATAIL 1.0 user's manual - a tailings basin model to evaluate transient water quality of acid mine drainage. (1.0). 1993. University of Waterloo.

SENES Consultants Limited. Waste rock sampling manual. MEND Project 4.5.1. 1998.

Singh G. and M. Bhatnagar. 1985. Bacterial formation of acid mine drainage: causes and control. Journal of Scientific and Industrial Research *44*:478-485.

Skinner B.J. and F.D. Luce. 1971. Stabilities and compositions of dmeykite and algodonite. Economic Geology *66*:133-139.

Smith, E. E., Svanks, K., and Shumate, K. Sulphide to sulphate reaction studies. 1-10. 1968. Proceeding of 2nd Symposium on Coal Mine Drainage Research.

Steger H.F. and L.E. Desjardins. 1978. Oxidation of sulpfide minerals, 4. pyrite, chalcopyrite and pyrrhotite. Chemical Geology *23*:225-237.

Steger H.F. 1982. Oxidation of sulfide minerals VII. effect of temperature and relative humidity on the oxidation of pyrrhotite. Chemical Geology *35*:281-295.

Stumm W. 1992. Chemistry of the solid-water interface - processes at the mineral-water and particle-water interface in natural systems. John Wiley & Sons, Inc.,

Sugio T., K.J. White, E. Shute, D. Choate and R.C.II. Blake. 1992. Existance of hydrogen sulfide: ferric ion oxidoreductase in iron-oxidizing bacteria. Applied and Environmental Microbiology *58*:431-433.

Suzuki I., T.L. Takeuchi, T.D. Yuthasastrakosol and J.K. Oh. 1990. Ferrous iron and sulfur oxidation and ferric iron reduction activities of *Thiobacillus ferrooxidans* are affected by growth on ferrous iron, sulfur, or a sulfide ore. Applied and Environmental Microbiology *56*:1620-1626.

Tewari P.H. and A.B. Campbell. 1976. Dissolution of iron sulphide (troilite) in aqueous sulphuric acid. Journal of Physical Chemistry *80*:1844-1848.

Thornber M.R. 1975. Supergene alteration of sulphides, II. a chemical study of the Kambalda nickel deposits. Chemical Geology *15*:117-144.

Thornber M.R. 1975. Supergene alteration of sulphides, I. a chemical model based on massive nickel sulphide deposits at Kambalda, Western Australia. Chemical Geology *15*:1-14.

Thornber M.R., P.D. Allchurch and E.H. Nickel. 1981. Variations in gossen geochemistry at the preseverance nickel sulfide deposit, Western Australia: a descriptive and experimental study. Economic Gelogy *76*:1764-1774.

Torma A.E., C.C. Walden, D.W. Duncan and R.M.R. Branion. 1972. The effect of carbon dioxide and particle surface area on themicrobiological leaching of a zinc sulfide concentrate. Biotechnology and Bioengineering *14*:777-786.

Toro L., B. Paponetti and C. Cantalini. 1988. Precipitate formation in the oxidation of ferrous ions in the presence of *Thiobacillus ferrooxidans*. Hydrometallurgy *20*:1-9.

Toulmin P. and P.B. Barton. 1964. A thermodynamic study of pyrite and pyrrhotite. Geochimica et Cosmochimica Acta *28*:641-671.

Tributsch H. and J.C. Bennett. 1981. Semiconductor-electrochemical aspects of bacterial leaching. 1. oxidation of metal sulphides with large energy gaps. Journal of Chemical Technology and Biotechnolog *31*:565-577.

Tributsch H. and J.C. Bennett. 1981. Semiconductor-electrochemical aspects of bacterial leaching. 2. survay of rate-controlling sulphide properties. Journal of Chemical Technology and Biotechnolog *31*:627-635.

Tuovinen O.H. 1986. Acid leaching of uranium ore materials with microbial catalysis. Biotechnology and Bioengineering Symp. *16*:65-72.

van Weert G., K. Mah and N.L. Piret. 1974. Hydrochloric acid leaching of nickerliferous pyrrhotites from the Sudbury district. CIM Bulletin 97-103.

Vaughan D.J. and J.R. Craig. 1978. Mineral chemistry of metal sulfides. Cambridge University Press,

Williamson M.A. and J.D. Rimstidt. 1994. The kinetics and electrochemical rate-determining step of aqueous pyrite oxidation. Geochimica et Cosmochimica Acta *58*:5443-5454.

Woods T.L. and R.M. Garrels. 1987. Thermodynamics values at low temperature for natural inorganic materials - an uncritical summary. Oxford University Press,

Wuensch B.J. 1963. Ont the suoerstructure and twinning of pyrrhotite. Mineral.Soc.Am.Spec.Pap. *1*:157-163.

Yakhontova L.K., L.G. Nesterovich and A.P. Grudev. 1983. New data on natural oxidation of pyrrhotite. Vestnik Moskovskogo Universiteta Geologiya *38*:41-44.

Yund R.A. and H.T. Hall. 1969. Hexagonal and monoclinic pyrrhotite. Economic Gelogy *64*:420-423.

Zheng C.Q., C.C. Allen and R.G. Bautista. 1986. Kinetic study of the oxidation of pyrite in aqueous ferric sulphate. Ind.Eng.Chem.Process Des.Dev. *25*:308-317.

LABORATORY STUDIES
OF PYRRHOTITE OXIDATION

Final Report - Appendices

(Appendix A – Material Characterization of Pyrrhotite Samples)

(Appendix B – Non-Oxidative Dissolution of Specimen Grade Pyrrhotite Samples)

(Appendix C – Ferric Iron Oxidation of Specimen Grade Pyrrhotite Samples)

(Appendix D – Kinetic Oxidation of Inco's Copper Cliff Pyrrhotite Concentrate)

(Appendix E – Column Studies of Inco's Copper Cliff Pyrrhotite Concentrate)

Principal Investigators

R.V. Nicholson, Department of Earth Sciences

J.M. Scharer, Department of Chemical Engineering

Research Assistants

E.C.M. Kwong, Department of Chemical Engineering

M.P. Janzen, Department of Earth Sciences

University of Waterloo

Waterloo, ON N2L 3G1

March, 1998

Appendix A

Material Characterization of Pyrrhotite Samples

Table A-1: Specific surface area values determined using BET method for the twelve pyrrhotite samples.

Sample ID	BET Surface Area Analysis (± 5% $m^2 \times g^{-1}$)				
	60-80 Mesh Grain Fraction	**80-120 Mesh Grain Fraction**	**120-170 Mesh Grain Fraction**	**170-230 Mesh Grain Fraction**	**230-325 Mesh Grain Fraction**
Po-M-1-93	—	—	0.107 ± 0.005	0.168 ± 0.008	0.18 ± 0.01
Po-M-2-94	—	0.26 ± 0.01	0.29 ± 0.01	0.36 ± 0.02	0.49 ± 0.02
Po-M-3-94	—	—	0.24 ± 0.01	0.27 ± 0.01	0.342 ± 0.02
Po-M-4-94	—	—	0.158 ± 0.008	1.78 ± 0.09	—
Po-C-5-94	—	0.184 ± 0.009	0.35 ± 0.02	0.48 ± 0.02	0.94 ± 0.05
Po-M-6-94	—	0.114 ± 0.006		0.22 ± 0.01	
Po-M-7-94	—	0.085 ± 0.04	0.115 ± 0.006	0.180 ± 0.009	0.29 ± 0.01
Po-M-8-93	0.079 ± 0.004	0.20 ± 0.01	0.34 ± 0.02	0.40 ± 0.02	0.74 ± 0.04
Po-M-9-91	—	—	—	—	0.52 ± 0.03
Po-M-15-93	—	—	—	2.1 ± 0.1	—
Po-M-17-93	—	—	0.20 ± 0.01	0.25 ± 0.01	—
Po-M-19-94	—	0.30 ± .01	0.29 ± 0.01	0.30 ± 0.02	0.70 ± 0.04

Table A-2: The impurities present in the twelve pyrrhotite samples determined by multi-acid extraction and ICP-AES.

SAMPLE ID	Ag (mg/kg)	Al %	As (mg/kg)	Ba (mg/kg)	Be (mg/kg)	Bi (mg/kg)	Ca %	Cd (mg/kg)	Co (mg/kg)	Cr (mg/kg)	Cu (mg/kg)
Po-M-1-93	5.9	0.15	0	7	5.9	0	0.03	0	1040	30	16500
Po-M-2-94	1.9	0	0	144	6.6	0	0.15	0	323	19	5280
Po-M-3-94	1.8	0	0	0	5.6	0	0	0	368	15	7370
Po-M-4-94	1.5	0.1	0	1	5.7	38	0	0	1390	68	839
Po-C-5-94	33.4	0.01	11	1	6.8	63	0	0	6	16	463
Po-M-6-94	2.7	0.06	0	9	7.4	0	0.02	0	1750	17	2020
Po-M-7-94	16.3	0.07	0	3	5.4	0	0	0	996	16	36300
Po-M-8-94	4.7	0.29	0	10	5.1	0	0.02	0	851	16	11600
Po-M-9-93	1.5	0.2	0	10	3.8	31	0.15	0	1850	33	286
Po-M-15-93	5	0.17	0	3	3.5	0	1.42	0	164	18	5710
Po-M-17-93	2.7	0.12	12	5	3.1	0	0	0	779	66	4020
Po-M-19-94	5	0.17	0	3	3.5	0	1.42	0	164	18	5710

SAMPLE ID	Fe %	K %	La (mg/kg)	Mg %	Mo (mg/kg)	Mn (mg/kg)	Na %	Ni (mg/kg)	P %	Pb (mg/kg)	Sb (mg/kg)
Po-M-1-93	54.6	0.03	1.6	0.04	0	34	0.05	456	0	322	0
Po-M-2-94	57.2	0	1.7	0.1	0	270	0.01	749	0	41	0
Po-M-3-94	54.5	0	0	0	0	19	0.02	70	0	48	0
Po-M-4-94	55.3	0	0	0.03	0	90	0.01	15800	0	48	0
Po-C-5-94	57.1	0	0	0	0	66	0	78	0	5120	23
Po-M-6-94	59.5	0	1.7	0	0	46	0	3710	0	192	0
Po-M-7-94	54.4	0	1	0.02	0	25	0.02	16	0	73	0
Po-M-8-94	53.3	0.05	0.9	0.05	0	43	0.02	13	0	77	0
Po-M-9-93	51.2	0.02	0	0.09	0	96	0.03	37900	0	33	0
Po-M-15-93	47.9	0.01	3.9	1.22	0	1260	0.02	143	0	621	0
Po-M-17-93	48.9	0.03	0	0.05	3	128	0.02	43500	0	53	0
Po-M-19-94	47.9	0.01	3.9	1.22	0	1260	0.02	143	0	621	0

SAMPLE ID	Sc (mg/kg)	Sn (mg/kg)	Sr (mg/kg)	Ti %	V (mg/kg)	W (mg/kg)	Y (mg/kg)	Zn (mg/kg)	Zr (mg/kg)
Po-M-1-93	0	286	1	0	43	0	1	159	0.7
Po-M-2-94	0	0	3	0	41	0	0.4	308	0
Po-M-3-94	0	19	0	0	40	0	0.3	0	0
Po-M-4-94	0	16	0	0.12	144	0	0.5	60	0
Po-C-5-94	0	0	0	0	42	0	0.4	274	0
Po-M-6-94	0	0	1.3	0	43	0	0.4	0	0
Po-M-7-94	0	0	0	0	40	0	0.4	565	0
Po-M-8-94	0	11	1.3	0	43	0	3.2	1570	20.1
Po-M-9-93	0	0	2.3	0.06	108	0	1.2	110	0
Po-M-15-93	0	24	11.4	0	37	0	2	8810	0
Po-M-17-93	0	0	0	0	43	0	0.5	140	0
Po-M-19-94	0	24	11.4	0	37	0	2	8810	0

Table A-3: Trace metal contents of the twelve pyrrhotite samples as determined by electron microprobe.

Po Sample	Co (mg/kg)	Cu (mg/kg)	Mn (mg/kg)	Ni (mg/kg)	Fe Norm Wt %	S Norm Wt %	Total Trace Metals (mg/kg)	Total Metals Norm Wt %
Po-M-1-93	1414	462	24	54	60.930	39.321	1954	61.125
Po-M-2-94 bright	694	45	0	5	63.248	36.679	744	63.322
Po-M-2-94 dark	1150	5	20	2898	59.976	39.6175	4073	60.383
Po-M-2-94 smoke	651	0	0	90	60.788	39.138	741	60.862
Po-M-3-94	935	5	5	63	60.620	39.280	1008	60.720
Po-M-4-94 dark	600	17	0	3477	60.801	38.791	4093	61.210
Po-M-4-94 bright	640	0	100	130	63.075	36.838	870	63.162
Po-C-5-94 dark	525	10	40	0	60.085	39.858	575	60.143
Po-C-5-94 light	520	0	100	0	60.759	39.180	620	60.821
Po-M-6-94	2407	0	0	3810	60.611	38.768	6217	61.233
Po-M-7-94	1577	0	0	27	60.859	38.981	1603	61.019
Po-M-8-94	1583	0	0	0	60.678	39.164	1583	60.836
Po-M-9-91	685	0	0	6794	59.455	39.796	7479	60.203
Po-M-15-93	765	0	0	15	60.842	39.026	780	60.920
Po-M-17-93	640	0	0	9450	59.223	39.769	10090	60.232
Po-M-19-94	513	10	10	27	60.762	39.182	560	60.818

Table A-4: Trace metal content for Po-M-1-93 as determined by electron microprobe.

	Grain 1		Grain 2		Grain 3		Grain 4		Grain 5		Average
Element	Atom %	Norm wt %	Atom %	Norm wt %	Atom %	Norm wt %	Atom %	Norm wt %	Atom %	Norm wt %	Norm wt %
Fe	47.160	60.82	47.208	60.862	47.429	61.063	47.409	61.049	47.209	60.856	60.93
Mn	0.000	0.000	0.000	0.000	0.010	0.012	0.000	0.000	0.000	0.000	0.0024
Co	0.100	0.136	0.099	0.134	0.115	0.156	0.109	0.148	0.098	0.133	0.1414
Ni	0.002	0.022	0.000	0.000	0.002	0.002	0.003	0.003	0.000	0.000	0.0054
Cu	0.000	0.000	0.000	0.000	0.000	0.000	0.000	0.000	0.016	0.231	0.0462
S	52.738	39.046	52.694	39.004	52.446	39.767	52.480	38.800	52.678	39.988	39.321
Total Metals											61.1254

Table A-5: Trace metal content for Po-M-2-94 as determined by electron microprobe.

	Grain 1 Bright		Grain 2 Smoke		Grain 3 Bright		Grain 4 Dark		Grain 5 Dark		Average	
Element	Atom %	Norm wt %	Atom %	Norm wt %	Atom %	Norm wt %	Atom %	Norm wt %	Atom %	Norm wt %	Dark Norm wt %	Bright Norm wt %
Fe	49.730	63.256	47.113	60.788	49.712	63.240	46.452	60.061	46.270	59.890	60.246	63.248
Mn	0.000	0.000	0.000	0.000	0.000	0.000	0.003	0.004	0.000	0.000	0.0013	0.000
Co	0.053	0.717	0.048	0.0651	0.050	0.067	0.082	0.112	0.117	0.118	0.0984	0.392
Ni	0.000	0.000	0.007	0.009	0.001	0.001	0.220	0.2995	0.206	0.280	.1962	0.0005
Cu	0.006	0.009	0.000	0.000	0.000	0.000	0.000	0.001	0.000	0.000	0.0003	0.0045
S	50.210	36.666	52.833	39.138	50.237	36.692	53.242	39.523	53.438	39.712	39.458	36.679
Total Metals											60.543	63.645

Table A-6: Trace metal content for Po-M-3-94 as determined by electron microprobe.

	Grain 1		Grain 2		Grain 3		Grain 4		Average
Element	Atom %	Norm wt %	Atom %	Norm wt %	Atom %	Norm wt %	Atom %	Norm wt %	Norm wt %
Fe	47.080	60.748	46.971	60.648	46.767	60.450	46.962	60.632	60.620
Mn	0.000	0.000	0.000	0.000	0.002	0.002	0.000	0.000	0.0005
Co	0.070	0.095	0.063	0.085	0.067	0.091	0.075	0.103	0.094
Ni	0.003	0.004	0.004	0.005	0.004	0.005	0.008	0.011	0.006
Cu	0.002	0.002	0.000	0.000	0.000	0.000	0.000	0.000	0.0005
S	52.847	39.151	52.962	39.262	53.161	39.452	52.955	39.254	39.280
Total Metals									60.72

Table A-7: Trace metal content for Po-M-4-94 as determined by electron microprobe.

	Grain 1 Dark		Grain 2 Bright		Grain 3 Dark		Grain 4 Dark		Average	
Element	Atom %	Norm wt %	Atom %	Norm wt %	Atom %	Norm wt %	Atom %	Norm wt %	Dark Norm wt %	Bright Norm wt %
Fe	47.259	60.839	49.541	63.075	47.056	60.629	47.355	60.934	60.801	63.075
Mn	0.000	0.000	0.008	0.010	0.000	0.000	0.000	0.000	0.000	0.010
Co	0.042	0.058	0.048	0.064	0.043	0.058	0.047	0.064	0.060	0.064
Ni	0.248	0.336	0.010	0.013	0.292	0.395	0.231	0.312	0.348	0.013
Cu	0.000	0.000	0.000	0.000	0.000	0.000	0.003	0.005	0.002	0.000
S	52.451	38.768	50.395	36.838	52.610	38.918	52.365	38.686	38.791	36.838
Totals									61.21	63.162

Table A-8: Trace metal content for Po-C-5-94 as determined by electron microprobe.

	Grain 1 Dark		Grain 2 Light		Grain 3 Dark		Average	
Element	Atom %	Norm wt %	Atom %	Norm wt %	Atom %	Norm wt %	Dark Norm wt %	Light Norm wt %
Fe	46.393	60.101	47.079	60.759	46.359	60.069	60.085	60.759
Mn	0.003	0.003	0.008	0.010	0.004	0.005	0.004	0.010
Co	0.038	0.052	0.038	0.052	0.039	0.053	0.0525	0.052
Ni	0.000	0.000	0.000	0.000	0.000	0.000	0.000	0.000
Cu	0.000	0.001	0.000	0.000	0.001	0.001	0.001	0.000
S	53.566	39.843	52.876	39.180	53.598	39.873	39.858	39.18
Totals							60.1425	60.821

Table A-9: Trace metal content for Po-M-6-94 as determined by electron microprobe.

	Grain 1		Grain 2		Grain 3		Grain 4		Average
Element	Atom %	Norm wt %	Atom %	Norm wt %	Atom %	Norm wt %	Atom %	Norm wt %	Norm wt %
Fe	47.207	60.716	47.301	60.808	46.751	60.309	47.1194	60.647	60.611
Co	0.183	0.249	0.179	0.243	0.169	0.230	0.160	0.217	0.241
Ni	0.303	0.409	0.302	0.409	0.240	0.325	0.2875	0.389	0.381
S	52.308	38.626	52.218	38.541	52.840	39.136	52.433	38.747	38.770
Total Metals									61.233

Table A-10: Trace metal content for Po-M-7-94 as determined by electron microprobe.

	Grain 1		Grain 2		Grain 3		Average
Element	Atom %	Norm wt %	Atom %	Norm wt %	Atom %	Norm wt %	Norm wt %
Fe	47.096	60.750	47.270	60.913	47.269	60.913	60.859
Co	0.107	0.146	0.122	0.166	0.119	0.161	0.158
Ni	0.006	0.008	0.000	0.000	0.000	0.000	0.003
S	52.791	39.096	52.608	38.922	52.613	38.926	38.981
Total Metals							61.019

Table A-11: Trace metal content for Po-M-8-94 as determined by electron microprobe.

	Grain 1		Grain 2		Grain 3		Average
Element	Atom %	Norm wt %	Atom %	Norm wt %	Atom %	Norm wt %	Norm wt %
Fe	47.075	60.728	47.009	60.666	46.982	60.640	60.678
Co	0.118	0.160	0.115	0.156	0.116	0.159	0.158
Ni	0.000	0.000	0.000	0.000	0.000	0.000	0.000
S	52.807	39.112	52.876	39.178	52.901	39.202	39.164
Total Metals							60.836

Table A-12: Trace metal content for Po-M-9-91 as determined by electron microprobe.

	Grain 1		Grain 2		Grain 3		Grain 4		Grain 5		Average
Element	Atom %	Norm wt %	Atom %	Norm wt %	Atom %	Norm wt %	Atom %	Norm wt %	Atom %	Norm wt %	Norm wt %
Fe	45.971	59.521	45.915	59.448	46.149	59.712	45.732	59.257	45.823	59.338	59.455
Co	0.049	0.067	0.047	0.0644	0.051	0.070	0.051	0.070	0.052	0.071	0.069
Ni	0.461	0.623	0.516	0.702	0.407	0.554	0.548	0.746	0.567	0.772	0.679
S	53.519	39.785	53.522	39.786	53.393	39.664	53.669	39.927	53.558	39.819	39.796
Total Metals											60.203

Table A-13: Trace metal content for Po-M-15-93 as determined by electron microprobe.

	Grain 1		Grain 2		Grain 3		Grain 4		Average
Element	Atom %	Norm wt %	Atom %	Norm wt %	Atom %	Norm wt %	Atom %	Norm wt %	Norm wt %
Fe	47.301	60.968	47.277	60.942	47.132	60.804	47.109	60.655	60.840
Co	0.053	0.072	0.060	0.082	0.056	0.077	0.055	0.075	0.077
Ni	0.000	0.000	0.000	0.000	0.005	0.006	0.000	0.000	0.002
S	52.646	38.956	52.663	38.976	52.807	39.113	52.835	39.057	39.030
Total Metals									60.92

Table A-14: Trace metal content for Po-M-17-93 as determined by electron microprobe.

	Grain 1		Grain 2		Grain 3		Average
Element	Atom %	Norm wt %	Atom %	Norm wt %	Atom %	Norm wt %	Norm wt %
Fe	45.881	59.376	45.655	59.110	45.714	59.182	59.228
Co	0.051	0.069	0.040	0.055	0.0497	0.068	0.064
Ni	0.619	0.842	0.756	1.033	0.705	0.960	0.945
S	53.450	39.713	53.546	39.803	53.531	39.790	39.769
Total Metals							60.232

Table A-15: Trace metal content for Po-M-19-94 as determined by electron microprobe.

	Grain 1		Grain 2		Grain 3		Average
Element	Atom %	Norm wt %	Atom %	Norm wt %	Atom %	Norm wt %	Norm wt %
Fe	47.015	60.701	47.132	60.811	47.094	60.773	60.762
Mn	0.002	0.003	0.000	0.000	0.000	0.000	0.001
Co	0.032	0.043	0.040	0.055	0.041	0.056	0.05133
Ni	0.002	0.003	0.003	0.004	0.001	0.001	0.003
Cu	0.000	0.000	0.000	0.000	0.002	0.003	0.001
S	52.949	39.250	52.825	39.130	52.863	39.167	39.182
Total Metals							60.812

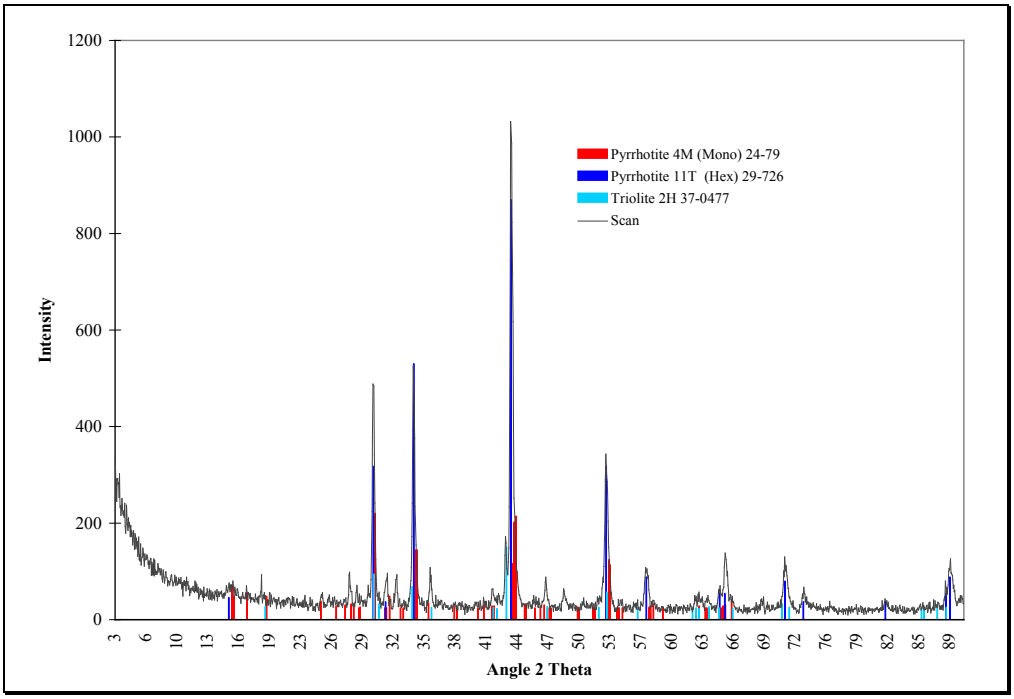

Figure A-1: Identification of pyrrhotite types for Po-M-2-94.

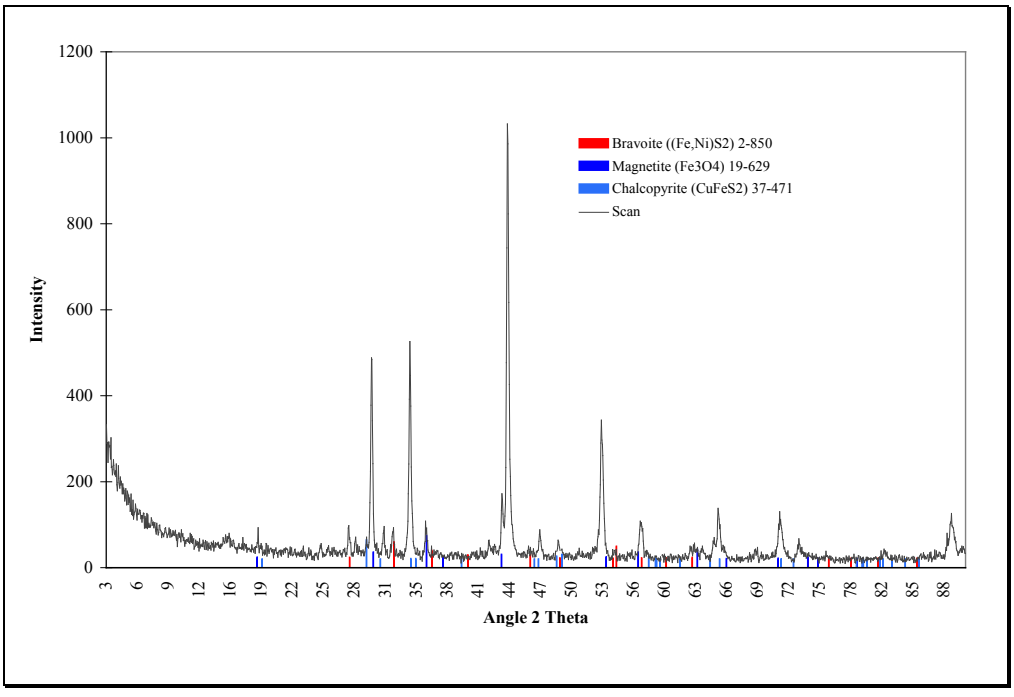

Figure A-2: Identification of accessory minerals for Po-M-2-94.

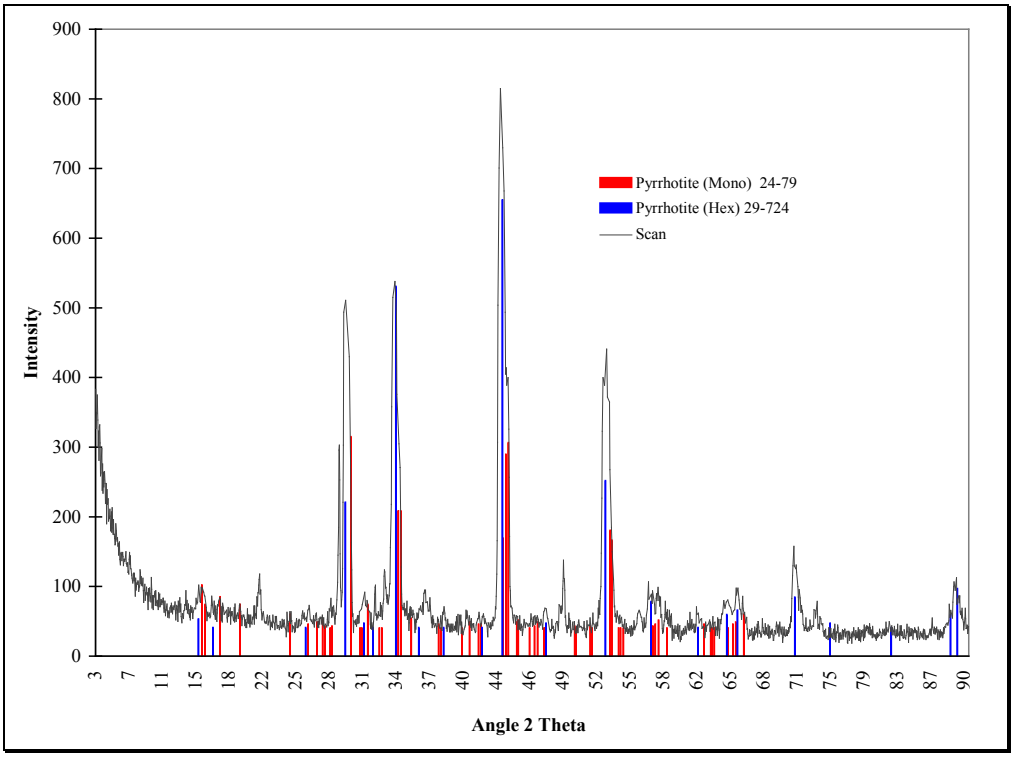

Figure A-3: Identification of pyrrhotite types for Po-M-3-94.

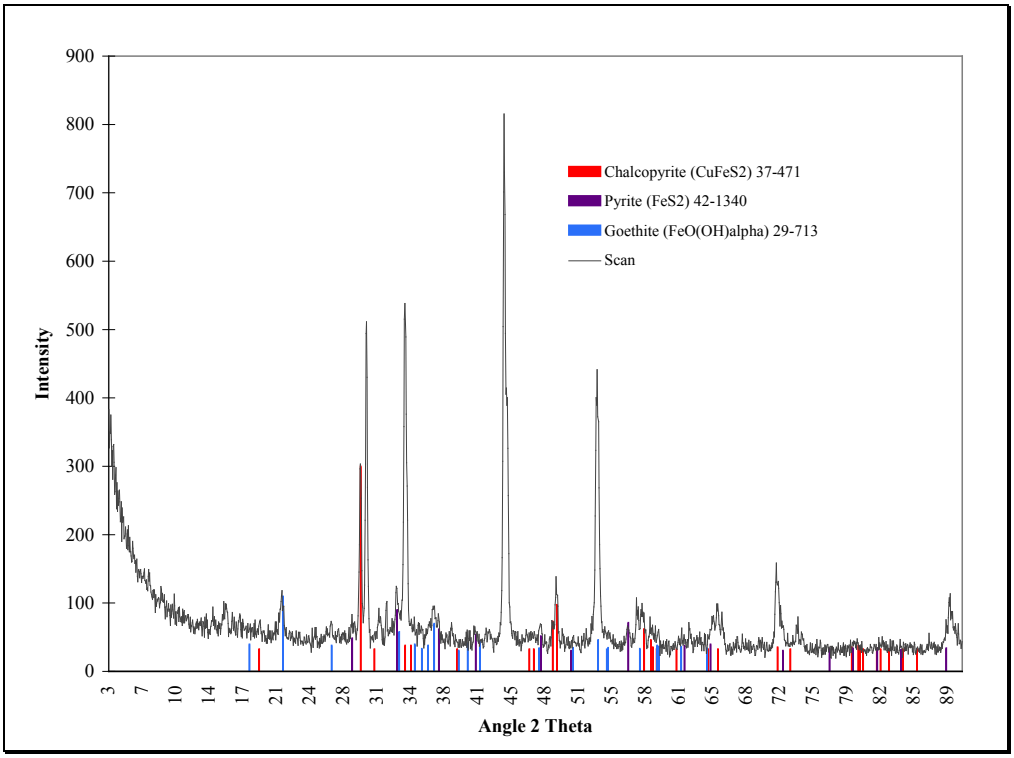

Figure A-4: Identification of accessory minerals for Po-M-3-94.

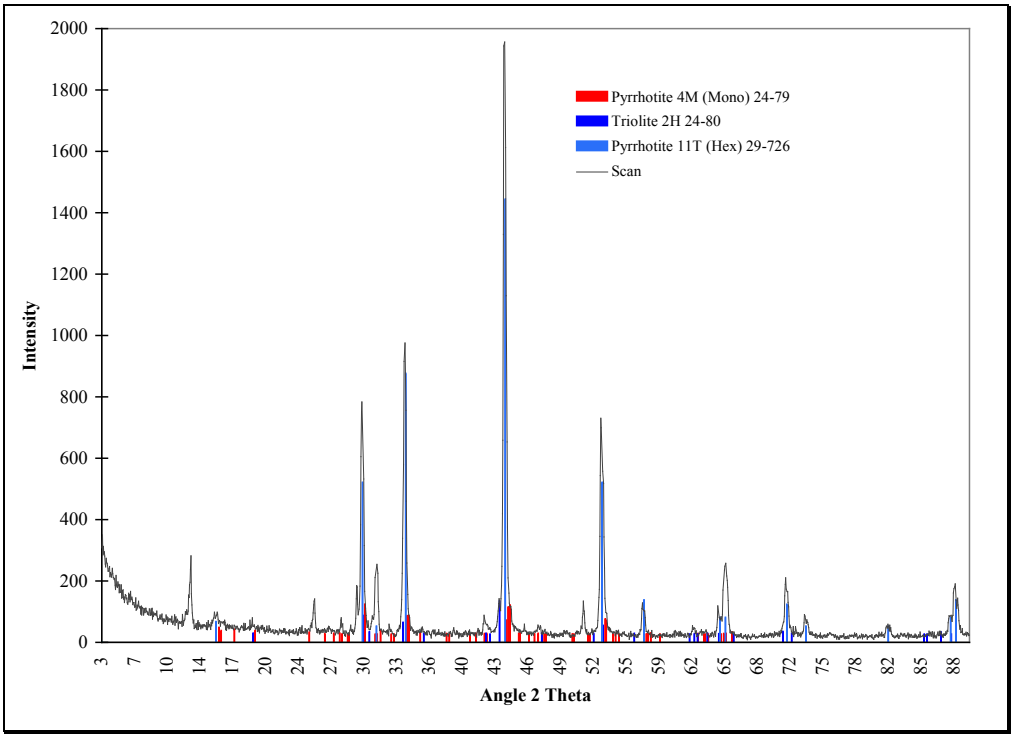

Figure A-5: Identification of pyrrhotite types for Po-M-4-94.

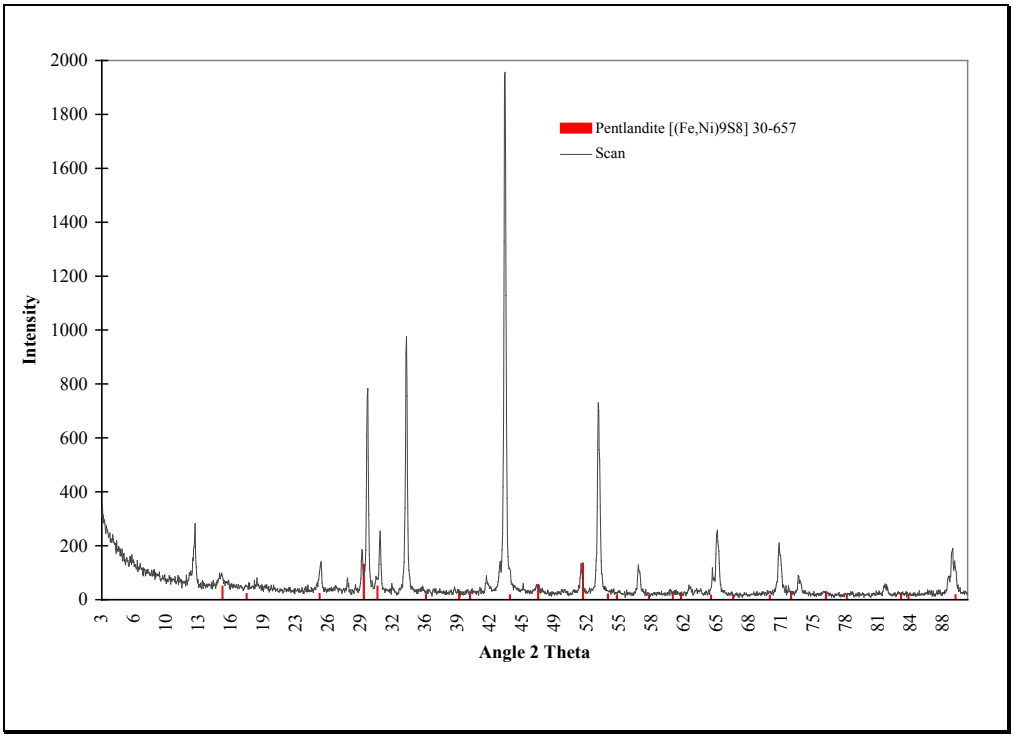

Figure A-6: Identification of accessory minerals for Po-M-4-94.

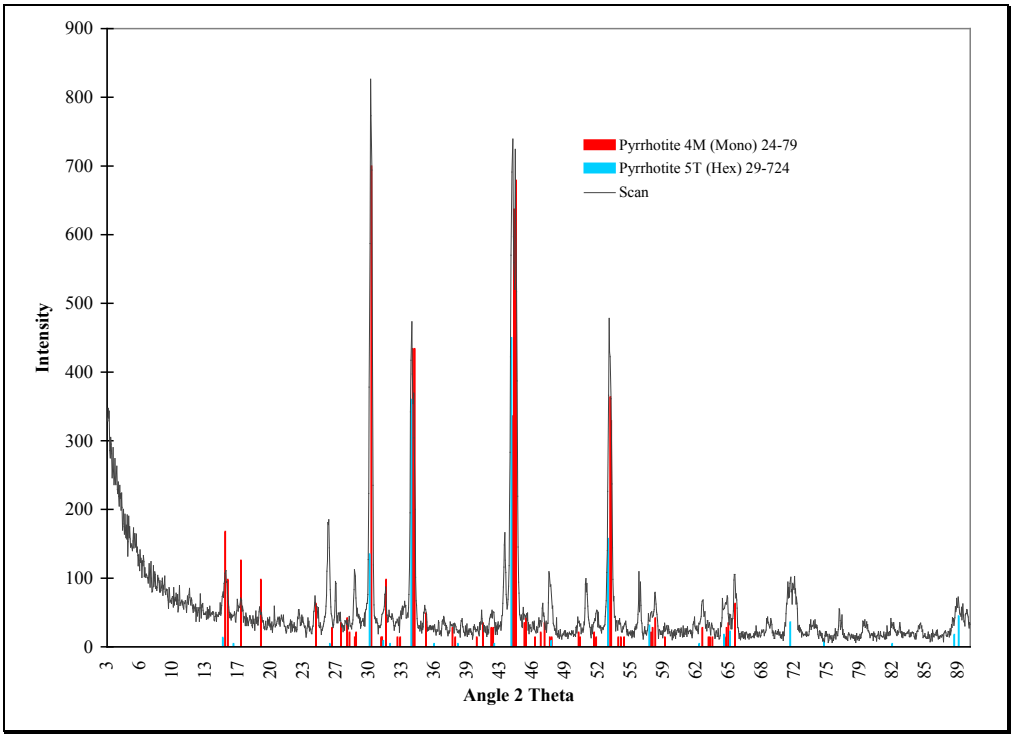

Figure A-7: Identification of pyrrhotite types for Po-C-5-94.

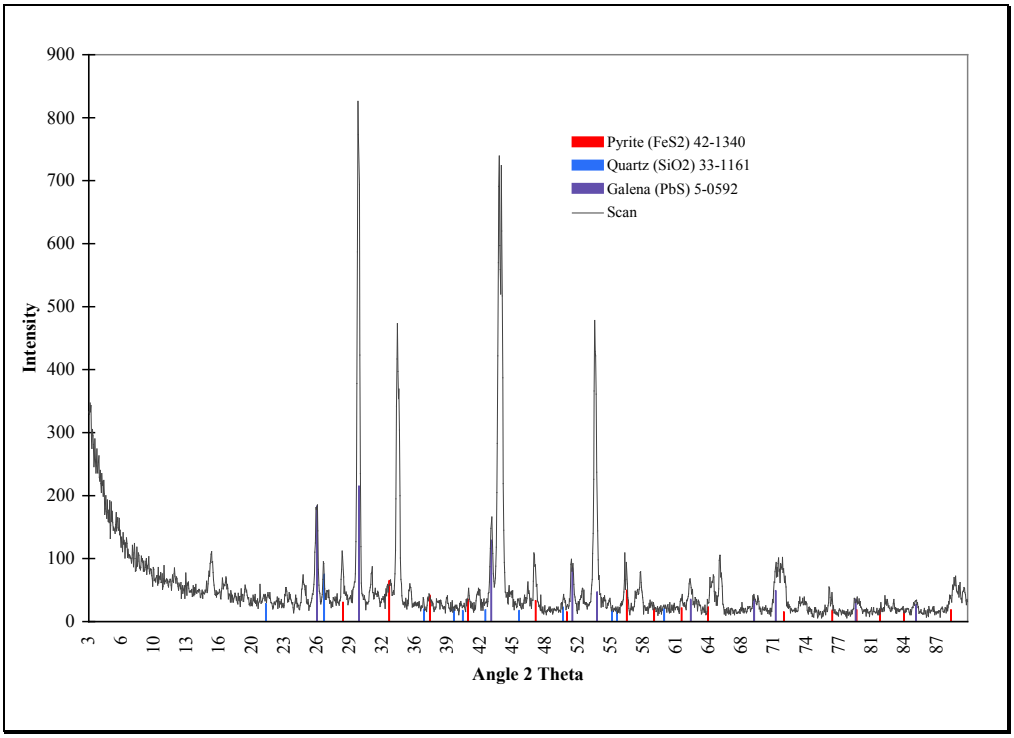

Figure A-8: Identification of accessory minerals for Po-C-5-94.

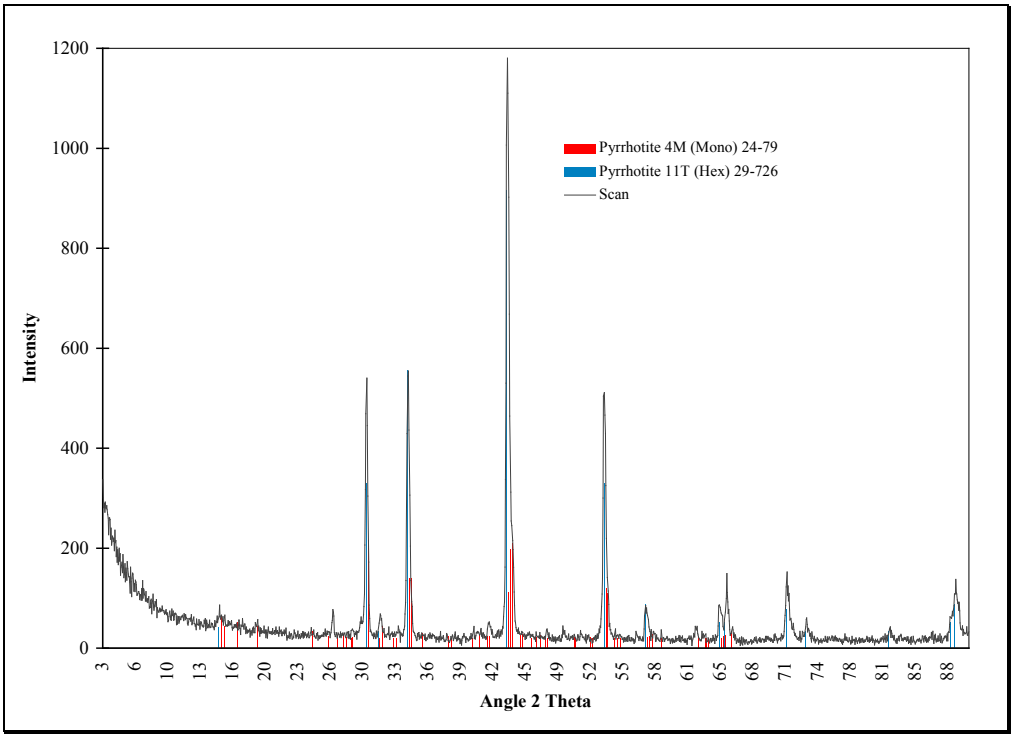

Figure A-9: Identification of pyrrhotite types for Po-M-6-94.

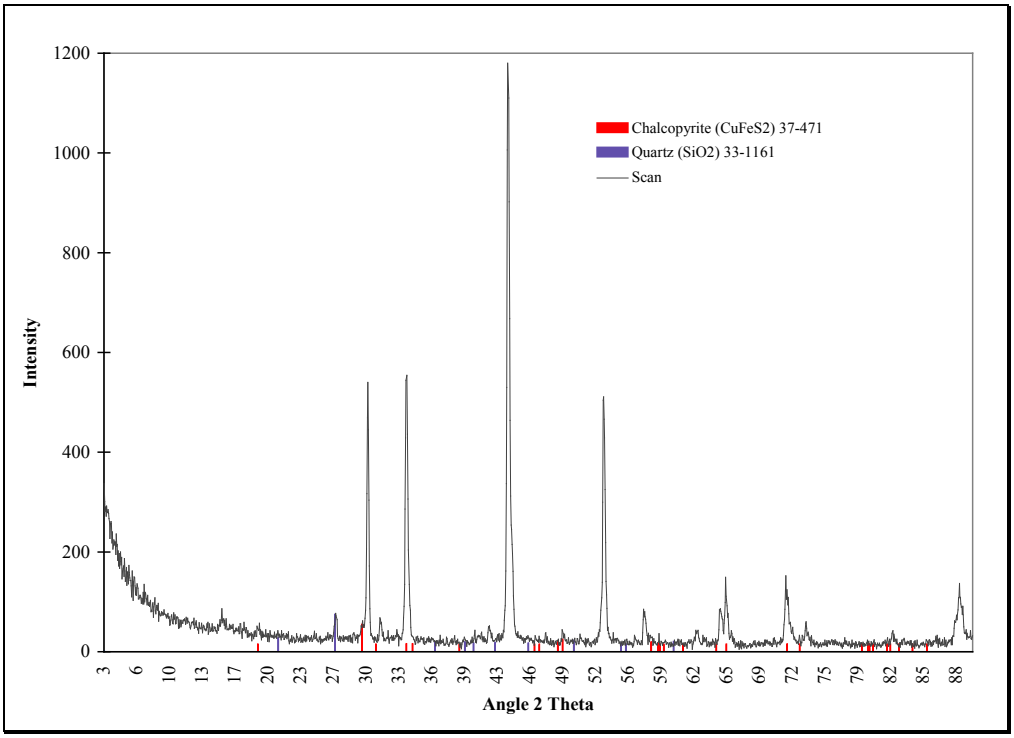

Figure A-10: Identification of accessory minerals for Po-M-6-94.

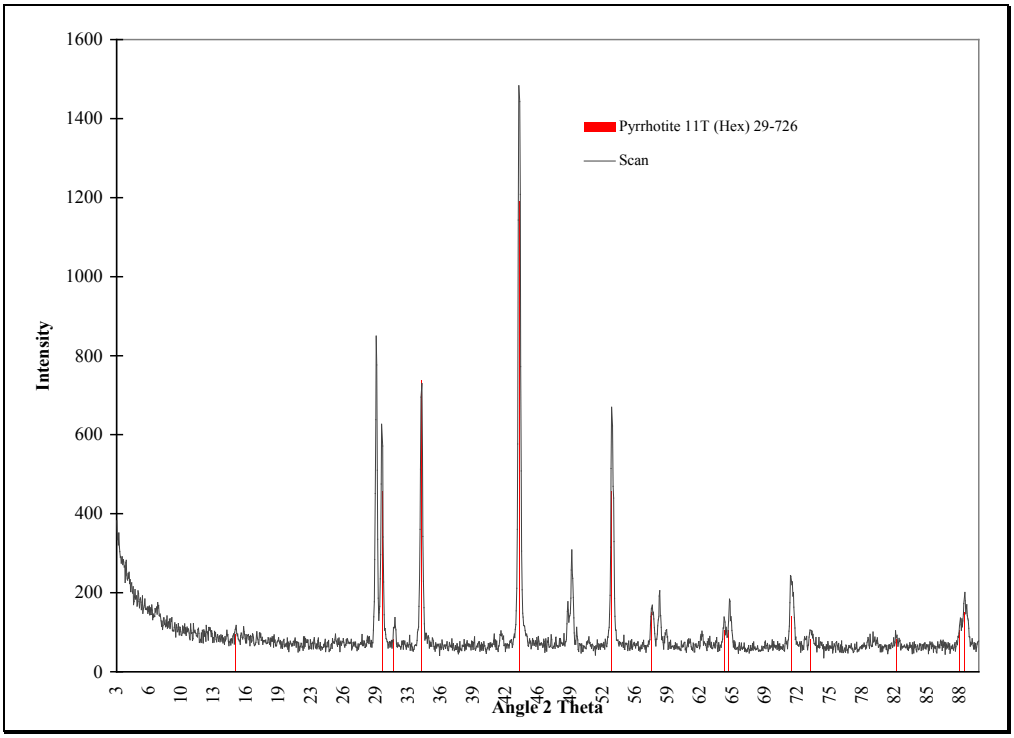

Figure A-11: Identification of pyrrhotite types for Po-M-7-94.

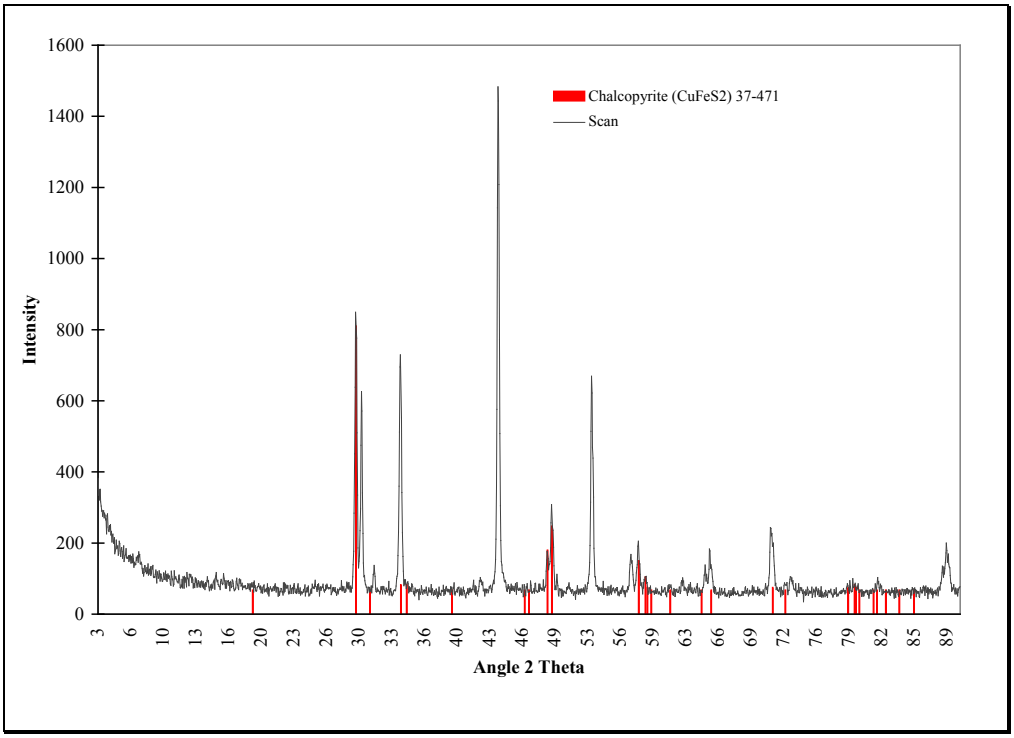

Figure A-12: Identification of accessory minerals for Po-M-7-94.

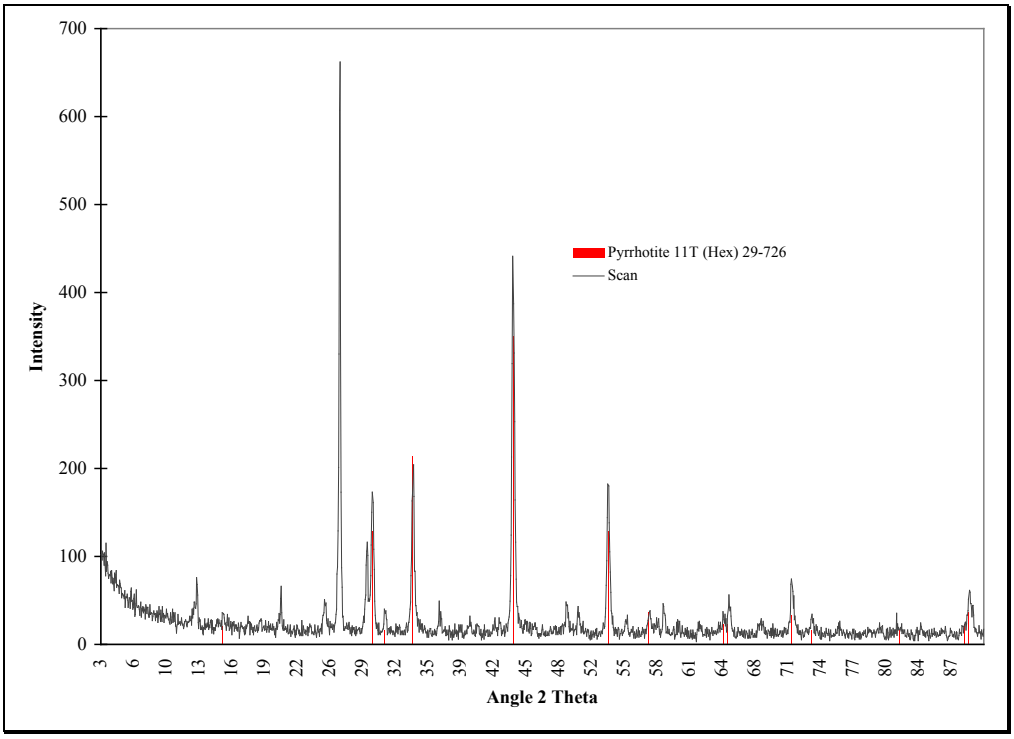

Figure A-13: Identification of pyrrhotite types for Po-M-8-93.

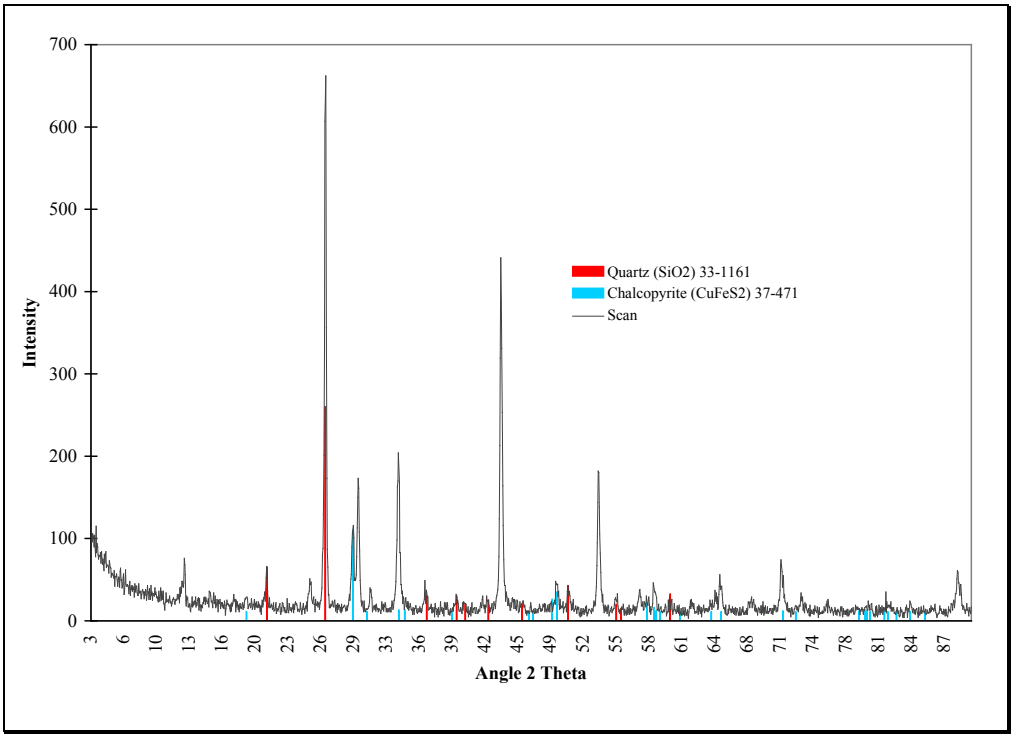

Figure A-14: Identification of accessory minerals for Po-M-8-93.

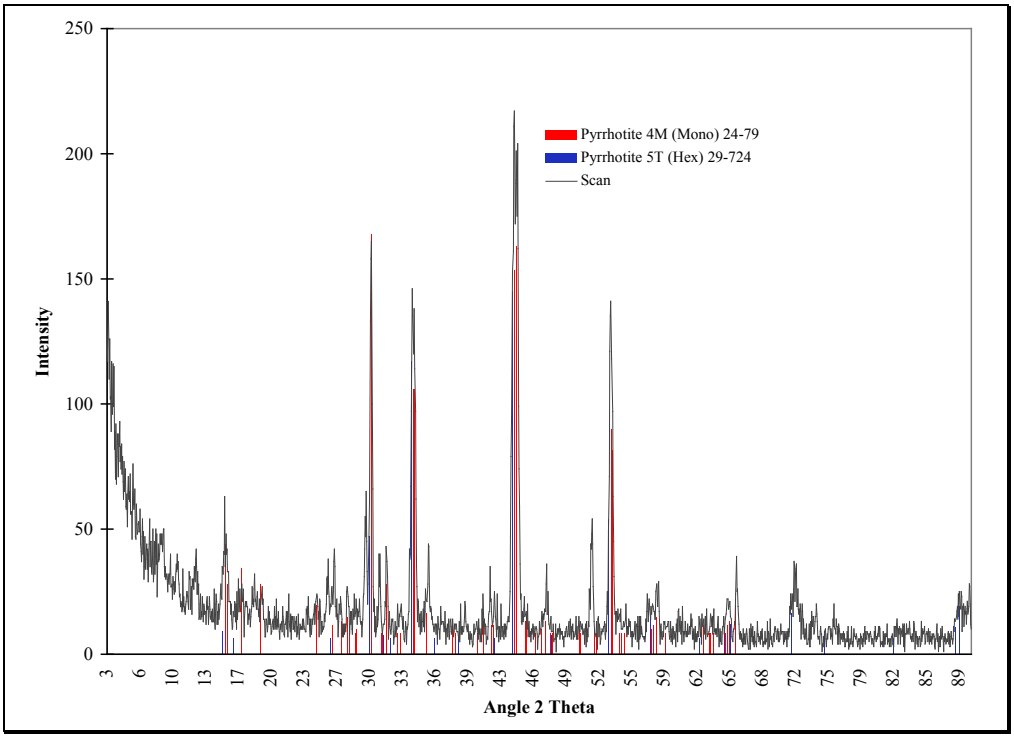

Figure A-15: Identification of pyrrhotite types for Po-M-9-91.

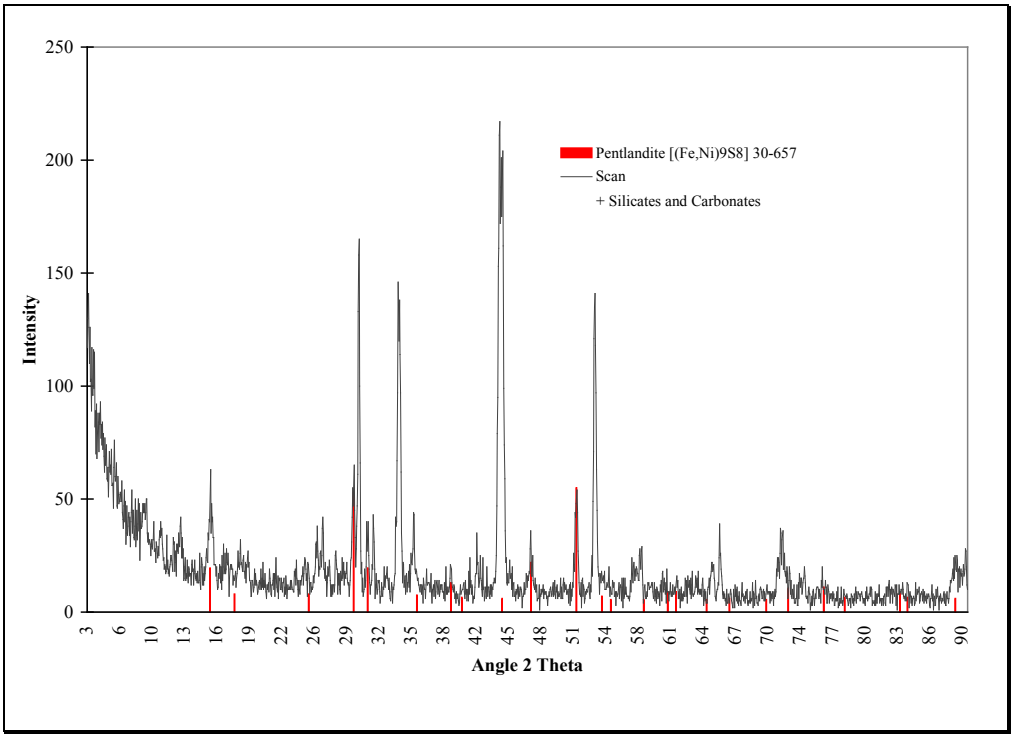

Figure A-16: Identification of accessory minerals for Po-M-9-91.

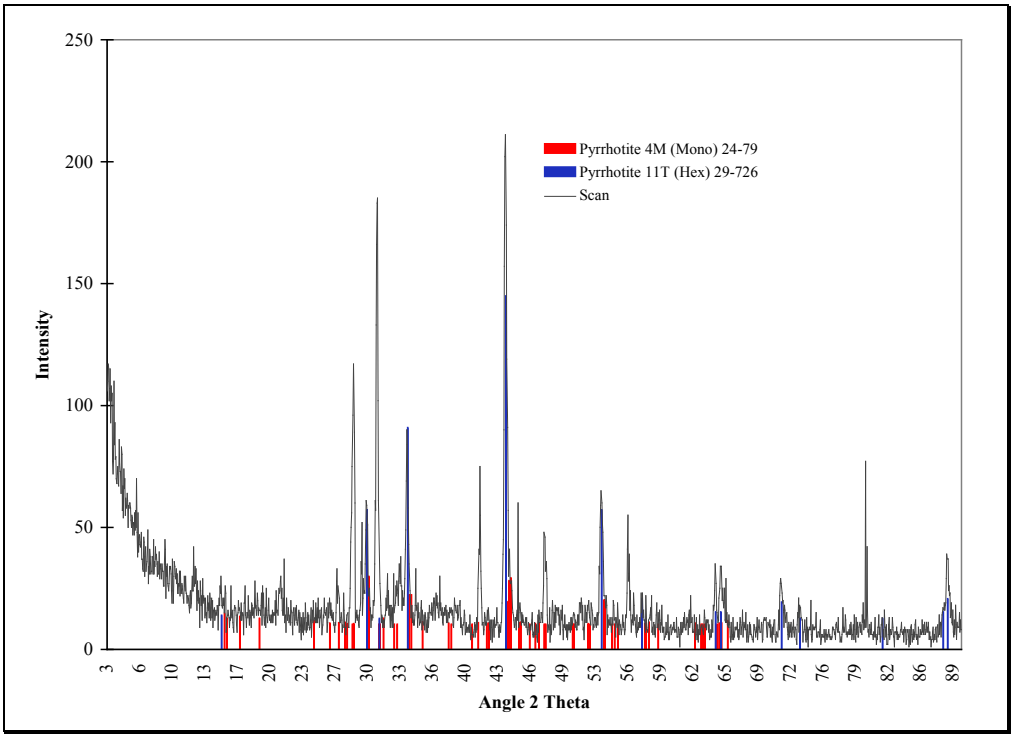

Figure A-17: Identification of pyrrhotite types for Po-M-15-93.

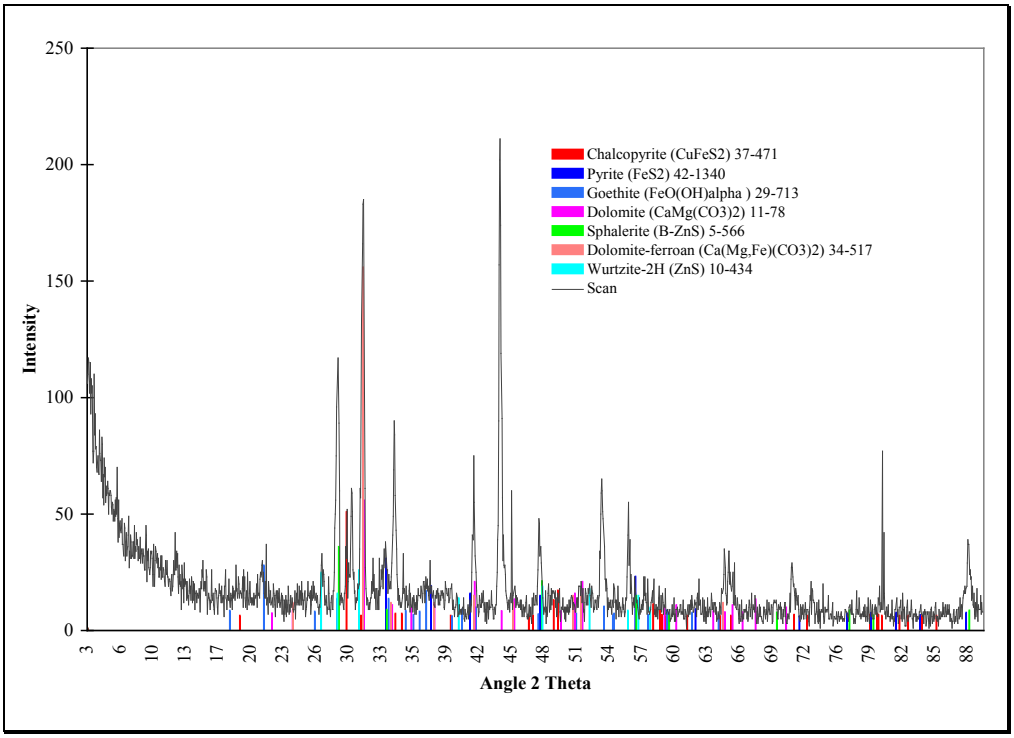

Figure A-18: Identification of accessory minerals for Po-M-15-93.

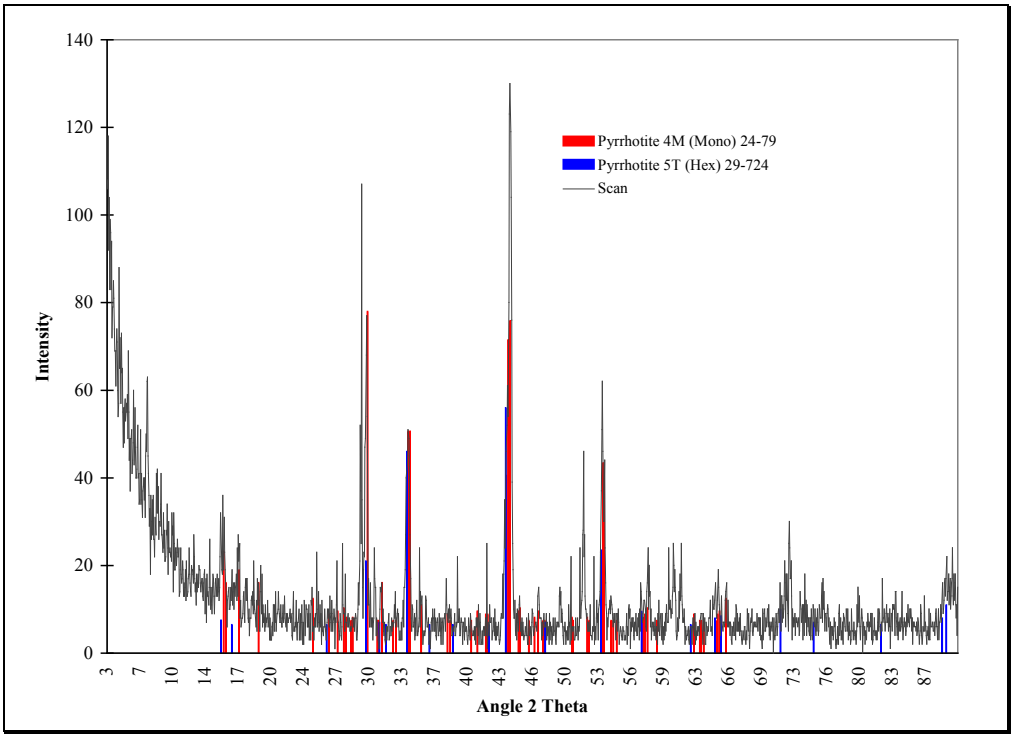

Figure A-19: Identification of pyrrhotite types for Po-M-17-93.

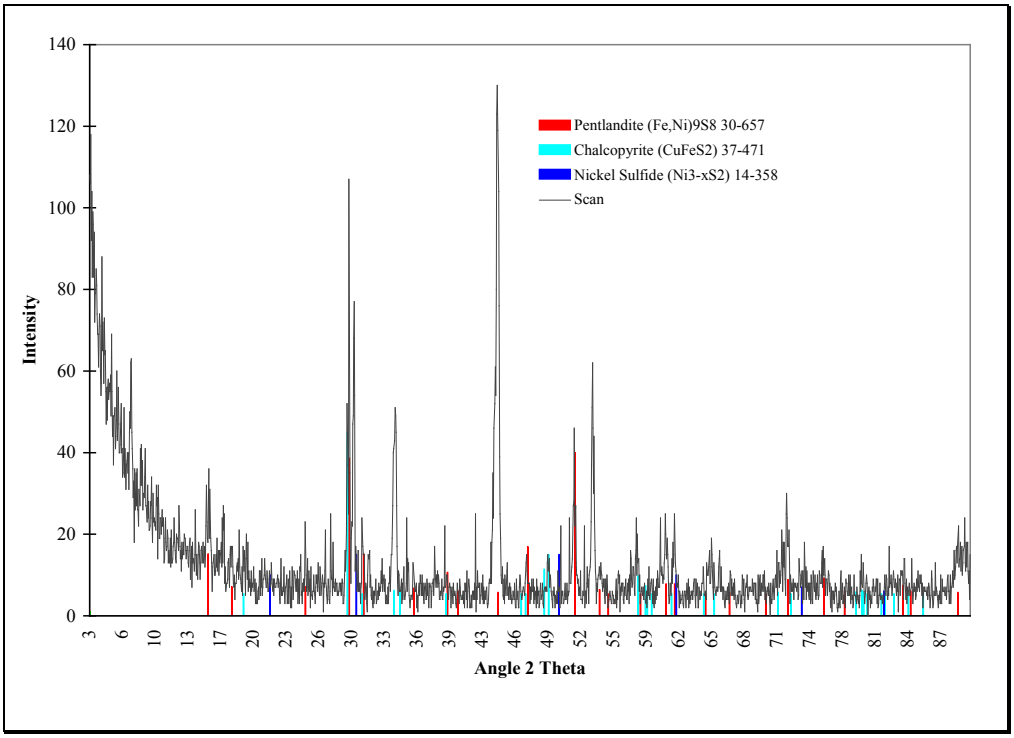

Figure A-20: Identification of accessory minerals for Po-M-17-93.

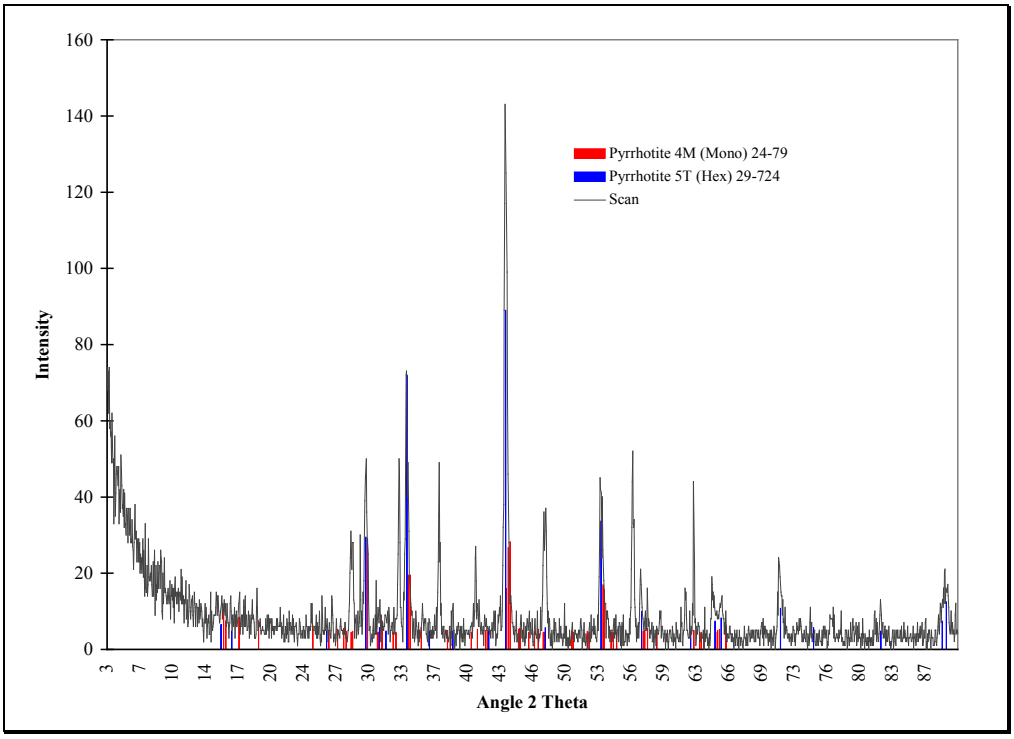

Figure A-21: Identification of pyrrhotite types for Po-M-19-94.

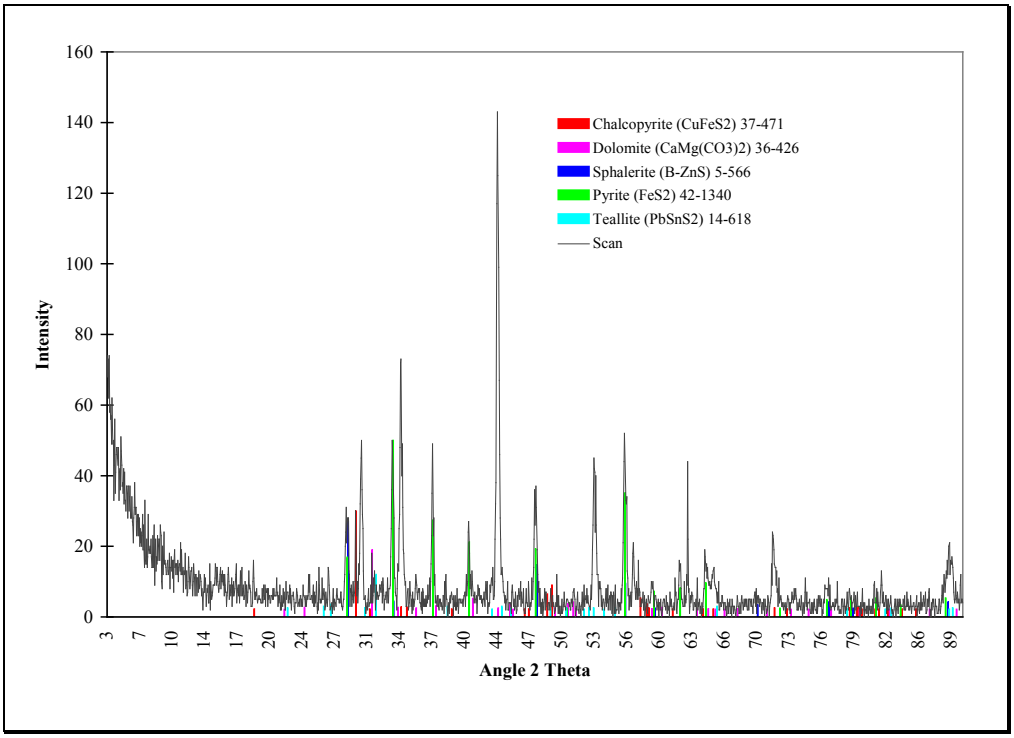

Figure A-22 Identification of accessory minerals for Po-M-19-94.

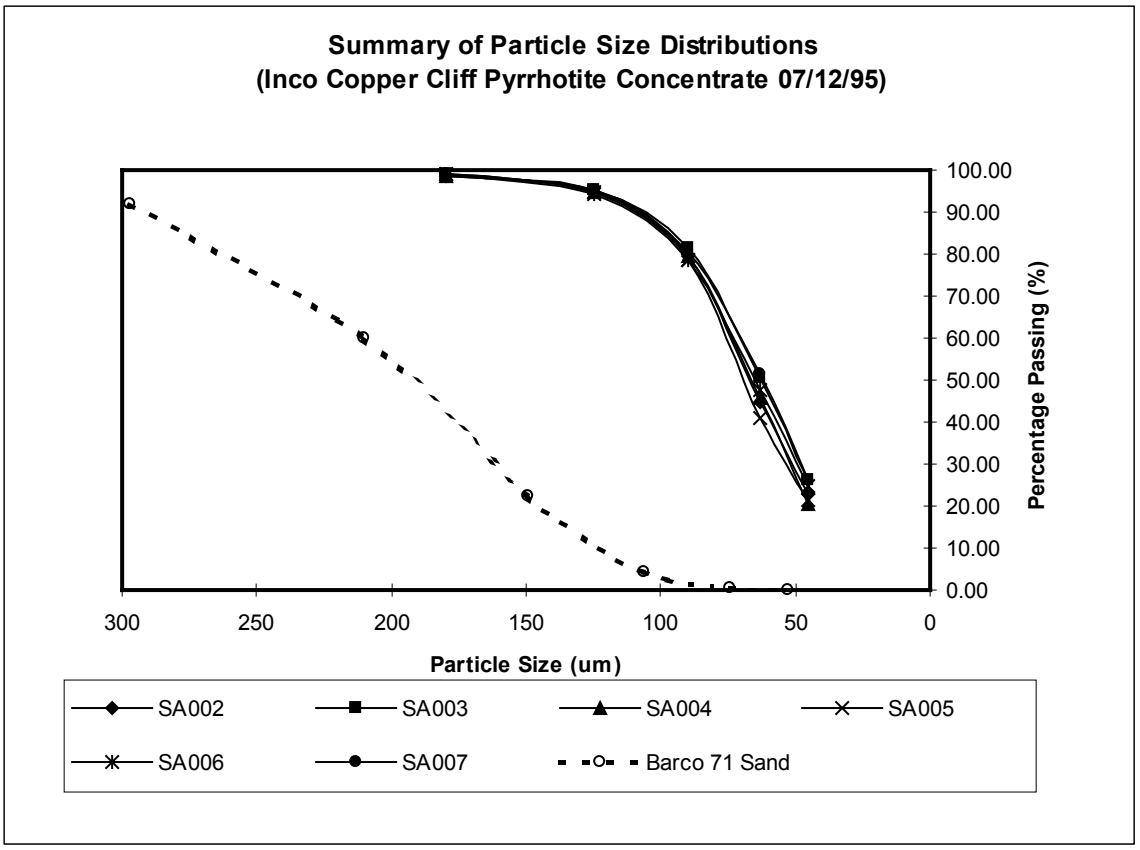

Figure A-23 Particle size distribution of pyrrhotite concentrate and quartz sand.

Table A-16: The impurities present in the Inco's Copper Cliff Po Conc.samples determined by multi-acid extraction and INAA-ICP & Leco anaysis.

SAMPLE ID	Ag (mg/kg)	Al %	As (mg/kg)	Ba (mg/kg)	Be (mg/kg)	Bi (mg/kg)	Ca %	Cd (mg/kg)	Co (mg/kg)	Cr (mg/kg)	Cu (mg/kg)
Bulk Sample #1	< 5	0.67	7.3	<50	< 2	< 5	0.46	< 0.5	200	260	680
Bulk Sample #2	< 5	0.65	6.5	110	< 2	< 5	0.44	0.9	210	280	665
Bulk Sample #3	< 5	0.66	6.4	<50	< 2	< 5	0.45	< 0.5	200	260	652
-180 / +125 µm	< 5	0.57	9.3	160	2	< 5	0.55	1.0	300	280	958
-125 / +90 µm	< 5	0.28	10.0	250	< 2	< 5	0.25	1.6	260	360	542
-90 / +63 µm	< 5	0.25	8.9	<50	< 2	< 5	0.22	< 0.5	220	390	407
-63 / +45 µm	< 5	0.21	8.1	160	< 2	< 5	0.17	0.5	220	510	546

SAMPLE ID	Fe %	K %	La (mg/kg)	Mg %	Mo (mg/kg)	Mn (mg/kg)	Na %	Ni (mg/kg)	P %	Pb (mg/kg)	Sb (mg/kg)
Bulk Sample #1	52.9	0.09	2.9	0.46	< 1	432	0.13	9200	0.002	51	0.2
Bulk Sample #2	56.7	0.07	3.5	0.43	< 1	400	0.15	9600	0.002	44	0.3
Bulk Sample #3	53.1	0.09	3.0	0.45	< 1	413	0.14	8900	0.002	51	0.2
-180 / +125 µm	59.3	0.10	4.9	0.51	< 1	372	0.20	11000	0.005	24	< 0.1
-125 / +90 µm	66.1	0.04	3.0	0.23	< 1	311	0.10	10000	0.002	18	0.4
-90 / +63 µm	65.3	0.05	3.1	0.20	15	297	0.09	8300	0.002	16	0.9
-63 / +45 µm	67.3	0.03	3.2	0.16	< 1	295	0.07	9100	0.002	17	0.4

SAMPLE ID	Sc (mg/kg)	Sn (mg/kg)	Sr (mg/kg)	Ti %	V (mg/kg)	W (mg/kg)	Y (mg/kg)	Zn (mg/kg)	S %	CO_2 %
Bulk Sample #1	3.0	< 0.01	< 0.05	0.20	139	< 1	6	61	22.8	0.062
Bulk Sample #2	3.4	< 0.01	< 0.05	0.19	133	< 1	6	55	25.9	0.040
Bulk Sample #3	3.0	< 0.01	< 0.05	0.20	138	< 1	6	61	23.1	0.029
-180 / +125 µm	4.7	< 0.01	< 0.05	0.17	97	< 1	7	109	27.0	
-125 / +90 µm	2.5	< 0.01	< 0.05	0.19	129	< 1	6	99	24.6	
-90 / +63 µm	2.3	< 0.01	< 0.05	0.19	145	< 1	5	93	27.0	
-63 / +45 µm	2.0	< 0.01	< 0.05	0.20	183	< 1	5	125	23.3	

Table A-17: The sulphide mineral present in the Inco's Copper Cliff Po Conc.samples calculated by chemical composition.

Sample ID	Cp %	Ga %	Sp %	Pn %	Po %	Total Sulphide Mineral %
Bulk Sample #1	0.196	0.006	0.009	1.496	56.139	57.846
Bulk Sample #2	0.192	0.005	0.008	1.216	64.207	65.628
Bulk Sample #3	0.188	0.006	0.009	1.505	56.895	58.603
-180 / +125 μm	0.277	0.003	0.017	1.555	66.619	68.471
-125 / +90 μm	0.157	0.002	0.015	1.353	60.835	62.362
-90 / +63 μm	0.118	0.002	0.014	0.930	67.286	68.350
-63 / +45 μm	0.158	0.002	0.019	1.153	57.716	59.048

Cp Chalcopyrite
Ga Galena
Sp Sphalerite
Pn Pentlandite
Po Pyrrhotite

Appendix B

Non-Oxidative Dissolution of Specimen Grade Pyrrhotite Samples

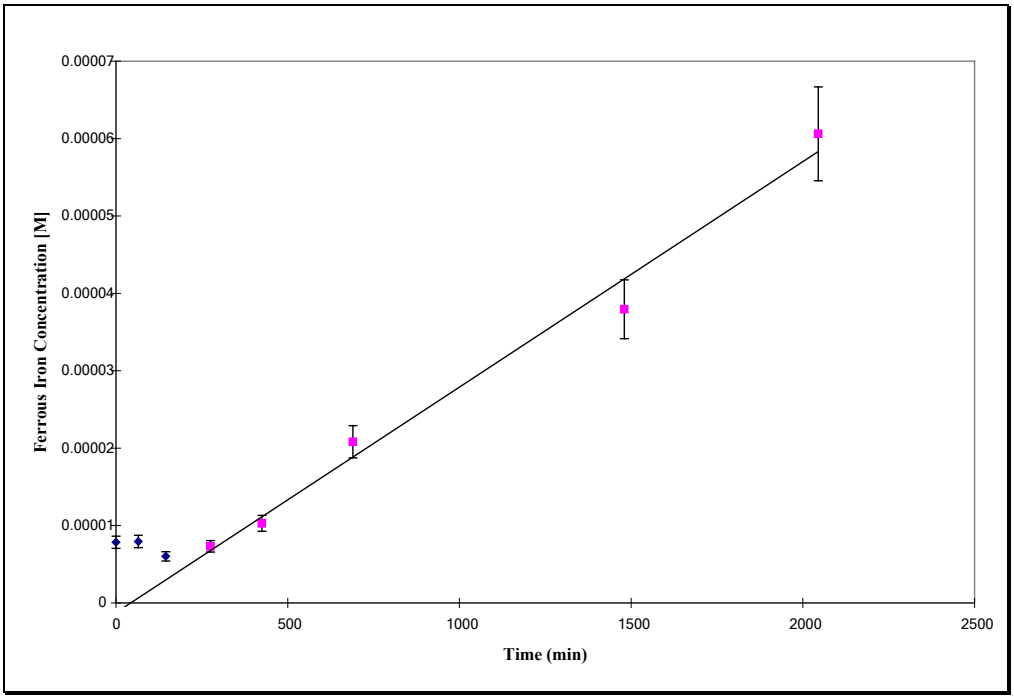

Figure B-1: Non-oxidative dissolution at pH=2.72, 25°C for Po-M-1-93.

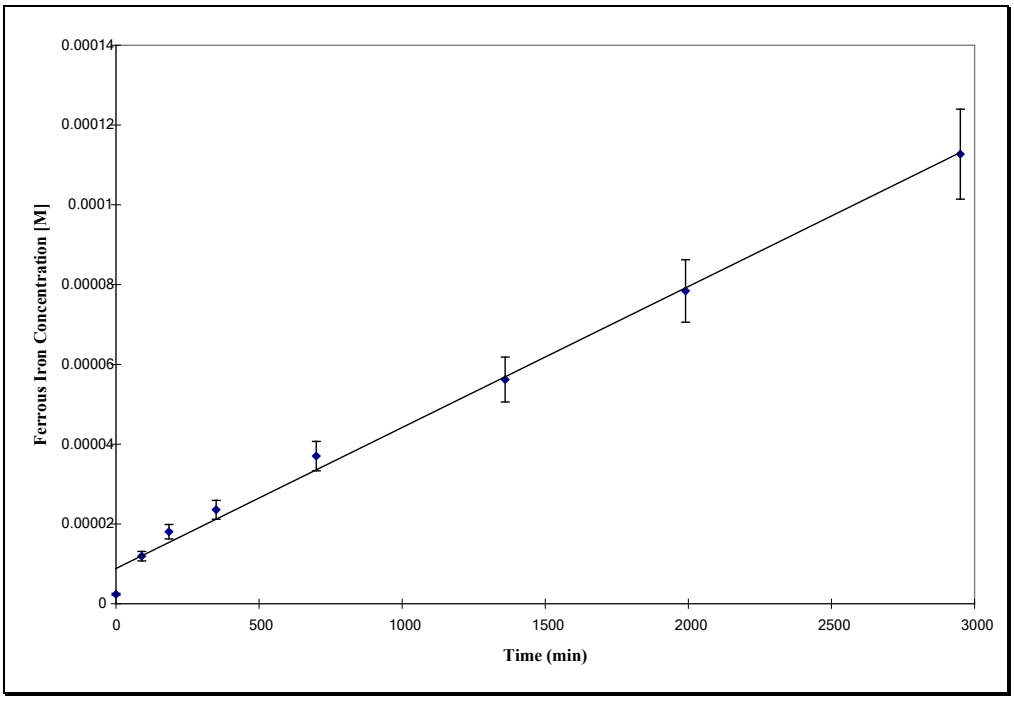

Figure B-2: Non-oxidative dissolution at pH=2.70, 25°C for Po-M-3-94.

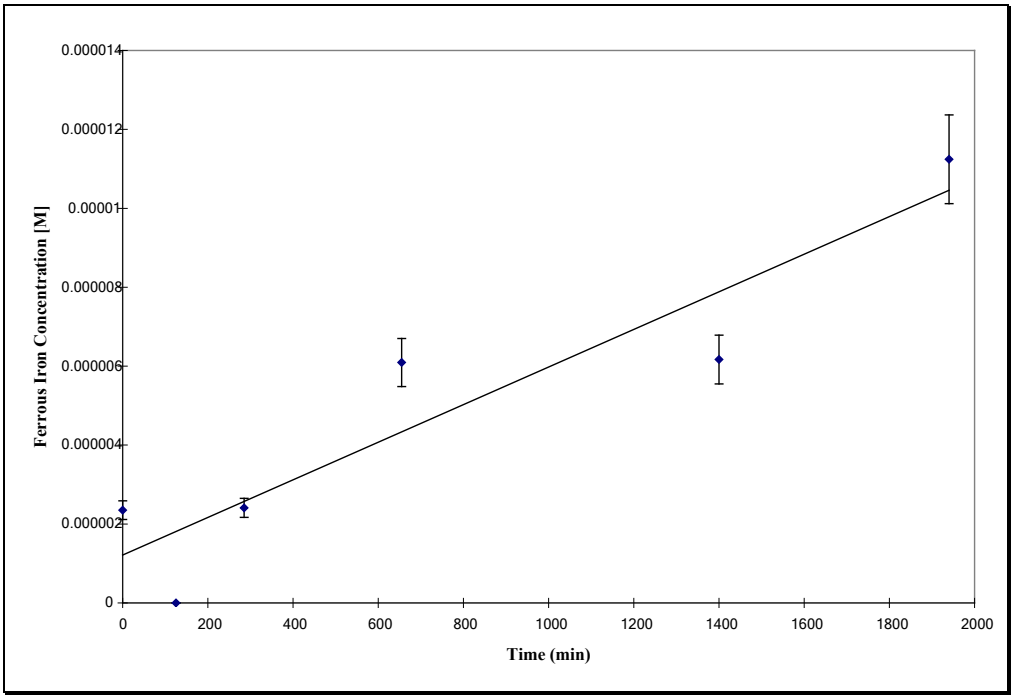

Figure B-3: Non-oxidative dissolution at pH=2.76, 25°C for Po-M-4-94.

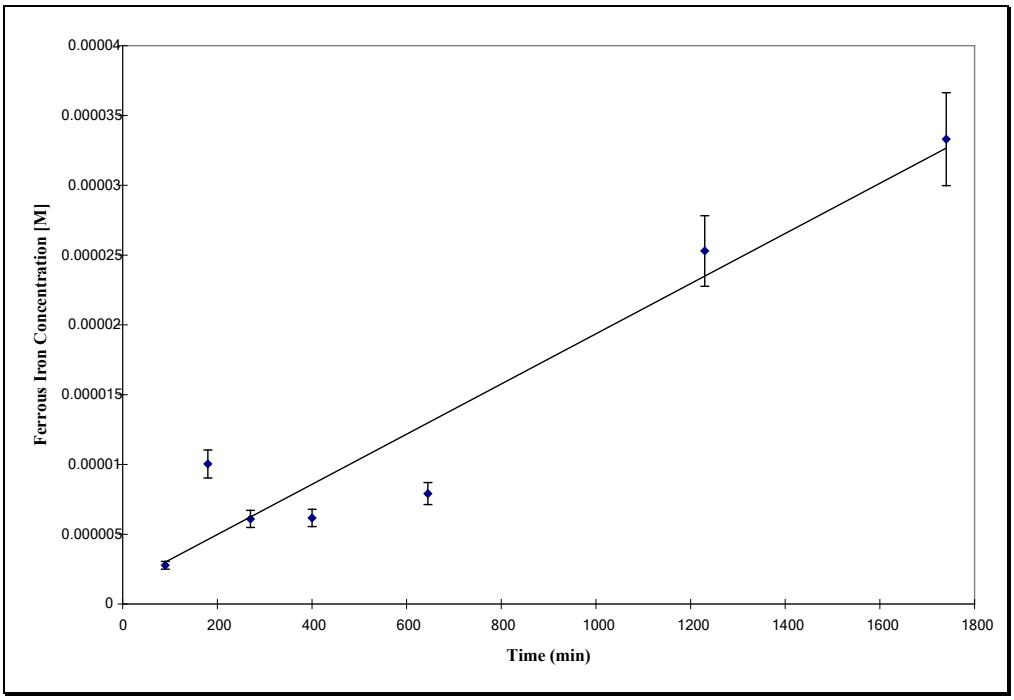

Figure B-4: Non-oxidative dissolution at pH=2.78, 25°C for Po-C-5-94.

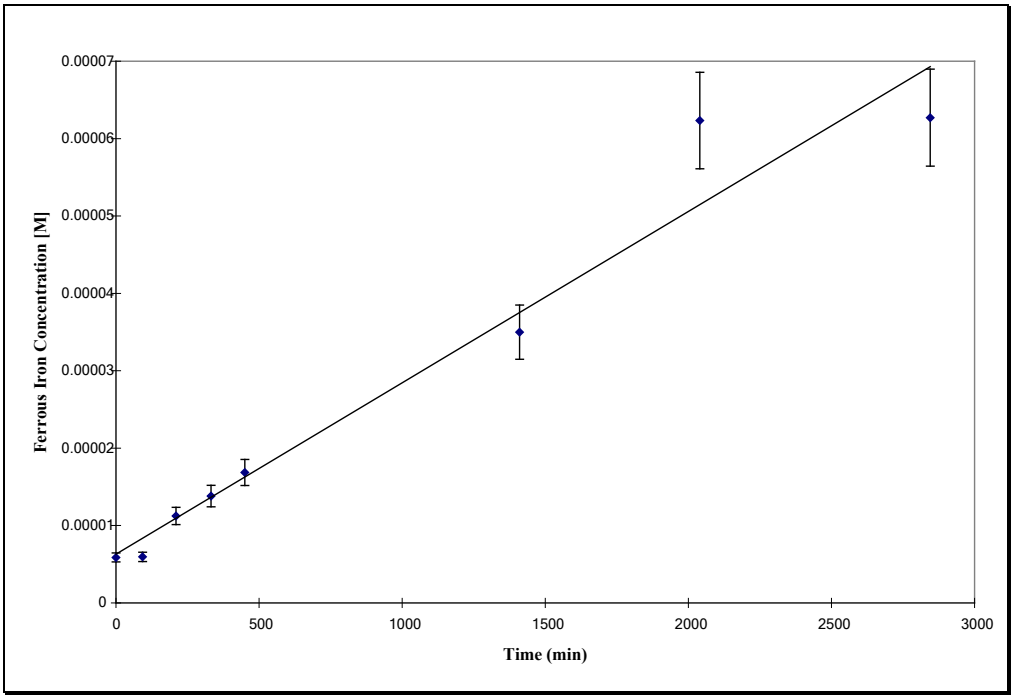

Figure B-5: Non-oxidative dissolution at pH=2.78, 25°C for Po-M-6-94.

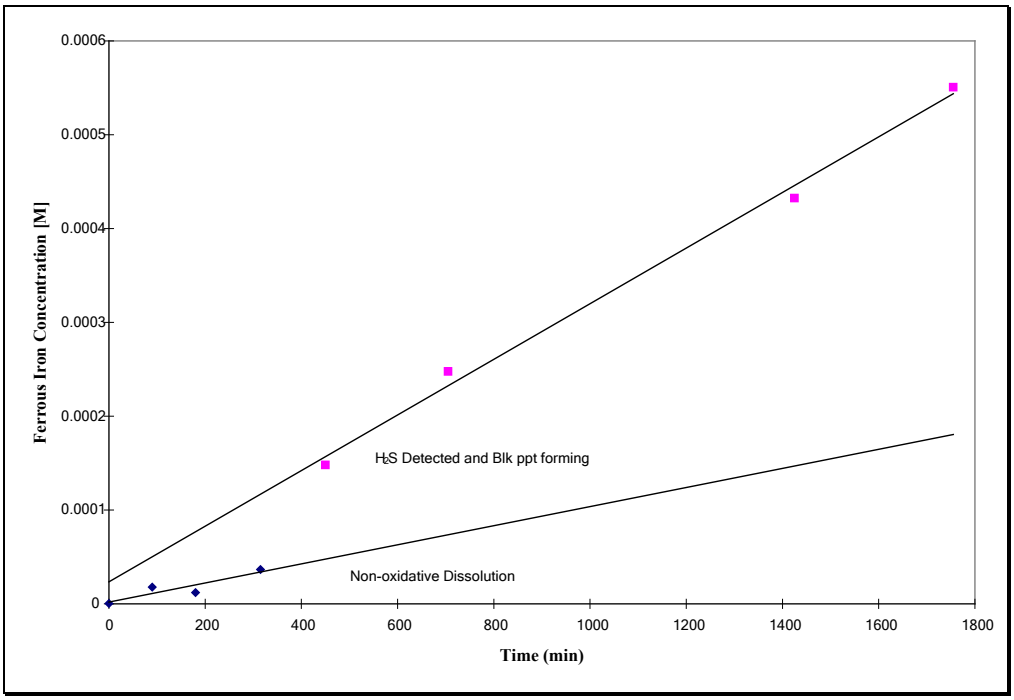

Figure B-6: Non-oxidative dissolution at pH=2.77, 25°C for Po-M-8-93.

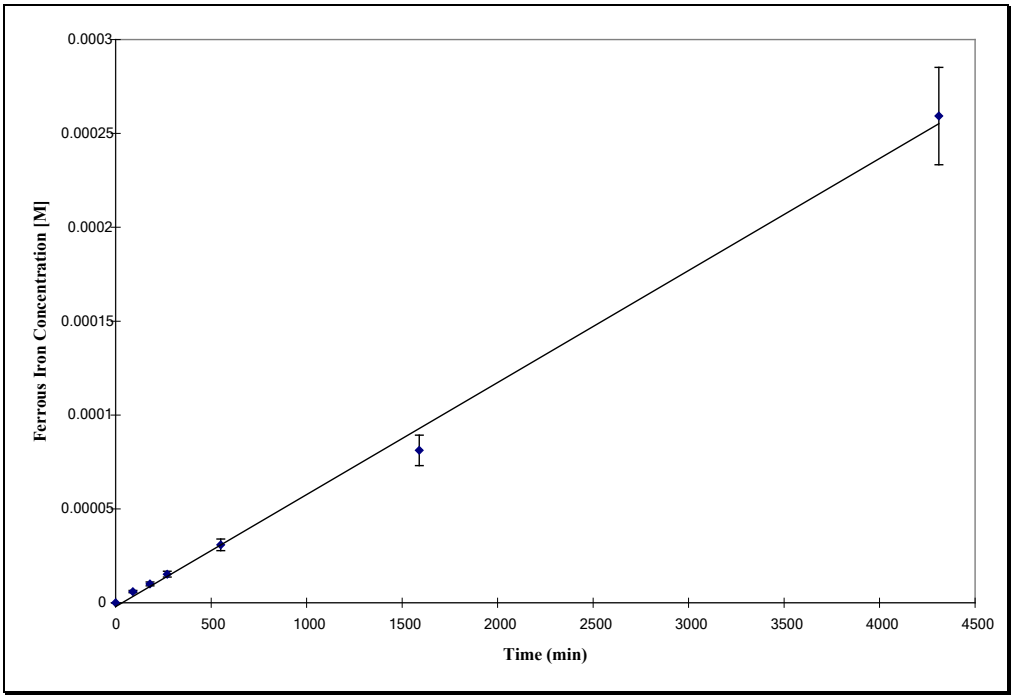

Figure B-7: Non-oxidative dissolution at pH=2.72, 25°C for Po-M-9-91.

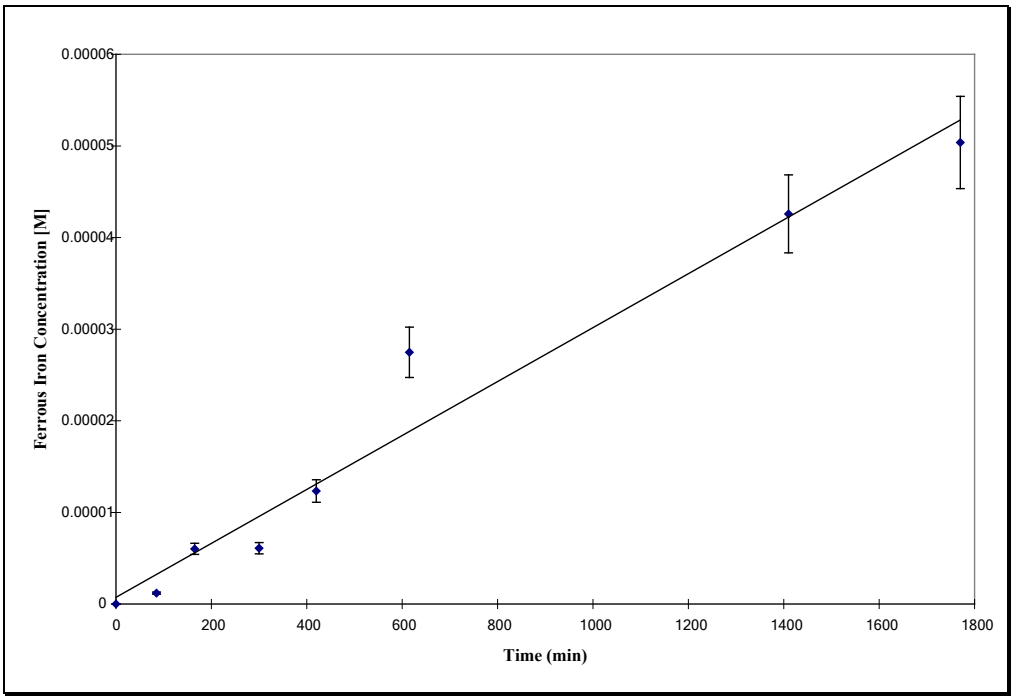

Figure B-8: Non-oxidative dissolution at pH=2.75, 25°C for Po-M-17-93.

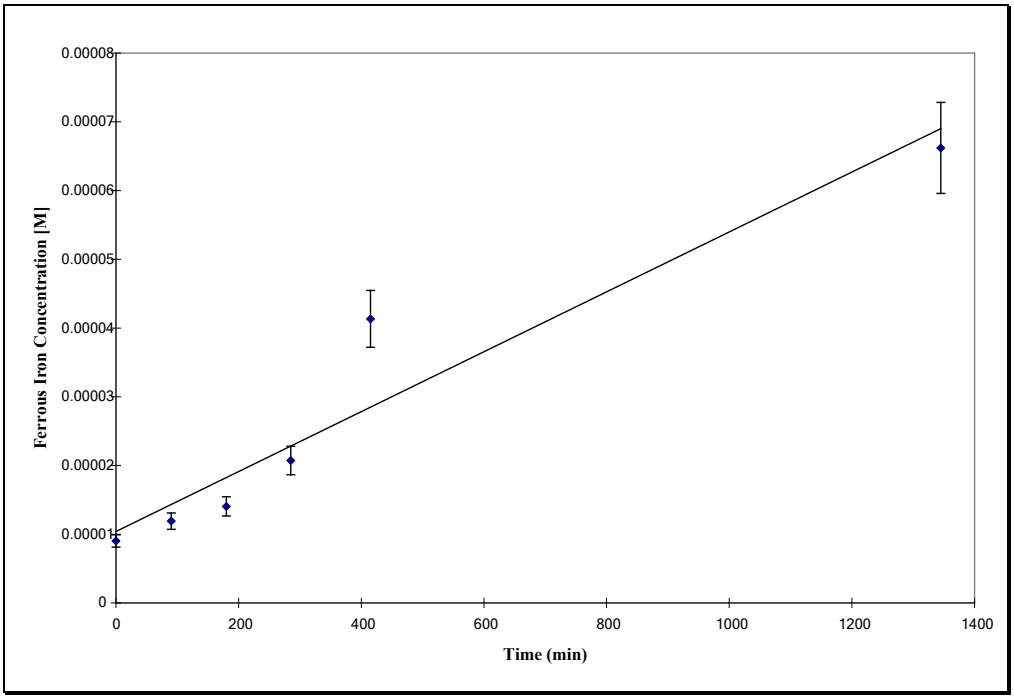

Figure B-9: Non-oxidative dissolution at pH=2.69, 25°C for Po-M-19-94.

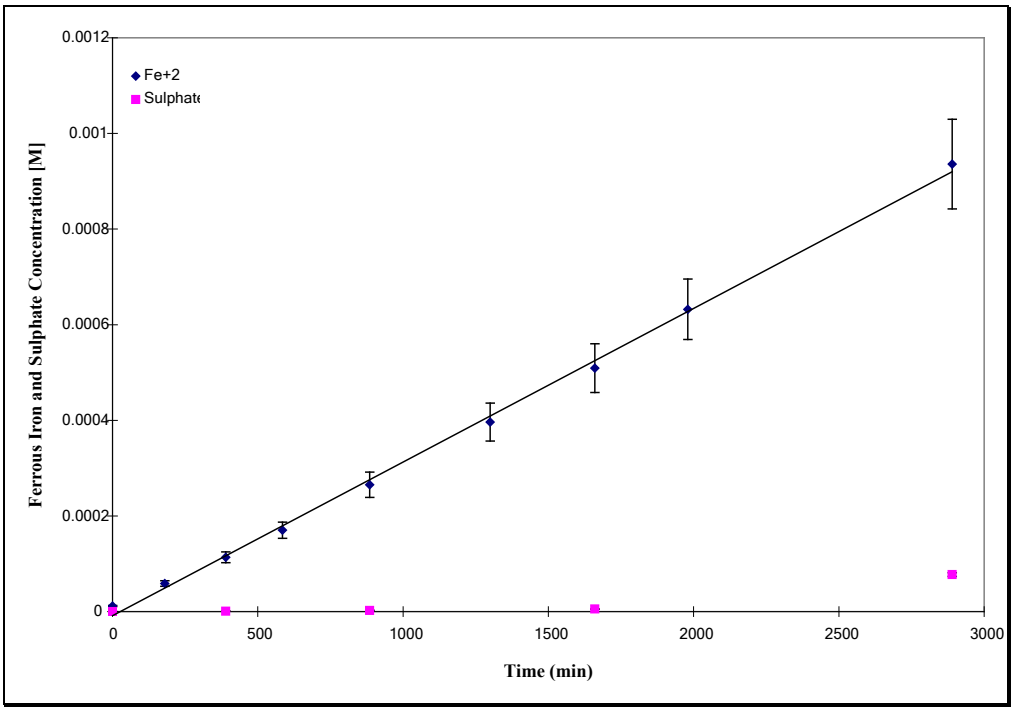

Figure B-10: Pyrrhotite oxidation by oxygen at pH=2.76, 25°C for Po-M-2-94.

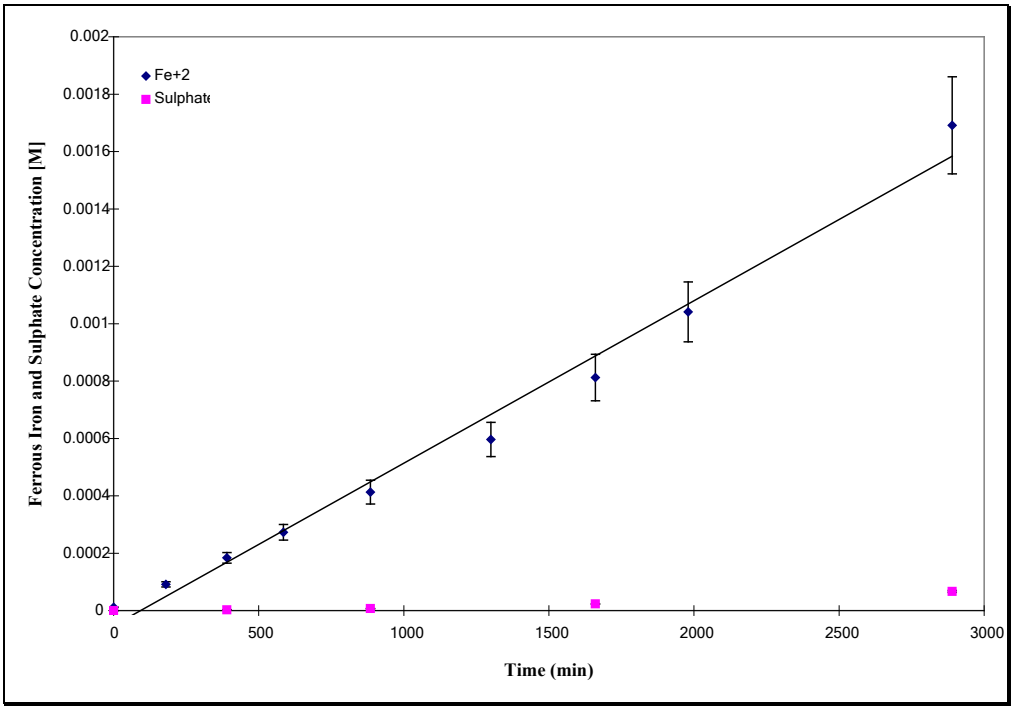

Figure B-11: Pyrrhotite oxidation by oxygen at pH=2.77, 25°C for Po-M-3-94.

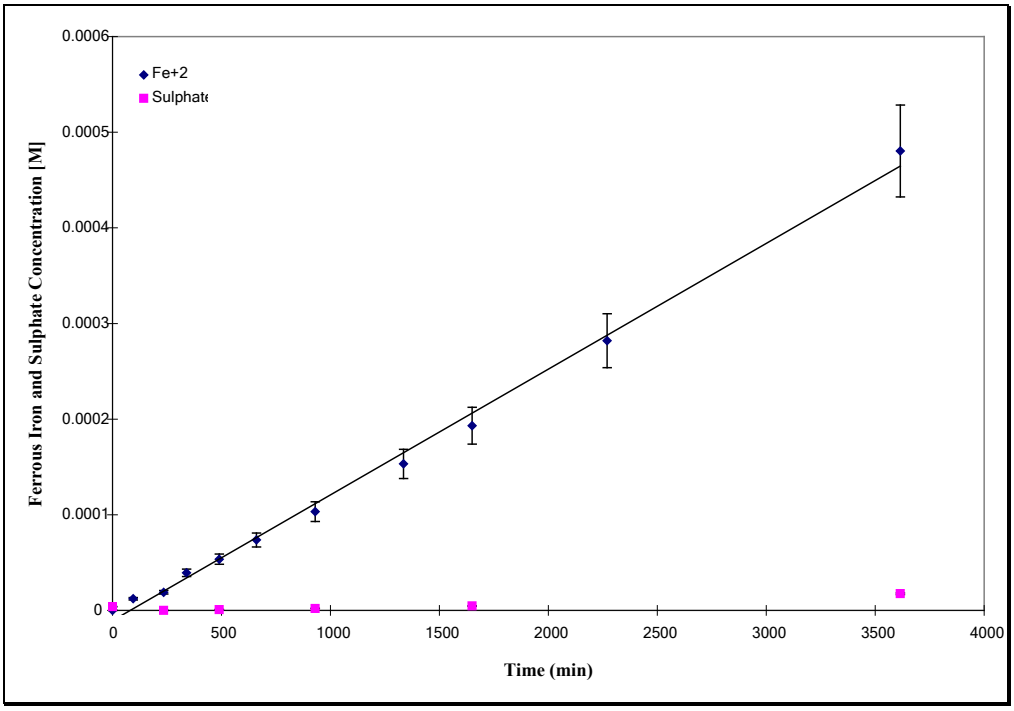

Figure B-12: Pyrrhotite oxidation by oxygen at pH=2.78, 25°C for Po-M-4-94.

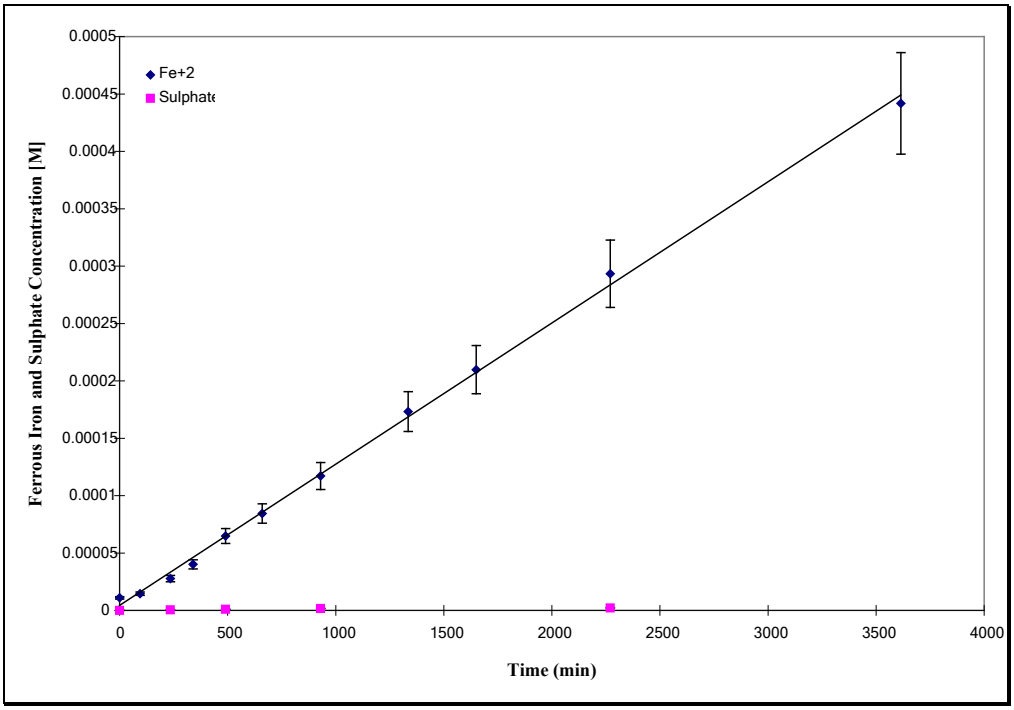

Figure B-13: Pyrrhotite oxidation by oxygen at pH=2.79, 25°C for Po-C-5-94.

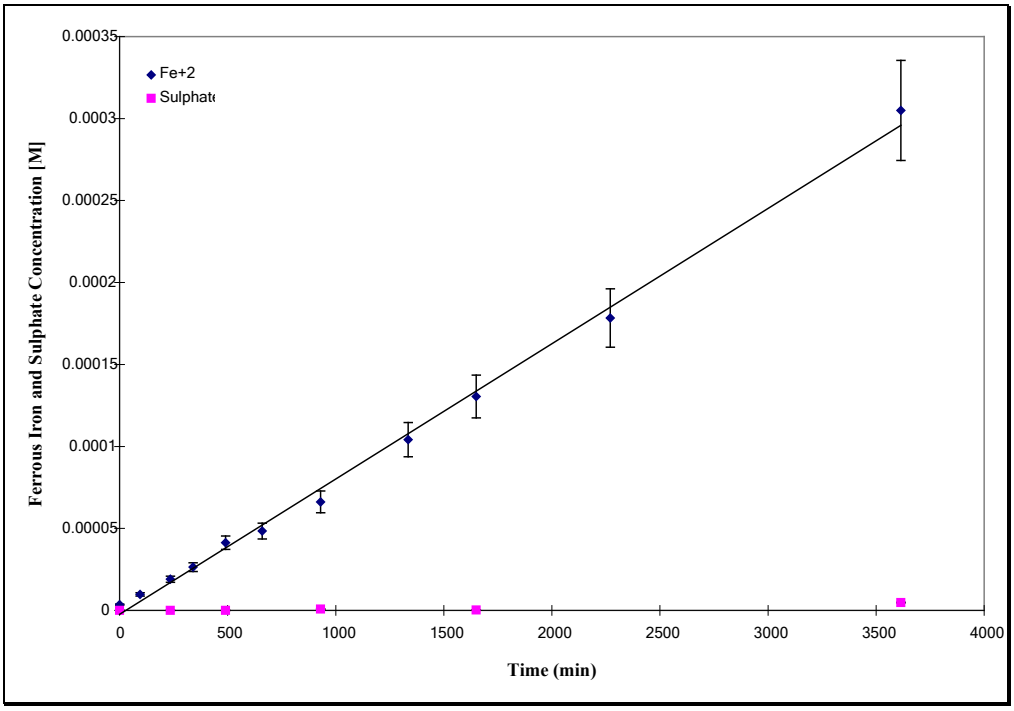

Figure B-14: Pyrrhotite oxidation by oxygen at pH=2.80, 25°C for Po-M-6-94.

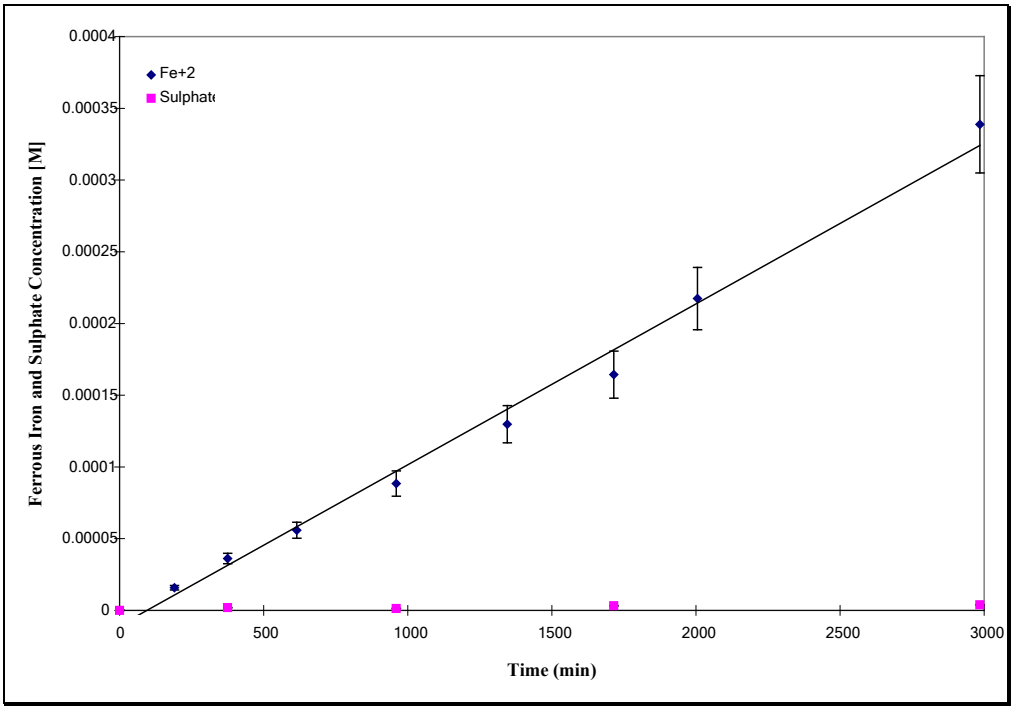

Figure B-15: Pyrrhotite oxidation by oxygen at pH=2.76, 25°C for Po-M-7-94.

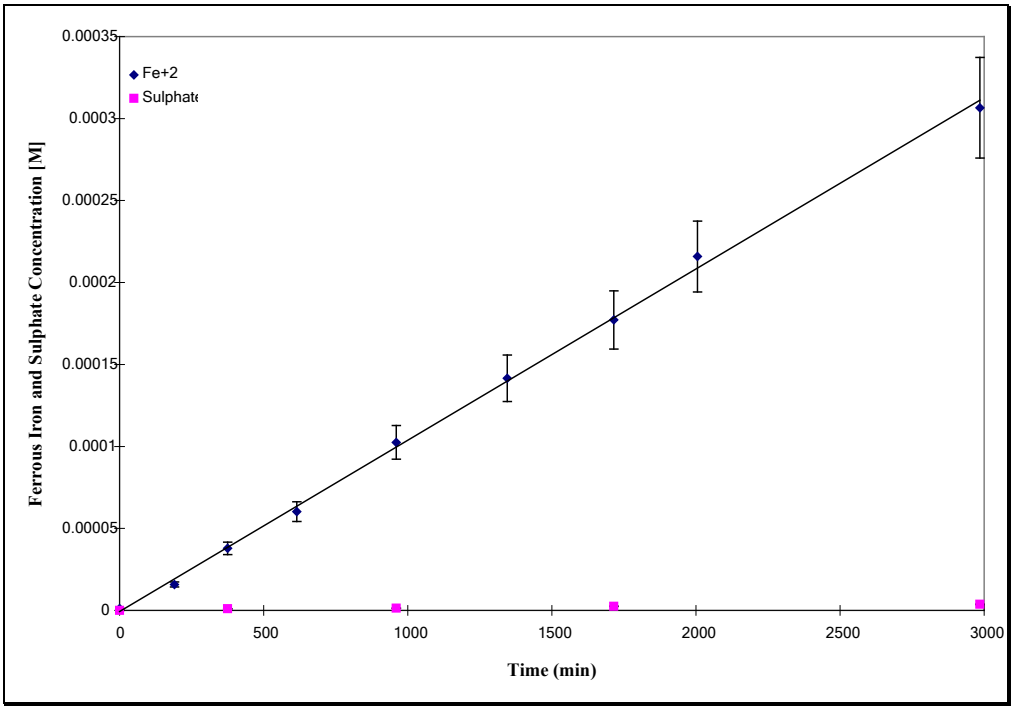

Figure B-16: Pyrrhotite oxidation by oxygen at pH=2.76, 25°C for Po-M-8-93.

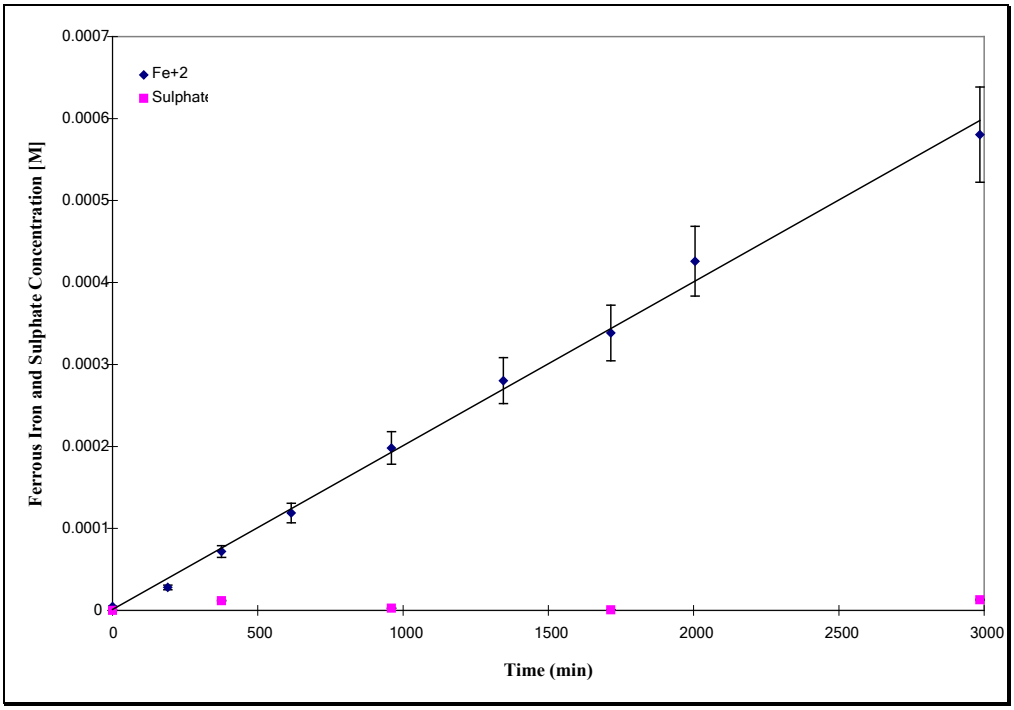

Figure B-17: Pyrrhotite oxidation by oxygen at pH=2.76, 25°C for Po-M-9-91.

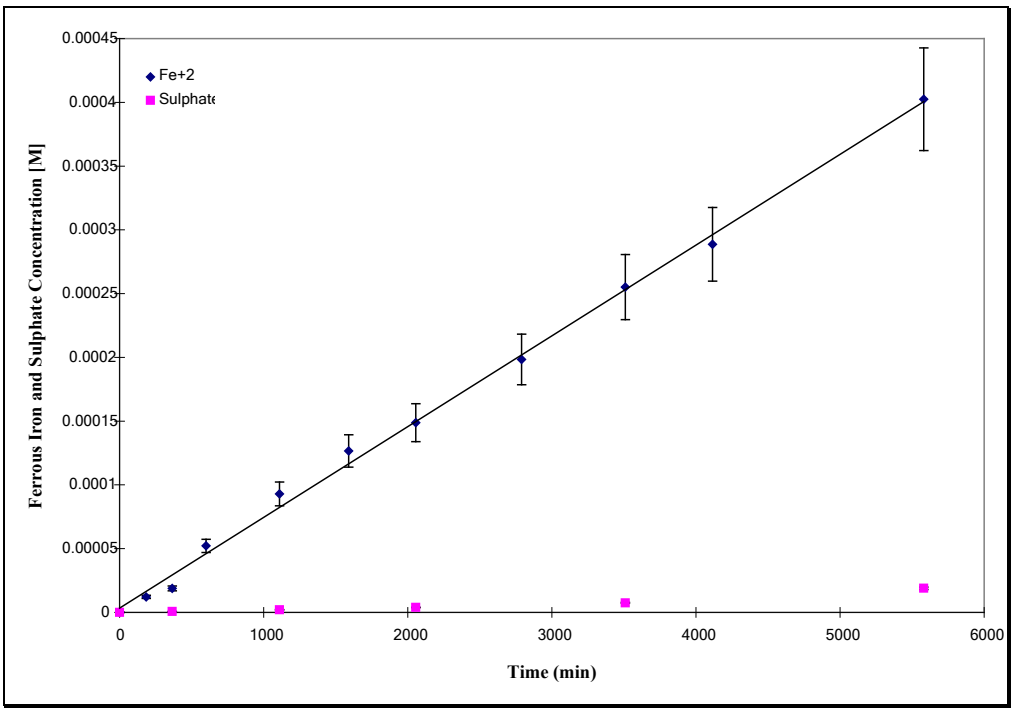

Figure B-18: Pyrrhotite oxidation by oxygen at pH=2.74, 25°C for Po-M-17-93.

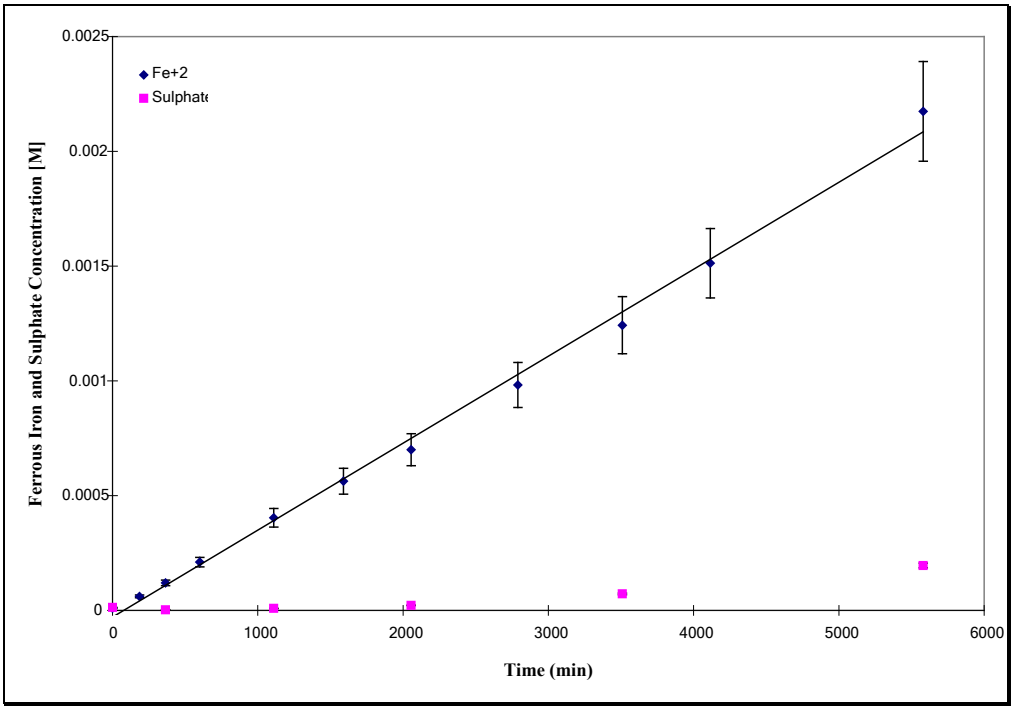

Figure B-19: Pyrrhotite oxidation by oxygen at pH=2.74, 25°C for Po-M-19-94.

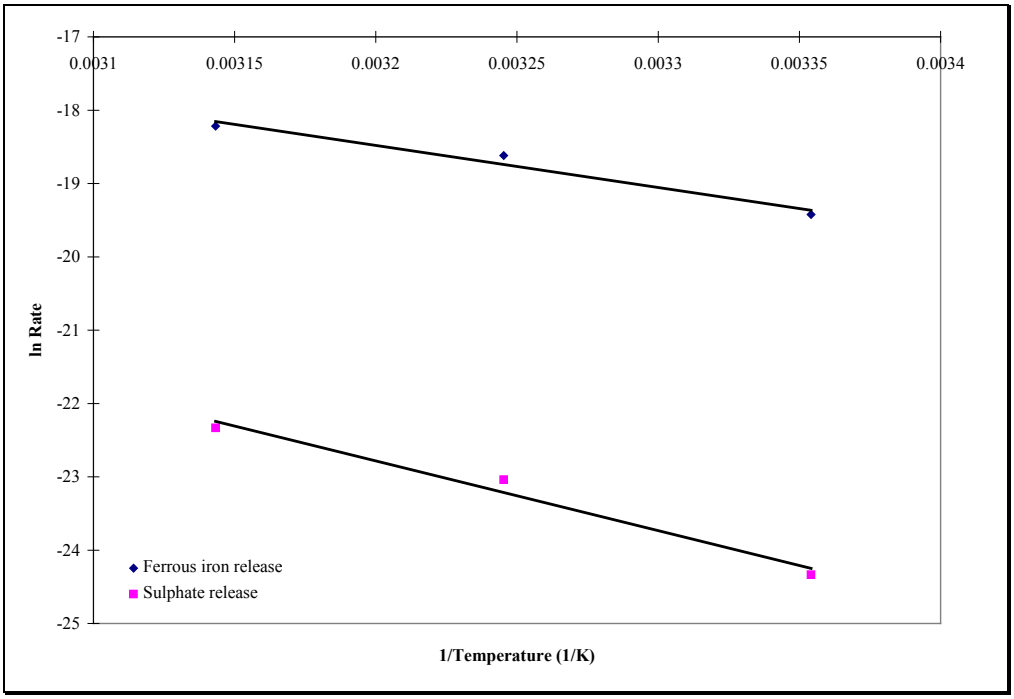

Figure B-20: The effects of temperature on O_2 oxidation reaction rate for Po-M-1-93.

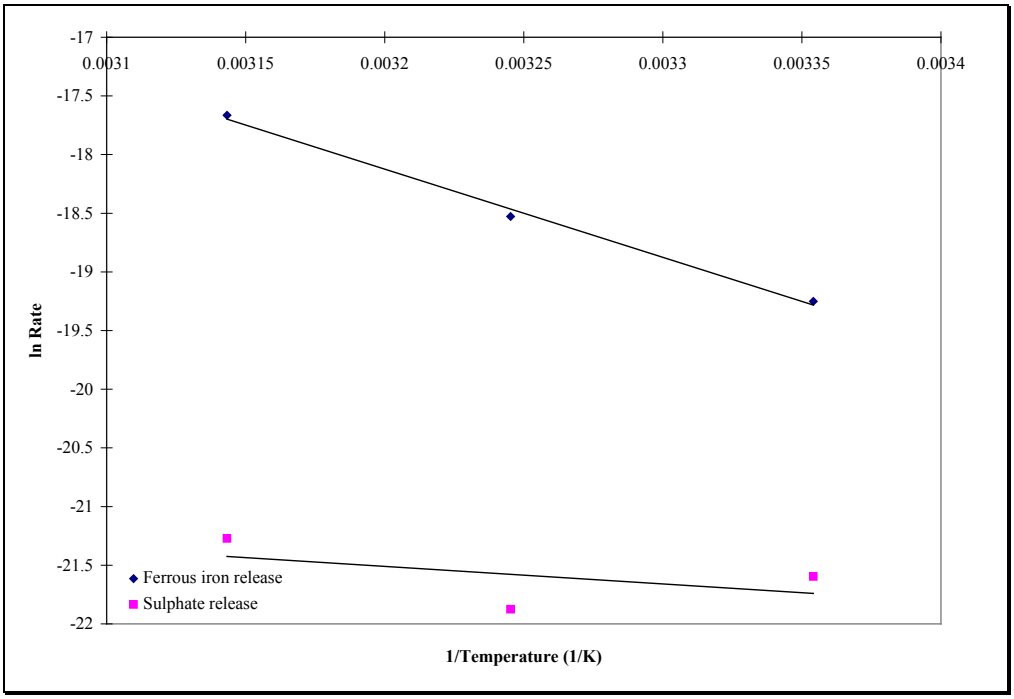

Figure B-21: The effects of temperature on O_2 oxidation reaction rate for Po-M-2-94.

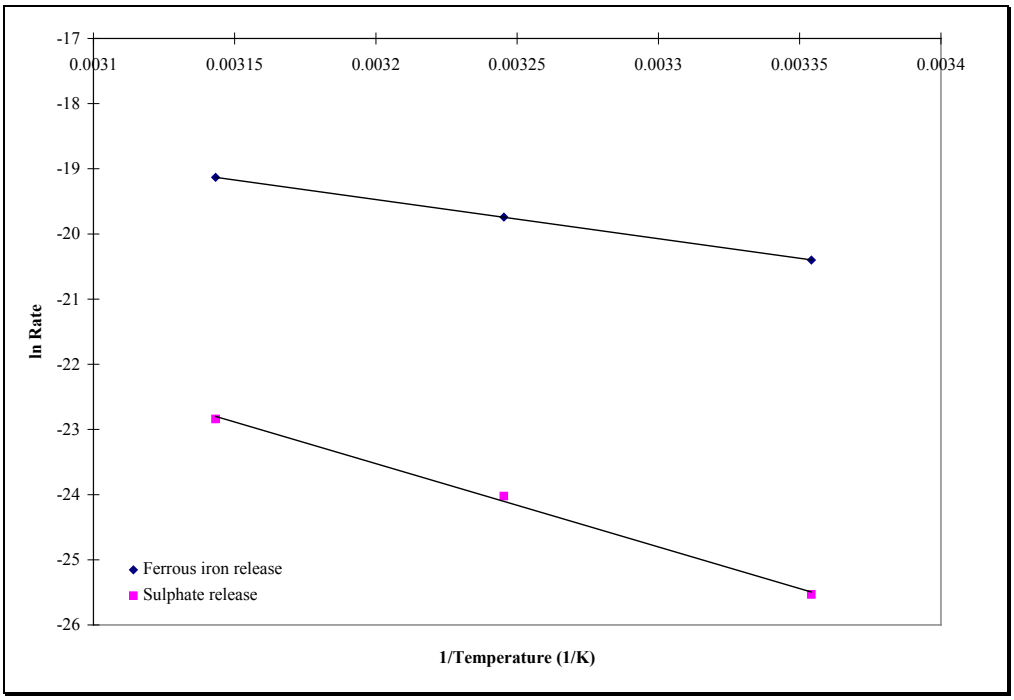

Figure B-22: The effects of temperature on O_2 oxidation reaction rate for Po-C-5-94.

Appendix C

Ferric Iron Oxidation of Specimen Grade Pyrrhotite Samples

Table C-1a: Complete listing of rates of pyrrhotite oxidation by ferric iron.

Po Sample	Fe^{+3}_{int} [M]	Temperature °C	pH	Oxidation Rate (moles-$Fe^{+3} \times m^{-2} \times s^{-1}$)
Po-M-1-93	2.00E-04	25	1.97	3.7E-08
Po-M-1-93	1.00E-03	25	2	8.1E-08
Po-M-1-93	1.00E-03	25	2	8.1E-08
Po-M-1-93	1.00E-03	35	2.4	1.3E-07
Po-M-1-93	6.00E-04	25	2.43	8.3E-08
Po-M-1-93	1.00E-03	7.5	2.46	1.2E-08
Po-M-1-93	2.00E-04	25	2.5	4.1E-08
Po-M-1-93	1.00E-03	25	2.5	5.3E-08
Po-M-1-93	2.00E-04	25	2.73	3.5E-08
Po-M-2-94	1.00E-02	35	1.75	1.7E-07
Po-M-2-94	2.00E-04	25	1.95	1.5E-08
Po-M-2-94	1.00E-03	25	2	5.9E-08
Po-M-2-94	1.00E-03	25	2	4.2E-08
Po-M-2-94	1.00E-02	25	2	8.2E-08
Po-M-2-94	1.00E-03	25	2	1.7E-07
Po-M-2-94	6.00E-04	25	2.48	6.5E-08
Po-M-2-94	1.00E-03	7.5	2.5	8.6E-09
Po-M-2-94	1.00E-03	35	2.5	7.9E-08
Po-M-2-94	1.00E-03	25	2.51	4.6E-08
Po-M-2-94	2.00E-04	25	2.51	2.7E-08
Po-M-2-94	2.00E-04	25	2.74	3.1E-08
Po-M-3-94	2.00E-04	25	1.98	3.2E-08
Po-M-3-94	1.00E-02	25	2.05	1.1E-07
Po-M-3-94	1.00E-03	7.5	2.43	5.1E-08
Po-M-3-94	6.00E-04	25	2.49	4.6E-08
Po-M-3-94	1.00E-03	35	2.5	1.2E-07
Po-M-3-94	1.00E-03	25	2.53	8.5E-08
Po-M-3-94	2.00E-04	25	2.53	3.2E-08
Po-M-3-94	2.00E-04	25	2.8	3.0E-08
Po-M-4-94	2.00E-04	25	2.02	2.5E-08
Po-M-4-94	1.00E-03	25	2.05	3.9E-08
Po-M-4-94	1.00E-03	35	2.45	9.4E-08
Po-M-4-94	6.00E-04	25	2.5	5.6E-08
Po-M-4-94	2.00E-04	25	2.5	1.7E-08
Po-M-4-94	1.00E-03	25	2.53	6.7E-08
Po-M-4-94	1.00E-03	15	2.54	2.6E-08

Table C-1b: Complete listing of rates of pyrrhotite oxidation by ferric iron.

Po Sample	Fe^{+3}_{int} [M]	Temperature °C	pH	Oxidation Rate (moles-$Fe^{+3}\times m^{-2}\times s^{-1}$)
Po-M-4-94	2.00E-04	25	2.75	1.8E-08
Po-C-5-94	1.00E-02	25	1.99	4.2E-08
Po-C-5-94	1.00E-03	25	2.02	2.2E-08
Po-C-5-94	2.00E-04	25	2.03	1.5E-08
Po-C-5-94	6.00E-04	25	2.51	5.4E-08
Po-C-5-94	1.00E-03	25	2.53	2.5E-08
Po-C-5-94	1.00E-03	7.5	2.54	4.7E-09
Po-C-5-94	2.00E-04	25	2.55	1.4E-08
Po-C-5-94	1.00E-03	35	2.55	3.0E-08
Po-C-5-94	2.00E-04	25	2.75	2.0E-08
Po-C-6-94	2.00E-04	25	2.8	5.2E-08
Po-C-6-94	2.00E-04	25	2.54	4.0E-08
Po-C-6-94	1.00E-03	25	2.48	6.8E-08
Po-M-7-94	2.00E-04	25	2.8	4.1E-08
Po-M-7-94	2.00E-04	25	2.55	3.4E-08
Po-M-7-94	1.00E-03	25	2.51	4.0E-08
Po-M-8-93	2.00E-04	25	2.75	1.4E-08
Po-M-8-93	2.00E-04	25	2.54	1.3E-08
Po-M-8-93	1.00E-03	25	2.49	2.3E-08
Po-M-9-91	2.00E-04	25	2.75	2.8E-08
Po-M-9-91	2.00E-04	25	2.5	2.8E-08
Po-M-9-91	1.00E-03	25	2.45	4.2E-08
Po-M-15-93	2.00E-04	25	2.63	2.8E-08
Po-M-15-93	1.00E-03	25	2.48	7.1E-08
Po-M-15-93	1.00E-02	25	2.02	1.1E-07
Po-M-17-93	2.00E-04	25	2.77	5.5E-08
Po-M-17-93	2.00E-04	25	2.53	3.8E-08
Po-M-17-93	1.00E-03	25	2.49	1.1E-07
Po-M-19-94	2.00E-04	25	2.75	6.3E-08
Po-M-19-94	2.00E-04	25	2.51	5.3E-08
Po-M-19-94	1.00E-03	25	2.51	1.9E-07

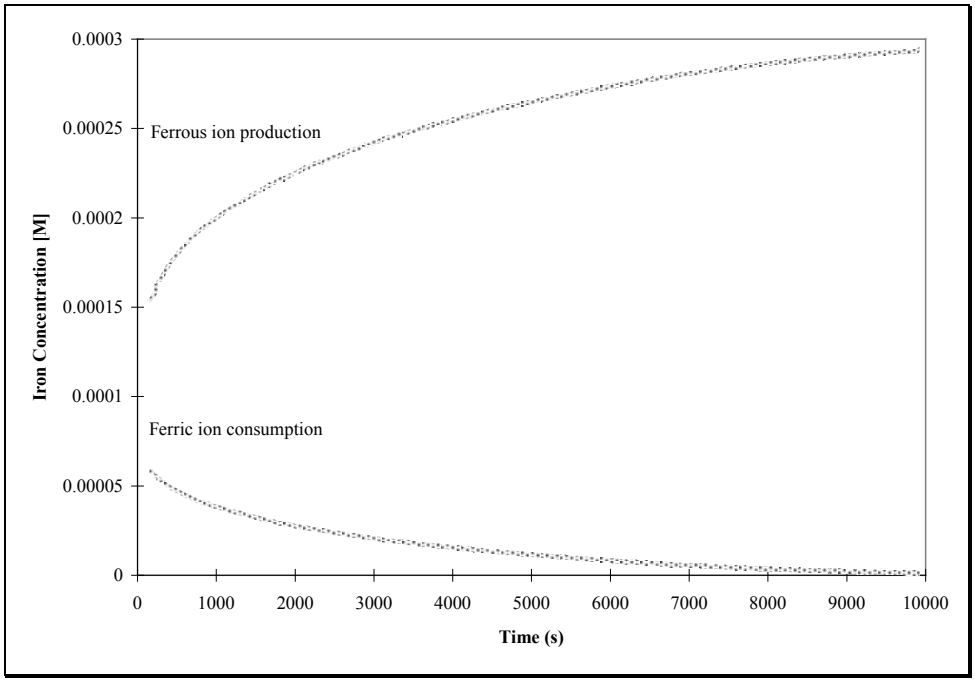

Figure C-1: Ferric iron oxidation of Po-M-1-93 at pH=2, 25°C, $Fe^{+3}_{int}=2\times10^{-4}$ [M], Experiment Sept 4D.

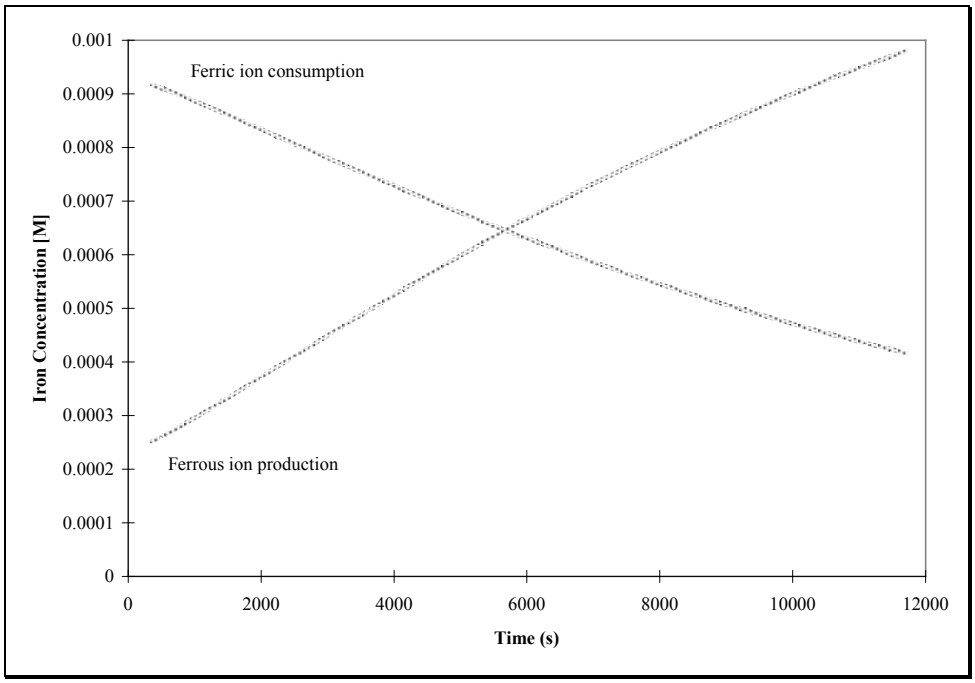

Figure C-2: Ferric iron oxidation of Po-M-1-93 at pH=2, 25°C, $Fe^{+3}_{int}=1\times10^{-3}$ [M], Experiment Aug 18B.

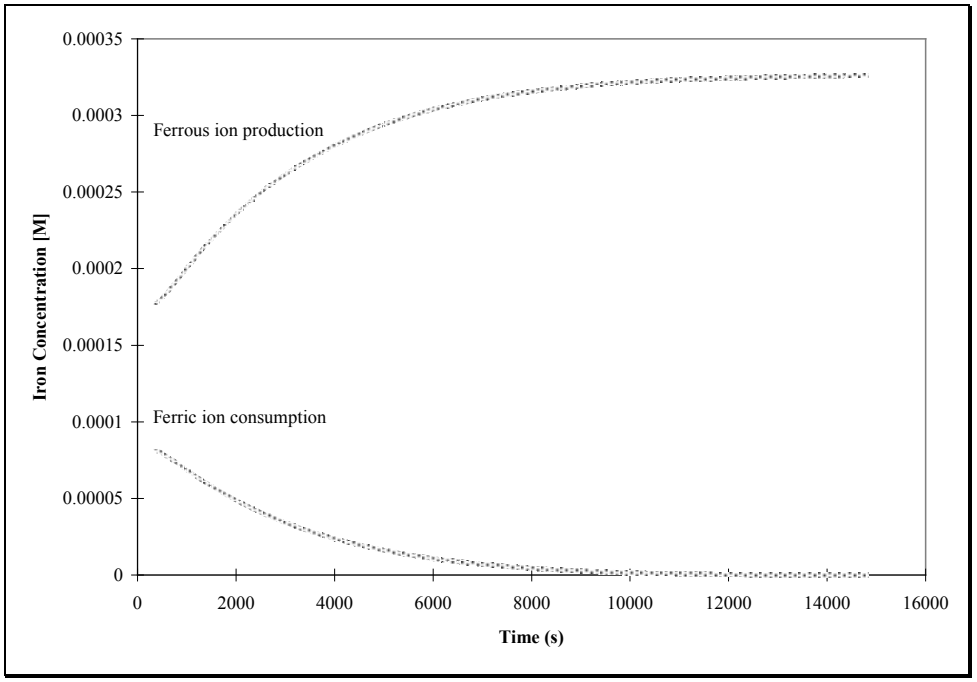

Figure C-3: Ferric iron oxidation of Po-M-1-93 at pH=2.5, 25°C, $Fe^{+3}_{int}=2\times10^{-4}$ [M], Experiment Aug 23B.

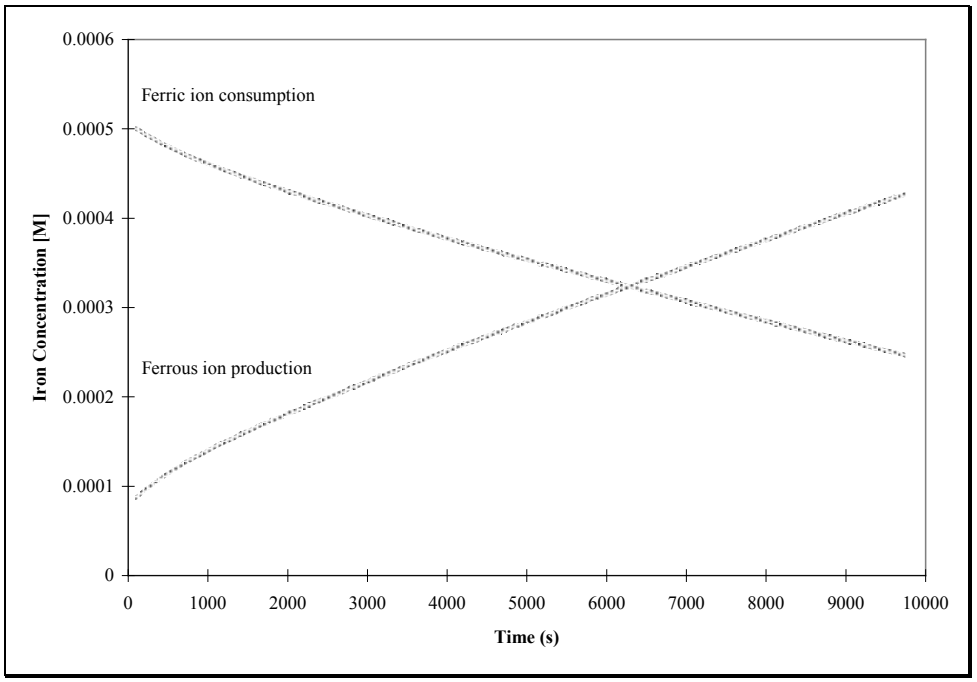

Figure C-4: Ferric iron oxidation of Po-M-1-93 at pH=2.43, 25°C, $Fe^{+3}_{int}=6\times10^{-4}$ [M], Experiment Sept 4C.

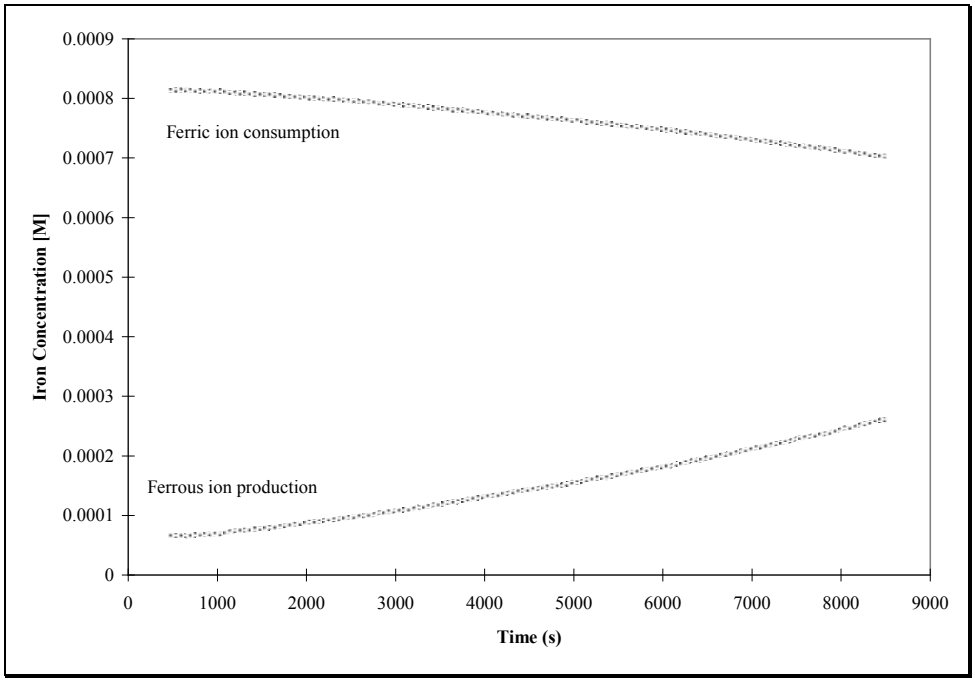

Figure C-5: Ferric iron oxidation of Po-M-1-93 at pH=2.46, 7.5°C, $Fe^{+3}_{int}=1\times10^{-3}$ [M], Experiment Sept 4B.

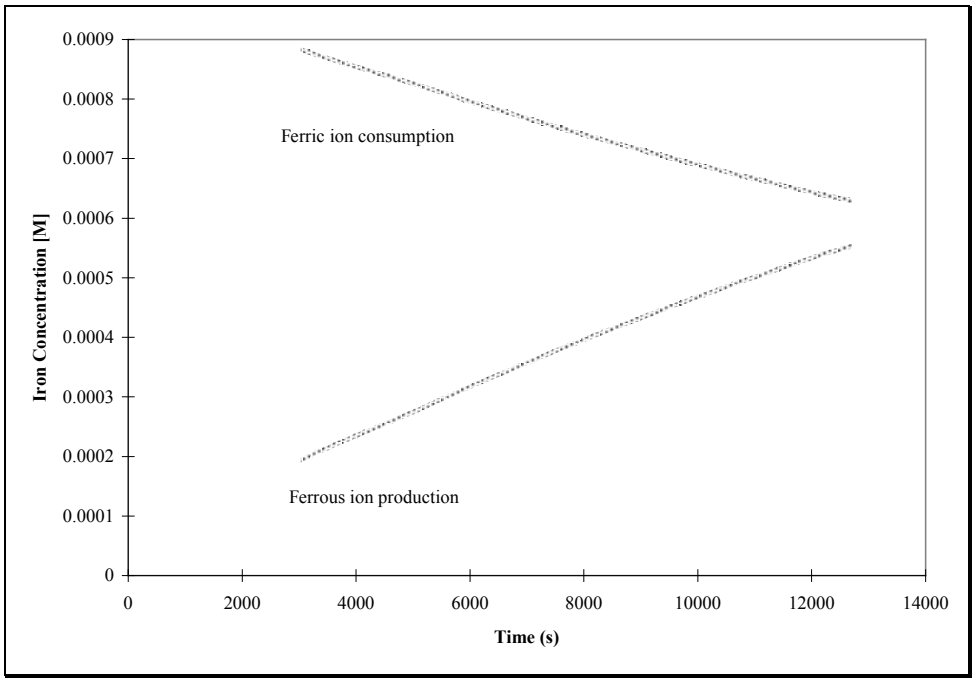

Figure C-6: Ferric iron oxidation of Po-M-1-93 at pH=2.5, 25°C, $Fe^{+3}_{int}=1\times10^{-3}$ [M], Experiment Aug 22.

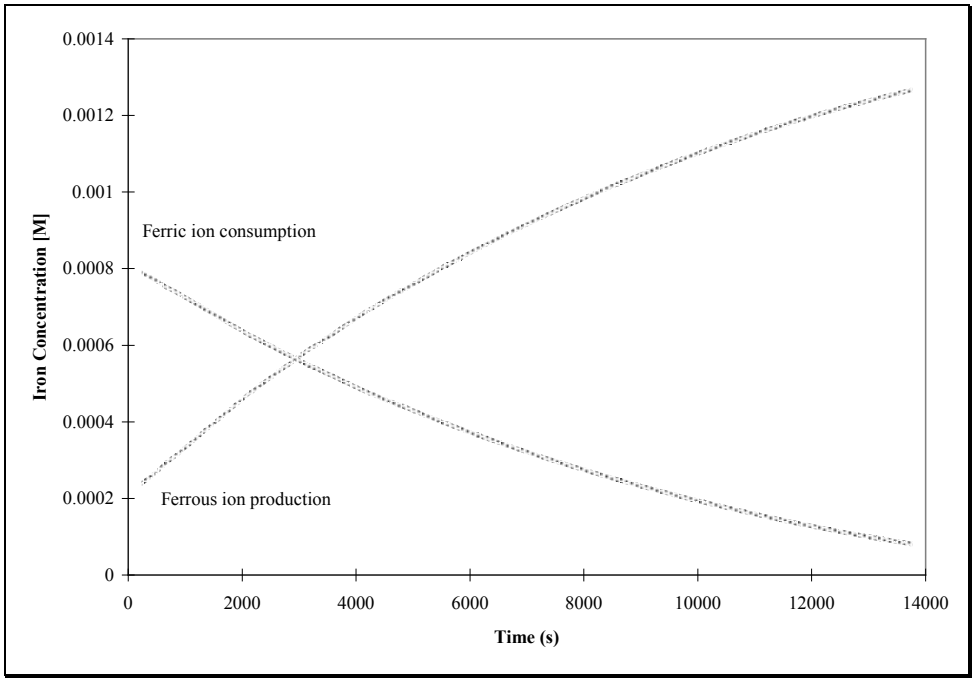

Figure C-7: Ferric iron oxidation of Po-M-1-93 at pH=2.4, 35°C, $Fe^{+3}_{int}=1\times10^{-3}$ [M], Experiment Aug23.

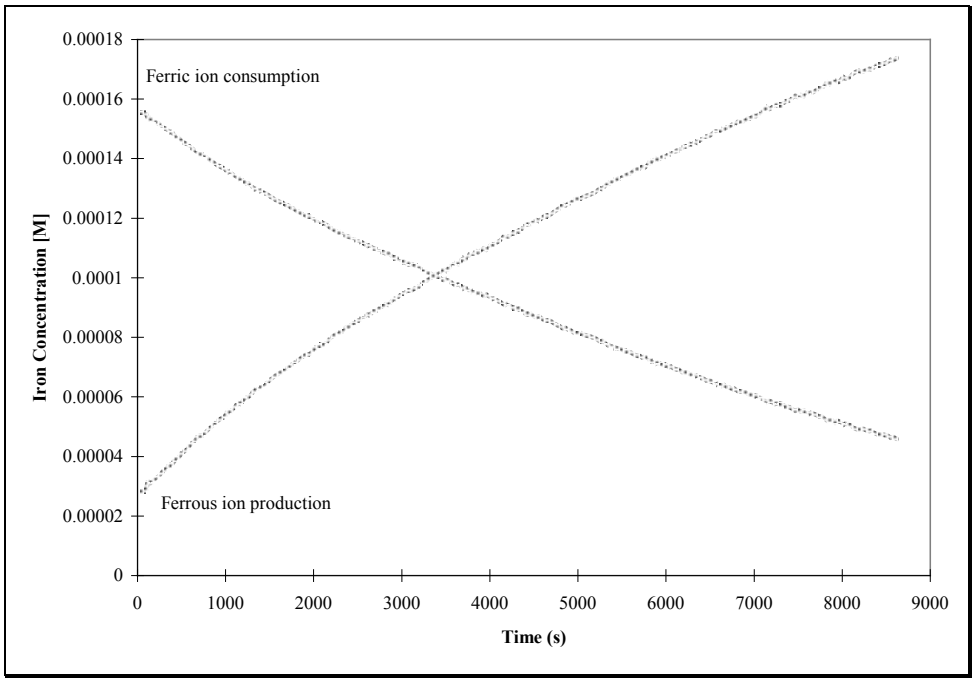

Figure C-8: Ferric iron oxidation of Po-M-1-93 at pH=2.73, 25°C, $Fe^{+3}_{int}=2\times10^{-4}$ [M], Experiment Sept 4.

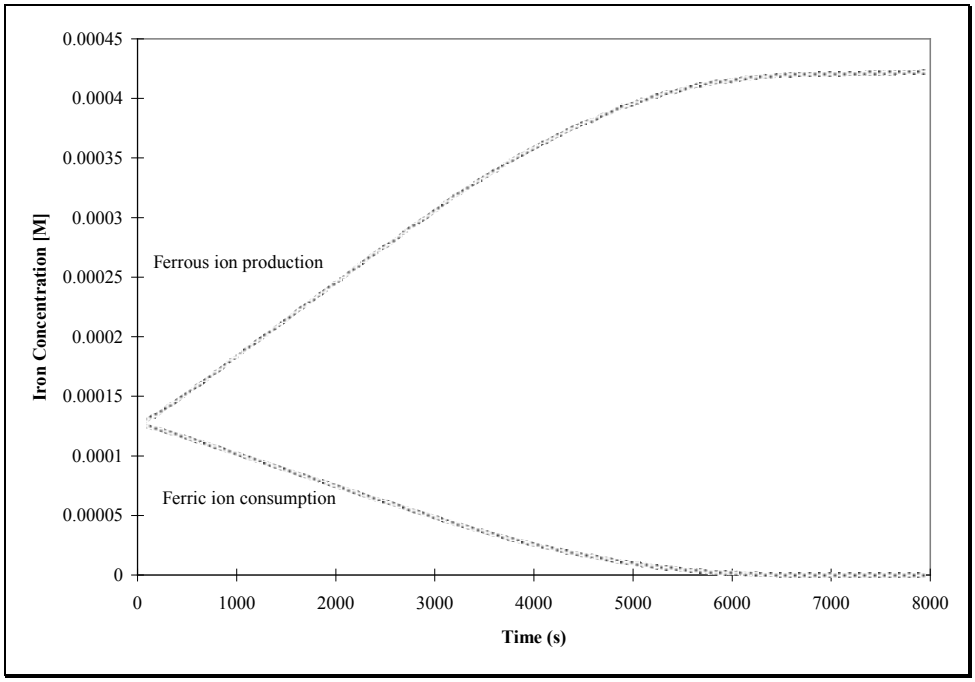

Figure C-9: Ferric iron oxidation of Po-M-2-94 at pH=1.95, 25°C, $Fe^{+3}_{int}=2\times10^{-4}$ [M], Experiment Sept 5D.

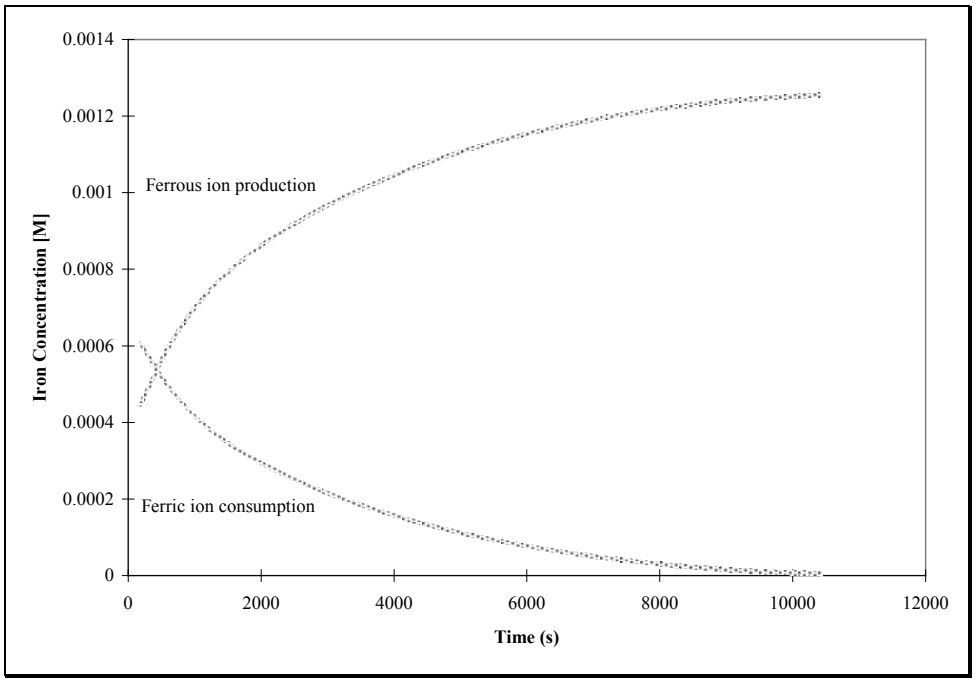

Figure C-10: Ferric iron oxidation of Po-M-2-94 at pH=2.0, 25°C, $Fe^{+3}_{int}=1\times10^{-3}$ [M], Experiment Aug 14.

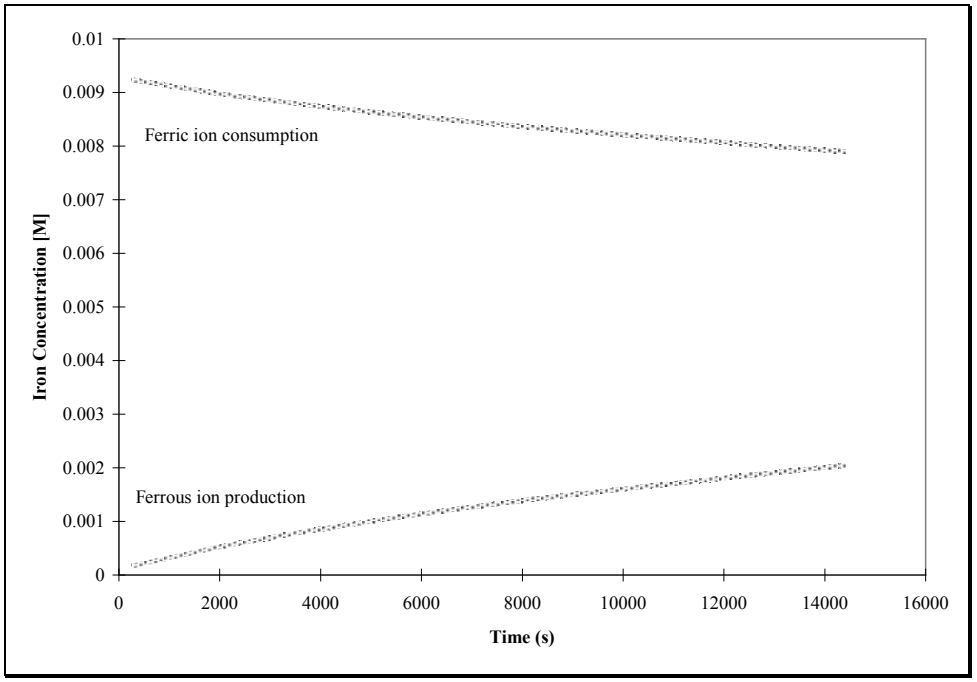

Figure C-11: Ferric iron oxidation of Po-M-2-94 at pH=2.0, 25°C, $Fe^{+3}_{int}=1\times10^{-2}$ [M], Experiment Aug 11.

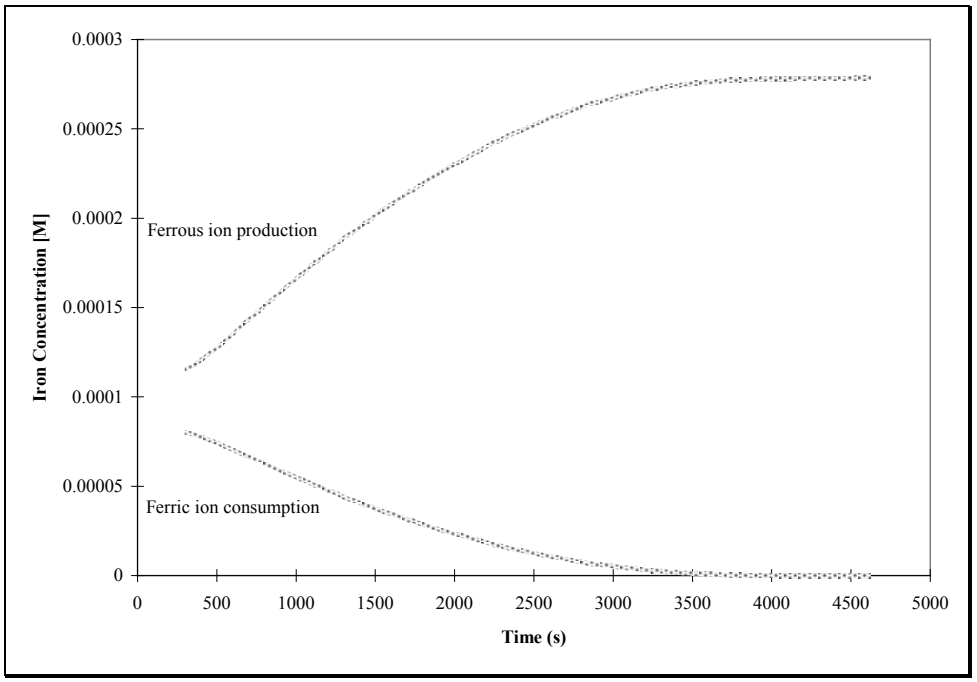

Figure C-12: Ferric iron oxidation of Po-M-2-94 at pH=2.51, 25°C, $Fe^{+3}_{int}=2\times10^{-4}$ [M], Experiment Sept 5B.

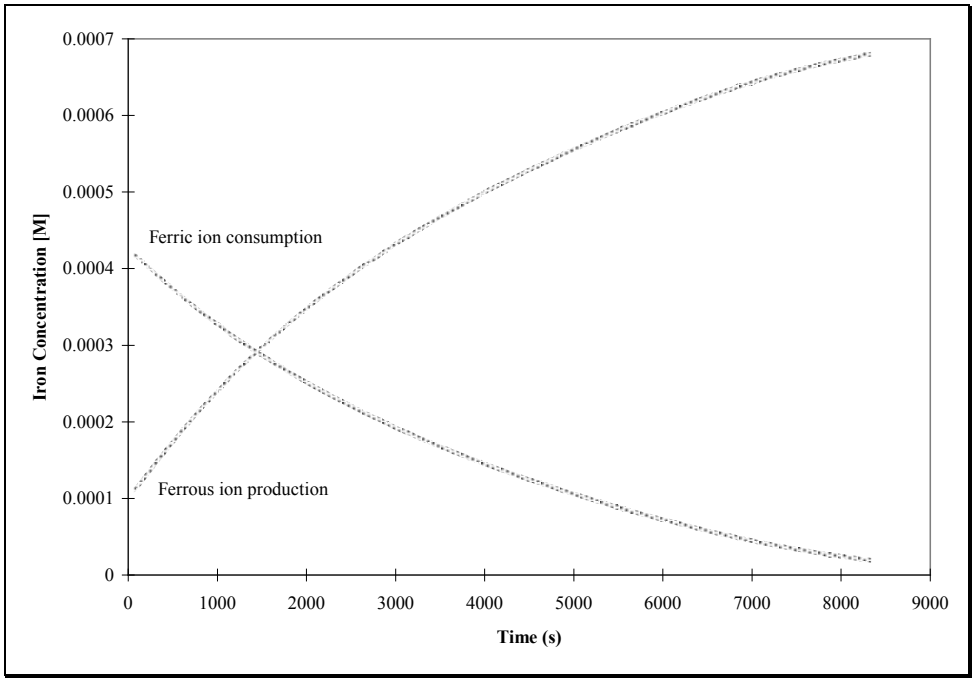

Figure C-13: Ferric iron oxidation of Po-M-2-94 at pH=2.48, 25°C, $Fe^{+3}_{int}=6´10^{-4}$ [M], Experiment Sept 5C.

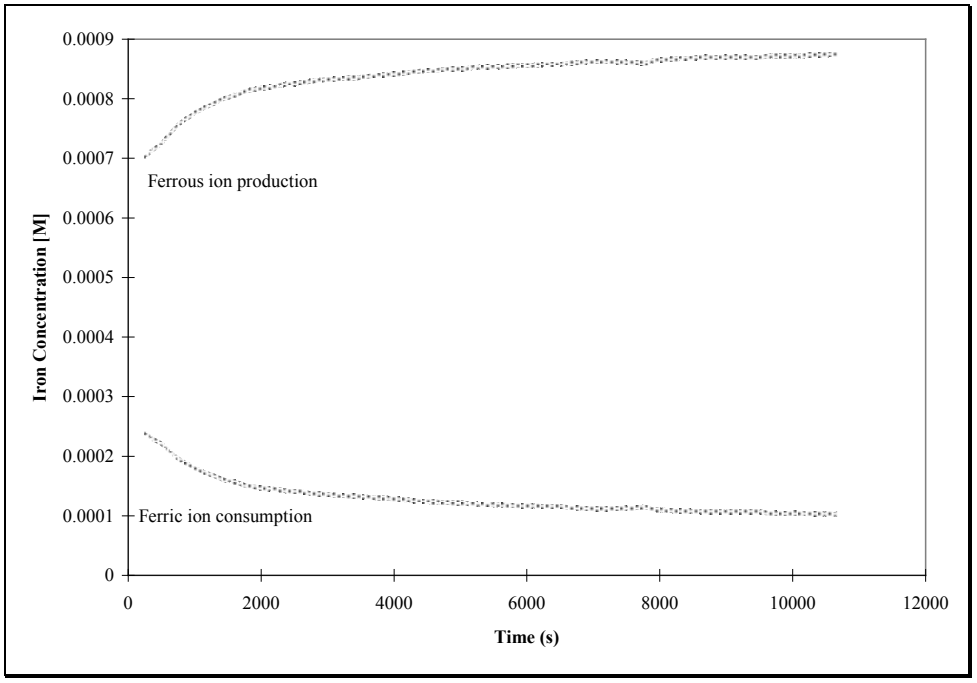

Figure C-14: Ferric iron oxidation of Po-M-2-94 at pH=2.50, 7.5°C, $Fe^{+3}_{int}=1´10^{-3}$ [M], Experiment Sept 2B.

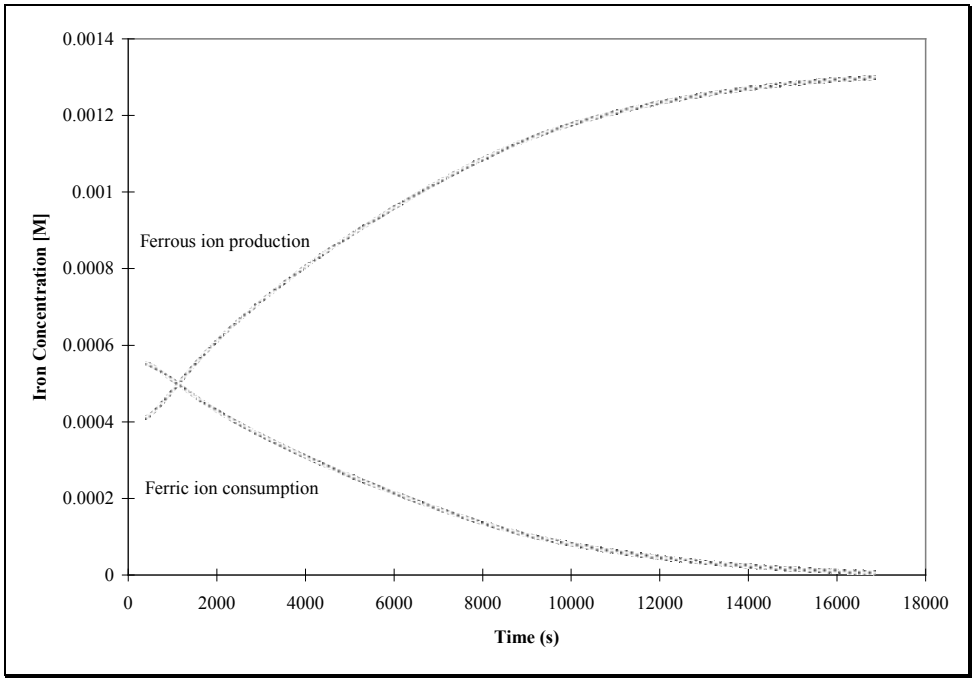

Figure C-15: Ferric iron oxidation of Po-M-2-94 at pH=2.51, 25°C, $Fe^{+3}_{int}=1\times10^{-3}$ [M], Experiment Sept 2.

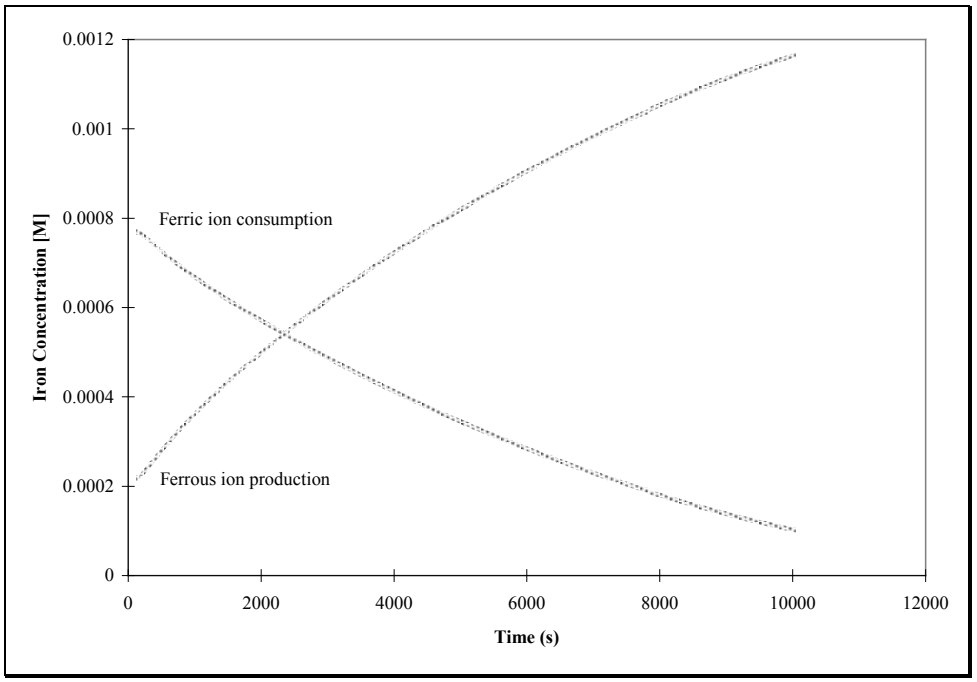

Figure C-16: Ferric iron oxidation of Po-M-2-94 at pH=2.50, 35°C, $Fe^{+3}_{int}=1\times10^{-3}$ [M], Experiment Sept 2C.

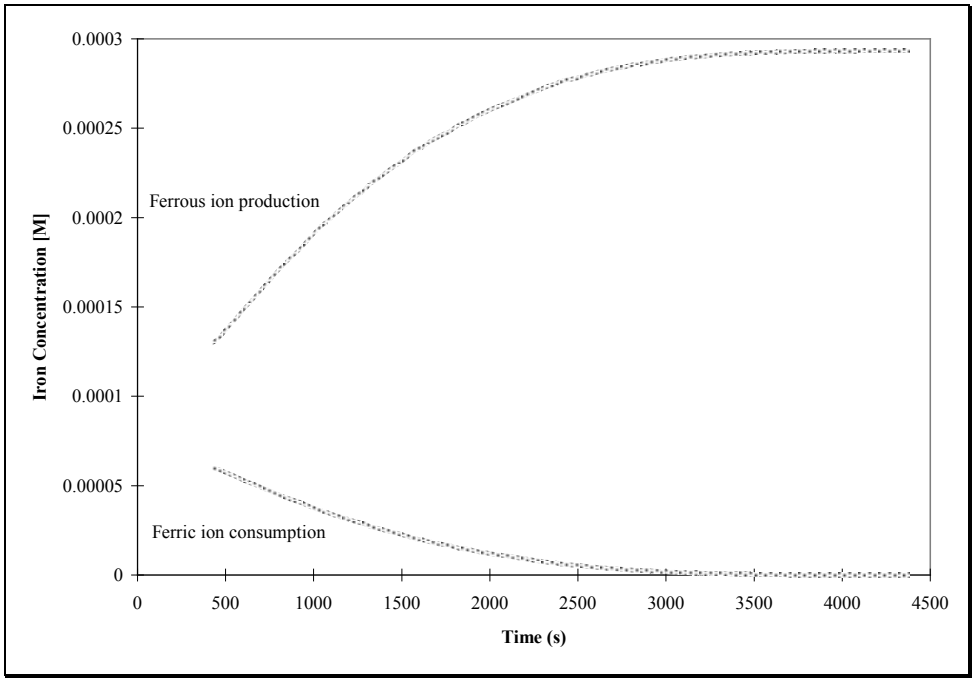

Figure C-17: Ferric iron oxidation of Po-M-2-94 at pH=2.74, 25°C, $Fe^{+3}_{int}=2\times10^{-4}$ [M], Experiment Sept 5.

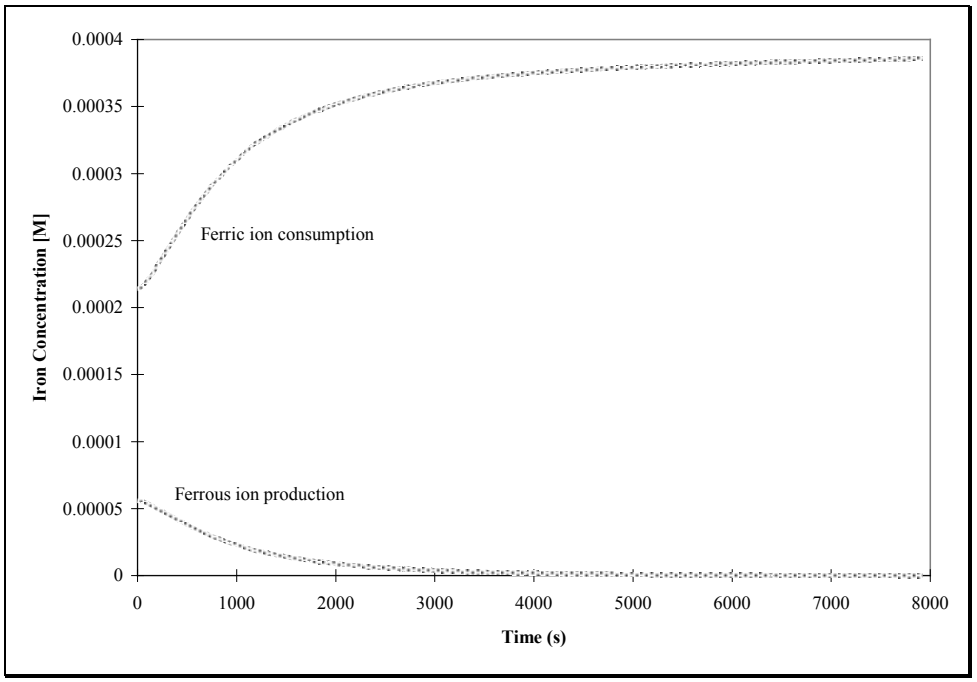

Figure C-18: Ferric iron oxidation of Po-M-3-94 at pH=1.98.0, 25°C, $Fe^{+3}_{int}=2\times10^{-4}$ [M], Experiment Aug 28.

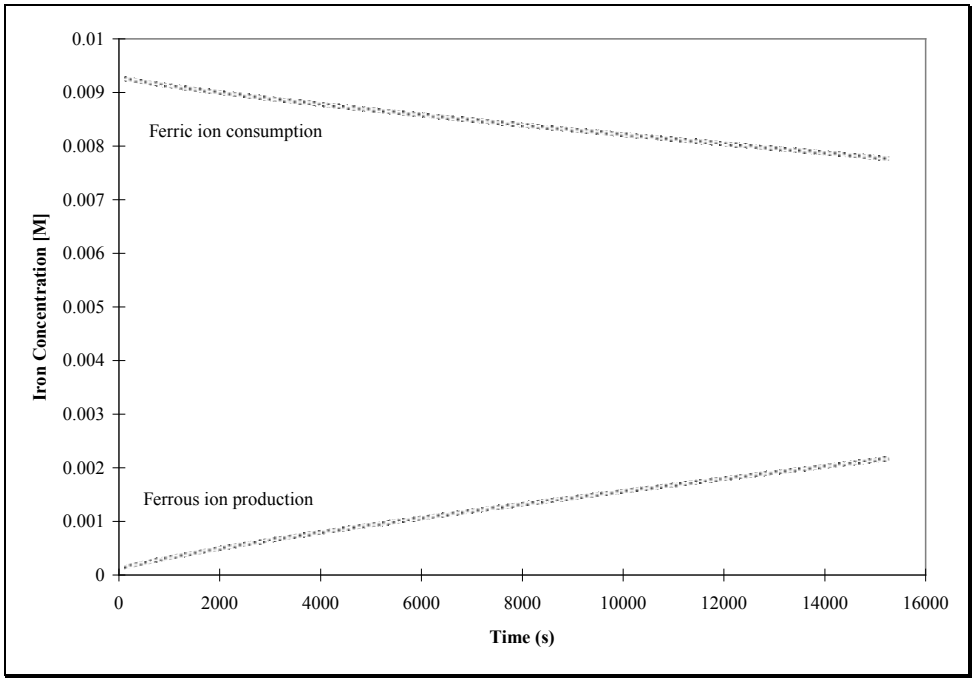

Figure C-19: Ferric iron oxidation of Po-M-3-94 at pH=2.05, 25°C, $Fe^{+3}_{int}=1\times10^{-2}$ [M], Experiment Aug 28C.

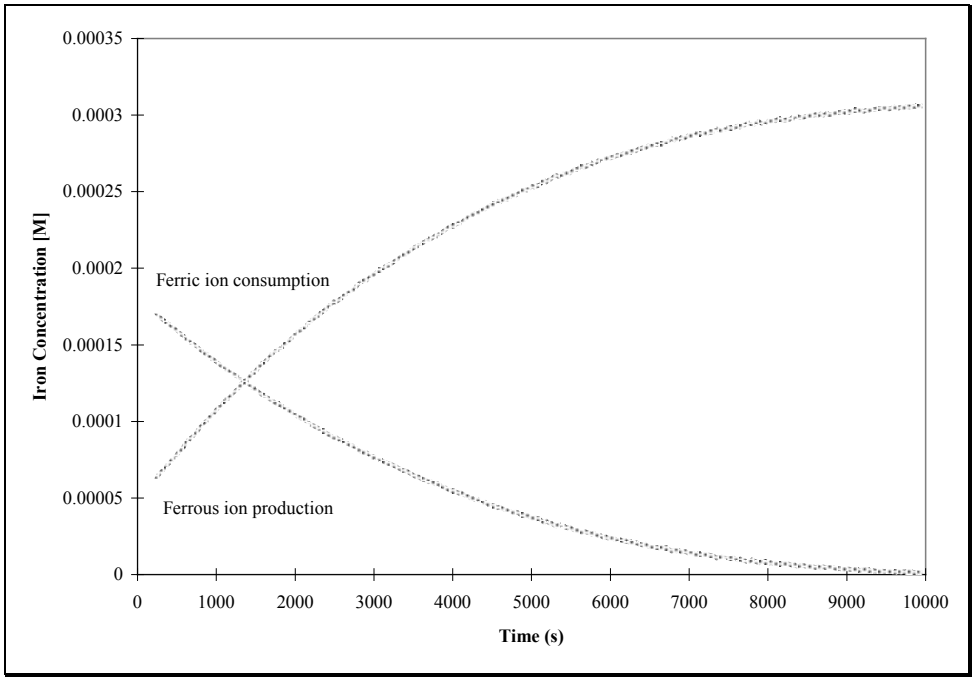

Figure C-20: Ferric iron oxidation of Po-M-3-94 at pH=2.53, 25°C, $Fe^{+3}_{int}=2\times10^{-4}$ [M], Experiment Aug 25B.

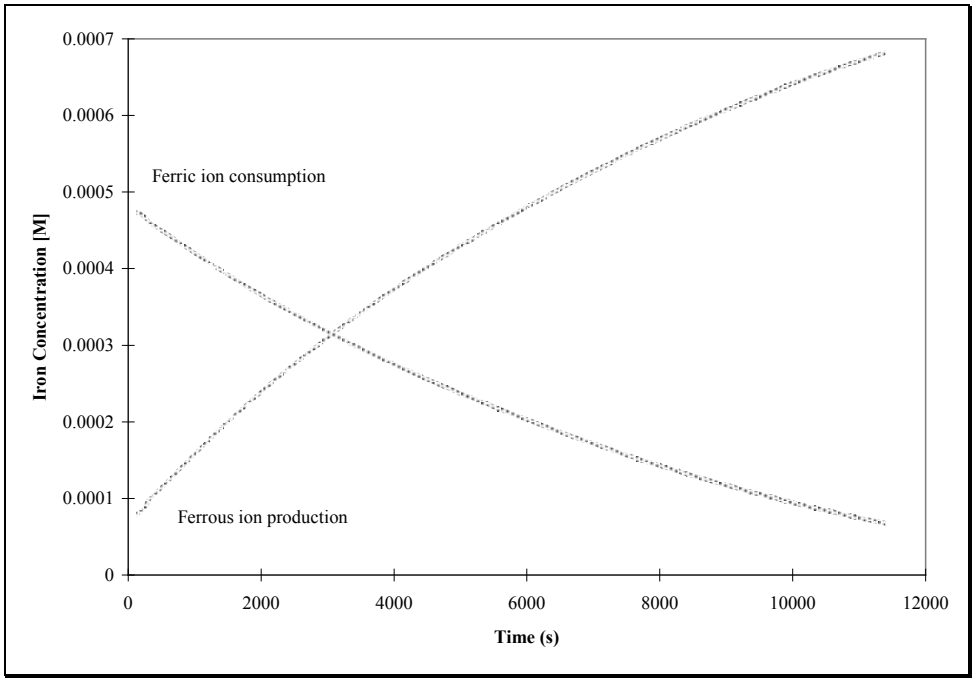

Figure C-21: Ferric iron oxidation of Po-M-3-94 at pH=2.49, 25°C, $Fe^{+3}_{int}=6\times10^{-4}$ [M], Experiment Aug 25C.

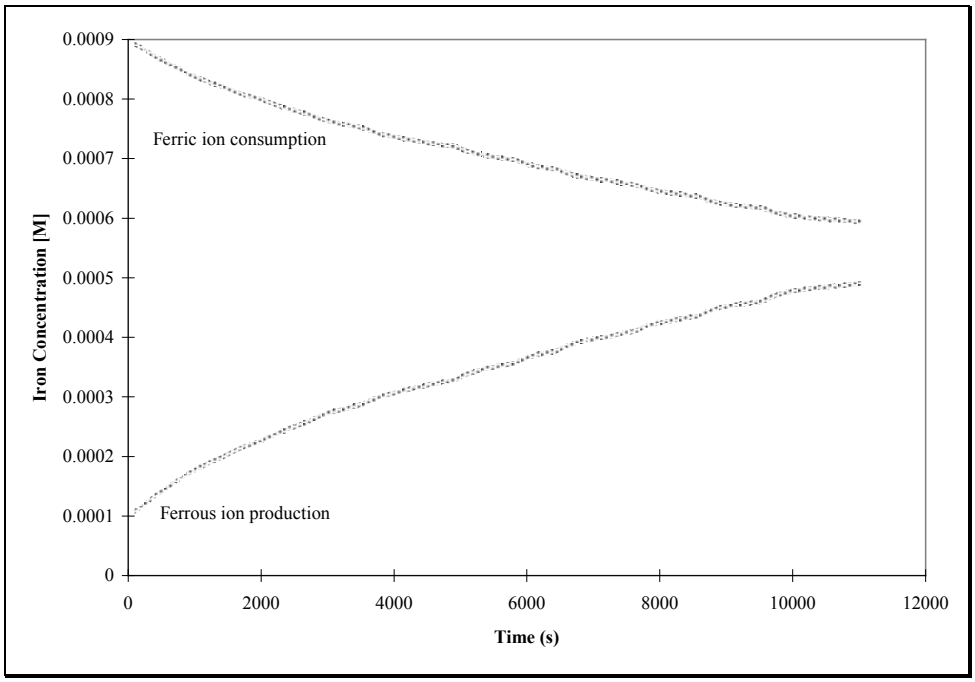

Figure C-22: Ferric iron oxidation of Po-M-3-94 at pH=2.43, 7.5°C, $Fe^{+3}_{int}=1\times10^{-3}$ [M], Experiment Aug 24.

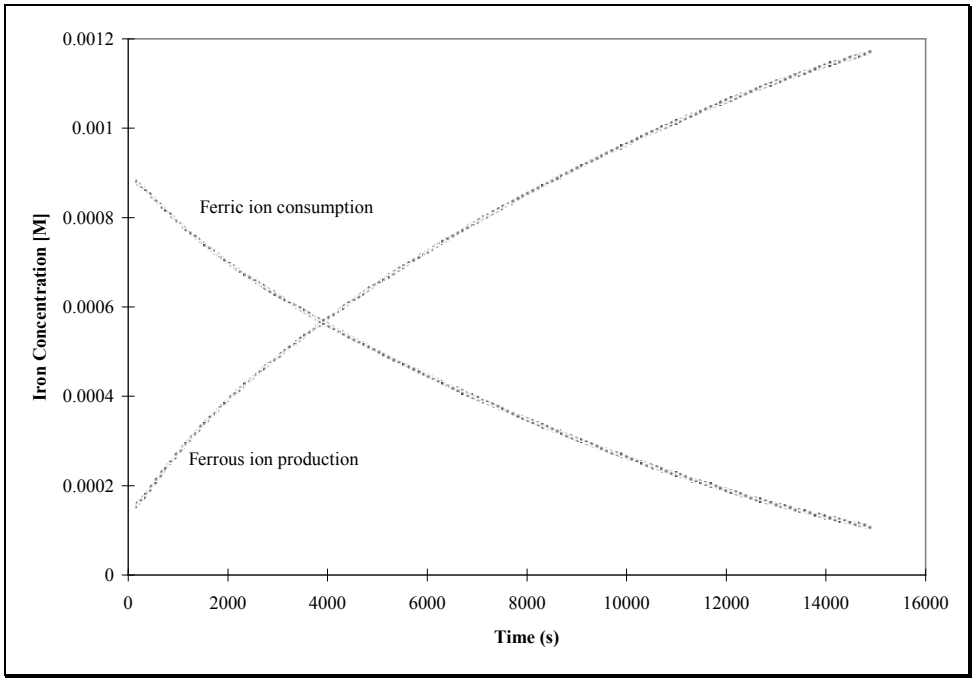

Figure C-23: Ferric iron oxidation of Po-M-3-94 at pH=2.53, 25°C, $Fe^{+3}_{int}=1\times10^{-3}$ [M], Experiment Aug 24B.

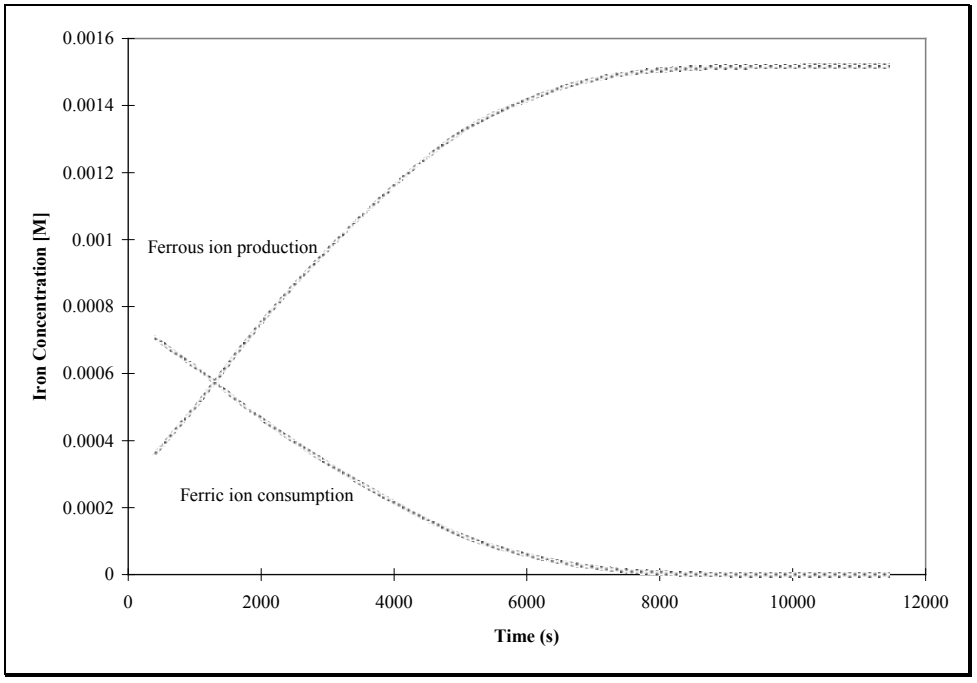

Figure C-24: Ferric iron oxidation of Po-M-3-94 at pH=2.50, 35°C, $Fe^{+3}_{int}=1\times10^{-3}$ [M], Experiment Aug 24C.

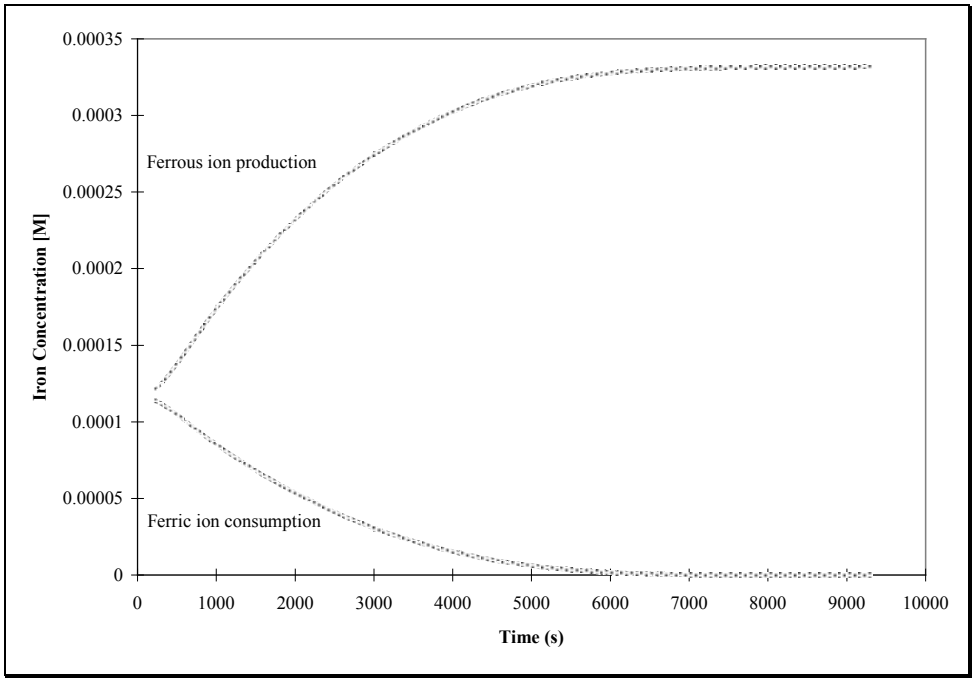

Figure C-25: Ferric iron oxidation of Po-M-3-94 at pH=2.80, 25°C, $Fe^{+3}_{int}=2\times10^{-4}$ [M], Experiment Aug 25.

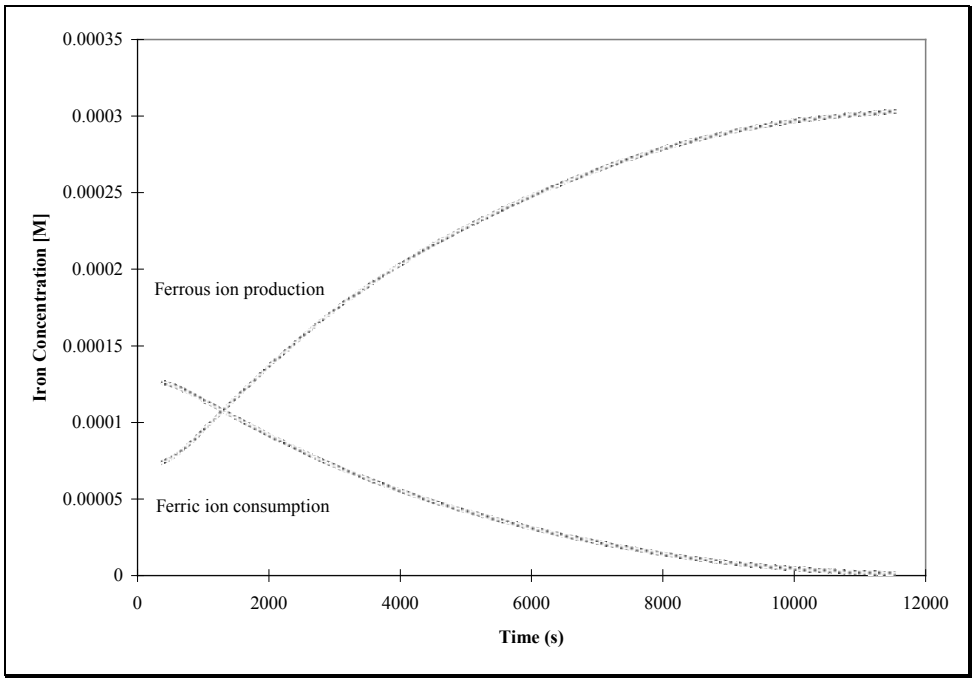

Figure C-26: Ferric iron oxidation of Po-M-4-94 at pH=2.02, 25°C, $Fe^{+3}_{int}=2\times10^{-4}$ [M], Experiment Aug 31B.

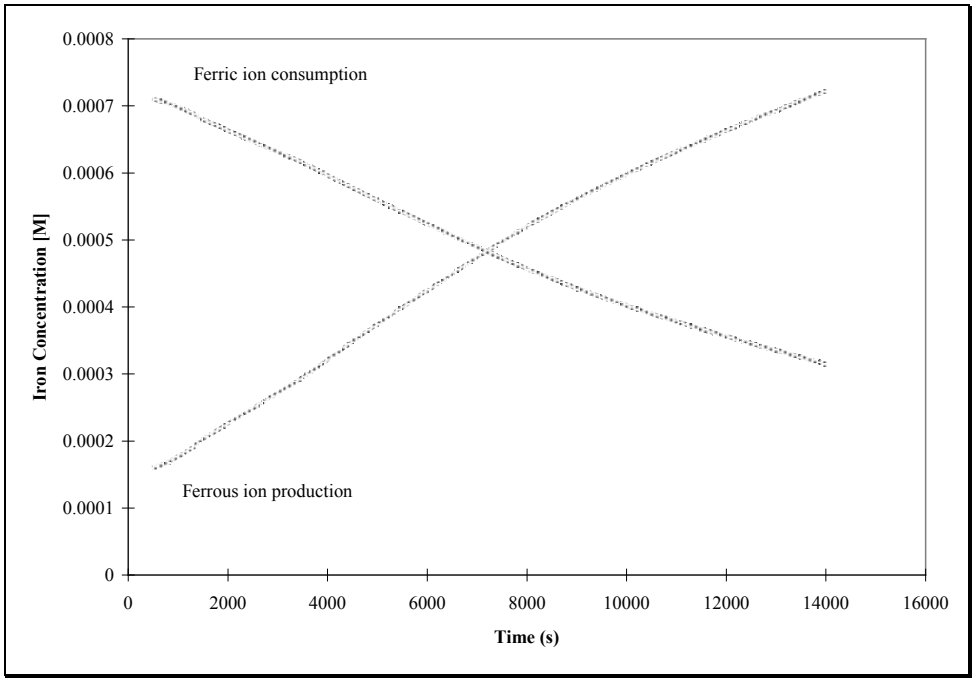

Figure C-27: Ferric iron oxidation of Po-M-4-94 at pH=2.05, 25°C, $Fe^{+3}_{int}=1\times10^{-3}$ [M], Experiment Aug 30C.

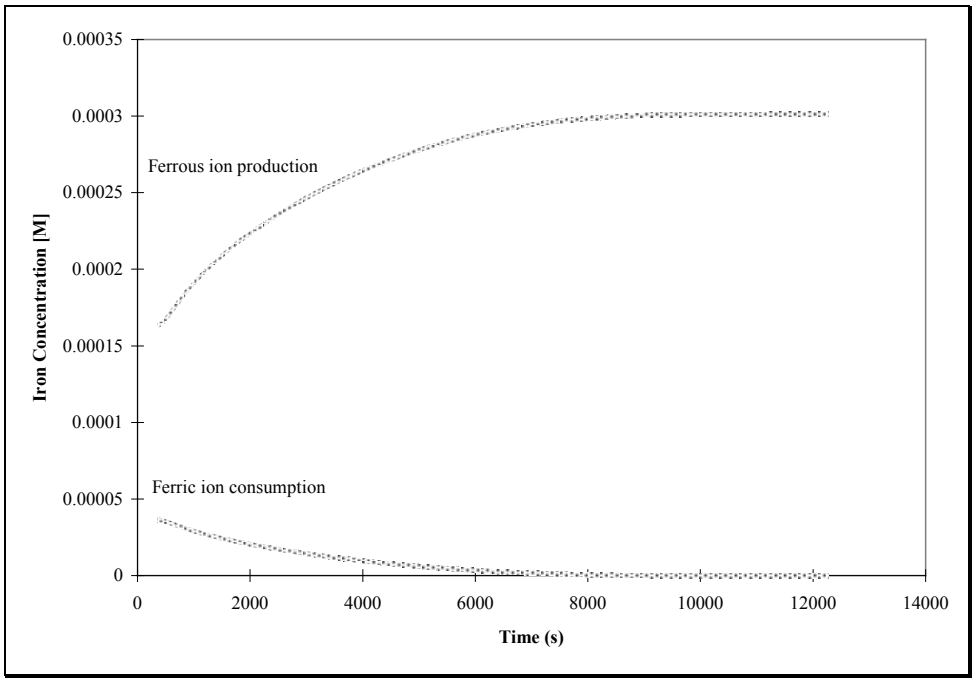

Figure C-28: Ferric iron oxidation of Po-M-4-94 at pH=2.50, 25°C, $Fe^{+3}_{int}=2\times10^{-4}$ [M], Experiment Aug 31.

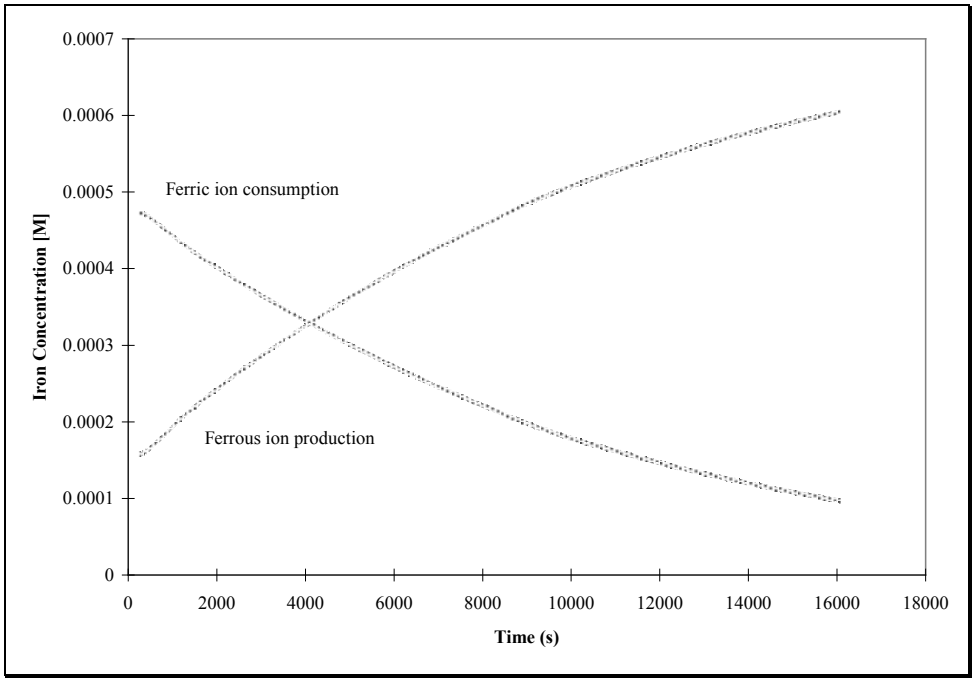

Figure C-29: Ferric iron oxidation of Po-M-4-94 at pH=2.50, 25°C, $Fe^{+3}_{int}=6\times10^{-4}$ [M], Experiment Aug 29B.

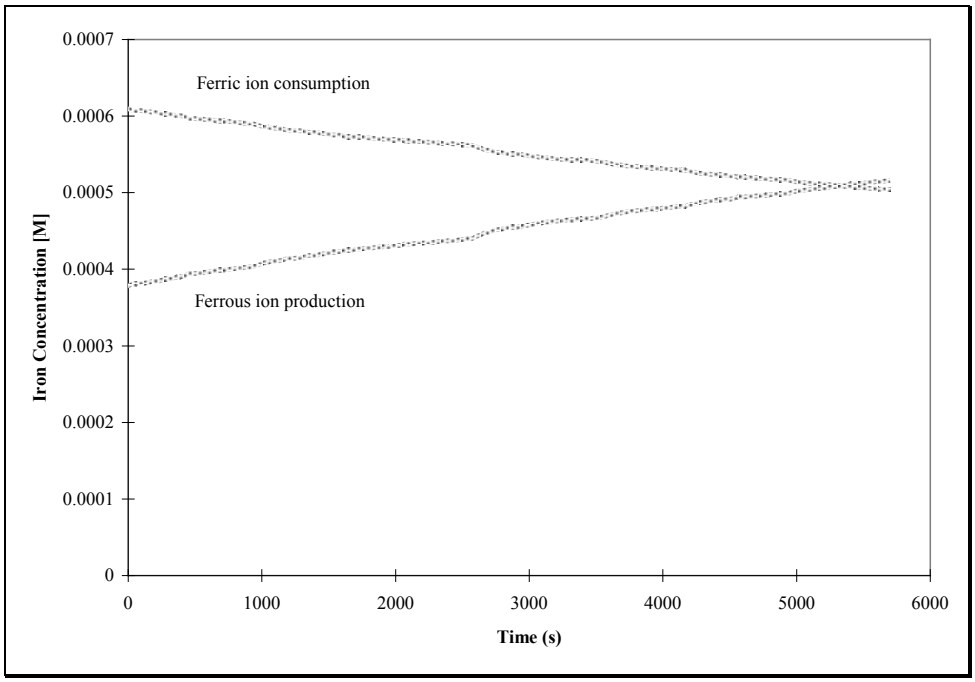

Figure C-30: Ferric iron oxidation of Po-M-4-94 at pH=2.54, 15°C, $Fe^{+3}_{int}=1\times10^{-3}$ [M], Experiment Aug 30.

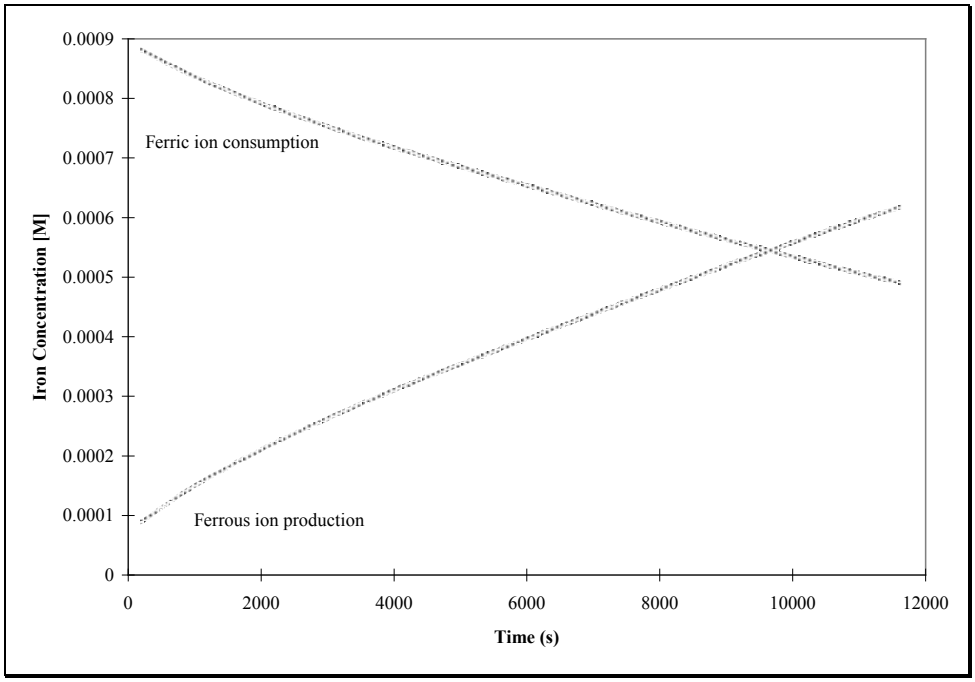

Figure C-31: Ferric iron oxidation of Po-M-4-94 at pH=2.53, 25°C, $Fe^{+3}_{int}=1\times10^{-3}$ [M], Experiment Aug 29.

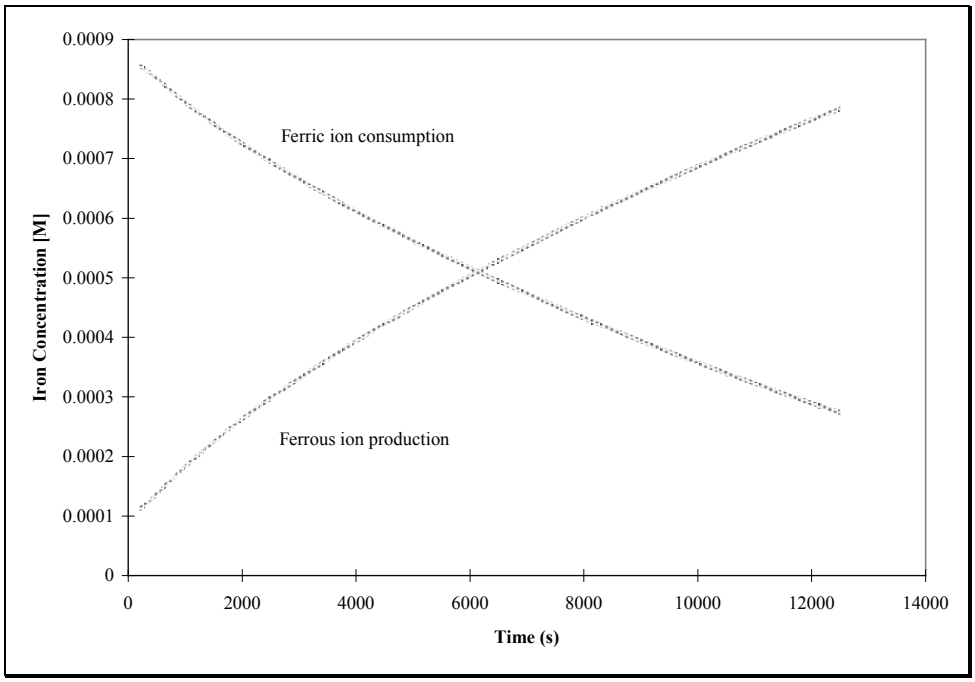

Figure C-32: Ferric iron oxidation of Po-M-4-94 at pH=2.45, 35°C, $Fe^{+3}_{int}=1\times10^{-3}$ [M], Experiment Aug 29C.

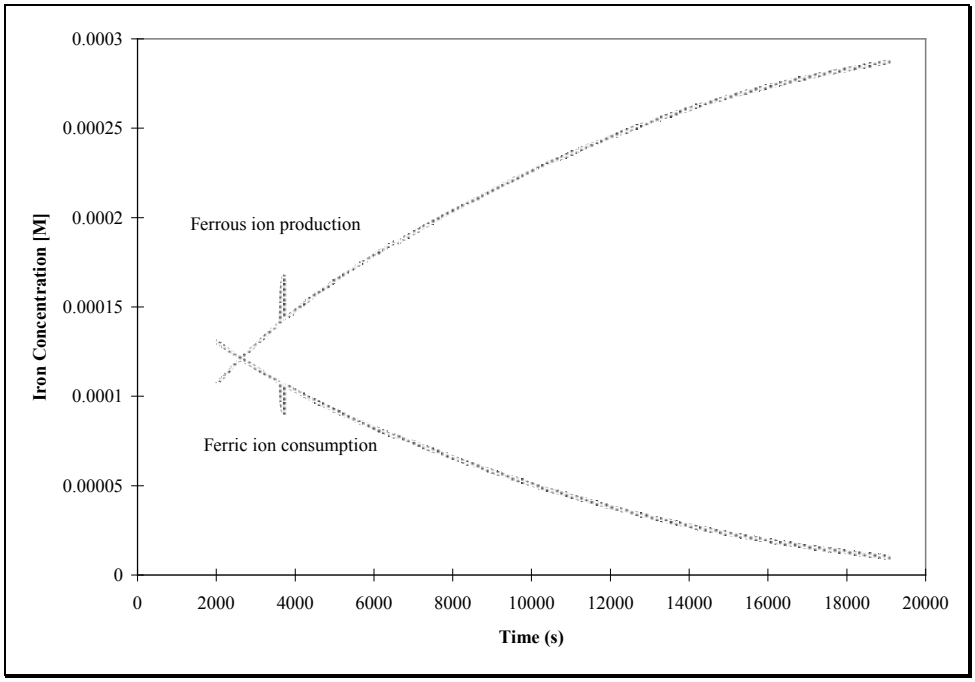

Figure C-33: Ferric iron oxidation of Po-M-4-94 at pH=2.75, 25°C, $Fe^{+3}_{int}=2\times10^{-4}$ [M], Experiment Aug 30B.

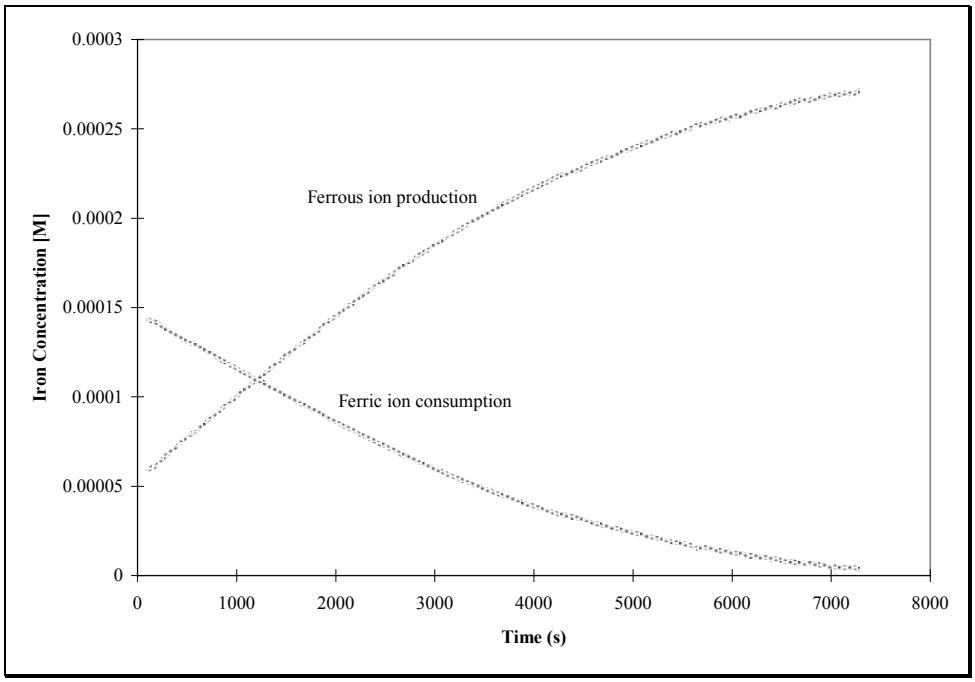

Figure C-34: Ferric iron oxidation of Po-C-5-94 at pH=2.03, 25°C, $Fe^{+3}_{int}=2\times10^{-4}$ [M], Experiment Sept 6.

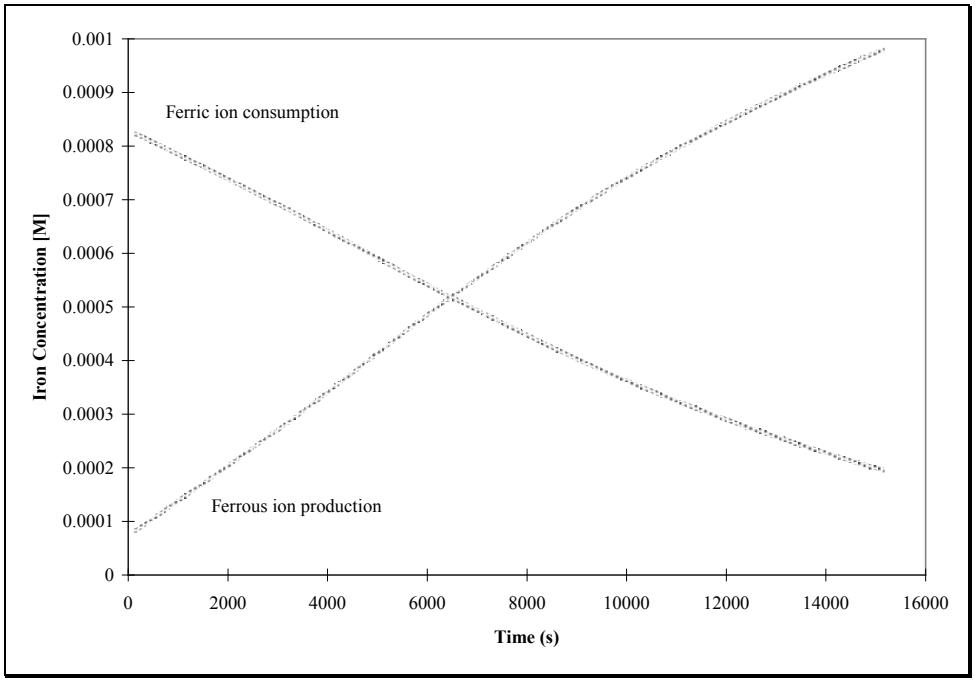

Figure C-35: Ferric iron oxidation of Po-C-5-94 at pH=2.02, 25°C, $Fe^{+3}_{int}=1\times10^{-3}$ [M], Experiment Sept 6B.

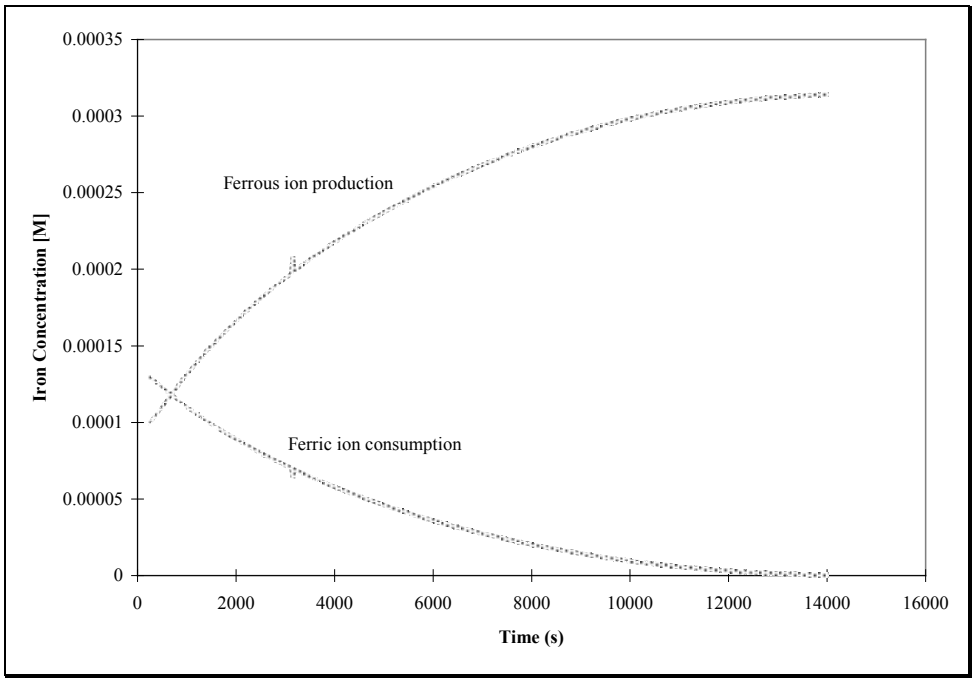

Figure C-36: Ferric iron oxidation of Po-C-5-94 at pH=2.55, 25°C, $Fe^{+3}_{int}=2\times10^{-4}$ [M], Experiment Sept 1B.

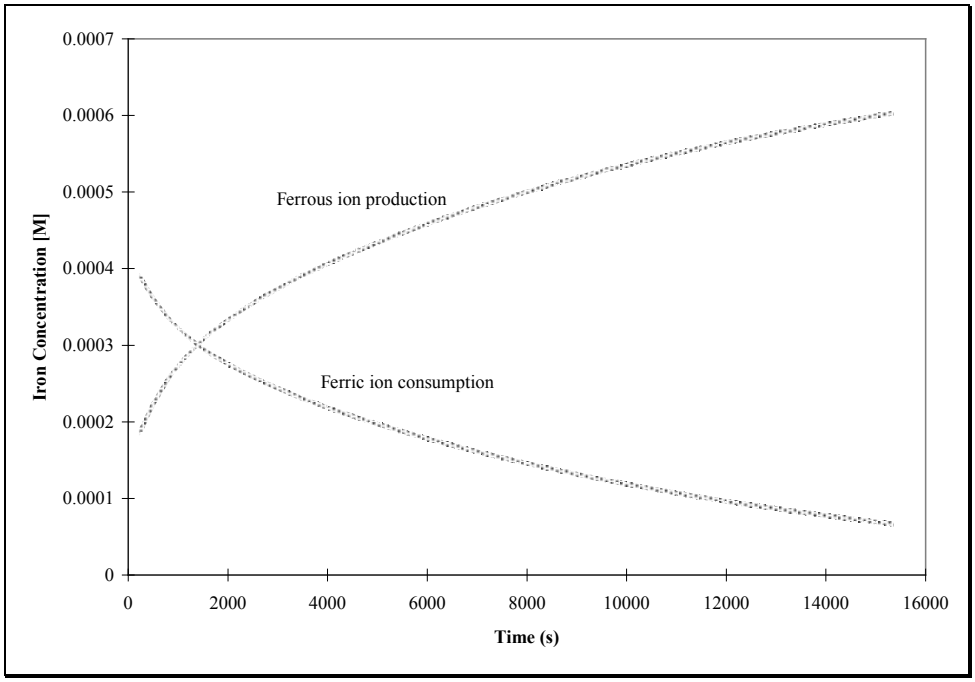

Figure C-37: Ferric iron oxidation of Po-C-5-94 at pH=2.51, 25°C, $Fe^{+3}_{int}=6\times10^{-4}$ [M], Experiment Sept 1C.

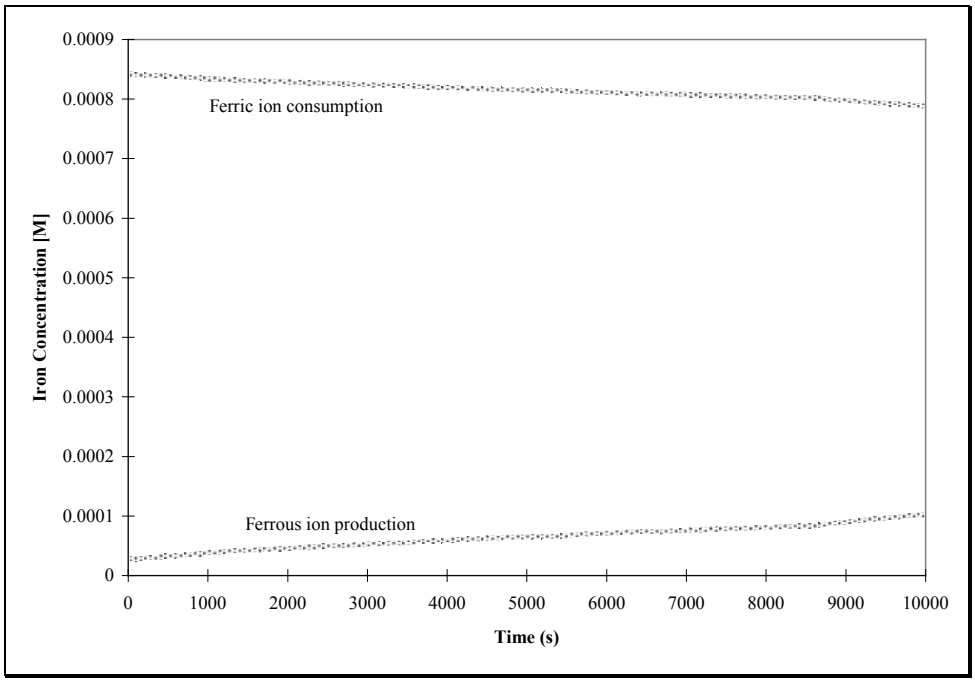

Figure C-38: Ferric iron oxidation of Po-C-5-94 at pH=2.54, 7.5°C, $Fe^{+3}_{int}=1\times10^{-3}$ [M], Experiment Sept 3B.

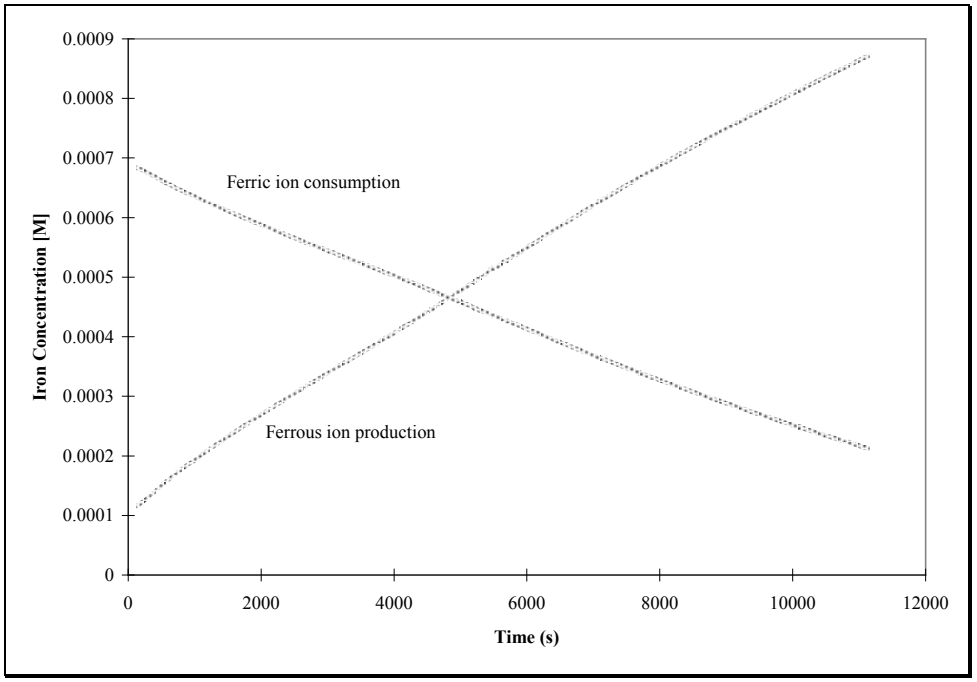

Figure C-39: Ferric iron oxidation of Po-C-5-94 at pH=2.55, 35°C, $Fe^{+3}_{int}=1\times10^{-3}$ [M], Experiment Sept 3C.

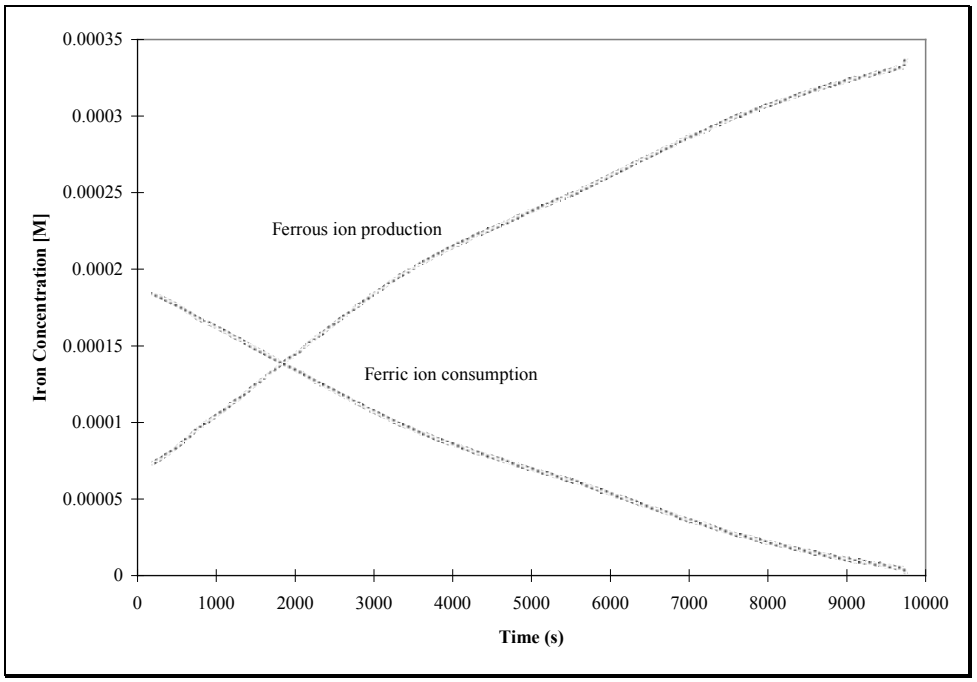

Figure C-40: Ferric iron oxidation of Po-M-6-94 at pH=2.54, 25°C, $Fe^{+3}_{int}=2\times10^{-4}$ [M], Experiment Oct 1B.

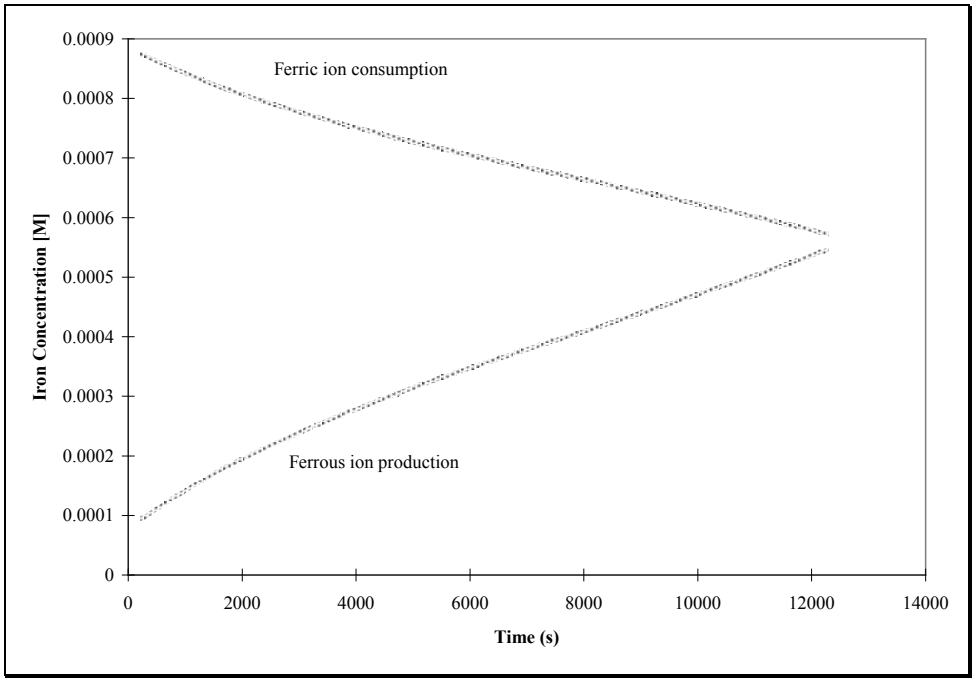

Figure C-41: Ferric iron oxidation of Po-M-6-94 at pH=2.48, 25°C, $Fe^{+3}_{int}=1\times10^{-3}$ [M], Experiment Oct 1C.

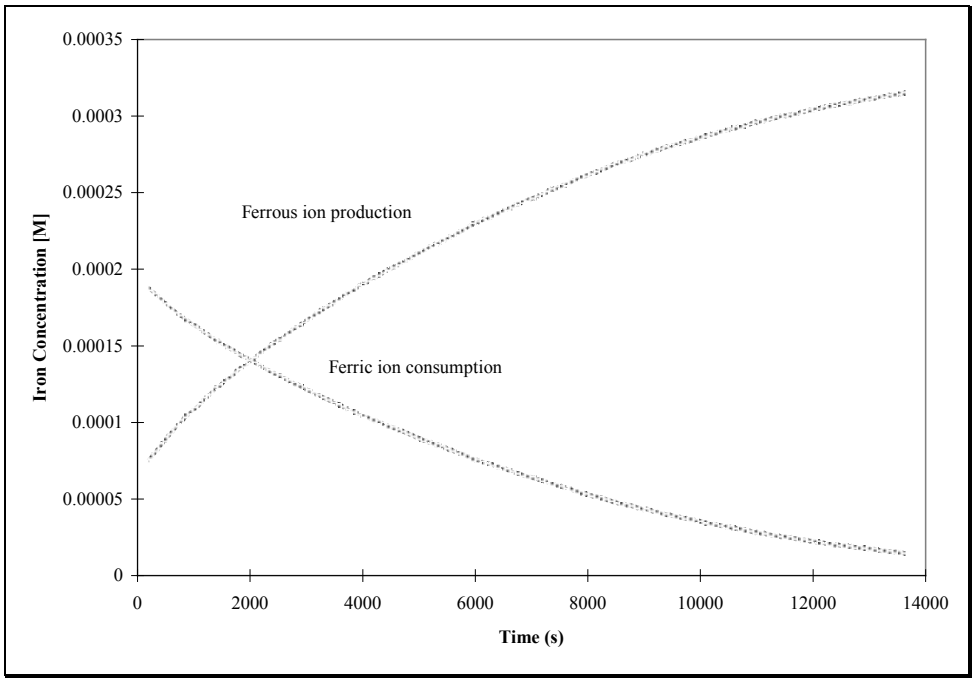

Figure C-42: Ferric iron oxidation of Po-M-6-94 at pH=2.80, 25°C, $Fe^{+3}_{int}=2\times10^{-4}$ [M], Experiment Oct 1.

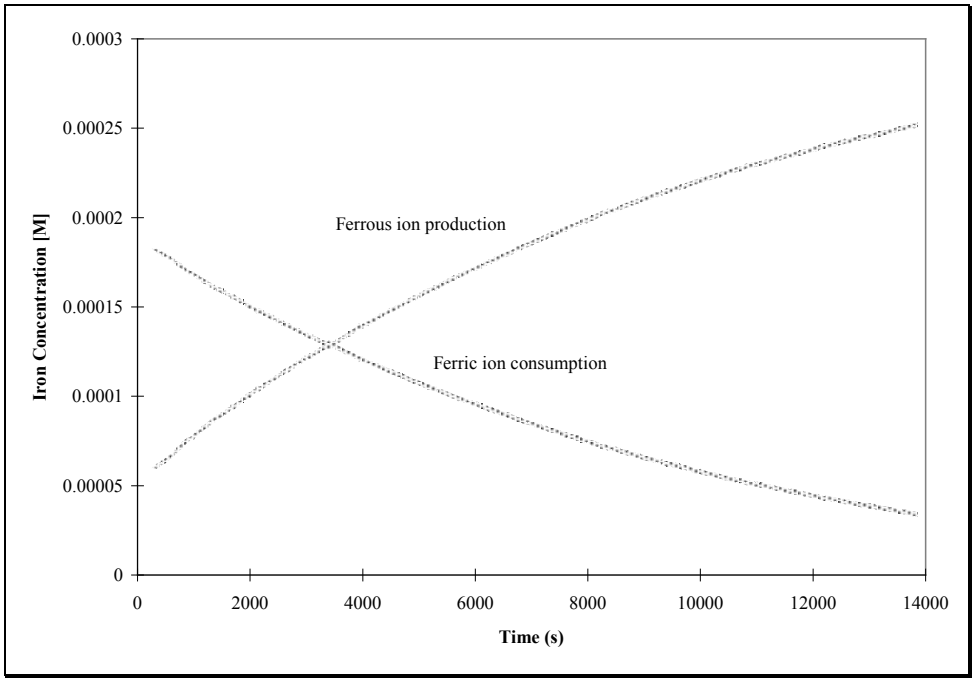

Figure C-43: Ferric iron oxidation of Po-M-7-94 at pH=2.55, 25°C, $Fe^{+3}_{int}=2\times10^{-4}$ [M], Experiment Oct 2B.

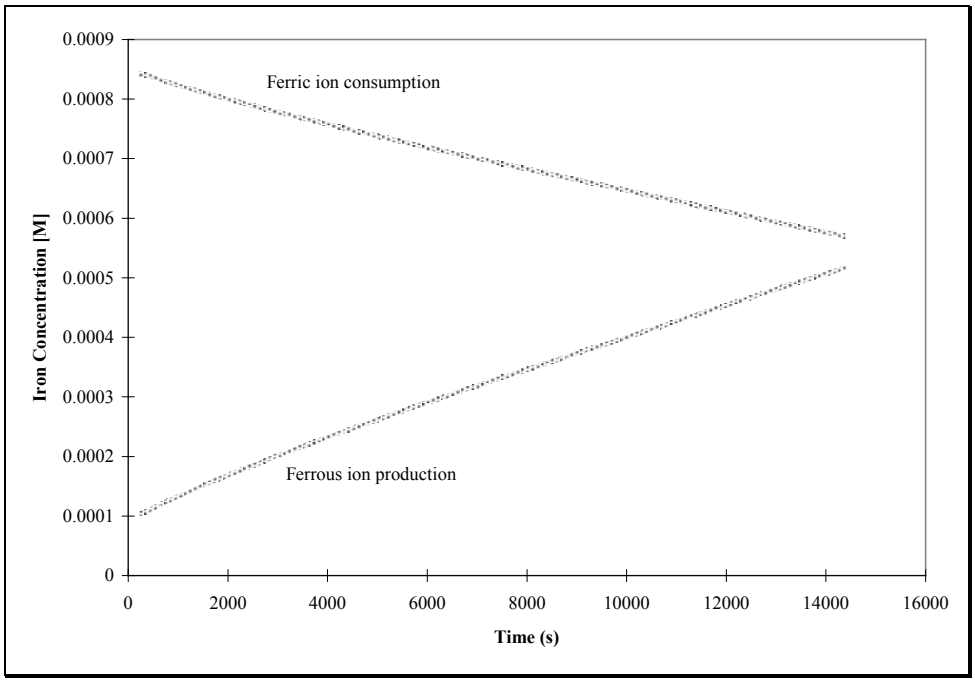

Figure C-44: Ferric iron oxidation of Po-M-7-94 at pH=2.51, 25°C, $Fe^{+3}_{int}=1\times10^{-3}$ [M], Experiment Oct 2C.

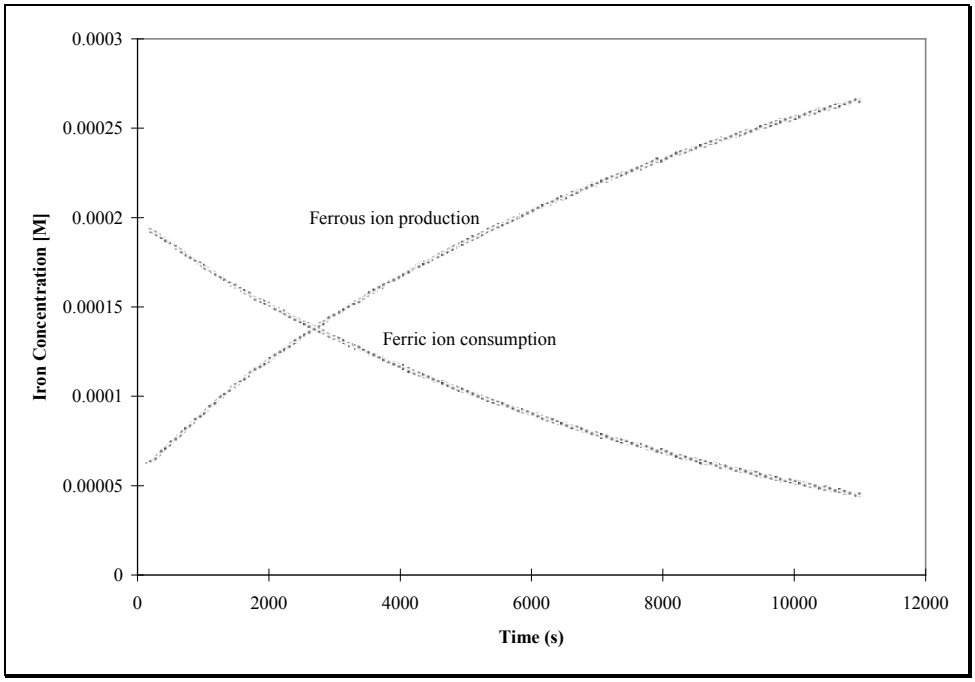

Figure C-45: Ferric iron oxidation of Po-M-7-94 at pH=2.80, 25°C, $Fe^{+3}_{int}=2\times10^{-4}$ [M], Experiment Oct 2.

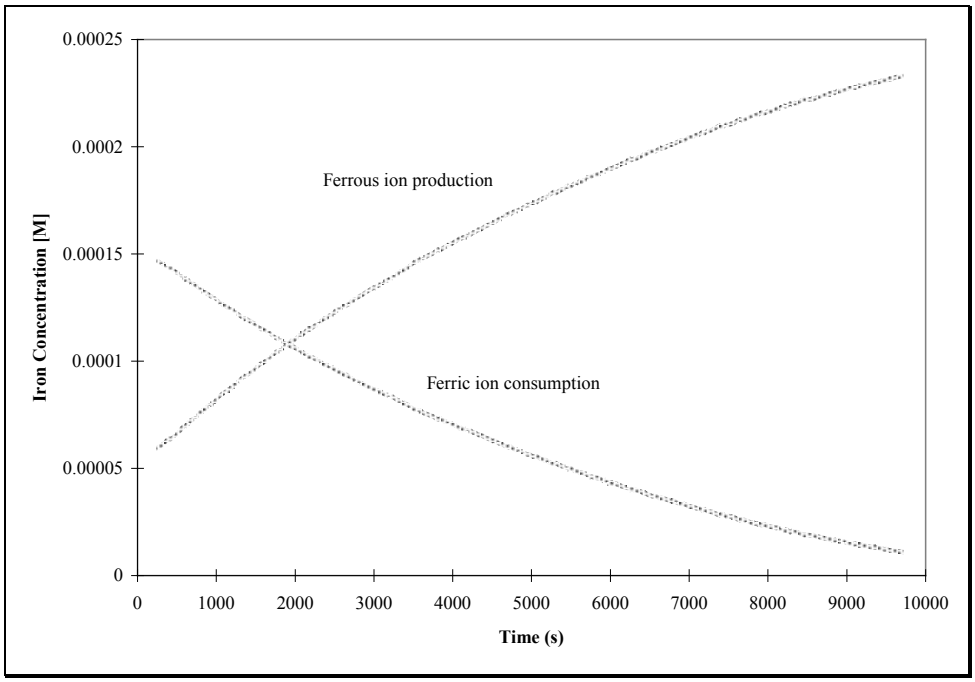

Figure C-46: Ferric iron oxidation of Po-M-8-93 at pH=2.54, 25°C, $Fe^{+3}_{int}=2\times10^{-4}$ [M], Experiment Oct 3B.

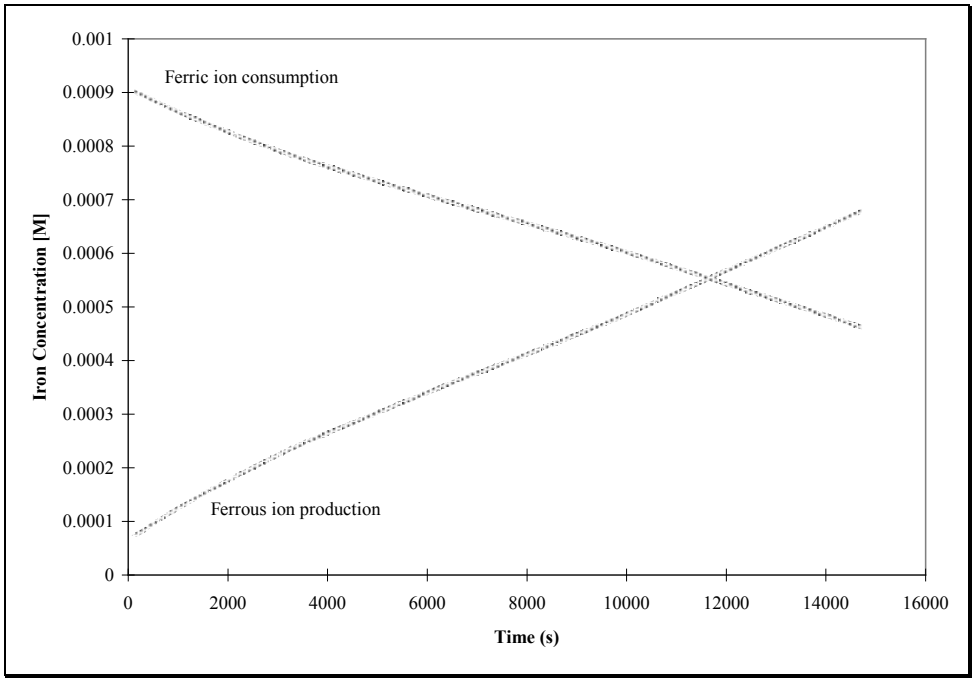

Figure C-47: Ferric iron oxidation of Po-M-8-93 at pH=2.49, 25°C, $Fe^{+3}_{int}=1\times10^{-3}$ [M], Experiment Oct 3C.

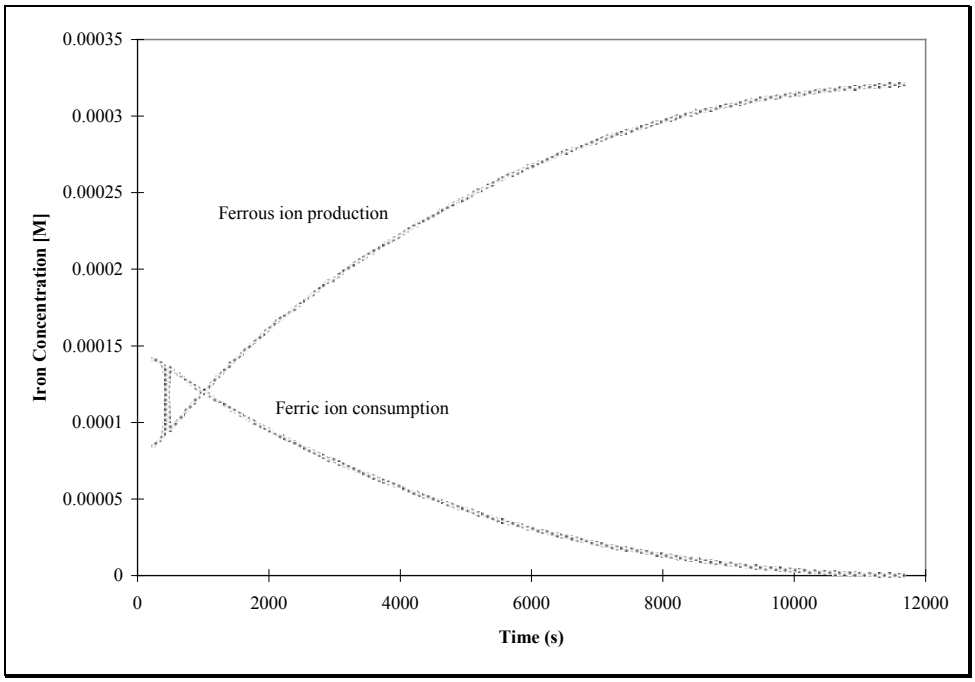

Figure C-48: Ferric iron oxidation of Po-M-8-93 at pH=2.75, 25°C, $Fe^{+3}_{int}=2\times10^{-4}$ [M], Experiment Oct 3.

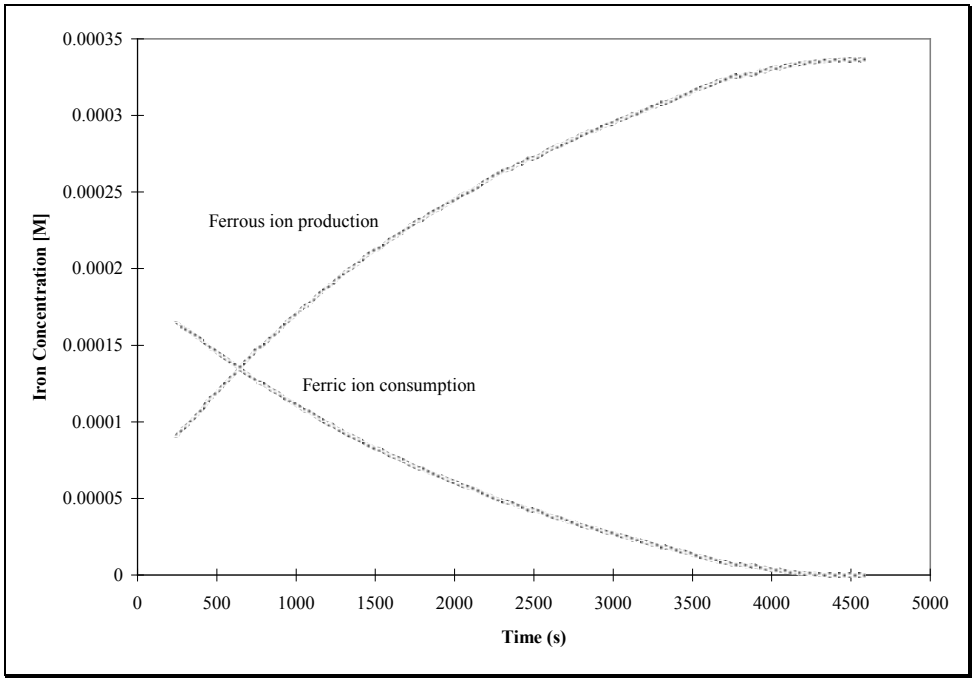

Figure C-49: Ferric iron oxidation of Po-M-9-91 at pH=2.50, 25°C, $Fe^{+3}_{int}=2\times10^{-4}$ [M], Experiment Oct 4B.

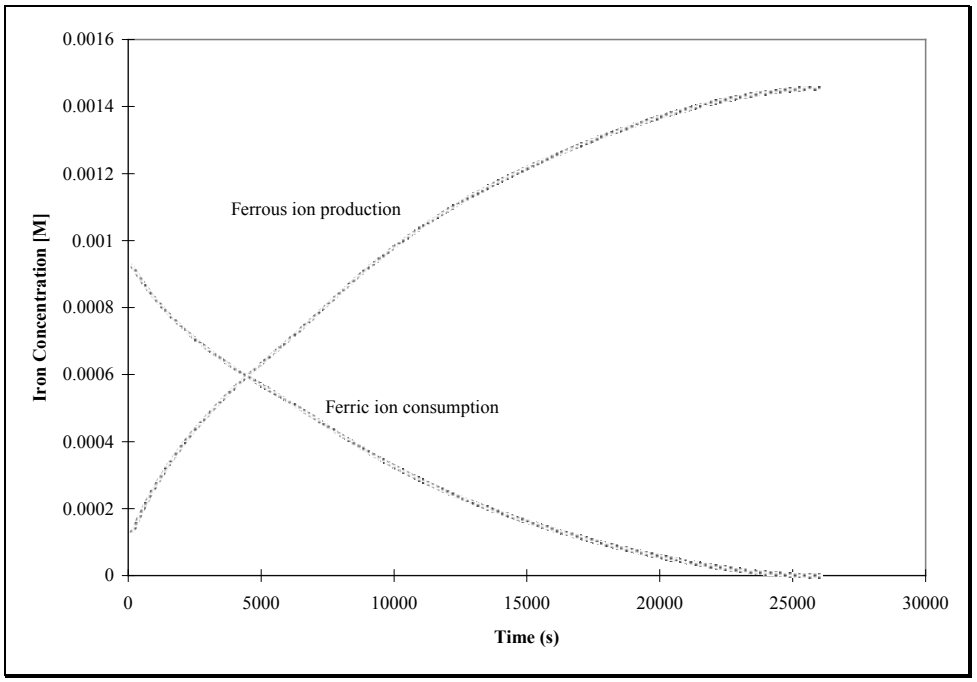

Figure C-50: Ferric iron oxidation of Po-M-9-91 at pH=2.45, 25°C, $Fe^{+3}_{int}=1\times10^{-3}$ [M], Experiment Oct 4C.

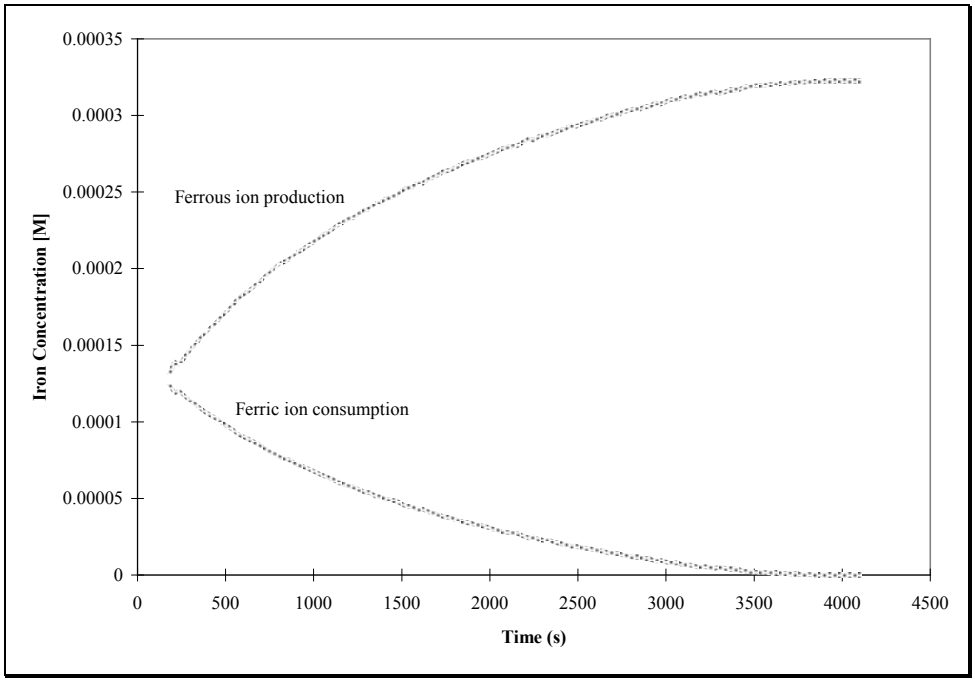

Figure C-51: Ferric iron oxidation of Po-M-9-91 at pH=2.75, 25°C, $Fe^{+3}_{int}=2\times10^{-4}$ [M], Experiment Oct 4.

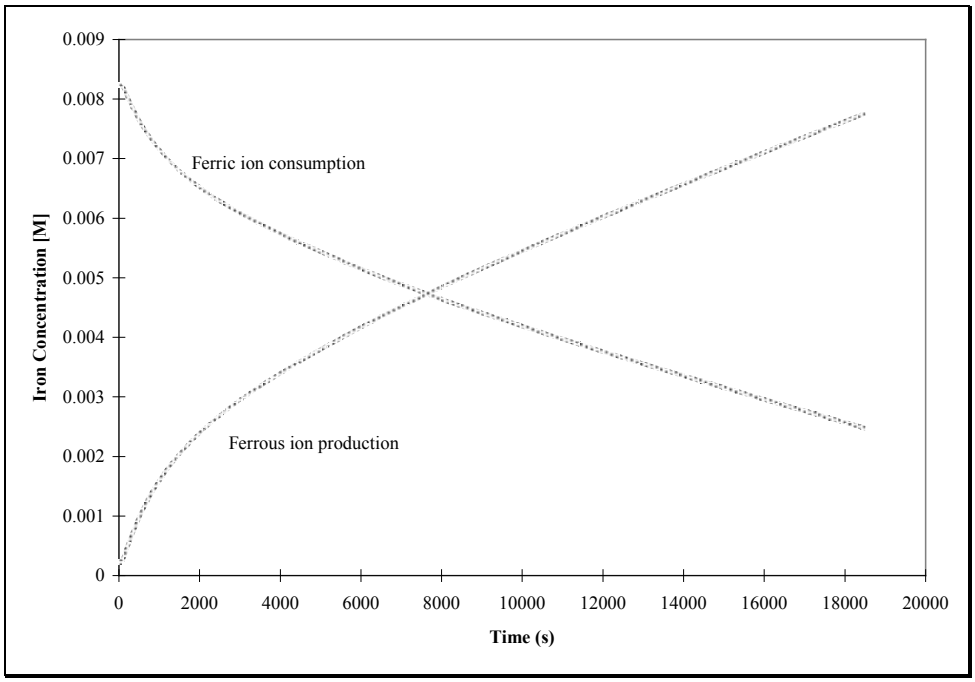

Figure C-52: Ferric iron oxidation of Po-M-15-93 at pH=2.02, 25°C, $Fe^{+3}_{int}=1\times10^{-2}$ [M], Experiment Oct 5C.

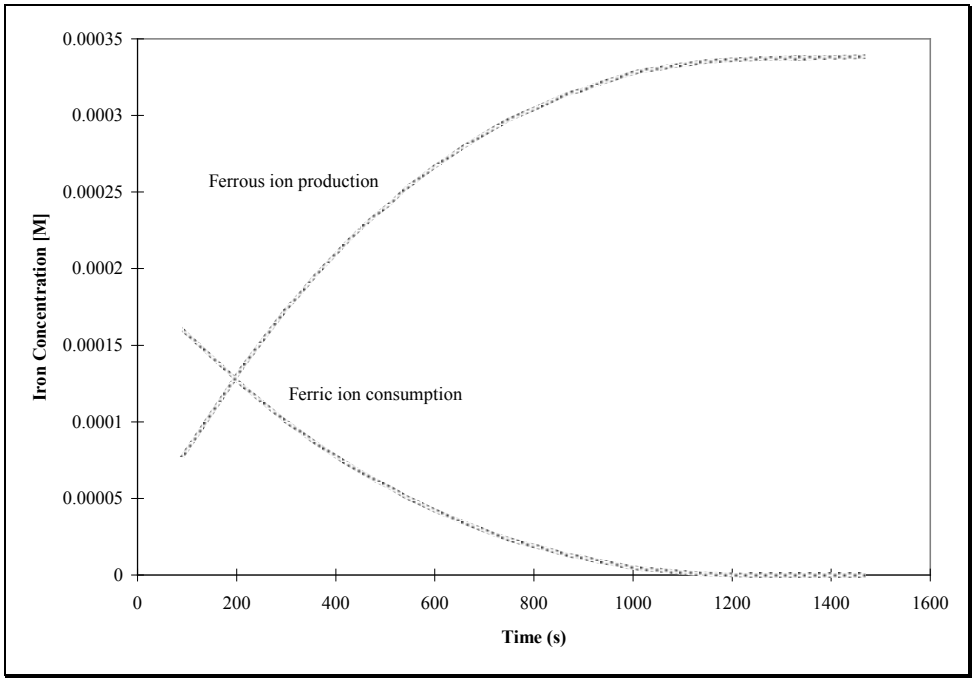

Figure C-53: Ferric iron oxidation of Po-M-15-93 at pH=2.68, 25°C, $Fe^{+3}_{int}=2\times10^{-4}$ [M], Experiment Oct 5.

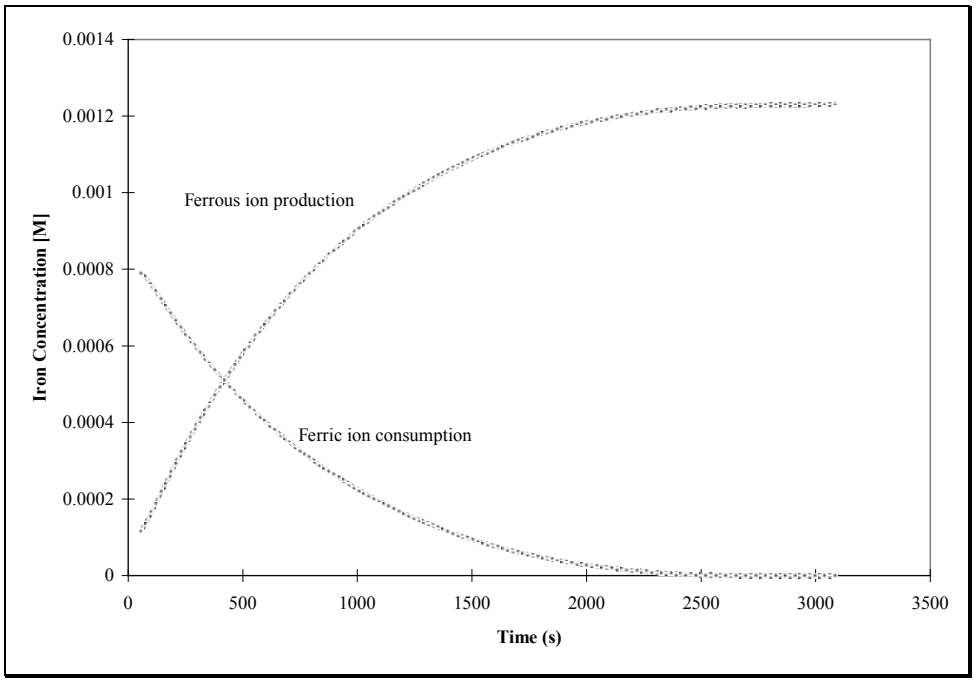

Figure C-54: Ferric iron oxidation of Po-M-15-93 at pH=2.48, 25°C, $Fe^{+3}_{int}=1\times10^{-3}$ [M], Experiment Oct 5B.

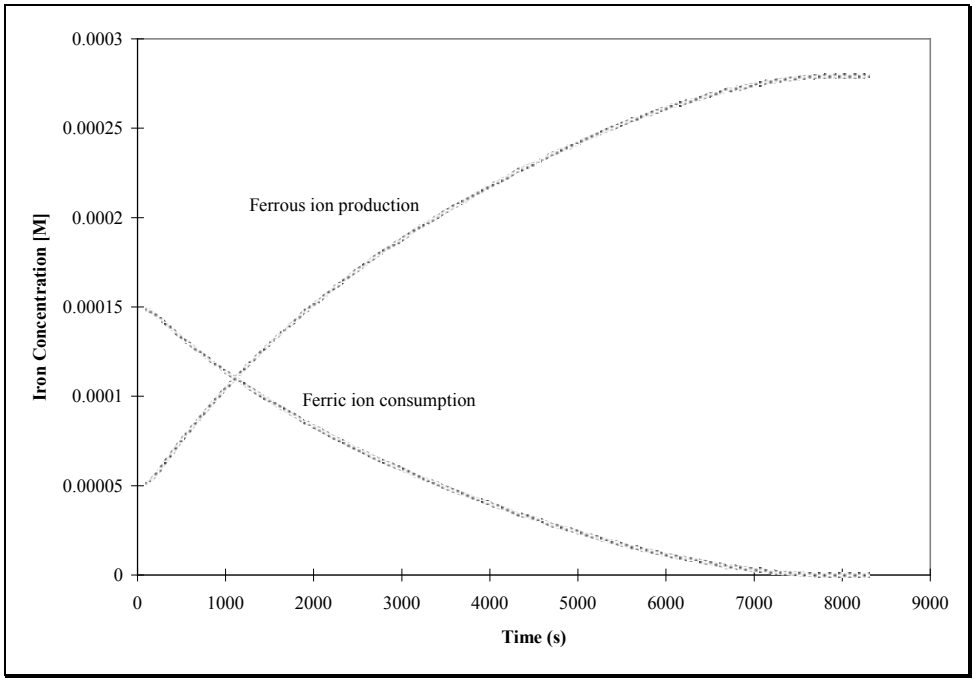

Figure C-55: Ferric iron oxidation of Po-M-17-93 at pH=2.53, 25°C, $Fe^{+3}_{int}=2\times10^{-4}$ [M], Experiment Oct 6B.

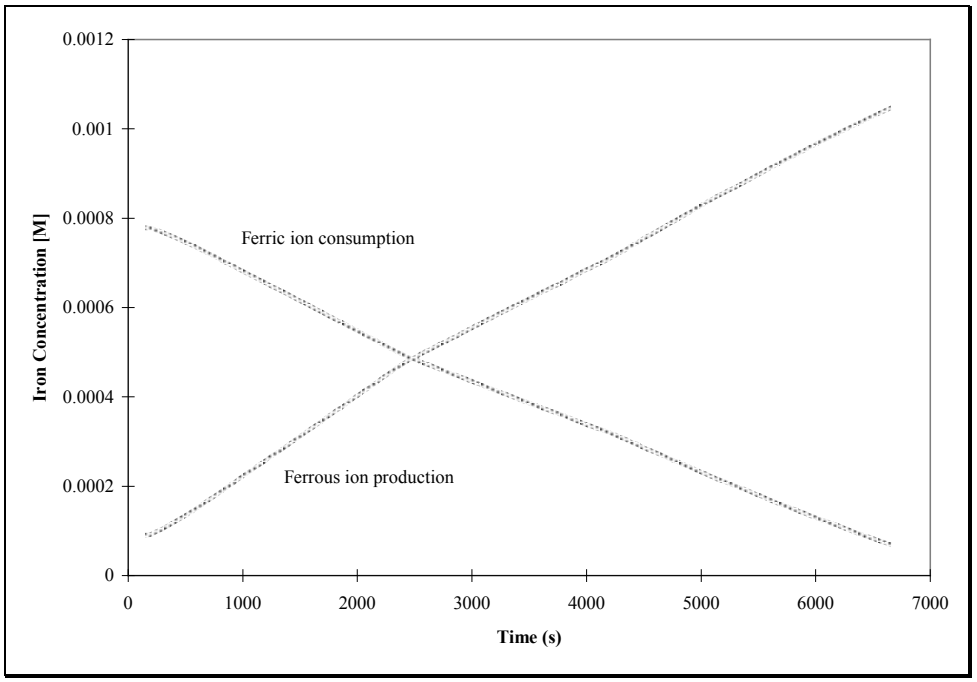

Figure C-56: Ferric iron oxidation of Po-M-17-93 at pH=2.49, 25°C, $Fe^{+3}_{int}=1\times10^{-3}$ [M], Experiment Oct 6C.

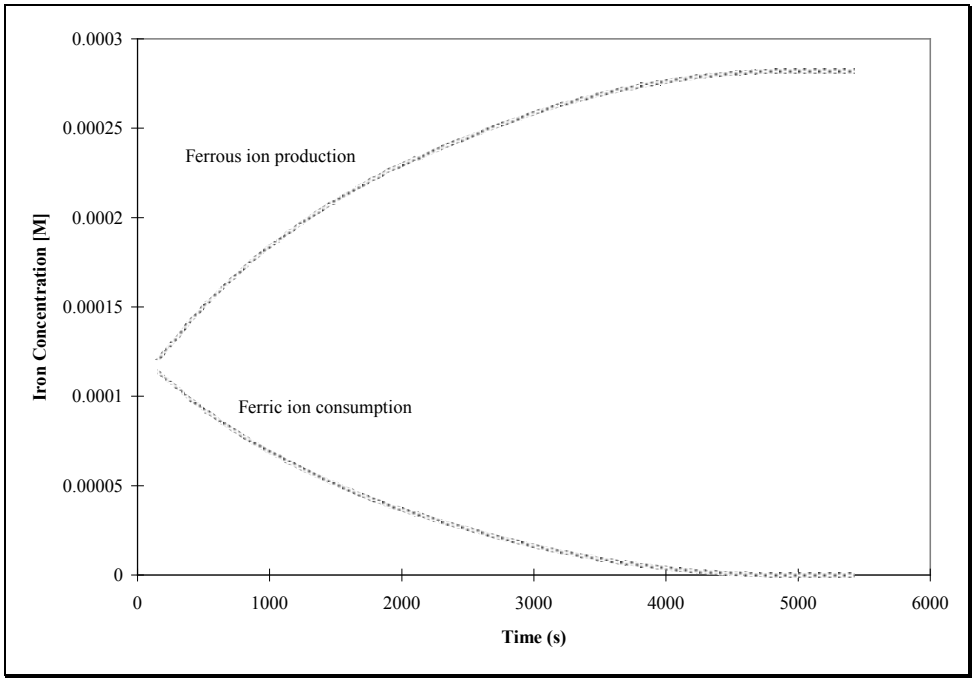

Figure C-57: Ferric iron oxidation of Po-M-17-93 at pH=2.77, 25°C, $Fe^{+3}_{int}=2\times10^{-4}$ [M], Experiment Oct 6.

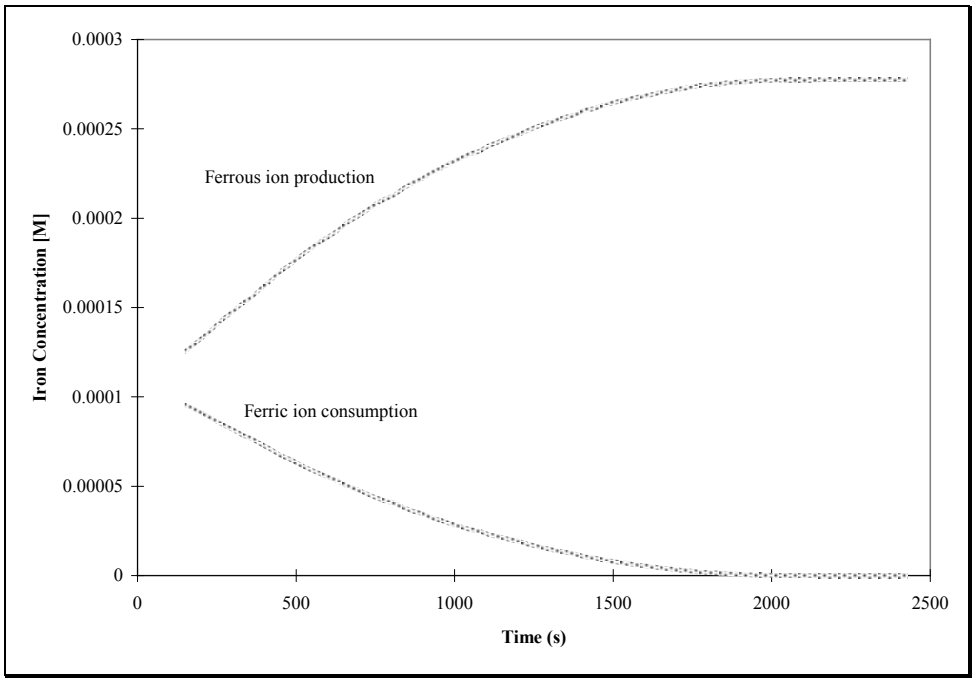

Figure C-58: Ferric iron oxidation of Po-M-19-94 at pH=2.51, 25°C, $Fe^{+3}_{int}=2\times10^{-4}$ [M], Experiment Oct 7.

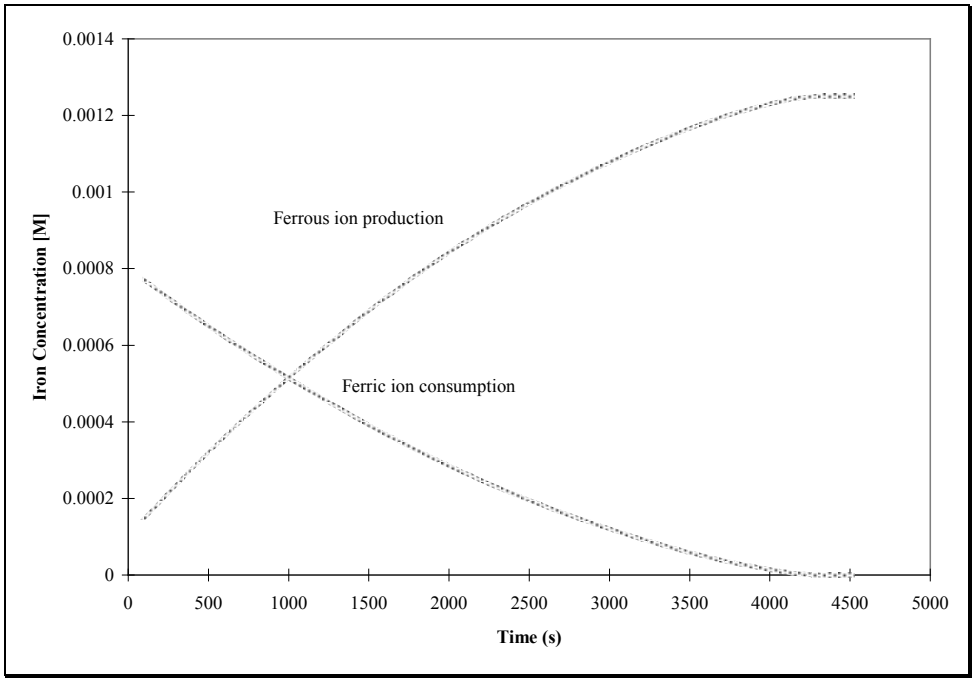

Figure C-59: Ferric iron oxidation of Po-M-19-93 at pH=2.51, 25°C, $Fe^{+3}_{int}=1\times10^{-3}$ [M], Experiment Oct 7C.

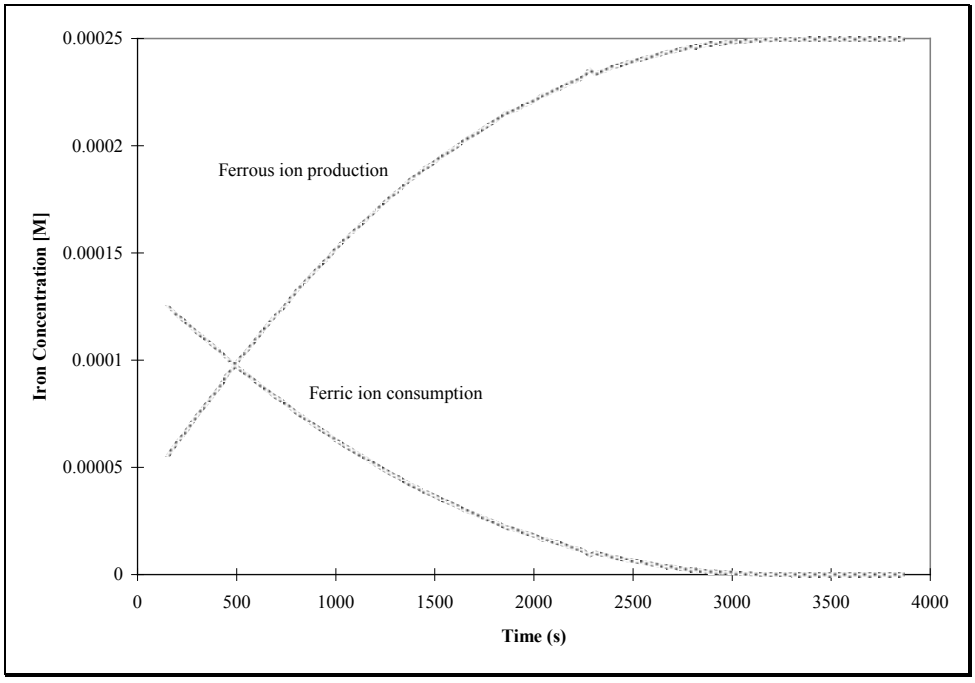

Figure C-60: Ferric iron oxidation of Po-M-19-94 at pH=2.75, 25°C, $Fe^{+3}_{int}=2\times10^{-4}$ [M], Experiment Oct 7B.

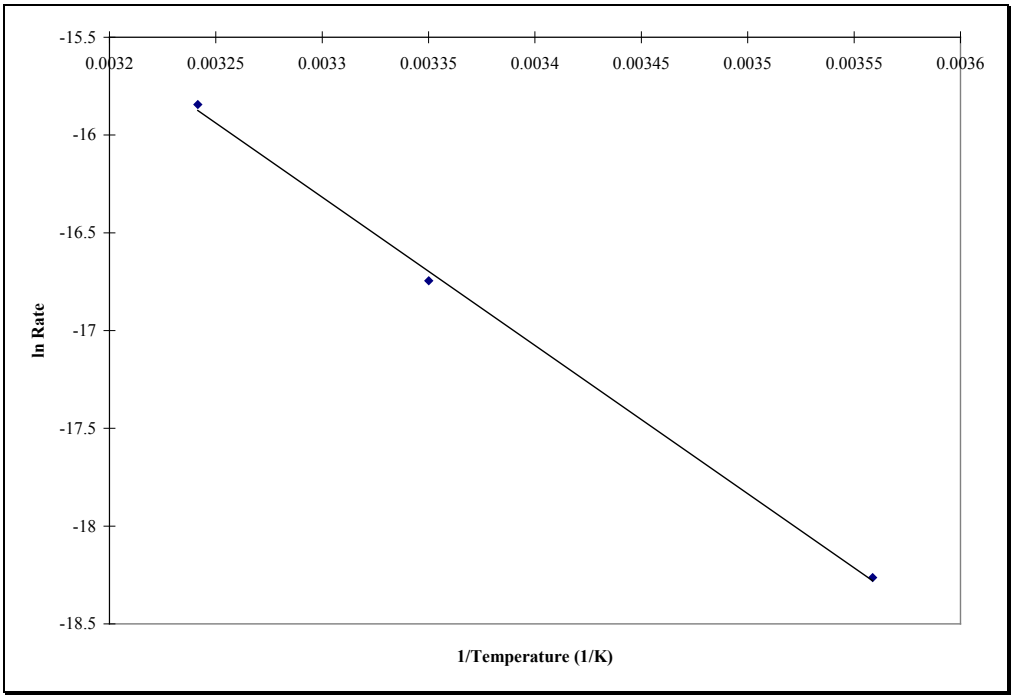

Figure C-61: The effects of temperature on pyrrhotite oxidation of Po-M-1-93 by Fe^{+3}.

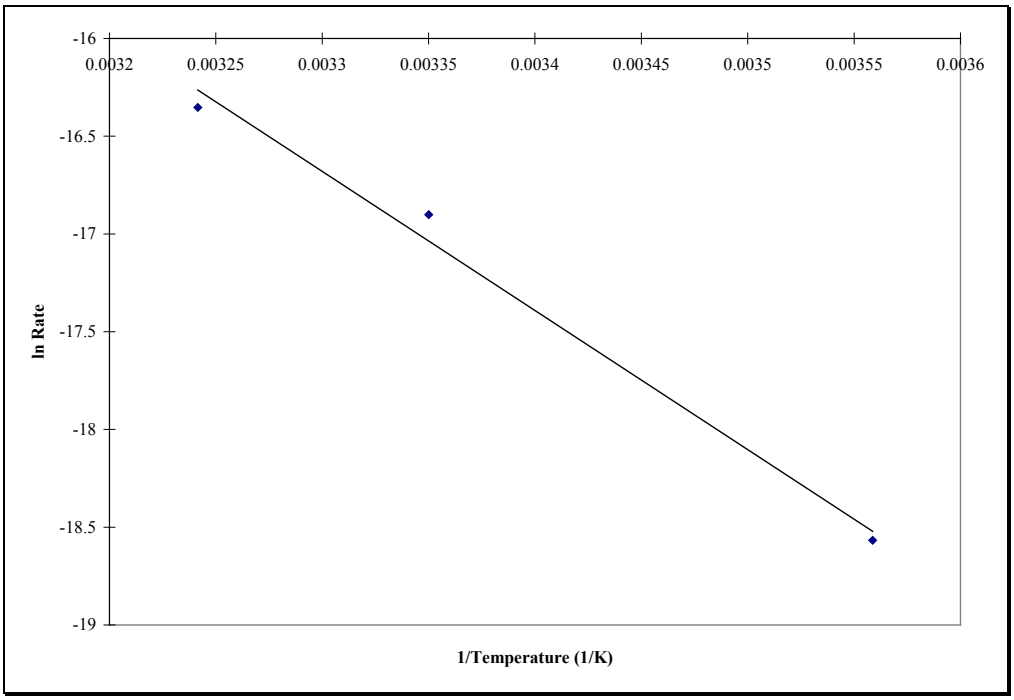

Figure C-62: The effects of temperature on pyrrhotite oxidation of Po-M-2-94 by Fe^{+3}.

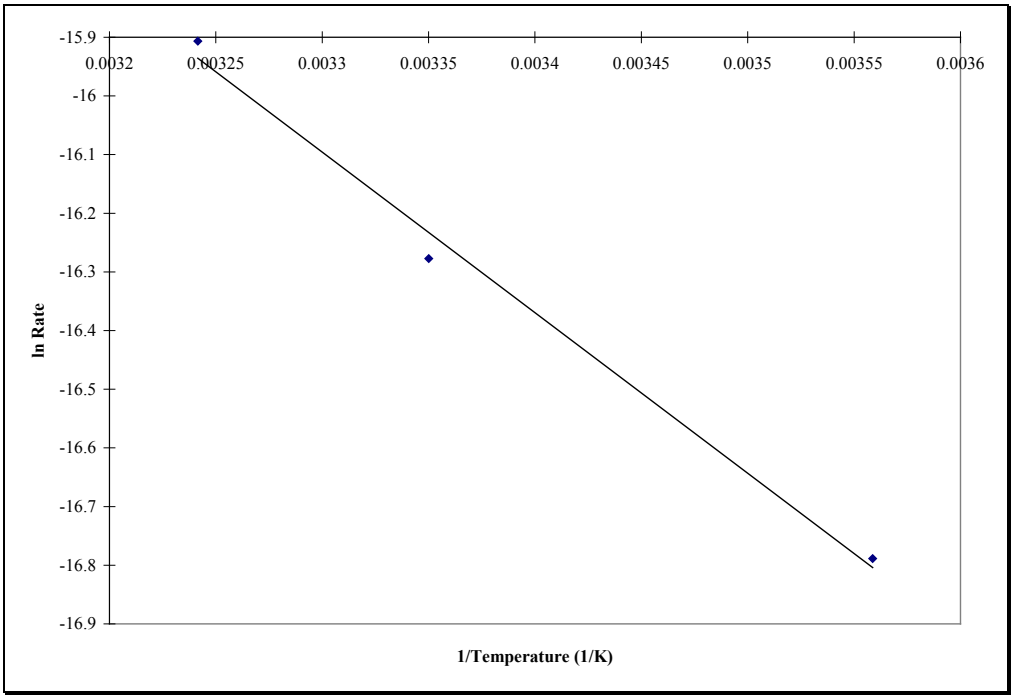

Figure C-63: The effects of temperature on pyrrhotite oxidation of Po-M-3-94 by Fe^{+3}.

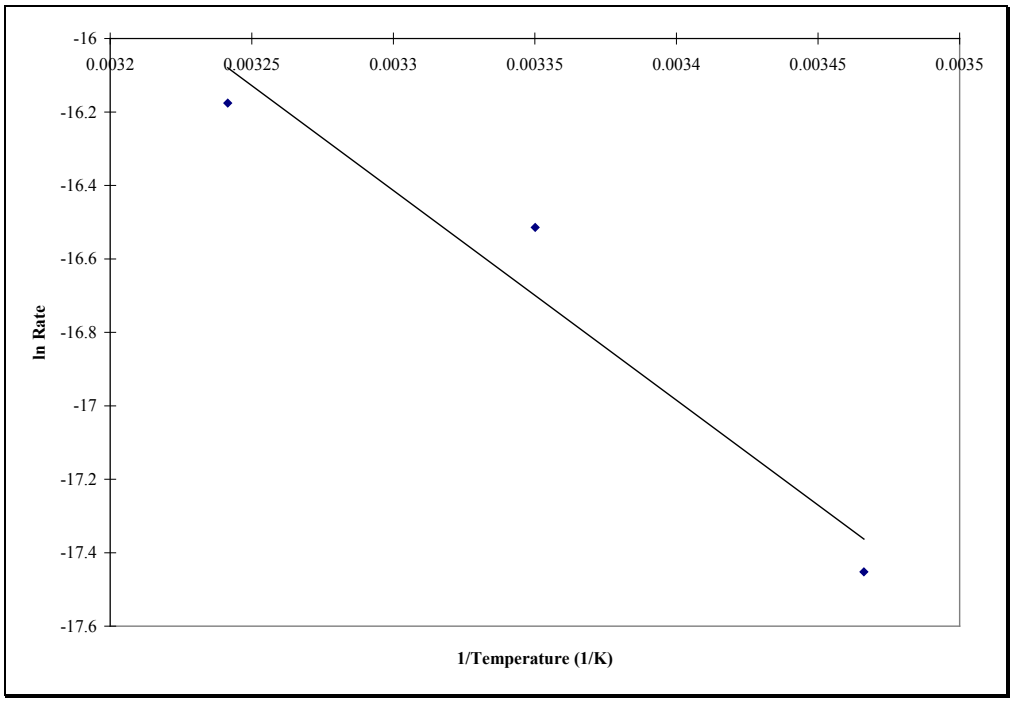

Figure C-64: The effects of temperature on pyrrhotite oxidation of Po-M-4-94 by Fe^{+3}.

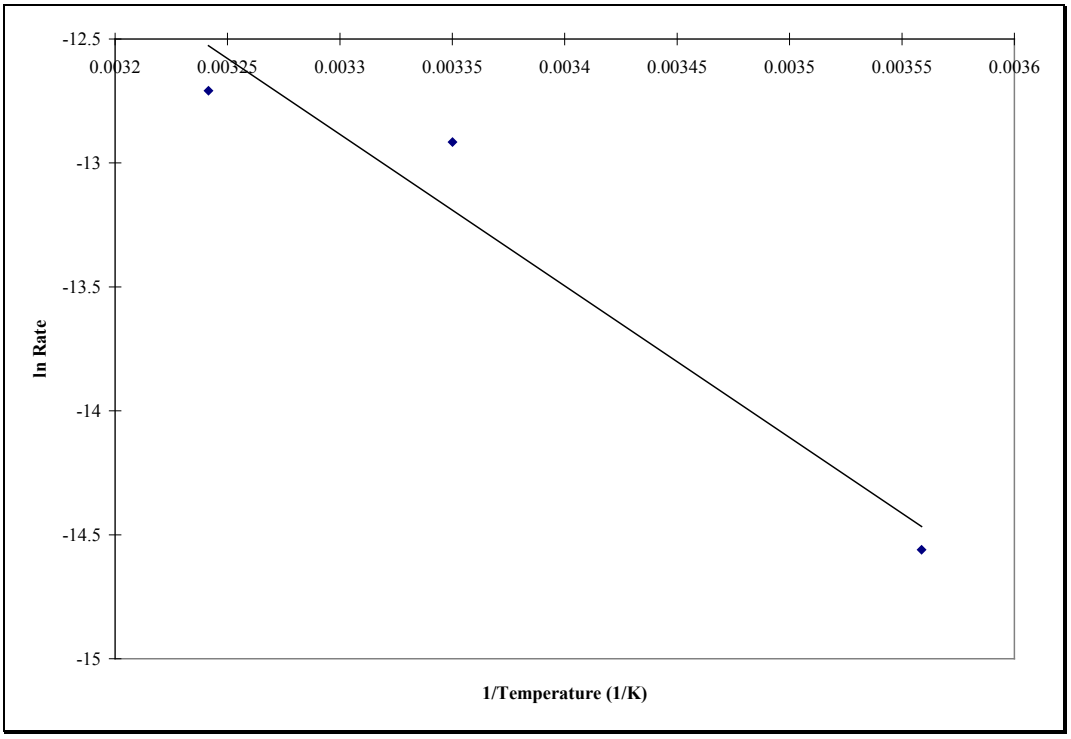

Figure C-65: The effects of temperature on pyrrhotite oxidation of Po-C-5-94 by Fe^{+3}.

Table C-2: Bulk chemical analysis of Po-M-3-94 and the precipitate formed from Po-M-3-94.

Element	Po-M-3-94	Precipitate of Po-M-3-94
Be ppm	5.6	< D.L.
Mg %	< D.L.	.02
Al %	< D.L.	< D.L.
P %	< D.L.	< D.L.
K %	< D.L.	< D.L.
Ca %	< D.L.	< D.L.
Sc ppm	< D.L.	< D.L.
Ti %	< D.L.	< D.L.
V ppm	40	29
Cr ppm	15	31
Mn ppm	19	56
Cd ppm	< D.L.	< D.L.
Sn ppm	19	< D.L.
Sb ppm	< D.L.	< D.L.
Ba ppm	< D.L.	98
La ppm	< D.L.	27
W ppm	< D.L.	< D.L.
Co ppm	368	368
Ni ppm	70	598
Cu ppm	7370	7100
Zn ppm	< D.L.	76
Sr ppm	< D.L.	< D.L.
Y ppm	0.3	< D.L.
Fe %	60.6 (Electron microprobe)	58.0 (ICP)
S %	39.3 (Electron microprobe)	42.1 (Leco furnace)

D.L. = Detection Limit

Appendix D

Kinetic Oxidation of Inco's Copper Cliff Pyrrhotite Concentrate

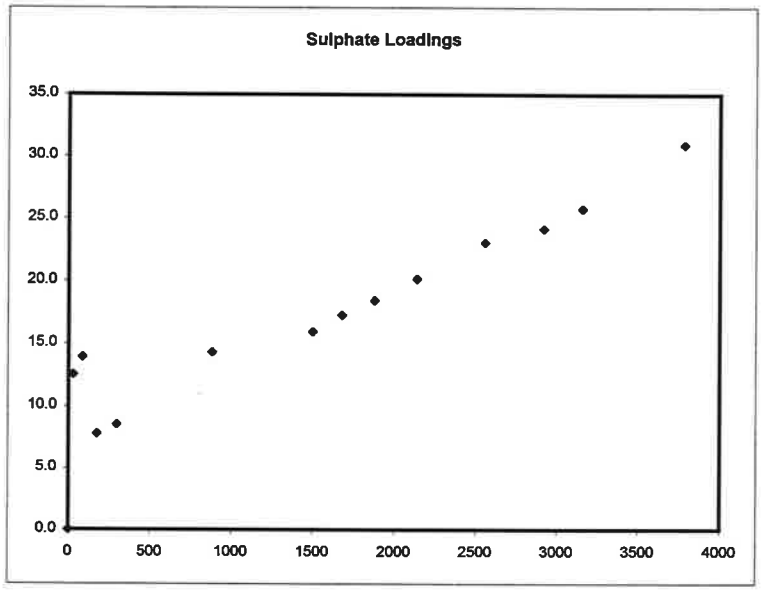

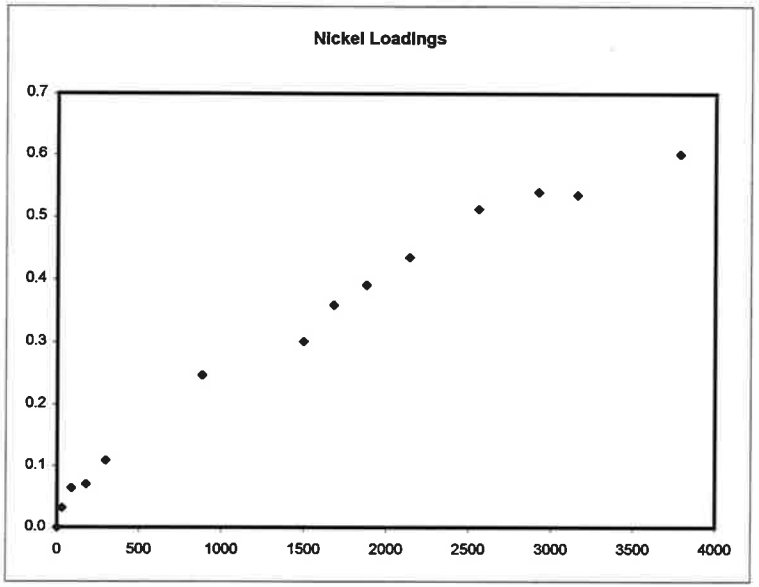

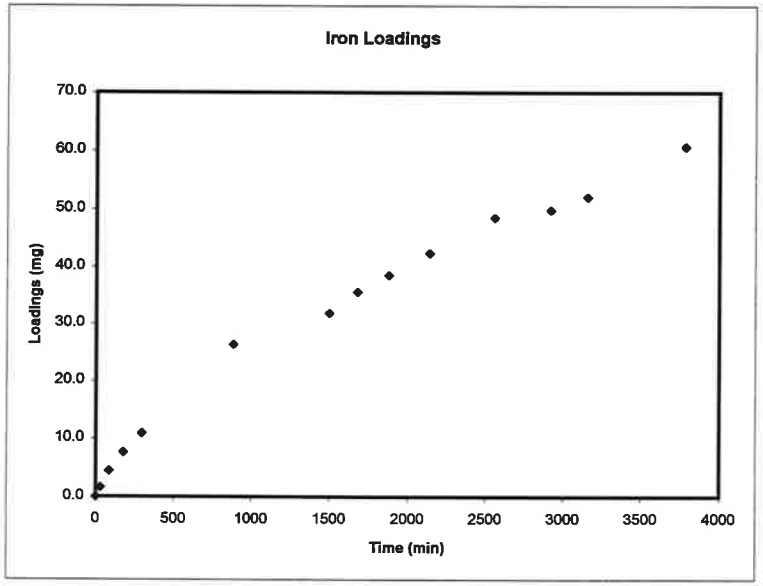

Regression
From 1500 To 3784

Production Rate (mol / min)

Sulphate	Iron	Nickel
6.49E-08	2.14E-07	2.15E-09

Oxidation Rate (mol / m2 s)

Sulphate	Iron	Nickel
2.42E-09	7.96E-09	8.02E-11

Figure D-1: Abiotic oxidation of Inco's Copper Cliff Po Conc at pH = 2, 30C (KS-006).

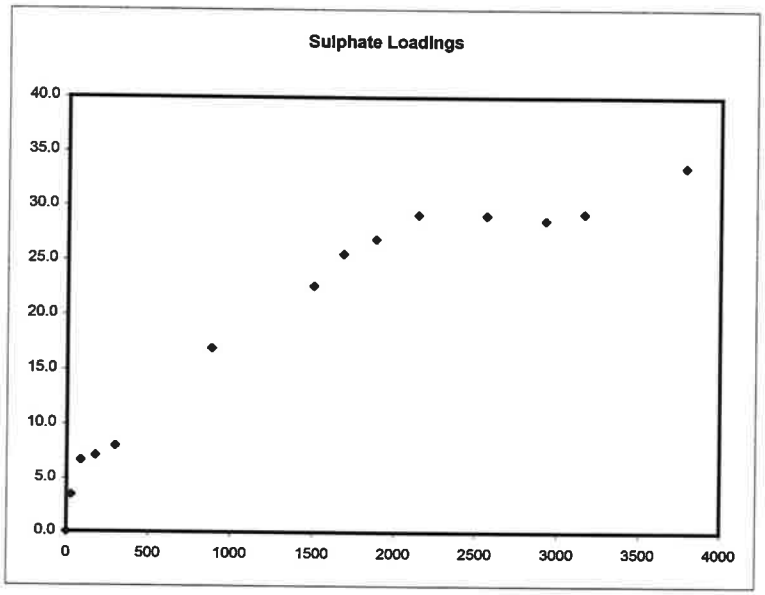

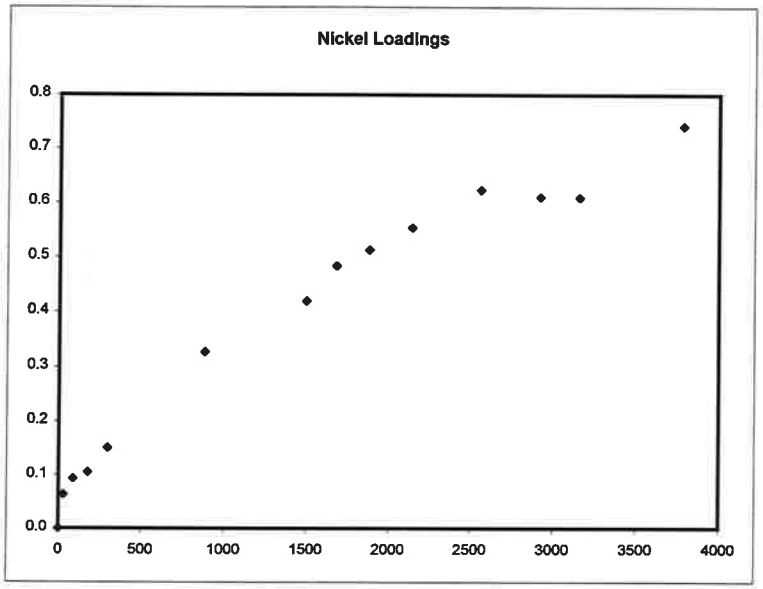

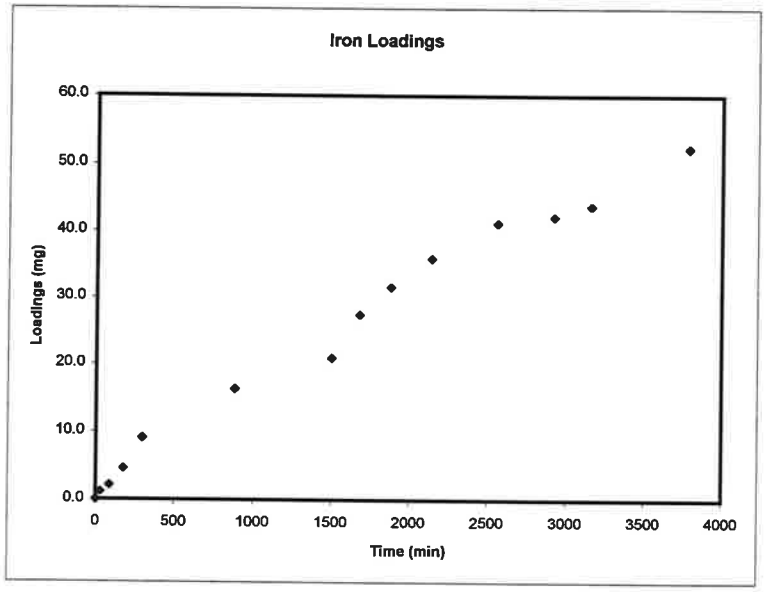

Regression
From 1500 To 3784

Production Rate (mol / min)

Sulphate	Iron	Nickel
3.76E-08	2.19E-07	2.03E-09

Oxidation Rate (mol / m2 s)

Sulphate	Iron	Nickel
1.4E-09	8.17E-09	7.56E-11

Figure D-2: Abiotic oxidation of Inco's Copper Cliff Po Conc at pH = 3, 30C (KS-007).

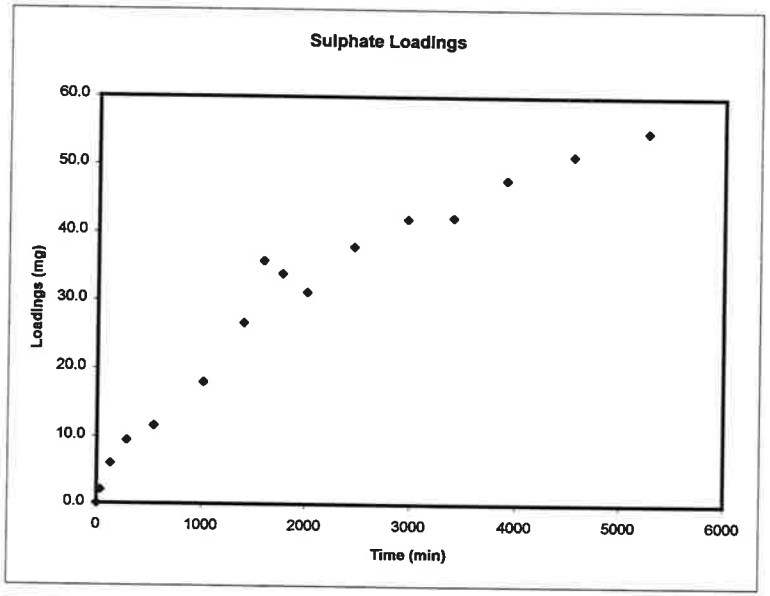

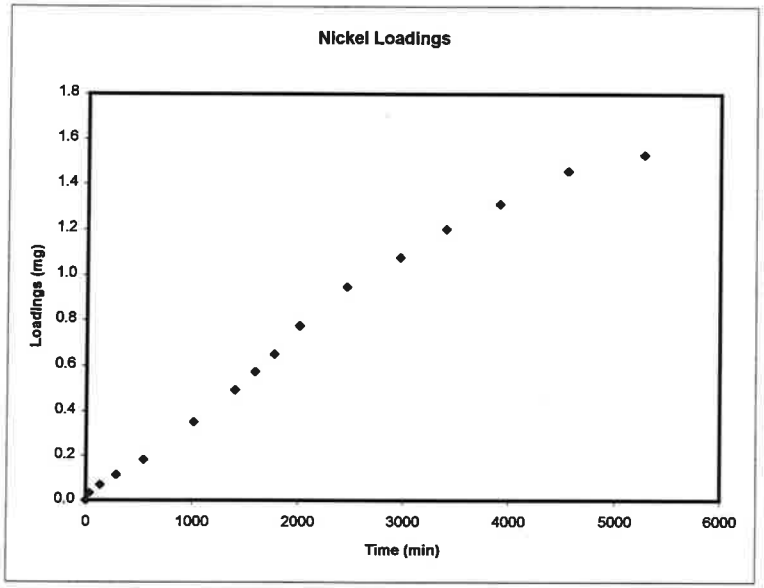

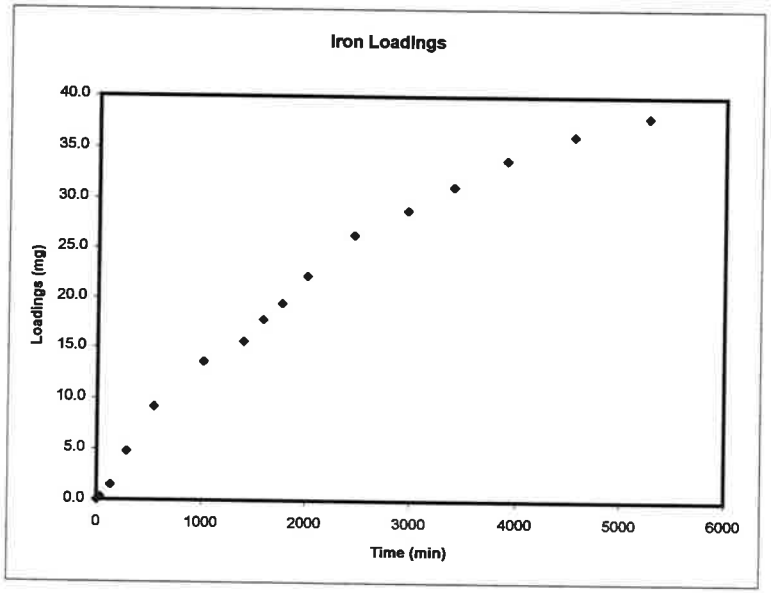

Regression
From 1767 To 5264

Production Rate (mol / min)

Sulphate	Iron	Nickel
6.9E-08	9.38E-08	4.28E-09

Oxidation Rate (mol / m2 s)

Sulphate	Iron	Nickel
2.57E-09	3.5E-09	1.6E-10

Figure D-3: Abiotic oxidation of Inco's Copper Cliff Po Conc at pH = 4, 30C (KS-008).

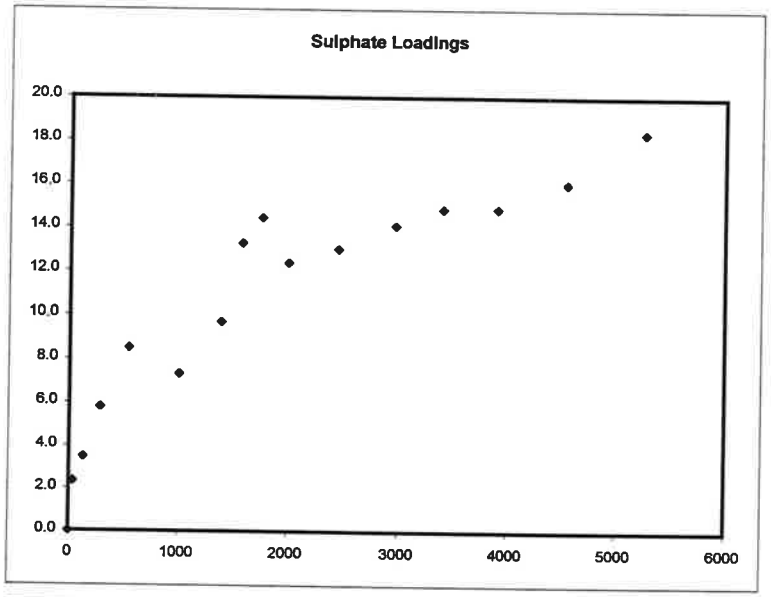

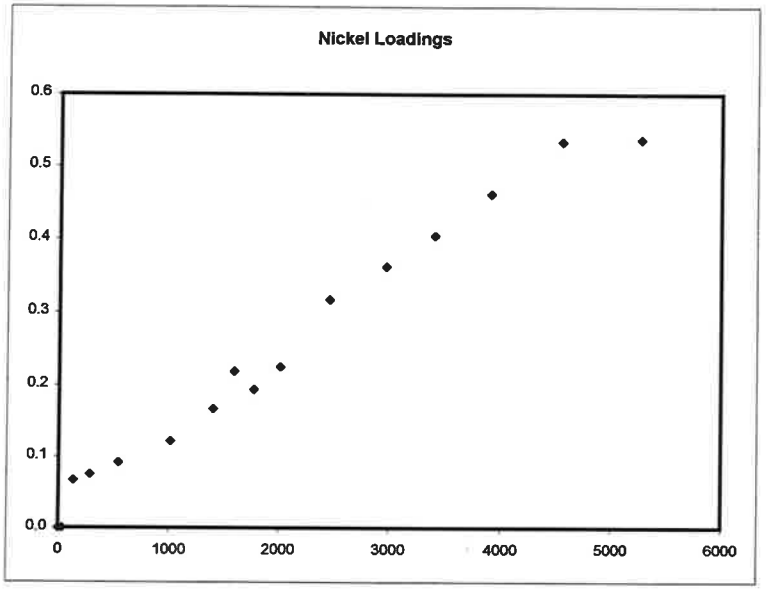

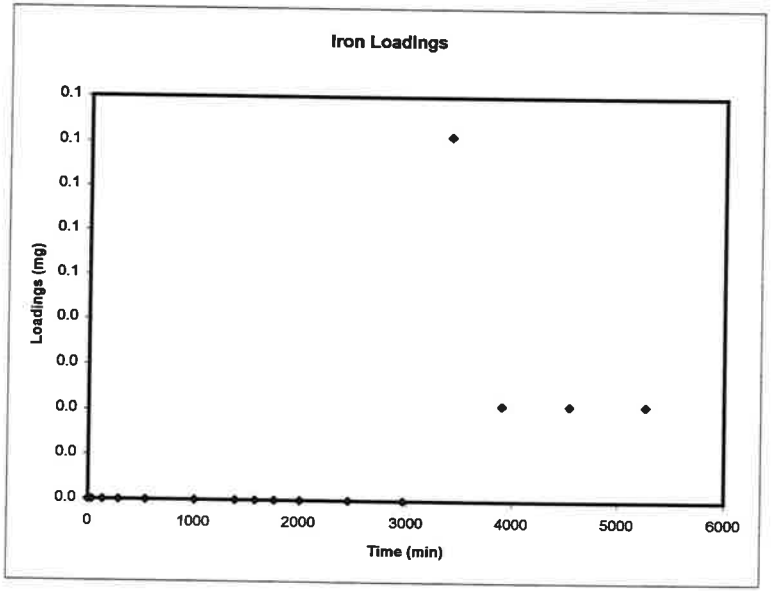

Regression
From 2007 To 5264

Production Rate (mol / min)

Sulphate	Iron	Nickel
1.75E-08	1.33E-10	1.65E-09

Oxidation Rate (mol / m2 s)

Sulphate	Iron	Nickel
6.51E-10	4.95E-12	6.14E-11

Figure D-4: Abiotic oxidation of Inco's Copper Cliff Po Conc at pH = 6, 30C (KS-009).

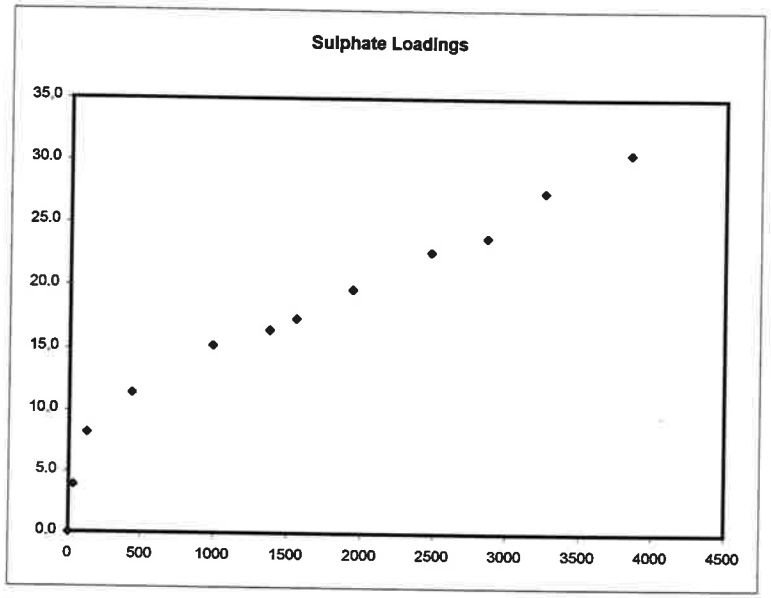

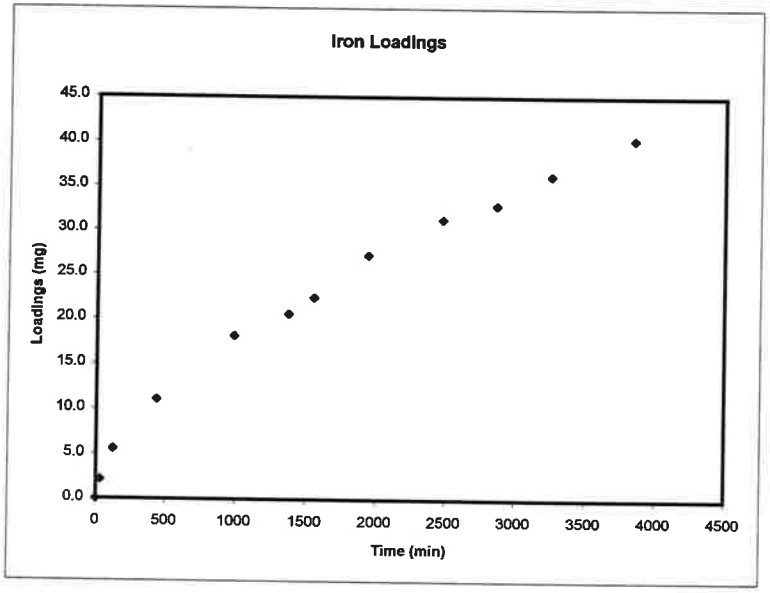

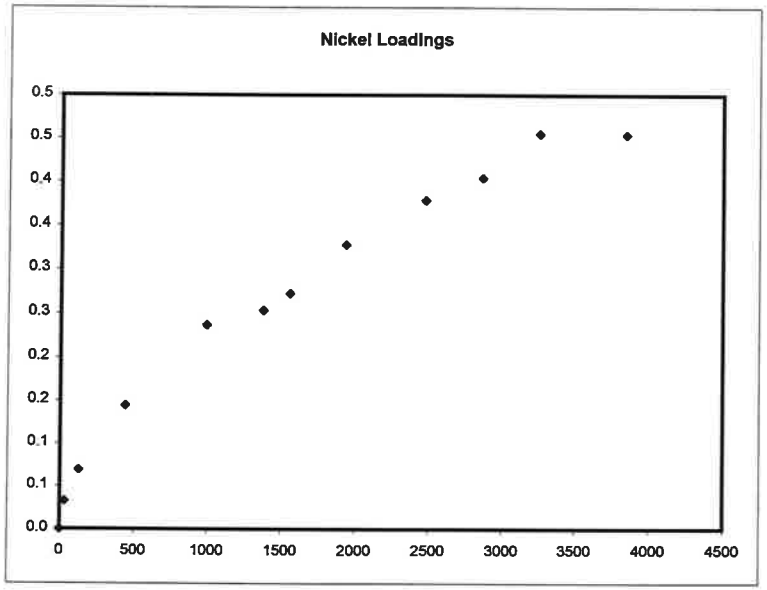

Regression
From 1376 To 3845

Production Rate (mol / min)

Sulphate	Iron	Nickel
5.91E-08	1.40E-07	1.49E-09

Oxidation Rate (mol / m2 s)

Sulphate	Iron	Nickel
2.2E-09	5.23E-09	5.54E-11

Figure D-5: Abiotic oxidation of Inco's Copper Cliff Po Conc at pH = 5, 20C (KS-016).

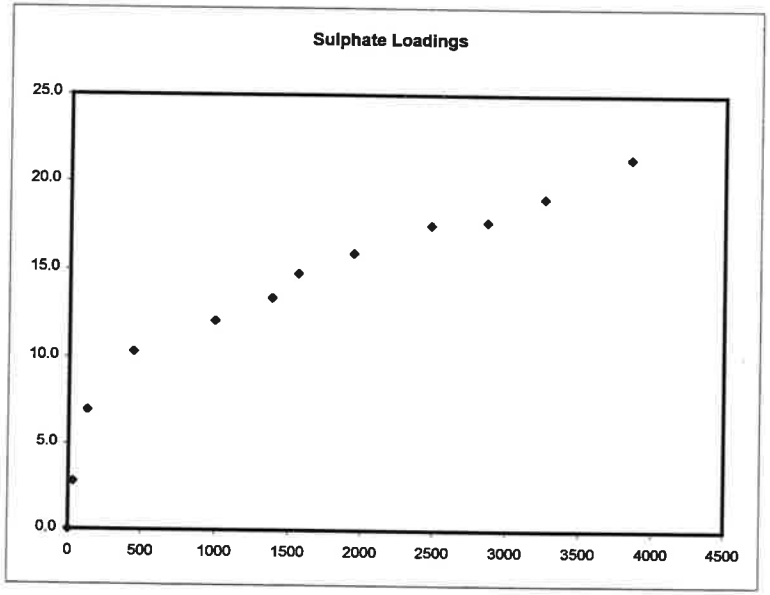

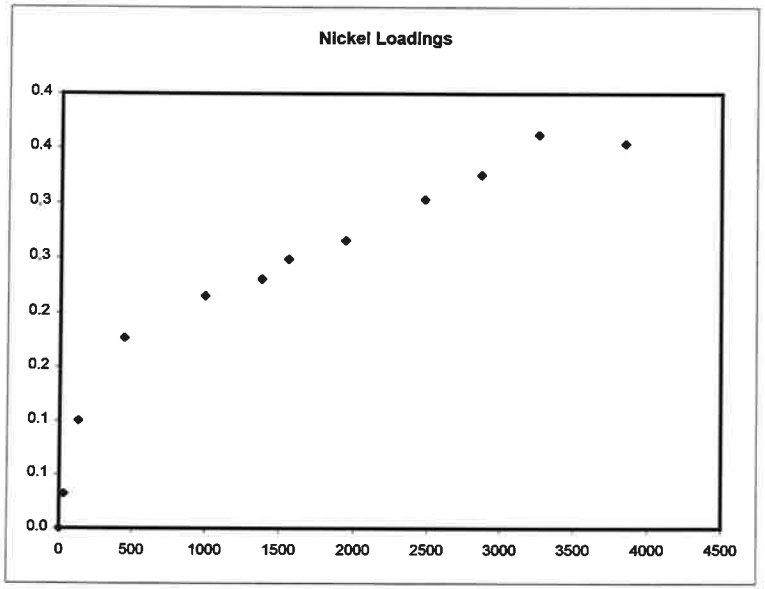

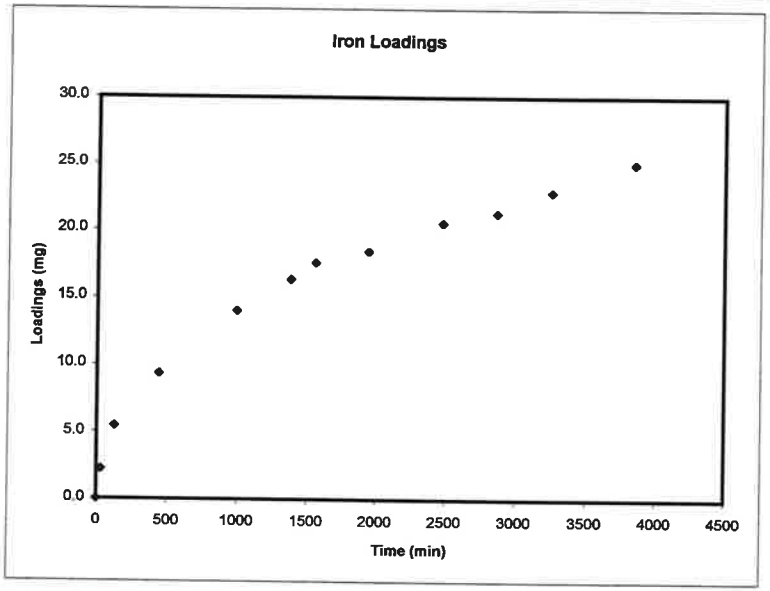

Regression
From 1376 To 3845

Production Rate (mol / min)

Sulphate	Iron	Nickel
3.01E-08	6.03E-08	9.35E-10

Oxidation Rate (mol / m2 s)

Sulphate	Iron	Nickel
1.12E-09	2.25E-09	3.49E-11

Figure D-6: Abiotic oxidation of Inco's Copper Cliff Po Conc at pH = 3, 20C (KS-017).

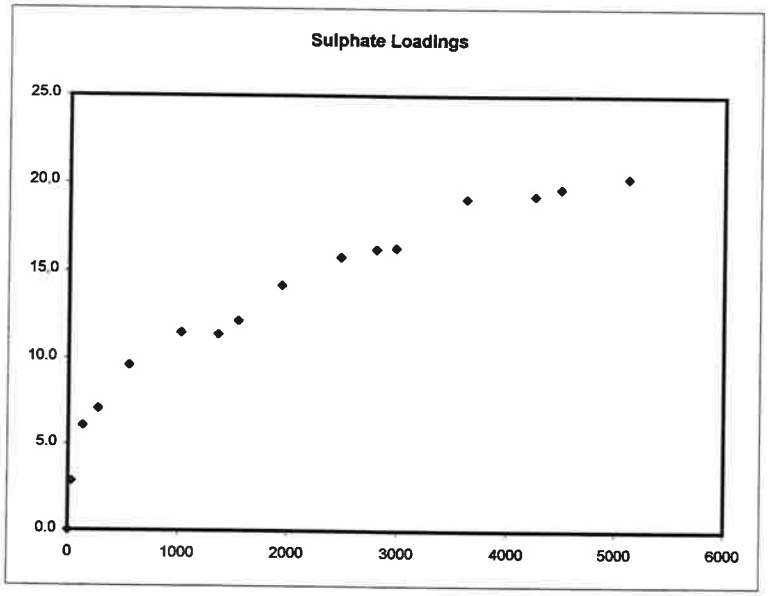

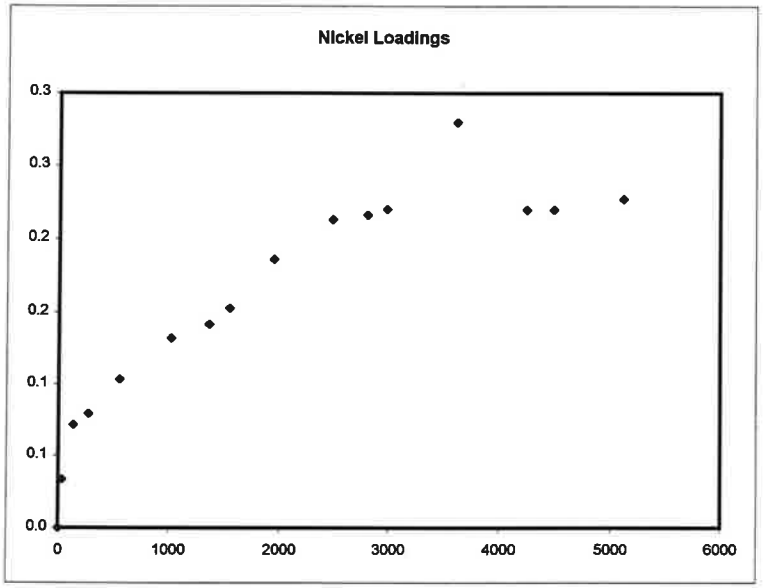

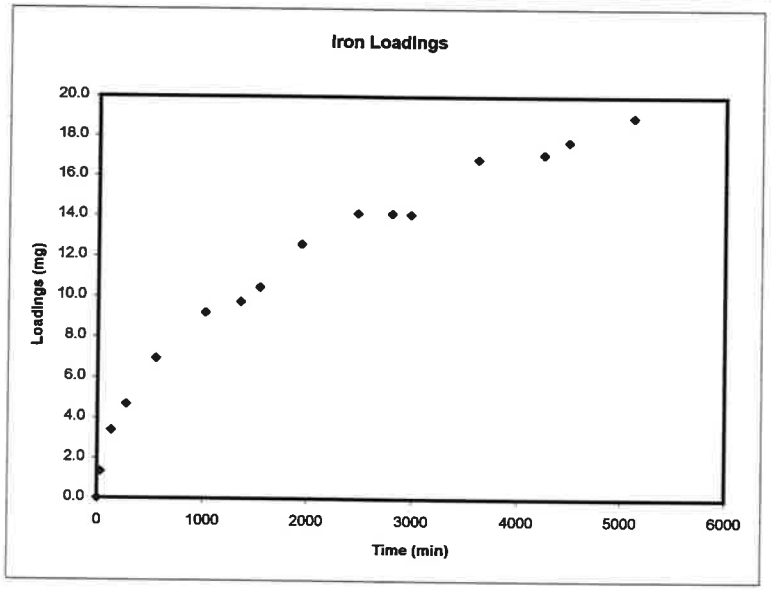

Regression
From 1354 To 5111

Production Rate (mol / min)

Sulphate	Iron	Nickel
2.48E-08	4.22E-08	3.72E-10

Oxidation Rate (mol / m2 s)

Sulphate	Iron	Nickel
9.25E-10	1.57E-09	1.39E-11

Figure D-7: Abiotic oxidation of Inco's Copper Cliff Po Conc at pH = 2, 10C (KS-018).

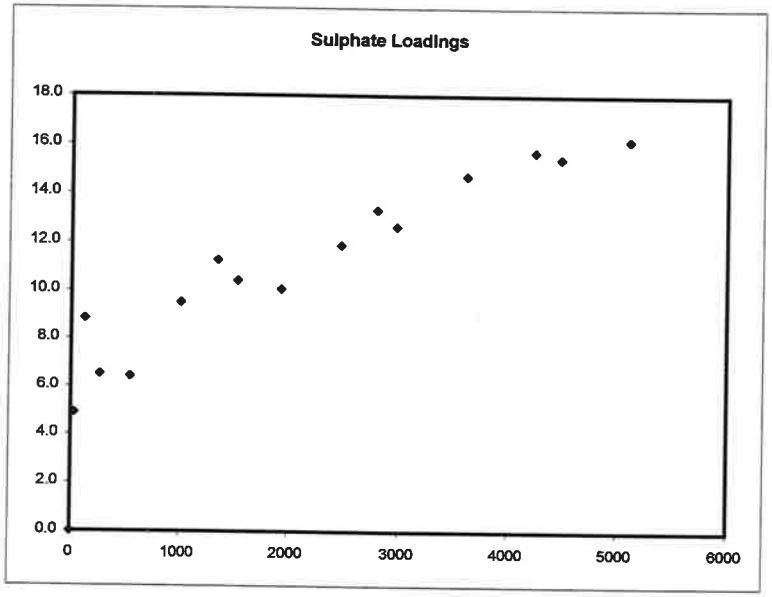

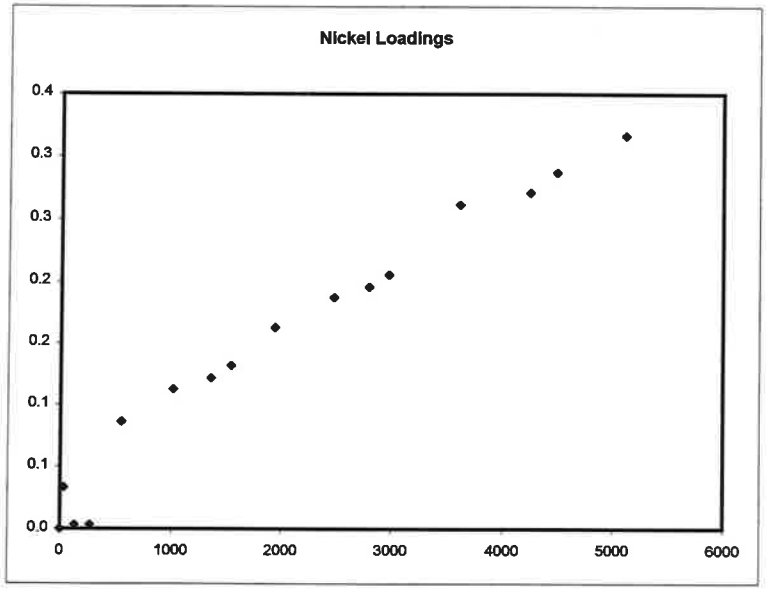

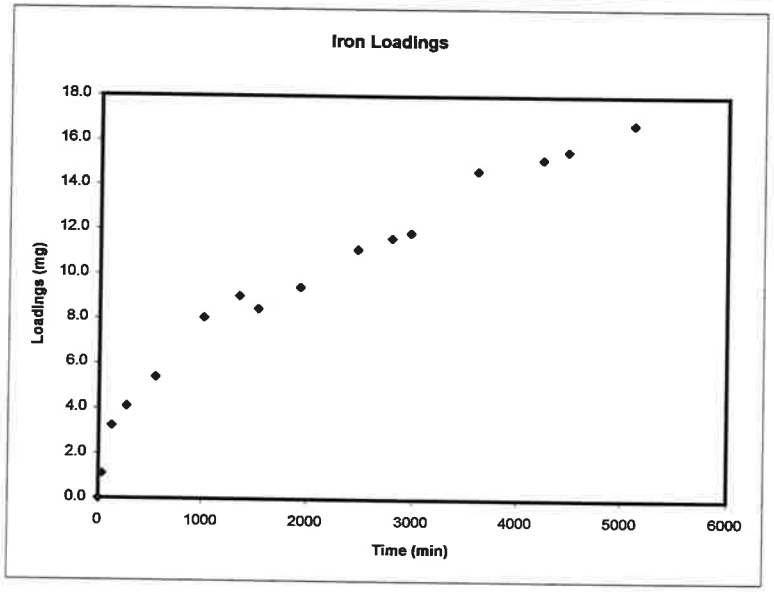

Regression
From 1539 To 5111

Production Rate (mol / min)

Sulphate	Iron	Nickel
1.91E-08	4.26E-08	8.7E-10

Oxidation Rate (mol / m2 s)

Sulphate	Iron	Nickel
7.12E-10	1.59E-09	3.24E-11

Figure D-8: Abiotic oxidation of Inco's Copper Cliff Po Conc at pH = 3, 10C (KS-019).

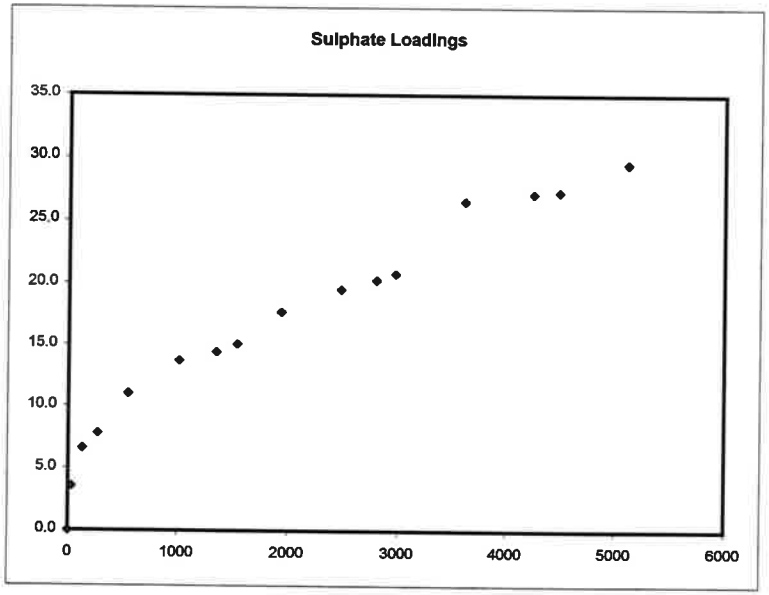

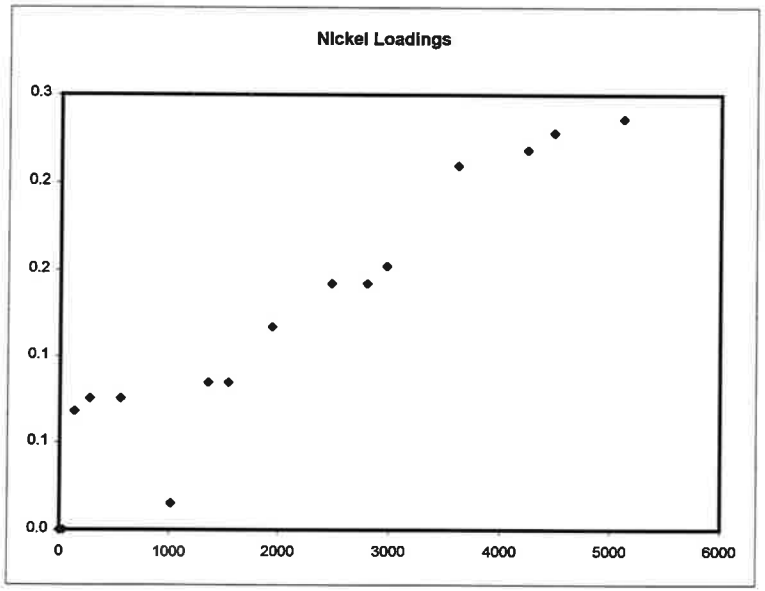

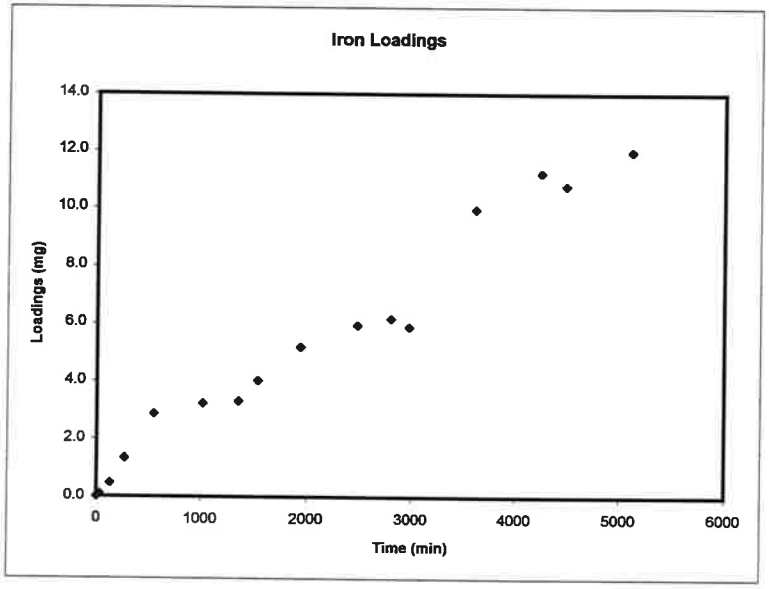

Regression
From 1354 To 5111

Production Rate (mol / min)

Sulphate	Iron	Nickel
4.36E-08	4.35E-08	7.53E-10

Oxidation Rate (mol / m2 s)

Sulphate	Iron	Nickel
1.62E-09	1.62E-09	2.81E-11

Figure D-9: Abiotic oxidation of Inco's Copper Cliff Po Conc at pH = 4, 10C (KS-020).

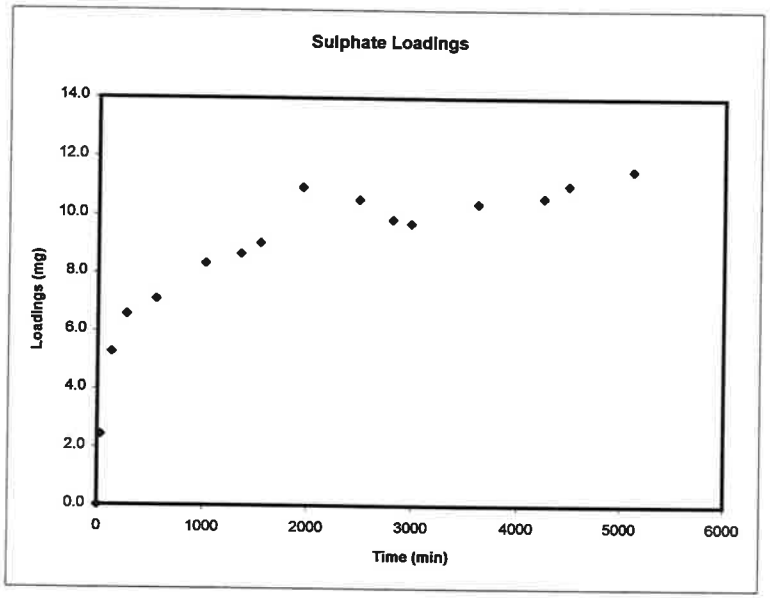

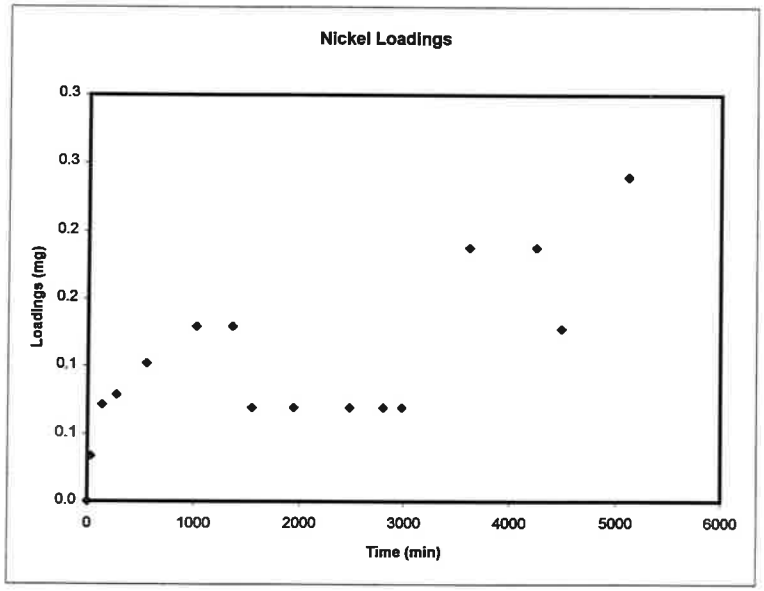

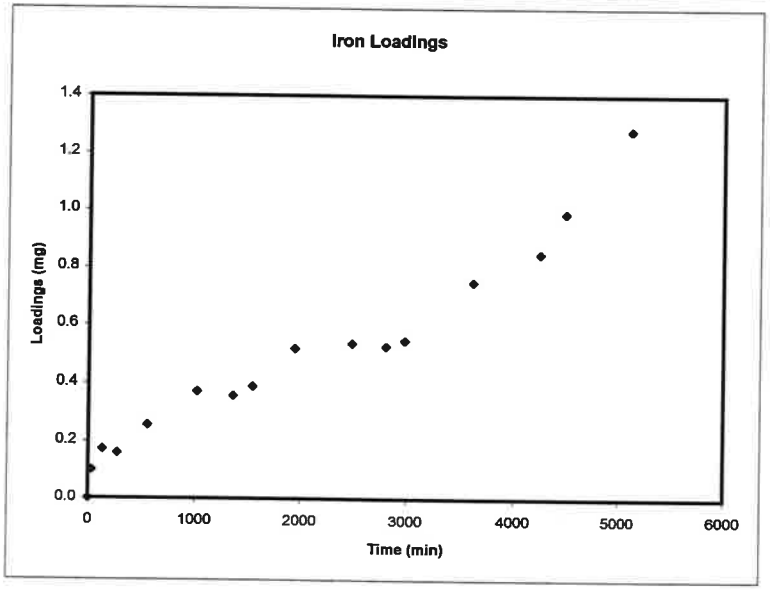

Regression
From 1354 To 5111

Production Rate (mol / min)

Sulphate	Iron	Nickel
5.56E-09	3.87E-09	6.19E-10

Oxidation Rate (mol / m2 s)

Sulphate	Iron	Nickel
2.07E-10	1.44E-10	2.31E-11

Figure D-10: Abiotic oxidation of Inco's Copper Cliff Po Conc at pH = 6, 10C (KS-021).

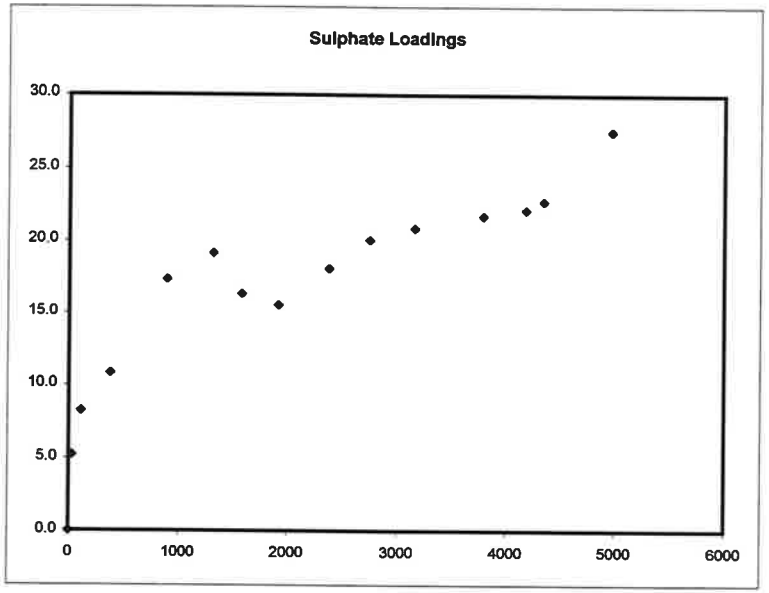

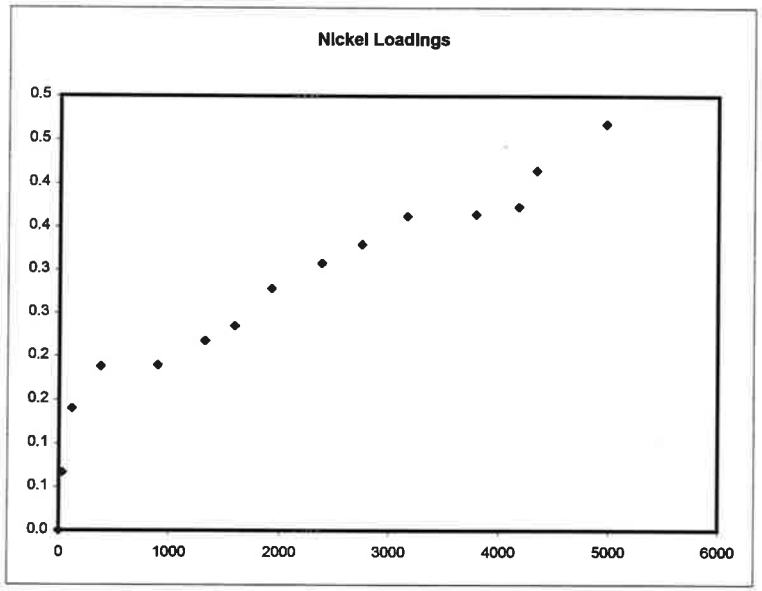

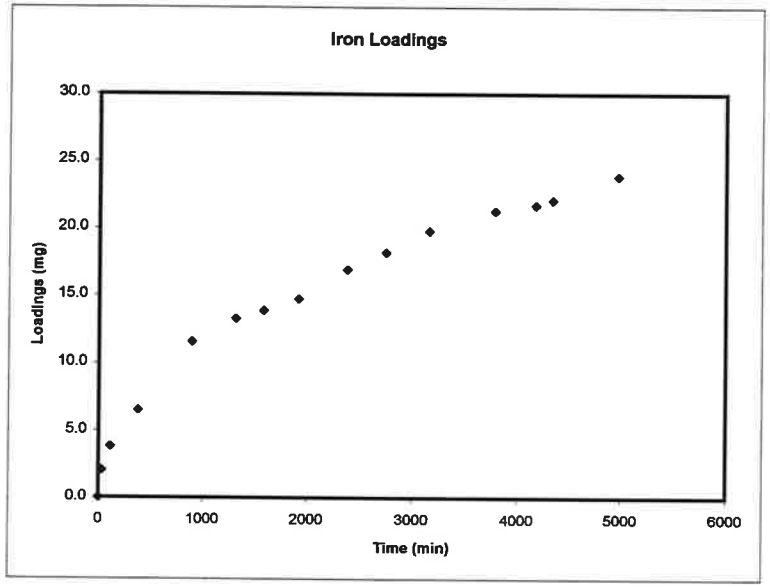

Regression
From 1583 To 4968

Production Rate (mol / min)

Sulphate	Iron	Nickel
3.12E-08	5.25E-08	9.95E-10

Oxidation Rate (mol / m2 s)

Sulphate	Iron	Nickel
1.16E-09	1.96E-09	3.71E-11

Figure D-11: Abiotic oxidation of Inco's Copper Cliff Po Conc at pH = 3, 20C (KS-023).

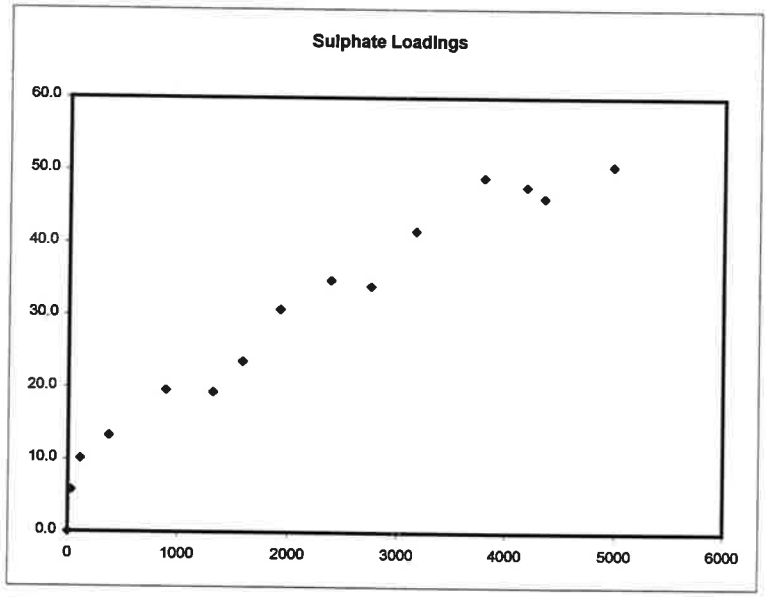

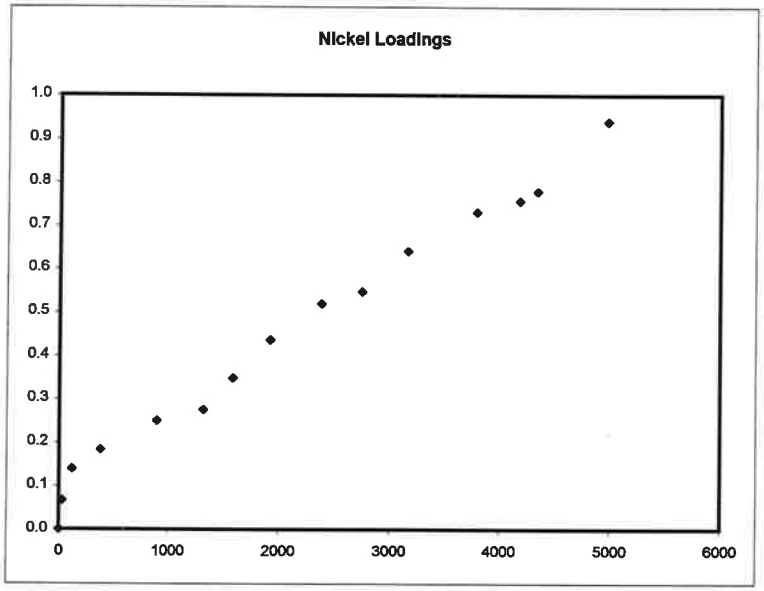

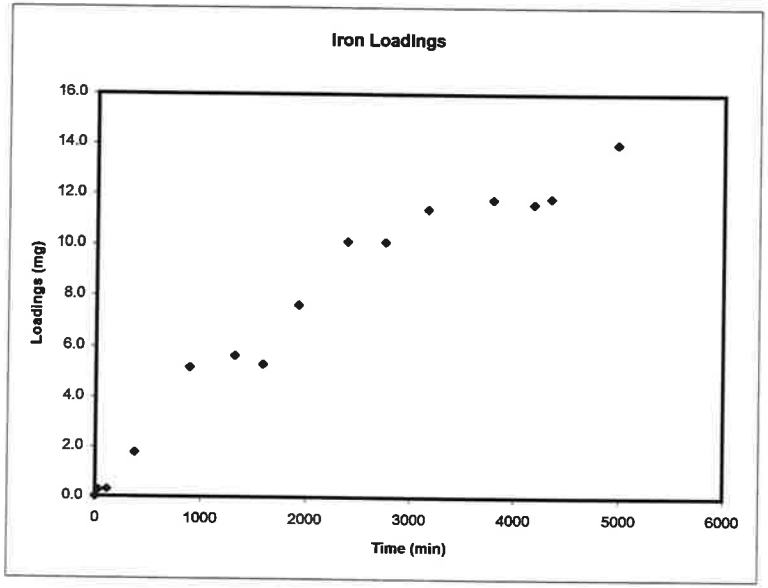

Regression
From 1583 To 4968

Production Rate (mol / min)

Sulphate	Iron	Nickel
8.09E-08	3.65E-08	2.72E-09

Oxidation Rate (mol / m2 s)

Sulphate	Iron	Nickel
3.02E-09	1.36E-09	1.01E-10

Figure D-12: Abiotic oxidation of Inco's Copper Cliff Po Conc at pH = 4, 20C (KS-024).

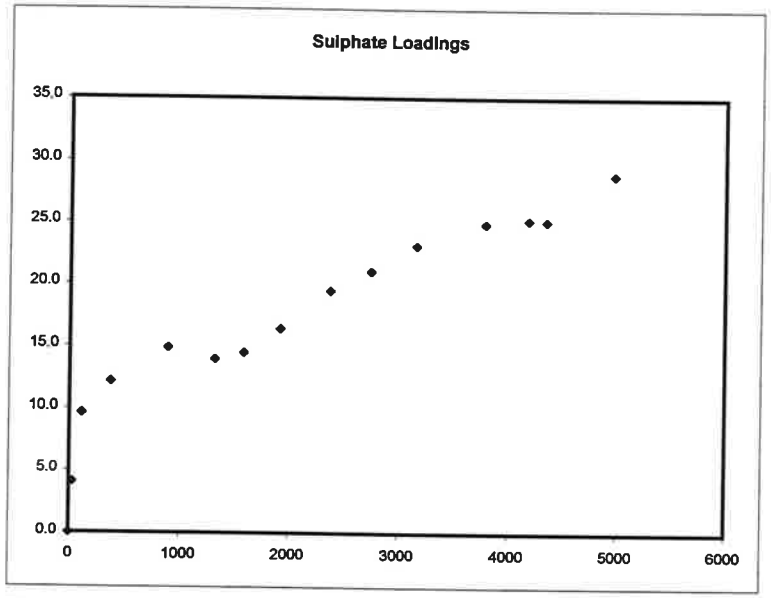

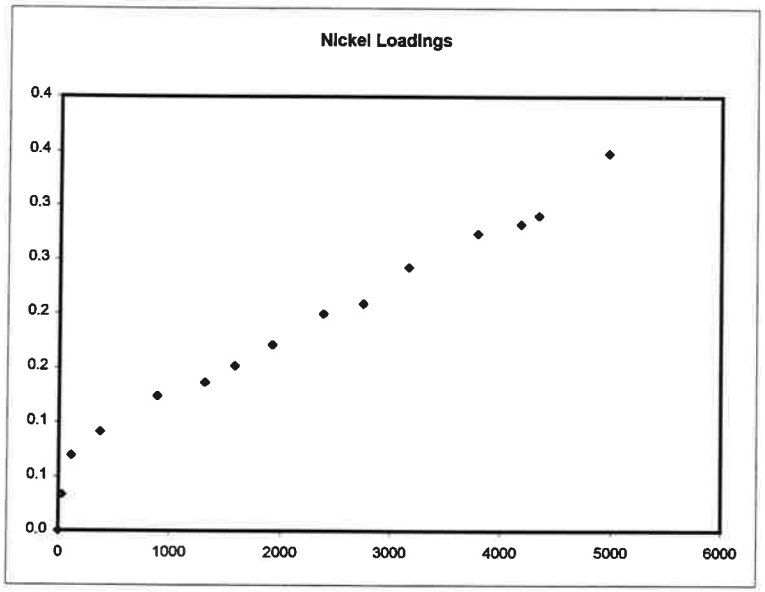

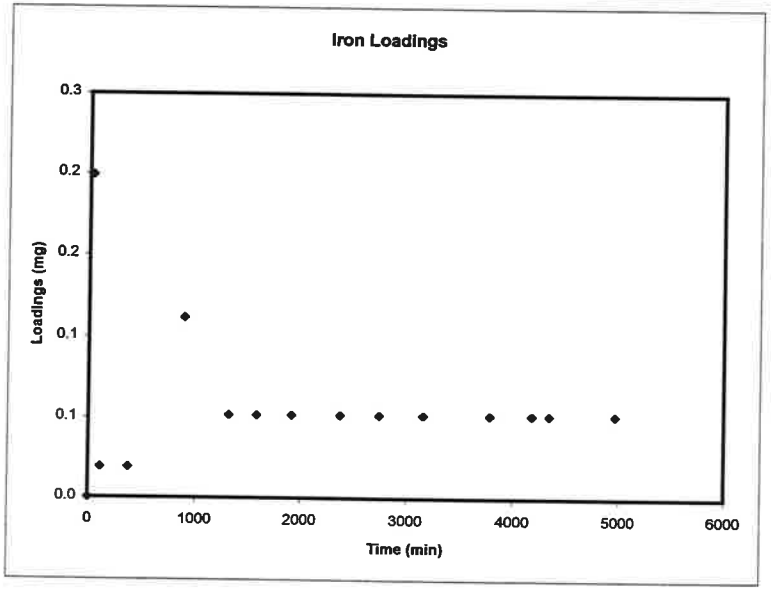

Regression
From 1583 To 4968

Production Rate (mol / min)

Sulphate	Iron	Nickel
4.06E-08	5.04E-25	9.22E-10

Oxidation Rate (mol / m2 s)

Sulphate	Iron	Nickel
1.51E-09	1.88E-26	3.44E-11

Figure D-13: Abiotic oxidation of Inco's Copper Cliff Po Conc at pH = 6, 20C (KS-025).

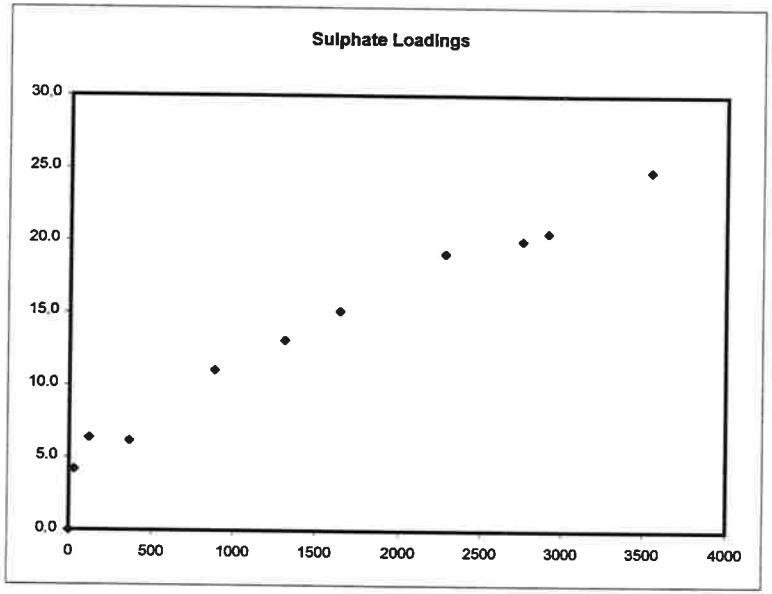

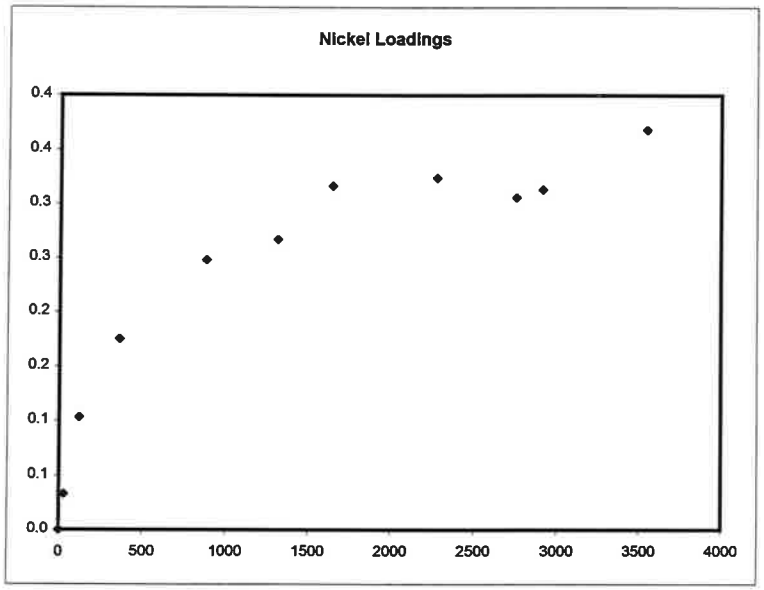

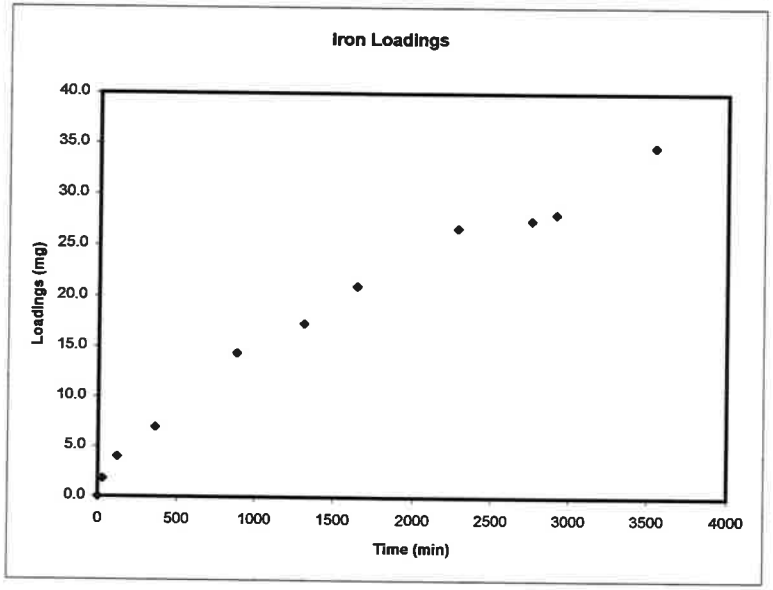

Regression
From 1311 To 3543

Production Rate (mol / min)

Sulphate	Iron	Nickel
5.14E-08	1.27E-07	5.24E-10

Oxidation Rate (mol / m2 s)

Sulphate	Iron	Nickel
1.92E-09	4.73E-09	1.95E-11

Figure D-14: Abiotic oxidation of Inco's Copper Cliff Po Conc at pH = 2, 20C (KS-026).

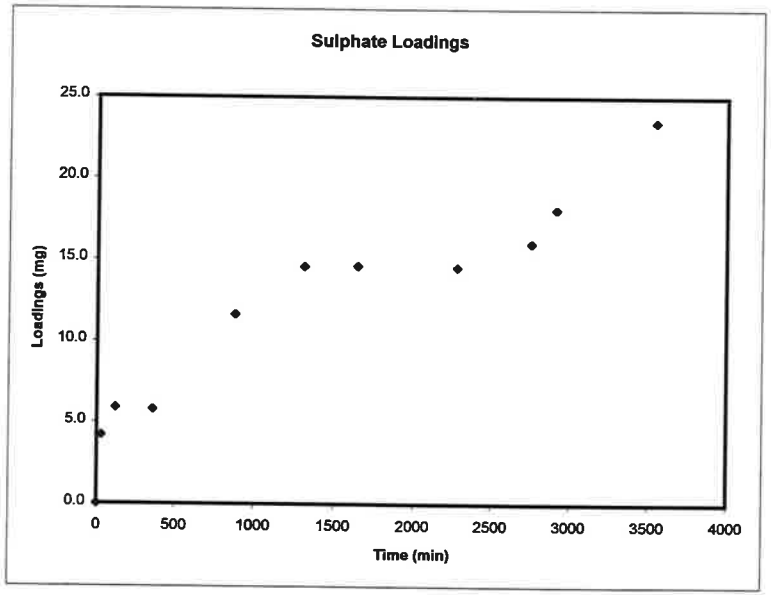

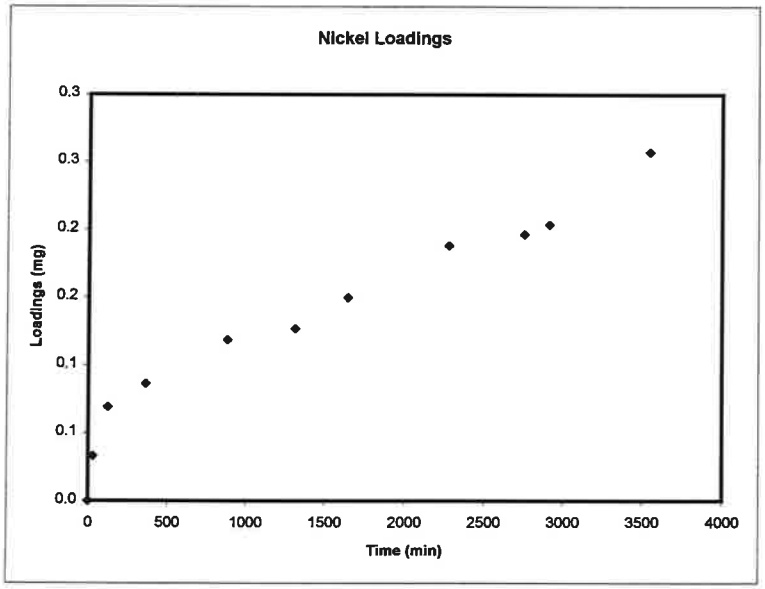

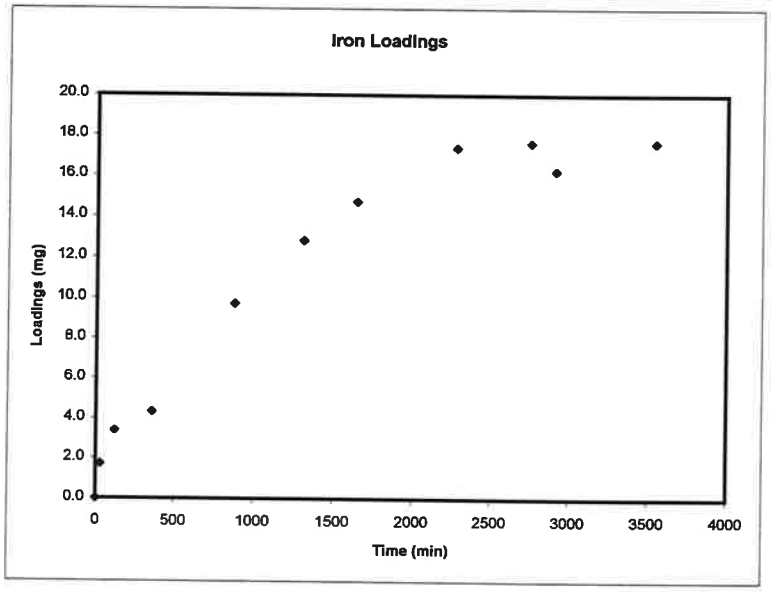

Regression
From 1311 To 3543

Production Rate (mol / min)

Sulphate	Iron	Nickel
3.72E-08	3.52E-08	9.10E-10

Oxidation Rate (mol / m2 s)

Sulphate	Iron	Nickel
1.39E-09	1.31E-09	3.39E-11

Figure D-15: Abiotic oxidation of Inco's Copper Cliff Po Conc at pH = 3, 20C (KS-027).

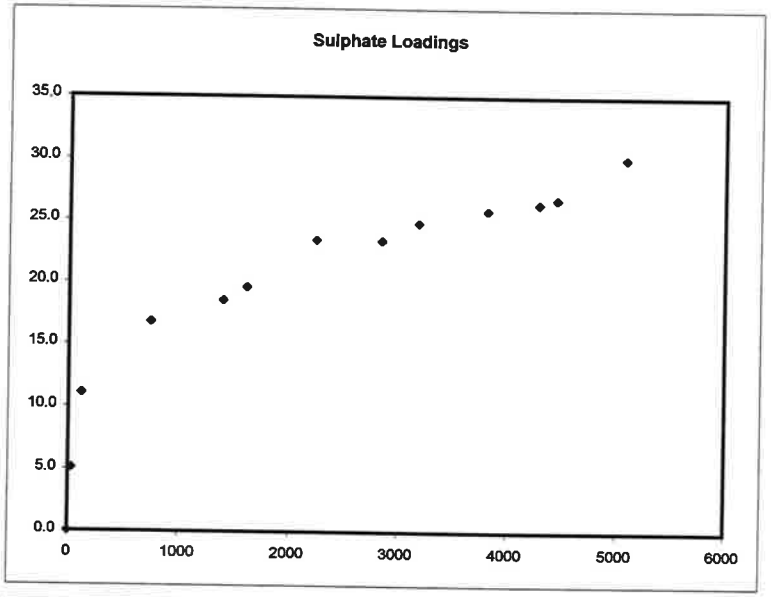

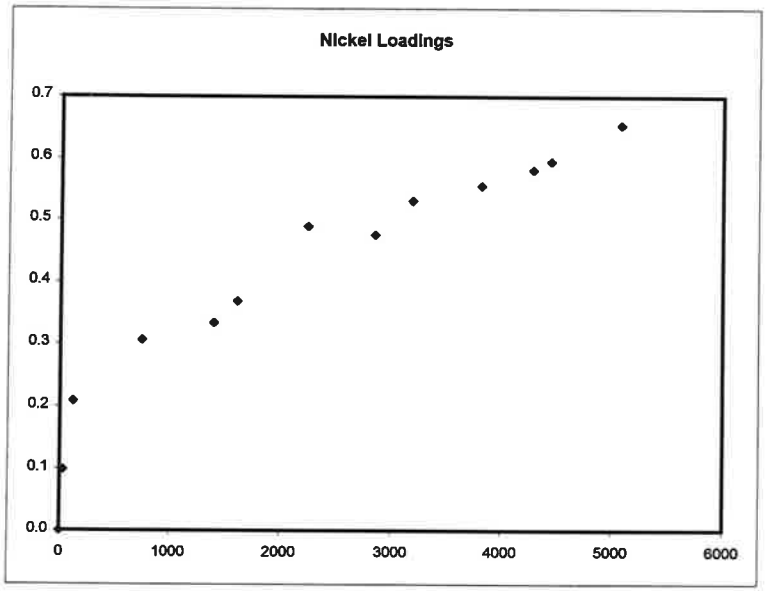

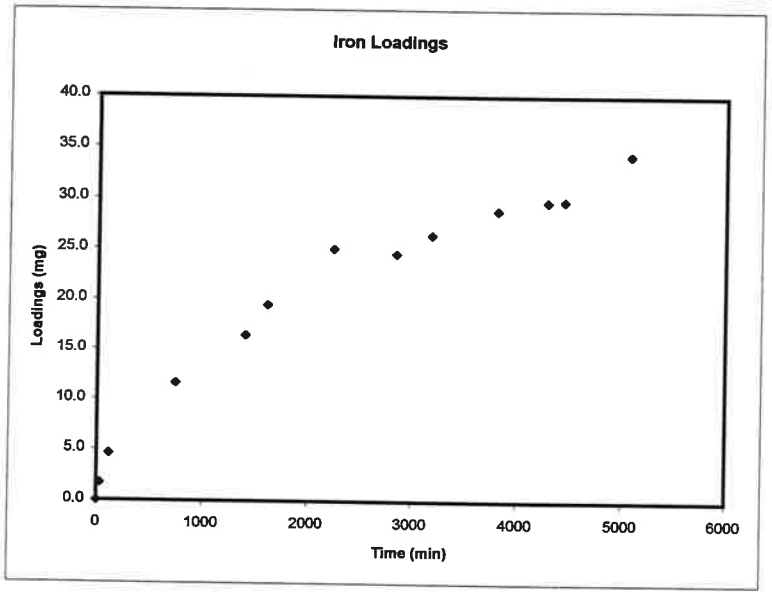

Regression
From 1402 To 5076

Production Rate (mol / min)

Sulphate	Iron	Nickel
2.80E-08	7.34E-08	1.34E-09

Oxidation Rate (mol / m2 s)

Sulphate	Iron	Nickel
1.55E-09	4.06E-09	7.4E-11

Figure D-16: Abiotic oxidation of Inco's Copper Cliff Po Conc at pH = 3, 20C (KS-029).

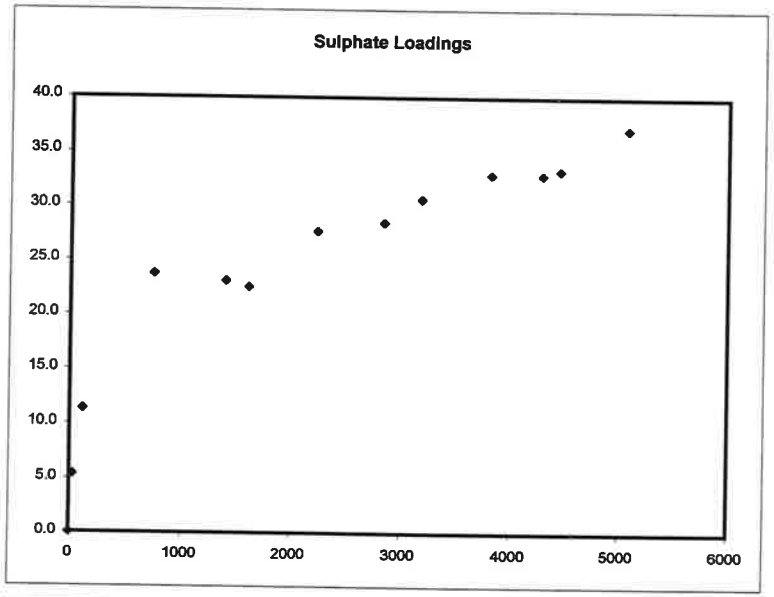

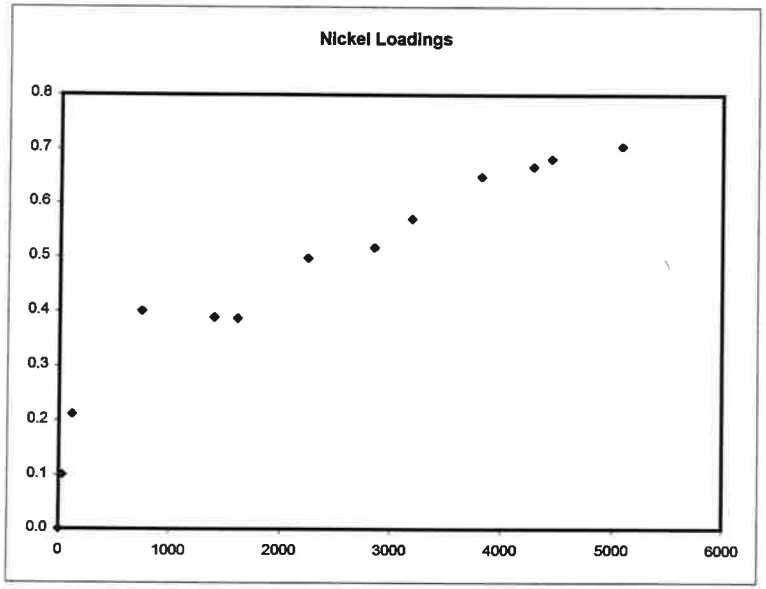

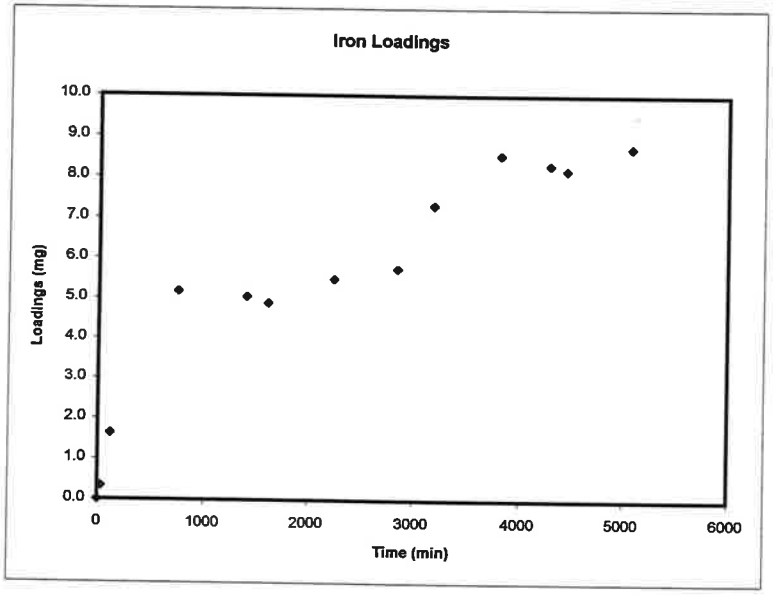

Regression
From 1402 To 5076

Production Rate (mol / min)

Sulphate	Iron	Nickel
3.84E-08	2.11E-08	1.59E-09

Oxidation Rate (mol / m2 s)

Sulphate	Iron	Nickel
2.12E-09	1.17E-09	8.76E-11

Figure D-17: Abiotic oxidation of Inco's Copper Cliff Po Conc at pH = 4, 20C (KS-030).

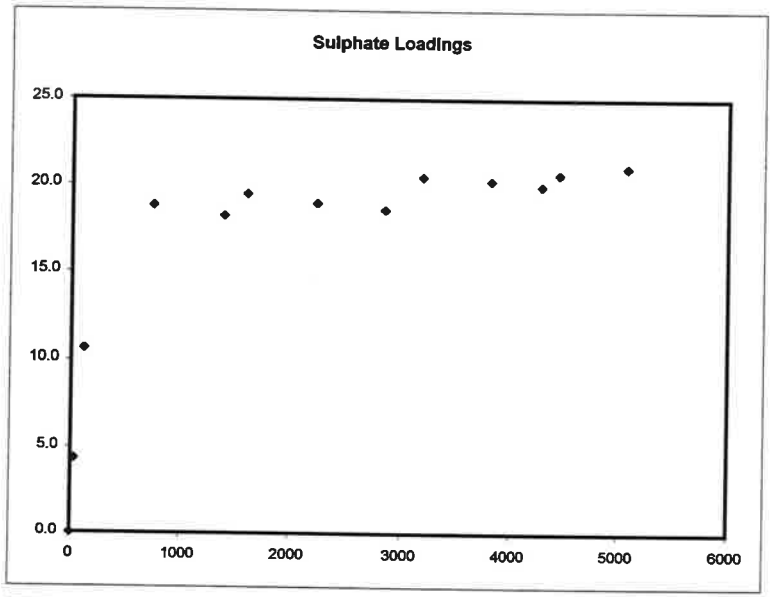

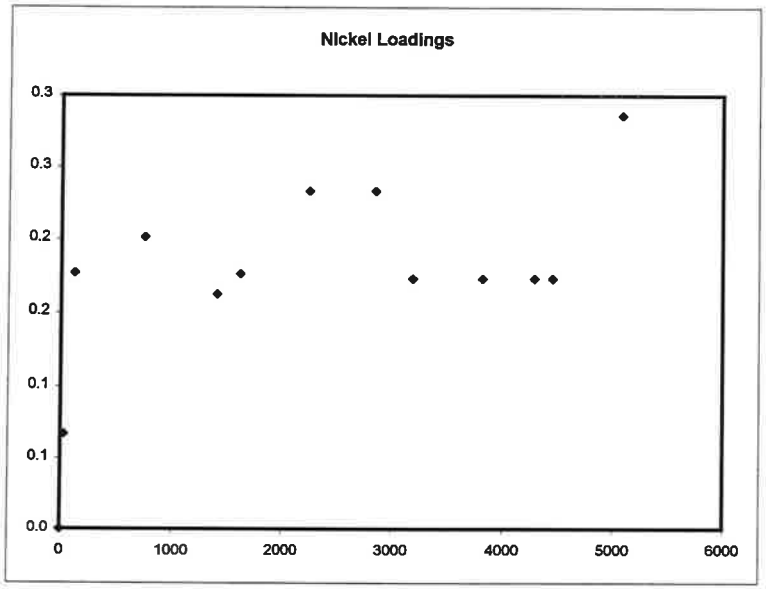

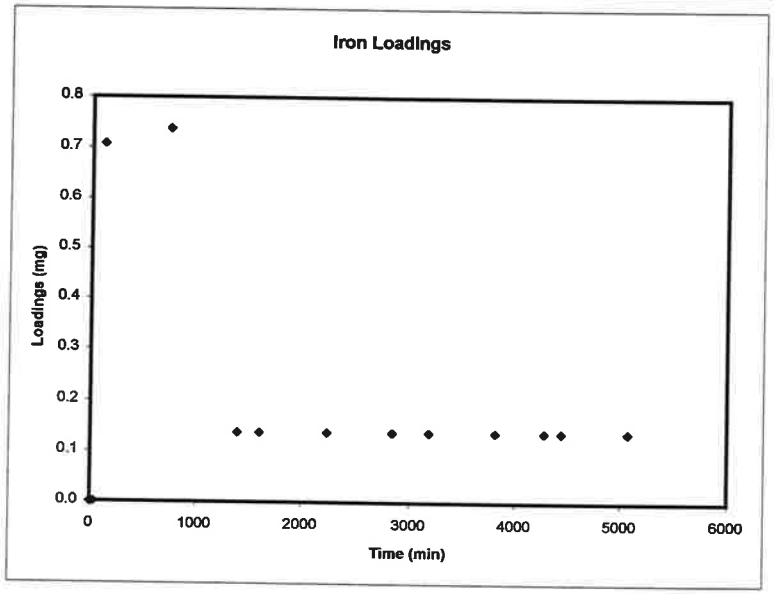

Regression
From 1402 To 5076

Production Rate (mol / min)

Sulphate	Iron	Nickel
6.57E-09	0.00E+00	1.83E-10

Oxidation Rate (mol / m2 s)

Sulphate	Iron	Nickel
3.63E-10	0.00E+00	1.01E-11

Figure D-18: Abiotic oxidation of Inco's Copper Cliff Po Conc at pH = 6, 20C (KS-031).

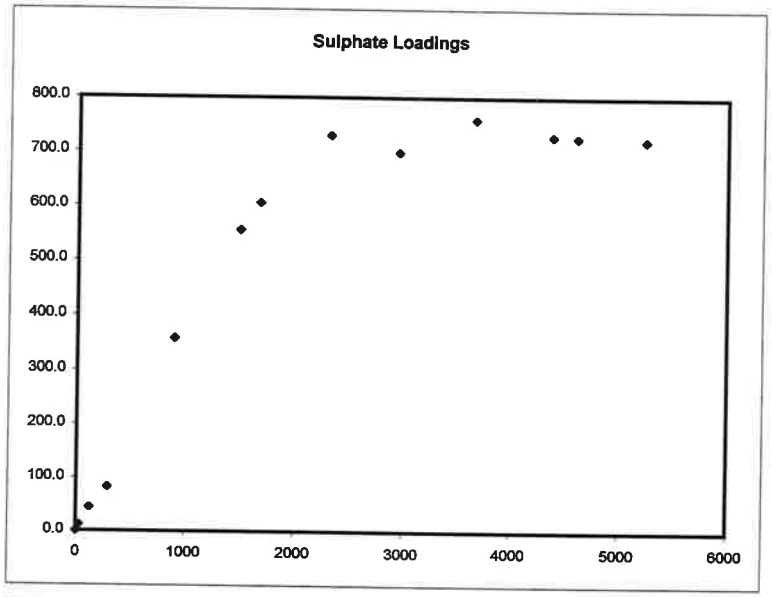

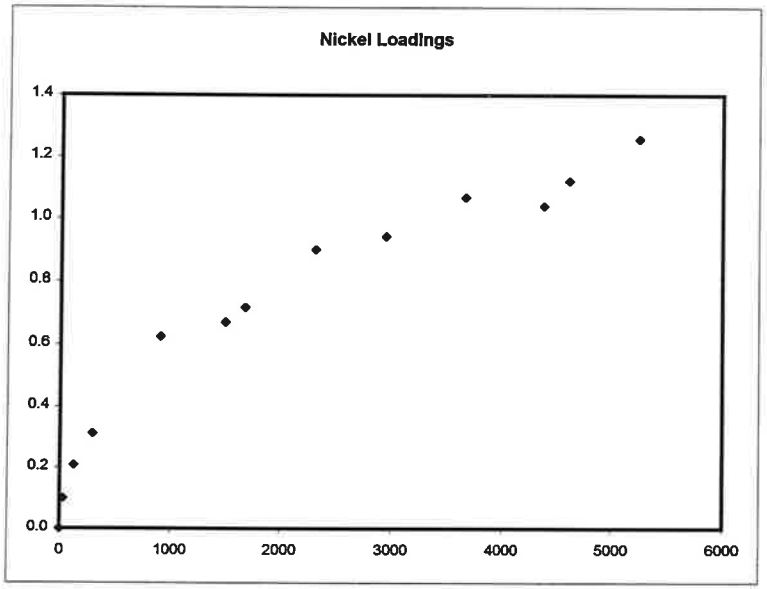

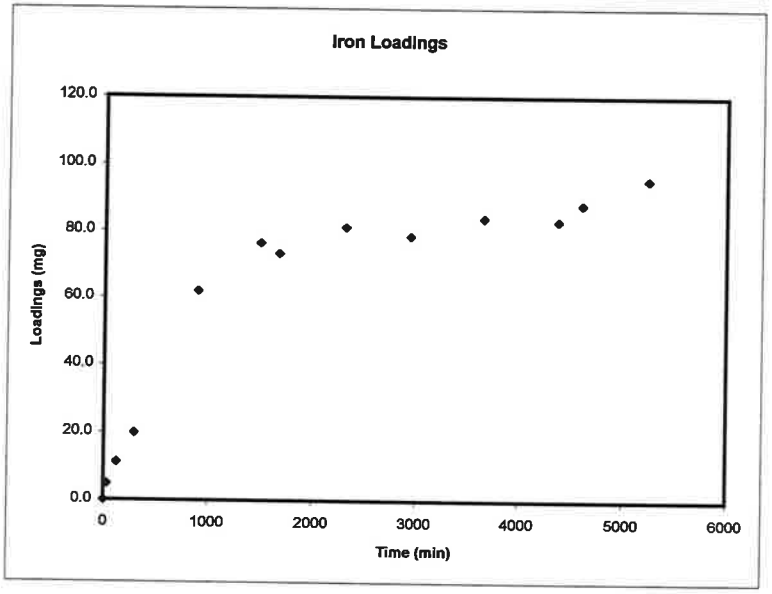

Regression
From 1675 To 5240

Production Rate (mol / min)

Sulphate	Iron	Nickel
2.43E-07	8.85E-08	2.18E-09

Oxidation Rate (mol / m2 s)

Sulphate	Iron	Nickel
9.06E-09	3.3E-09	8.12E-11

Figure D-19: Abiotic oxidation of Inco's Copper Cliff Po Conc at pH = 2, 40C (KS-036).

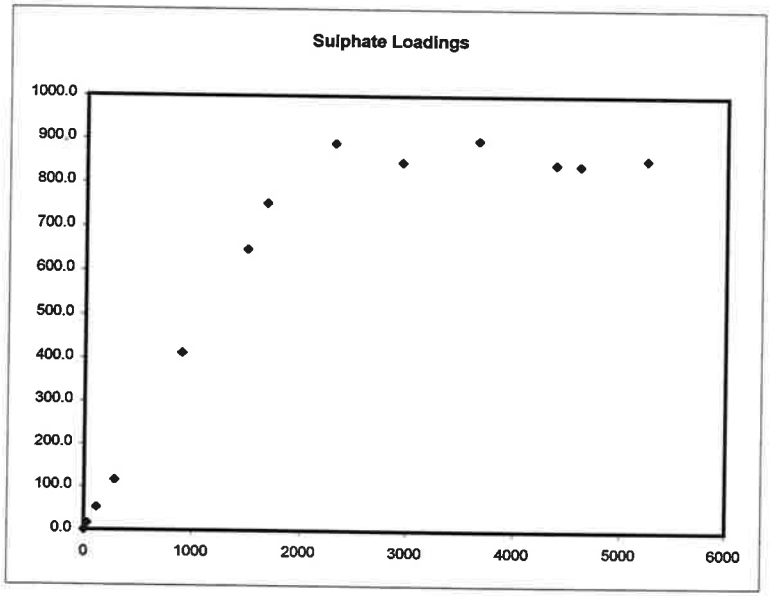

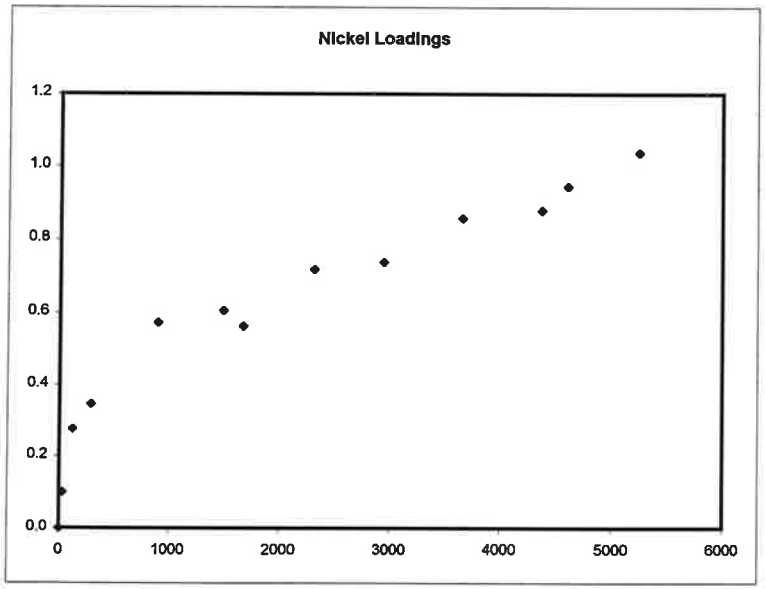

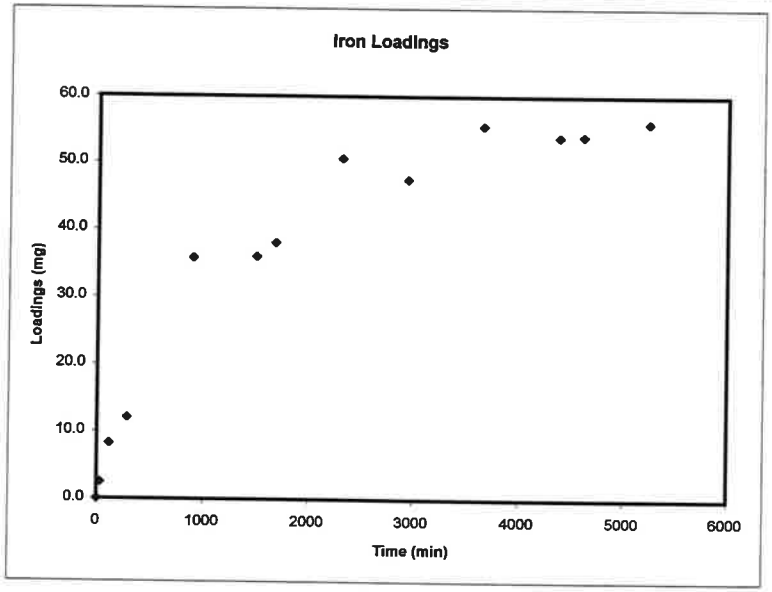

Regression
From 1675 To 5240

Production Rate (mol / min)

Sulphate	Iron	Nickel
1.37E-07	7.38E-08	2.04E-09

Oxidation Rate (mol / m2 s)

Sulphate	Iron	Nickel
5.12E-09	2.75E-09	7.6E-11

Figure D-20: Abiotic oxidation of Inco's Copper Cliff Po Conc at pH = 3, 40C (KS-037).

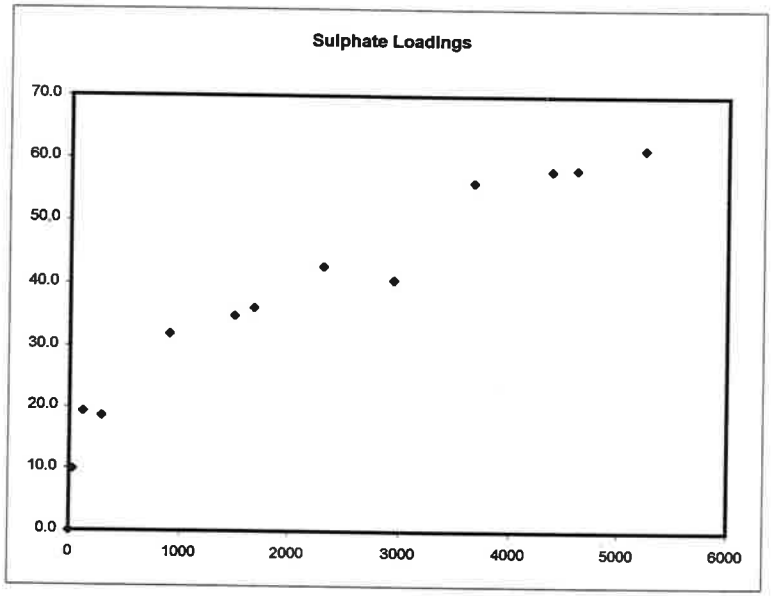

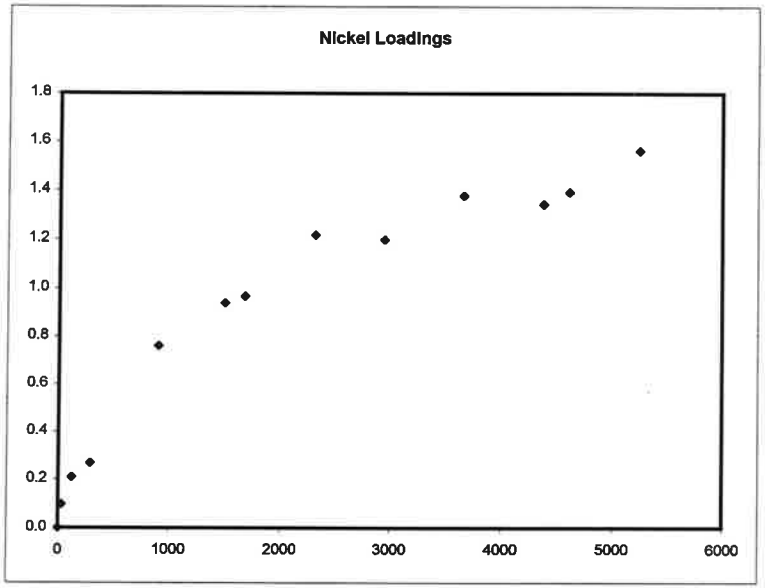

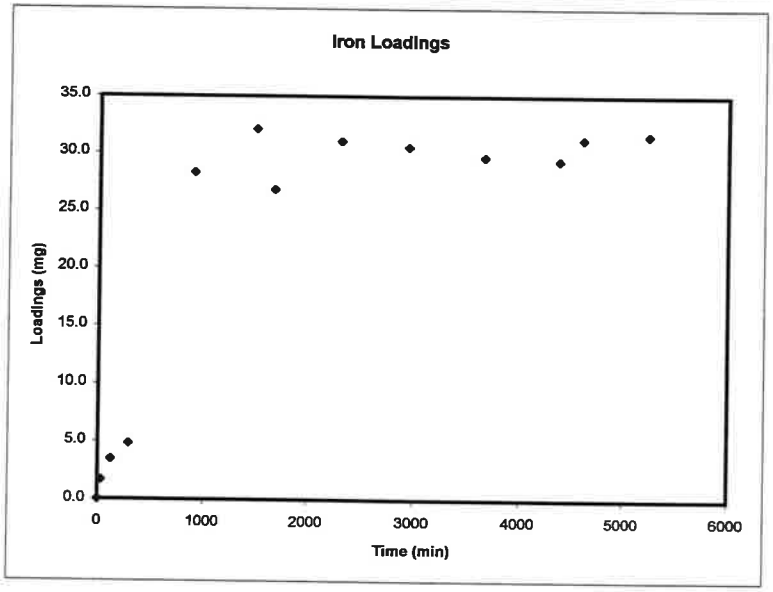

Regression
From 1675 To 5240

Production Rate (mol / min)

Sulphate	Iron	Nickel
7.82E-08	1.38E-08	2.32E-09

Oxidation Rate (mol / m2 s)

Sulphate	Iron	Nickel
2.92E-09	5.15E-10	8.64E-11

Figure D-21: Abiotic oxidation of Inco's Copper Cliff Po Conc at pH = 4, 40C (KS-038).

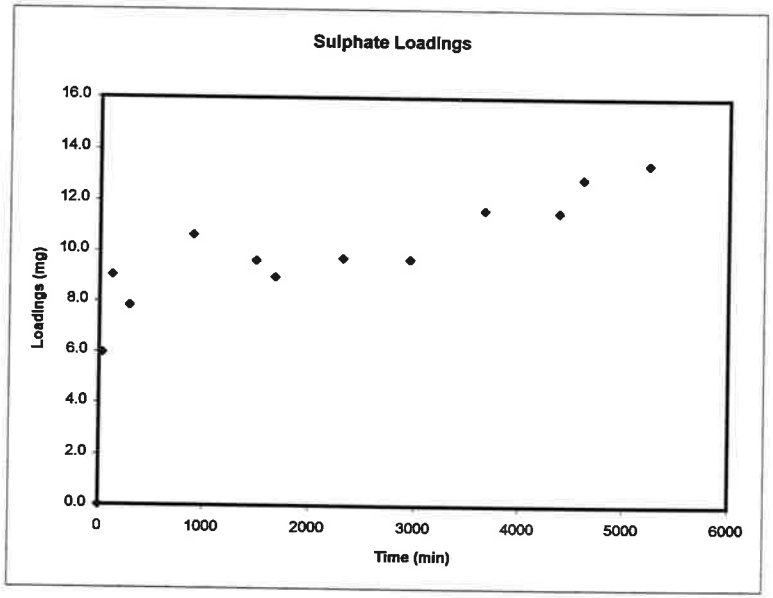

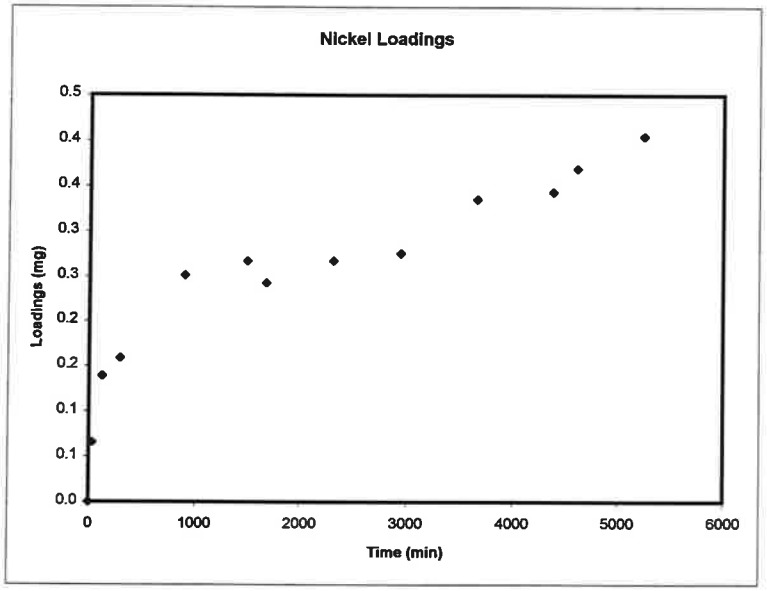

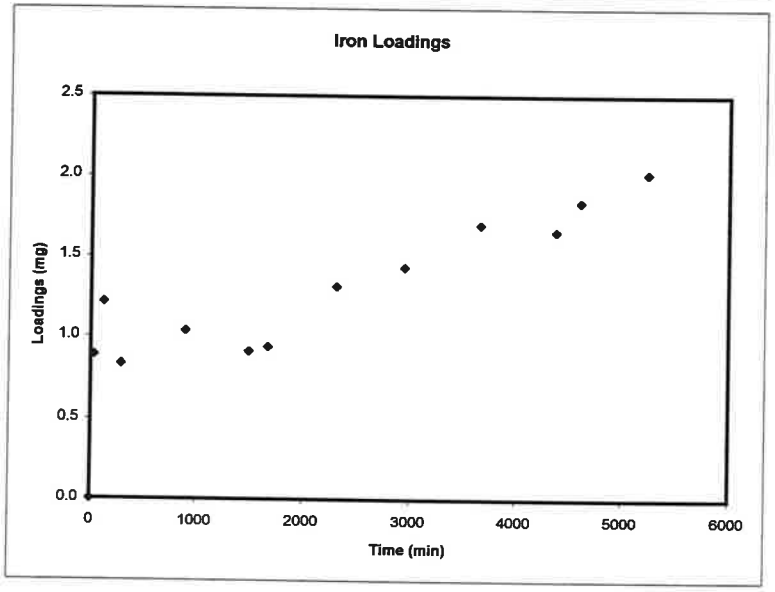

Regression
From 1675 To 5240

Production Rate (mol / min)

Sulphate	Iron	Nickel
1.32E-08	4.80E-09	7.65E-10

Oxidation Rate (mol / m2 s)

Sulphate	Iron	Nickel
4.9E-10	1.79E-10	2.85E-11

Figure D-22: Abiotic oxidation of Inco's Copper Cliff Po Conc at pH = 6, 40C (KS-039).

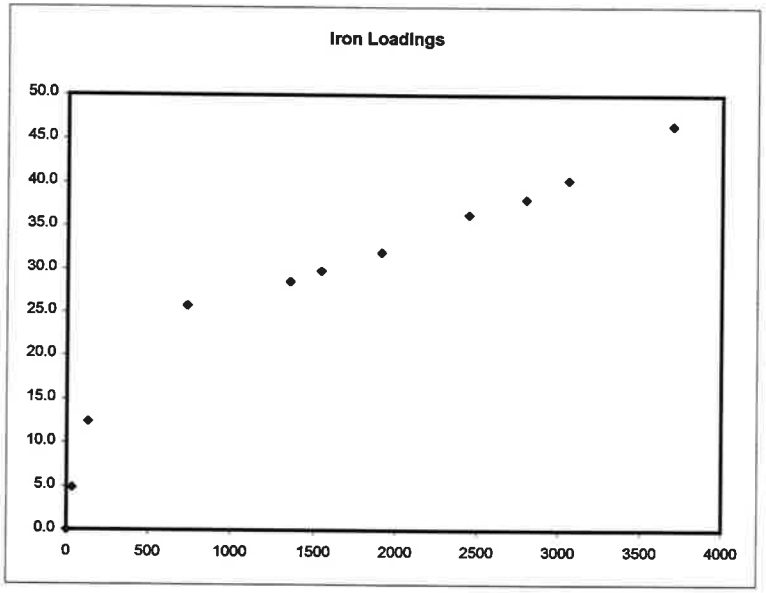

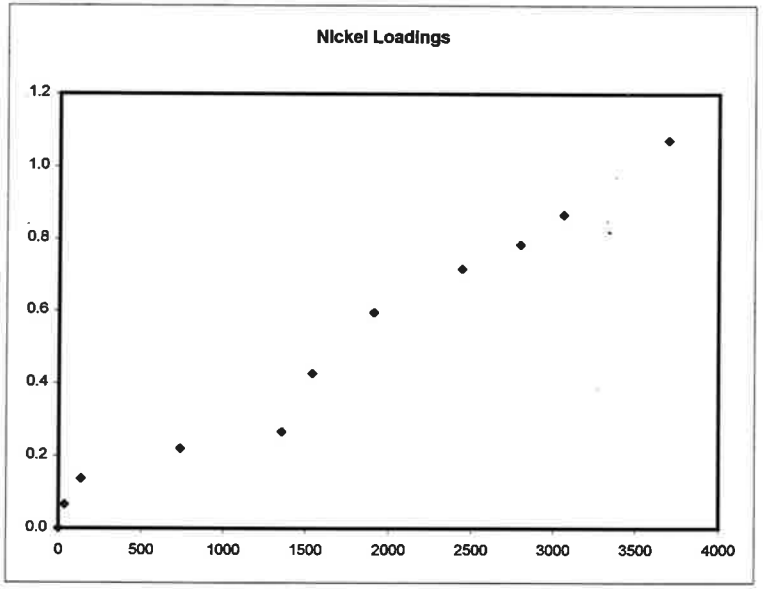

Regression
From 1353 To 3694

Production Rate (mol / min)

Sulphate	Iron	Nickel
	1.34E-07	5.35E-09

Oxidation Rate (mol / m2 s)

Sulphate	Iron	Nickel
	4.98E-09	2E-10

Figure D-23: Abiotic oxidation (with 10E-3M EDTA) of Inco's Copper Cliff Po Conc at pH = 2, 30C (KS-012).

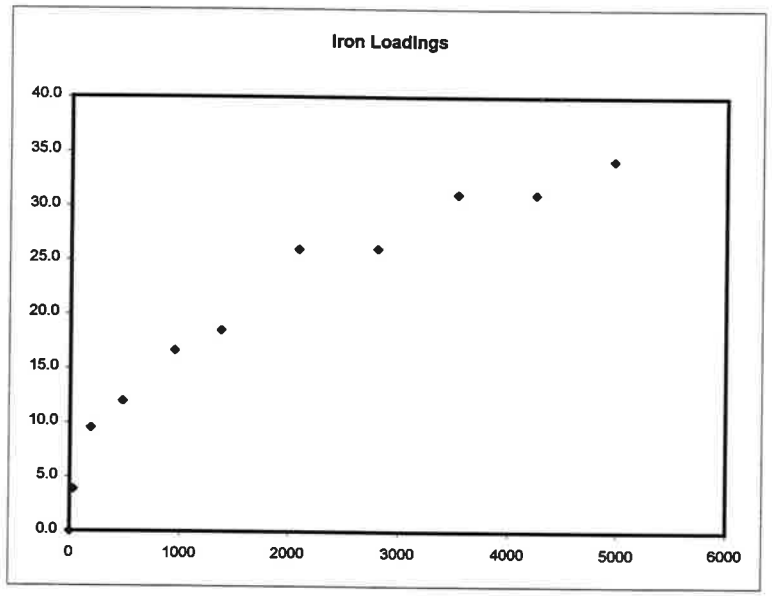

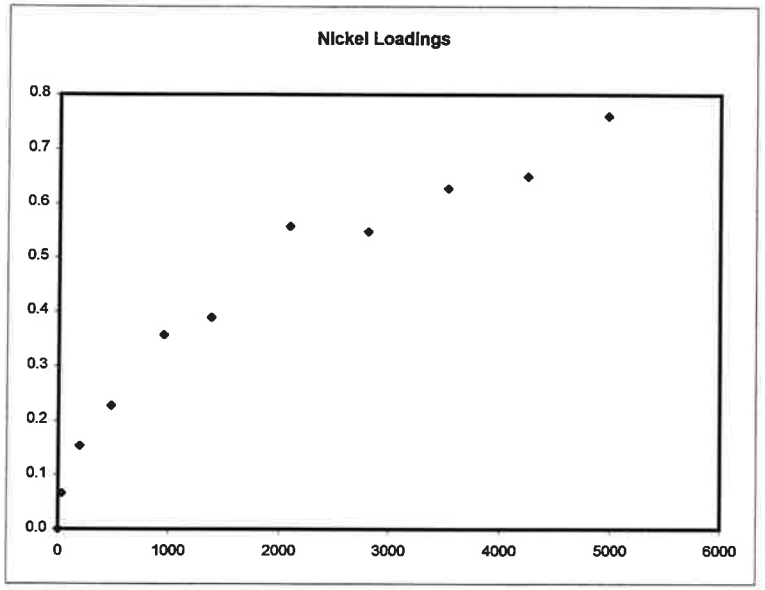

Regression
From 1378 To 4971

Production Rate (mol / min)

Sulphate	Iron	Nickel
	7.04E-08	1.5E-09

Oxidation Rate (mol / m2 s)

Sulphate	Iron	Nickel
	2.62E-09	5.59E-11

Figure D-24: Abiotic oxidation (with 10E-3M EDTA) of Inco's Copper Cliff Po Conc at pH = 3, 30C (KS-010).

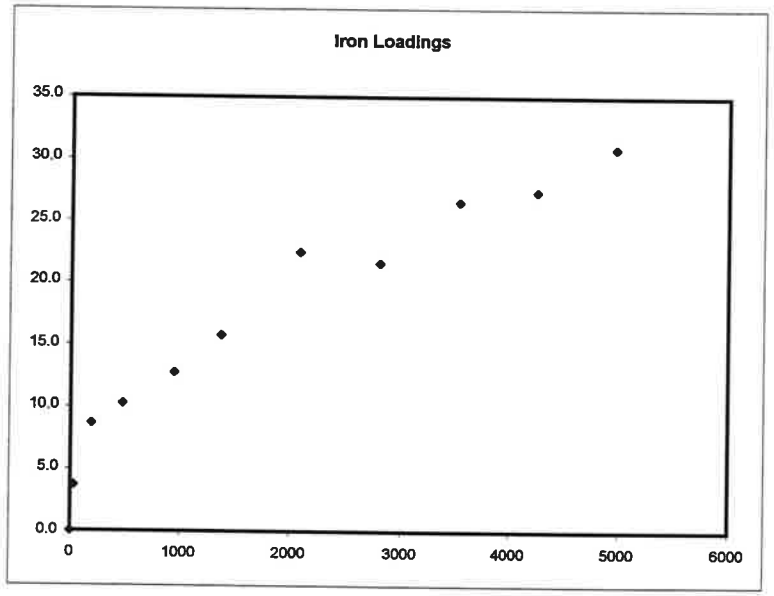

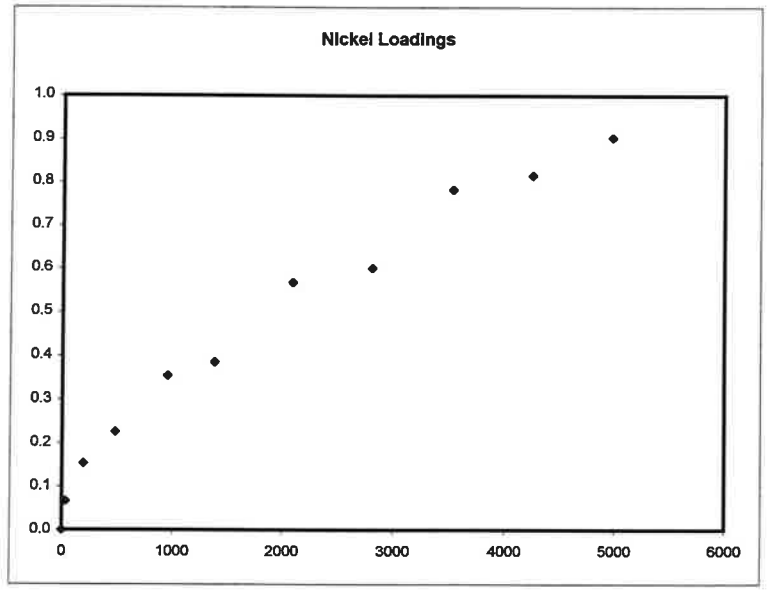

Regression
From 1378 To 4971

Production Rate (mol / min)

Sulphate	Iron	Nickel
	6.78E-08	2.38E-09

Oxidation Rate (mol / m2 s)

Sulphate	Iron	Nickel
	2.53E-09	8.86E-11

Figure D-25: Abiotic oxidation (with 10E-3M EDTA) of Inco's Copper Cliff Po Conc at pH = 4, 30C (KS-011).

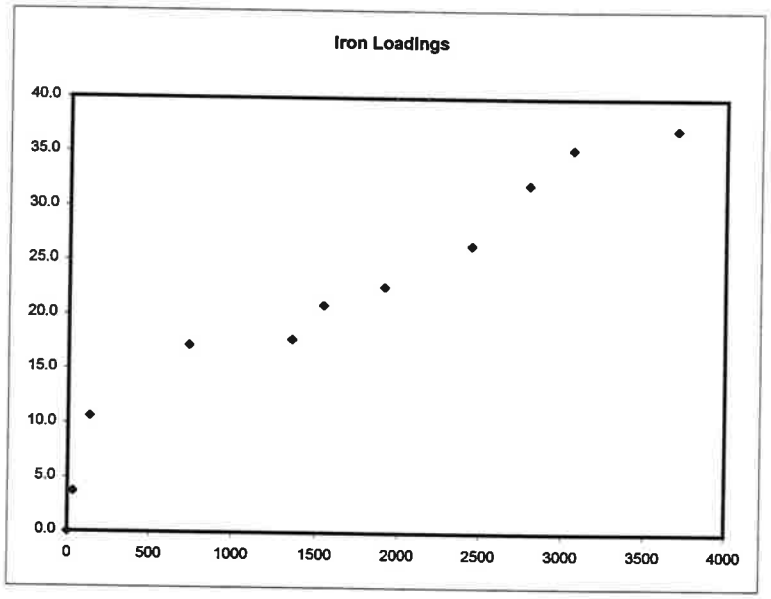

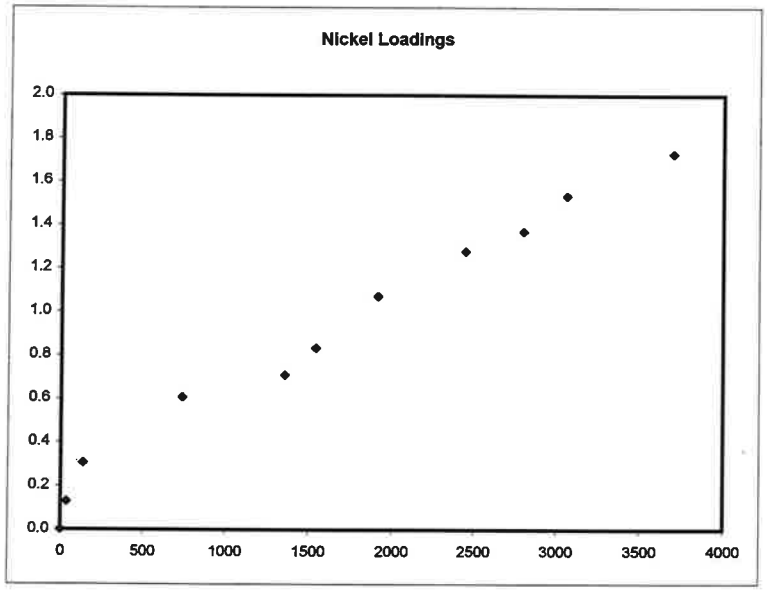

Regression
From 1353 To 3694

Production Rate (mol / min)

Sulphate	Iron	Nickel
	1.55E-07	7.33E-09

Oxidation Rate (mol / m2 s)

Sulphate	Iron	Nickel
	5.79E-09	2.73E-10

Figure D-26: Abiotic oxidation (with 10E-3M EDTA) of Inco's Copper Cliff Po Conc at pH = 6, 30C (KS-013).

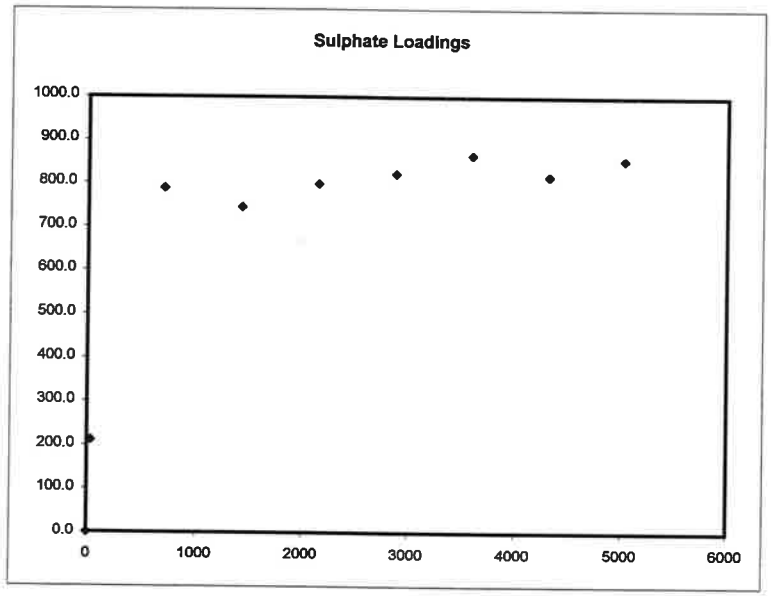

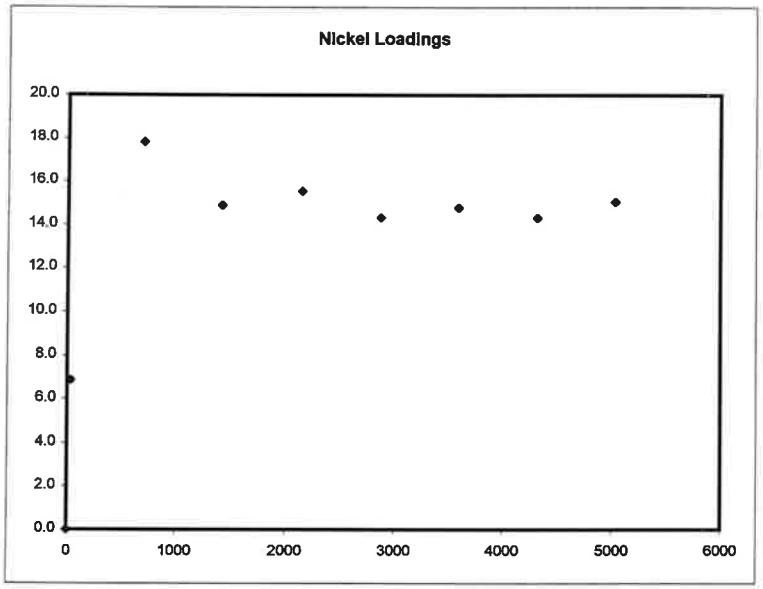

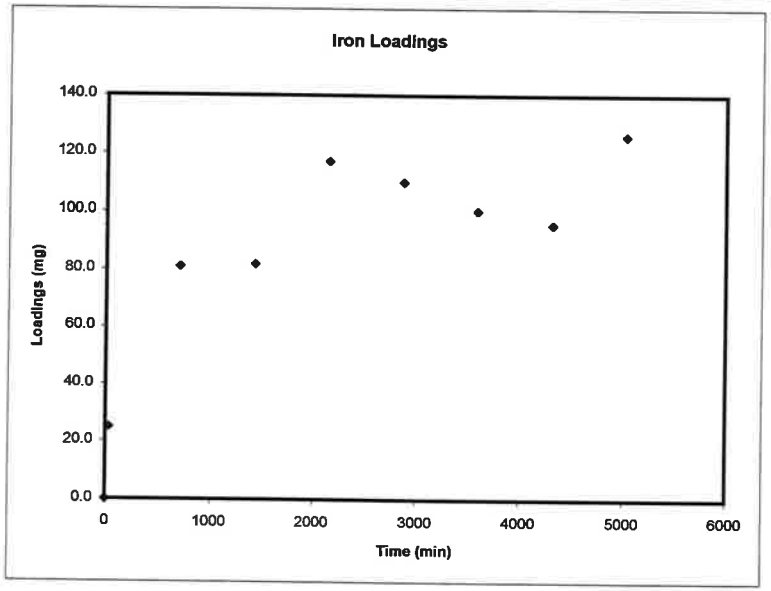

Regression
From 1420 To 5023

Production Rate (mol / min)

Sulphate	Iron	Nickel
2.67E-07	1.04E-07	-1.65E-09

Oxidation Rate (mol / m2 s)

Sulphate	Iron	Nickel
9.96E-09	3.87E-09	-6.1E-11

Figure D-27: Bacterial inoculated oxidation of Inco's Copper Cliff Po Conc at pH = 2, 40C (KS-040).

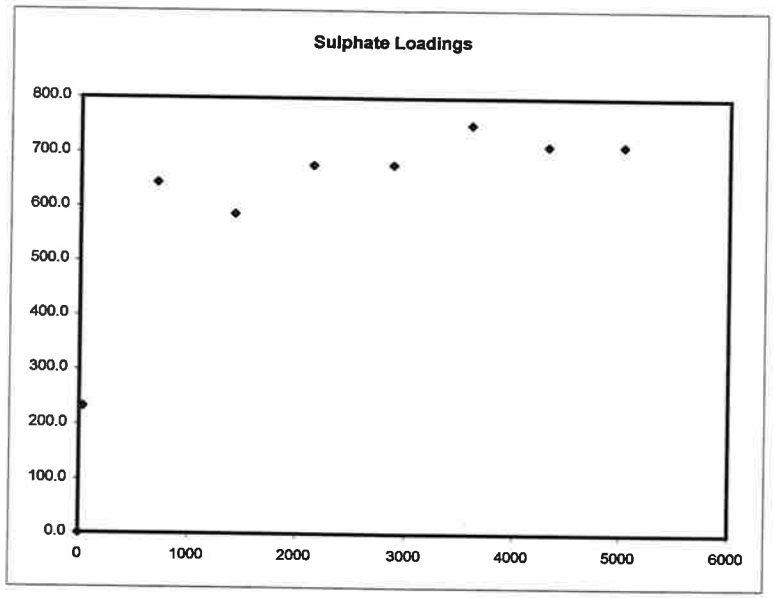

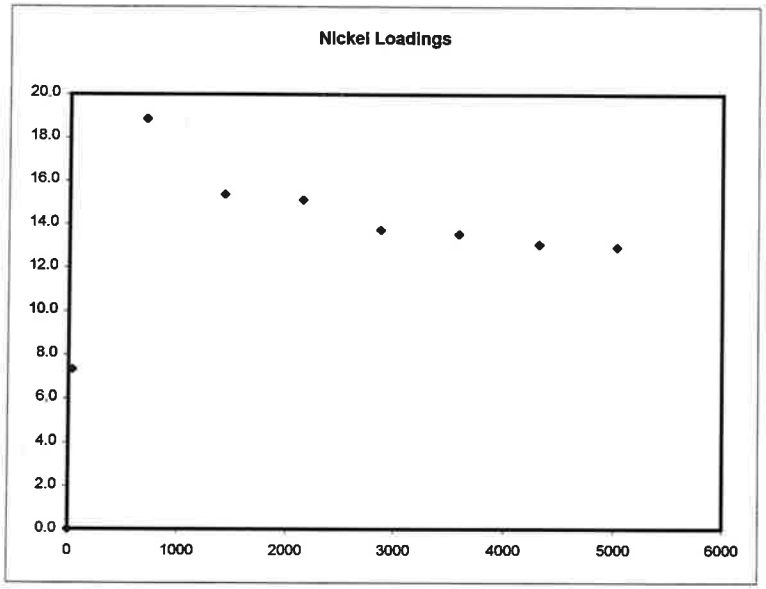

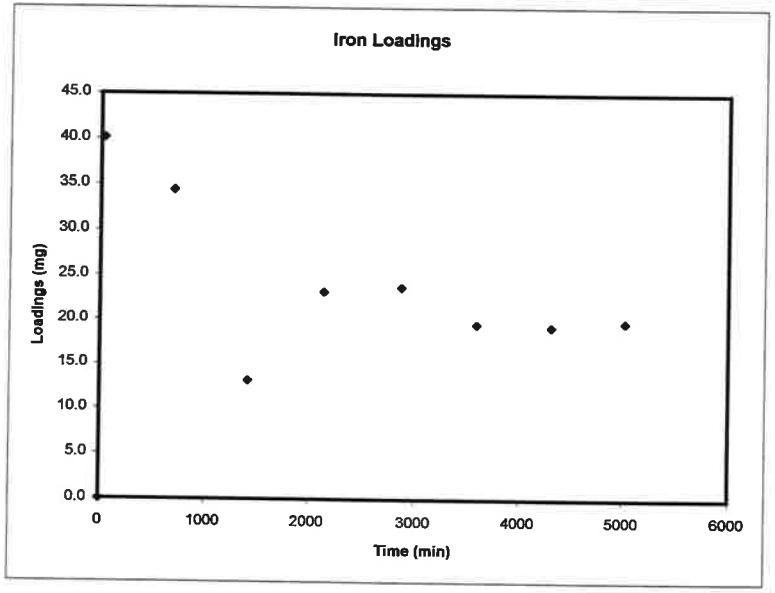

Regression
From 1420 To 5023

Production Rate (mol / min)

Sulphate	Iron	Nickel
3.36E-07	1.22E-08	-1.25E-08

Oxidation Rate (mol / m2 s)

Sulphate	Iron	Nickel
1.25E-08	4.55E-10	-4.7E-10

Figure D-28: Bacterial inoculated oxidation of Inco's Copper Cliff Po Conc at pH = 3, 40C (KS-041).

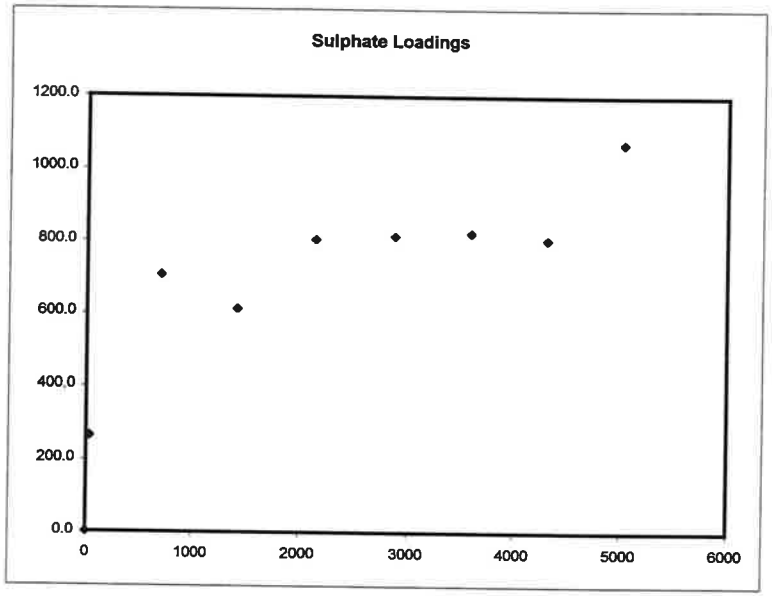

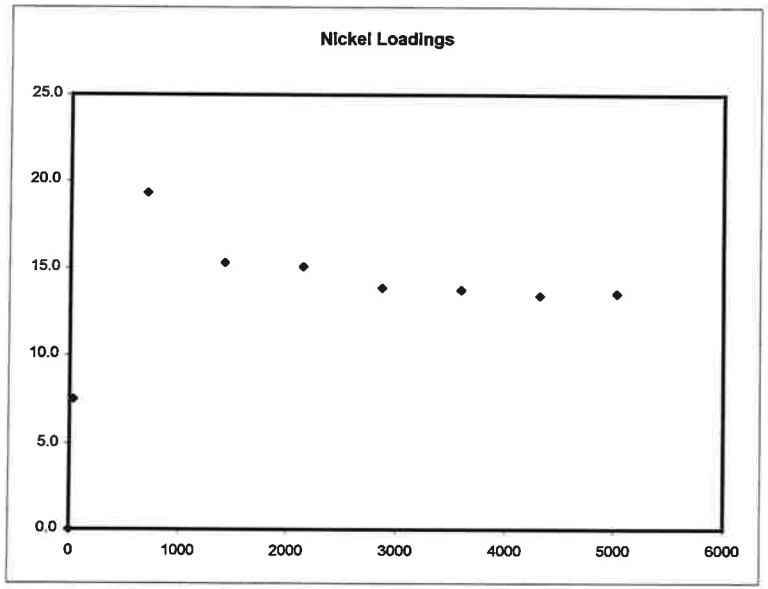

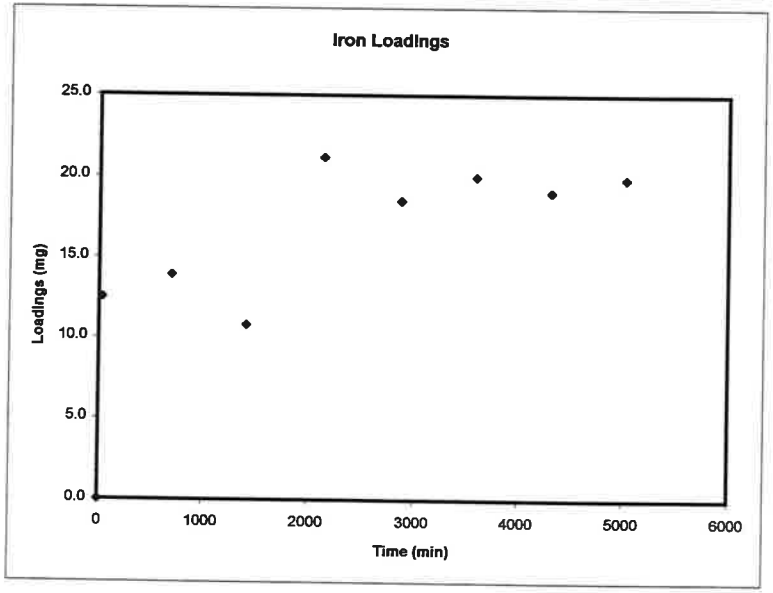

Regression
From 1420 To 5023

Production Rate (mol / min)

Sulphate	Iron	Nickel
9.47E-07	2.88E-08	-9.37E-09

Oxidation Rate (mol / m2 s)

Sulphate	Iron	Nickel
3.53E-08	1.08E-09	-3.5E-10

Figure D-29: Bacterial inoculated oxidation of Inco's Copper Cliff Po Conc at pH = 4, 40C (KS-042).

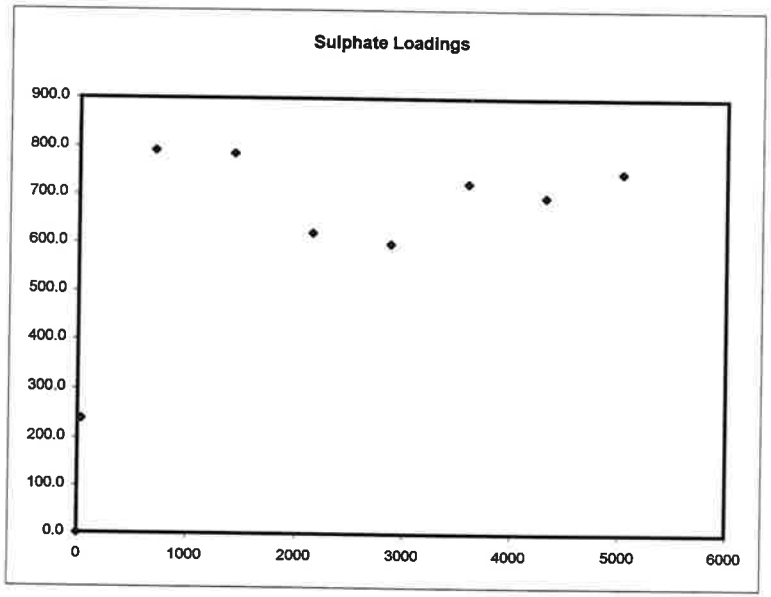

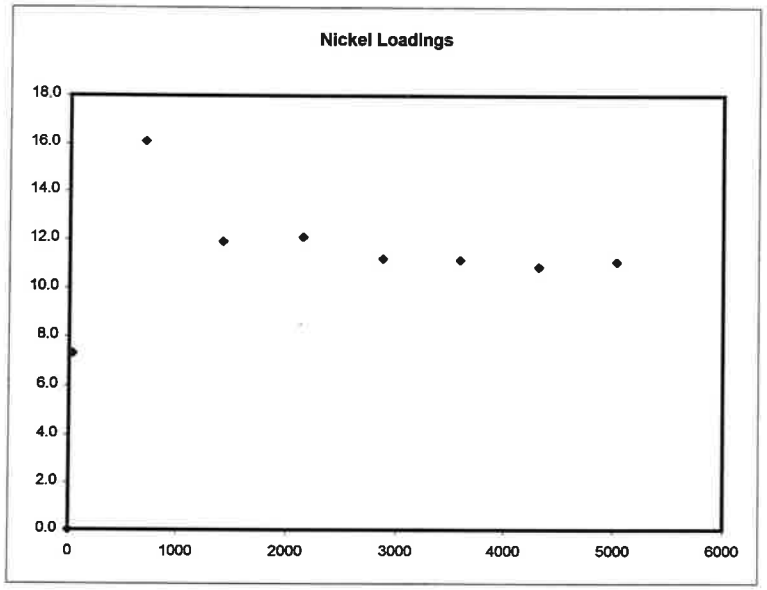

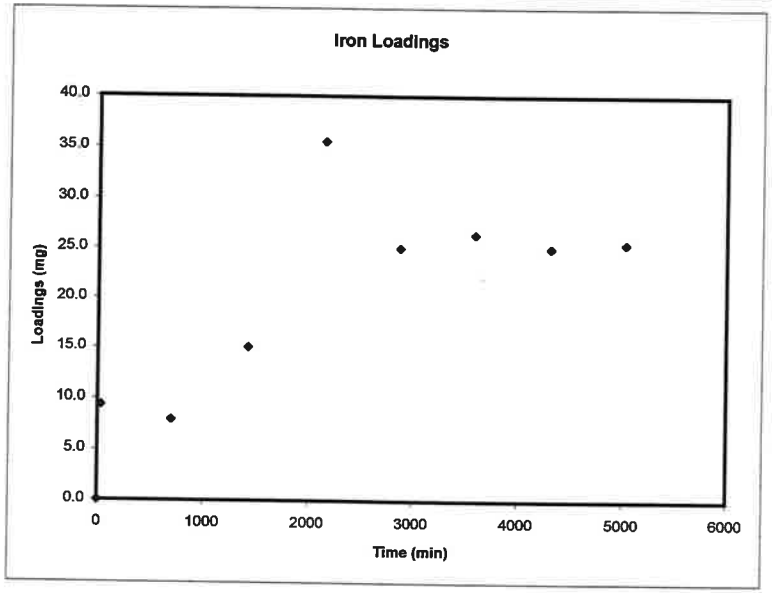

Regression
From 1420 To 5023

Production Rate (mol / min)

Sulphate	Iron	Nickel
6.21E-08	1.56E-08	-5.35E-09

Oxidation Rate (mol / m2 s)

Sulphate	Iron	Nickel
2.31E-09	5.82E-10	-2E-10

Figure D-30: Bacterial inoculated oxidation of Inco's Copper Cliff Po Conc at pH = 6, 40C (KS-043).

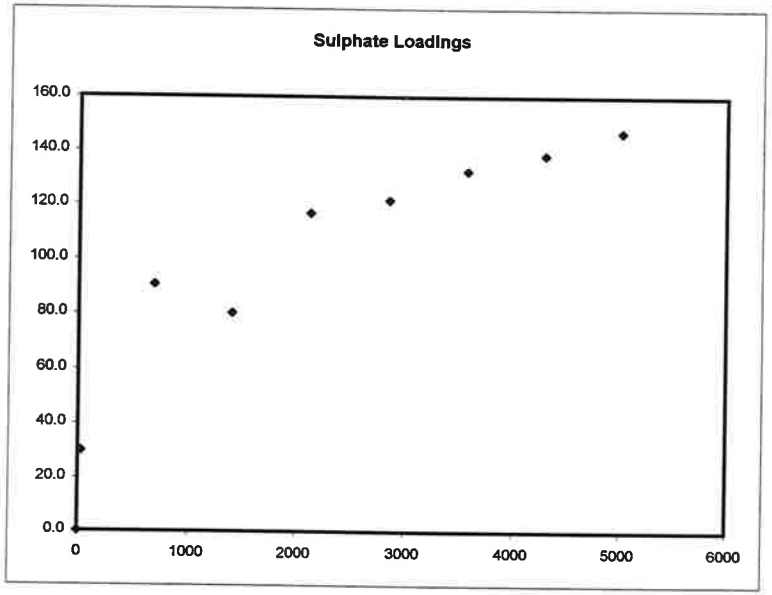

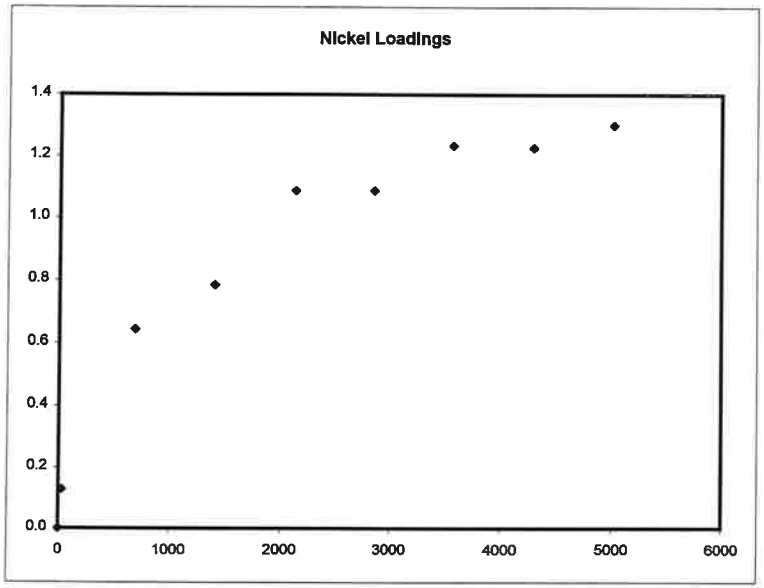

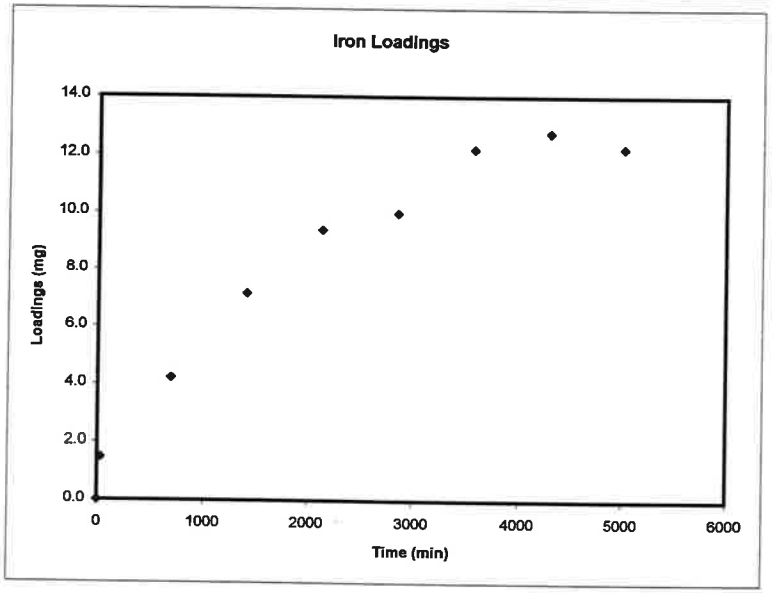

Regression
From 1405 To 5010

Production Rate (mol / min)

Sulphate	Iron	Nickel
1.69E-07	2.68E-08	2.11E-09

Oxidation Rate (mol / m2 s)

Sulphate	Iron	Nickel
6.3E-09	9.98E-10	7.88E-11

Figure D-31: Abiotic oxidation (with growth medium) of Inco's Copper Cliff Po Conc at pH = 2, 40C (KS-044).

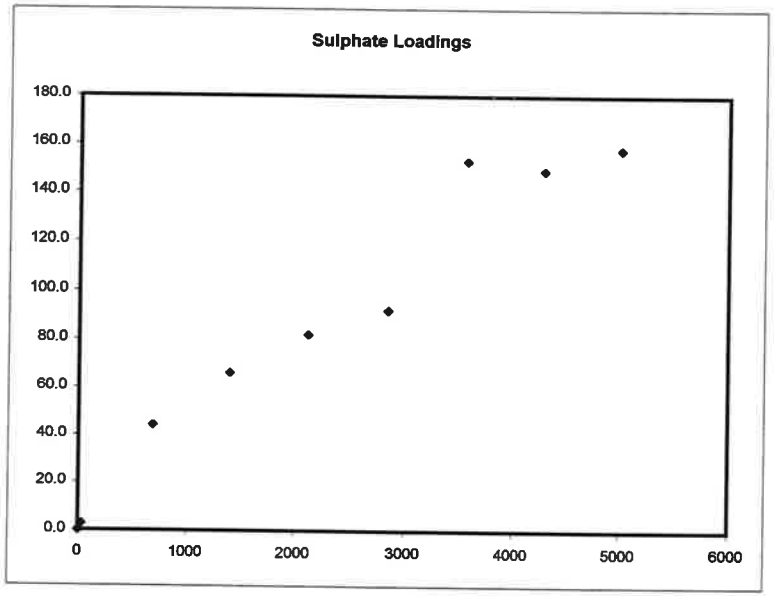

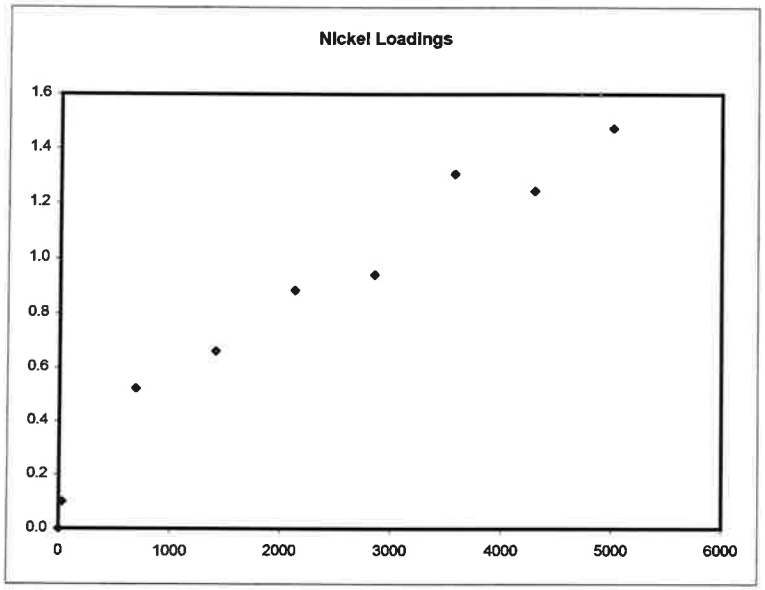

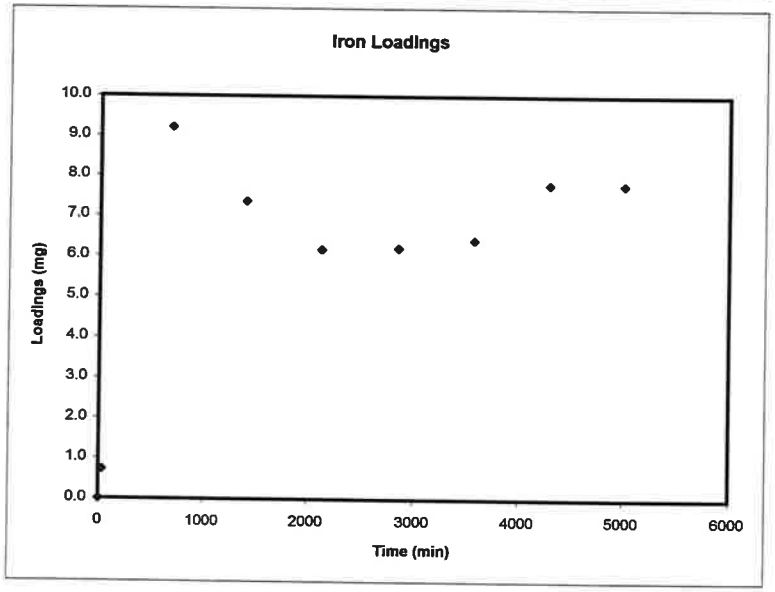

Regression
From 1405 To 5010

Production Rate (mol / min)

Sulphate	Iron	Nickel
2.97E-07	5.07E-09	3.71E-09

Oxidation Rate (mol / m2 s)

Sulphate	Iron	Nickel
1.11E-08	1.89E-10	1.38E-10

Figure D-32: Abiotic oxidation (with growth medium) of Inco's Copper Cliff Po Conc at pH = 3, 40C (KS-045).

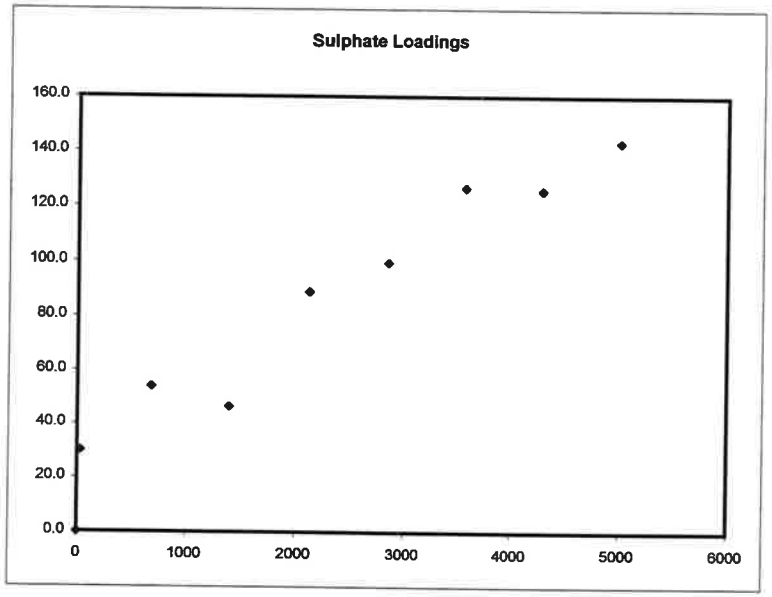

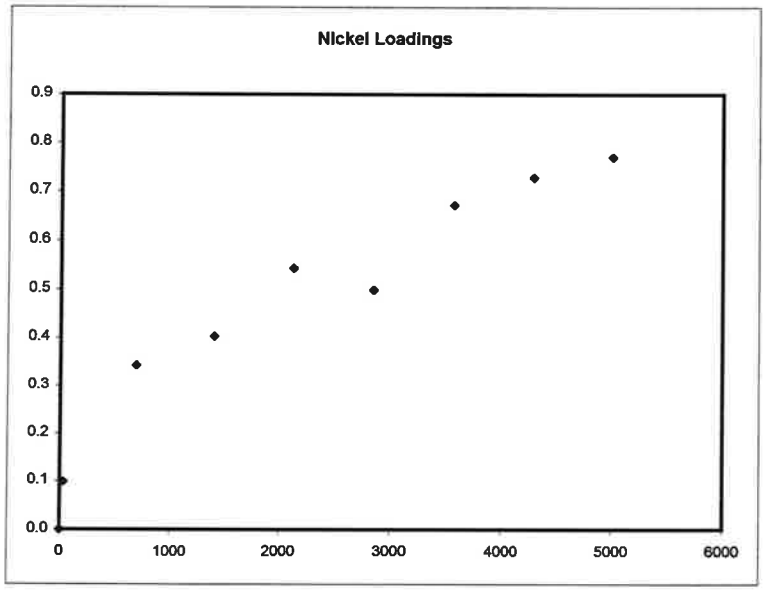

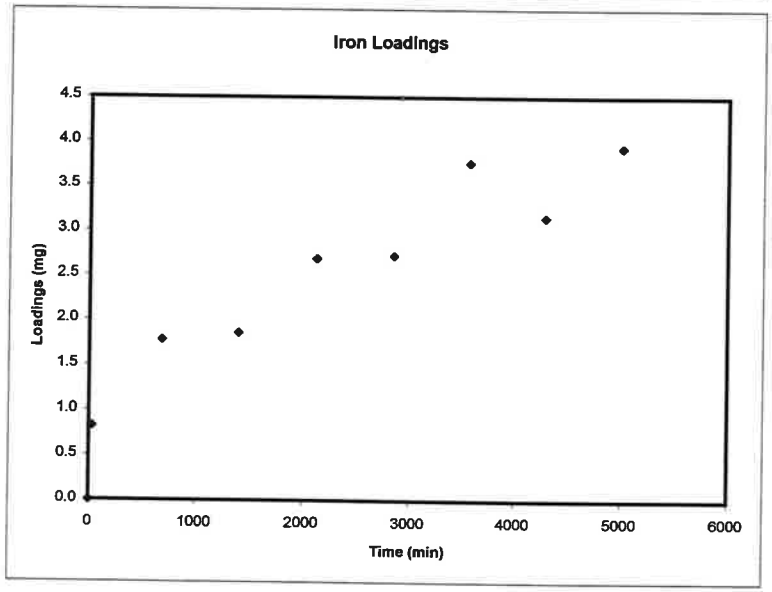

Regression
From 1405 To 5010

Production Rate (mol / min)

Sulphate	Iron	Nickel
2.56E-07	9.09E-09	1.73E-09

Oxidation Rate (mol / m2 s)

Sulphate	Iron	Nickel
9.55E-09	3.39E-10	6.44E-11

Figure D-33: Abiotic oxidation (with growth medium) of Inco's Copper Cliff Po Conc at pH = 4, 40C (KS-046).

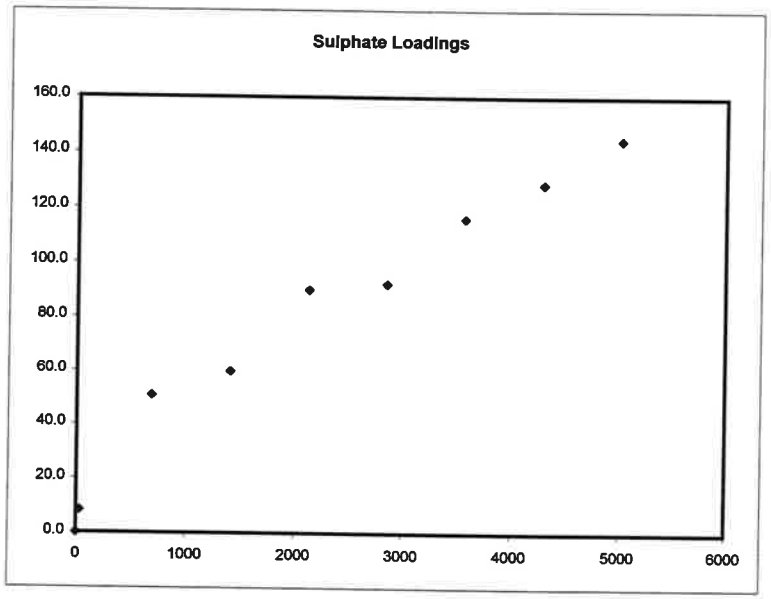

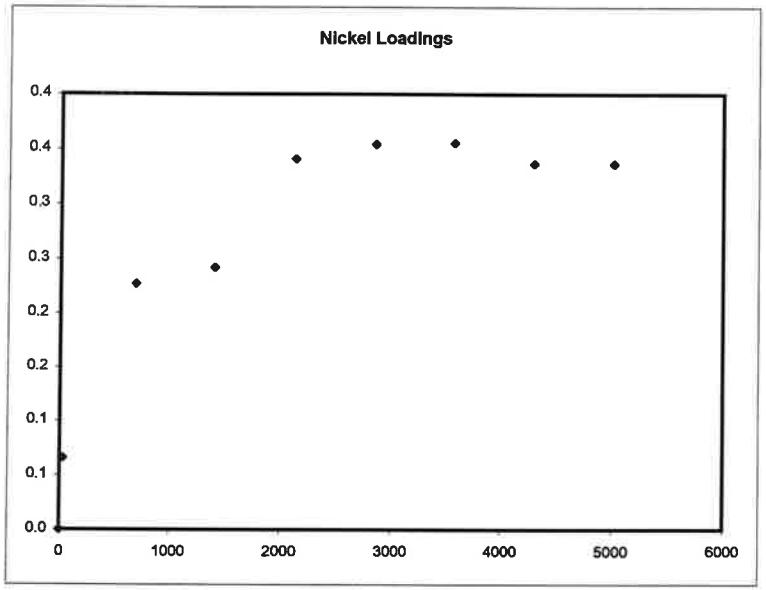

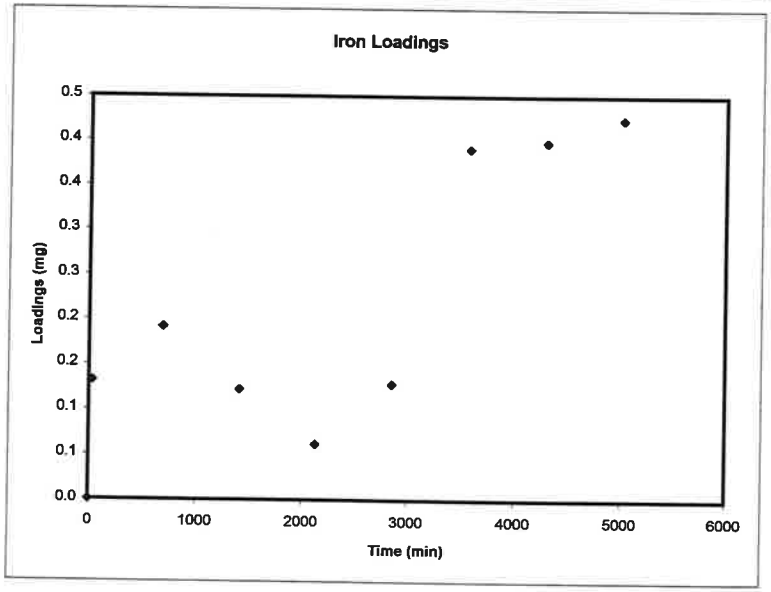

Regression
From 1405 To 5010

Production Rate (mol / min)

Sulphate	Iron	Nickel
2.32E-07	1.97E-09	3.10E-10

Oxidation Rate (mol / m2 s)

Sulphate	Iron	Nickel
8.65E-09	7.36E-11	1.16E-11

Figure D-34: Abiotic oxidation (with growth medium) of Inco's Copper Cliff Po Conc at pH = 6, 40C (KS-047).

Appendix E

Column Studies of Inco's Copper Cliff Pyrrhotite Concentrate

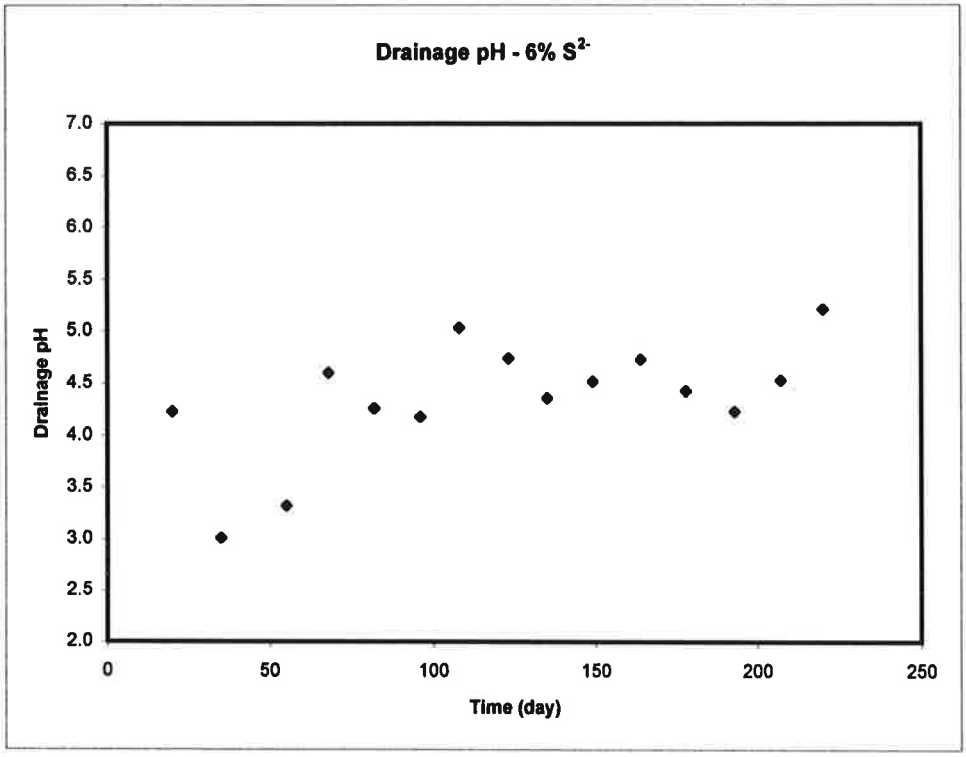

Figure E-1: Drainage pH of base case (6 % S^{2-}) column.

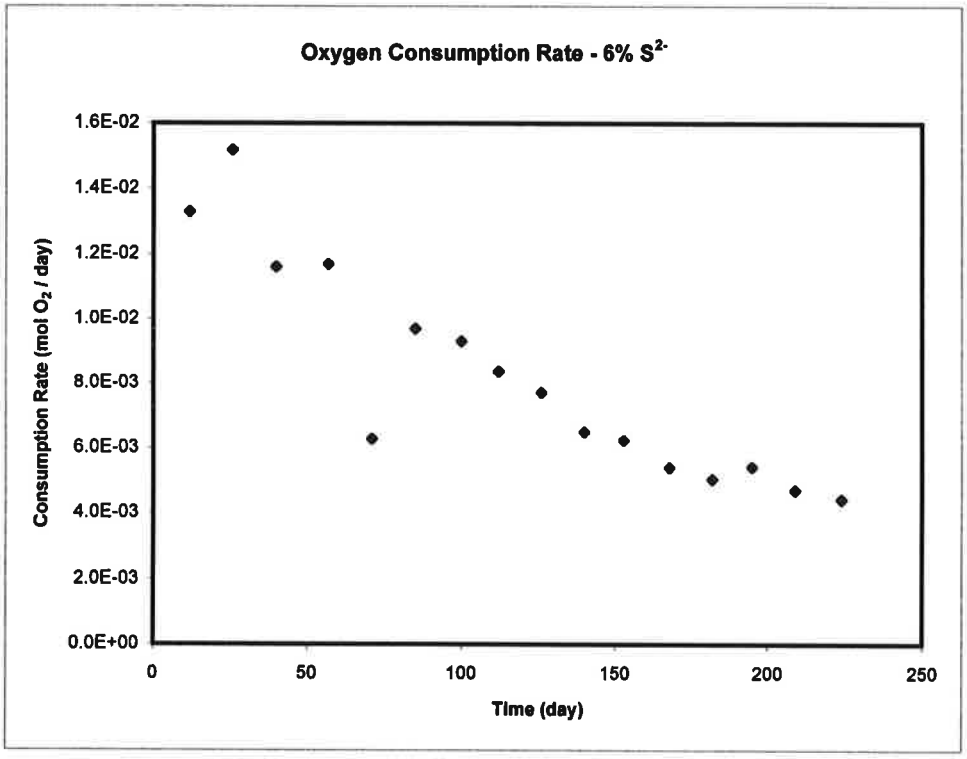

Figure E-2: Oxygen consumpation rate of base case (6 % S^{2-}) column.

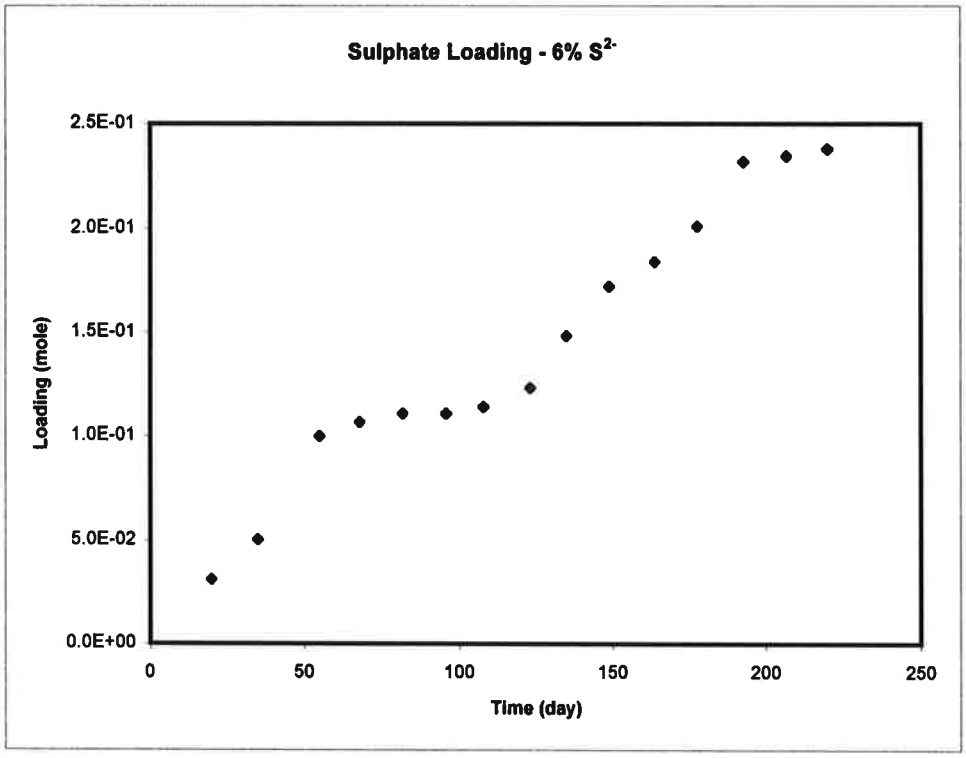

Figure E-3: Sulphate loading of base case (6 % S^{2-}) column.

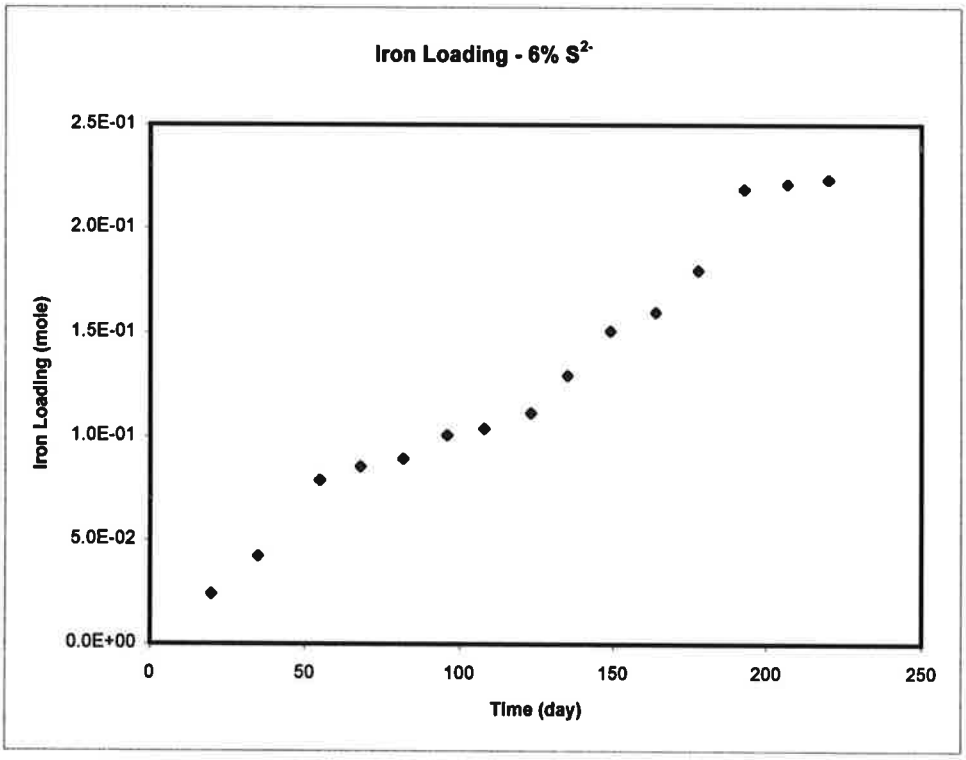

Figure E-4: Iron loading rate of base case (6 % S^{2-}) column.

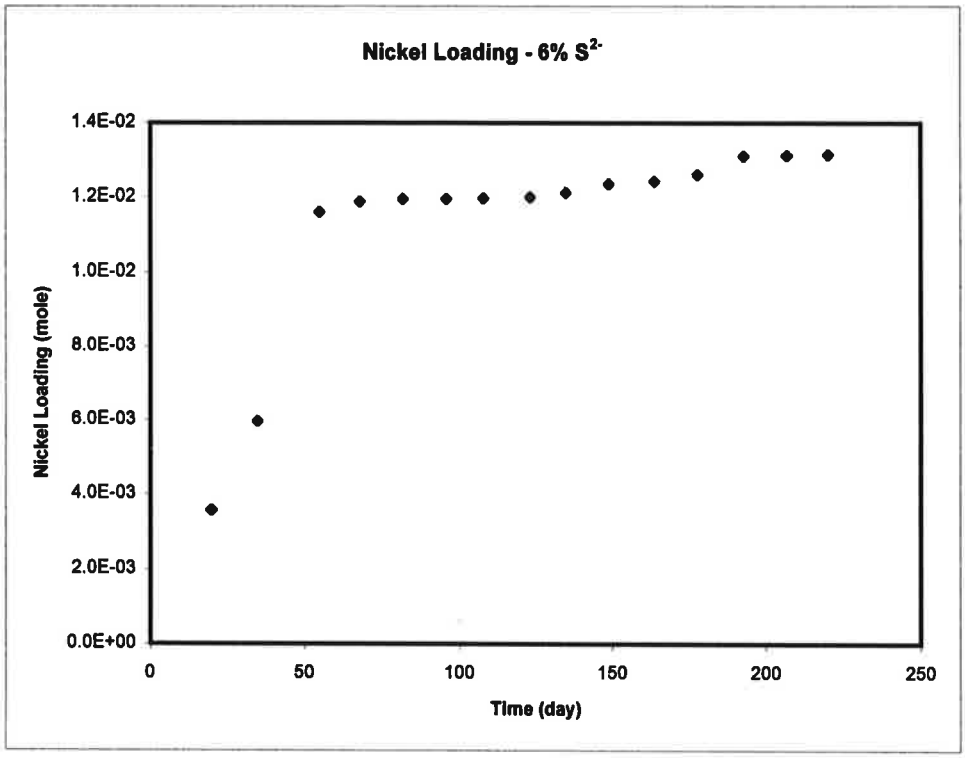

Figure E-5: Nickel loading of base case (6 % S^{2-}) column.

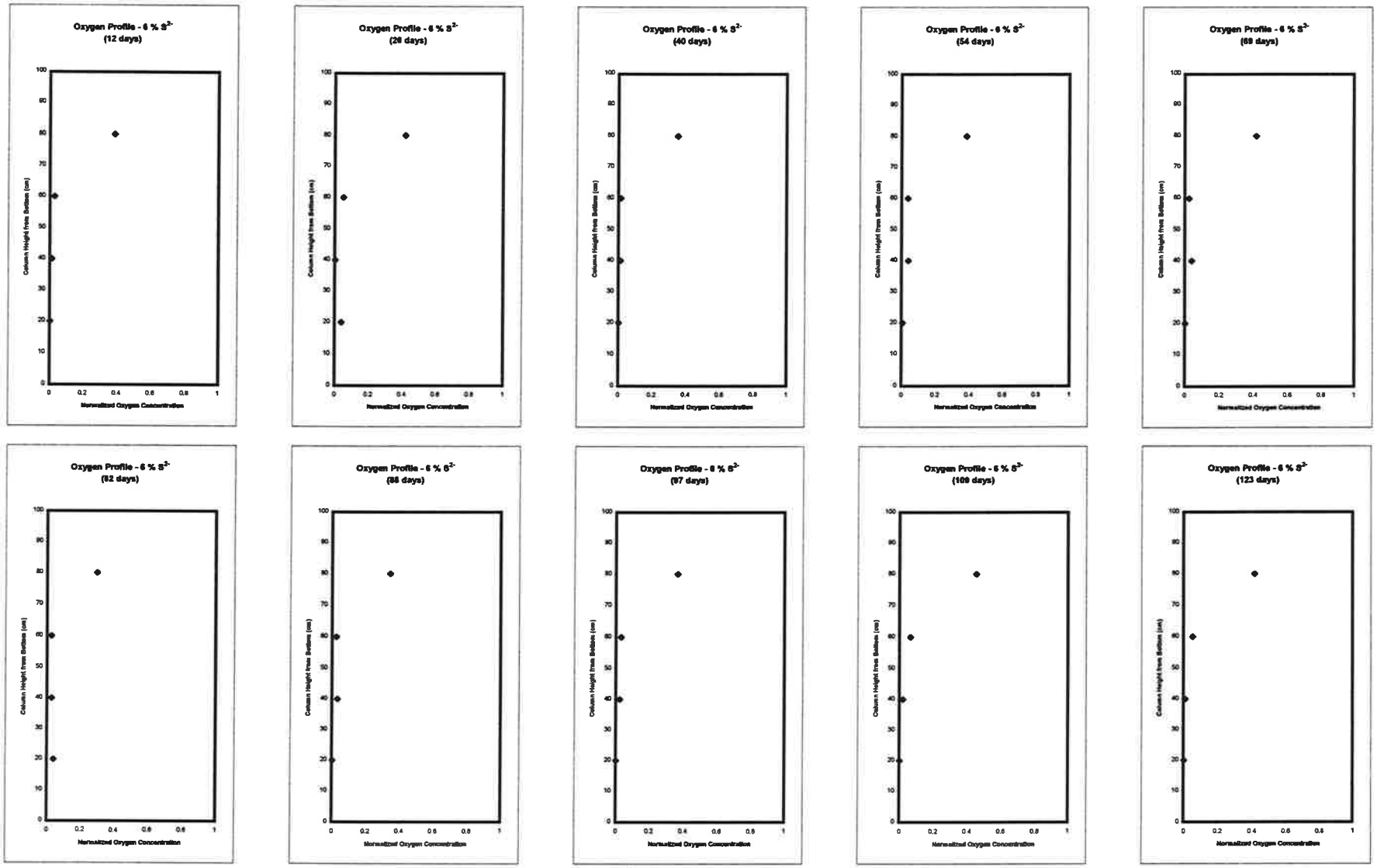

Figure E-6a: Pore space oxygen concentration profiles in the base case (6 % S^{2-}) column.

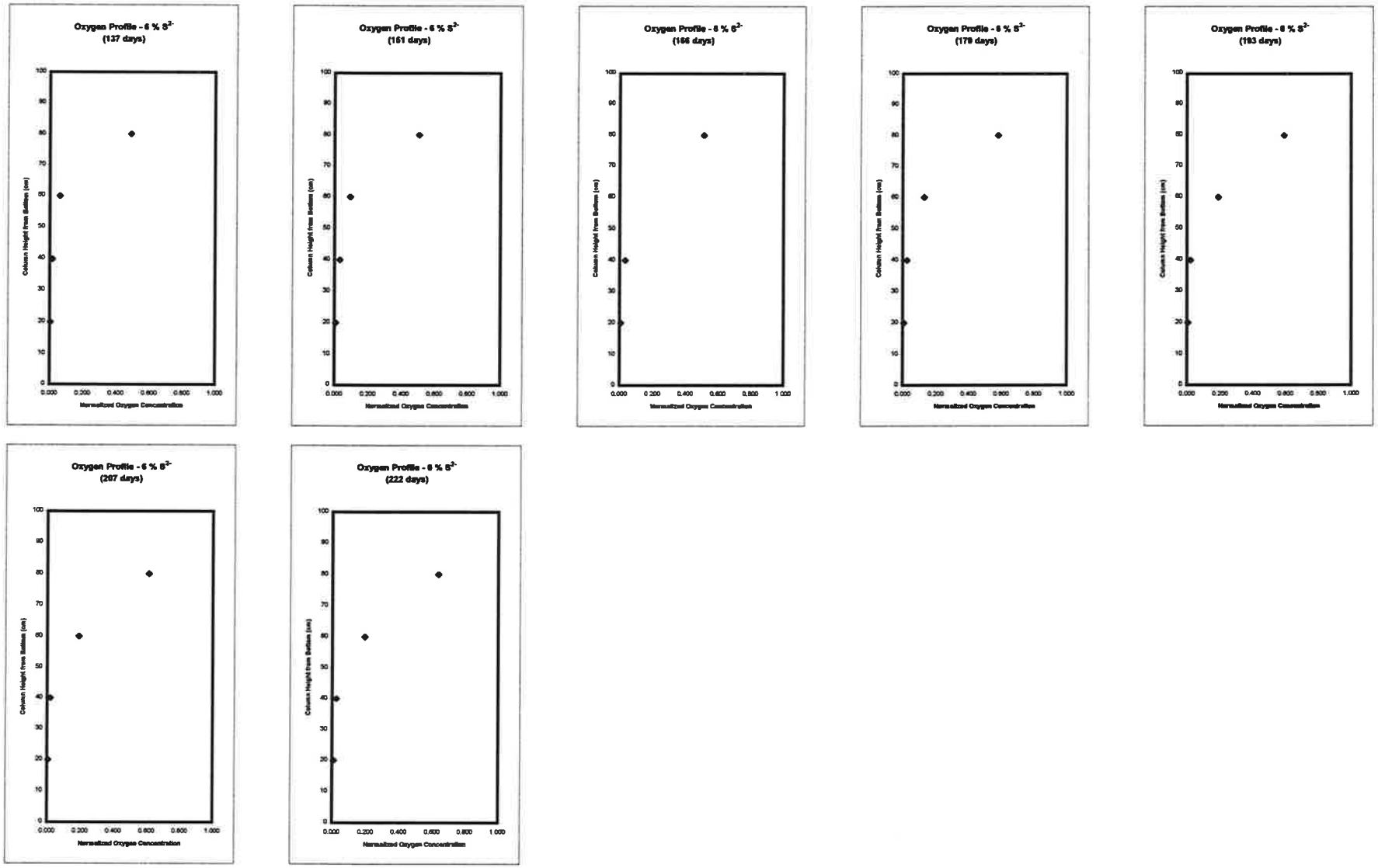

Figure E-6b: Pore space oxygen concentration profiles in the base case (6 % S^{2-}) column.

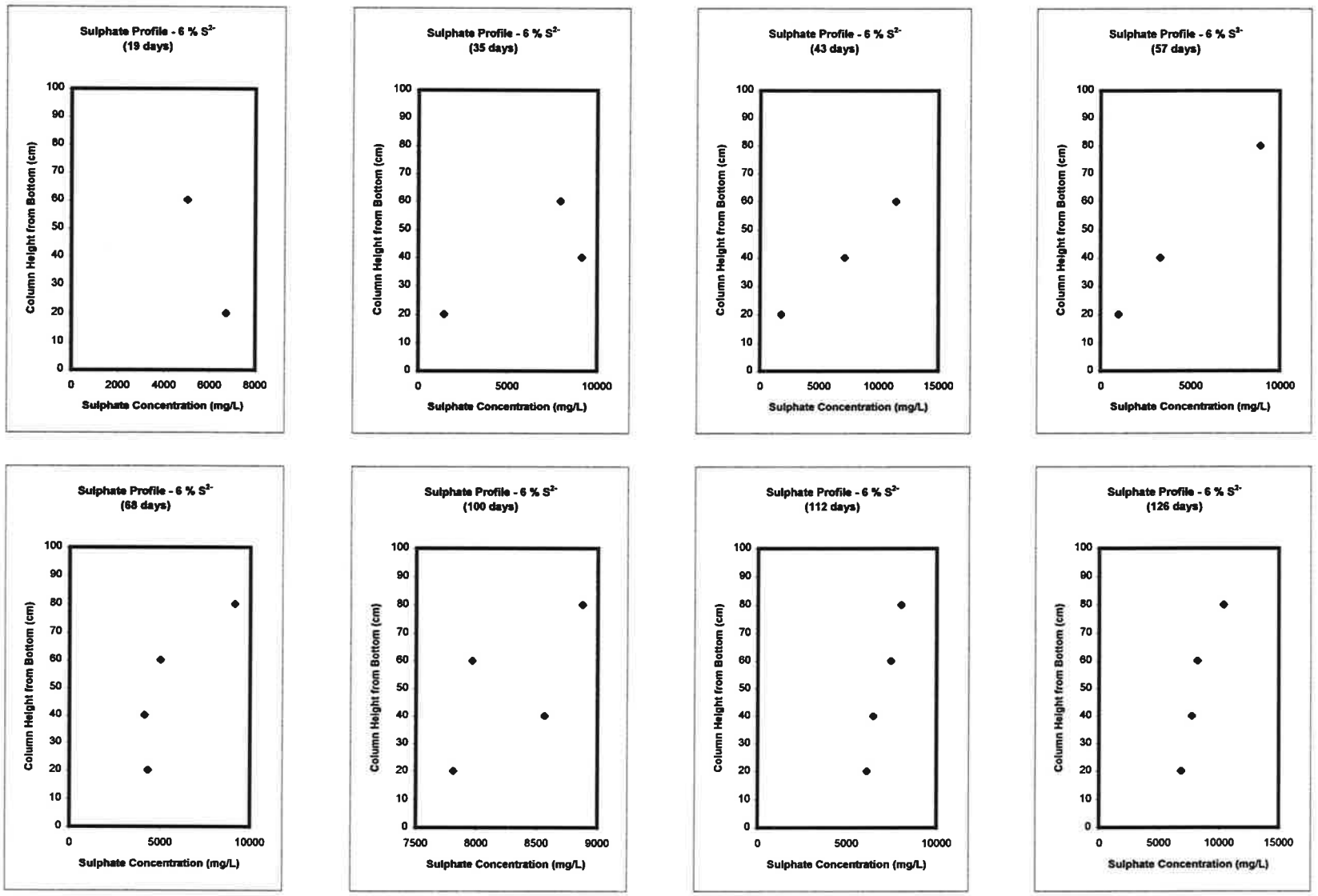

Figure E-7: Porewater sulphate concentration profiles in the base case (6 % S^{2-}) column
(note differences in scales for the sulphate concentration axis)

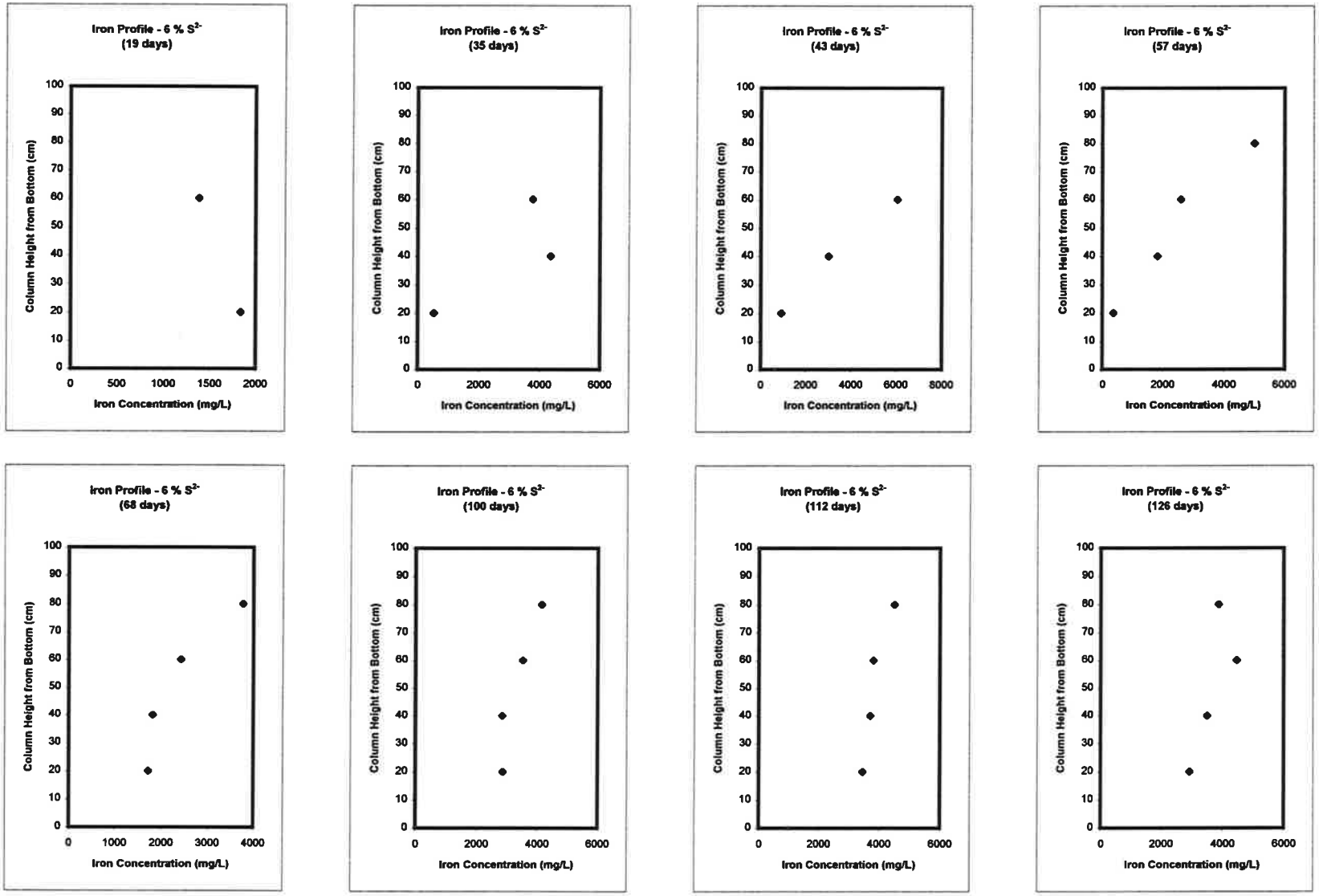

Figure E-8: Porewater iron concentration profiles in the base case (6 % S^{2-}) column
(note differences in scales for the iron concentration axis)

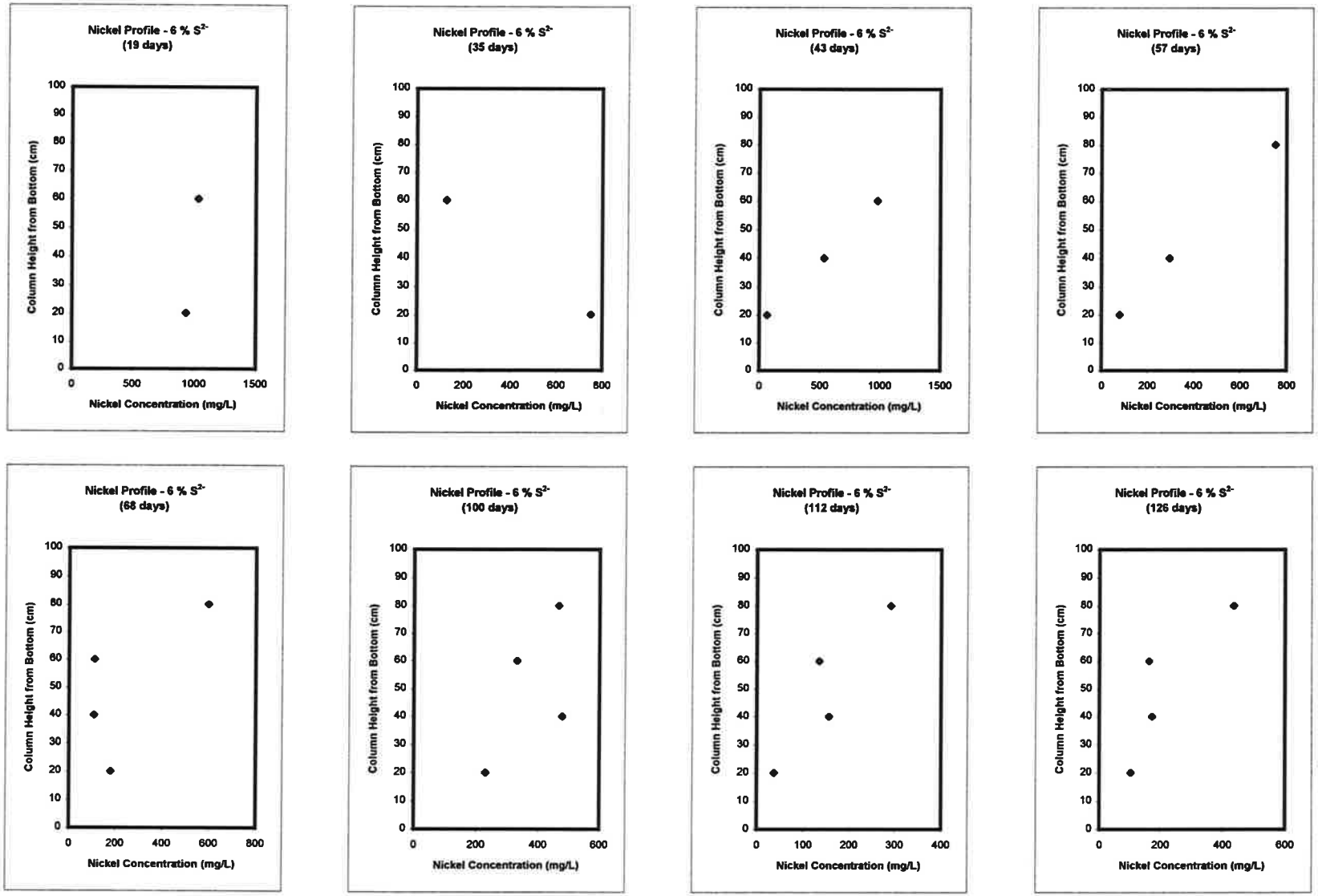

Figure E-9: Porewater nickel concentration profiles in the base case (6 % S^{2-}) column
(note differences in scales for the nickel concentration axis)

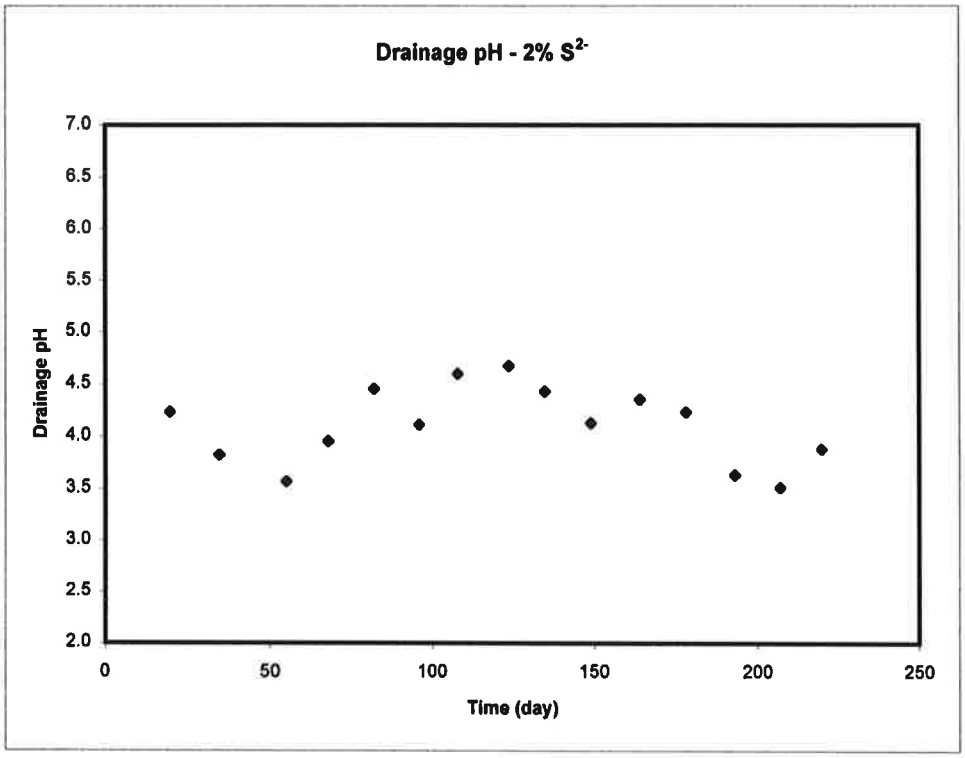

Figure E-10: Drainage pH of 2 % S^{2-} column.

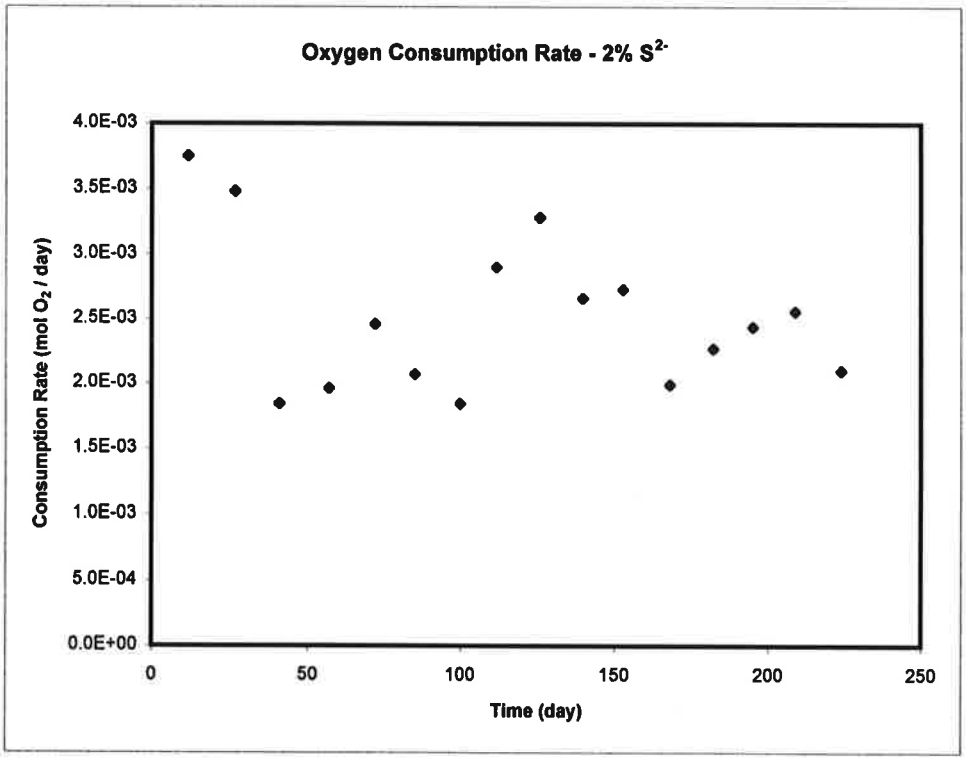

Figure E-11: Oxygen consumpation rate of 2 % S^{2-} column.

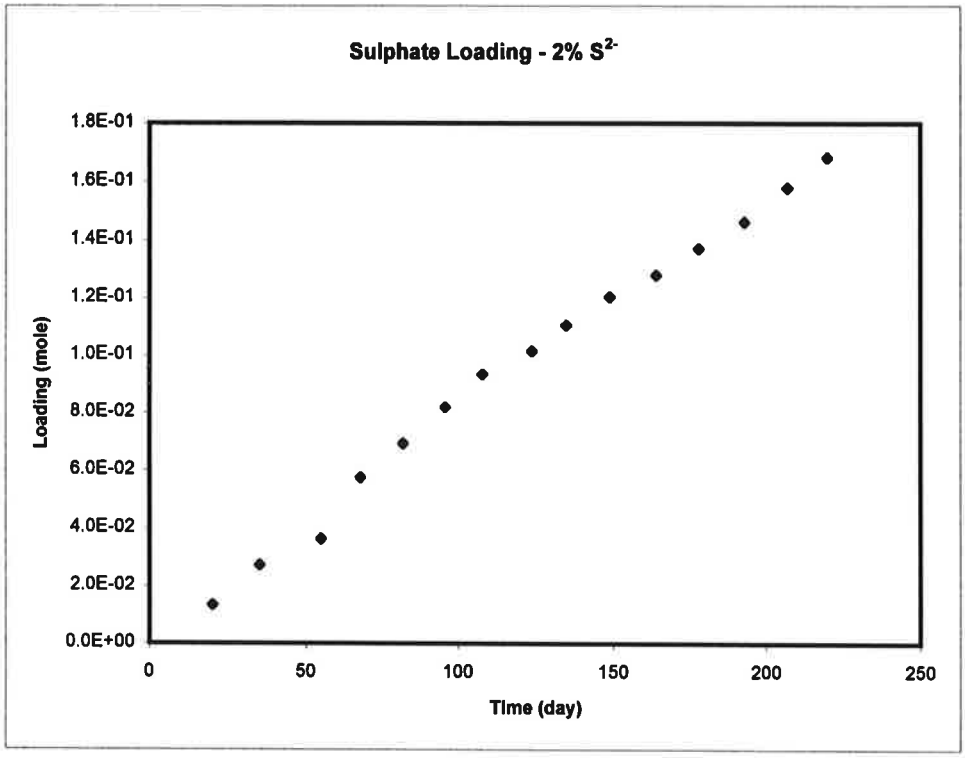

Figure E-12: Sulphate loading of 2 % S^{2-} column.

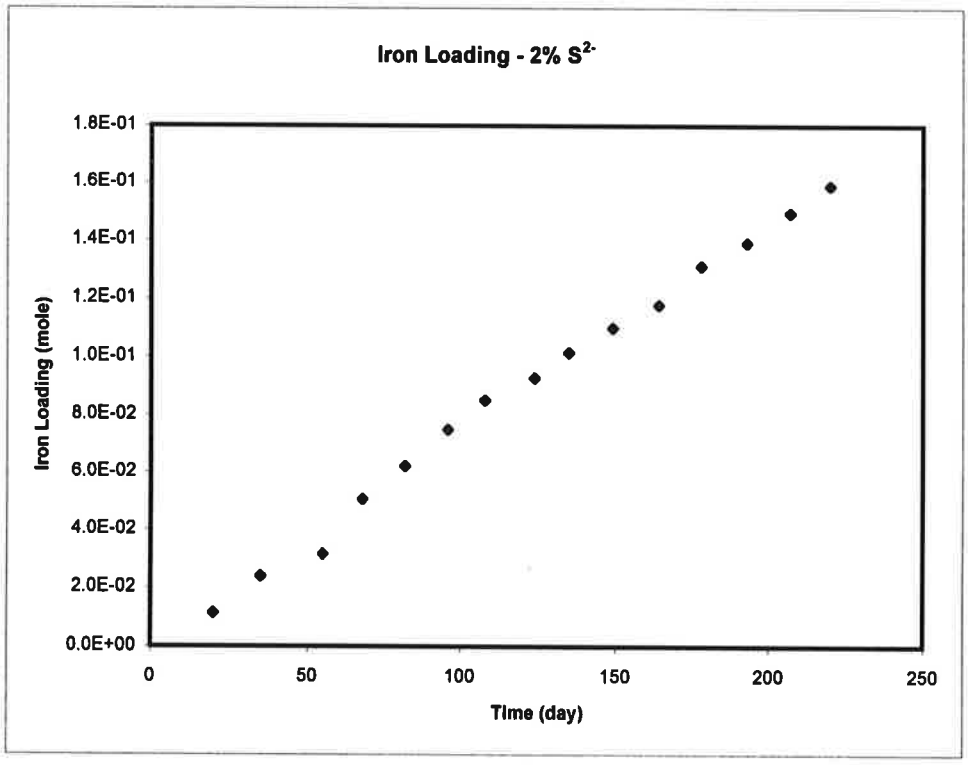

Figure E-13: Iron loading rate of 2 % S^{2-} column.

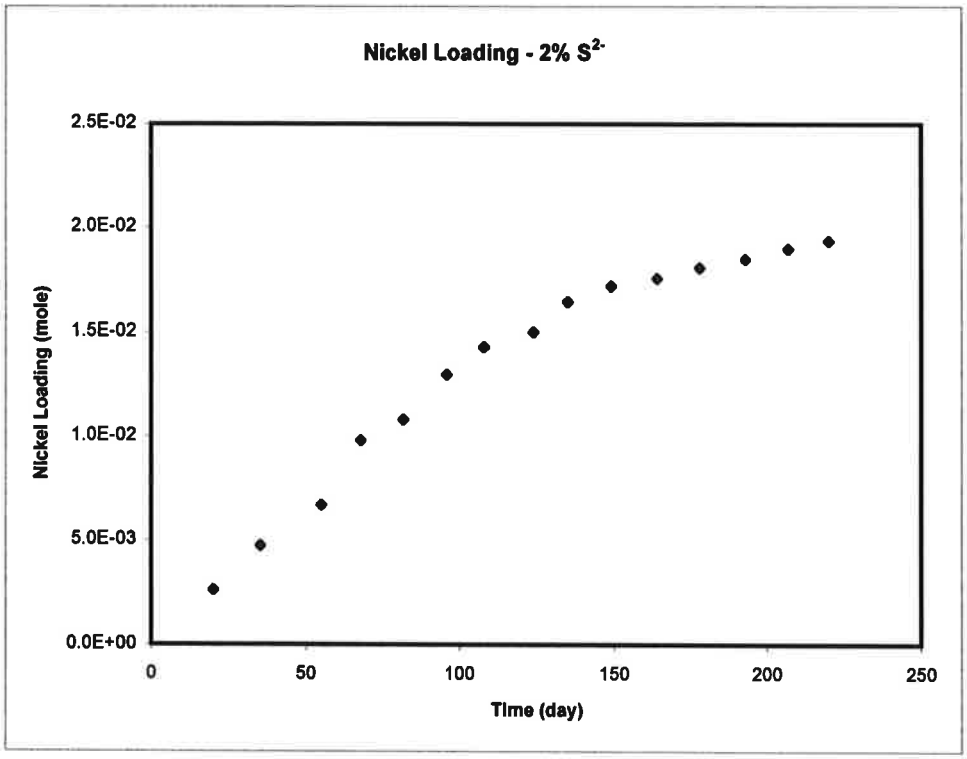

Figure E-14: Nickel loading of 2 % S^{2-} column.

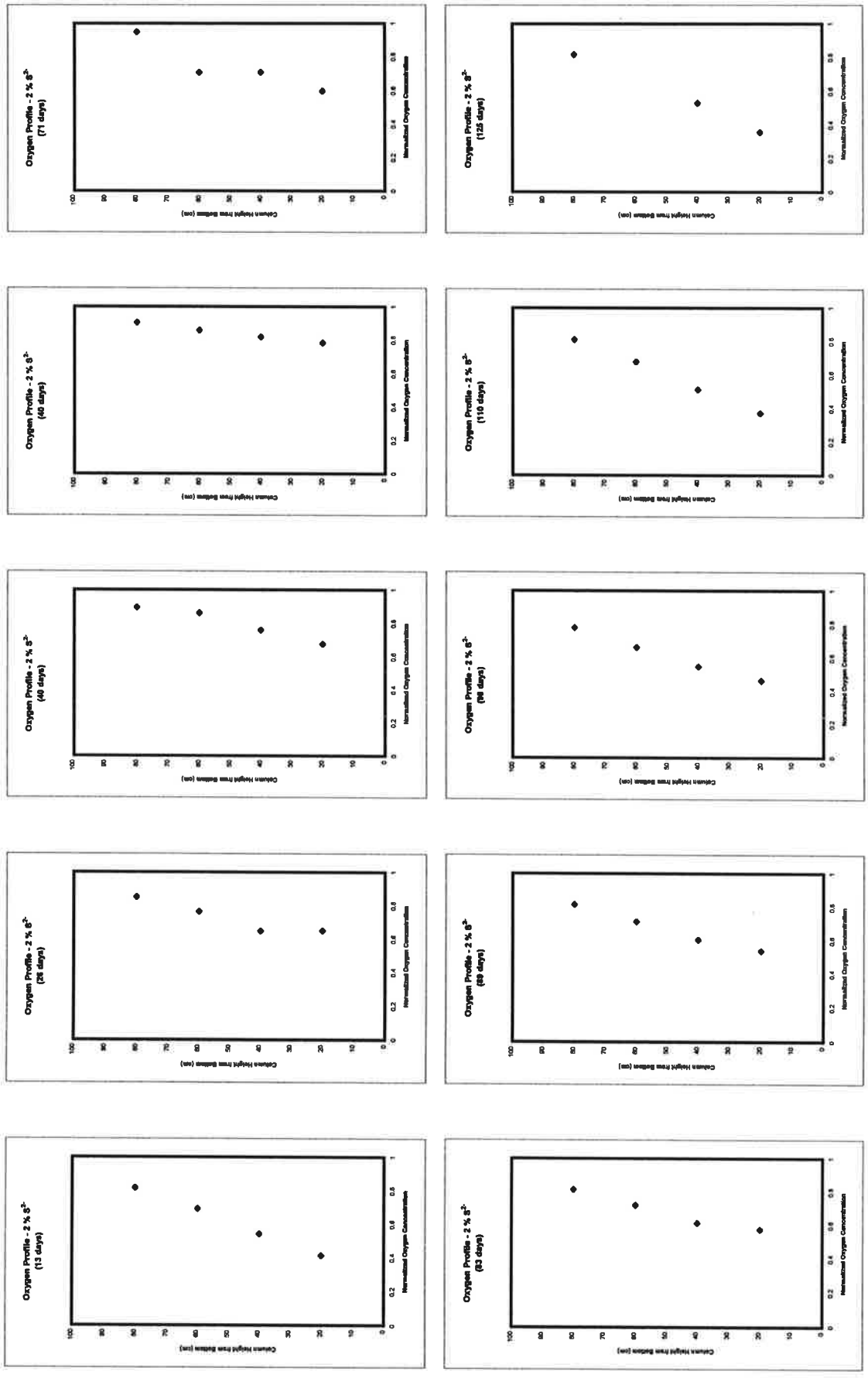

Figure E-15a: Pore space oxygen concentration profiles in the 2 % S^{2-} column.

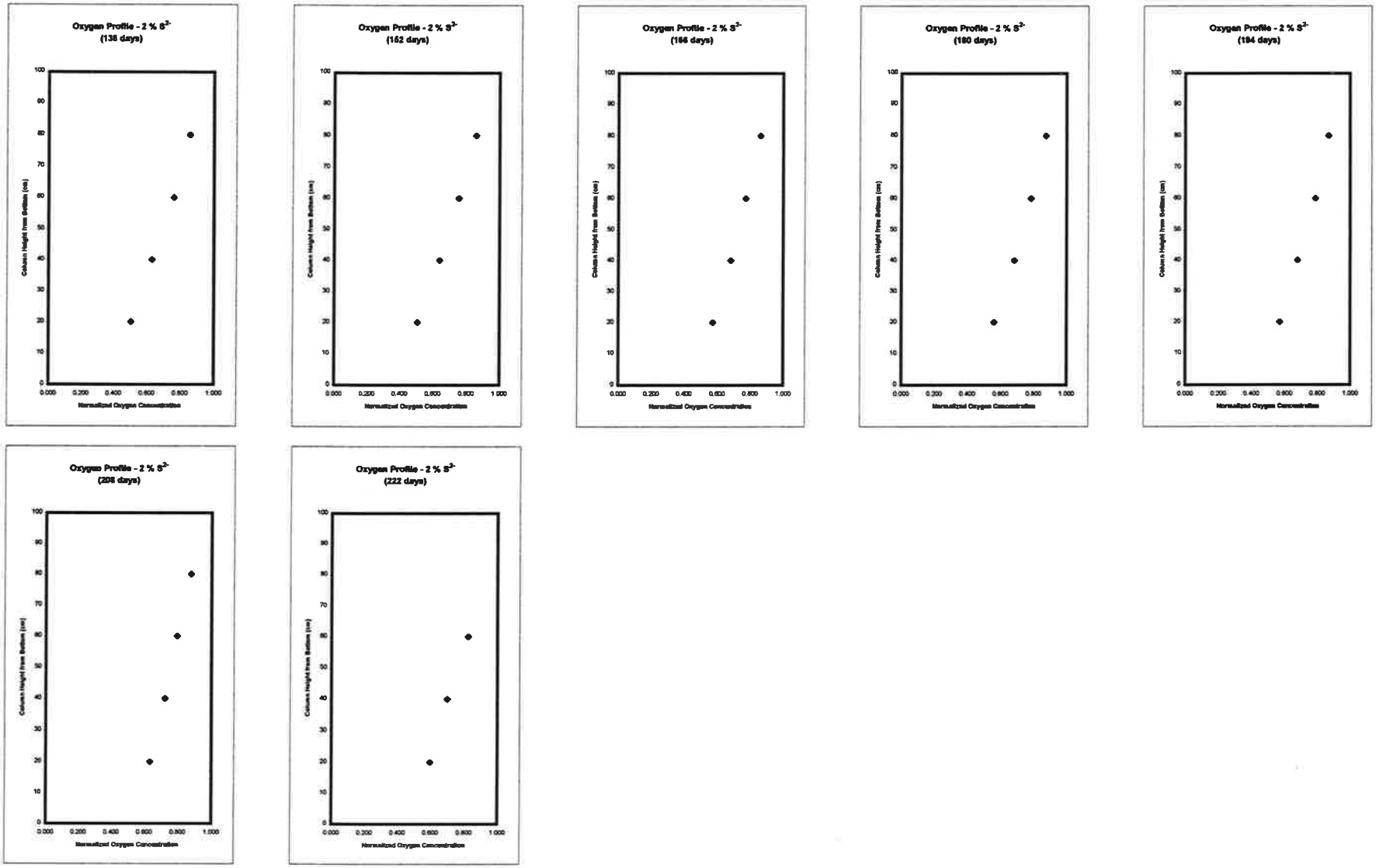

Figure E-15b: Pore space oxygen concentration profiles in the 2 % S^{2-} column.

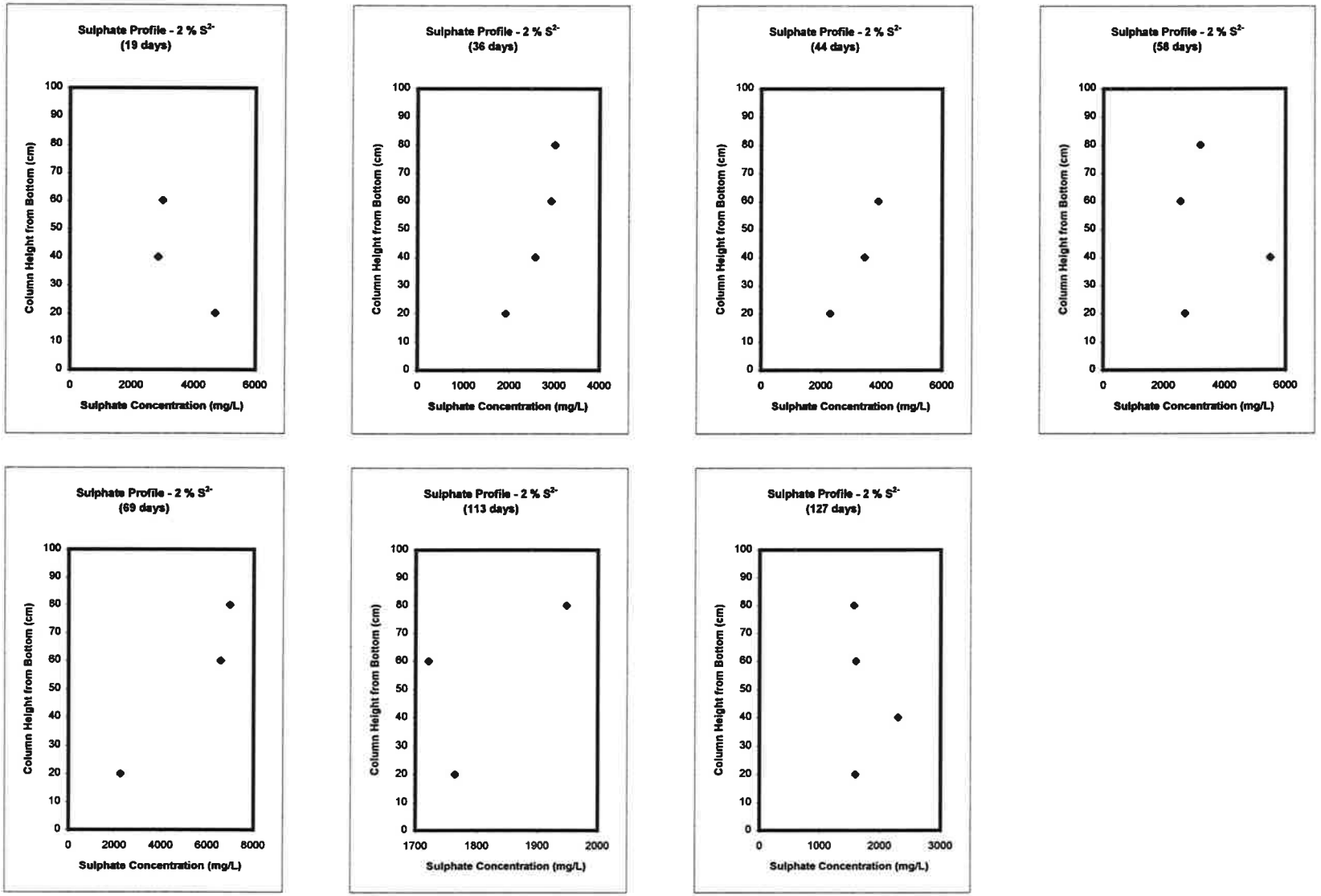

Figure E-16: Porewater sulphate concentration profiles in the 2 % S^{2-} column.
(note differences in scales for the sulphate concentration axis)

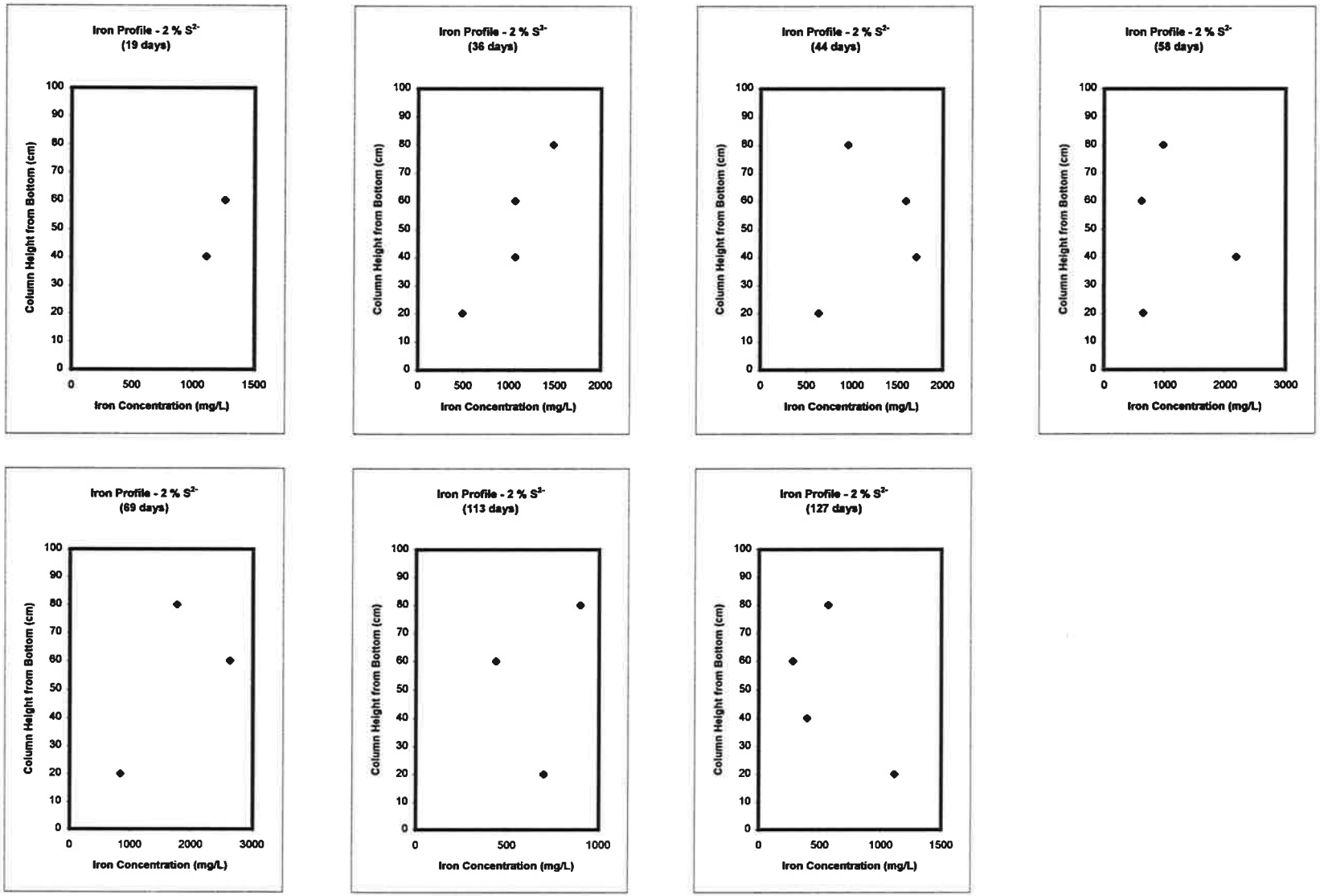

Figure E-17: Porewater iron concentration profiles in the 2 % S^{2-} column.
(note differences in scales for the iron concentration axis)

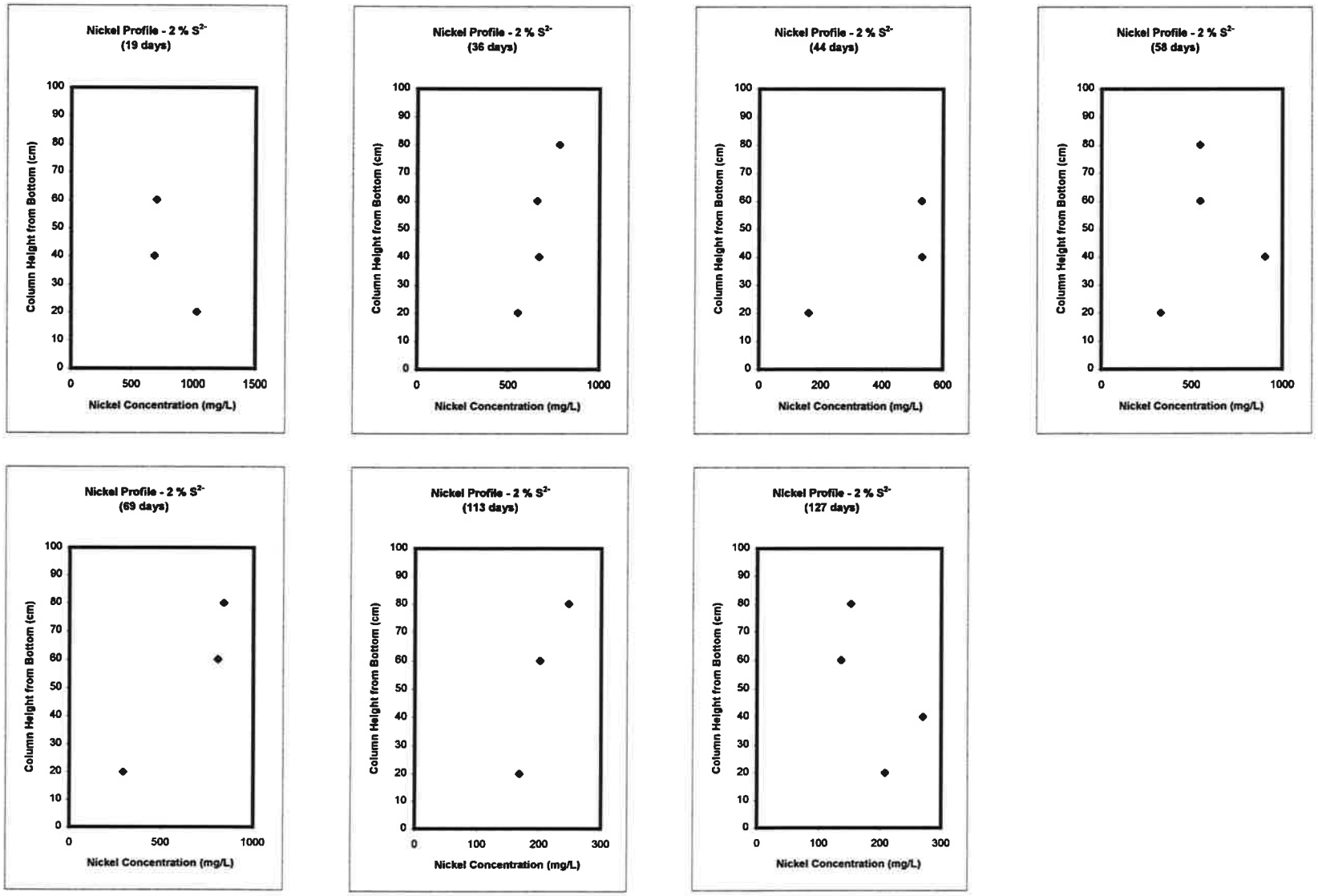

Figure E-18: Porewater nickel concentration profiles in the 2 % S^{2-} column.
(note differences in scales for the nickel concentration axis)

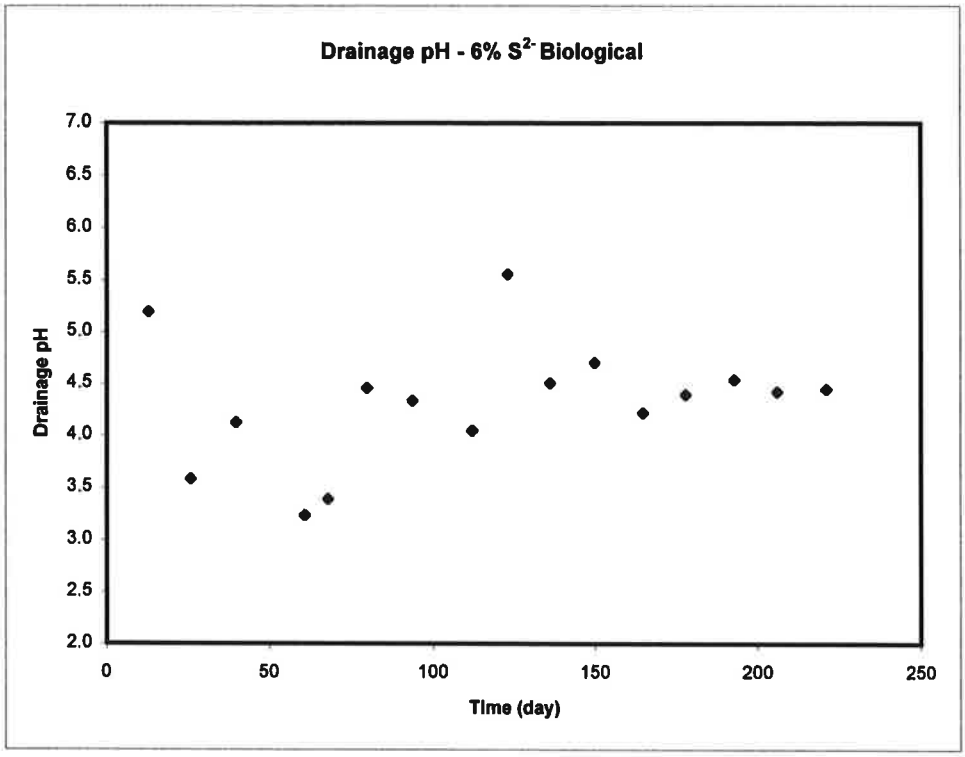

Figure E-19: Drainage pH of bacterial inoculated (6 % S^{2-}) column.

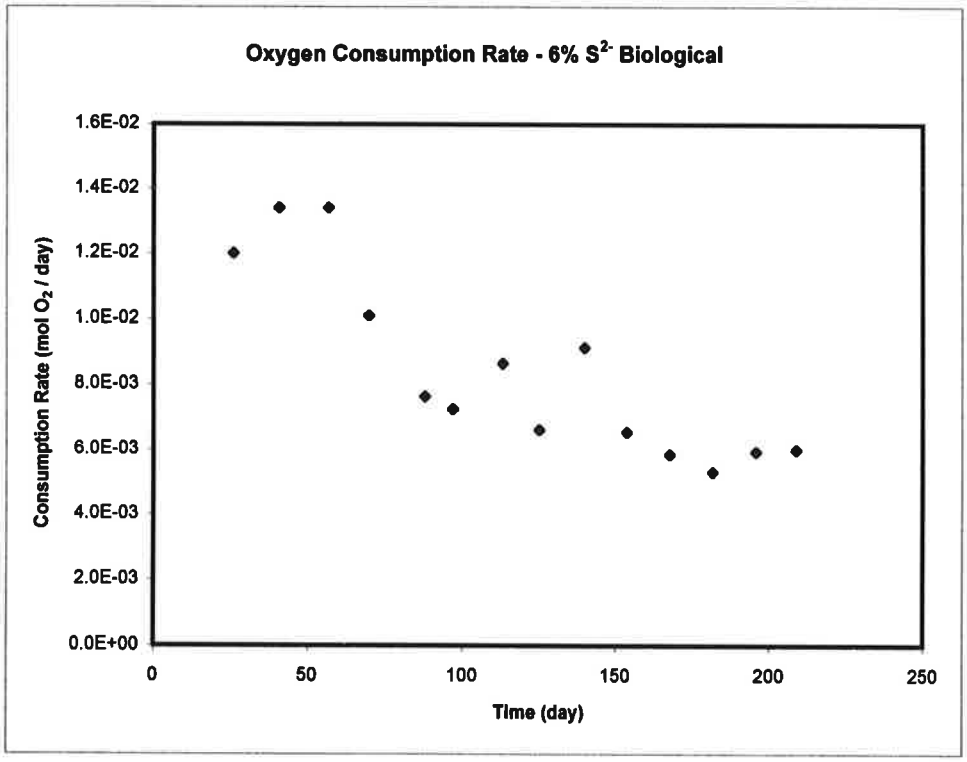

Figure E-20: Oxygen consmption rate of bacterial inoculated (6 % S^{2-}) column.

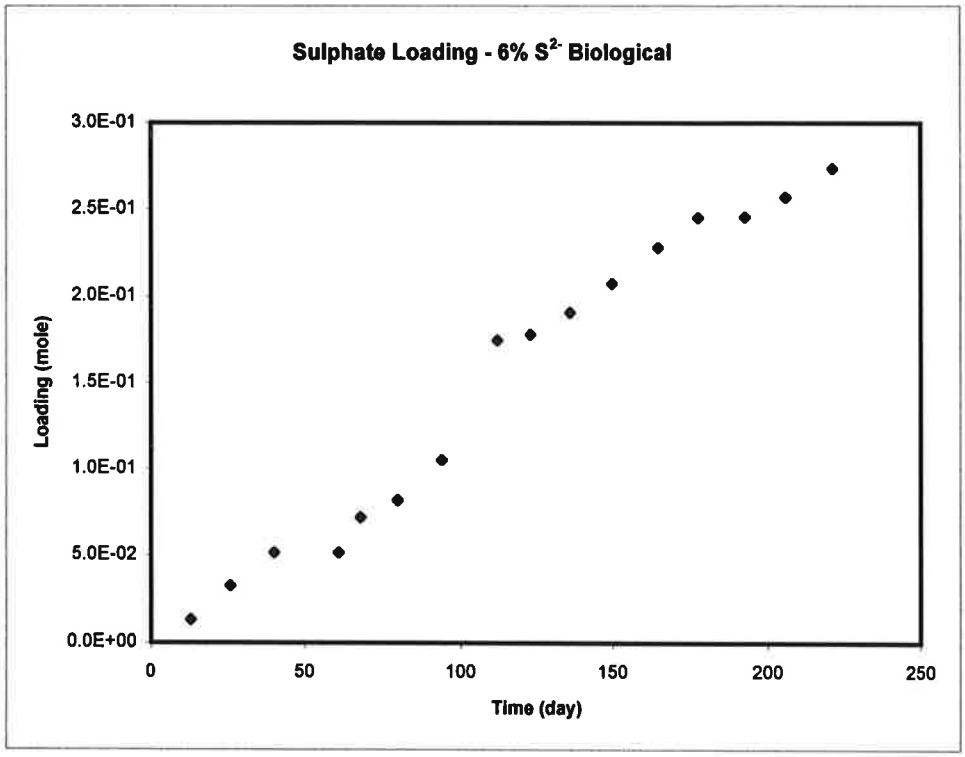

Figure E-21: Sulphate loading of bacterial inoculated (6 % S^{2-}) column.

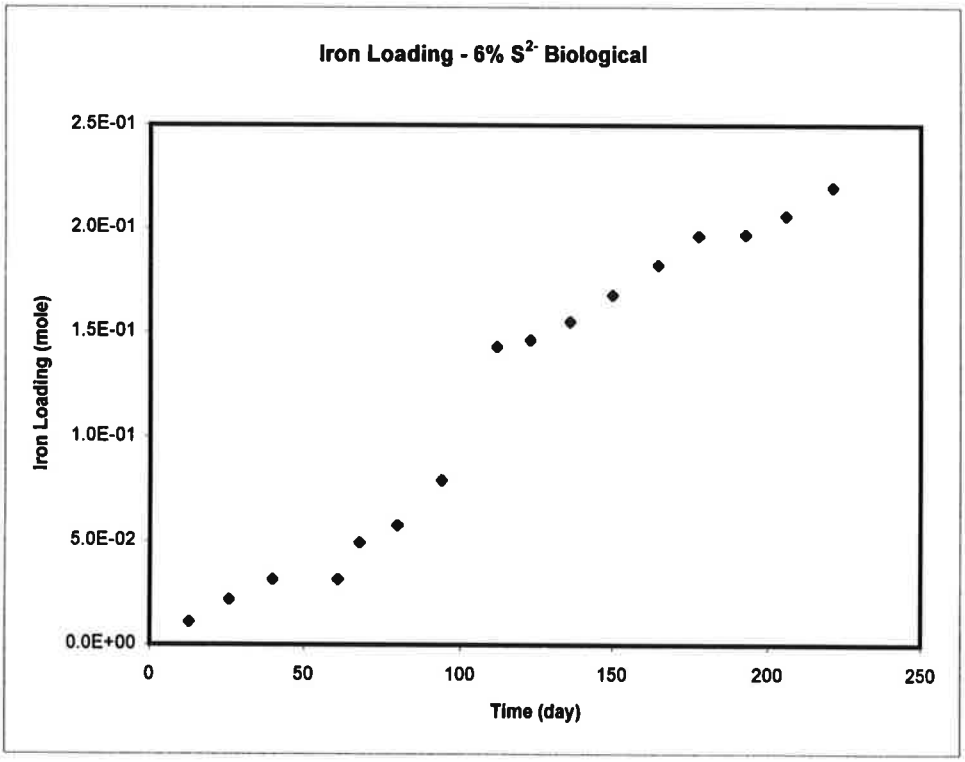

Figure E-22: Iron loading of bacterial inoculated (6 % S^{2-}) column.

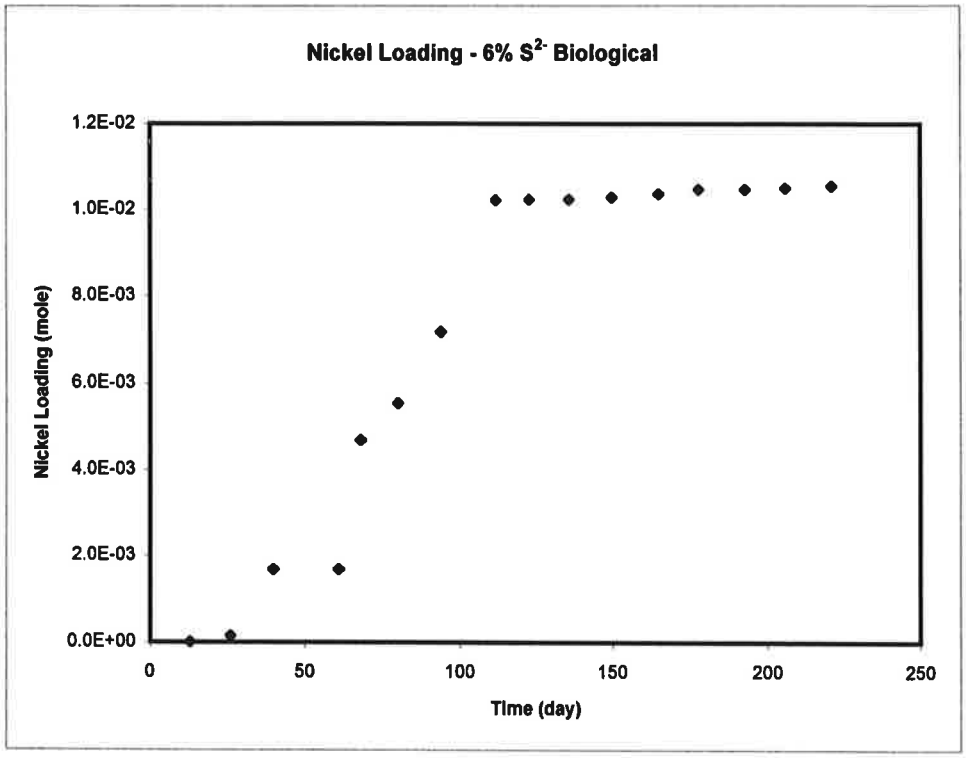

Figure E-23: Nickel loading of bacterial inoculated (6 % S^{2-}) column.

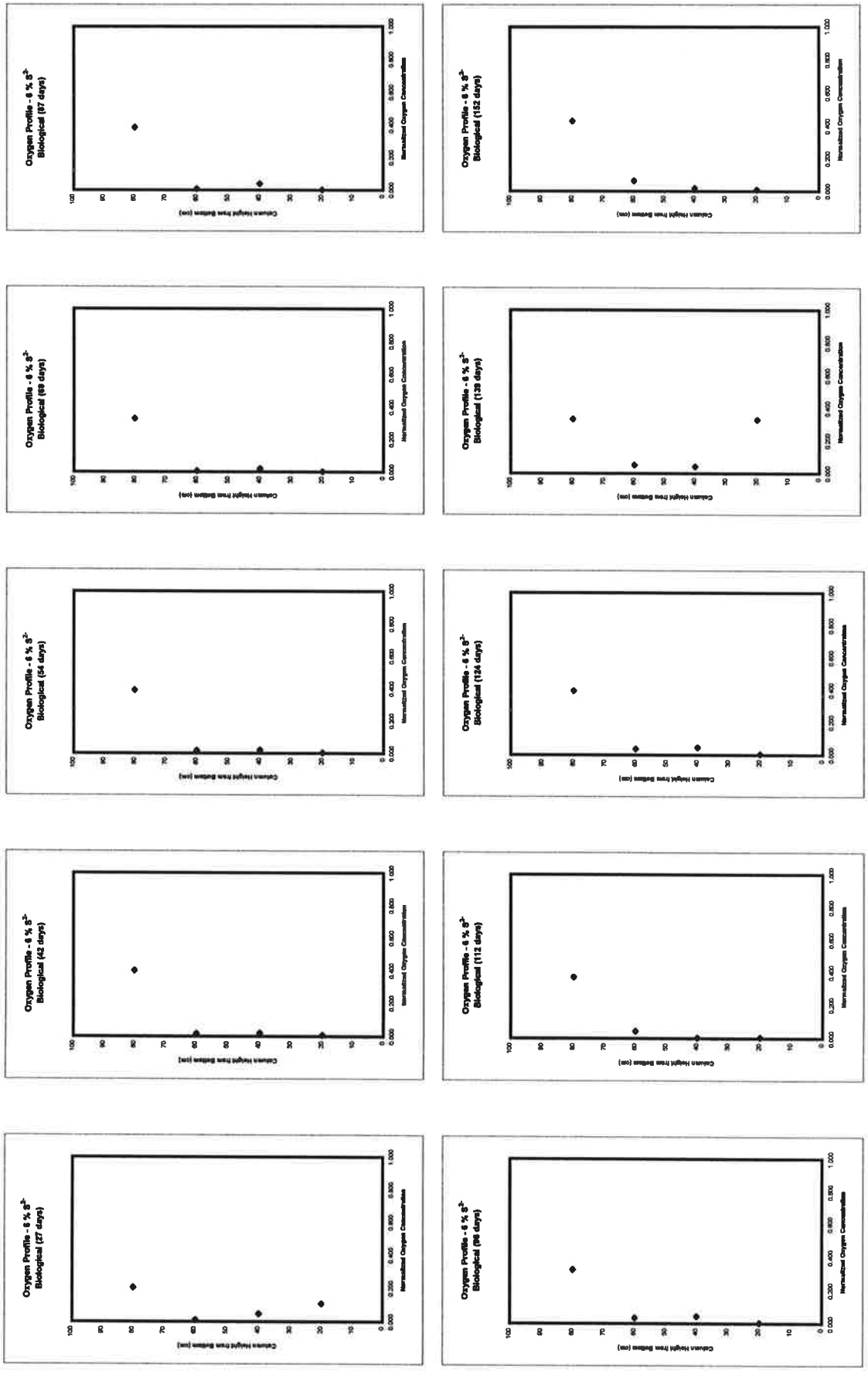

Figure E-24a: Pore space oxygen concentration profiles in the bacterial inoculated column.

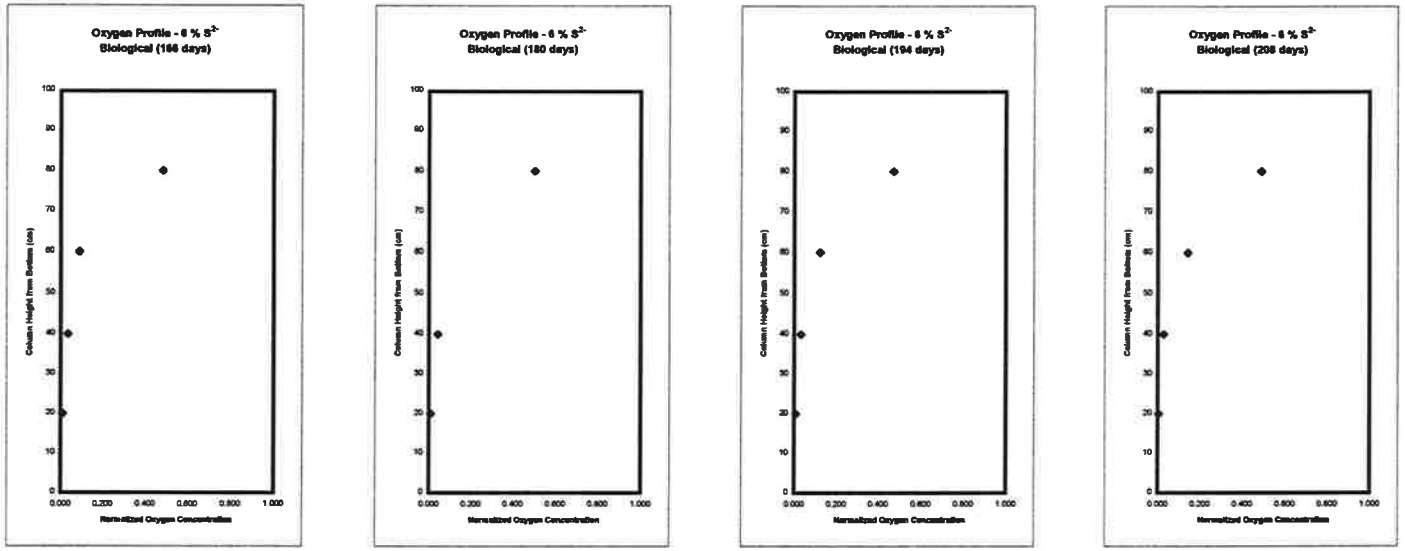

Figure E-24b: Pore space oxygen concentration profiles in the bacterial inoculated column.

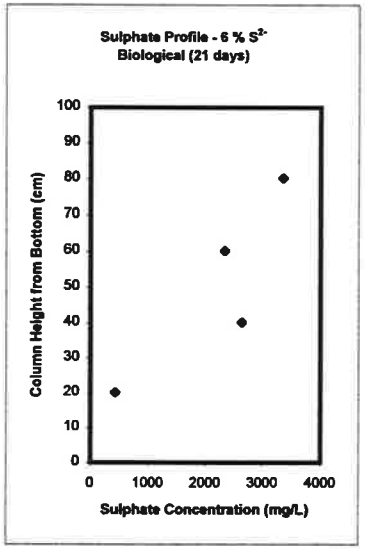

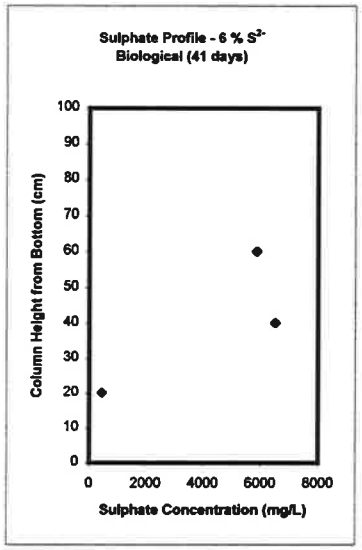

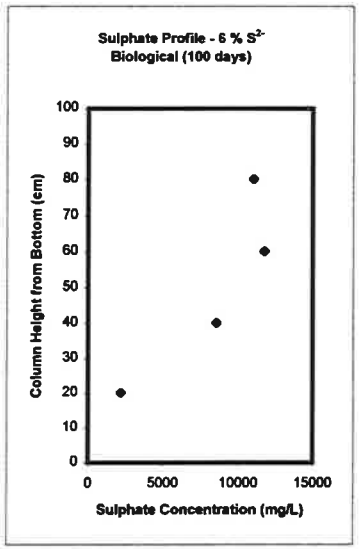

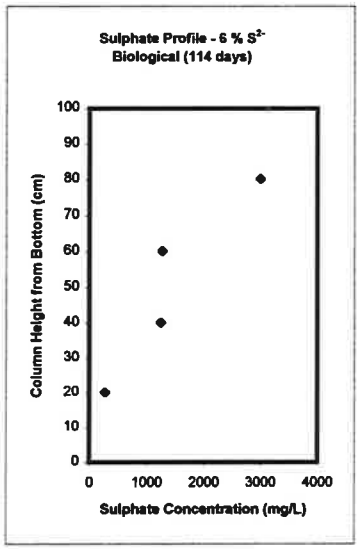

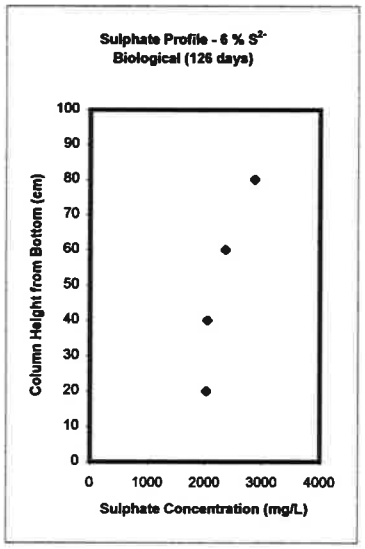

Figure E-25: Porewater sulphate concentration profiles in the bacterial inoculated column
(note differences in scales for the sulphate concentration axis)

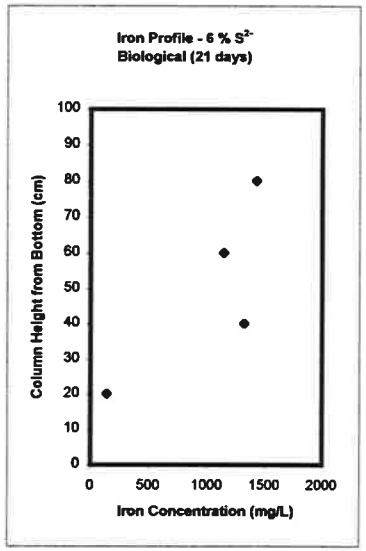

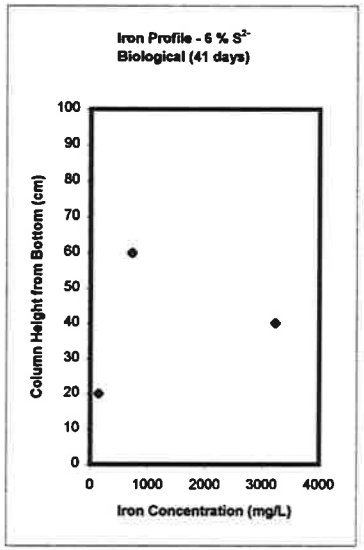

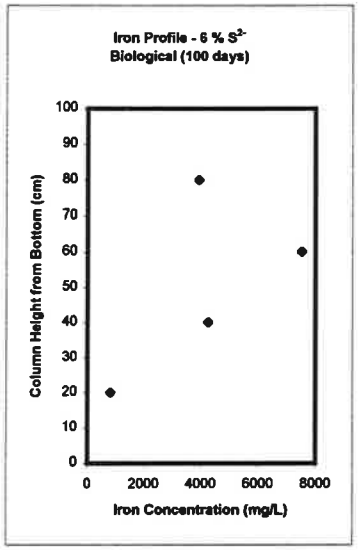

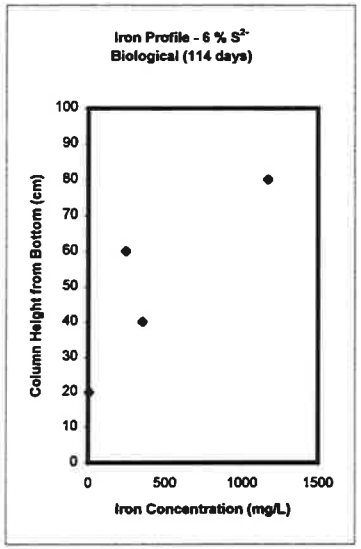

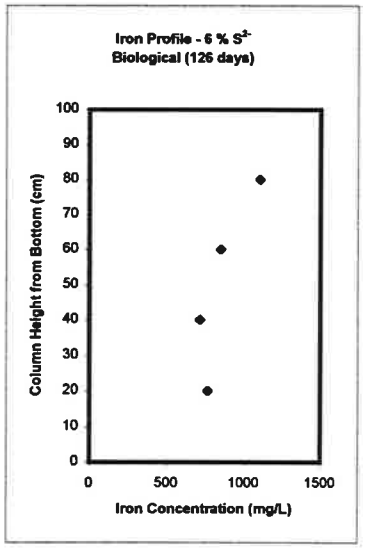

Figure E-26: Porewater iron concentration profiles in the bacterial inoculated column
(note differences in scales for the iron concentration axis)

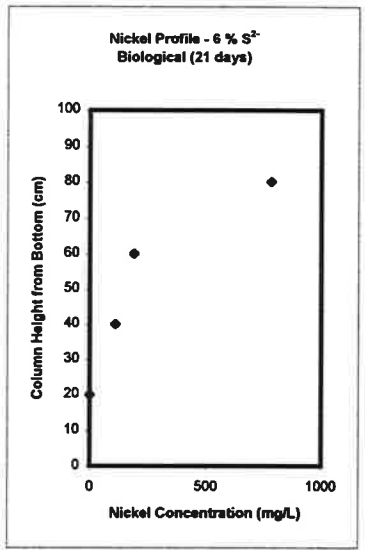

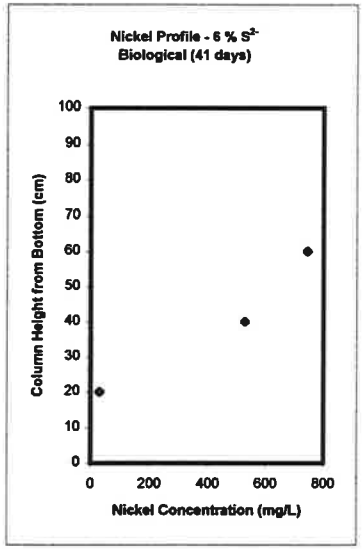

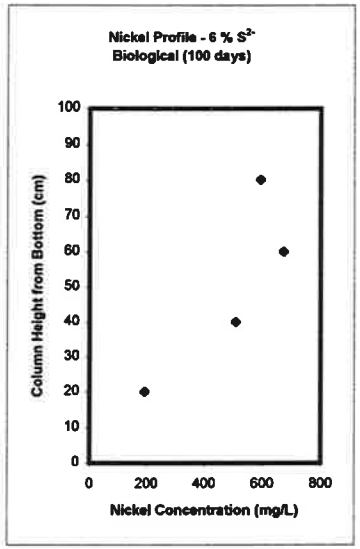

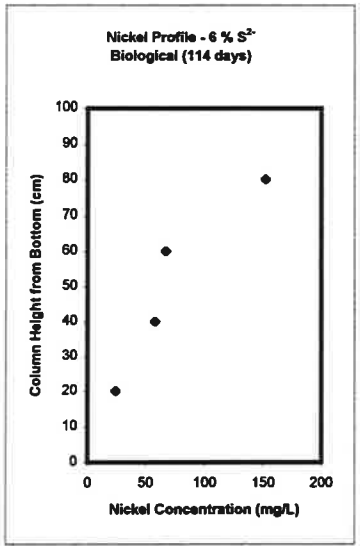

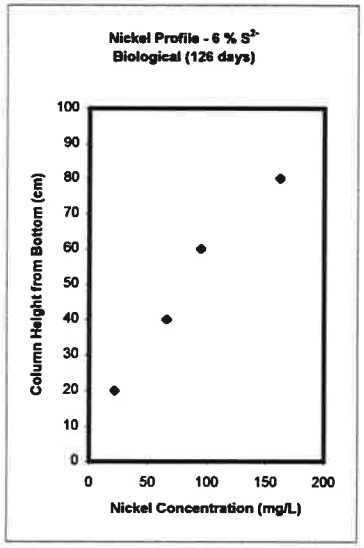

Figure E-27: Porewater nickel concentration profiles in the bacterial inoculated column
(note differences in scales for the nickel concentration axis)

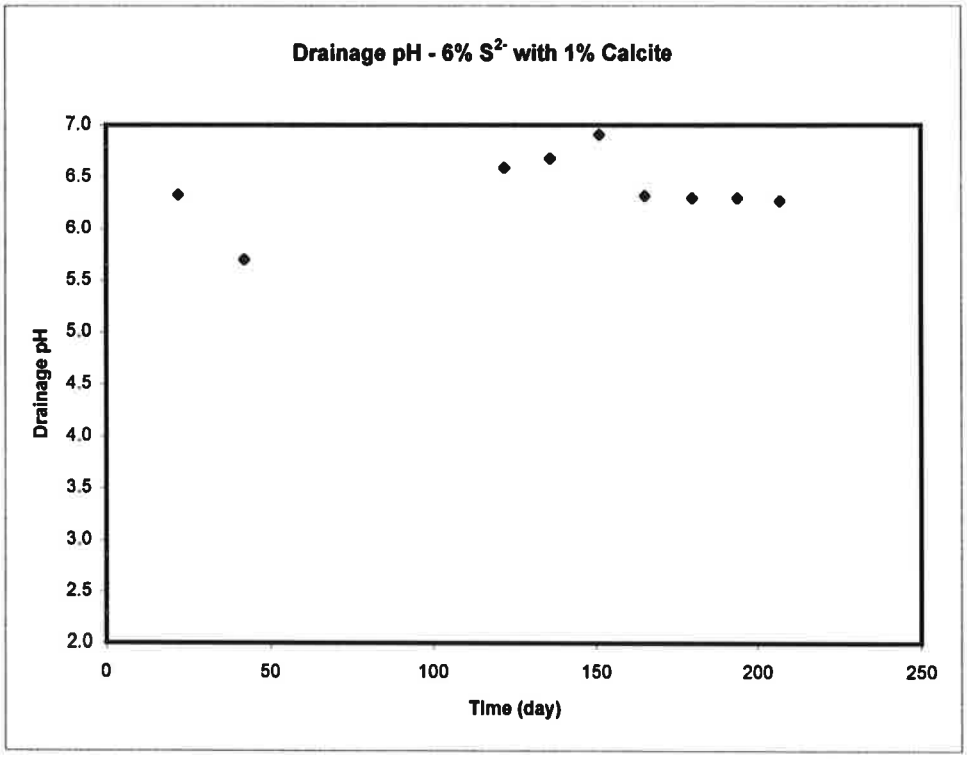

Figure E-28: Drainage pH of 1 % calcite buffered (6 % S^{2-}) column.

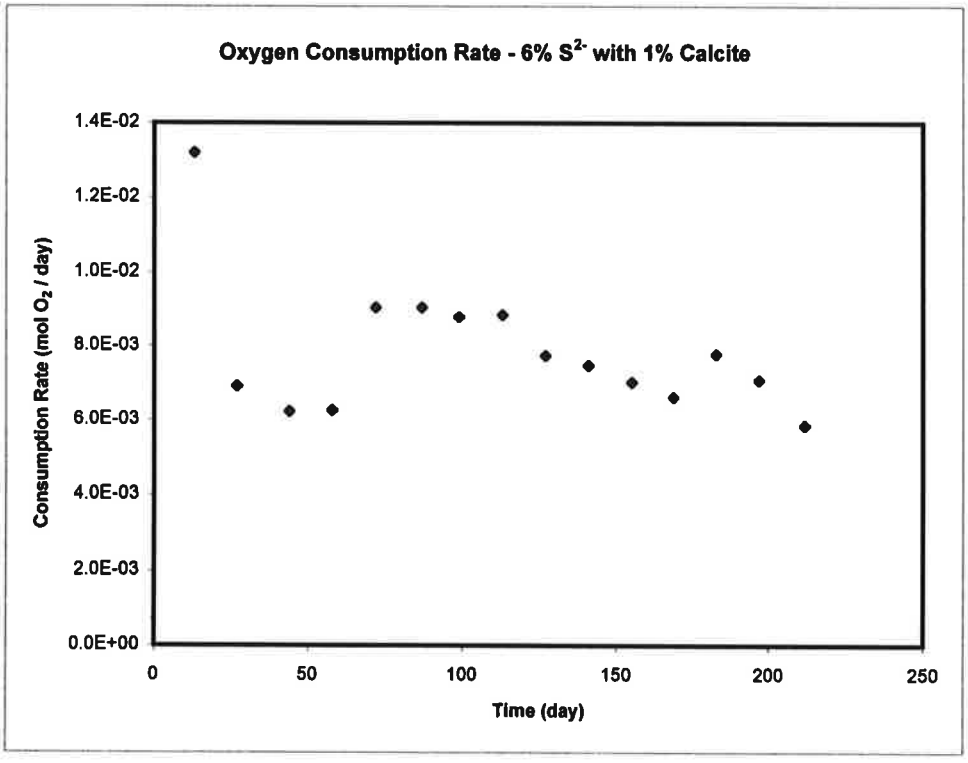

Figure E-29: Oxygen consumption rate of 1 % calcite buffered (6 % S^{2-}) column.

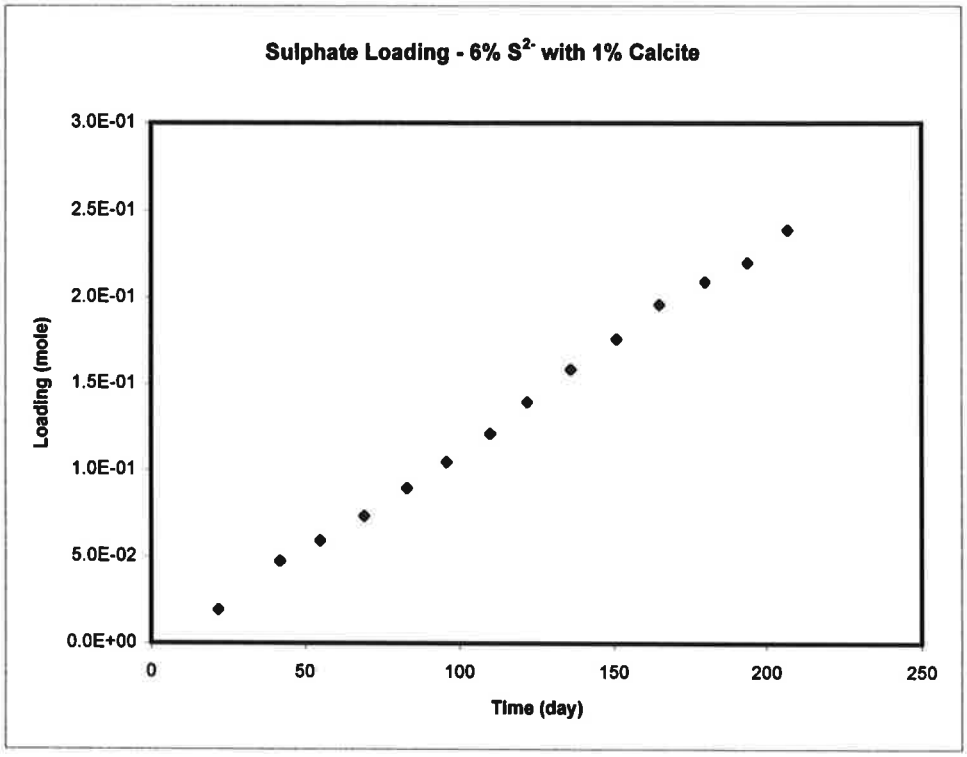

Figure E-30: Sulphate loading of 1 % calcite buffered (6 % S^{2-}) column.

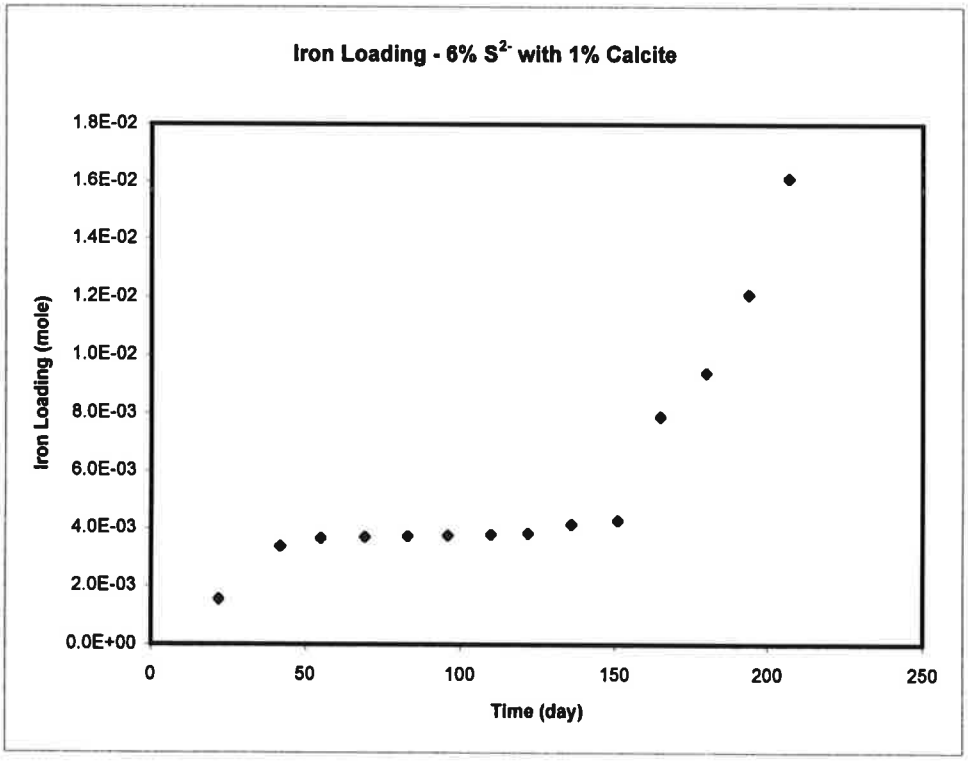

Figure E-31: Iron loading of 1 % calcite buffered (6 % S^{2-}) column.

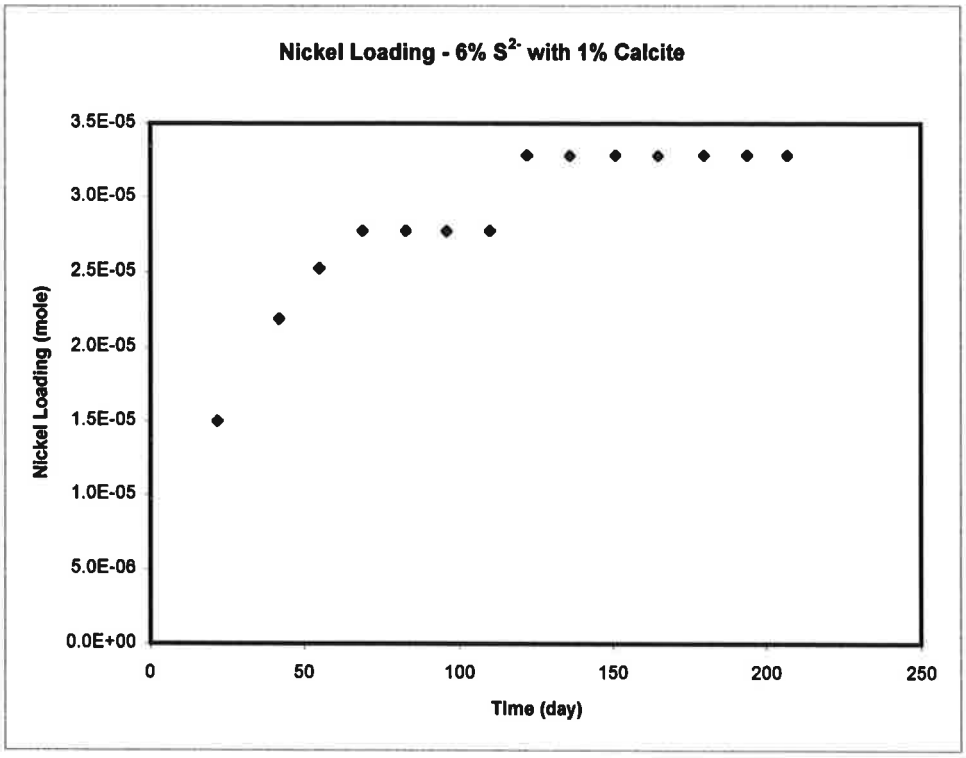

Figure E-32: Nickel loading of 1 % calcite buffered (6 % S^{2-}) column.

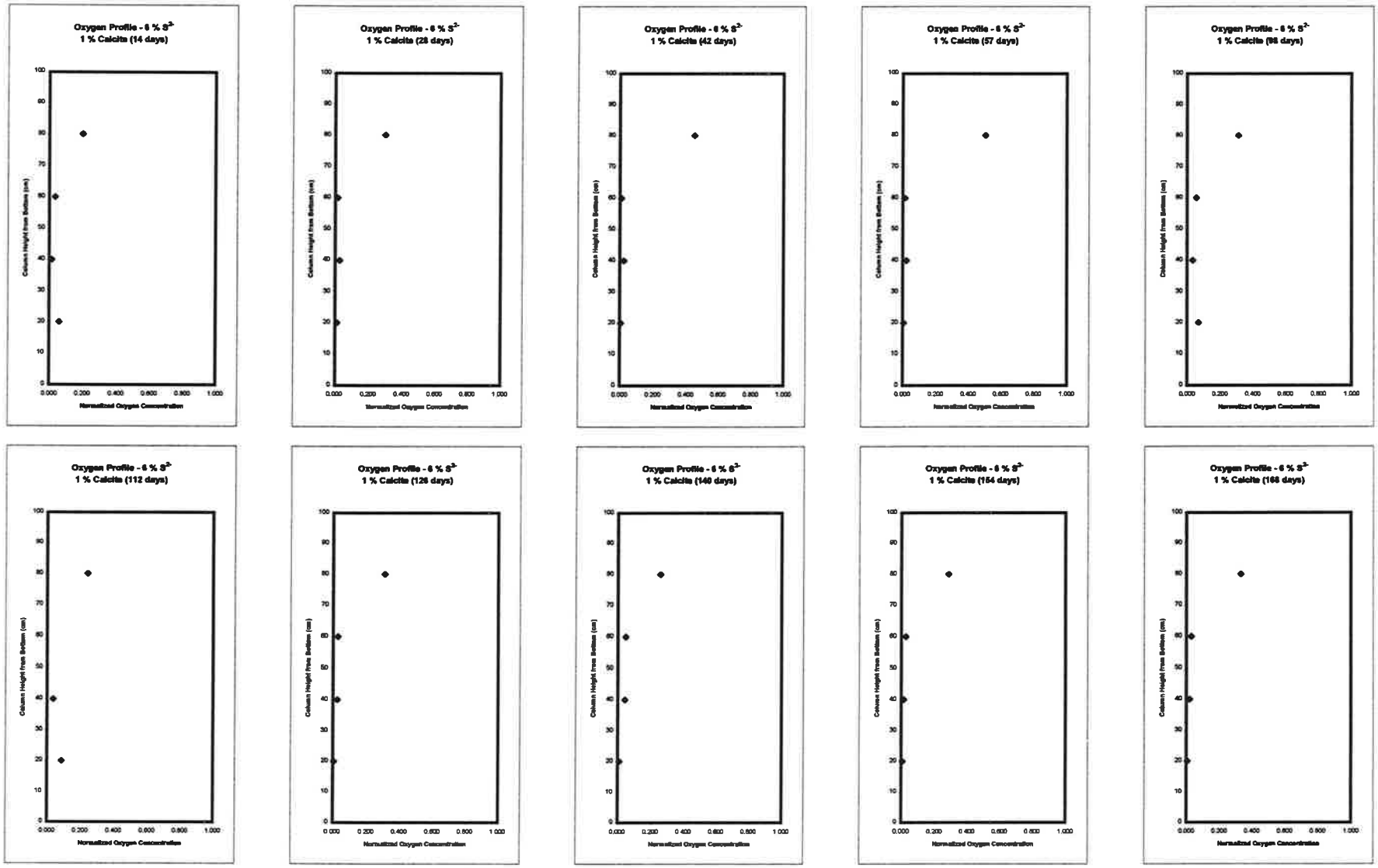

Figure E-33a: Pore space oxygen concentration profiles in the 1 % calcite column.

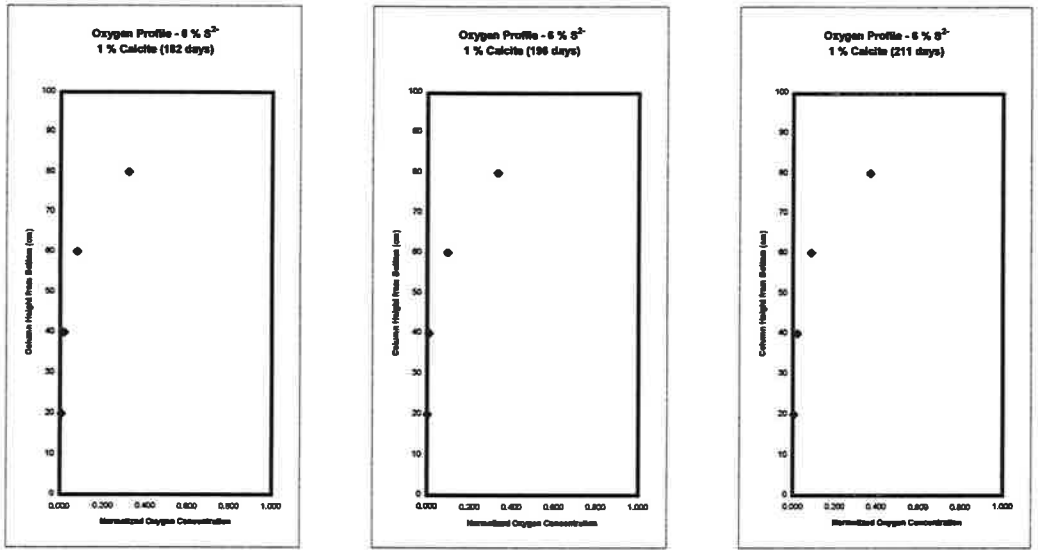

Figure E-33b: Pore space oxygen concentration profiles in the 1 % calcite column.

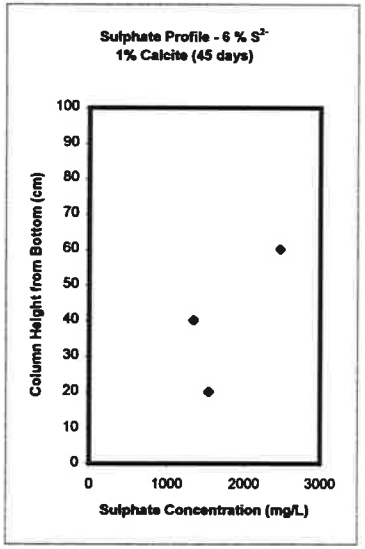

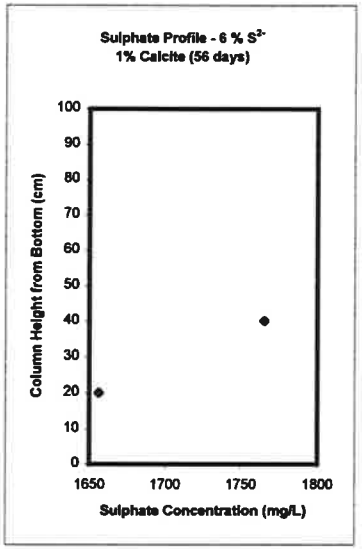

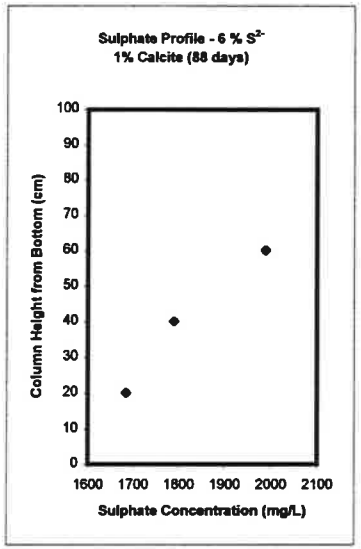

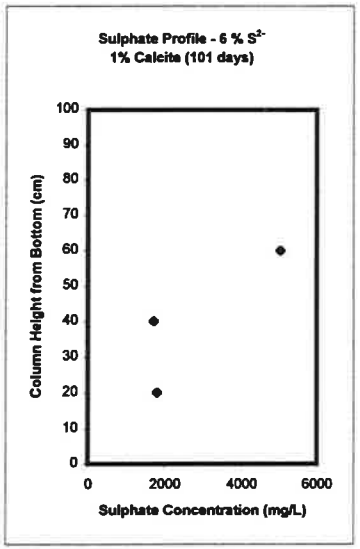

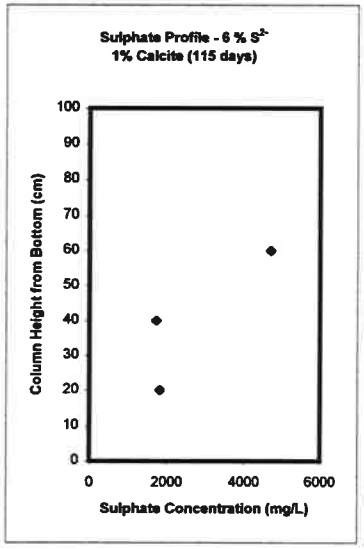

Figure E-34: Porewater sulphate concentration profiles in the 1 % calcite column
(note differences in scales for the sulphate concentration axis)

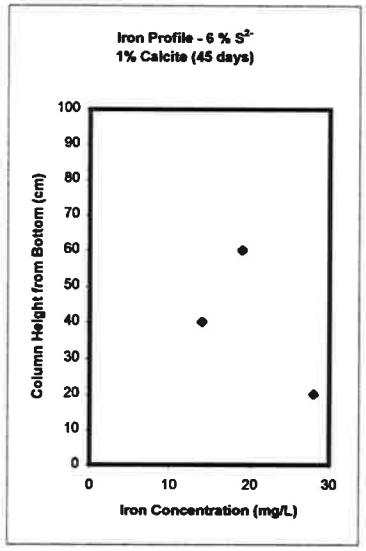

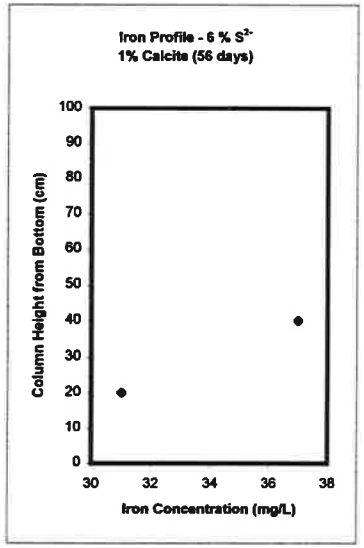

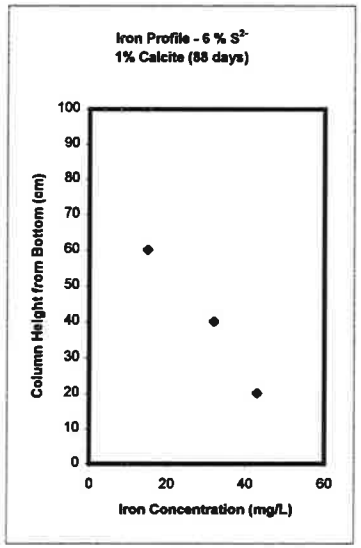

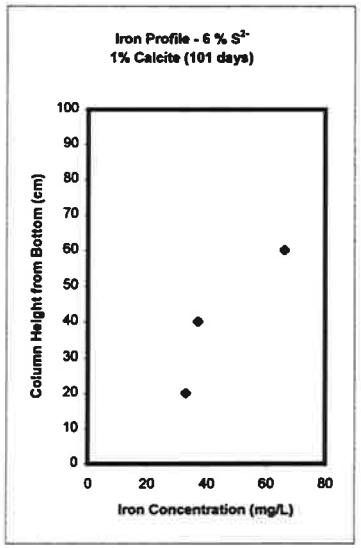

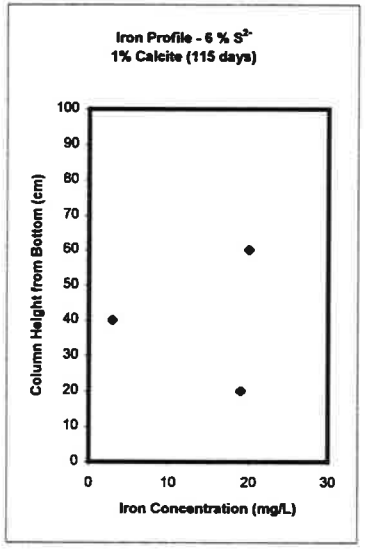

Figure E-35: Porewater iron concentration profiles in the 1 % calcite column
(note differences in scales for the iron concentration axis)

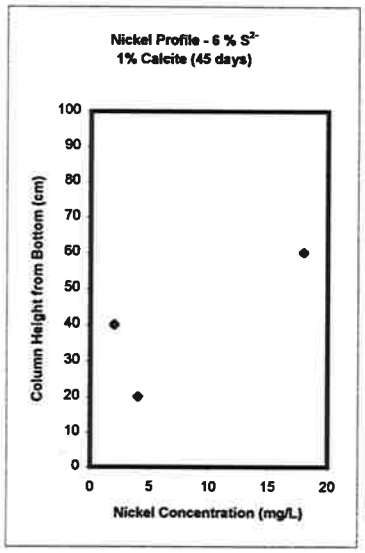

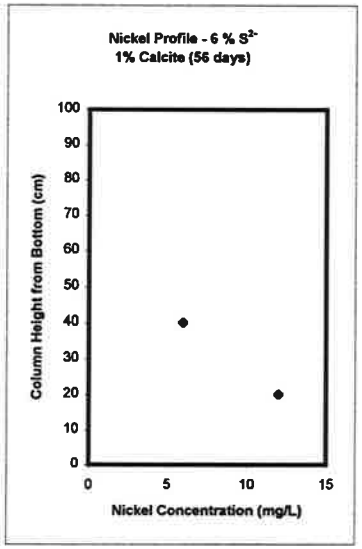

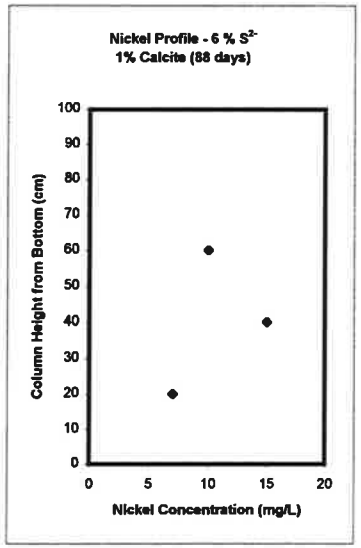

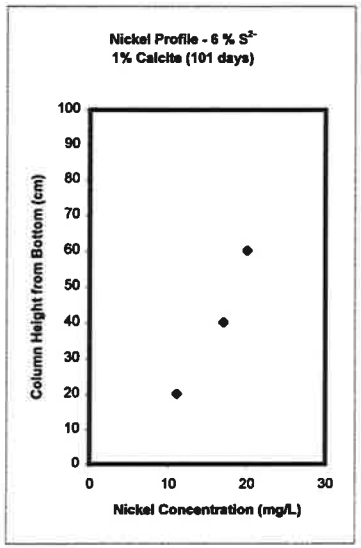

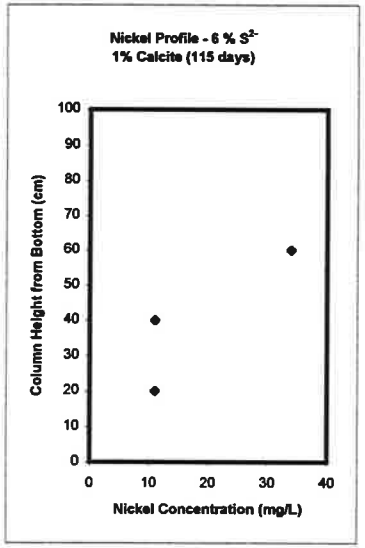

Figure E-36: Porewater nickel concentration profiles in the 1 % calcite column
(note differences in scales for the nickel concentration axis)

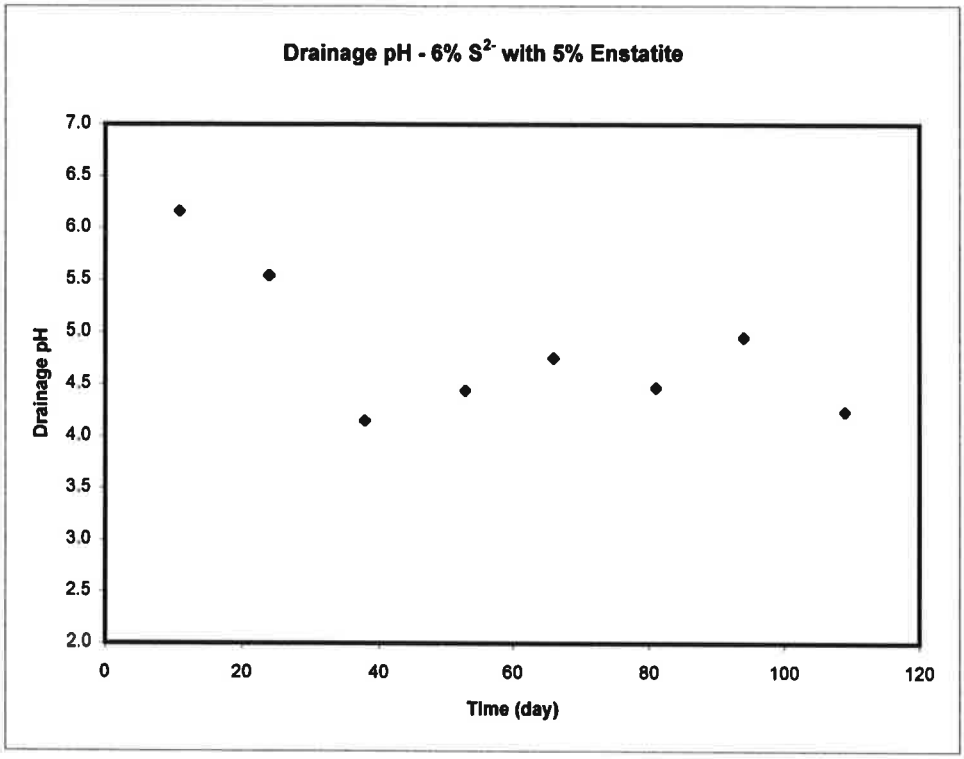

Figure E-37: Drainage pH of 5 % enstatite buffered (6 % S^{2-}) column.

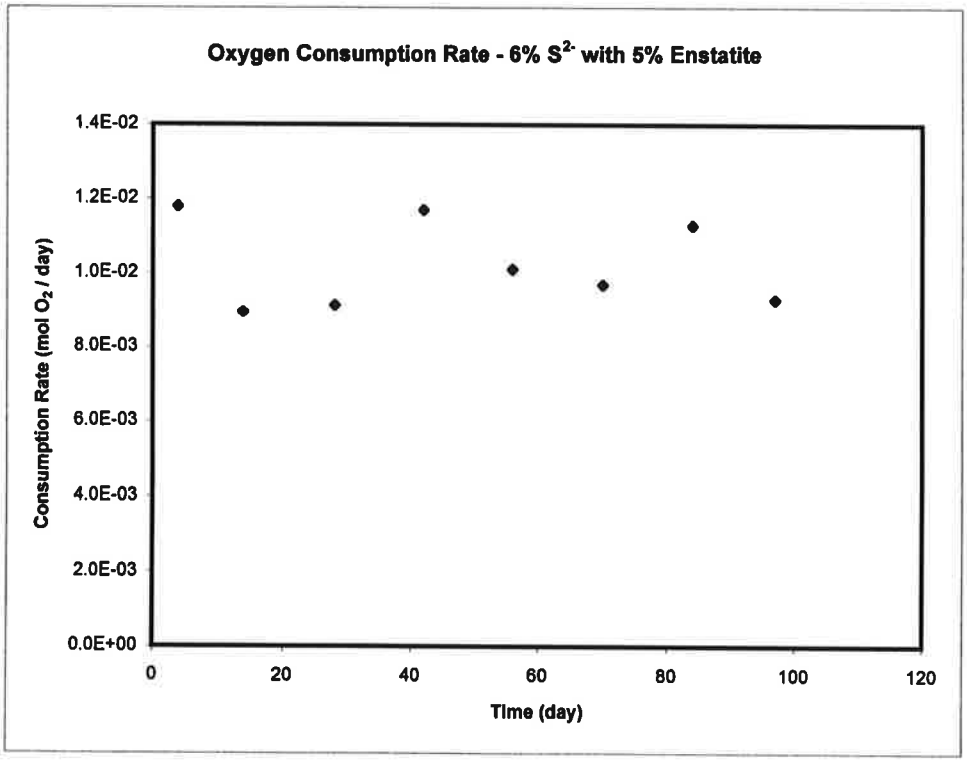

Figure E-38: Oxygen consumption rate of 5 % enstatite buffered (6 % S^{2-}) column

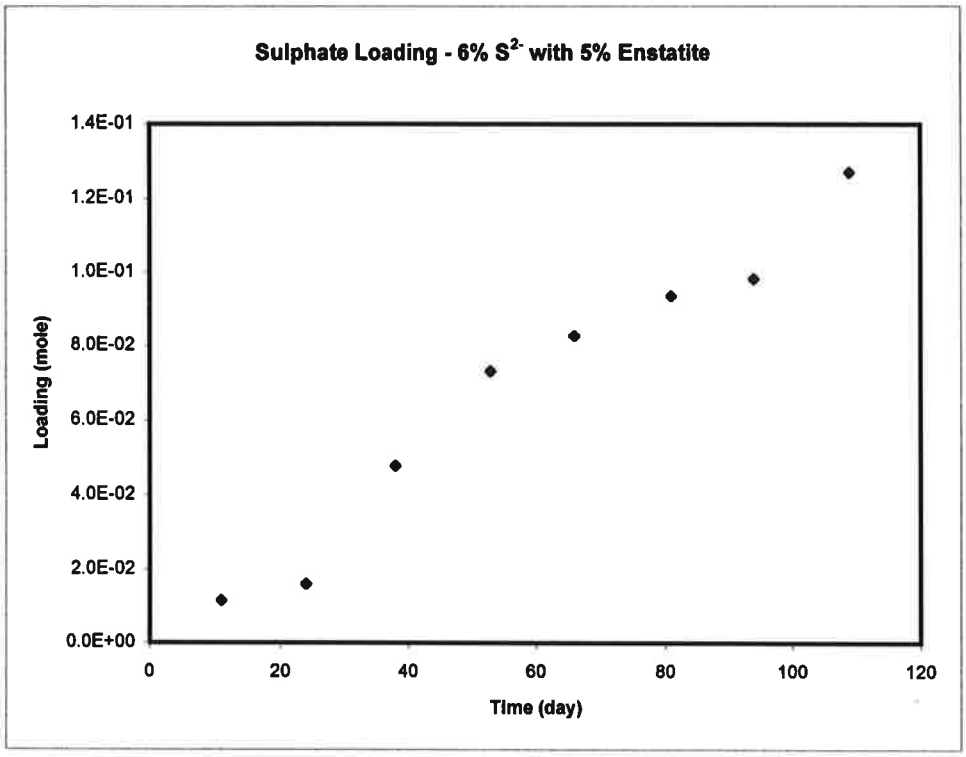

Figure E-39: Sulphate loading of 5 % enstatite buffered (6 % S^{2-}) column.

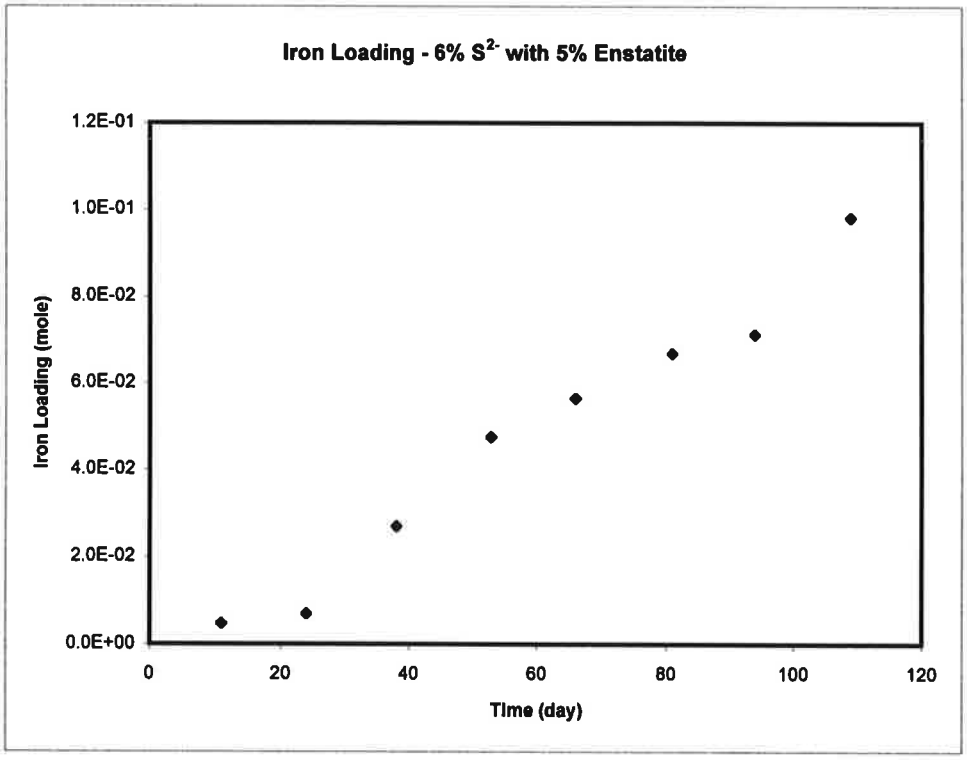

Figure E-40: Iron loading of 5 % enstatite buffered (6 % S^{2-}) column.

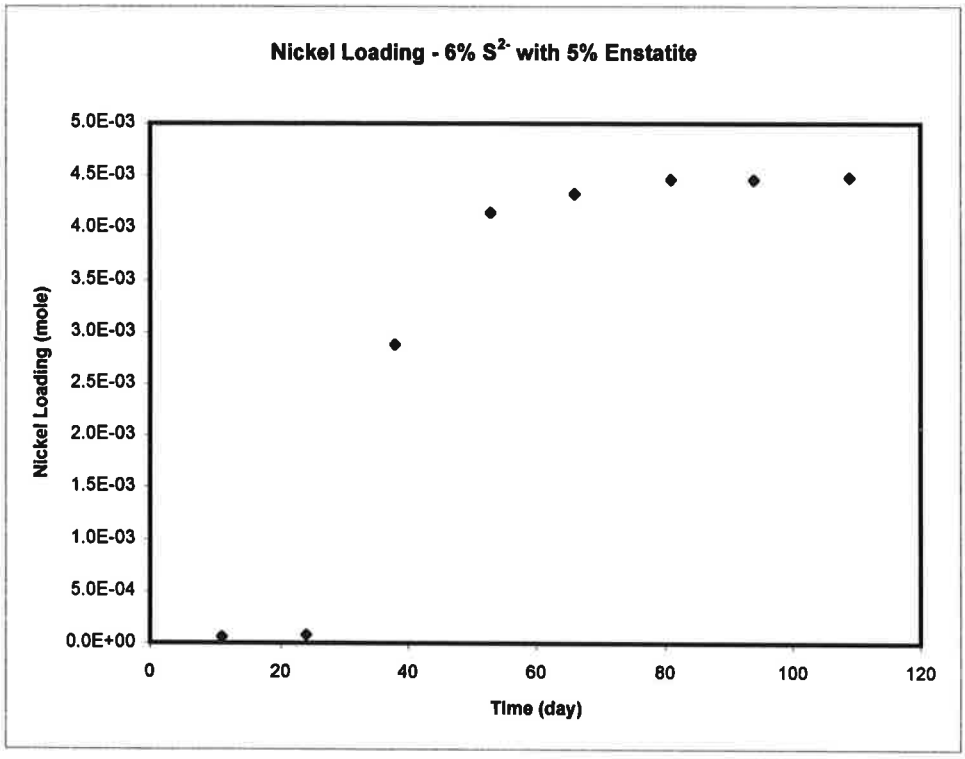

Figure E-41: Nickel loading of 5 % enstatite buffered (6 % S^{2-}) column.

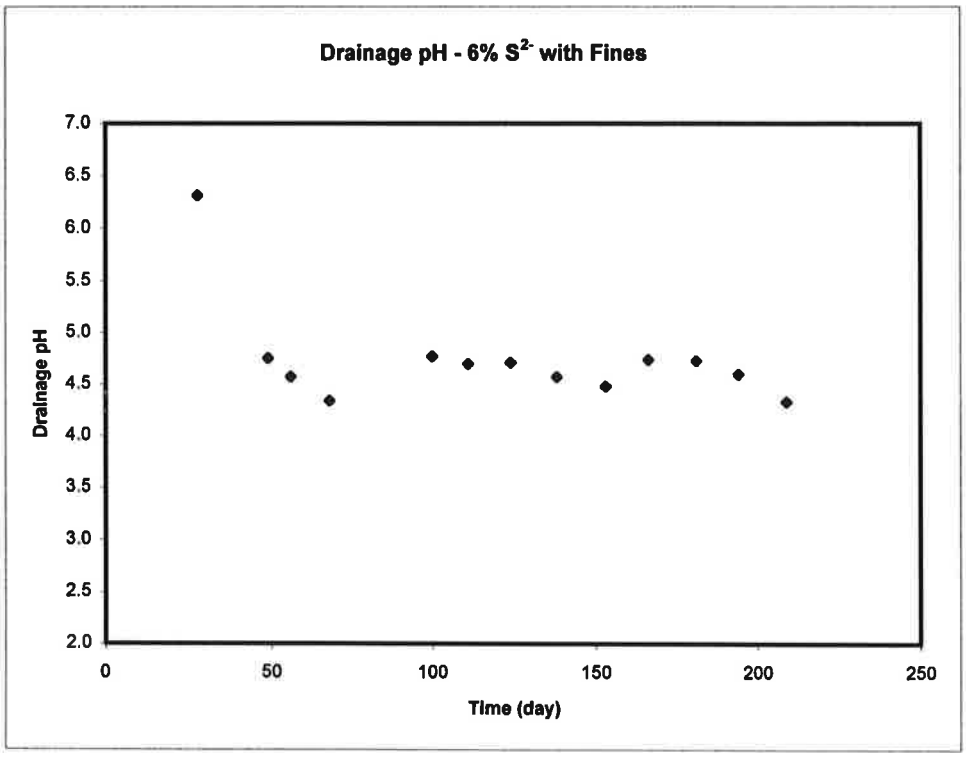

Figure E-43: Drainage pH of (6 % S^{2-}) column with fines.

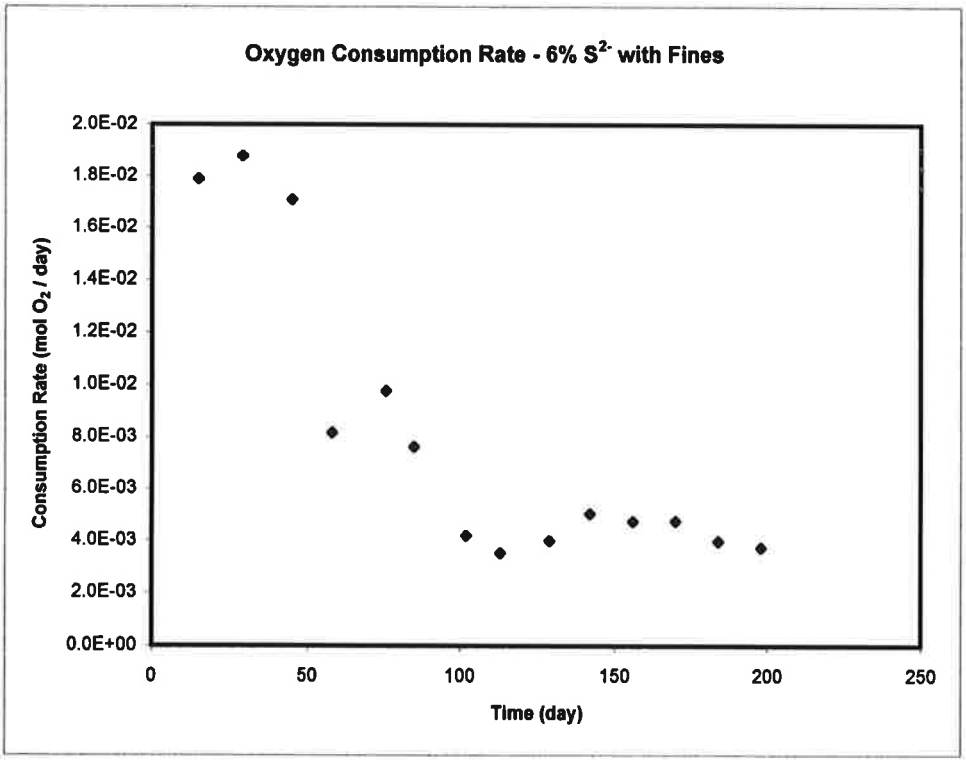

Figure E-44: Oxygen consumption rate of (6 % S^{2-}) column with fines.

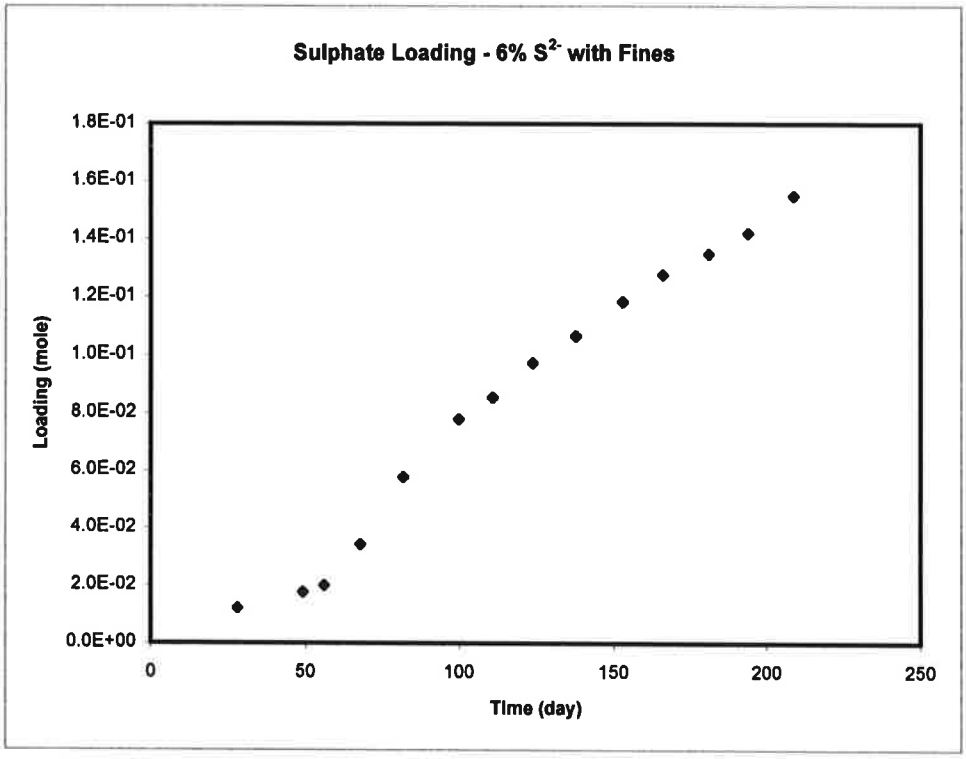

Figure E-45: Sulphate loading of (6 % S^{2-}) column with fines.

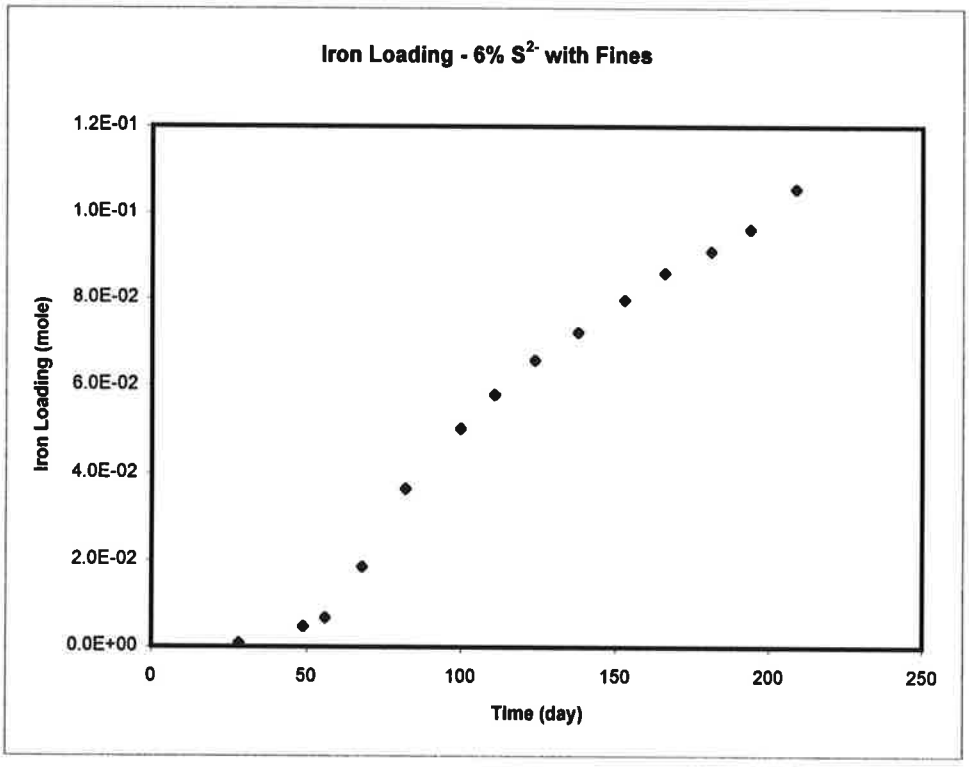

Figure E-46: Iron loading of (6 % S^{2-}) column with fines.

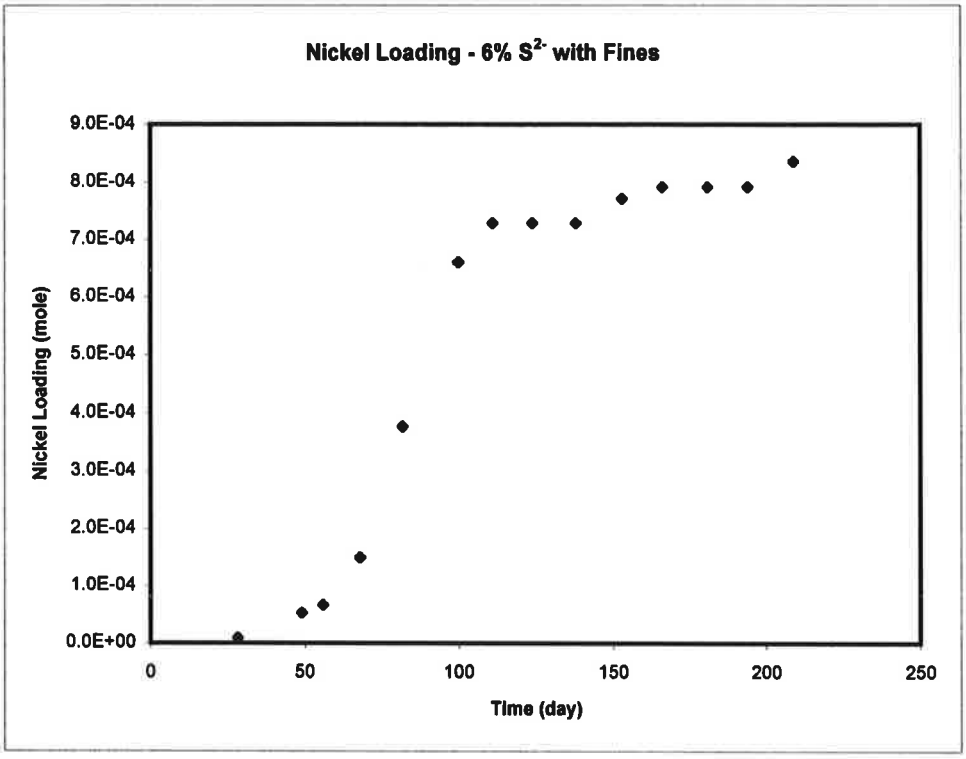

Figure E-47: Nickel loading of (6 % S^{2-}) column with fines.

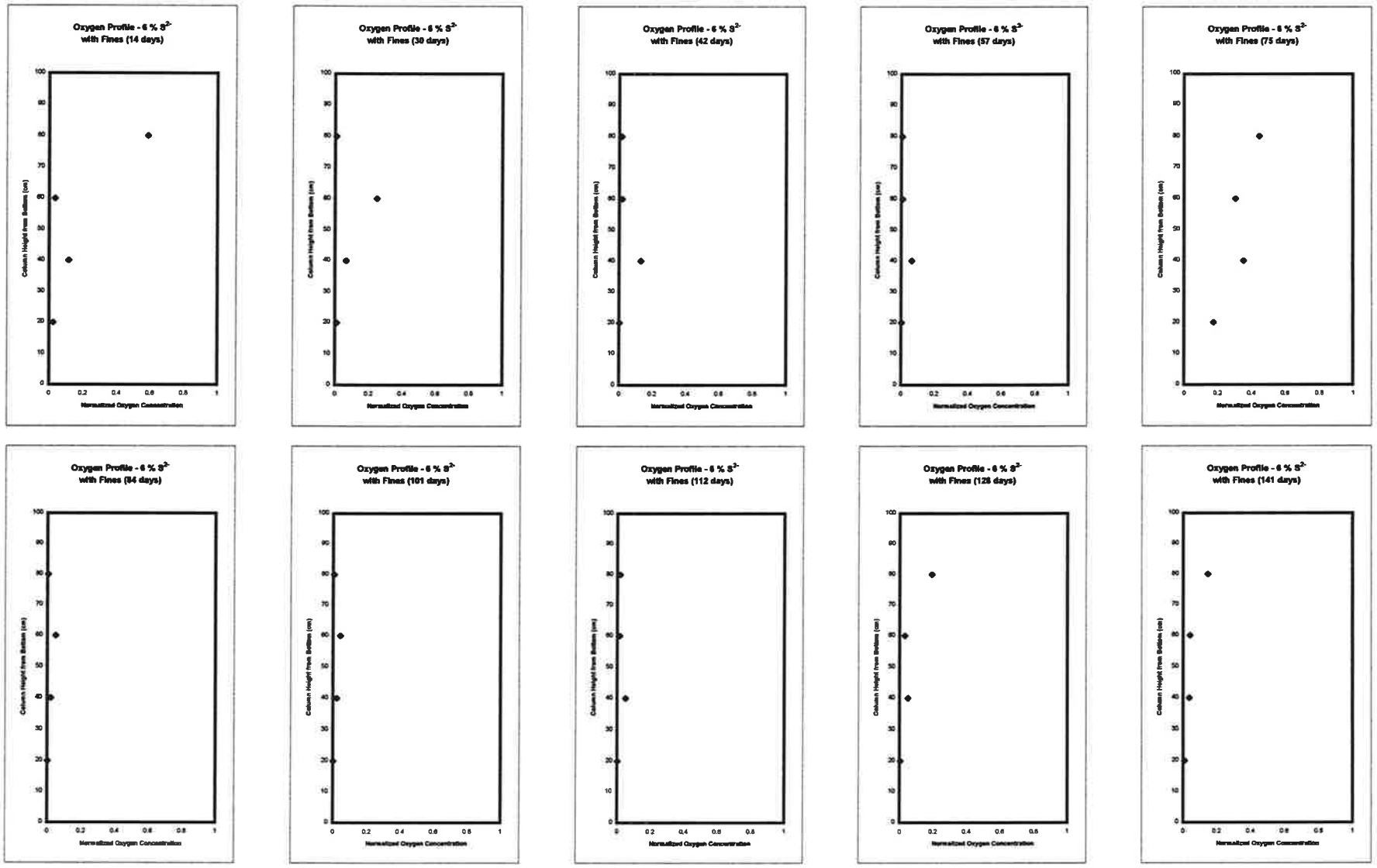

Figure E-48a: Pore space oxygen concentration profiles in the 6 % S^{2-} column with fines.

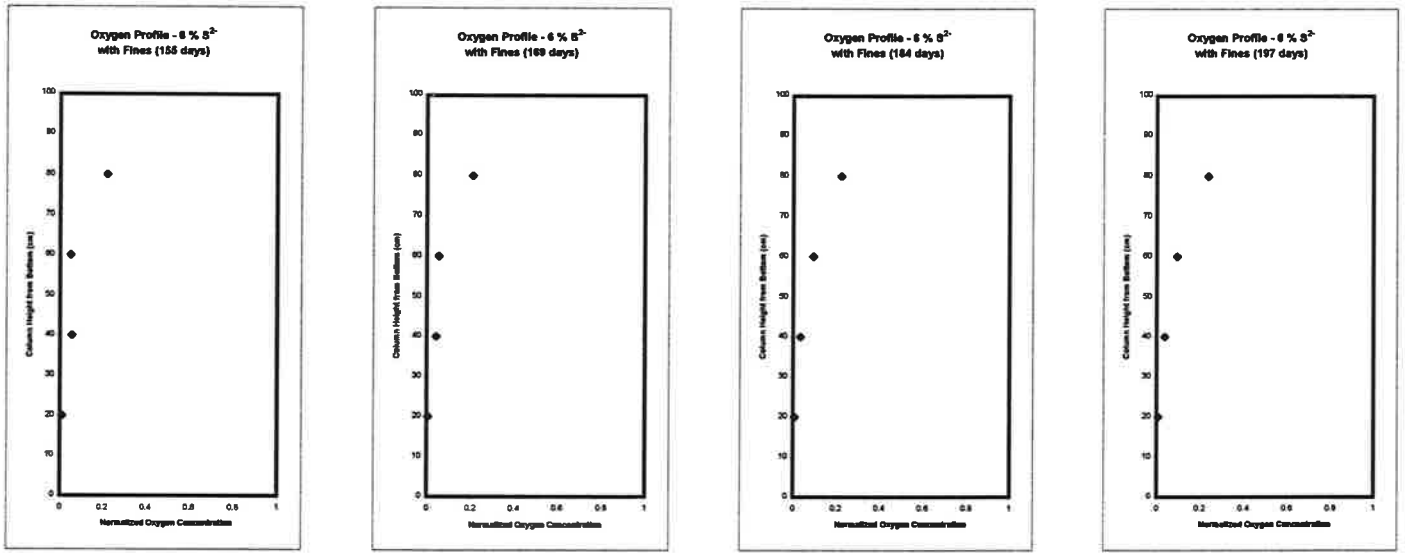

Figure E-48b: Pore space oxygen concentration profiles in the 6 % S^{2-} column with fines.

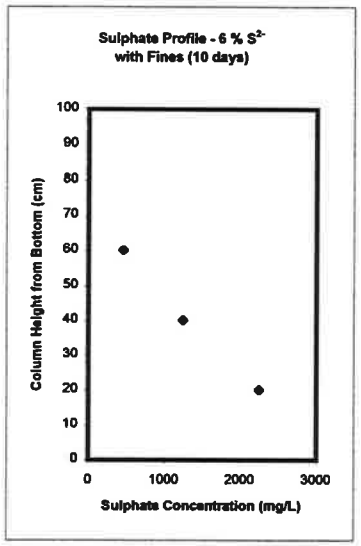

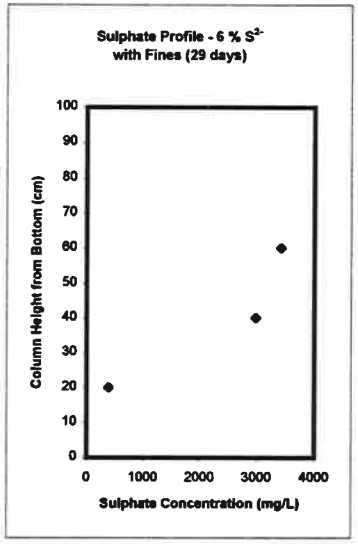

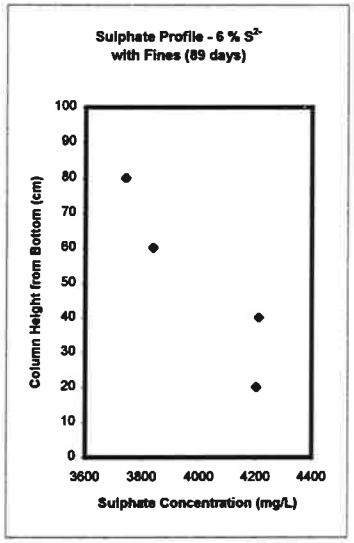

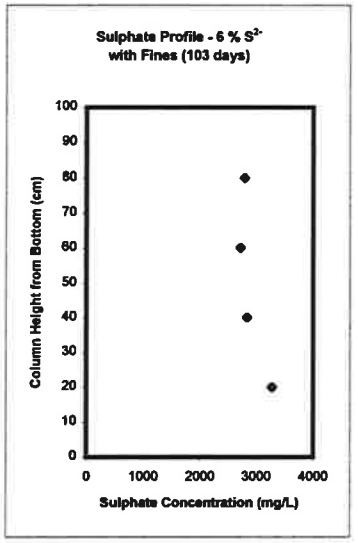

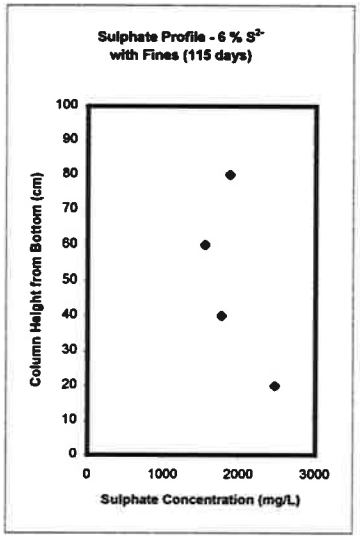

Figure E-49: Porewater sulphate concentration profiles in the 6 % S^{2-} column with fines
(note differences in scales for the sulphate concentration axis)

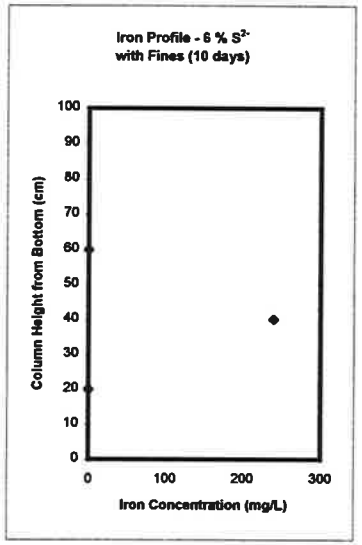

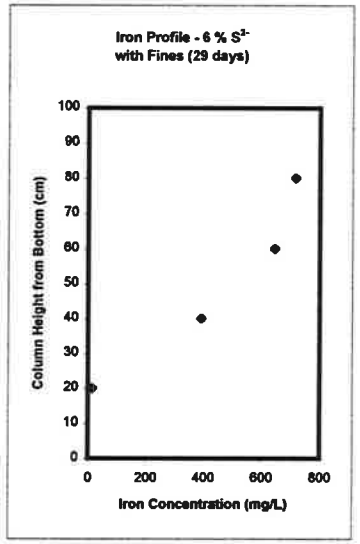

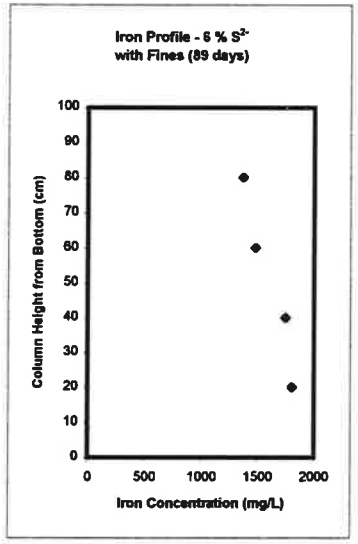

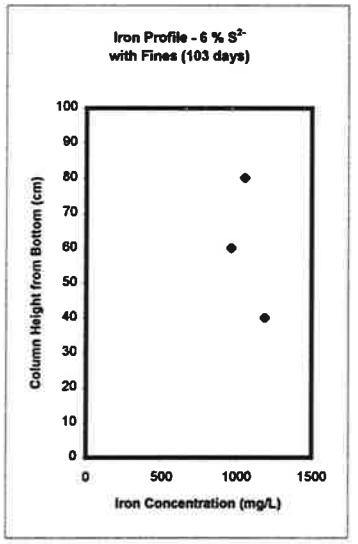

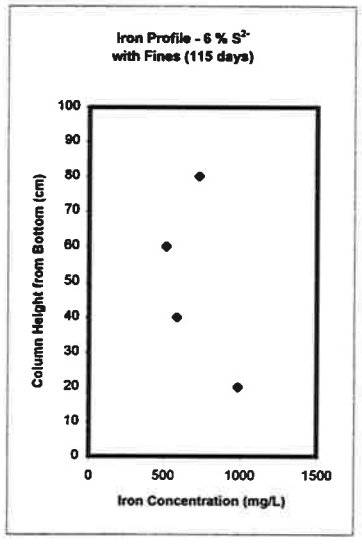

Figure E-50: Porewater iron concentration profiles in the 6 % S^{2-} column with fines
(note differences in scales for the iron concentration axis)

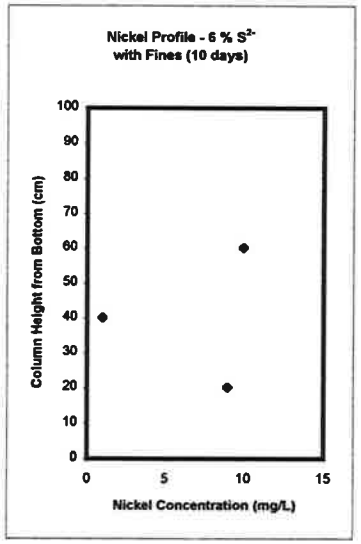

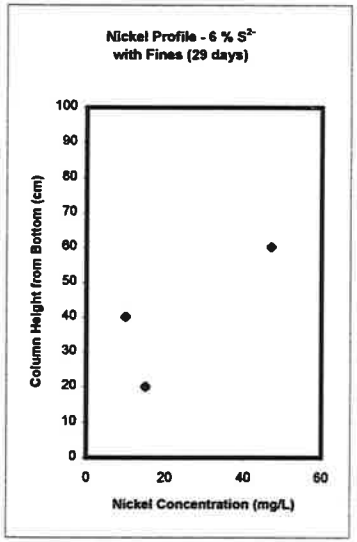

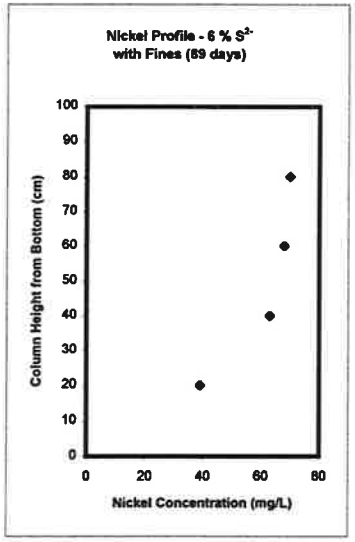

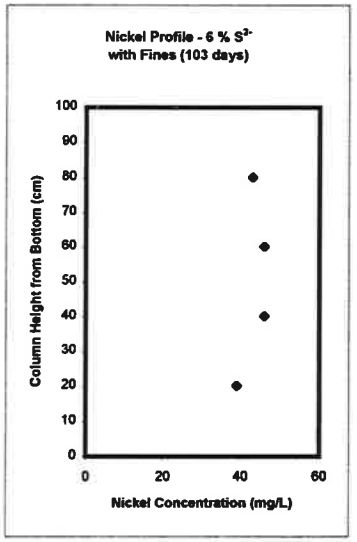

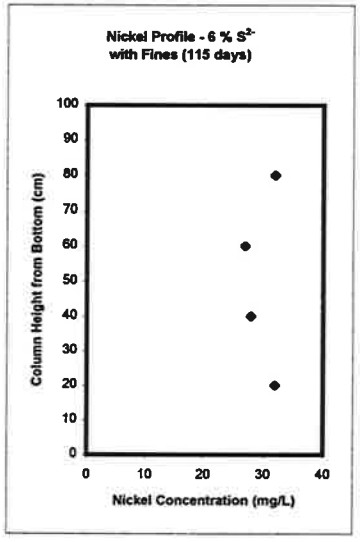

Figure E-51: Porewater nickel concentration profiles in the 6 % S^{2-} column with fines
(note differences in scales for the nickel concentration axis)